THE UNIVERSITY *of* EDINBURGH

Results from the ZEPLIN-III Experiment

Anthony Hollingsworth

A thesis submitted in fulfilment of the requirements
for the degree of Doctor of Philosophy
to the
University of Edinburgh
August 2012

Abstract

The majority of matter in the Universe is dark. World wide efforts to understand this dark component of the Universe are underway and the current evidence suggests the existence of a non-relativistic, non-baryonic and weakly interacting massive particle (WIMP). This weakly interacting dark matter should occasionally couple to baryonic matter, primarily through nuclear interactions. The predicted event rates are low ($< \mathcal{O}(1)$ events/kg/day). The energy deposited is also expected to be low ($\lesssim 50$ keV), and so distinguishing a WIMP signal above the radioactive and cosmic backgrounds is a difficult challenge.

The ZEPLIN–III device was designed to meet this challenge and achieve a competitive sensitivity to WIMP-nucleon interactions. The ZEPLIN–III detector is a two phase time projection chamber using liquid xenon as a target. The instrument was designed to detect dark matter by measuring scintillation and ionisation. Measuring two signals produced by incident radiation allows for discrimination between event types. This allows separation of the main component of the background radiation (primarily electron recoils) from any population of WIMP events that may be present in the data. The ZEPLIN–III detector completed its first science run in 2008, achieving a discrimination power of 1:7800 between nuclear and electron recoils, the highest of any liquid xenon detector. This result limited the WIMP-nucleon cross section to less than 8.4×10^{-8} pb at 90% confidence level (double sided) for a WIMP mass of 55 GeV/c^2.

The ZEPLIN–III detector then entered an upgrade phase. The two main improvements included the installation of a new ultra-low background PMT array, significantly reducing the main source of background events, and the addition of

a veto detector. The veto detector significantly increased the detector's ability to reject WIMP-like background signals, which may be produced by background neutron events. The veto detector also aided background discrimination by detecting 28% of γ-ray events from the fiducial volume of ZEPLIN–III. The second science run of ZEPLIN–III began in June 2010 and continued until May 2011. During the second science run the discrimination power was 1:280 between nuclear and electron recoils. A total of 8 events were observed in the WIMP search region, which is consistent with background expectations. Assuming a null detection allowed the exclusion of the scalar cross-section above 4.8×10^{-8} pb near a WIMP mass of 51 GeV/c^2. This result was combined with the result from a re-analysis of the first science run using more recent results for the relative scintillation yield, $\mathcal{L}_{\mathbf{eff}}$, to give a total limit on the spin independent cross-section of 3.9×10^{-8} pb at 90% confidence near 52 GeV/c^2 WIMP mass for the ZEPLIN–III experiment. The WIMP-neutron spin-dependent cross-section limit is 8.0×10^{-3} pb at 50 GeV/c^2 at 90% confidence for the combined first and second science runs. At the time of publication, these were the world's second best, and best results, respectively.

Declaration

Except where otherwise stated, the research undertaken in this thesis was the unaided work of the author. Where the work was done in collaboration with others, a significant contribution was made by the author.

A. Hollingsworth
May 2011

Acknowledgements

Firstly I would like to thank my supervisor, Dr. Alex Murphy, and my second supervisor, Dr. Chamkaur Ghag. Their support, advice and encouragement have been invaluable throughout my Ph.D.. The guidance I received from them over the last few years has allowed me to complete my Ph.D. and develop the skills I will need in the future. I owe a great deal to both of them.

I would also like to thank all the members of the ZEPLIN–III collaboration. Working in this collaboration has provided me with opportunities to participate in all aspects of producing a science result in experimental physics, from building and running a detector to interpreting the data. In particular I would like to thank Henrique Araùjo for all the useful advice and for driving the ZEPLIN–III project forward with such enthusiasm and determination. I would like to thank Francisco Neves for teaching me how to program properly! I would also like to thank Sean Pailing for all his help in the laboratory. My experience with the ZEPLIN–III collaboration has been both a valuable learning experience and a lot of fun. I'm very thankful for all the fond memories I have of my time with this collaboration.

The fellow members of the ZEPLIN–III team at Edinburgh also deserve special mention; Emma for patiently listening to all my attempts to explain my problems and Paul and Lea for their valuable advice (some of which was even related to physics). I would also like to acknowledge all of my office mates at the University of Edinburgh; their antics have helped me keep my sanity throughout my Ph.D. I would also like to thank Pauline, Ailsa and Ben for ensuring that I experienced the widest possible range of hangover types throughout my time at Edinburgh.

The funding for my Ph.D., along with the experiment, was provided by the STFC and I am grateful for their support. I would like to acknowledge the the Scottish government for their provision of the RTSG grant which allowed me to attend conferences throughout my Ph.D.. I would like to thank Cleveland Potash Ltd for the use of their mine for our low background laboratory. The University of Edinburgh has provided me with an excellent environment to complete my Ph.D.. I would like to acknowledge some of the staff at the university in particular; I would like to thank Jane Patterson for her help, along with that of my supervisor Alex Murphy, in providing me with a 2 month interruption after my motorbike accident. I would also like to thank Martin Evans for securing me an extra months funding to cover the same incident. Their help was invaluable in ensuring I was able to complete my studies without any problems due to the time it took for me to recover fully. I would also like to thank Fiona McNaughton for her assistance in processing my expenses, her help ensured I never went bankrupt throughout my Ph.D..

Contents

List of Figures

List of Tables

Chapter 1

Introduction

1.1 The Dark Matter Problem

Since the early 1930's evidence for dark matter has been accumulating. The missing matter problem began with measurements showing that galaxies in clusters experience much stronger accelerating forces than can be produced by the gravity of the luminous matter observed within them. Since this initial observation many new studies, from observing gravitational effects to comparing cosmic density measurements to big bang nucleosynthesis models, show that the matter we can see is only a small fraction of the matter in the Universe. The current cosmological model, known as the ΛCDM model, attributes only $\sim 4.6\%$ of the energy density of the Universe to baryonic matter. 23% is attributed to cold dark matter (CDM) and 72% is dark energy (Λ), see [311, 372] and references therein.

Grand Unified Theory (GUT) predicts that the three gauge interactions of the standard model of particle physics should merge at some energy scale into a single interaction characterised by a larger gauge symmetry and a single coupling constant. Experimental results indicate that the Higgs mass should be far below this energy scale [1]. This leads to a hierarchy problem where seemingly unnatural fine tuning would be required to explain the different strengths of the fundamental forces at lower energy scales. A possible solution to this problem is supersymmetry (SUSY). This theory postulates that all elementary particles have a supersymmetric partner, so they are the same apart from a half unit of

spin. However since these superpartners have not yet been observed SUSY would be a broken symmetry as the supersymmetric partners must be heavier than their standard model partners. If SUSY exists then it may also provide an excellent dark matter candidate particle. To conserve a supersymmetric quantum number known as R-parity the lightest supersymmetric particle (LSP) would be stable, massive and weakly interacting [232]. This theoretical particle fits the bill quite well for a dark matter particle needed to explain astronomical observations and so is strongly favoured. Chapters 2 and 3 detail the evidence for dark matter and possible methods of detection.

1.2 Thesis Outline

The ZEPLIN–III collaboration consists of five institutions located in three countries. In the United Kingdom there are the Rutherford Appleton Laboratory, the University of Edinburgh and Imperial College London. In Portugal there is O Laboratório de Instrumentacão e Fìsica Experimental de Artìculas (LIP-Coimbra) and in Russia there is the Alikhanov Institute for Theoretical and Experimental Physics (ITEP Moscow). The ZEPLIN–III collaboration constructed and successfully operated the ZEPLIN–III dark matter detector between February 2008 and May 2011. ZEPLIN–III is a two phase time projection chamber designed to detect dark matter interactions using liquid xenon as a target. It operated at the Palmer underground laboratory in the Boulby mine, UK, between February 2008 and May 2008 during its first science run. Then following an upgrade it operated from June 2010 to May 2011 for its second science run. Details of the detector are given in Chapter 4. The ZEPLIN–III veto detector was provided by the University of Edinburgh and ITEP Moscow, details of the commissioning of this detector are given in Chapter 5. The performance of this detector is assessed in Chapter 6. During its second science run the veto operated in conjunction with ZEPLIN–III. The operation and results of the second science run are detailed in Chapter 7.

The ZEPLIN–III collaboration is relatively small and so this provided a situation where I was able to be involved in many different aspects of achieving the collaborations science goals. I was heavily involved in the commissioning

and upgrading of the instrument and the design, construction and commissioning of its shielding, as well as the daily operation of both detectors, data analysis and calibration. As my institute was responsible for supplying the veto detector I was heavily involved in all aspects of this detector. This included taking a leading role in the veto operation and data analysis (both producing the software required for the veto and performing the analysis). My lead role in the veto data analysis also allowed me to identify other uses for the veto data such as identifying contaminations, as detailed in Chapter 7, searching for exotic forms of dark matter, as detailed in Section 6.6 and also investigating muons, detailed in Section 6.5. Identifying and measuring contaminations included obtaining a measurement of the ^{85}Kr contamination of the xenon. This isotope is a potentially dangerous threat to the sensitivity of the instrument and this measurement shows that the purity achieved in the ZEPLIN–III target allowed the instrument to reach its target sensitivity.

To summarise my main achievements; I wrote the veto analysis and reduction software, I assembled the instrument for the science run, I calibrated the veto, I was responsible for the veto data and performed the reductions and much of the analysis, I identified new analyses which utilised the veto and I contributed to data analysis which produced the final result of the ZEPLIN–III experiment.

Chapter 2

A Review of Cosmology

2.1 Introduction

The first observations indicating that the Universe contained significant dark components came in the early 30s when Fritz Zwicky published velocity measurements of galaxies within the Coma cluster [390]. These observations showed that the mass present within the cluster was far in excess of the mass of all the luminous matter. Since this initial observation of missing matter there have been many complementary observations which also point to a large fraction of the mass of the Universe being both non-luminous and non-baryonic. This chapter describes the current state of cosmology, the evidence for dark matter and possible solutions to the dark matter problem.

2.2 Modern Cosmology

The currently favoured cosmological model, known as the ΛCDM model, is very successful at describing our observations of the Universe. The key principles underpinning this theory are the hot big bang and the cosmological principle. In this model the Universe is composed of two main components, both of which are dark. These components are dark energy, denoted by Λ, and dark matter, denoted by CDM. The C is for 'cold' which refers to the kinetic energy of the dark matter particles in relation to their mass so that $m_\chi c^2 \gg \frac{p_\chi^2}{2m_\chi}$ and the particles have non-relativistic velocities at the time of decoupling.

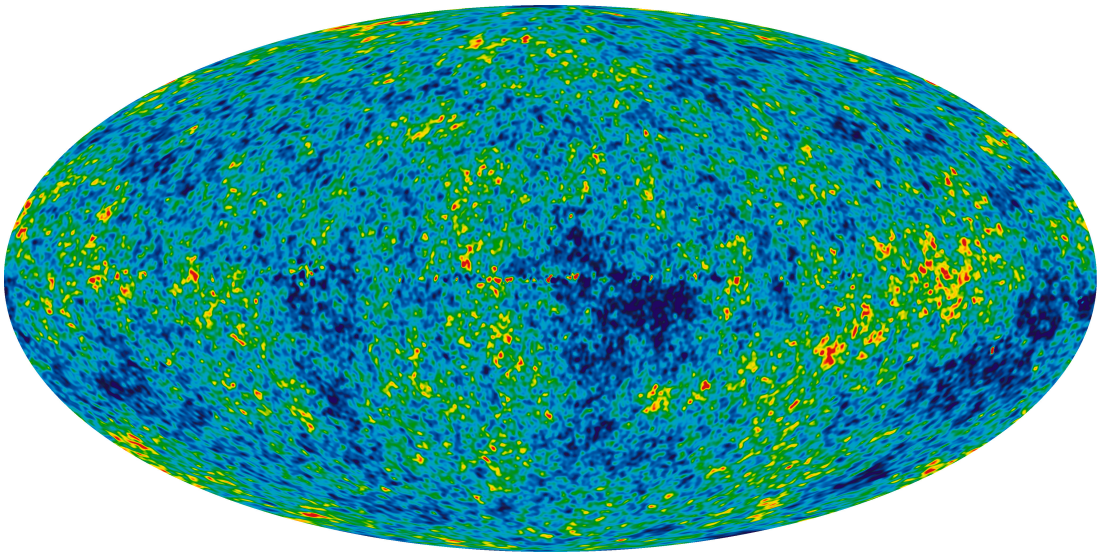

Figure 2.1: The seven year WMAP primary temperature anisotropies data shown in galactic co-ordinates centred on the center of the Milky Way. The range of temperature covered by the colour map is $\pm 200\mu$K with red representing hot areas and blue representing cold areas [231].

The cosmological principle states that the Universe should have no preferred directions or places, i.e. it should be isotropic and homogeneous. Although this seems incorrect on the small scales inhabited by people, and even up to larger scales observed in the early part of the 20$^{\text{th}}$ century, once scales above $\sim$100 Mpc are considered both of these principles can generally be seen in the structure of the Universe. The hot big bang theory states that the Universe as we know it has expanded from an ancient singularity. The most compelling piece of evidence for both the cosmological principle and the hot big bang is the evidence from the Wilkinson Microwave Anisotropy Probe (WMAP) which shows the black body radiation emitted during a much earlier period of the Universe, just after it first became transparent after having cooled enough to allow neutral atoms to form. The microwave background, observed by WMAP [231], shows that the density of the early Universe is very close to uniform, as discussed in Section 2.3.3 and shown in Figure 2.1.

In the mid 20$^{\text{th}}$ century the biggest debate in cosmology was the nature of the Universe's evolution; was it in a steady state or did it change over time? In the late 20's Edwin Hubble measured the red shifts of galaxies and found that, on average, extra-galactic objects were moving away from us [224]. The relation

between recession velocity and distance is called Hubble's law and this effect is causing the expansion of the Universe. This was a key piece of evidence for an evolving Universe and it is an important piece of evidence for the big bang theory. This law states that the recession velocity of distant objects depends on the distance to those objects as the space in-between them is expanding:

$$\vec{v} = H_0 \vec{r} \tag{2.1}$$

where $\vec{v}$ is the recession velocity, $\vec{r}$ is the distance to the object and H_0 is the Hubble parameter defining the rate of expansion of space. This is often written as a function of the dimensionless parameter, h_0, defined as:

$$H_0 = h_0 \times 100 \text{ km}^{-1}\text{s}^{-1}\text{Mpc}. \tag{2.2}$$

Recent observations of Cepheid variables and Type 1a supernovae (SNIa) [313] puts the value at:

$$h_0 = 0.738 \pm 0.024 \tag{2.3}$$

using a simultaneous fit to all Cepheid and SNIa data. This relation suggests that further back into the past points in space within the Universe were much closer together. A fit to just SNIa data is shown in Figure 2.2, showing the relation between distance and recession velocity caused by the expansion of the Universe. The evidence showing an expanding Universe eventually lead to the big bang theory [35] suggesting that at the beginning of time the Universe we now inhabit expanded from a singularity on the Planck length scale.

Another key piece of evidence for this theory came in 1965 with the discovery of the cosmic microwave background (CMB) [297]. This radiation is thought to be an after-glow of the hot big bang, more details of which are given in Section 2.3.3. As the Universe expanded, it cooled, this cooling effect allowed particles, and eventually neutral atoms, to 'freeze out'. This effect is defined by the thermal energy of the Universe. In the very early Universe the thermal energy was high enough to provide enough energy for pair production of all particles, but as the Universe expanded the available thermal energy dropped. Once the thermal energy dropped below the energy threshold for pair production of a particle species, thermal production ceased and the particle freezes out

(see Section 2.2.1.3). This early environment did not allow the transmission of electromagnetic radiation as the optical path length was very small. Due to this, the early Universe was almost a perfect black body radiator. Once the Universe had expanded enough to allow enough of the tail of the distribution of the thermal energy to drop below the ionisation energy of hydrogen then free electrons were captured by protons to form neutral hydrogen atoms, which is known as the recombination epoch. This happened about 380,000 years after the big bang, as depicted in Figure 2.3, and after this time the Universe became transparent as the optical path length dramatically increased due to the drop in free-free scattering. This is referred to as photon decoupling as photons are no longer continually scattered by free electrons.

Once the Universe became transparent all the thermal radiation was released as a black body spectrum, so the thermal spectrum's peak was determined only by its temperature as $\lambda \propto \frac{1}{T}$. As radiation from this last scattering surface at the 380,000 year horizon reaches Earth we can see this afterglow (but no further with electromagnetic radiation). This radiation was red shifted whilst it travelled through expanding space towards the Earth. The 0.4 ionisation fraction, the accepted point of the release of the CMB, corresponding to a temperature of $\sim$4000 K gives a redshift of $\sim$1500, given that the temperature can be calculated by $T = 2.72548(1 + z)$.

The observation of the cosmic microwave background is the strongest piece of evidence supporting the theory of the hot big bang. The peak wavelength corresponds to a temperature of 2.72548 ± 0.00057 K [179]. The radiation spectrum currently incident on Earth from the period of photon decoupling peaks in the microwave region, as shown in Figure 2.4. This snap shot of the early Universe provides an excellent tool for determining the contents of the Universe; more discussion of how this reveals the dark matter content is contained within Section 2.3.3. A parameter vital to the cosmological model is the age of the Universe, this too can be derived from CMB observations, as discussed in Section A.1.

Another development in physics in the early part of the 20^{th} century was the

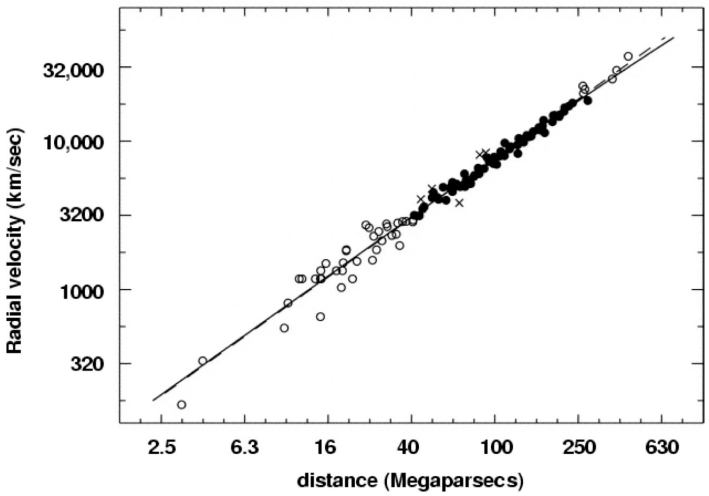

Figure 2.2: A plot showing the relation between recession velocity and distance caused by the expansion of the Universe. The proper motion of the objects means that this relation will always show some spread about the true value, the proportion of this decreases with distance however the accuracy with which distance can be determined also has a tendency to decrease with increasing distance. The fit line assumes $\Omega_m = 0.3$ and $\Omega_\Lambda = 0.7$, the dashed line assumes a matter dominated Universe. Adapted from [310].

theory of General Relativity [158, 159]. The brief review presented was written with the aid of general relativity course notes [205]. General relativity describes how the curvature of space-time, expressed by the Einstein tensor $G_{\mu\nu}$ (given by equation A.7), is defined by the mass contained within it which is described by the stress-energy-momentum tensor $T_{\mu\nu}$. The gravitational field equations can be written as:

$$R_{\mu\nu} - \frac{1}{2} g_{\mu\nu} R + \Lambda g_{\mu\nu} = \frac{8\pi G}{c^4} T_{\mu\nu} \tag{2.4}$$

where G is the gravitational constant, c is the speed of light in a vacuum, $R_{\mu\nu}$ is the Ricci curvature tensor (representing the difference in volume element between curved Riemannian space and flat Euclidean space), R is the Ricci scalar (representing the curvature of the Riemannian space), $g_{\mu\nu}$ is the space-time metric and Λ is the cosmological constant. The cosmological constant was originally set to zero, however with the discovery of the accelerating expansion of the Universe in 1998 this constant has now been equated to dark energy [312]. This value is the equivalent of an energy density of the vacuum and acts like a negative pressure accelerating the expansion rate of the Universe. Equation 2.4 can be rewritten

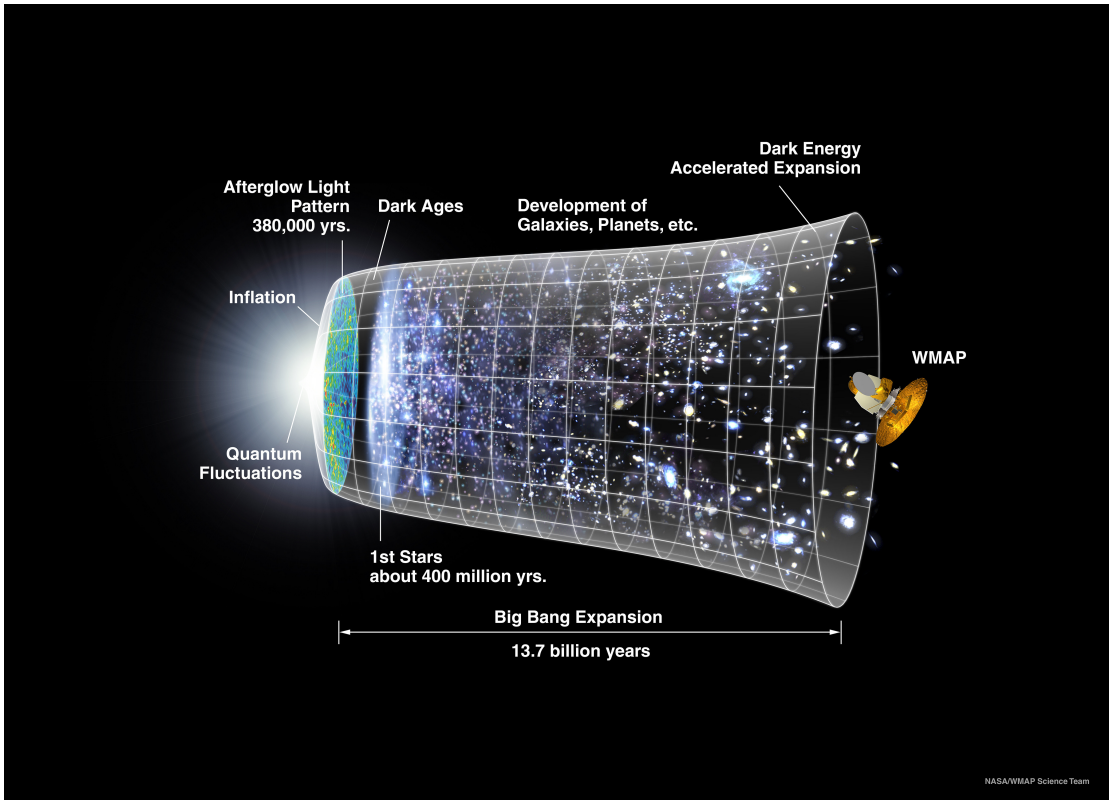

Figure 2.3: The expansion of the Universe depicted as a function of its age. The different epochs of the Universe are indicated, begging with the big bang then followed by a period of inflation which seeded large scale structure via quantum density fluctuations. This is followed by recombination before which the Universe was opaque. Image obtained from the WMAP website [284].

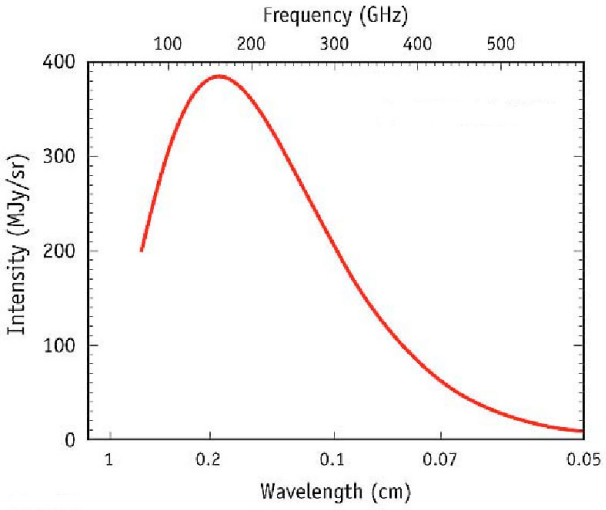

Figure 2.4: The cosmic microwave background spectrum. This is a blackbody spectrum whose peak is defined by the temperature of the black body radiator. The position of the peak indicates the current temperature of the Universe. Image obtained from the WMAP website [284].

as:

$$G_{\mu\nu} + \Lambda g_{\mu\nu} = \frac{8\pi G}{c^4} T_{\mu\nu} \tag{2.5}$$

by defining the Einstein tensor as:

$$G_{\mu\nu} = R_{\mu\nu} - \frac{1}{2} g_{\mu\nu} R. \tag{2.6}$$

In Equation 2.4 the Ricci tensor and Ricci scalar are contractions of the general Riemann curvature tensor, described in Section A.2.

General relativity was first tested in 1915 where it is was used to explain the precession of perihelion of the planet Mercury. This is observed at 574.10 ± 0.69 arcseconds per century [123] which can be explained by the addition of 531.63 ± 0.69 arcseconds per century from gravitational interactions with other planets plus 0.0254 arcseconds per century from the oblateness of the Sun. The missing component is attributed to the curvature of space-time as described by general relativity. This is calculated as 42.98 ± 0.04 arcseconds per century [90] and explains the observed precession. General relativity is a key tool used in modern cosmology and indeed much of the evidence for the existence of dark matter relies on our understanding of gravity. Its description of how matter bends space-time

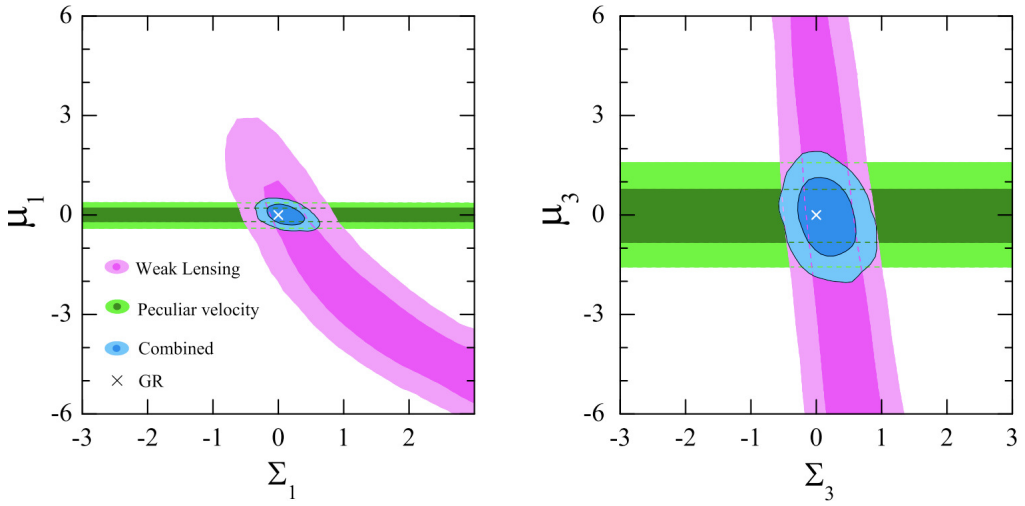

Figure 2.5: Combining results from weak lensing surveys with peculiar velocity measurements allows the comparison of gravitational bending of space and time. The origin in this plot represents gravity having an equal effects on each [338].

is key to mapping the dark matter of the Universe. The description does not distinguish between the bending of space and time and so these are expected to be equivalent. Survey data can be used to measure this and shows that this is indeed the case, as shown in Figure 2.5 [338].

For an isotropic and homogeneous expanding Universe, the distance between any two points at a given time, $\vec{x}(t)$, is related to a system of co-moving co-ordinates accounting for the expansion as:

$$\vec{x}(t) = R(t)\vec{x}(t_0) \tag{2.7}$$

where $\vec{x}(t_0)$ is the co-moving distance and $R(t)$ is the cosmological expansion scale factor. Its time derivative can be multiplied by Equation 2.7 rearranged for $\vec{x}(t_0)$ to give:

$$\dot{\vec{x}}(t) = \dot{R}(t)\vec{x}(t_0) = \frac{\dot{R}(t)}{R(t)}\vec{x}(t). \tag{2.8}$$

We can define a Hubble parameter in terms of the scale factor ratio as it gives a velocity proportional to distance, so:

$$H(t) = \frac{\dot{R}(t)}{R(t)} \tag{2.9}$$

since cosmic time, t, is not directly observable (there is still some debate about the exact age of the Universe) the relative expansion rate, $\tilde{H}$, is defined. This is normalised to the present day value of the Hubble constant and is given as a function of the red shift, z, caused by the expansion:

$$\tilde{H}(z) = \frac{H(z)}{H_0} \tag{2.10}$$

where the red shift, which measures the recession velocity (and also the stretching of the wavelength of light as it travels through expanding space) is given by $z = \frac{R_0}{R(t)} - 1$ and $H(z)$ can be defined by differentiating R with respect to cosmic time and changing variables, $\frac{dR}{dt} \rightarrow \frac{dR}{dz}\frac{dz}{dt}$ so that rearranging for $\frac{dz}{dt}$ gives:

$$\frac{dz}{dt} = \frac{dR}{dt}\frac{d}{dR}\left(\frac{R_0}{R(t)} - 1\right) \Rightarrow \dot{z} = -\frac{R_0\dot{R}}{R(t)^2} = -(1+z)H(z). \tag{2.11}$$

The evolution of the Universe can be described using the Friedmann-Lemaitre-Robertson-Walker (FLRW) solutions to the field equations. These assume the cosmological principle and using comoving spherical polar co-ordinates $x^\mu = (ct, r, \theta, \phi)$, where r is an angular diameter distance, then the separation of points in space is given by:

$$dl^2 = f(r)dr^2 + r^2(d\theta^2 + \sin^2\theta d\phi^2). \tag{2.12}$$

From this, the Robertson-Walker metric has the form:

$$ds^2 = c^2dt^2 - R^2(t)\left[f(r)dr^2 + r^2(d\theta^2 + \sin^2\theta d\phi^2)\right] \tag{2.13}$$

where s is the proper distance between space-time points. Using Peter Scheuer's argument for $f(r)$ [264] this can be written as:

$$ds^2 = c^2dt^2 - R^2(t)\left[\frac{dr^2}{1-kr^2} + r^2(d\theta^2 + \sin^2\theta d\phi^2)\right] \tag{2.14}$$

where length units can be chosen so that the curvature, k, can be either 0 for no curvature, -1 for negative curvature or 1 for positive curvature. The metric

tensor is calculated by:

$$g_{\mu\nu} = \frac{\partial \xi^\alpha}{\partial x^\mu}\frac{\partial \xi^\beta}{\partial x^\nu}\eta_{\alpha\beta} \tag{2.15}$$

where $\eta_{\alpha\beta}$ is the Minkowski spacetime metric $\text{diag}(-1,1,1,1)$, $x^\mu(\tau)$ is any co-ordinate system and $\xi^\alpha = (ct, \vec{x})$ is a co-ordinate system where a freely-moving particle in a gravitational field follows a straight world line so that $\frac{d^2\xi^\alpha}{d\tau^2} = 0$ where τ is the proper time. By the equivalence principle stating that gravity is an acceleration this may always be found. Trivially from Equation 2.14 the Robertson-Walker metric tensor is thus $\text{diag}(1, -\frac{R^2}{a}, -R^2r^2, -R^2r^2\sin^2\theta)$[1], where $a = 1 - kr^2$. The Einstein tensor in this case is derived in Appendix A.3.

The space-time curvature can be related to the contents of the Universe by equation 2.5, as outlined in Section A.4. From equation A.9 the energy-momentum tensor for a stationary fluid with $U^\mu = (1, \vec{0})$ is:

$$T^{\mu\nu} = \begin{pmatrix} \rho & \cdot & \cdot & \cdot \\ \cdot & \frac{ap}{R^2} & \cdot & \cdot \\ \cdot & \cdot & \frac{p}{R^2r^2} & \cdot \\ \cdot & \cdot & \cdot & \frac{p}{R^2r^2\sin^2\theta} \end{pmatrix} \tag{2.16}$$

and by substituting this into the Einstein field equations (Equation 2.5), and using the contravariant Einstein tensor (Equation A.7, where the contravariant tensor is given by the covariant tensor as $\text{diag}(G^{\mu\nu}) = -\text{diag}(G_{\mu\nu})$), the solutions are two differential equations for the scale factor, $R(t)$, and its time derivatives:

$$\frac{\dot{R}^2}{R^2} + \frac{k}{R^2} - \frac{\Lambda}{3} = \frac{8\pi G\rho_t}{3} \tag{2.17}$$

$$2\frac{\ddot{R}}{R} + \frac{\dot{R}^2}{R^2} + \frac{k}{R^2} - \Lambda = -8\pi G p \tag{2.18}$$

where $\rho_t = \rho_\gamma + \rho_m$ represents the total density of matter and radiation. As a consistency check, Equation 2.18 can be derived from Equation 2.17 by differentiating with respect to time and assuming a conservation law. The

[1]Note that natural units are used in this section where $c = 1$

conservation of energy for a perfect fluid is:

$$\frac{d}{dt}(\rho R^3) = -p\frac{d}{dt}R^3 \tag{2.19}$$

which shows that for a positive pressure the density of the Universe will decrease whilst the volume (R^3) increases.

Equation 2.17 can be further simplified by incorporating the cosmological constant into the density so that $\rho_T = \rho_t + \frac{\Lambda}{8\pi G}$. If the Hubble parameter defined in equation 2.9 is also used then equation 2.17 becomes:

$$\underbrace{H^2}_{\text{Expansion}} + \underbrace{\frac{k}{R^2}}_{\text{Curvature}} = \underbrace{\frac{8\pi G\rho_T}{3}}_{\text{Density}} \tag{2.20}$$

i.e. a flat Euclidean Universe, ($k = 0$), will occur for a critical value of the density given by:

$$\rho_c \equiv \frac{3H^2}{8\pi G} \tag{2.21}$$

where the present critical density is $\rho_c(0) \sim 1.88 \times 10^{-26} h_0^2$ kg m^{-3} or $\sim 1.50 \times 10^{-5} h_0^2$ Gev cm^{-3}. Using the Hubble constant value given in 2.3 this is approximately nine protons per cubic metre. This definition of the critical density can be used to define a dimensionless density parameter, Ω, governing the behaviour of the expansion, as outlined in Section A.5.

2.2.1 The Hot Big Bang

As was outlined in the previous section the big bang is the key component of current cosmological theories. A brief outline of the early evolution of the Universe and how it relates to dark matter is given here; for a full review of the big bang theory see [295]. The beginning of our understanding of the Universe starts at the Planck time, $t_p \equiv \sqrt{\frac{\hbar G}{c^5}}$, about 10^{-43} seconds after the initial singularity. The redshift of this period is approximately the Planck energy ($E_p = m_p c^2 \equiv \sqrt{\frac{\hbar c^5}{G}} \sim 10^{19}$ GeV) divided by the CMB energy ($k_B T \sim 10^{-3.6}$ eV) which gives $z_p \sim 10^{31.6}$. Following this the Universe expanded. The expansion may be treated as adiabatic with pV^γ =constant, although this is just an approximation as there are many irreversible changes. The early Universe is

also thought to have undergone a brief period of inflationary expansion [197].

2.2.1.1 Inflation

Inflation theory states that exponential expansion of space dramatically increased the volume of the Universe by many orders of magnitude ($> e^{60}$ if inflation began at the GUT scale). This would have meant that particles were effectively moving away from each other at speeds greater than c, although since this was an effect caused by expanding space and no particles were accelerated to these effective velocities general relativity is not violated. This theory offers a solution to many cosmological observations which otherwise seem to have no natural explanation (see Section 2.2.2). More detail on inflation are given in Section A.6.

2.2.1.2 Eras of the Universe

As the Universe expanded it evolved through several distinct phases. During each different phase the dynamics of the Universe were dominated by a different component. The inflationary period was followed by a period of radiation domination. This gave way to a matter dominated Universe and finally the Universe is now dominated by vacuum energy. More detail is given in Section A.7.

2.2.1.3 Nucleosynthesis and Freezeout

The high thermal energy in the early Universe allowed the creation of particles whose rest mass energy was less than the available thermal energy. Both matter and anti-matter were created so annihilation also took place, due to the extreme densities the interaction times are often much shorter than the expansion time-scale. As such, a perfect fluid in thermal equilibrium is a reasonable approximation. In equilibrium, the number density of a particle species can be calculated by either the Bose-Einstein or Fermi-Dirac distribution depending on the nature of the particle. The calculation is briefly outlined in Section A.8 along with a description of the matter anti-matter asymmetry.

The time variation of the number density of a species can be estimated with the Boltzmann equation:

$$\dot{n} + 3Hn = -\langle \sigma v \rangle n^2 \tag{2.22}$$

where σ is the interaction cross section, v is the particle velocity and $3Hn$ represents the dilution due to the expansion of the Universe. The number density n, evolves on two time-scales; the expansion time-scale, $H(z)^{-1}$, and the interaction time-scale, $(\langle \sigma v \rangle n)^{-1}$. During the radiation era the Hubble time scales with $\propto R^2$ but the interaction time scales with density and energy so that is varies as $\propto R^3$. This shows there is some cross over point between thermal equilibrium at early times and decoupling at late times. This decoupling is known as freeze out and occurs as the interaction time-scale becomes too long for the species to maintain thermal equilibrium. This process leaves a set of frozen out relic particles (such as the CMB in the case of photons). Freeze out of a species can occur when it is behaving as radiation, $kT \gg mc^2$, or matter, $kT \ll mc^2$. The former, relativistic freeze out, leaves a "hot relic", and the latter, massive freeze out, leaves a "cold relic". Figure 2.6 illustrates the freeze-out of several particle species with different interaction strengths. Dark matter WIMPs are thought to appear at the weak scale, $M_\chi \sim 100$ GeV/c^2, and so have interactions with a cross section of order $\sigma \sim G_F^2 T^2$, where the Fermi energy $G_F = \frac{\alpha}{M_\chi}$ and α is the fine structure constant. Hence freeze-out occurs at $\langle \sigma v \rangle \sim n\sigma v \sim G_F^2 (kT)^5$. This gives $\frac{\langle \sigma v \rangle}{H} \simeq G_F^2 (kT)^3 m_{planck}^{-1}$, which is ∼unity at $kT \sim 1$ MeV/c. It is important to note that dark matter particles are expected to follow this freeze-out trend, indicating that they do annihilate, simply because density measurements indicate $\Omega \simeq 1$, otherwise there would be an over-abundance of dark matter. This also indicates, by crossing symmetry, that dark matter particles should have some interaction with baryonic matter.

At some point during its expansion and cooling the Universe passed through a phase where the conditions were favourable for nuclear reactions, similar to those occurring in the cores of stars. This period is described by Big Bang nucleosynthesis, as briefly outlined in Section A.9.

The relic abundances of light elements are sensitive to baryon density and may be used to weigh the baryons in the Universe. Nucleosynthesis is a well

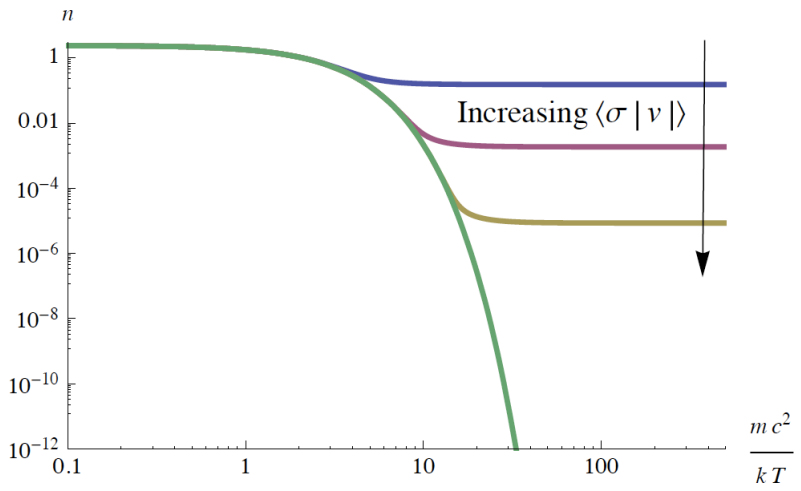

Figure 2.6: Freeze-out of particle species as a function of interaction strength, $\langle\sigma v\rangle$. The green curve shows the equilibrium abundance which decays exponentially after the temperature drops below threshold. The lines which "peel off" from equilibrium correspond to increasing values of $\langle\sigma v\rangle$ for lower values of the final abundance and freeze-out temperature. Image adapted from [229].

understood process as it can be tested in laboratories on Earth. Comparisons of predictions of the ratios of light elements to the measured ratios in regions thought to have primordial abundances are shown in Figure 2.7. This shows good agreement apart from lithium. The mismatch from lithium data could be due to systematic errors in the observations, uncertainties in stellar astrophysics (since the abundance is measured in metal poor stars), uncertainties in nuclear inputs, or new physics [178]. The fit provides limits on the baryon content of the Universe of:

$$0.019 \leq \Omega_b h^2 \leq 0.024(95\%\ \text{CL}). \tag{2.23}$$

As this is considerably less than the matter density, $\Omega_m h^2$, this indicates most matter is non-baryonic.

2.2.2 Problems With the Big Bang

The framework of the hot big bang contains some major problems; these are outlined here along with a possible solution. As was mentioned in Section 2.2.1.1 the Universe is believed to have undergone a brief period of inflation before the radiation dominated era began. This inflation offers a neat solution to these

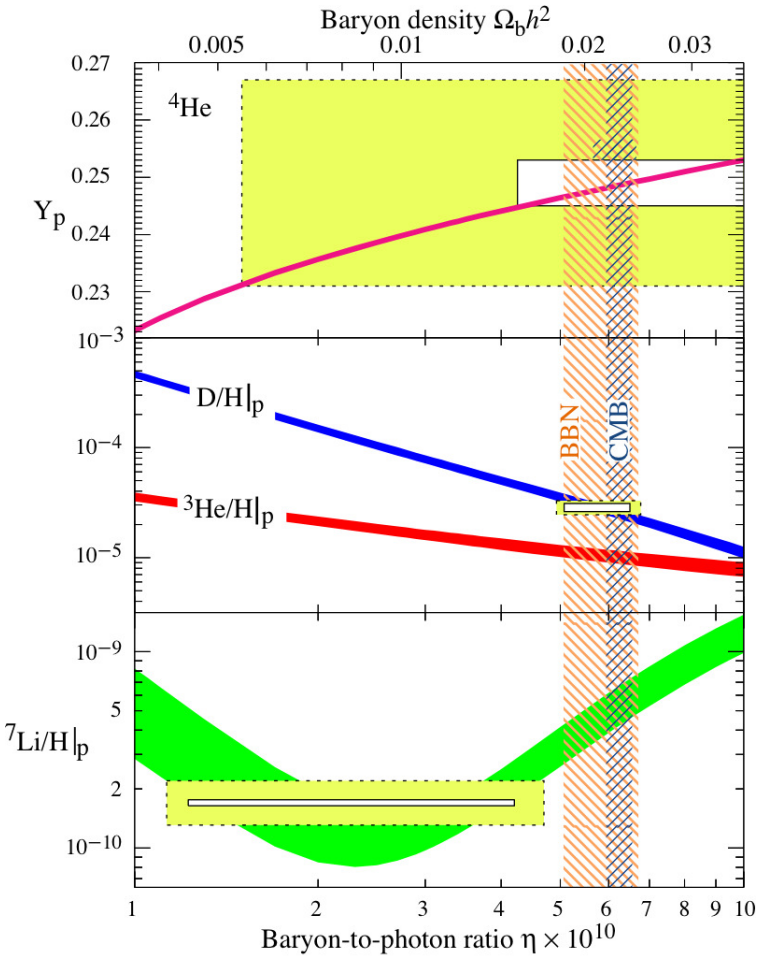

Figure 2.7: The abundance ratios of light elements predicted by the standard model of big bang nucleosynthesis [139] where the bands show the 95% CL range. Boxes show observed light element abundance ratios, the small box is $\pm 2\sigma$ statistical errors and the large box is $\pm 2\sigma$ statistical and systematic errors. The vertical bands show the concordance range of direct measurements of the light element abundances (orange) and the CMB measurement of the cosmic baryon density (blue).

problems and indeed this is the motivation for the inflation theory.

2.2.2.1 The Expansion Problem

At $t = 0$ the Universe was expanding. This suggests a mechanism is needed to launch the expansion of the Universe. The standard big bang model does not account for how all parts of the Universe began expanding simultaneously, but if inflation occurred then this occurs naturally during the inflation period.

2.2.2.2 The Flatness Problem

The expansion of the Universe would seem to need to be launched at a very precise value for space to be as flat as it is observed to be in the current era. To expand from the Planck scale to the current scale of the Universe (a factor of over 10^{30}) would seem to require significant fine tuning. The density of the Universe is observed to be very close to $\Omega = 1$. Rearranging the Friedmann equation, A.12, for the curvature gives:

$$k = \frac{R^2 H^2}{c^2}(\Omega - 1) \tag{2.24}$$

which shows that if the Universe initially has $\Omega \neq 1$ then Ω rapidly changes with time as it scales with the curvature. To achieve a value of $\Omega = 1 \pm 0.01$ [346] today would require $\Omega(t_{Planck}) = 1 \pm 10^{-62}$. If inflation occurred in the early Universe then a value of $\Omega = 1$ occurs naturally as any deviation from the critical value is washed out by the vast change in scale, rearranging equation 2.20 and substituting in the critical density, equation 2.21, gives:

$$(\Omega^{-1} - 1)\rho R^2 = -\frac{3kc^2}{8\pi G} \tag{2.25}$$

during inflation the scale factor, R, grows exponentially. Since the right hand side of equation 2.25 is constant the $(\Omega^{-1} - 1)$ term must decrease with time.

2.2.2.3 The Horizon Problem

The CMB shows that all the observable Universe is the same temperature to within $\sim 10^{-5}$. The angular size of the horizon, given by the angular diameter distance over horizon distance $\theta_H = \frac{d_H}{d_A}$, is approximately 1.7° and the maximum size of causally connected regions at the time of photon decoupling was $\sim 9 \times 10^5$ light years, but the temperature invariance covers a volume many orders of magnitude larger than this. The uncertainty principle suggests that the Universe should not have a uniform temperature as an initial condition. A period of inflation explains this observation as the observable Universe was in thermal equilibrium before inflation. The exponential increase in scale factor means that regions of the Universe larger than the current horizon distance were once causally connected and should have been in equilibrium at decoupling.

2.2.2.4 The Monopole Problem

If grand-unified theory (GUT), see Section 2.4, is correct and the standard model $SU(3) \times SU(2) \times U(1)$ groups all fit into a single group at high energy, unifying the strong and electro-weak forces then it is expected that magnetic monopoles were produced when this single force split as the Universe cooled to below T_{GUT} (after between 10^{-43} and 10^{-36} seconds) [217]. With a single particle per horizon volume the current number density of magnetic monopoles, with no inflation, should be $\sim 10^{-4}$ cm^{-3} and with a predicted mass of $\sim 10^{16}$ GeV these particles would have closed the Universe after only a few decades. These particles have not been observed and limits have been placed on their abundance of $\sim 10^{-23}$ cm^{-3} for a monopole velocity of $10^{-3}c$, from observations of galactic magnetic field lines [140] (known as the Parker limit). Direct detection approaches have also set limits on monopoles, such as the Monopole, Astrophysics, and Cosmic Ray Observatory (MACRO). This experiment was the first to set a limit on the local magnetic monopole flux significantly below the Parker limit for the whole range of expected velocities at 1.4×10^{-16} cm^{-2} s^{-1} sr^{-1} [37]. Although both inflation and GUT are hypothetical they both have strong theoretical grounds and the existence of an inflationary period of the Universe allows for GUT monopoles to exist and remain consistent with observations.

2.3 Evidence for Dark Matter

So far dark matter has been discussed as a requirement of the current cosmological model. A significant non-baryonic cold dark matter component of the Universe is required by the current ΛCDM model and fits well with our observations of the Universe being at or very close to critical density. There is more direct evidence for the existence of dark matter which is outlined in this section.

2.3.1 Dark Matter in Galaxies and Clusters

Measurements of the velocity dispersions in galaxy clusters provided the inspiration for the dark matter hypothesis. In 1933 Fritz Zwicky published a paper showing results of velocity dispersion measurements of the Coma cluster [390]. By measuring the velocities of galaxies near the edge of the cluster, and using the virial theorem to calculate the mass enclosed by their orbits, he found that the cluster was around four hundred times heavier than could be accounted for by the mass of the visible matter within the cluster. The method, along with details of more modern methods including X-ray measurements, is discussed in more detail in Section A.10. The Sunyaev-Zeldovich Effect may also be used to measure the mass of galaxy clusters. The results agree with X-ray measurements, as discussed in Section A.11.

The strong gravitational field of clusters enables them to retain heavy elements from high-energy supernova explosions. Thus studying the chemical composition of the intracluster medium as a function of redshift also gives a record of the chemical evolution of the Universe [276]. This information is required for nucleosynthesis models and also once again reinforces the ancient origins of the Universe.

An important piece of evidence for dark matter comes from measuring the rotation curves of galaxies. These show dark matter on much smaller scales than that observed in the intracluster medium. Observations across the electromagnetic spectrum allow the mass of the luminous matter to be estimated and in some cases, depending on the galaxies orientation and type, spectrograph

results can be used to measure the rotation velocity as a function of radius. The morphology of galaxies shows that they are gravitationally bound, which is also consistent with the crossing time given the age of the Universe. The luminous matter within the rotating galaxies may then provide measurements of the rotation velocity by the Doppler effect. Spiral galaxies provide the best candidates for these types of measurements as they consist of a central bulge and a flattened disc. For the disc to be bound it should obey Virial theorem where $2K + T \leq 0$, this means that the maximum velocity of bound objects orbiting at a given radius is:

$$V_{max} = \sqrt{\frac{GM(< r)}{r}}, \tag{2.26}$$

where $M(< r)$ represents the mass contained within the galaxy out to a radial distance r. At large radii the mass contained within would have converged and a Keplerian fall off of orbiting velocities is expected with $V \propto r^{-\frac{1}{2}}$. Accurate spectrograph results became available in the 70s and results showed rotation curves remaining flat out to large radii [320]. These results also show approximately flat rotation curves [335]. Figure 2.8 shows an example of a rotation curve for a spiral galaxy and Figure 2.9 shows the rotation curve for the Milky Way galaxy. The calculations of dark matter density in the solar region of the Milky Way are particularly difficult, although this result is of vital importance to direct detection experiments. Recent measurements presented in Reference [87] suggest that the local dark matter density is lower than 10^{-3}M$\odot$ pc^{-3} (0.04 GeV cm^{-3}). These results were obtained by analysing the kinematics of 412 stars at heights ranging from 1 to 4 kpc from the Galactic mid plane [87]. One of the assumptions made during this analysis was that the mean azimuthal velocity is independent of Galactocentric radius at all heights from the mid plane, however this assumption has been shown to be unsupported by the data [96]. The data imply that only the circular speed is independent of radius in the mid-plane [170]. In the solar neighbourhood, the circular speed is larger than the mean azimuthal velocity by over 35 km s^{-1} due to asymmetric drift [96]. A reanalysis accounting for this is consistent with the standard estimates of local dark matter density and provides the most robust direct measurement of the local dark-matter density to date of 0.008 ± 0.002 M$\odot$ pc^{-3} (0.3 ± 0.1 GeV cm^{-1}) [96].

The observed rotation curves with constant velocity imply $M(< r) \propto r$, hence

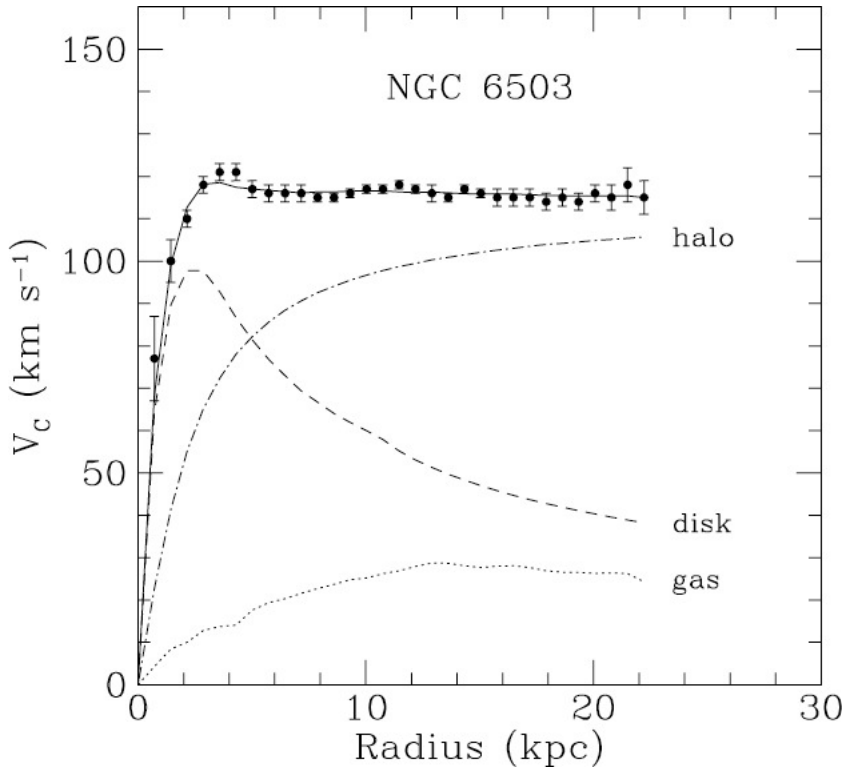

Figure 2.8: The rotation curve of the spiral galaxy NGC 6505. This flat rotation curve can be explained as being due to the sum of masses from the three components shown on the plot [234]. The "halo" refers to the dark matter halo.

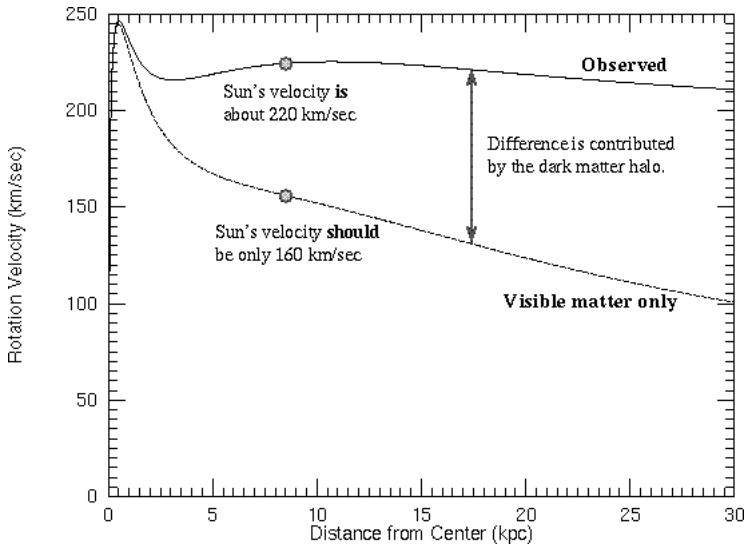

Figure 2.9: The rotation curve of the Milky Way. The Sun is travelling ~ 60 km s^{-1} faster than can be accounted for by luminous matter [354].

a density relation of $\rho \propto r^{-2}$. This observed density profile can be explained by the presence of an isothermal sphere of dark matter. Although the flat rotation curve alone does not necessarily require an isothermal sphere (a disc could give the same relation) further observations of polar-ring galaxies with material orbiting out of the orbital plane of the galaxy show an approximately spherical distribution, although results also favour slightly flattened halos with axial ratios of $\sim 1.3:1$ [385].

Elliptical galaxies are more difficult to analyse due to their morphology. Some elliptical galaxies contain faint discs of neutral hydrogen which allow similar methods as used for spiral galaxies to be employed, for example, measurements of NGC 2974 using the Very Large Array detected an HI disc for which the rotation curve could be measured [381]. The velocity dispersion and mass-to-light ratio data acquired from this analysis was combined with X-ray measurements from ionised gas to give the velocity profile shown in Figure 2.10. Measuring emission from ionised gas is a more common technique for probing the dark matter halos of elliptical galaxies. These regions typically extend out to ~ 50 kpc [181]. The gravitating mass within a region can be derived from the X-ray flux under the assumption that the emitting gas is in hydrostatic equilibrium, so long as the gas temperature and density profiles are known [167]. Further evidence of dark matter halos in elliptical galaxies also comes from strong gravitational lensing observations [246].

In general it is found that the dynamics of galaxies are often dominated by non-radiating matter, although there are some null results for elliptical galaxies showing that a dark matter halo is not required (for example NGC 3379 [141]). A large number of systems have now been studied and a general trend has emerged. The current paradigm is that each galaxy lies within a self-gravitating dark halo of size R_{vir} and mass M_{vir} [329]. The size, R_{opt}, and mass, $M_\star$, of the baryonic component are related to the dark matter halo by the relations:

$$R_{vir} \sim 15 R_{opt} \tag{2.27}$$

$$M_{vir} = 3 \times 10^{12} \left(\frac{M_\star}{2 \times 10^{11} M_\odot} \right)^{0.4} M_\odot \tag{2.28}$$

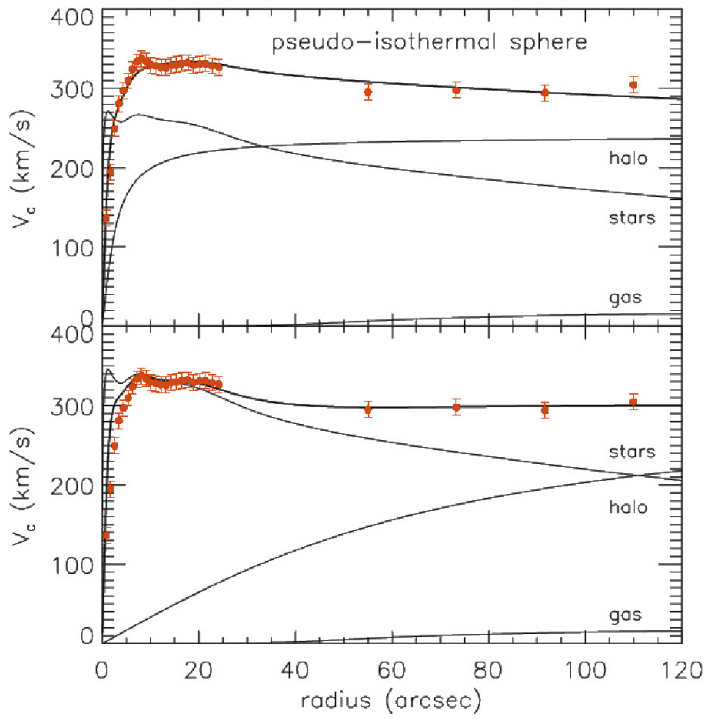

Figure 2.10: Best-fitting models for a pseudo-isothermal sphere of dark matter around the elliptical galaxy NGC 2974. The top image has a mass-to-light ratio of $2.34\frac{M_\odot}{L_\odot}$ estimated from stellar population models ($\odot$ represents the solar value). The bottom image has a mass-to-light ratio of $3.8\frac{M_\odot}{L_\odot}$ estimated by the maximal disc model [381]. The red points show the data from ionised gas and H_I gas measurements and the solid curve shows the fit from a combination of the three components shown separately below.

Figure 2.11 shows the relation between dark matter halo size and the size of the luminous component. The close matching of data, simulation and analytical formulas suggest that this phenomenon is well understood and there is a strong link between the two components. This is consistent with the current theory of galaxy formation where the baryons fell into cold dark matter over-densities, see [350] and references therein.

2.3.2 Gravitational Lensing

Fritz Zwicky coined the term "dark matter", based on observations of the inferred and observed mass of the Coma cluster, and suggested the potential of gravitational lensing as a viable technique for measuring mass [391]. This relies on the general relativistic principle covered in Section 2.2 which shows how matter bends space-time, see equation A.2. This means that images of background objects will be distorted by mass along the line of sight. As the degree of distortion is related to the strength of the lens it is possible to use the effects of gravitational lensing to measure mass. Gravitational lensing effect can be sub-divided into four categories, strong lensing, micro lensing, weak lensing and flexion.

Strong lensing occurs when the lens is very massive and a background object is close to the line of sight to the lens, as illustrated in Figure 2.12. Strong lensing produces highly distorted images, the light from a background object may take several different paths and multiple images may be seen, an example of this is shown in Figure 2.13. The peak distortion occurs at the Einstein radius which scales as $r_E \propto \sqrt{M(< r)}$. With the correct alignment this scenario would distort the background image such that a ring, known as an Einstein ring, is observed. If the mass was mostly contained within the galaxies then these rings would appear around the individual galaxies. Observations show them to appear around the cluster as a whole, so the mass must be much more evenly distributed. Strong lensing can also be used to constrain cosmological parameters such as the cosmological constant. The number of lensing events can constrain Ω_Λ by determining the volume of space between the observer and source [117]. As the light may take different paths around the gravitational lens there may also be

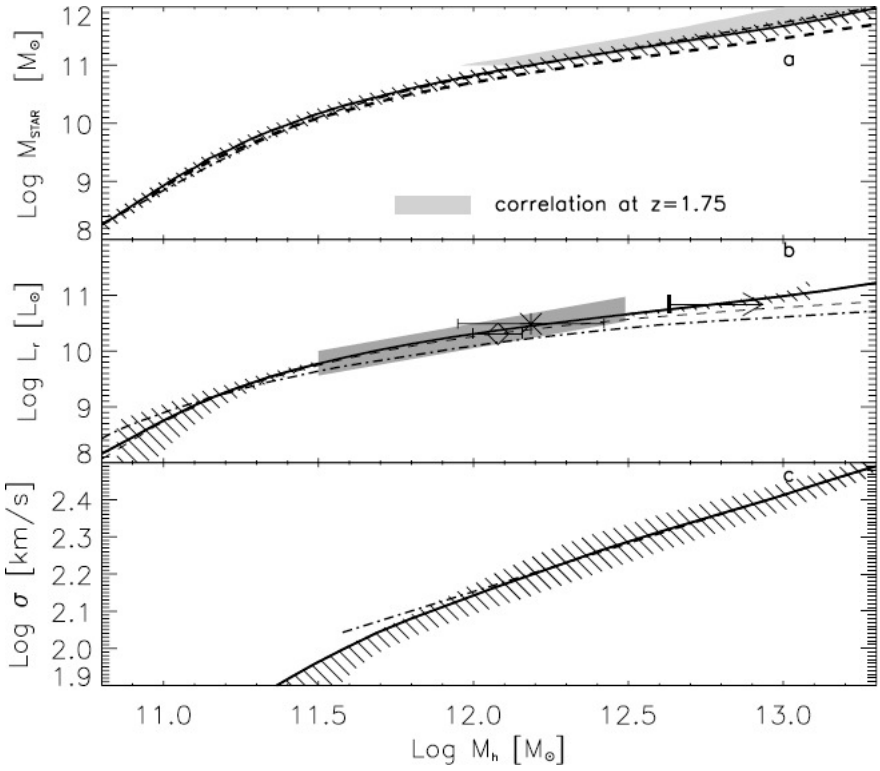

Figure 2.11: Relations between the dark matter halo and the baryonic matter of galaxies, from [329]:
(a) The mass in stars plotted against the dark matter halo mass. The thick solid line shows the numerical results while the dot-dashed line represents the analytical fitting formula. The barred area shows the uncertainty in the mass-to-light ratio and the shaded area shows data from [180].
(b) The $r^\star$ band luminosity as a function of dark matter halo mass. the solid line shows numerical results and the analytical fit as they are indistinguishable, the dashed line shows the numerical result including galaxy groups and clusters in the halo mass function. The barred area shows the uncertainty, the dot-dashed line is the corresponding result from [374] and the shaded region is the result from [244]. The data points are from the following results; arrow [292], diamond [215] and star [198].
(c) The relation between velocity dispersion, σ, and dark matter halo mass. The solid line shows the numerical results and the dot-dashed line shows the analytical formula, $\sigma \simeq 110\ \mathrm{kms}^{-1} \left(\frac{M_{vir}}{6.3\times10^{11}M_\odot}\right)^{\frac{1}{3}}$. The barred area shows the uncertainty.

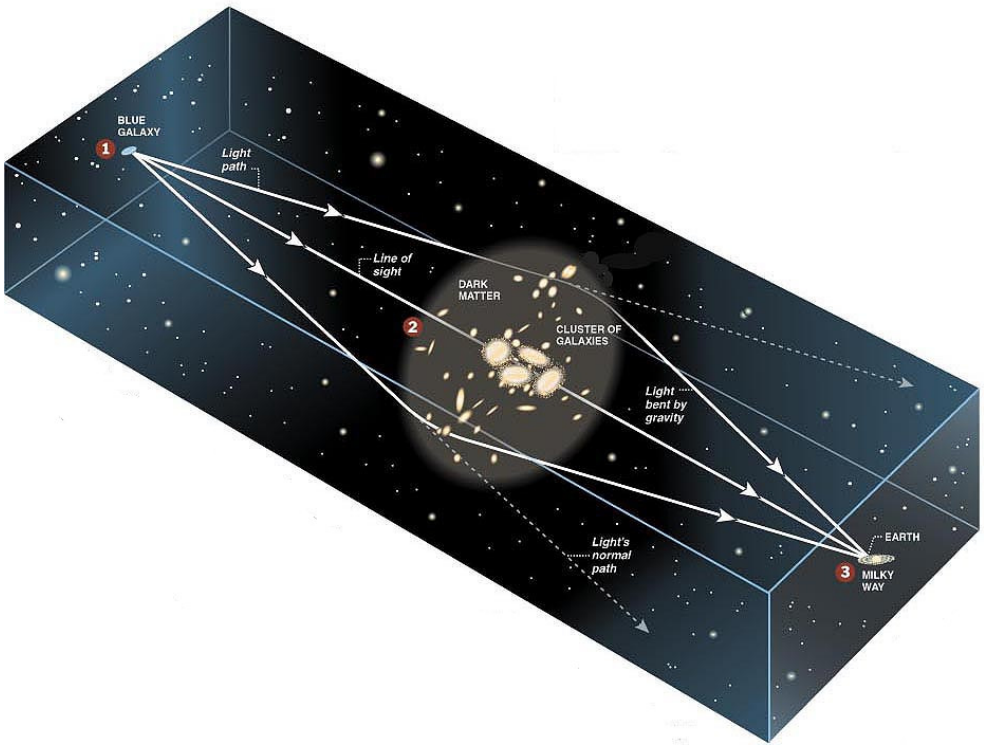

Figure 2.12: Light from a background object (1) is bent around a massive galaxy cluster along the line of sight (2). This galaxy cluster acts similarly to an optical lens and the properties of the lensing cluster can be inferred from the distortion of the background image (3). Image obtained from [77].

time delays for changes in the images. The time delays may be used to measure the Hubble constant [252]. The matter density can also be constrained from strong lensing studies, giving $\Omega_m = 0.31\,^{+0.27}_{0.14}$ [367].

Microlensing occurs when an image becomes more intense as a gravitational lens bends more light from a background object towards the observer. This transient phenomenon allows observations of objects down to small mass scales, such as planets. It can be used to detect objects that emit little or no light and may therefore be used to detect dark matter in the form of Massive Compact Halo Objects (MACHOs) and microlensing surveys allow limits to be placed on the amount of matter in this form, as described in Section A.16.

Most gravitational lensing data is of weak lensing. Strong lensing requires that multiple light paths are bent around a massive object towards an observer.

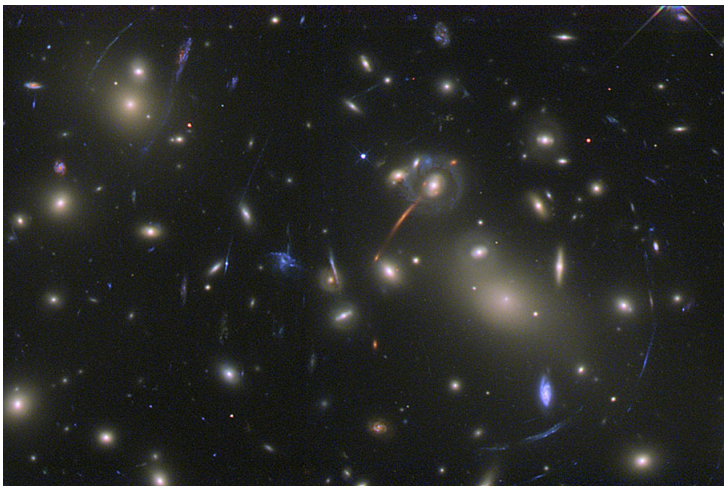

Figure 2.13: Strong lensing by the galaxy cluster Abell 2218 [185]

This effect is a rare occurrence as it requires the observer to be in a special position along the focal plane. Observations of weak lensing requires no such special position and instead the observations rely on statistical analyses of the distortion caused as light from background sources passes through relatively weak gravitational fields. These regions are away from the core of clusters and the deflection is only slight.

While it is difficult, and usually impossible, to tell if an individual background source has been weakly lensed, a large survey may show a trend in the shape of background sources that is inconsistent with what is known about their morphology, as illustrated in Figure 2.14. These distortions take the form of shear, magnification, twist and rotation [60]. The most commonly used distortions are the shear or magnification, as these can be approximated using first order terms in local linear transformation of the sky represented by a 2×2 matrix. The shear tends to have a higher signal-to-noise ratio than the magnification and most weak lensing surveys therefore measure this, where one of the factors contributing to the noise in these measurements is the intrinsic shape of the lensed galaxies. Typically, weak lensing alters the major-to-minor axis of distant galaxies by $\sim 2\%$ [272]. The observable shear field is proportional to a second derivative of the gravitational potential along the line of sight; A convolution can then be used to convert the shear field into a map of the projected mass distribution along the

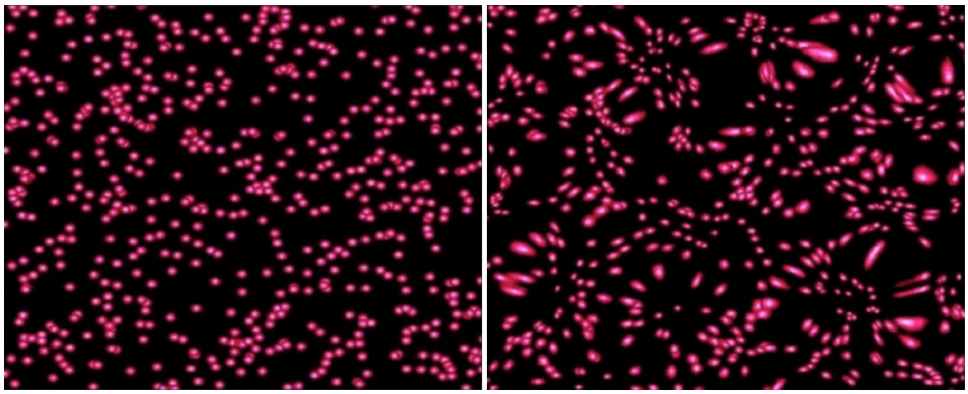

Figure 2.14: Results from a simulation demonstrating the weak lensing effect. The left image shows sources with no intervening mass between them and the observer; the right image shows the distortion created as the light passes through a gravitational field [379].

line of sight with a resolution only limited by the density of background sources.

If redshift is also measured then the weak lensing survey can be used to produce 3D dark matter maps, as shown in Figure 2.15. Results from these analyses can be used to constrain the matter density of the Universe. Recent COSMOS results show $\left(\frac{\Omega_m}{0.3}\right)^{0.44} = 0.866^{+0.085}_{-0.068}$ at 68% C.L. (so $\Omega_m \simeq 0.216$) [271]. Lensing results also provide pure geometric tests of the structure of space-time, as mentioned in Section 2.2. By comparing the relative shear of many low mass source-lens pairs in the COSMOS survey data, a variation in shear was detected as a function of distance behind the lens. This result was used to constrain the equation of state of the Universe, equation A.25, giving $-2.5 \leq \omega \leq -0.1$ at greater than 99% confidence [361]. In the case of $\omega = -1$ these results give a value of the cosmological constant density parameter of $\Omega_\Lambda = 0.85^{+0.044}_{-0.19}$ (68%C.L.) and detect cosmic acceleration at 98% C.L.. The Sloan Digital Sky Survey results show that, from a sample of around a third of a million galaxies, the typical halo mass is $1.4 \times 10^{12} M_\odot$ with a stellar mass of $6.0 \times 10^{10} M_\odot$ [267]. This study also indicated that the stars account for $\sim 16\%$ of baryons, which is in agreement with X-ray observations (although it should be noted that these results show most of the baryons within galaxies are in stars and the difference between the two results above is attributed to non-baryonic dark matter). Results using the COSMOS survey data can be used to decompose the mass into its various components, as shown in Figure 2.16. A more direct measurement using the Hubble space

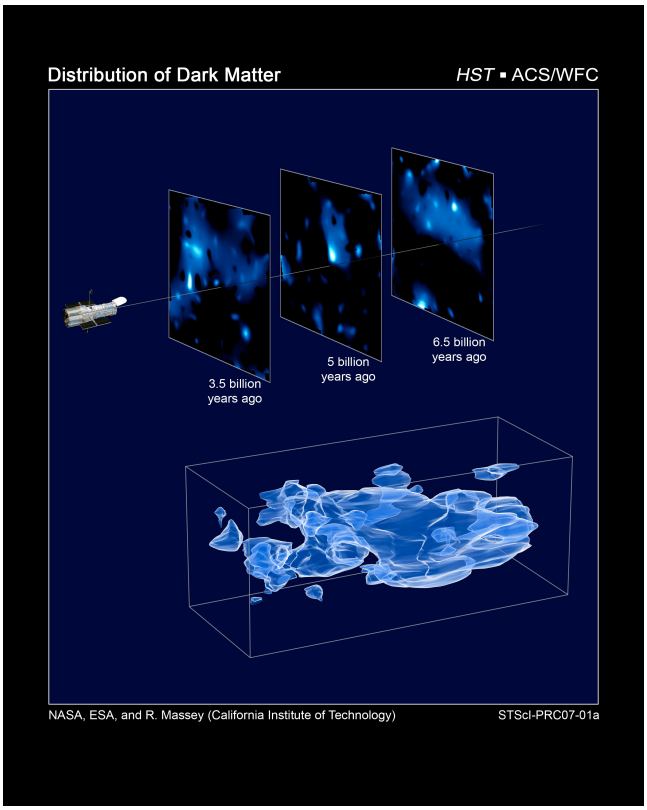

Figure 2.15: Data from the HST COSMOS survey was used to create this 3D dark matter map [270].

telescope SLACS survey data gives a higher result of $(1.2 \pm 0.3) \times 10^{13} M_{\odot}$ and $(2.6 \pm 0.3) \times 10^{11} M_{\odot}$ for the halo and stellar mass respectively [188].

Flexion is the regime between weak and strong lensing. As the strength of the gravitational field along the line of sight increases, background images begin to curve (although in this regime it is still too weak for strong lensing to occur), as shown in Figure 2.17. Although the amplitude of the shear signal is larger than the flexion signal the intrinsic curvature of typical galaxies is very low so these measurements have much lower noise. This allows statistical techniques similar to those of weak lensing to be used and flexion surveys are useful to plug the gap between strong lensing and weak lensing in regions where the statistics are too low for significant weak lensing results but the field is too weak for strong lensing [293].

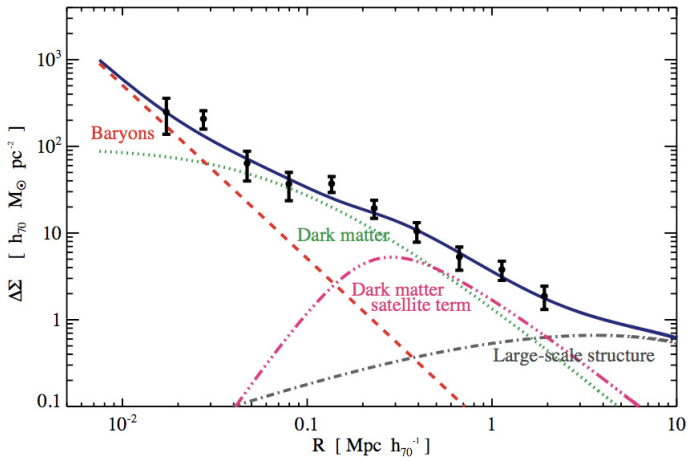

Figure 2.16: The observed radial distribution of mass around elliptical galaxies, shown decomposed into its various components [253]. The solid blue curve shows the total surface mass density from the weak lensing signal. The baryons (red dashes) are seen to dominate the core of the galaxy, with dark matter (green dots) becoming increasingly dominant with increasing radius. The triple dotted magenta line shows the contribution from occasions when the analysis focuses on satellite galaxies in the halo of the larger host and the dot-dash grey line shows that on large scales (above ~ 3 Mpc) the galaxy-galaxy lensing signal reverts to the cosmic shear signal from large-scale structure around where the galaxy is located.

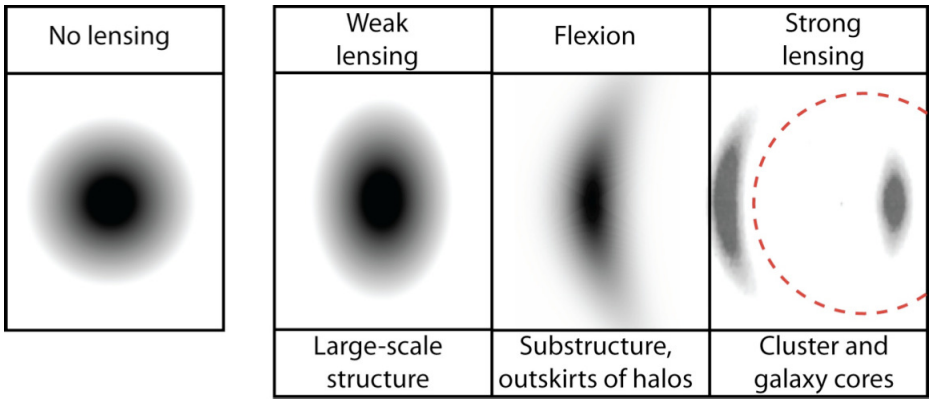

Figure 2.17: The three regimes of gravitational lensing. The degree of distortion increases from left to right (although the weak lensing is exaggerated compared to a typical distortion) and increases with the strength of the gravitational field. Image obtained from [272].

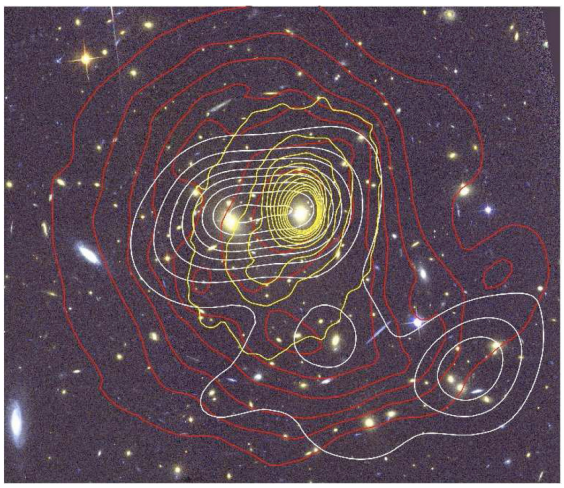

Figure 2.18: A colour composite image of the cluster RX J1347.5-1145. Red contours show the surface mass density from strong and weak lensing mass reconstruction. X-ray brightness is shown with yellow contours and K-band light, mapping the stars, is shown with white contours. All contours are linearly spaced. Obtained from [98].

2.3.2.1 Colliding Clusters

Lensing results are often complemented by X-ray and optical results to map the different mass components of objects. Figure 2.18 shows an overlay from strong and weak lensing to map the dark matter of the cluster RX J1347.5-1145 along with X-ray measurements and optical surveys to map the baryons. When galaxy clusters collide, the fluid-like x-ray emitting gas containing the majority baryonic component may become separated from the dispersionless stellar component. Using a combination of the measurements discussed above the different matter components may be mapped separately allowing a measurement of the relative mass that is independent of the assumptions regarding the nature of the gravitational force law. Figure 2.18 shows the results from measurements of the merging cluster 1E 0657-557, also known as the bullet cluster. Lensing measurements shows the gravitational potential does not map the X-ray emitting gas, showing an 8σ spatial offset. Since this gas contains the majority of visible matter this indicates that the majority of the mass is dark.

Since the initial observation of the bullet cluster several other merging clusters have been measured (for example see [31]). Figure 2.20 shows an optical image of two merging galaxy clusters where measurements of the different mass

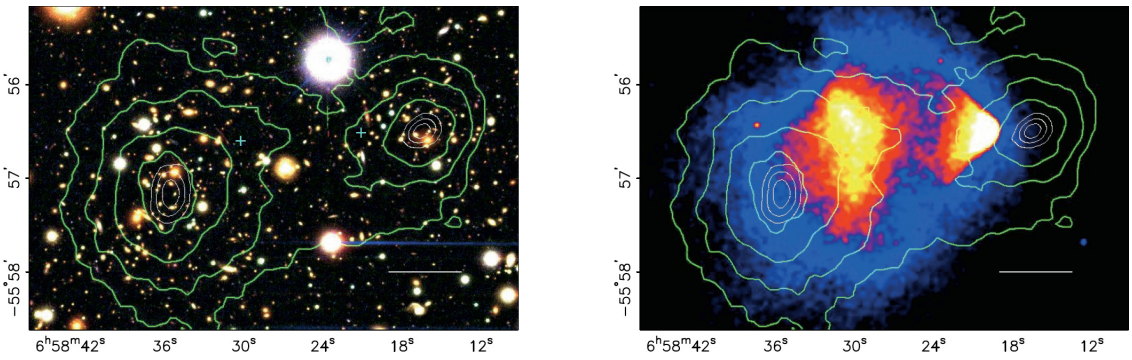

Figure 2.19: Maps showing the mass distribution of the merging cluster 1E 0657-558 [126] the white bars indicate 200 kpc, the green contours show weak lensing reconstructions:
Left image: Colour image from the Magellan images showing the stellar distribution.
Right image: Chandra image showing the distribution of X-ray emitting gas.

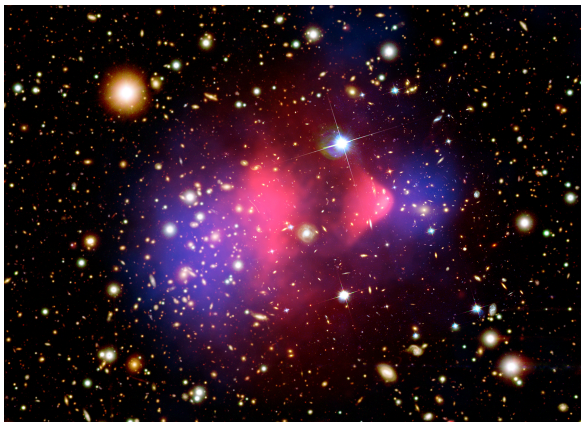

Figure 2.20: Composite image of the bullet cluster, obtained from the Chandra website [125]. Blue shows the mass measured by weak lensing, pink shows the X-ray emitting gas.

components have been overlaid in false colour. These measurements show that, independently of the nature of the gravitational force at large scales, there is some form of non-interacting dark matter in these clusters which contains the majority of the mass [126].

2.3.3 The Cosmic Microwave Background

The cosmic microwave background (CMB) is a key tool in modern cosmology, and as such has already been mentioned several times in section Section 2.2. This relic

Table 2.1: WMAP parameters from the seven year CMB data set [231]. The uncertainties presented are 68% CL.

Description	Symbol	WMAP	WMAP+BAO+H_0
Age of the Universe	t_0	13.75 ± 0.13 Gyr	13.75 ± 0.11 Gyr
Hubble constant	H_0	71.0 ± 2.5 kms^{-1}Mpc^{-1}	$70.4^{+1.3}_{-1.4}$ kms^{-1}Mpc^{-1}
Physical baryon density	$\Omega_b h^2$	$0.02258^{+0.00057}_{-0.00056}$	0.02260 ± 0.00053
Baryon density	Ω_b	0.0449 ± 0.0028	0.0456 ± 0.0016
Physical dark matter density	$\Omega_{dm} h^2$	0.1109 ± 0.0056	0.1123 ± 0.0035
Dark matter density	Ω_{dm}	0.222 ± 0.026	0.227 ± 0.014
Dark energy density	Ω_Λ	0.734 ± 0.029	$0.728^{+0.05}_{-0.016}$
Curvature fluctuation amplitude	Δ^2_R	$(2.43 \pm 0.11) \times 10^{-9}$	$(2.441^{+0.088}_{-0.092}) \times 10^{-9}$
Scalar spatial index	n_s	0.963 ± 0.014	$0.963/pm0.012$
Redshift of photon decoupling	$t_\star$	$1090.79^{+0.94}_{-0.92}$	$1090.89^{+0.68}_{-0.69}$
Reionisation optical depth	τ	0.88 ± 0.015	0.87 ± 0.014
Total density	Ω	$1.080^{+0.093}_{-0.071}$	$1.0023^{+0.0056}_{-0.0054}$
Equation of state	ω	$-1.12^{+0.42}_{-0.43}$	-0.980 ± 0.053
Physical neutrino density	$\Omega_\nu h^2$	< 0.014(95%C.L.)	< 0.0062(95%C.L.)
Number of light neutrino families	N_{eff}	> 2.7(95%C.L.)	$4.34^{+0.86}_{-0.88}$

radiation field left over from the big bang shows that the Universe is homogeneous and isotropic on large scales. Although the CMB is very uniform after corrections there are small temperature fluctuations, known as primary anisotropies, as shown in Figure 2.1. Many parameters of the ΛCDM model can be measured using CMB data, as discussed in more detail in Section A.12. Some of the parameters are listed in Table 2.1.

2.3.4 Large Scale Structure

Following the photon decoupling, the density perturbations, thought to have originated from quantum fluctuations which were then inflated, continued to grow. Surveys of the Universe measuring the distribution of matter can be used to constrain cosmological parameters. Galaxy surveys use redshift to create 3 dimensional maps of the Universe as shown in figures 2.21 and 2.22. Evidence of acoustic oscillation is seen in the large scale structure of the Universe.

The surveys show filamentary features separated by large voids. An

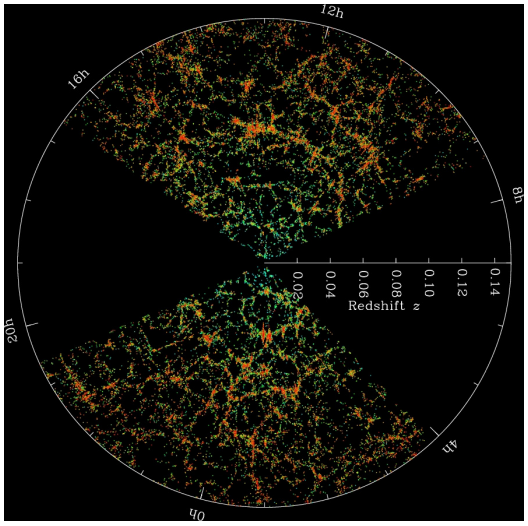

Figure 2.21: Large scale structure in the northern equatorial slice the Sloan Digital Sky Survey (SDSS) main galaxy redshift survey. The slice is 2.5 degrees thick and the galaxies are colour-coded by luminosity [91].

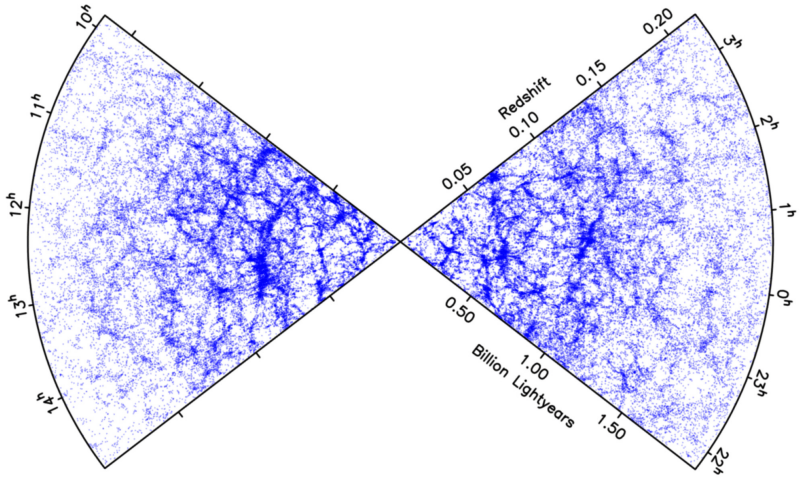

Figure 2.22: Map of large scale structure obtained by the Two-degree-Field Galaxy Redshift Survey (2dF GRS) [133].

autocorrelation function can be defined for the density field as:

$$\xi(\vec{r}) \equiv \langle \delta(\vec{x})\delta(\vec{x}+\vec{r})\rangle \tag{2.29}$$

where the density perturbation field is $\delta(\vec{x}) \equiv \frac{\rho(\vec{x})-\langle\rho\rangle}{\langle\rho\rangle}$. A power-law spectrum implies a power-law correlation function:

$$\xi(r) = \left(\frac{r}{r_0}\right)^{-\gamma} \tag{2.30}$$

where $\gamma = n + 3$ can be measured from the density map. The largest survey, the Sloan Digital Sky Survey (SDSS), measured $n = 0.983 \pm 0.035$. The case for $n = 1$ is known as the Harrison-Zeldovich spectrum and corresponds to a fractal metric, i.e. a scale-invariant spectrum where space time has the same 'wrinkliness' on all scales which further supports the idea that structure originated from magnified quantum fluctuations from the inflationary period. This survey also constrained several other cosmological parameters, $\Omega_m h^2 = 0.135 \pm 0.008$, $\omega = -0.8 \pm 0.18$ and $h = 0.648 \pm 0.045$. A significant (3.4σ) feature was also found in the power spectrum at $\sim 100 h^{-1}$ [160]. This is in good agreement with ΛCDM models, as shown in Figure 2.23, and evidence seen in the CMB at this scale indicates that large scale structure today grew linearly from ancient density perturbations.

N-body simulations have been used to test cosmological models. The millennium simulation [348] uses the concordance ΛCDM model to attempt to simulate large scale structure formation. The simulation models growth of dark matter structure and the results closely resemble the filament like structure observed by sky surveys, as shown in Figure 2.24 and more recently with increased spatial resolution shown in Figure 2.25. The ΛCDM model predicts a filament structure between galaxy clusters, as seen in the simulations. Although detection of these structures is difficult due to the low signal to nose ratio a recent analysis of the area between the Abel 222 and 223 clusters has confirmed a robust detection [144].

There are three types of dark matter usually considered, as mentioned in Section 2.2.1.3, depending on the properties of the particles:

- **Hot dark matter:** These particles would have de-coupled when relativistic

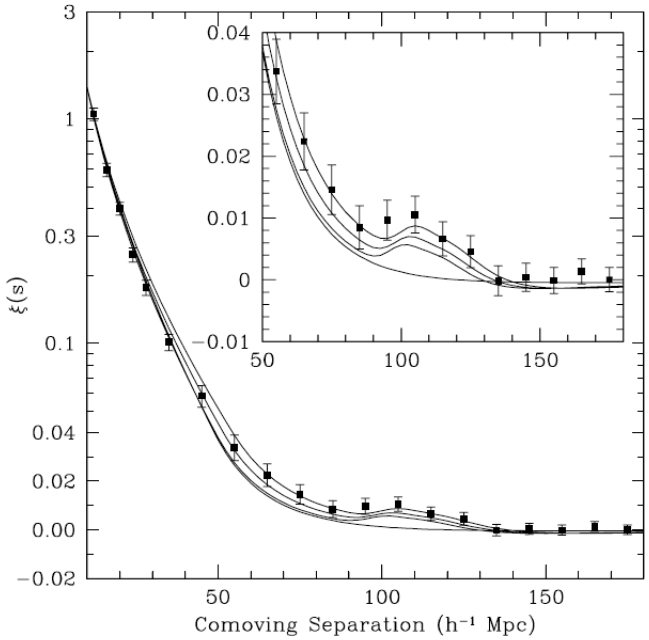

Figure 2.23: Large scale redshift-space correlation function of the SDSS Luminous Red Galaxy (LRG) sample. The models are $\Omega_m h^2 = 0.12$ (top line), $\Omega_m h^2 = 0.13$ (middle line), $\Omega_m h^2 = 0.14$ (third line) and all have $\Omega_b h^2 = 0.024$ and $n = 0.98$. The bottom line shows pure CDM model with $\Omega_m h^2 = 0.105$ and has no acoustic peak. The fluctuation at $100\mathrm{h}^{-1}$ is statistically significant. Image from [160].

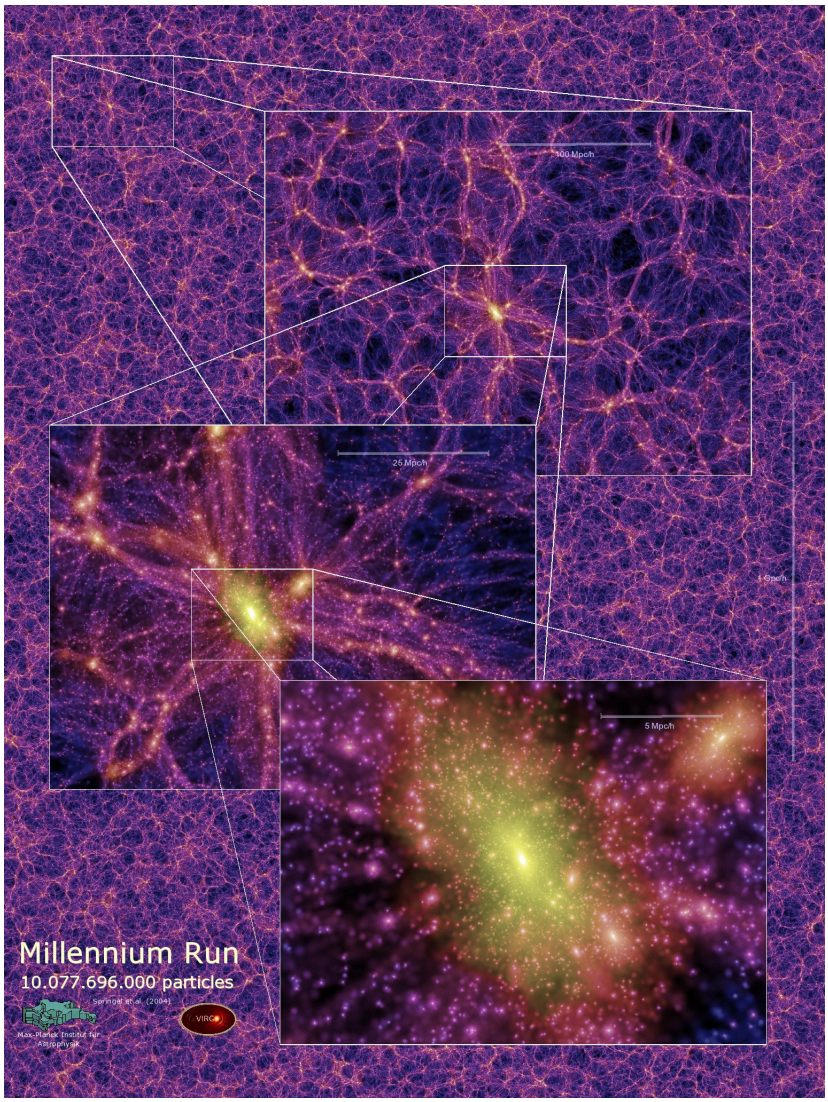

Figure 2.24: Graphical output of the millennium simulation showing structure formation on different scales [348].

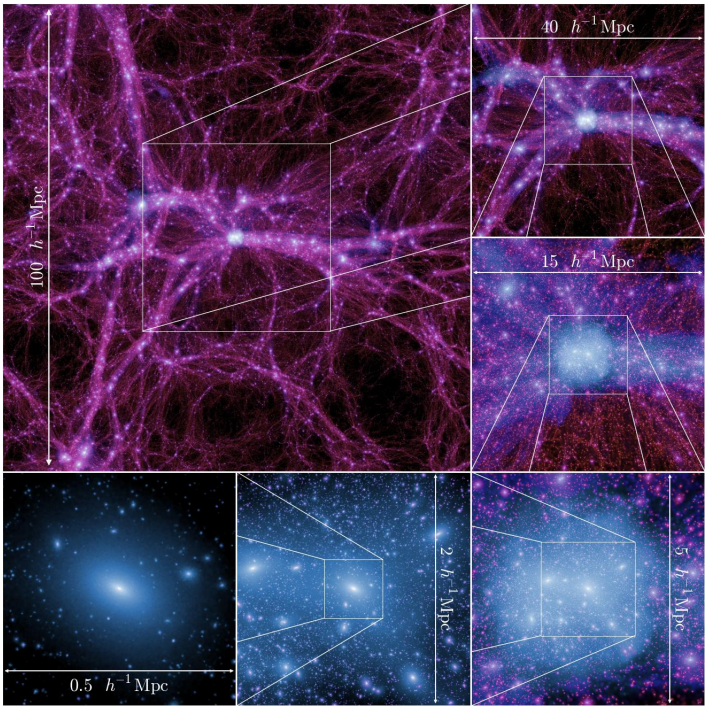

Figure 2.25: Graphical output from the second millennium simulation performed with higher spatial and mass resolution [97].

and would have a number density similar to photons (such as eV-mass neutrinos).

- **Warm dark matter:** If the particles de-couple sufficiently early the relative abundance of photons can be boosted by annihilations other than just $e^{\pm}$. The mass range here would be around $1 - 10$ keV.

- **Cold dark matter:** If the particles de-couple when nonrelativistic the number density is exponentially suppressed, for a freeze-out temperature of ~ 1 MeV this is $n \sim e^{-M}$ and falls with increasing mass and cannot correspond to known neutrinos purely due to this consideration.

Large scale structure can constrain the quantities of dark matter in each form. Since structure formation is seen very early on in the Universe this indicates that dark matter (or the majority of it) is not hot. This matches simulation results which show sharp features with weak filaments (from bottom up structure formation) rather than weak features along the filaments (top down formation). Warm and cold dark matter become distinguishable at smaller scales such as large galaxies. There are some suggestions that dark matter in galaxies appears warmer than first thought [193]. One reason for this is the apparent lack of smaller satellite galaxies orbiting larger galaxies as part of the bottom up structure formation process. Cold dark matter remans the favoured candidate from the CMB power spectrum and it is possible that the smaller satellite galaxies are not luminous enough to have yet been observed, although this is an active area of research.

2.4 Particle Physics Beyond the Standard Model

It seems natural that the dark matter should consist of as yet undiscovered particles. Particle physics may then be used to guide the search for dark matter. As baryonic dark matter would violate Big Bang nucleosynthesis models, as discussed in Section 2.2.1.3, a non-baryonic candidate is required. The current

theory describing particle physics is known as the standard model (SM).

The SM of particle physics, developed over the 20$^{\text{th}}$ century, is very successful at describing the known particles and their interactions. The SM is a quantum field theoretical model consistent with both quantum mechanics and special relativity. Figure 2.26 shows a summary of known SM particles. In addition to the particles shown there is an additional particle required to complete this model, known as the Higgs boson, whose discovery is the main aim of both the TeVatron and the LHC[2]. This particle, thought to be responsible for the existence of mass structure, is associated with a Higgs field in which massive particles interact and gain mass [209], and is a scalar field with a non-zero vacuum expectation value. This particle is also required within the electroweak theory to prevent the s-wave scattering amplitude of $e^+e^- \rightarrow W^+W^-$ from diverging. The general form for the observable mass of the Higgs particle is given by:

$$M_H^2 = (M_H^2)_0 + \frac{kg^2\Lambda^2}{16\pi^2} \tag{2.31}$$

where the second term is the one loop correction in which k is a constant, g is the electroweak coupling and Λ is the energy scale of new physics. Figure 2.27 shows the bounds of the Higgs mass. This particle is expected to be discovered at the LHC. Section A.13 contains more discussion on particle physics beyond the SM.

2.4.1 Supersymmetry

Independently of astronomical observations of dark matter, there are potential solutions to the outstanding problems with the SM that naturally lead to new stable particles. As these new particles could also account for the dark matter required by astronomical observations, these theories are strongly favoured and are used as a guide when designing experiments to detect dark matter. SUSY is an ingredient which appears in many theoretical extensions to the SM. This theory postulates that the SM particles have superpartners differing only by a half unit of spin and as such the symmetry relates bosonic integer-spin particles to fermionic

[2]The graviton is also not included. This is a hypothetical particle which mediates the force of gravity.

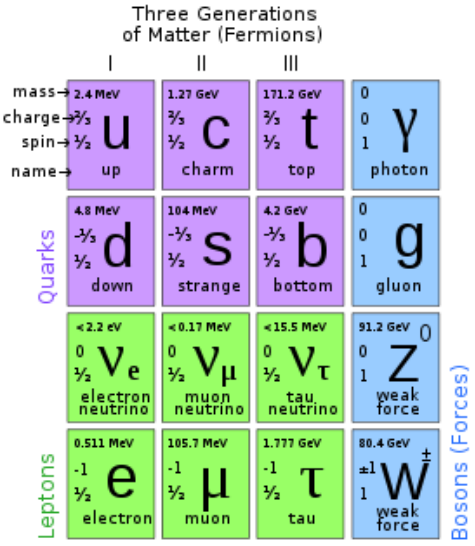

Figure 2.26: The known particles of the standard model of particle physics.

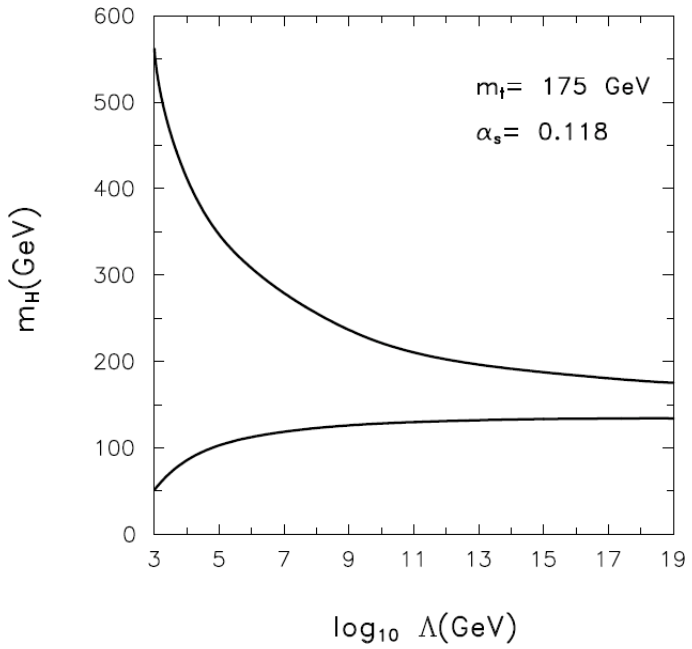

Figure 2.27: Bounds on the Higgs particle mass as a function of Λ for $M_t = 175$ GeV. The stable region is between the two lines. The region above represents phase space where the Higgs would be non-pertubative and the potential cannot be normalised. Below represents phase space where the particle is unstable [5].

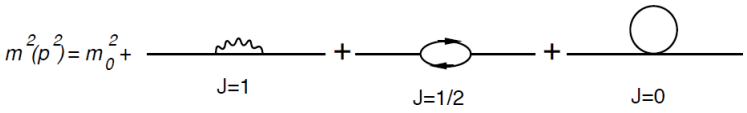

Figure 2.28: Radiative corrections to the scalar mass, image from reference [305].

half-integer-spin particles. The effect of this it to stabilise the radiative corrections that otherwise require fine tuning of high-energy parameters to allow for stable particles. Essentially, the cancellations of basic mass terms by the superpartners remove the sensitivity of the mass to the value of Λ. If supersymmetry exists then it is a broken symmetry as the superpartners have not yet been observed and must have much larger masses than their SM counterparts.

As mentioned previously, scalar mass parameters receive quantum corrections from loops that contain particles of spins $J = 1, \frac{1}{2}$ and 0, as shown in Figure 2.28. The loop integrals are potentially divergent but must be normalised. SUSY provides an alternative to fine tuning to solve the gauge hierarchy. Virtual bosons and virtual fermions contribute with opposite signs and would cancel each other out if there existed a bosonic superpartner for every fermion and a fermionic superpartner for every boson. Such a Fermi-Bose symmetry would relate the fermion and boson spin states via:

$$Q \mid \text{Fermion} >= \mid \text{Boson} > \text{ and } Q \mid \text{Boson} >= \text{Fermion} > \tag{2.32}$$

Where Q is the "supercharge" operator. The Q operators must carry spin $\frac{1}{2}$ which implies supersymmetry is a space-time symmetry. This gives a potential path to quantum gravity.

The new supersymmetric Yukawa interactions, from SUSY, violating baryon and lepton number lead to rapid proton decay. It is possible to set the Yukawa couplings to 0 and this forces conservation of baryon and lepton number, and so agrees with observations, by introducing a new symmetry term. For SUSY this is known as R-Parity and is expressed as:

$$R = (-1)^{3(B-L)+2S} \tag{2.33}$$

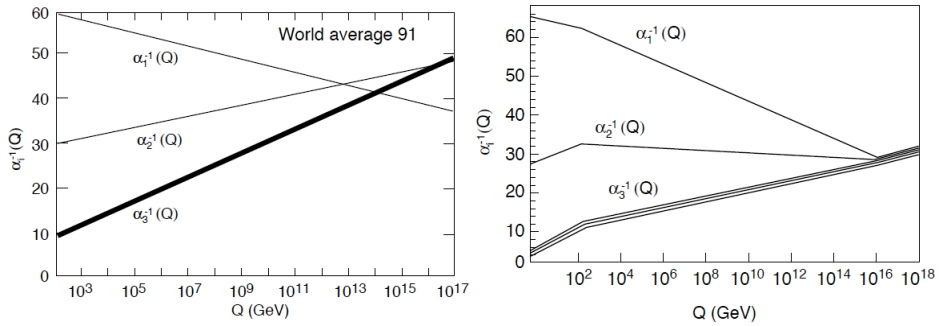

Figure 2.29: The unification of the SM forces. The three gauge couplings, g_3, g and g' representing the gauges $SU(3)_C$, $SU(2)_L$ and $U(1)_Y$ respectively do not unite for the non-SUSY SM case shown on the left. The right hand shows the SUSY case where strong force ($\alpha_s = \frac{g_3^2}{4\pi}$), electromagnetic force ($\alpha_{EM} = \frac{e^2}{4\pi}$) and weak force ($\sin\theta_W{}^2 = \frac{(g')^2}{g^2+(g')^2}$) unite into a single force at $\mu \simeq 2^{16}$ GeV [162, 84].

where B is the baryon number, L is the lepton number and S is the spin. Standard model particles have $R = 1$ and SUSY particles have $R = -1$. Conservation of R-Parity forbids SUSY particles from decaying into SM particles and so unstable SUSY particles decay to lighter SUSY particles, possibly to just one stable SUSY particle which is prevented from further decay by energy and R-Parity conservation. This particle is known as the lightest supersymmetric particle (LSP) and is stable, colourless and neutral making it an excellent candidate for dark matter.

CP violation by SUSY theories tend to produce larger neutron dipole moments than SM expectations. Consequently measurements of the neutron dipole moment can be used to constrain SUSY models. Several new experiments are aiming to improve sensitivity enough to put strong constraints on current SUSY models, such as the Cryogenic Neutron Electric Dipole Moment (cryoEDM) experiment [66]. SUSY extensions to the SM may also be tested by measurements of the proton decay lifetime, estimated to be $10^{34} - 10^{38}$ years [298]. More detail on SUSY models is given in Section A.14.

2.4.1.1 Neutralinos

There are a number of dark matter candidates produced by SUSY theories that would be suitable to explain cosmological observations. In some models the Gravitino [164], sneutrino [84] or gluino [207] could be the LSP. In MSSM the lightest neutralino, $\tilde{\chi}_1^0$, sometimes denoted only by χ, is the LSP. The linear combination of neutral gauge and Higgs bosons (Wino, Bino and Higginos) form four neutralinos, these are colourless and electrically neutral. Further details are provided in Section A.15.

All SUSY particles would have been produced in thermal equilibrium during the Big Bang via ($l\tilde{l} \rightarrow \chi\tilde{\chi}$) and annihilate via ($\chi\tilde{\chi} \rightarrow l\tilde{l}$) where l is a lepton. In many cases the neutralino is a Majorana particle and is able to self annihilate ($\chi = \tilde{\chi}$). The number density of neutralinos is described by the boltazmann equation, 2.22. Using typical weak-scale values, the freezeout temperature is $T_f \simeq \frac{m_\chi}{20}$. The entropy per comoving volume remains constant after this time so that $\left(\frac{n_\chi}{s}\right)_f = \left(\frac{n_\chi}{s}\right)_0$ where $s \simeq 0.4 g_\star T^3$, $g_\star$ is the effective number of relativistic degrees of freedom and the subscripts 0 and f denote the values now and at freezeout [232]. Using the freezeout condition for the annihilation rate $\Gamma = n_\chi \langle \sigma v \rangle = H$ this gives:

$$\left(\frac{n_\chi}{s}\right)_0 \simeq \frac{10^{-8}}{\left[\left(\frac{m_\chi}{\mathrm{GeV}}\right)\left(\frac{\langle \sigma v \rangle}{10^{-27}\ \mathrm{cm^3 sr^{-1}}}\right)\right]} \tag{2.34}$$

The current entropy density and critical density are $s_0 \simeq 4000\ \mathrm{cm}^{-3}$ and $\rho_c \simeq 10^{-5} h^2\ \mathrm{GeV\ cm}^{-3}$ so that the present neutralino density would be given by:

$$\Omega_\chi h^2 = \frac{m_\chi n_\chi}{\rho_c} \simeq \frac{3 \times 10^{-27}\ \mathrm{cm^3 s^{-1}}}{\langle \sigma v \rangle} \tag{2.35}$$

which is almost independent of the neutralino mass and inversely proportional to the annihilation cross section. For weakly interacting particles the annihilation cross section can be estimated as $\langle \sigma v \rangle \sim \alpha^2 (100\ \mathrm{GeV}^{-2})$ [232]. For $\alpha \sim 10^{-2}$ this gives $\langle \sigma v \rangle \sim 10^{-25}\ \mathrm{cm^3 s^{-1}}$ which gives a neutralino density between $0.06 \leq \Omega_\chi \leq 0.35$, in good agreement with observations showing $\Omega_{CDM} = 0.227$.

This remarkable match between astronomical observations of dark matter density and predictions from particle physics has motivated much study of SUSY.

The theoretical parameter space is well defined and experimental results from particle colliders, direct searches and indirect searches are currently being utilised to explore this parameter space. Given the theoretical predictions of the most likely LSP properties the required sensitivity for a discovery has now been reached by experiments such as the LHC and the next generation of ∼ton scale direct detection searches.

2.4.2 Axions

The Quantum ChromoDynamics (QCD) Lagrangian includes a CP-violating term with an effective strong-CP violating parameter Θ. This parameter may lie anywhere in the range $-\pi \leq \Theta \leq \pi$. Measurements of the neutron dipole moment indicate that $\mid \Theta \mid \leq 10^{-10}$ [65], although a value of ~ 0 is allowed it seems unnatural that this should occur naturally with no mechanism to set Θ to the observed value. A solution to this problem leads to the postulation of the axion, a potential dark matter candidate. More details on axion dark matter is given in Section A.16.1.

2.5 Conclusions

Current astronomical surveys yield data that are well fitted by the ΛCDM model. This model includes a significant matter component, $\Omega_m \approx 0.27$, the majority of which has not been observed by any technique other than those involving gravity; hence the main matter component is dark. Nuclear physics calculations of Big Bang nucleosynthesis indicate that most of the matter in the Universe is non-baryonic and has little or no interaction with baryonic matter apart from via gravity. Current particle physics theories naturally provide additional weakly interacting particles in the correct quantities to account for the observed cosmological density. These independent results all lead to similar conclusions which indicate that most of the matter in the Universe is in the form of Weakly Interacting Massive Particles (WIMPs). Leading theories predicting the form of the dark matter are provided by SUSY extensions to the SM, although there are other theories as discussed in Section A.16. Carefully constructed detectors may

be able to directly observe the rare interactions of these particles with ordinary matter and thus begin to solve one of the greatest mysteries in physics.

Chapter 3

Detecting dark matter

3.1 Indirect Detection

Many different techniques fall into the category of indirect methods of detecting dark matter. These methods all rely on observations of the secondary effects of dark matter interactions. To date, indirect methods include the only experiments to have robustly confirmed observations of dark matter.

3.1.1 Gravitational Effects

The gravitational effects of dark matter were how the phenomenon was first discovered. Experiments looking at gravitational phenomena caused by dark matter have so far proved the only successful method of detection and as such were covered in detail in Section 2.3. This is still an active area of research and there are several missions in progress to improve scientific knowledge in this area. The Planck satellite is currently mapping the CMB with high resolution and sensitivity, down to 5 arcmin over higher frequencies. Several performance and results papers have been published at the time of writing, with the main result expected in 2013 [359].

The Cluster Lensing And Supernova survey with Hubble (CLASH) [121] collaboration will use both strong and weak gravitational lensing to measure the dark matter content of the Universe. This mission will be utilising the panchromatic imaging capabilities of the recently upgraded Hubble space

telescope to perform this search. This mission will also observe type 1a supernovae out to a redshift of ∼2 in order to measure the strength of dark energy over the history of the Universe. This mission is currently in progress and the complete dataset is expected to be released by mid 2013 [303].

The Large Synoptic Survey Telescope (LSST) will perform weak lensing surveys. As described in Section 2.3, these are used to map the distribution of matter in the Universe. Although the project is still in the design phase at the time of writing the first mirrors have been cast and first light is expected 4 years after construction begins, with the 10 year survey expected to begin near the end of the decade [389]. The Canada-France Hawaii Lensing Survey (CFHTLenS) is also mapping the matter distribution of the Universe with a weak lensing survey using a 155 square degree camera [210]. The largest survey is the Sloan Digital Sky Survey (currently in phase three, SDSS-III). This survey uses a 2.5 m optical telescope, between 2000 and 2008 it covered over a quarter of the sky (almost a million galaxies). The survey is ongoing with the 9^{th} data release due by 2014 [317].

3.1.2 Dark Matter Annihilation

If dark matter is a Majorana particle the annihilation products from self interactions could be detected. As described in Section 2.4, the dark matter particles would be their own anti-particles. Regions with a higher density of dark matter, such as the centre of galaxies or massive starts, should have an excess of these signals. The dark matter self annihilation signature could be in the form of photons or baryonic particles and there are several experiments searching for each type of signal.

The light emitted by the annihilation of two such heavy particles would be extremely high energy and appear in the γ-ray end of the electromagnetic spectrum. Although a continuous spectrum is possible there should be a monochromatic component from the decays via $\chi\chi \rightarrow \gamma\gamma$ and $\chi\chi \rightarrow Z^0\gamma$. The photon energy would be $E_\gamma \approx m_\chi c^2$ with a peak wavelength given by $\lambda = \frac{hc}{m_\chi} = (1.2 \times 10^{-6}\text{Å}) m_{10}^{-1}$ where $m_{10} \equiv m_\chi c^2/(10\ \text{GeV/c}^2)$ [227]. The standard

deviation can be related to the velocity dispersion of the dark matter particles by $\sigma_\lambda = \frac{2v_c\lambda}{c}$. For the standard value of $v_c \sim 220\mathrm{km\,s^{-1}}$ and $m_{10} \sim 1$ this is about 10^{-9} Å. The luminosity form a dark matter halo is given by:

$$L_\gamma = 2m_\chi c^2 \langle\sigma v\rangle \mathcal{P} \tag{3.1}$$

where $\langle\sigma v\rangle$ is the annihilation cross-section and $\mathcal{P} \equiv \frac{1}{m_\chi^2}\int \rho_\chi^2(r) 4\pi r^2 dr$ depends on the dark matter density distribution $\rho_\chi(r)$ [227].

There are currently several telescopes searching for photon signals from either the continuous spectrum, which is expected to be about 2 orders of magnitude lower than the Galactic background but with a sharp increase towards the Galactic centre, or discrete lines. The space telescopes currently operating are the Fermi γ-ray space telescope [67] and the INTErnational Gamma-Ray Astrophysics Laboratory (INTEGRAL) [122]. There are also several ground based instruments such as the Very Energetic Radiation Imaging Telescope Array System (VERITAS) [386], the High Energy Stereoscopic System (HESS) telescope array [11, 10] and the Major Atmospheric Gamma-ray Imaging Cherenkov Telescopes (MAGIC) observatory [30]. The upcoming Cherenkov Telescope Array (CTA) will extend the search out to higher energies [216, 99].

There are also experiments searching for particles created by dark matter annihilation. These include; the balloon borne experiment the Advanced Thin Ionization Calorimeter (ATIC) [114], the space instruments the Alpha Magnetic Spectrometer (AMS2) [29] and the Payload for Antimatter Matter Exploration and Light-nuclei Astrophysics (PAMELA) experiment [300]. Dark matter annihilation in the sun or the earth could give rise to an excess of upward going muon neutrinos through the earth, these neutrinos would have energies of $\sim \frac{1}{3}$ of the WIMP mass and so would not be confused with standard solar neutrinos. There are several experiments searching for this signal, notably the balloon borne Antarctic Impulse Transient Antenna (ANITA) experiment, the IceCube experiment [306], the Sudbury Neutrino Observatory (SNO+) [17] and the Astronomy with a Neutrino Telescope and Abyss environmental RESearch (ANTARES) experiment [15]. The Pierre Auger Observatory is also searching for a dark matter signal in cosmic rays striking the earths atmosphere [12].

Recently data from the Fermi Large Area Telescope show evidence of a γ-ray line at $\sim$130 GeV. The significance of this line emission is 3.3σ, although in regions close to the Galactic center this increases to 4.6σ [384]. If this line were due to dark matter self-annihilations to γ-rays then this would imply a dark matter particle of mass $129.8 \pm 2.4^{+7}_{-13}$ GeV/c^2 with an annihilation cross-section of $\langle\sigma v\rangle_{\chi\chi\to\gamma\gamma} = (1.27 \pm 0.32^{+0.18}_{-0.28} \times 10^{-27})$ cm^3 s^{-1} using the Einasto dark matter profile [301]. Analysis presented in Reference [183] suggests that this is just below the limit of the current best direct detector, XENON100, but will be within range of future detectors with larger target masses.

3.1.3 Creating Dark Matter

Another route to discovering dark matter particles is to create them. Large accelerators such as the LHC at CERN could produce new dark matter particles [107]. The signature for these would be missing transverse energy (MEt) where energetic jets, a mono-jet, leptons or photons show a large imbalance in the momentum flow of the collision. If this signal were detected then the size of the momentum imbalance can be used to infer the properties of the dark matter created and so this method could be very complementary to direct detection searches. A possibility is that SUSY particles may be created at CERN which may include the dark matter particles sought by direct and indirect experiments. Given the recent announcement of the potential discovery of the Higgs boson at $\sim$125 GeV/c^2 [365, 366] the parameter space for SUSY models is constrained. However it may be unnatural to expect the gaugino masses to be unity at the GUT scale [110]. If the LHC Higgs is confirmed and non-universal gaugino masses are considered then the current non-detection of SUSY at the LHC is to be expected.

3.2 Direct Detection

The review provided here is guided by References [232] and [256]. For a more in-depth review see [232, 256] and references therein. Assuming that WIMPs are the solution to the dark matter problem, and they have a cosmological density of order unity, then they can be expected to have a small but finite coupling to ordinary matter, as discussed in Section 2.2.1.3. This coupling stems from the

expectation that dark matter in the early Universe should have annihilated to produce the astronomical observations we see today[3]. By crossing symmetry, the amplitudes of WIMP annihilation and WIMP interaction with baryonic matter are related. Detecting the signals produced by these interactions is the main focus of many experiments currently operating in labs all around the world. The weak interactions would primarily be with the nucleus of the target material. In the non-relativistic limit they would couple to either the mass (scalar interaction) or the spin of the nucleus (axial-vector interaction) [194] known as spin-independent and spin-dependent interactions respectively. Spin-independent scattering is generally more sensitive due to the coherent summation of scattering amplitudes from each nucleon in the nucleus, whereas the spin-dependent coupling would only be to an odd unpaired nucleon as spins from pairs would cancel out. The differential energy spectrum of such nuclear recoils is expected to be featureless and of the form:

$$\frac{dR}{dE_R} = \frac{R_0}{E_0 r} \exp^{-E_R/E_0 r} \tag{3.2}$$

where the kinematic factor $r = \frac{4M_\chi M_t}{(M_\chi + M_t)^2}$, E_R is the recoil energy and E_0 is the most probable kinetic energy of incident dark matter particles of mass M_χ. This simple form would need to be modified to account for the properties of real dark matter detectors to be of use in dark matter searches. In practice there are several important corrections:

1. The peculiar motion of the detector must be accounted for. This includes the motion of the solar system through the galaxy and also the Earths relative motion to that of the Sun, $v_\oplus = 244 + 15 \sin(2\pi y)$ km/s, where y is the time elapsed since March 2^{nd} in years.

2. The true recoil energy will differ from the observed recoil energy due to the relative efficiency factor between WIMP recoils and background recoils, as described in detail in Section 8.2.2.

3. Instrumental resolution and threshold effects.

4. A finite energy dependent form factor (< 1) due to the finite size of the nucleus.

[3]In fact the annihilation cross-section appears to be close to the weak scale, implying that the dark matter particles should interact weakly. This is known as the "WIMP miracle".

Accounting for these factors Equation 3.2 becomes:

$$\left.\frac{dR}{dE}\right|_{observed} = R_0 S(E) F^2(E) I \tag{3.3}$$

where $F(E)$ is the energy dependent form factor, $S(E)$ is the energy dependent spectral function accounting for points $1 \rightarrow 3$ and I is the interaction function accounting for the difference between spin-dependent and spin-independent interactions [256].

3.2.1 WIMP-nucleon Cross-Section

The dominant factor deciding if an experiment is able to detect a dark matter signal is the size of the WIMP-nucleon interaction cross-section. Until a detection can be confirmed, experiments produce limit plots to show the sensitivity achieved in terms of this value. The cross-section has two components:

$$\sigma(qr_n) = \sigma_0 F^2(qr_n) \tag{3.4}$$

where the first, σ_0, is the interaction cross-section at zero momentum transfer and contains all the information about the specific interaction. The second, F, is the nuclear form factor and depends only on the momentum transfer. The momentum transfer $q = \sqrt{2M_t E_R}$ is multiplied by the effective radius r_n so that qr_n is a dimensionless quantity[3]. M_t is the target mass.

For a given theoretical particle the properties of the interaction can be predicted from current knowledge of particle physics. For example, since a neutralino would be composed of a combination of super-symmetric counterparts to standard model particles, the weak interactions they would have with quarks and gluons can be described by an effective Lagrangian containing the relevant information and predictions. The cross-section (Equation 3.4) can be calculated in stages [232]. Firstly the interactions between WIMPs and quarks and gluons are considered. Since diagrams with internal quark loops appear, the couplings for all six quarks must be considered along with the gluon couplings, rather than just

[3]Where natural units are considered, i.e. $\hbar = 1$

couplings to the up and down quarks found in target nucleons. Although there are many experimental constraints narrowing the parameter space somewhat, the parameters of the supersymmetric model used introduces the largest uncertainty in the cross-section. The next step is to translate these interactions into nucleon interactions using matrix elements of quark and gluon operators in a nucleon state, using hadronic matrix elements from scattering data wherever possible. Finally the nuclear wave functions are included by the nuclear form factor. The nuclear form factor is used to model the coherent loss of cross-section for interactions between WIMPs and nuclei [166].

Accounting for the first two steps listed above gives σ_0. It is a function of the Fermi weak-coupling, G_F, describing the strength of the interaction and of the enhancement factor, C_A carrying information from the particle physics model describing the type of interaction (axial-vector or scalar) and information about the quark and nucleon distribution:

$$\sigma_0 = 4G_F^2 \mu_A^2 C_A \tag{3.5}$$

where $\mu_A = \frac{m_t m_\chi}{m_t + m_\chi}$ gives the reduced mass of the WIMP-nucleon system.

There are several contributions to the interaction cross-section such as tensor, vector, axial-vector, scalar and pseudo-scalar which add differently inside the nucleon. Astronomical observations favour dark matter interactions occurring in the extreme non-reletavistic regime which simplifies the interactions greatly. The axial-vector current becomes the interaction between the WIMP spin and the quark spin. The tensor current has the same form as the scalar current, as would the vector current, however since neutralinos are Majorana fermions they do not have vector interactions. This leads to only two dominant contributions to the WIMP-nucleon cross-section which need to be considered. The scalar spin-independent interaction where the WIMP couples to the mass of the nucleons in the target nucleus and the axial-vector spin-dependant interaction where the WIMP couples to the spin of any unpaired nucleon within the target nucleus.

The form factor describes the spatial extent of the target nucleus. It acts as a correction to the simple Rutherford scattering case which becomes less accurate

with increasing momentum transfer q. For large values of q the differential cross-section becomes:

$$\left(\frac{d\sigma}{\Omega}\right) = \left(\frac{d\sigma}{\Omega}\right)_R \cdot |F(q^2)|^2 \tag{3.6}$$

where the subscript $_R$ is for Rutherford scattering, $F(q^2)$ is the Fourier transform of the mass (or charge) density of the target nucleus, σ is the scattering cross-section and Ω is the scattering angle. The Helm approximation of the form factor uses a "folded" distribution [208]. This approximation breaks the nucleus up into two components, treating the nucleus as hard sphere surrounded by a softer skin. For spin-dependent interactions the Fourier transform approximating a single outer shell nucleon is:

$$F^2(qr_n) = j_0(qr_n) = \frac{\sin(qr_n)}{qr_n} \tag{3.7}$$

however this approximation is quite poor if the odd nucleon is not in an s-state. The Fourier transform for a solid sphere used to approximate spin-independent interaction with the whole nucleus is:

$$F^2(qr_n) = \frac{3j_1(qr_n)}{qr_n} = \frac{3[\sin(qr_n) - qr_n\cos(qr_n)]}{(qr_n)^3} \tag{3.8}$$

The Helm approximation used for the xenon target in this experiment is:

$$F^2(qr_n) = \frac{3j_1(qr_n)}{qr_n}\exp^{-(qs)^2} \tag{3.9}$$

the nuclear radius, r_n, used for xenon is 5.6 fm. The skin thickness parameter, s, used for xenon is 0.9 fm. Figure 3.1 shows how the form factor varies with recoil energy for several different target nuclei. Other form factors are available, for example those presented in Reference [154] and [165].

3.2.2 Spin-independent Interactions

The paper [232] was used as a guide for this section. The scalar neutralino-nucleon cross-section has contributions from squark exchange and Higgs exchange, as shown in figures 3.2 and 3.3, giving rise to couplings to quark currents and one-loop amplitudes for interactions with gluons. A notable difference between

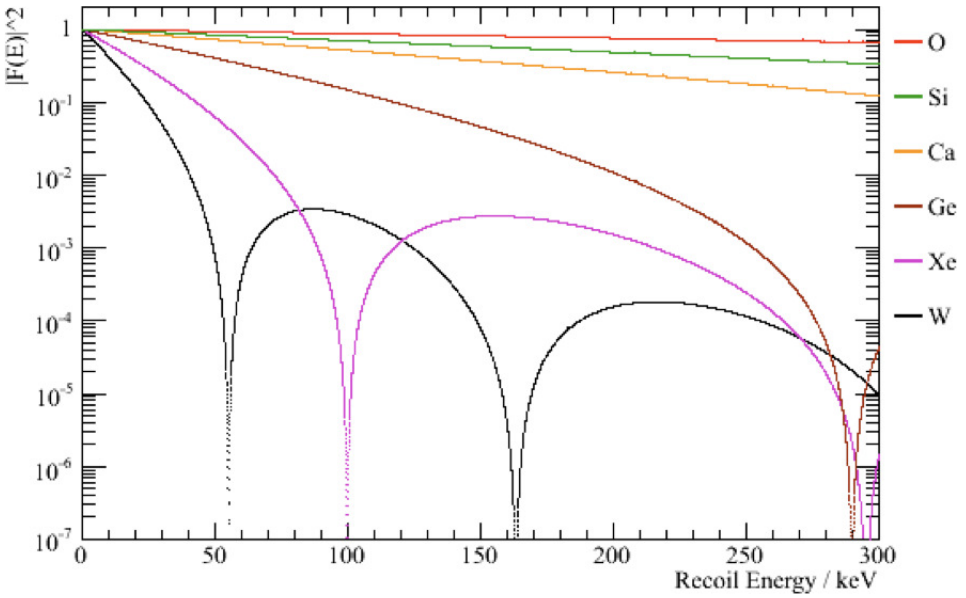

Figure 3.1: Measurements of the form factors of several common dark matter detector target nuclei. The characteristic minima for xenon can be seen at recoil energies of 100 keV and $\sim$ 300 keV. Despite the form factor for xenon being relatively low in the region of interest (up to 20 keV electron-recoil equivalent energy (keV_{ee})) its large mass compensates for this through the A^2 term in the scalar interaction in Equation 3.10. Image obtained from [327].

the scalar and axial-vector interactions is the coherent enhancement factor. This benefits high mass targets as the amplitudes from the scalar coupling to the mass add coherently to give a boost to the cross-section that scales with the number of nucleons as:

$$\sigma_{\chi-T} \propto A^2 \sigma_{\chi-n} \tag{3.10}$$

the spin-independent cross-section, σ_{SI}, from Equation 3.5 becomes:

$$\sigma_{SI} = 4G_F^2 \mu_A^2 C_{SI} \tag{3.11}$$

where the spin-independent enhancement factor, C_{SI} is given by:

$$C_{SI} = \frac{1}{\pi G_F^2}(Z f_p + (A - Z) f_n)^2 \tag{3.12}$$

where f_p and f_n are the effective WIMP-proton and WIMP-neutron couplings given by:

$$f_{p,n} = \sum_{q=u,d,s} f_{T_q}^{(p,n)} a_q \frac{m_{p,n}}{m_q} + \frac{2}{27} f_{TG}^{(p,n)} \sum_{q=c,b,t} a_q \frac{m_{p,n}}{m_q} \tag{3.13}$$

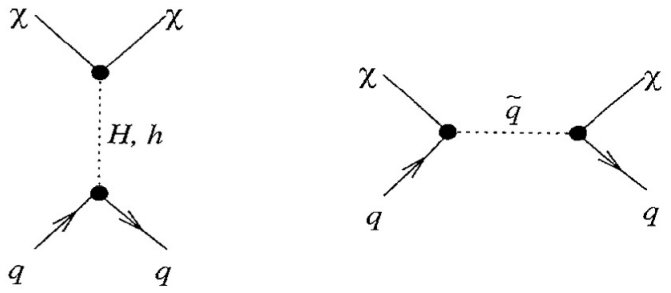

Figure 3.2: Feynman diagrams showing contributions to the spin-independent elastic scattering of neutralinos from quarks. Image obtained from [232].

the WIMP-quark couplings are represented by a_q, $f_{T_q}^{(p,n)}$ denotes the quark content of the nucleon. The first term of Equation 3.13 corresponds to the interactions with quarks shown in Figure 3.2. The second term corresponds to the interactions with gluons, as in diagram 3.3, where $f_{TG}^{(p)} = 1 - f_{T_u}^{(p)} - f_{T_d}^{(p)} - f_{T_s}^{(p)} \approx 0.84$ and similarly $f_{TG}^{(n)} \approx 0.83$ [218].

3.2.3 Spin-dependent Interactions

The axial-vector contributions to the cross-section come from Z^0 and quark exchange, shown in Figure 3.4. Equation 3.2 becomes:

$$\sigma_{SD} = 4G_F^2 \mu_A^2 C_{SD} \tag{3.14}$$

where the spin-dependent enhancement factor is given by:

$$C_{SD} = \frac{8}{\pi} \Lambda^2 J(J+1) \tag{3.15}$$

and

$$\Lambda = \frac{1}{J} \left[a_p \langle S_p \rangle + a_n \langle S_n \rangle \right] \tag{3.16}$$

where $\langle S_p \rangle = \langle N \mid S_p \mid N \rangle$ is the expectation value of the spin content of the proton group in the nucleus, and similarly for $\langle S_n \rangle$. Typically it is assumed that all the nuclear spin is carried by the "odd group", either the protons or neutrons depending on which is most unpaired. The value of the odd-group spin is found

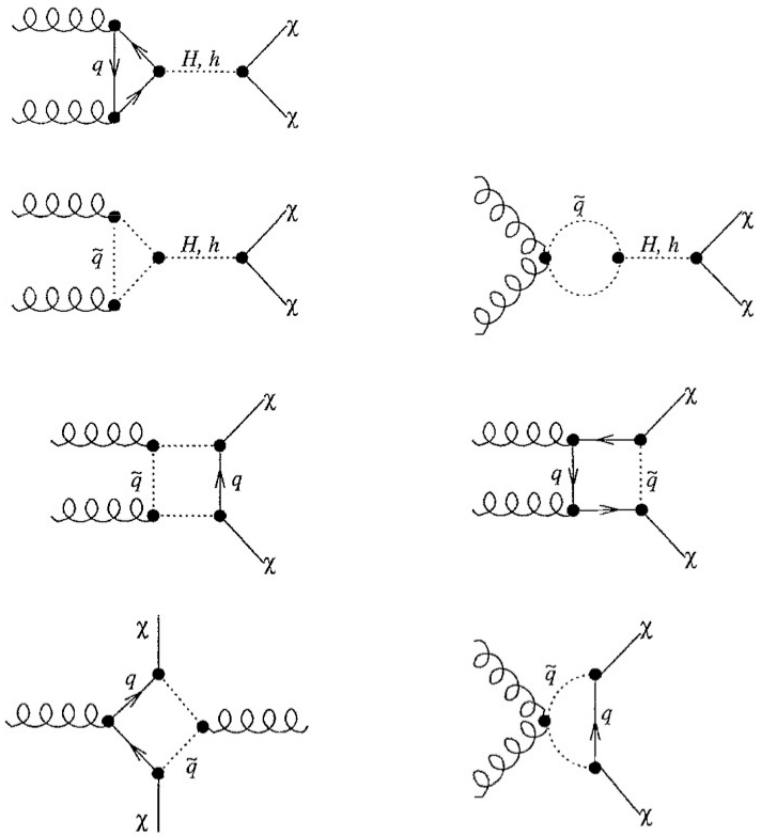

Figure 3.3: Feynman diagrams showing contributions to the spin-independent elastic scattering of neutralinos from gluons. These contribute to the scalar elastic-scattering amplitude from interactions with nuclei. Image obtained from [232].

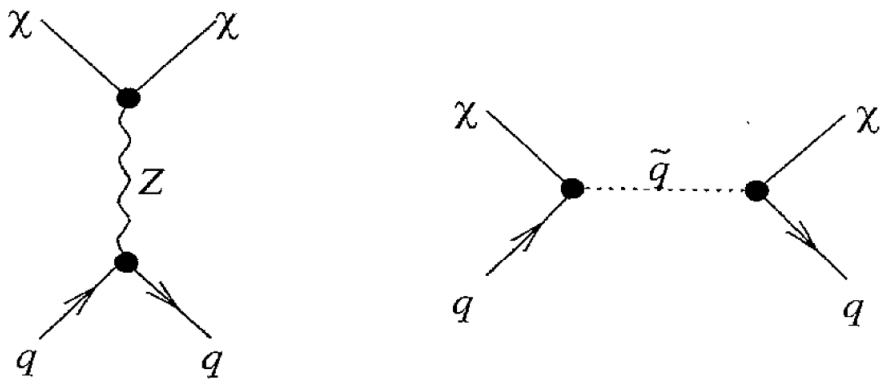

Figure 3.4: Feynman diagrams sowing contributions to the spin-dependent elastic scattering of neutralinos from quarks. Image obtained from [232].

by measuring the nuclear magnetic moment:

$$\langle S_{odd} \rangle = \frac{\mu - g^l_{odd} J}{g^s_{odd} - g^l_{odd}} \tag{3.17}$$

where odd stands for either the proton or neutron depending on the make up of the nucleus involved, and J is the spin of the nucleus. The values for protons are $g^s_p = 5.586$ and $g^l_p = 1$. The values for neutrons are $g^s_n = -3.826$ and $g^l_n = 0$ [232]. For some elements these values give rather poor estimates and more detailed calculations are needed. For example for ^{131}Xe the interacting-boson-fermion odd-group model [235, 225] gives $\langle S_p \rangle = -0.041$ and $\langle S_n \rangle = -0.236$.

3.2.4 Dark Matter Detectors

The energy deposited by the WIMP interactions varies with the WIMP mass, with a maximum where the WIMP mass is equal to the target mass. The recoil energy seen by the detector is given by:

$$\langle E_R \rangle = \frac{2 v^2_\chi m_t}{(1 + \frac{m_t}{m_\chi})^2}. \tag{3.18}$$

For most detectors the apparent observed energy deposited by a recoil, E_v, is some function of the true energy deposition, E_R. The factor relating these

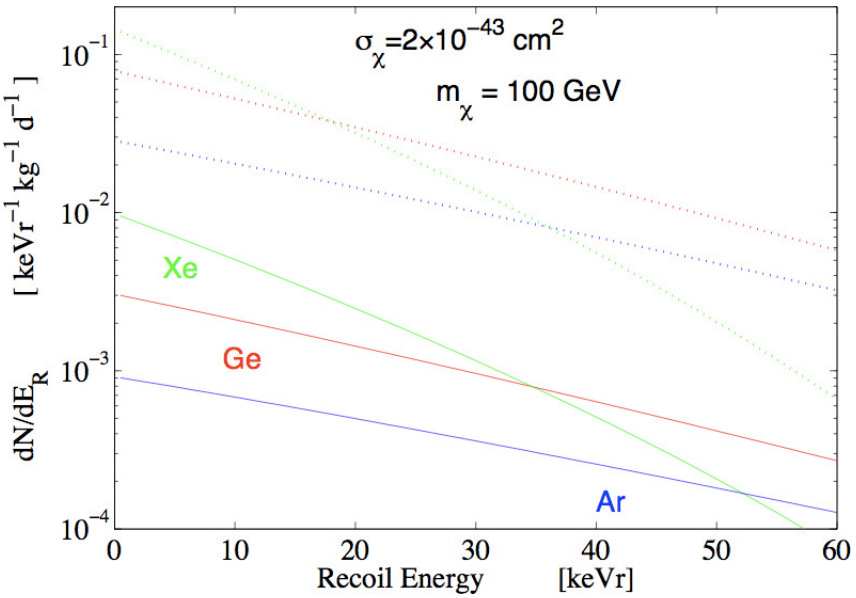

Figure 3.5: The expected differential energy deposition rates for some common targets. The solid line shows the differential rate and the dashed line shown the rate integrated over all energies. Image obtained from [339].

two values is known as the 'quenching factor' and it may vary with both energy deposition and interaction type. The differential rate is given by:

$$\frac{dR}{dE_R} = f_n \left(1 + \frac{E_R}{f_n}\frac{df_n}{dE_R}\right)\frac{dR}{dE_v} \tag{3.19}$$

where the terms are as defined in previous equations in this chapter.

The expected rates for some common target materials are shown in Figure 3.5. As an example, for a 100 GeV c^{-2} WIMP mass with a Ge target where the WIMP-nucleon cross-section is $\sigma_{\chi-n} = 2 \times 10^{-7}$pb the rate above a 10 keV threshold is $\sim 5 \times 10^{-2}$ kg^{-1} day^{-1}, which would give about 1 interaction per 20 kg per day.

When the energy deposited drops below a threshold energy there is expected to be a rapid drop in ionisation and/or scintillation efficiency. The threshold energy is the excitation energy required to produce ionisation, E_g. For nuclear

recoils this threshold energy is of the order E_c where:

$$E_c = \frac{m_t}{4m_e} E_g \tag{3.20}$$

where m_e is the mass of an electron.

Experiments designed to detect dark matter directly must take into consideration the key factors discussed in this section. The recoil rate is expected to be maximal at low energies so they must have a very low energy threshold. Heavy target nuclei are preferred as they both maximise the kinematic factors and the scalar interaction cross-section, however lighter targets are preferred if the WIMPs are lighter than the currently favoured theory suggests. Including isotopes with net spin gives sensitivity to spin-dependent interaction. Also the low interaction rate means that the background must be eliminated as far as possible. For this reason most detectors now use two channels to measure the recoil energy which provides good discrimination between event types. Another potential method of discriminating between electron and nuclear recoils is by using timing information from the pulse shape, although this method provides weaker discrimination than using multiple channels. This is further discussed in Section 4.3. Neutrons are a particularly problematic background for most dark matter detectors as low energy elastic scattering interactions from neutrons are expected to populate the same phase space as WIMP interactions. As such, dark matter detectors must be manufactured from very radio-pure materials. Muon induced neutrons are another potential threat, although cosmic rays themselves are easily identified and eliminated as dark matter candidate events, a high muon flux may lead to neutron emission via activation or spallation. As such, dark matter detectors are typically located in low background laboratories deep underground to minimise the muon flux. Figure 3.6 shows the muon flux as a function of depth for several of these laboratories.

The most sensitive dark matter detectors are currently divided into two groups, liquefied noble gas detectors and cryogenic detectors. The most popular phenomena utilised for detecting energy deposits are scintillation, ionisation and heat in the form of lattice vibrations (phonons), with most detectors now utilising more than one of these channels concurrently to improve event type

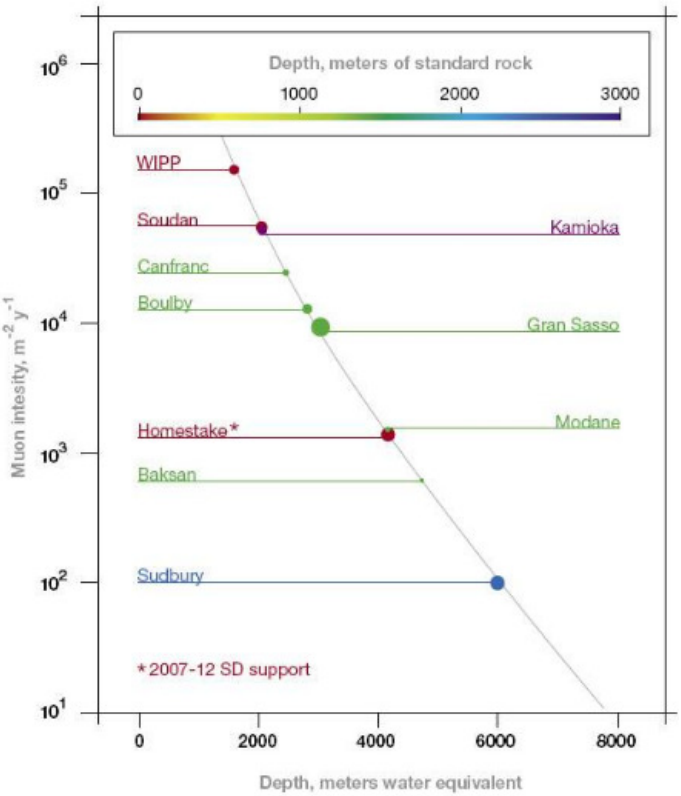

Figure 3.6: The muon intensity as a function of depth for a selection of underground laboratories. Image obtained from [327].

discrimination. A brief summary is given below listing the current dark matter detection experiments in these two categories and several other experiments using other techniques.

3.2.5 Noble Gas Detectors

There are several dark matter detectors using liquified noble gas as a target. Due to the chemical nature of these elements it is possible to achieve the extremely high purity needed to reach the required level of sensitivity. These detectors measure scintillation light, usually with an array of photomultiplier tubes. Some of these detectors also measure the ionisation; this is achieved by applying an electric field to drift the ionisation charge through the liquified noble gas target and measure its size by observing a photoluminescent flash during extraction into a thin gas phase at the surface of the target. An attractive benefit of this type of detector is the relative ease with which it can be scaled up since the targets are essentially a tub of liquid. Also, since the temperature required to liquify the noble gases used is above the boiling point of nitrogen, these detectors do not require the kind of sophisticated cooling systems as cryogenic detectors. The ZEPLIN-III detector falls into this category and this instrument is discussed in detail in Section 4.

The two predecessors of ZEPLIN-III both used liquified noble gas as a target. The ZEPLIN-I [32] and ZEPLIN-II [34] instruments both set world competing limits using liquid xenon targets. The ZEPLIN-II detector was the first noble gas dark matter detector to use 3D position reconstruction, realised by using the time projection chamber (TPC) concept, to fiducialise the target and take advantage of the self shielding properties of liquid xenon. In a TPC an electric field is used to extract some of the ionisation charge from the interaction site in the liquid phase. This charge is then drifted through the liquid phase, by the same electric field, into the gas phase. Thus a signal is produced in each phase of the xenon. If the drift time of electrons through the liquid xenon is known then the time between the two signals gives the depth of the interaction. The other co-ordinates required to reconstruct the position of the interaction are given by the hit pattern observed by the PMT array. Here follows a brief review of some of the current noble gas target detectors.

The XENON collaboration operate liquid xenon target detectors at the LNGS Gran Sasso laboratory. The current detector is the two phase XENON100 detector containing 161 kg of liquid xenon (99 kg veto and 62 kg target). The large target mass and low background of this detector means that it is currently the most sensitive instrument in the world [46, 45]. The instrument uses two arrays containing a total of 242 photomultipliers measuring light in both the fiducial volume and the outer layer of xenon which is used as a veto. The WIMP ARgon Programme (WARP) is also located at the Gran Sasso laboratory. This two phase detector uses a 140 kg argon target [78]. The Large Underground Xenon Detector (LUX) experiment is currently undergoing surface testing and is expected to be deployed underground shortly [23]. This experiment is a two phase detector using a 300 kg active region of liquid xenon observed by 122 2-inch PMTs [275]. The Argon Dark Matter (ArDM) experiment is being deployed at the Canfranc Underground Laboratory (Spain) following expensive testing at CERN. This detector features a 1-tonne double phase chamber with PMT readout of scintillation light and ionisation detection using Large Electron Multipliers in the gas [238]. This two phase detector will use argon as a target [202]. The DARKSIDE experiment, to be located at Gran Sasso, will use 50 kg of depleted argon as a target and serve as a prototype for a ton scale detector [36]. The Xenon MASSive detector (XMASS) is currently operating at Kamioka. Although this experiment only measures scintillation light it is expected to achieve very high sensitivity due to the size of the target ($\sim$ton) [8]. The Dark matter Experiment with Argon and Pulse shape discrimination (DEAP) experiment is currently under construction at SNOlab. This detector is also single phase (scintillation only) but compensates for this with an extremely large target mass of 3.6 tons [95].

3.2.6 Cryogenic Detectors

Cryogenic detectors use crystals cooled to mK temperatures. These super-cooled crystals convert most of the energy transferred by interactions into lattice vibrations (phonons). The energy transferred is not quenched for nuclear recoils (unlike with scintillation and ionisation) and so very low thresholds are possible. Many of these detectors combine phonon detection with a measurement of either

scintillation or ionisation to achieve discrimination. The phonon measurement provides an excellent measure of the energy since it is unquenched, allowing high sensitivity from relatively low mass targets. By combining this measure with a second channel these detectors achieve the highest discrimination of all the detection techniques. Current cryogenic detectors include the Cryogenic Dark Matter Search (CDMS) located in the Soudan underground laboratory [136]. This experiment measures phonons and ionisation from silicon and germanium crystals. The current generation of detectors themselves are know as iZIPs (interleaved Z-sensitive Ionization Phonon), featuring thin film super-conducting technology. Each detector consists of a 600 g germanium cylindrical crystal (r = 76 mm, z = 25 mm) [100]. The electric field used to drift the ionisation to the readout electrodes is strong enough that the CDMS detector may also be used to search for axion signals [19]. The Expérience pour DEtecter Les Wimps En Site Souterrain (EDELWEISS) experiment [55] located in the Modane underground laboratory uses 10 ultra-pure 400 g germanium crystals as a target. These detectors are equipped with thermal "Ge-NTD" (Neutron Transmutation Doping) sensors to enable the measurement of phonons and ionisation in order to achieve discrimination between interaction types. The Cryogenic Rare Event Search with Superconducting Thermometers (CRESST) experiment located at Gran Sasso measures phonons and scintillation from $CaWO_4$ crystals. This modular detector uses 300 g targets with a tungsten superconducting phase-transition thermometer (W-SPT) evaporated onto the surface for photon detection. The resistance of the thermometer is measured by passing a constant current through the readout circuit in which the thermometer is in parallel with a small shunt resistor and the input coil of a dc-SQUID (Superconducting QUantum Interface Device). The dc-SQUID is used to measure the phonons produced by the interaction. The use of scintillating molecules containing three elements adds a further feature to the discrimination power of the instrument, there are six 'bands' to be populated here on the discrimination plot (energy verses ratio of the energy in each channel) consisting of two bands (electron recoil and nuclear recoil) from each element in the crystal [43]. The EDELWEISS and CRESST collaborations are collaborating on the European Underground Rare Event Calorimeter Array (EURECA) project to build a ton scale cryogenic detector [249]. The Heidelberg Dark Matter Search (HDMS) operates high purity germanium crystals, one a 202 g *p*-type enriched

^{73}Ge crystal surrounded by the second 2.111 kg Ge crystal [75]. This experiment is currently testing technology for the proposed GErmanium NItrogen Underground Setup (GENIUS) proposed at Gran Sasso [242]. The Rare objects SEarch with Bolometers UndergrounD (ROSEBUD) experiment [138] is located in the Modane underground laboratory and uses a set of sapphire, germanium, $CaWO_4$ and Al_2O_3 bolometers to measure phonons.

3.2.7 Other WIMP Detectors

There are several other techniques employed to detect dark matter. The Coherent Germanium Neutrino Technology (CoGeNT) experiment, housed in the Soudan underground laboratory, uses P-type Point Contact (PPC) high purity germanium crystals cooled to liquid nitrogen temperatures [69]. It measures only ionisation but has achieved a very low threshold due to the low electronic noise (~ 0.5 keV$_{ee}$), giving this detector enhanced sensitivity to light WIMPs [4]. The Korea Invisible Mass Search (KIMS) is located in the Yangyang underground laboratory (Y2L) [241]. This detector measures scintillation from 12 CsI(Ti) crystals weighing 104.4 kg, this gives the instrument excellent sensitivity to spin-dependent interactions. The annual modulation with NAI Scintillators (ANAIS) experiment [240] is located at the Canfranc underground laboratory (LSC). Rather than discrimination of interaction species this experiment aims to detect dark matter by observing the annual modulation in the event rate as the earth orbits the sun and moves into and out of the 'WIMP wind'. This detector aims to further investigate the signal observed by the DArk MAtter search with Large sodium Iodide Bulk for RAre processes (DAMA/LIBRA). This experiment measures scintillation light from 250 kg of thallium doped NaI crystals. It aims to detect a dark matter signal by the annual modulation and this experiment has observed a modulation in the event rate [82]. The annual modulation measurement, the latest results of which are shown in Figure 3.7, is at a significance of 8.9σ and so is quite compelling. However the dark matter interpretation of this signal is still under debate as many other experiments have ruled out a signal in the DAMA/LIBRA region for most favourable WIMP models.

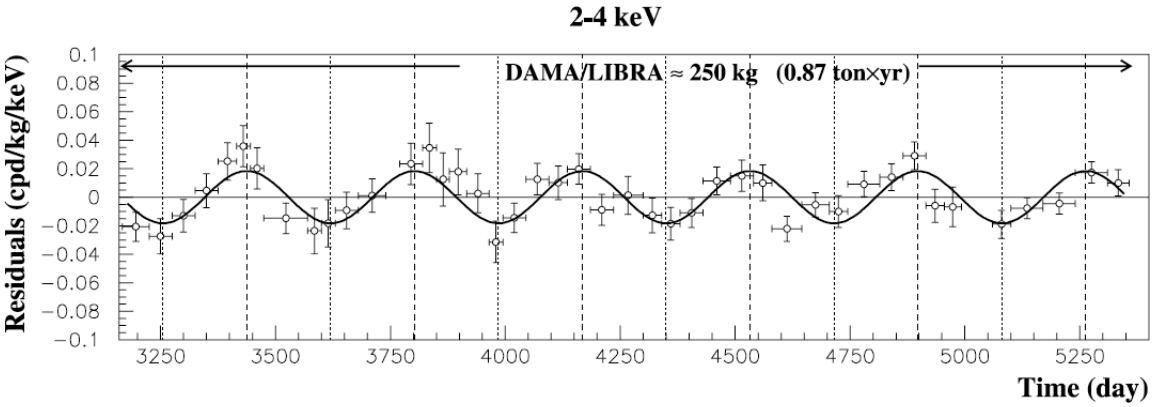

Figure 3.7: Latest results from the DAMA/LIBRA experiment showing an annual modulation in the event rate [82].

There are also several experiments searching for a dark matter experiment using time projection chambers. These experiments aim to reconstruct the track of incoming particles by measuring the track of the recoiling molecule, for example by using a multi wire proportional counter (MWPC). This requires low pressure gas hence the target masses of these experiments is quite low. However they have a distinct advantage in terms of discrimination as the extra information gained from reconstruction of the incoming track can be used to help eliminate background and also to improve the significance of a dark matter signal. The significance is improved because the direction of the track should correspond to the time of day due to the Earth's rotation as it moves into the WIMP wind. These detectors include the Directional Recoil Identification From Tracks (DRIFT) experiment. This negative ion time projection chamber is located at the Boulby mine and uses a CS_2 and CF_4 target [108]. The NEw generation WIMP search with an Advanced Gaseous tracking dEvice (NEWAGE) detector is currently operating in the Kamioka underground observatory. This experiment uses a CF_4 target at 0.2 atm [280]. The MIcro-tpc MAtrix of Chambers of He_3 (MIMAC) experiment is primarily aimed at detecting axial-vector interactions. The He_3 target is very low mass but has $\langle S_p \rangle = -0.05$ and $\langle S_n \rangle = 0.49$ (compared to Ge with $\langle S_p \rangle = 0.03$ and $\langle S_n \rangle = 0.38$), although its low mass may make it quite sensitive to low WIMP masses [88]. The Dark Matter Time Projection Chamber (DM-TPC) is currently located at the Waste Isolation Pilot Plant (WIPP) facility. It uses a CF_4 target and CCD (charge coupled device) cameras rather than MWPCs [18].

Another category of dark matter detectors use superheated fluids. Typically, small droplets of superheated fluid are suspended in a gel. Due to the surface tension of the target fluid there is an energy cost required to collapse it into a bubble. Energy depositions within the droplets may cause the fluid to undergo a phase change and create a bubble, the formation of which may be detected. The conditions in the liquid can be set such that backgrounds from electron recoils cannot produce bubbles and so the only background would be produced by nuclear recoils, rejection factors of $> 10^9$ for electron recoils have been reported [93], and neutrons can be rejected by multiple scattering. Detectors currently operating include the Project in Canada to Search for Supersymmetric Objects (PICASSO) experiment housed at snolab. This experiment uses freon (C_4F_{10}) droplets with an average radius of $\sim 50\mu$m and array of piezo electric sensors to detect bubble formation [54]. The Chicagoland Observatory for Underground Particle Physics (COUPP) experiment is housed in the MINOS hall near Fermi lab. This detector uses CF_3I droplets [93] and has recently completed a test run with a 2 kg target. The Superheated Instrument for Massive ParticLe Experiments (SIMPLE) experiment is located at the laboratoire souterrain à Bas Bruit. This detector uses ∼208 g of C_2ClF_5 droplets with an average radius of $\sim 30\mu$m in a viscoelastic 900 ml gel matrix [173].

Ultimately any confirmation of the detection of dark matter particles would require measurement using a combination of these techniques. The liquified noble gas and cryogenic detectors are the most sensitive and would be the first to see a positive signal, this would need conformation from both other detection techniques and an annual modulation of the event rate. To further improve the significance of a signal, directional detectors would be required, the signal is expected to come from the direction of Cygnus and so the ionisation track direction would depend on the time of day as the Earth rotates. These detections are unlikely to reveal much about the underlying physics defining these particles and so collider results will also be needed. However collider experiments cannot test the stability of these particles or their cosmological abundance. Even then detecting dark matter in the milky way may not necessarily solve the dark matter problem as there is no guarantee that this is the same substance making up ∼23%

of the energy density of the Universe. Given the complexity seen within the small fraction of the Universe we know about it would seem a distinct possibility for more than one form of dark matter. Indirect searches would be needed to establish if dark matter detected on Earth is the only form of dark matter or merely a component of the Universes dark matter content. Figures 3.8 and 3.9 show limit plots for some of the experiments mentioned in this section.

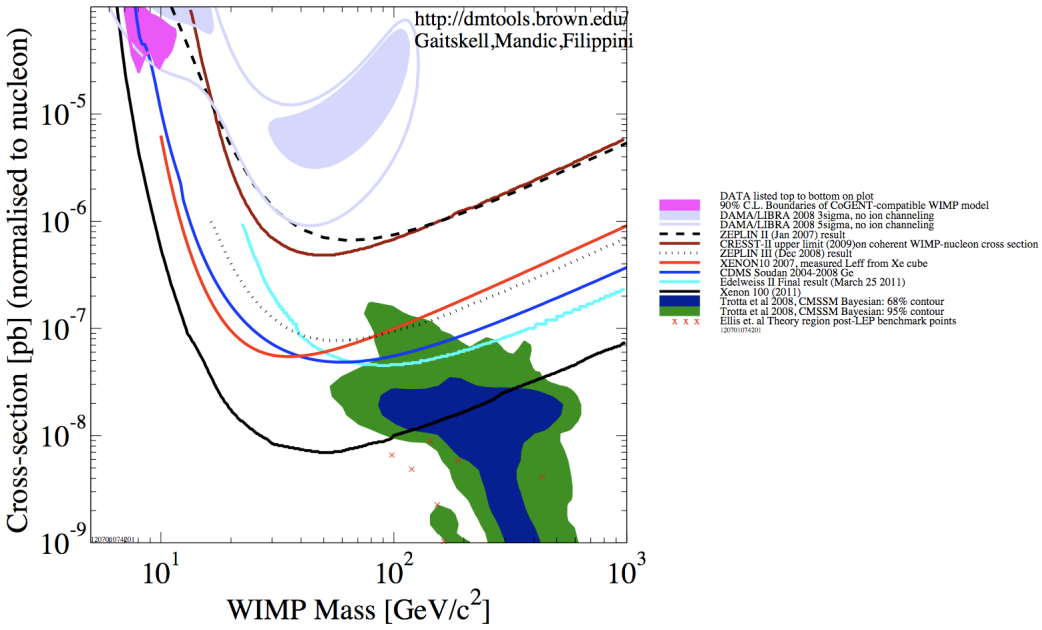

Figure 3.8: Spin-independent WIMP-nucleon cross-section limits from several direct detection experiments. Image obtained from [80].

3.2.8 Axion Detectors

Axions are another favourable candidate for dark matter particles, as discussed in Section A.16.1. There are several detectors dedicated to axion detection. Axions are expected to couple to photons and there are several detection techniques designed to search for the signals this would produce. In a strong magnetic field axions may be converted into photons via the Primakoff effect. The Axion Dark Matter eXperiment (ADMX) exploits this principle using a 7.6 T field inside a cryogenic microwave cavity. If the energy of the axion matches the resonant frequency of the chamber then axions may be converted into microwave photons. The ADMX experiment aims to probe the 2-20 μeV range. The instrument is

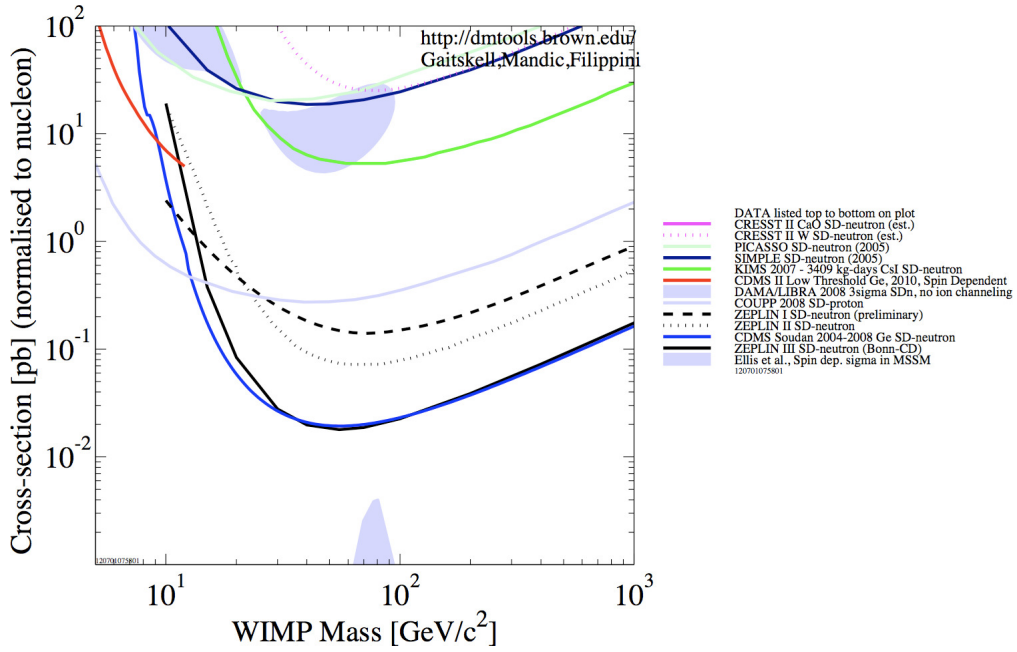

Figure 3.9: Spin-dependent WIMP-neutron cross-section limits from several direct detection experiments. Image obtained from [80].

currently undergoing an upgrade at the University of Washington [221]. The Polarizzazione del Vuoto con LASer (PVLAS) experiment aims to detect an axion signal by observing its effects on polarised light in a magnetic field. The experiment uses a 5 T rotating dipole magnet and linearly polarised laser light at 1064 nm and 532 nm [375]. In the presence of a magnetic field, photons with parallel polarisation will preferentially create axion particles. Since the speed of massive particles is slower than the speed of light then if virtual particles are briefly created by this effect the light becomes birefringed, the beam is split depending on the alignment of the polarisation and the magnetic field.

Current limits set by axion searches are shown in Figure 3.10. Upcoming missions to search for axions include the Nuclear Spectroscopic Telescope ARray (NuSTAR) satellite which will employ the first high energy X-ray focusing telescope to image the $6 - 79$ keV region of the suns electromagnetic spectrum [203]. The Any Light Particle Search (ALPS) located at the Deutsches Elektronen Synchrotron (DESY) lab in Hamburgh successfully finished the first phase of data taking in 2009, placing limits on very Weakly Interacting Sub-eV Particles

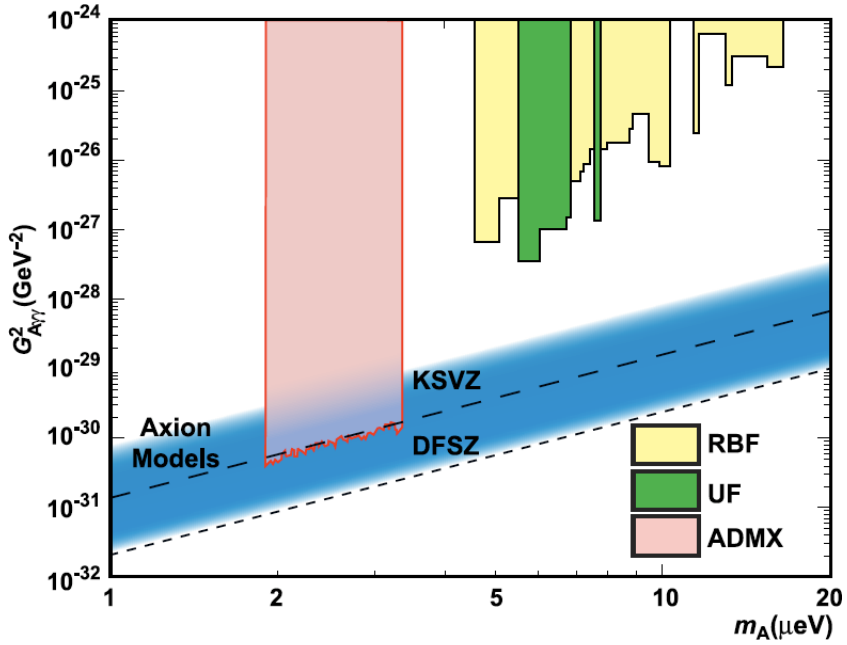

Figure 3.10: Exclusion region for axion dark matter reported by the microwave cavity experiments RBF and UF [200] and ADMX [58] assuming a local dark matter density of 450 MeV cm^{-3}. Image from the CERN particle data group website [199].

(WISPS) [157] after upgrades strict limits are expected to be placed on axions.

3.2.9 Notable Recent Results form Dark Matter Detectors

Several experiments have recently published results which include events within their respective WIMP search regions. The CoGeNT detector has reported and excess of low energy events [4]. These are bulklike events (i.e. not electronic noise) below 3 keV in ionisation energy. As the CoGeNT detector can reject surface events using a rise time cut these events originate from either a currently unknown background source or dark matter interactions. The CoGeNT data also show signs of an annual modulation as may be expected from dark matter interactions. The statistical significance of this modulation is only $\sim 2.8\sigma$ [3], limited by the 15 month exposure. Figure 3.11 shows the CoGeNT low energy spectrum and Figure 3.12 shows the modulation in event rate as a function of energy.

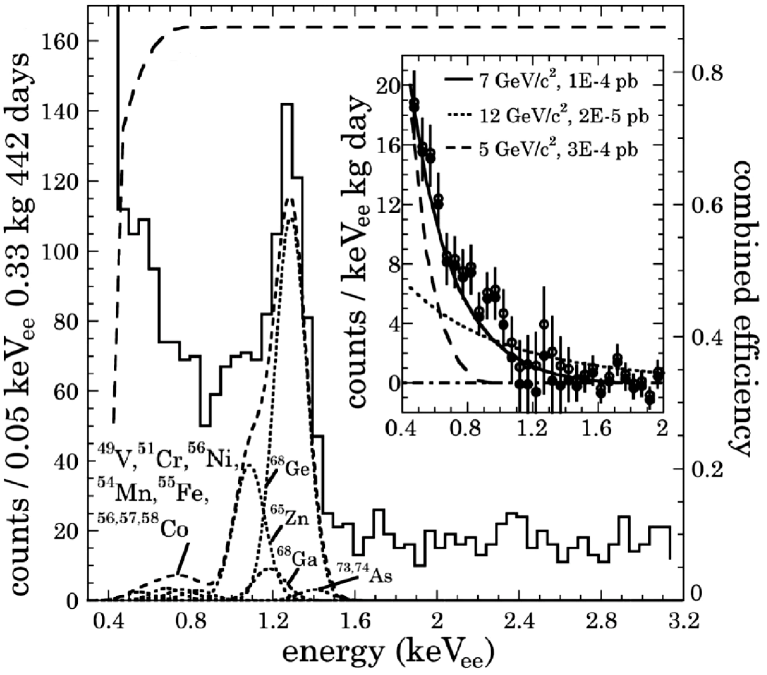

Figure 3.11: The uncorrected low-energy CoGeNT spectrum following the removal of surface events. The predicted L-shell peaks are shown by dotted Gaussian curves and the dashed line traces their envelope. The dashed line above shows the combined efficiency (trigger and software cuts, scale shown on right axis). The inset image shows spectra corrected for the efficiency, stripped of L-shell contributions and corrected for flat background components. Examples of expected light-WIMP signals are shown overlaid. Image obtained from Reference [3].

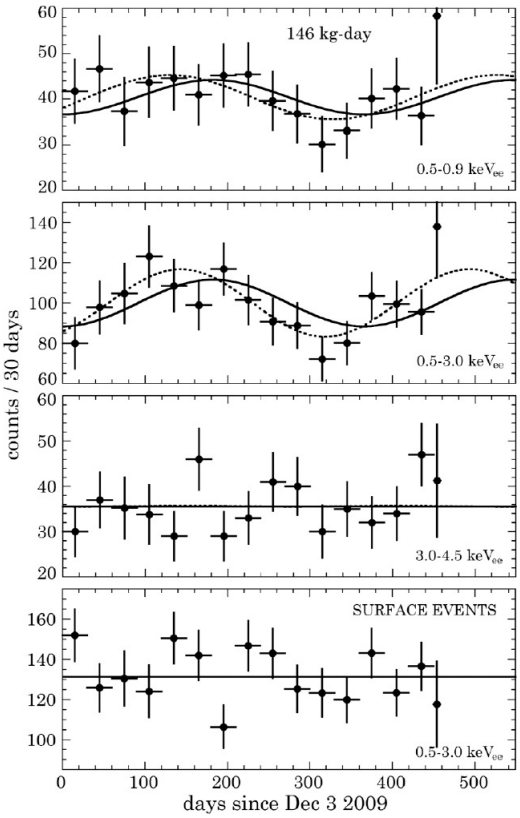

Figure 3.12: The rate of CoGeNT events over time. A dotted line shows the best-fit modulation and a solid line indicates a prediction for a 7 GeV/c^2 WIMP in a galactic halo with Maxwellian distribution. It is noted that for a non-Maxwellian halo the peak position is shifted and so may align with the data. Image obtained from Reference [3].

Although results from several other experiments have excluded the parameter space for favoured WIMP models, the CoGeNT data may be interpreted under a light WIMP hypothesis. If this is a dark matter signal it could indicate a light WIMP in the range $\sim 7 - 11$ GeV/c^2 [4]. Reconciliation's between the CoGeNT signal and results from other detectors exist, under a dark matter interpretation of the signal. For example a re-analysis of the Xenon-10 and Xenon-100 limit curves using up to date $\mathcal{L}_{eff}$ data (from Reference [220], discussed in Section 8.2.2) show that results from the xenon collaboration are not incompatible with the CoGeNT signal [132]. Another possibility for the discrepancy between results from detectors with xenon targets and the CoGeNT signal could be a difference between the dark matter coupling to protons and neutrons (isospin-violating dark matter [174, 115]) where, for example, a coupling ratio of $\frac{f_n}{f_p} \approx -0.7$ (see Equation 3.13) would weaken the constraints from xenon experiments by a factor of $\sim$20 [219]. It has also been suggested that the DAMA modulation, shown in Figure 3.7, may be compatible with the CoGeNT signal [184, 182]. Methods of reconciliation include isospin-violating dark matter and non-standard dark matter halos [168, 285]. A more difficult reconciliation is with CDMS data, which has also excluded this parameter space [21]. The CDMS uses germanium detectors and operates in the same facility as the CoGeNT detector. This detector also has approximately 10 times the low energy exposure of CoGeNT and has over 4 annual cycles available for modulation analysis. It has been suggested that the data are compatible, considering the calibration choices made by the CDMS collaboration [131]. A recent analysis of CDMS-II data found no evidence of an annual modulation in their low energy data [22].

The CRESST–II experiment has also reported an excess of events at low energies [43]. A maximum likelihood analysis combining the effects of know background sources show, at high significance, that these are not responsible for the observed signal. The data have been interpreted under a WIMP hypothesis as shown in Figures 3.13 and 3.14. Under a WIMP hypothesis these data favour two regions of phase space, corresponding to two minima produced by the maximum likelihood fitting, shown in Figure 3.13. The "M1" minimum rejects the background at 4.7σ significance and the "M2" minimum rejects the background at 4.2σ significance. These results are centred on low WIMP masses of 25 GeV/c^2

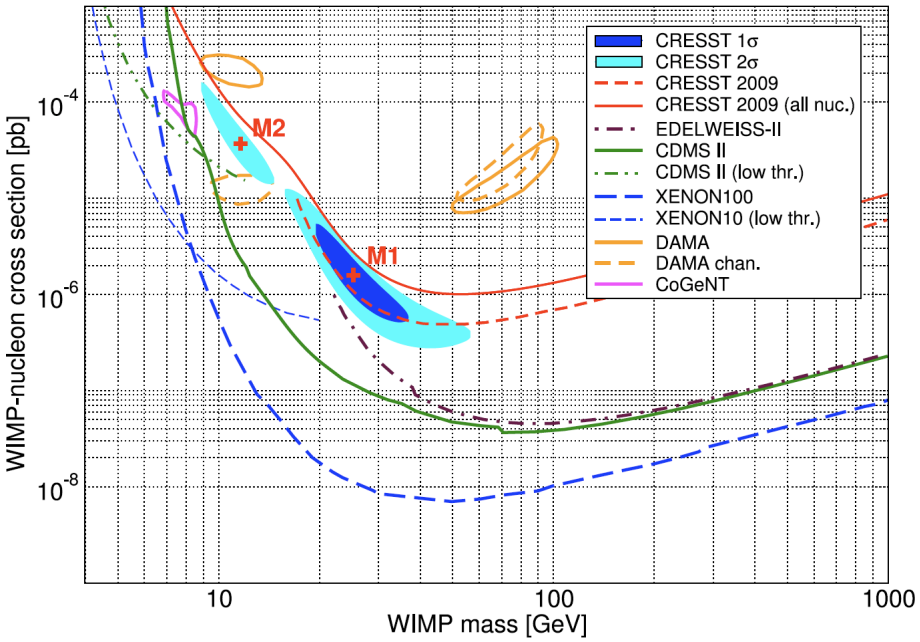

Figure 3.13: The WIMP parameter space compatible with the CRESST–II results. The results show limits from several other experiments as well as the 90% confidence regions favoured by CoGeNT and DAMA/LIBRA. Image obtained from [43].

and 12 GeV/c^2, respectively [352]. It should be noted that the M2 region may be compatible with the upper boundary of the WIMP interpretation of the CoGeNT result. Recent analysis of the CRESST–II data optimised for low mass WIMPS suggests that this result may be compatible with the DAMA annual modulation [101].

The EDELWEISS–II experiment observe 5 events in the WIMP acceptance region [55]. With a background expectation of 3 events no WIMP hypothesis analysis is offered. Recent analysis for the EDELWEISS–II data optimised for low mass WIMPS shows no evidence of an exponential increase of events at low energies and the observation of 1 event in the low mass WIMP search region allows a 90% C.L. limit of 1.0×10^{-5} pb on the spin-independent WIMP-nucleon scattering cross-section [56]. This result constrains the parameter space of CoGeNT, CRESST and DAMA as shown in Figure 3.15.

The XENON100 experiment recently release a pre-print result [45] showing the most sensitive dark matter result yet. Analysis of a 34 kg fiducial region providing

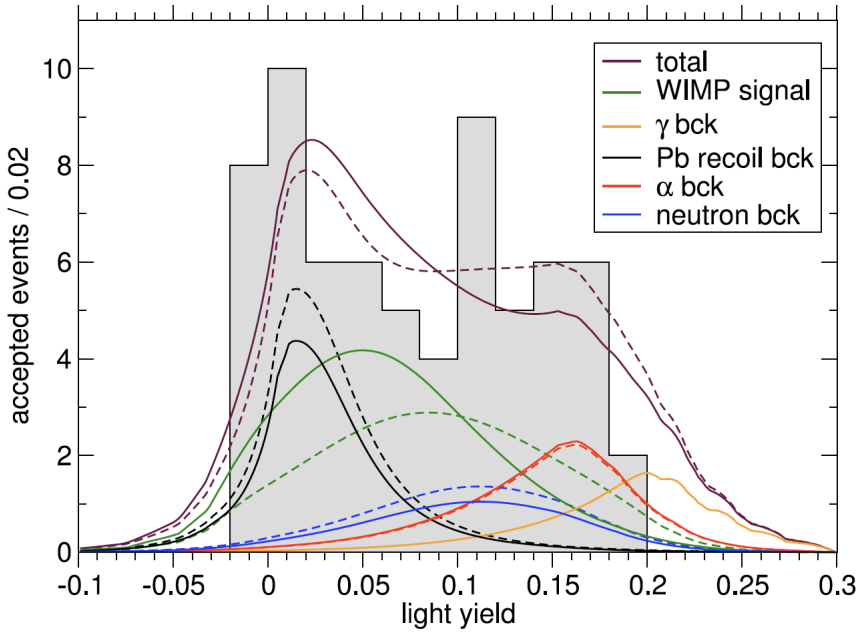

Figure 3.14: The light yield distribution of the accepted CRESST–II events, together with the expected contributions of the known backgrounds. Also shown (green) is the possible WIMP signal. The two minima, produced by the maximum likelihood fitting, are shown by solid and dashed lines. These represent the M1 and M2 regions, respectively. Image obtained from [43].

2323.7 kg·days of data yielded 2 events in the WIMP acceptance region. This is inline with the background expectation of 1.0 ± 0.2 events and allows a limit on the cross-section of the WIMP-nucleon interaction of 2×10^{-45} cm^2 to be set for a 55 Gev/c^2 WIMP at 90% C.L.. The exclusion curve is shown in Figure 3.16.

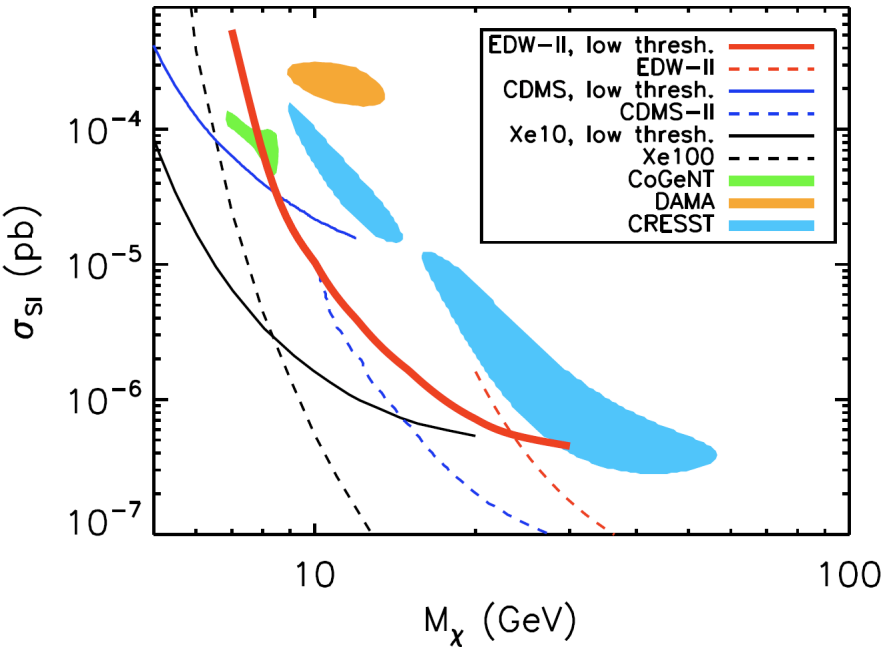

Figure 3.15: 90% C.L. Poisson limit on the WIMP-nucleon σ_{SI} as a function of WIMP mass derived from the analysis of four bolometers (solid red curve). Several other limits are shown along with the 90% favoured regions of the DAMA, CRESST and CoGeNT experiments. Image obtained from [56].

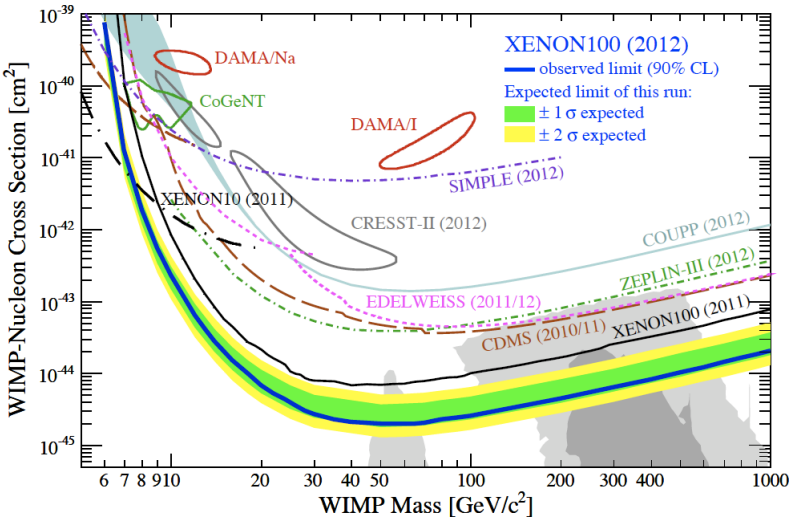

Figure 3.16: Exclusion limits from the XENON100 experiment [45]. The expected sensitivity is shown by the green (yellow) band at 1σ (2σ). The 90% C.L. exclusion curve is shown in blue. The dark (light) grey shaded region shown the 1σ (2σ) preferred cMSSM region [353].

Chapter 4

ZEPLIN-III

4.1 Introduction

The ZEPLIN-III detector is the third dark matter detector of the ZEPLIN (ZonEd Proportional scintillation in LIquid Noble gases) series and is designed to achieve the optimum conditions for WIMP detection. The ZEPLIN–III detector has been described in detail elsewhere [25]. The two predecessors, ZEPLIN-I [32] and ZEPLIN-II [33], both set competitive limits on the WIMP-nucleon cross-section of 1.1×10^{-6} pb for an 80 GeV c^{-2} WIMP mass and 6.6×10^{-7} pb for a WIMP mass of 65 GeV c^{-2}, respectively. The ZEPLIN-II instrument was the first dark matter detector to operate using a liquid xenon TPC. A TPC works by drifting charge through a target. The drift time can be used to provide a spatial co-ordinate which may be used to reconstruct the position of the initial interaction. This is the same technology used by the ZEPLIN-III detector. The ZEPLIN-III TPC is a thin cylinder of liquid xenon with a small gas layer above the liquid surface. Radiation may interact with the liquid xenon in the target. This causes VUV scintillation light to be emitted at the interaction site. The interaction also causes ionisation of the liquid xenon. An electric field is applied to the liquid xenon target and some of the ionisation charge is extracted from the interaction site and drifted through the liquid xenon up to the xenon gas layer. A higher strength field present in the gas phase accelerates the charge producing an electroluminescent flash. If the drift velocity of electrons through the liquid xenon is known, then the time between the primary scintillation signal (also known as the S1 signal) and the electroluminescent signal (also known as

the S2 signal) gives the depth of the interaction. The hit pattern seen by the PMTs can be used to calculate the position in the x-y plane and thus the 3D position of the interaction site may be reconstructed. This allows for a fiducial volume to be defined within the target xenon.

The ZEPLIN-III instrument consists of a xenon target that is located within a vacuum jacket for thermal insulation. The target is mounted on top of a liquid nitrogen vessel which is used to maintain temperature stability. This allows the target medium to exist in two phases, liquid and gas. Figure 4.1 shows a CAD drawing of the instrument and Figure 4.2 shows a photograph of the detector. The detector is located in the Palmer laboratory at the Boulby mine. This laboratory is 1070 m underground, this is equivalent to 2850 m of water overhead [26] as shown in Figure 3.6. The shielding provided by the rock overburden reduces the muon flux by a factor of $\sim 10^6$ to $(3.39 \pm 0.15) \times 10^{-8}$ muons cm^{-2} s^{-1} [52]. Muon interactions deposit enough energy to completely saturate the detector and so introduce a dead time required for the detector to recover following a muon interaction. Neutrons from muon spallation and secondary cascades may also lead to nuclear recoils within the ZEPLIN-III target. Although the single scatter events could potentially be mis-identified as a WIMP interaction, these events are also likely to produce a veto signal. Muons may also activate detector components leading to the generation of internal radioactive backgrounds. Due to the irreducible background of muon induced neutrons the ZEPLIN-III detector is located deep underground.

To help achieve the required level of radiopurity for a rare event search the instrument is made of oxygen-free copper (type C103) and was constructed using electron beam welding to prevent contamination. The target volume is a flat cylinder (fiducial $(r, z) \sim (15\text{ cm}, 4\text{ cm})$) with 31 close-packed 2 inch PMTs immersed within the target medium, viewing it from below. The target medium is liquid xenon, a material that has many characteristics to make it favourable for dark matter searches, as discussed in Section 4.3. The xenon is cooled to around -100°C [355] where it contains two phases of xenon (liquid and gas). The PMTs are held in place using a tight fitting PMT screen which also reduces cross-talk between PMTs. The thin geometry ($z < 4$cm) of the target improves the light

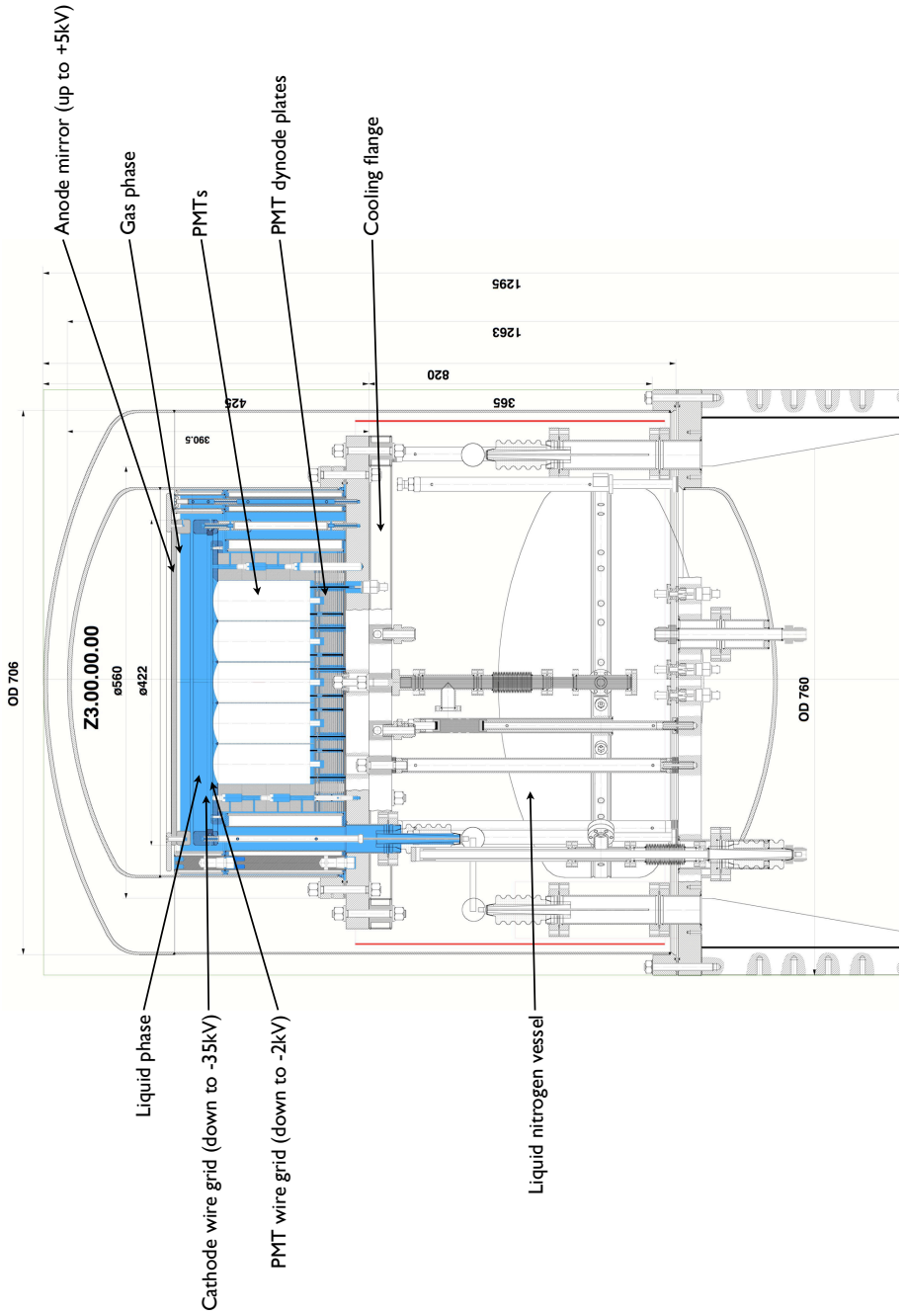

Figure 4.1: A CAD drawing of the ZEPLIN-III instrument, annotated with some of the features mentioned in the body of the text [128].

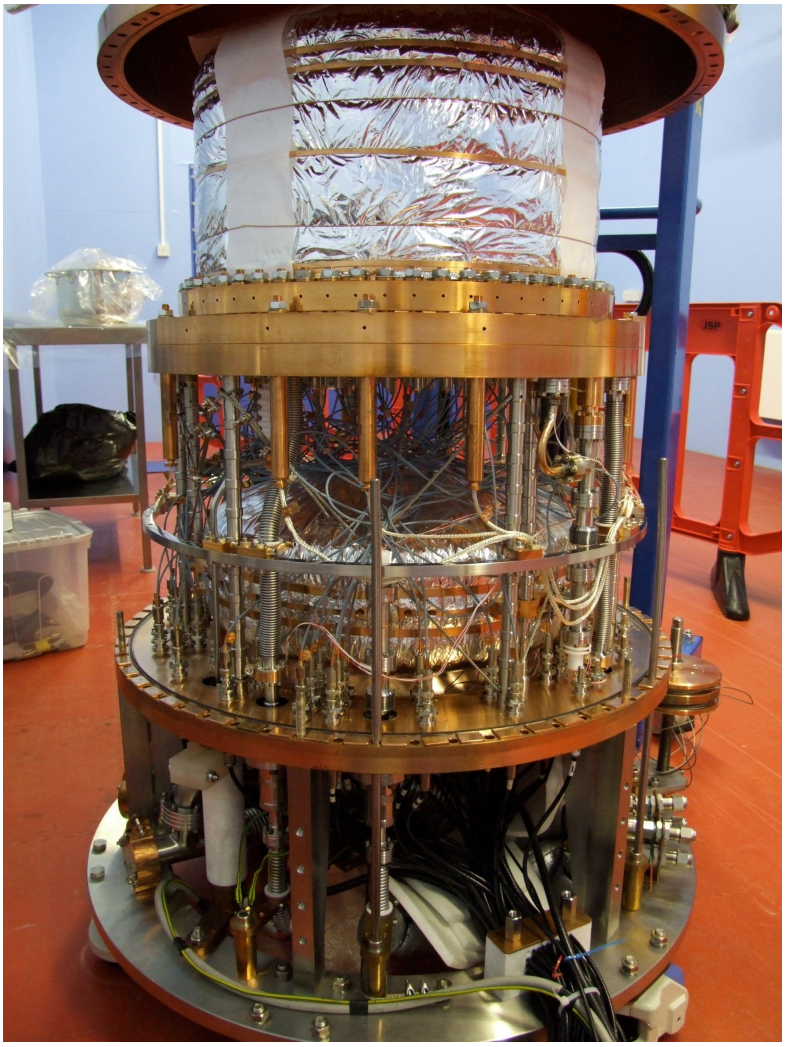

Figure 4.2: A photograph of the ZEPLIN-III detector with the vacuum jacket lifted to show the internal components.

collection for primary scintillation by increased total internal reflection from the liquid surface, as this is much larger than the area of the outer perimeter of the cylinder. This geometry also enables good position reconstruction in the X-Y plane. As the energy threshold is limited by the size of the primary scintillation signal, these two factors ensure a very low energy threshold is achieved by the instrument allowing it to probe much lower WIMP-nucleon cross-sections.

The light yield of the electroluminescence signal is increased by using a very highly polished copper surface for the anode used to provide the electric field (hence this is referred to as the anode mirror). The light yield is also increased by the change in refractive index between the liquid and gas layers creating a focusing effect as the photons enter the liquid phase. The use of an anode plate and a single wire-grid cathode to generate the drift field allows a highly uniform field within the target volume without the use of a dedicated charge extraction grid or field shaping rings [42] as shown in Figure 4.3. A uniform field is required to reduce the number of corrections needed for charge extracted from different areas, and hence increase the accuracy of the experiment. Achieving this with minimal material allows a fiducial volume to be defined which is unbounded by solid surfaces, hence without introducing further potential sources of unwanted background. This removes spurious surface effects and allows the self shielding effects of the xenon to be utilised to increase rejection of unwanted background events.

A third wire grid is positioned just above the PMTs. This PMT grid is kept at the same voltage as the photo-cathodes to protect the PMTs from the high electric field in the fiducial volume. The PMT grid and PMT screen are shown in Figure 4.4. The PMT screen has the added effect of creating a reverse field region between the PMTs and the cathode. In any dark matter search there is background radiation produced by contamination of the surrounding material. The key to a successful dark matter detector is the ability to discriminate between this background radiation and a WIMP signal. This is further helped if the rate of background radiation is minimised. The reverse field further reduces the number of unwanted background events by suppressing secondary signals from this region. Due to the construction requirements, a large proportion of the background events

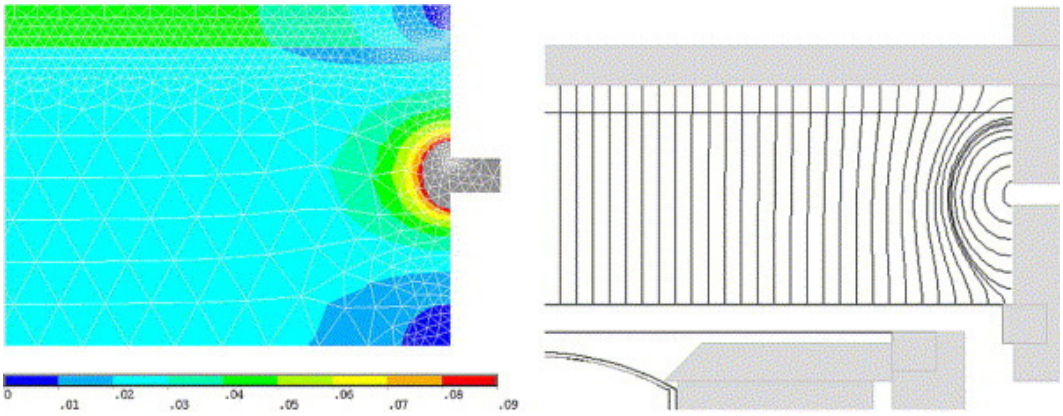

Figure 4.3: The electric field within the ZEPLIN-III target, adapted from [50].
Left image: A contour map of the electric field in the peripheral region of the target. This is the result from a simulation using ANSYS finite element software. This shows the fiducial volume has a very uniform field.
Right image: Results from the ANSYS simulation were fed into a GEANT4 simulation, this image shows the electric field lines in the target volume. These begin at the cathode, pass up through the gas-liquid phase boundary and terminate at the anode.

are produced by radioactive contaminants contained within the PMTs. However many of these will interact within the reverse field region and be excluded due to the lack of an electroluminescence signal. The internally generated background is further reduced by careful selection of building materials and a design which minimises the amount of material required. All components were radio-assayed to determine their contribution to the background. To further reduce the internal background the 31 PMTs, having 15 connections each, are powered by a common voltage supply reducing the number of feed-throughs required to 47. Sixteen 2 mm thick copper plates (dynode plates) separated by quartz spacers are used to supply voltages to each PMT pin. As all 31 PMTs are held at the same voltage attenuators are used to flat-field the output signal. This significantly reduces the amount of material required inside the detector. External background radiation is attenuated using shielding. Both external γ-rays and neutrons were reduced by a factor of 10^5 by using 20 cm of high-purity lead and 30 cm of polypropylene shielding. During the second science run the outer 15 cm of the neutron shielding was used as an active veto, as discussed in detail in chapter 5.

Figure 4.4: This image shows the ZEPLIN-III PMT screen and PMT grid, holding the PMTs within the target volume and isolating them from the charge drift field respectively.

4.2 ZEPLIN-III Event Discrimination

The ZEPLIN-III instrument is a two phase time projection chamber. This allows for accurate event discrimination which is vital for a dark matter search looking for rare events. The WIMP interactions are expected to be nuclear recoils whereas the background events are primarily electron recoils. The primary signal is produced via scintillation as radiation interacts within the liquid phase of the detector. The luminescence has two components, see Section 4.3, and some discrimination may be achieved by the shape of the primary signal. The main discrimination factor is given by the ratio of size of the scintillation signal to the size of the secondary electroluminescence signal from the gas phase. This secondary signal is generated by extracting charge from the interaction site using a strong electric field applied to the target volume. This causes some of the separated electrons to drift along the field lines and into the gas phase where a much stronger electric field accelerates the electrons. This typically leads to a much larger signal being generated in the gas phase and provides a measure of the amount of ionisation in the original interaction.

The potential difference used to supply the charge drift field during the second science run of ZEPLIN-III was 15kV. The field in the liquid phase may be calculated by:

$$E_l = \frac{V}{\epsilon_r d_g + d_l} \tag{4.1}$$

where V is the potential difference applied across the target, $\epsilon_r = \frac{\epsilon_l}{\epsilon_g}$ is the relative electrical permittivity between the liquid and gas phases and $d_{l/g}$ are the thicknesses of the liquid/gas phases. The relative permittivity is about two ($\epsilon_l \approx 1.96$) and so the electric field in the gas phase is about twice that in the liquid phase:

$$E_g = \epsilon_r E_l \tag{4.2}$$

For the second science run voltage, with $d_g = 3.5$ mm, this gives $E_l = 3.46$ kV cm^{-1} and $E_g = 6.78$ kV cm^{-1}. The emission coefficient at the liquid gas interface is approximately unity above 5 kV cm^{-1} so this field negates any efficiency loss at this boundary [196]. At 6.8 kV cm^{-1} the gas phase produces ~ 200 photons per cm per electron [50]. The uniformity of the electric field is limited by variations in the total distance between the anode mirror and the cathode grid, $L = d_l + d_g$,

and also by d_l as:

$$\frac{\Delta E_l}{E_l} = \frac{\epsilon_r \Delta L + \Delta d_l(\epsilon_r + 1)}{\epsilon_r d_g + d_l} \tag{4.3}$$

where ΔL is limited by three factors, the planarity of the anode mirror, the planarity of the cathode grid and their degree of relative parallelism. The combination of these gives $\Delta L \sim 100$ μm [25]. Δd_l depends on the degree of parallelism of the liquid surface with the two electrodes. There are three capacitive sensors which are used to measure the liquid level with sub-millimeter precision (corresponding to ± 0.03 pF). Three screws allow for height adjustments and levelling of the detector. In the fiducial volume this translates to $\Delta d_l \sim 500$ μm. With $L = 40$ mm and using the second science run conditions this gives $\frac{\Delta E_l}{E_l} < 8.4\%$ for the fiducial volume. In practice calibration data was used to measure the tilt of the detector and, in combination with accurate position measurements, corrections to the data could be applied to account for a variance of the electric field due to detector tilt, as discussed in Section 8.2.6.

To achieve event discrimination, precise three-dimensional event reconstruction is required even with the highly uniform electric field and high level of target purity achieved by the ZEPLIN-III detector. The depth of the interaction is calculated by the drift time of the charge in the liquid phase. For ZEPLIN-III operating voltages the drift velocity is ~ 2.5 mm μs^{-1} and the distance between the primary and secondary signal is used to correct the secondary signal for lost ionisation charge due to the finite electron lifetime within the xenon (the second science run corrections are discussed in Section 8.2.1). The PMT array allows for position reconstruction in the x-y plane by analysis of the hit pattern. Centroid calculations provide a reasonable estimate of the interaction site however a custom software package called '`mercury`' was created which uses likelihood estimators to accurately reconstruct event positions. The precision achieved in the second science run is discussed in Section 8.2.1. The position reconstruction is vital for fiducialisation of the target, allowing a large proportion of the unwanted background events to be rejected by sacrificing some of the outer layer of the target. Figure 4.5 shows the discrimination power of the ZEPLIN-III detector using conservative ionisation yields. The factors achieved by the experiment were highly dependent on the PMTs used. The first and second science run results for the discrimination power are given in Sections 4.5 and 8.2.4, respectively.

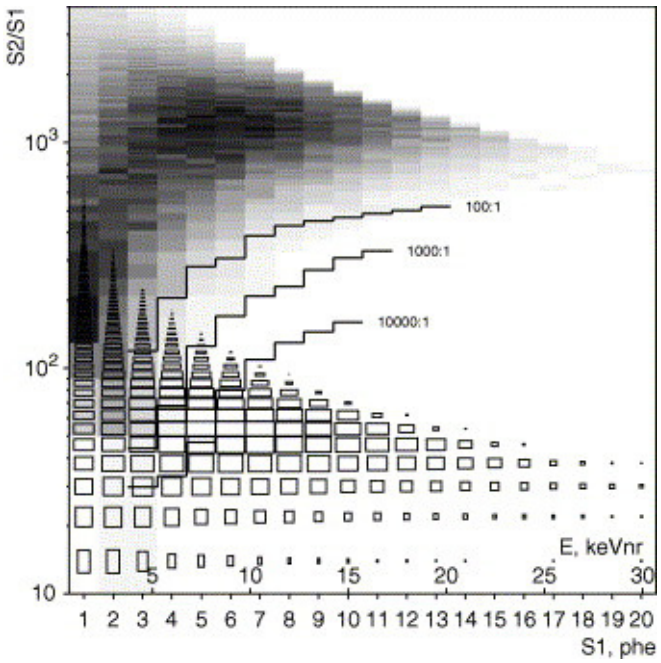

Figure 4.5: The discrimination power of the ZEPLIN-III detector within the inner 8 kg fiducial volume. The discrimination is found using the size of the secondary signal over the size of the primary ($S2/S1$). The upper population are electron recoils and the lower population are nuclear recoils. The thick lines represent the boundaries for a given γ-ray discrimination efficiency [50].

4.3 Xenon Physics

Xenon has several qualities which make it an excellent target material for a dark matter search. It has a high scintillation yield (relative to sodium iodide) producing broad spectrum vacuum ultra-violet (VUV) photons centered on 177.6 nm with a spectral width of 14 nm. As xenon is transparent to VUV light (attenuation length = 36.4 ± 1.8 cm [337]) large targets may be used. Coupled with reasonable PMT quantum efficiency for VUV light this ensures good efficiency can be achieved using xenon targets. High sensitivity is also achieved in the ionisation channel. The limiting factor for drifting charge being the level of electronegative impurities within the liquid xenon, which is relatively easy to purify. For example the XMASS collaboration have achieved 10^{-12} purity on some contaminants [7]. A fiducial volume may be defined with an outer layer of xenon used as a shield due to its high stopping power ($Z = 54$, $\rho_l = 2.95$ g cm^{-3}). Figure 7.4 shows the stopping power as a function of photon energy. The large size of the xenon atom also provides a relatively high cross-section for spin independent interactions, see Equation 3.2.2, and also makes it a favourable kinematic match to expected WIMP masses providing high event rates at low energies, see Figure 3.5. The breadth of natural isotopes in xenon provides sensitivity to spin dependent interactions, as discussed in Section 3.2.3. Xenon itself is a very radio-pure material, the longest lived isotope is ^{127}Xe with a half life of 36.346 days [204], hence for xenon which has been stored in a low background environment these isotopes are only introduced at very low levels by activation during neutron calibration[2].

The energy transferred to the target medium, E_0, by an interacting particle is split between three channels; scintillation, ionisation and heat. For electrons this can be written as:

$$E_0 = N_i E_i + N_{ex} E_{ex} + N_i \epsilon \tag{4.4}$$

where E_i and E_{ex} are the mean energies spent to ionise or to excite an atom;

[2]The isotope ^{136}Xe has also been observed to decay by the Enriched Xenon Observatory (EXO-200) experiment via double beta decay, however the half life for this decay is $t_{\frac{1}{2}} = 2.11 \pm 0.04(\text{stat}) \pm 0.21(\text{syst}) \times 10^{21}$ years [13]. This instrument demonstrates the benefits of xenon for rare event searches in general.

N_i and N_{ex} are the mean numbers of ionised and excited atoms, respectively; and ϵ is the mean energy of sub-exciton electrons left over following excitation and ionisation, as in Reference [41] and references therein. The value of ϵ has been estimated to lie between 4.65 eV and 5.25 eV for liquid xenon [148]. The production of scintillation light and ionisation charge in liquid xenon involves several steps. For the low energy elastic nuclear recoils of interest to WIMP searches, the recoil velocity is expected to be below the Fermi velocity of the electrons, and consequently, the xenon atom remains neutral during scattering. The recoiling atom will then scatter off neighbouring atoms, and although most scatters will be elastic there will be occasional inelastic interactions that create excitation or ionisation. This thermalisation process leaves behind a large number of ionised and excited xenon atoms, their number being proportional to the initial energy deposit. The free electrons from the ionised atoms will either recombine to form excited xenon atoms or escape, the fraction escaping depending on the strength of the electric field. The excited xenon atoms form self-trapped excimers (within a few picoseconds) which subsequently decay to emit scintillation photons. Occasionally two excited xenon atoms combine to produce only one scintillation photon in a process called biexcitonic quenching; this reduces the scintillation yield and the rate is proportional to the excitation density. The exciton scintillation signal has two components, one fast and one slow, corresponding to the singlet ($^1\Sigma_u^+ \rightarrow^1 \Sigma_g^+$) and triplet ($^3\Sigma_u^+ \rightarrow^1 \Sigma_g^+$) transitions. The recombination scintillation signal is slower than either of the direct signals due simply to the extra time required to form an exciton. The lifetimes of the direct excitation (exciton luminescence) states and indirect excitation (recombination luminescence) states are summarised in Table 4.3 and a diagram illustrating the processes is shown in Figure 4.6.

Although the number of scintillation photons produced is proportional to the energy deposition, the exact photon yield remains uncertain. Measurements show that, on average, each scintillation photon requires between 12 and 40 eV [149, 118]. Table 4.3 shows the difference in scintillation time constants and intensities between the different scintillation components for electron recoils and nuclear recoils. This is caused by the difference in track topologies following a recoil. The fast component from exciton luminescence dominates the scintillation

Table 4.1: Decay times for the fast singlet $^1\Sigma_u^+$ excited molecular state (τ_s) and the slow triplet $^3\Sigma_u^+$ excited molecular state (τ_t). τ_r is the recombination time and $\left(\frac{I_s}{I_t}\right)$ is the intensity ratio of the fast and slow components. Values with [a] are adapted from [251], values with [b] are adapted from [214] and values with † were measured in a 4 keV cm^{-1} electric field [214].

measurement	1 MeV electrons	α-particles
τ_s	2.2 ± 0.3 ns$^{\dagger a}$	4.3 ± 0.6 ns^b
τ_t	34 ± 2 ns^a	22 ± 1.5 ns^b
	27 ± 1 ns$^{\dagger a}$	
τ_r	45 ns^a	
$\left(\frac{I_s}{I_t}\right)$	$0.05^{\dagger a}$	0.45 ± 0.07^b

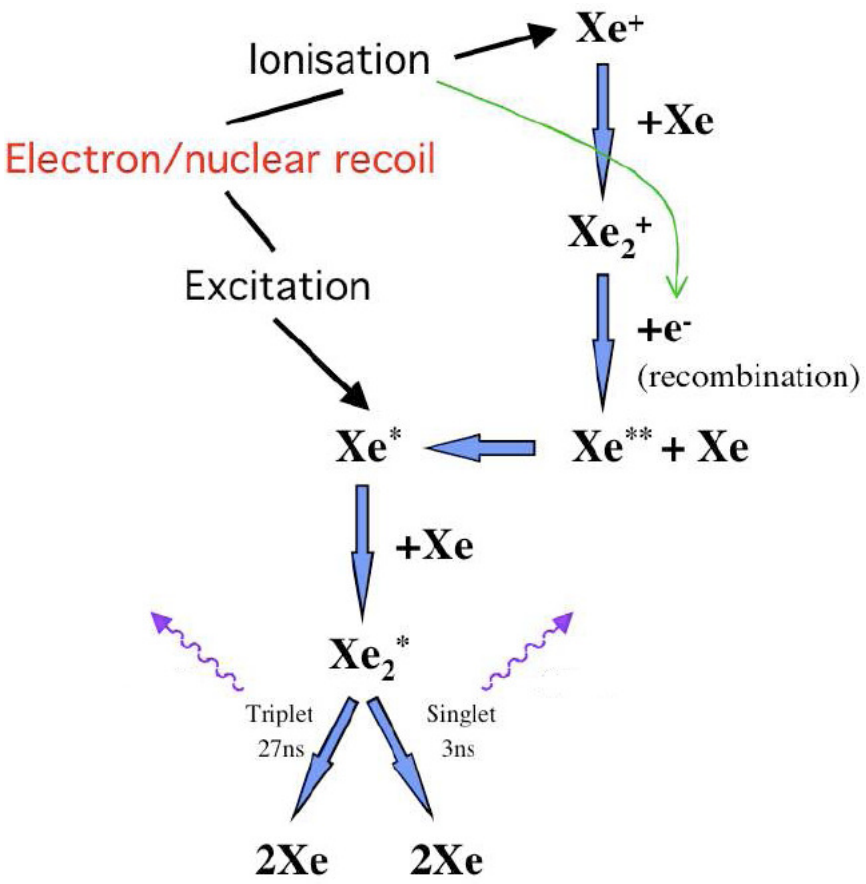

Figure 4.6: A schematic of the scintillation process in liquid xenon following an interaction with radiation. Some of the ionisation charge, the green arrow, is extracted by the electric field and produces the secondary signal in the gas phase.

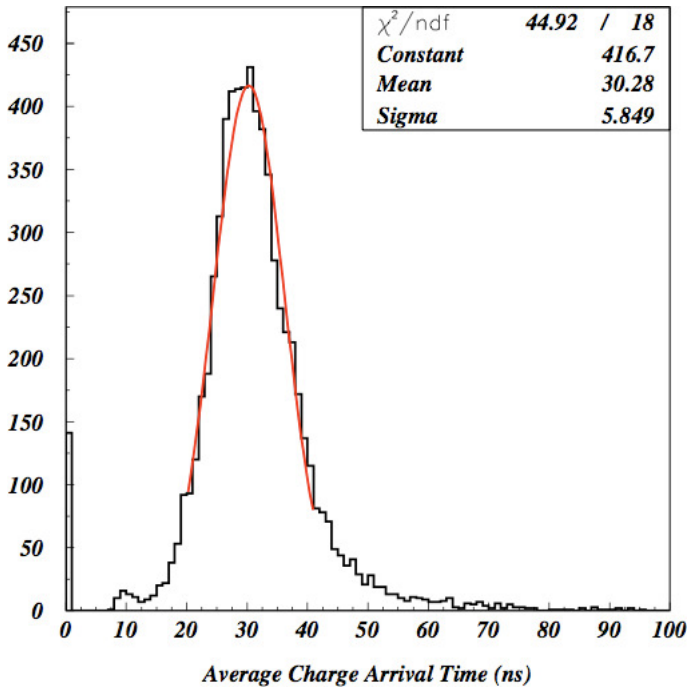

Figure 4.7: A histogram showing the average charge arrival time of unsaturated pulses for zero electric field data measuring ZEPLIN-III background radiation. This is in good agreement with expectations for electron recoils.

signal for nuclear recoils where the track is shorter and more densely populated by excitons, whereas the electron recoils produce a longer ionisation track and recombination luminescence becomes significant. This will produce a time constant in the region of $22-45$ ns for electron recoils. Figure 4.7 shows ZEPLIN-III background data taken at 0-field (i.e. no drift field), as this is dominated by γ-ray radiation the mean arrival time spectrum of resulting electron recoils is expected have a time constant in agreement with this value.

Another key difference between electron and nuclear recoils in liquid xenon is the relative scintillation yield, $\mathcal{L}_{\mathbf{eff}}$. This factor relates the energies deposited by electron and nuclear recoils by:

$$\mathcal{L}_{\mathbf{eff}} = \frac{E_{ee}}{E_{nr}} \frac{S_e}{S_n} \tag{4.5}$$

where E_{ee} is the true energy deposited by an electron recoil, E_{nr} is the true energy deposited by a nuclear recoil and $S_{e/n}$ are factors accounting for suppression of

scintillation yields from electron/nuclear recoils due to the electric field. In the second (first) science run the values are $S_e = 0.38$ (0.39) and $S_n = 0.92$ (0.92) [220]. As liquid xenon dark matter detectors are typically calibrated using γ-ray sources it is vital to obtain an accurate measurement of the nuclear quenching factor to be able to estimate the energy of a nuclear recoil. A relatively large proportion of energy (E) deposited by nuclear recoils is transferred into atomic motion, whereas most energy from electron recoils is transferred into the electronic subsystem (T). This results in a quenching of the observed energy, denoted by $q = \frac{T}{E}$. The simple Lindhard model [259] where the energy given to atomic motion is given by $K = E - T$, does not account for the observed quenching in liquid xenon. The relative scintillation yield for liquid xenon may be expressed, in the absence of a drift field, as a combination of factors:

$$\mathcal{L}_{\mathbf{eff}} = q_{nc} \times q_{esc} \times q_{el} \tag{4.6}$$

where q_{nc} is the Lindhard factor, q_{esc} accounts for escaping electrons and q_{el} is the electric quenching factor [269].

Escape electrons occur even in the absence of an electric field as some electrons may have a thermalisation distance comparable to the Onsager radius, $r_{th} \sim r_O$, where an electron has an equal probability to recombine or escape [291]. Although this factor is known to effect electron recoils, it was not until more recently that it has been considered to significantly effect nuclear recoils too, due to their higher than expected ionisation yield [269]. Electronic quenching becomes significant for high linear energy transfer (LET $= -\frac{dE}{dx}$). Here, scintillation light is lost because of the larger number of biexcitonic collisions [213, 212] due to the higher exciton density along nuclear recoil tracks. The three quenching factors that contribute to the relative scintillation efficiency are energy dependent, however the energy dependence has only been measured accurately for energies somewhat higher than those of interest to WIMP searches. The Hitachi model attributing the majority of the additional quenching beyond the Lindhard model to biexcitonic collisions does not hold below 10 $\mathrm{keV_{nr}}$ [49, 85]. Accounting for quenching due to escape electrons brings the theoretical model much closer to measurements [269], however the relative scintillation yield is still poorly understood at low energies. Recent results indicate that $\mathcal{L}_{\mathbf{eff}}$ is independent of the applied electric field [269],

so although the primary and secondary signal are strongly anti-correlated the loss of energy to escaping electrons does not contribute significantly to the secondary signal indicating that q_{esc} should be a very small effect. Measurements also show that the quenching occurs prior to self trapping, as the lifetimes of VUV emission do not depend on LET or the amount of quenching [214]. The second science run $\mathcal{L}_{\mathbf{eff}}$ was measured using neutron calibration data and the results are shown in Section 8.2.2. There is also a kinematic cut off for scintillation production which causes a drop off below a few tens of keV$_{nr}$ [341].

No satisfactory theory currently exists for the saturation characteristics of the ionisation yield as a function of applied electric field, $\frac{Q_y(F)}{Q_0}$, where F is the field, $Q_y(F)$ is the charge collected and $Q_0 = \frac{E}{W}$ is the charge produced by an incident particle depositing energy E creating electron-ion pairs with a minimum ionisation energy of W. The measurement of the ZEPLIN-III second science run Q_y is given in Section 8.2.2. For xenon W is typically given as 15.6 eV [358] this was also measured from ZEPLIN-III data and is quoted in Section 8.2.2. The anti-correlation between the scintillation signal and the electroluminescence signal which measures ionisation is shown in Figure 4.9 as a function of the drift field. This demonstrates the difference in ionisation yield between electron and nuclear recoils as clearly the electron recoil scintillation signals are more strongly suppressed by the drift field. As previously mentioned the extracted charge is drifted to the liquid/gas interface by an electric field and then a fraction of this charge, depending of the field strength, is emitted into the gas phase. Figure 4.8 shows the emission fraction as a function of field strength in the ZEPLIN-III detector.

Following emission into the gas phase, the electrons are accelerated by the strong electric field and collide with xenon atoms generating an electroluminescence signal which is proportional to the ionisation (proportional scintillation). The electroluminescence per unit track length, Y, is a function of the electric field in the gas:

$$Y = A \times E_g - B \times P_{eq} \tag{4.7}$$

where A and B are the electroluminescence yield constants which are determined experimentally, E_g is the electric field and P_{eq} is an expression for the gas density

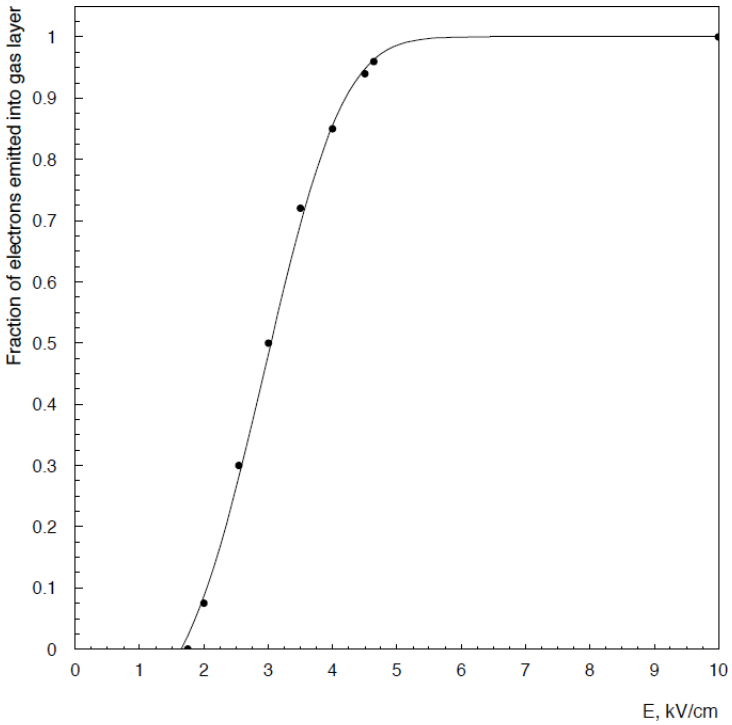

Figure 4.8: The cross-phase emission probability for electrons at the liquid/gas boundary in xenon [196]. The line shows the parameterisation used by the ZEPLIN-III simulation of [50].

compared to gas at the equivalent pressure at 0°C. Figure 4.10 shows the yield as a function of electric field for several models as outlined in [50]. Gaseous contamination represents a significant threat to two-phase xenon detectors. For example a contamination of $< 1\%$ of nitrogen can cause a significant enough increase in the drift velocity of the gas phase as to suppress the ionisation signal to a point where two phase operation in not feasible. Figure 4.11 shows the change in drift velocity as a function of drift field for several contaminants. This suppression is due to the decrease in time spent drifting through the gas phase, leading to a significantly lower energy deposit. During the commissioning of ZEPLIN-III for the second science run this effect was observed.

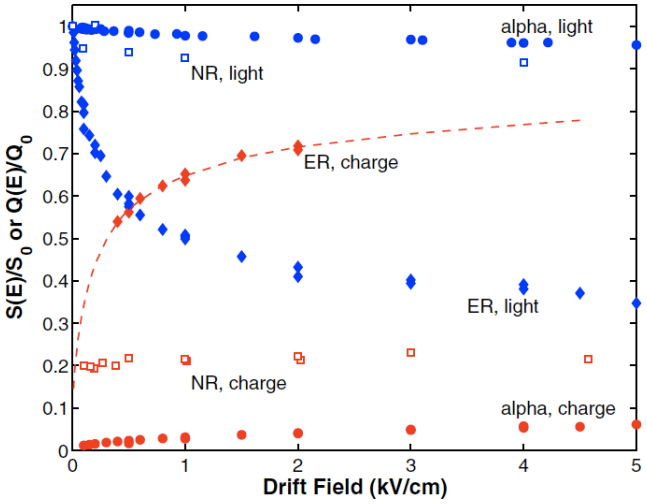

Figure 4.9: The field dependence of scintillation and ionisation yield in liquid xenon for 122 keV$_{ee}$ electron recoils (ER) from γ-rays and 56.5 keV$_{nr}$ nuclear recoils (NR) from alphas. $\frac{S(E)}{S_0}$ and $\frac{Q(E)_y}{Q_0}$ are the scintillation and ionisation yields compared to their zero field values.

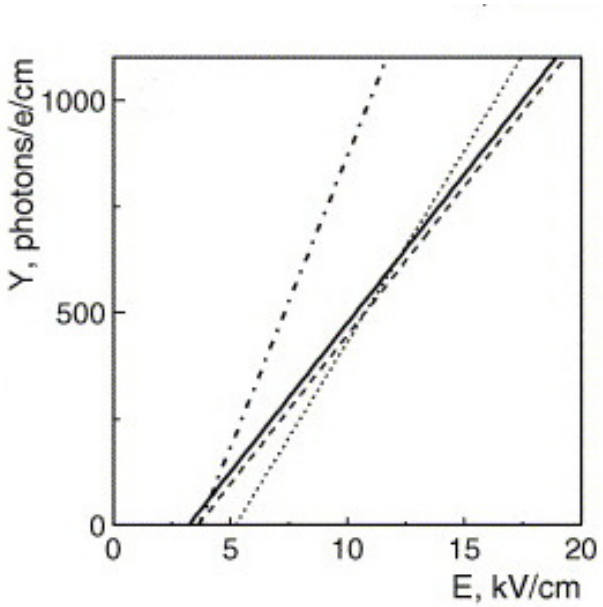

Figure 4.10: The electroluminescence yields for gaseous xenon at 4 bar equivalent pressure at 0°C. Electroluminescence constants (A,B) are; continuous line (70,56), dashed line (70,63), dotted line (90,117) and for saturated vapour represented by the dash-dotted line (137,125). Adapted from [50].

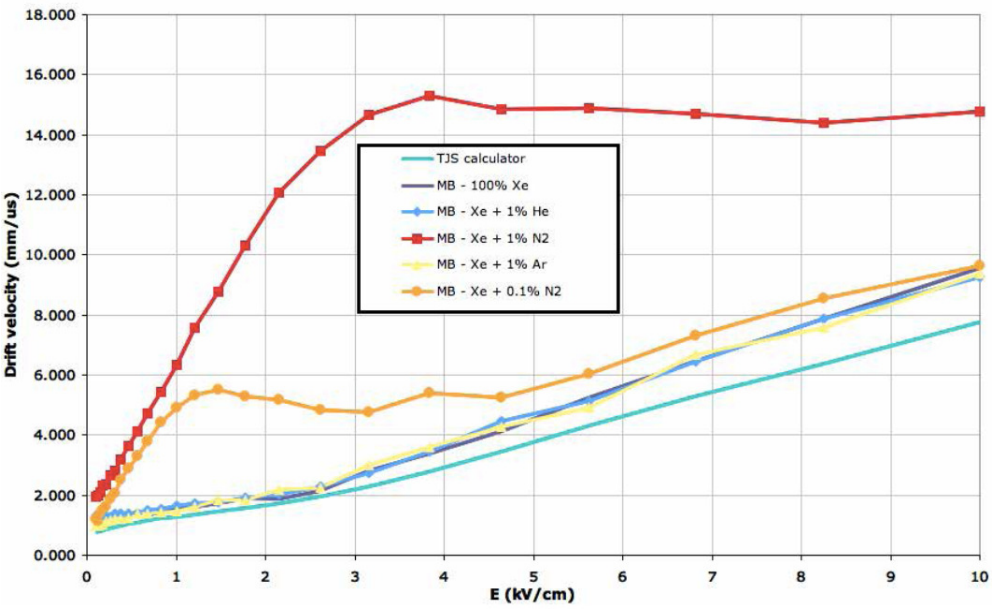

Figure 4.11: Electron drift velocity in xenon gas given various levels of contamination. Calculated by `Magboltz` software. TJS is for the case of pure xenon as calculated by T. J. Sumner. N_2 gives the most significant increase in drift velocity [86].

4.4 ZEPLIN-III Ancillary Systems

4.4.1 Cooling system

The target is cooled using liquid nitrogen (LN_2). The LN_2 is stored in a 36 l vessel below the target. The LN_2 vessel is also housed within the vacuum jacket to maintain thermal isolation. The heat load is approximately 40 W at two phase operating temperature allowing over a day between LN_2 refills. The refilling process has been observed to generate spurious data hence the science run is halted during cryogenic refills to ensure good quality data. The LN_2 vessel has two thermal couplings to the target. One is provided by thick bundles of copper wire for which one end is dipped into the LN_2 and the other is thermally coupled to the copper cooling flange on the underside of the target vessel, as shown in Figures 4.1 and 4.12. The wire bundles are designed to be flexible in order to decouple acoustic and mechanical noise in the LN_2 vessel from the target. The second thermal link is provided by a direct connection between the LN_2 vessel and the hollow cooling flange below the target, as shown in Figure 4.12. This allows boil-off gas to be used for active thermal control of the target

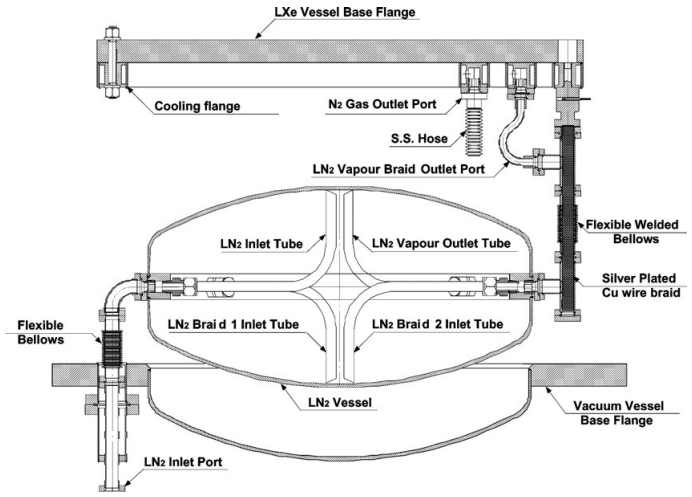

Figure 4.12: The thermal control system elements of ZEPLIN-III.

with minimal cryogen usage. A vapour outlet tube is open at the top of the LN_2 vessel. A control valve may then allow this vapour to flow out of the system via the hollow copper flange on the bottom of the target allowing further cooling of the target. This fine temperature control allows stable two phase operation with the temperature of the target maintained to within 1°C. A slow control system monitors the temperature, switching the valve on and off depending on which side of a pre-set temperature the target is at. This leads to temperature oscillations with a period of about 30 minutes, as shown in Figure 4.13. The time constant for a pressure change in reaction to a temperature change within the target is much longer than this oscillation period and so a high level of pressure stability is maintained, constant to within 0.01 bar. Figure 4.14 shows an example of the pressure during science data acquisition and demonstrates the high level of stability achieved.

4.4.2 Purification and Safety Systems

To achieve successful two phase operation the xenon must be extremely pure. Charge extracted by the drift field is used to measure ionisation. However, the signal size may be affected by electro-negative impurities (mainly oxygen rich molecules) within the xenon. For the maximum drift time in ZEPLIN-III of

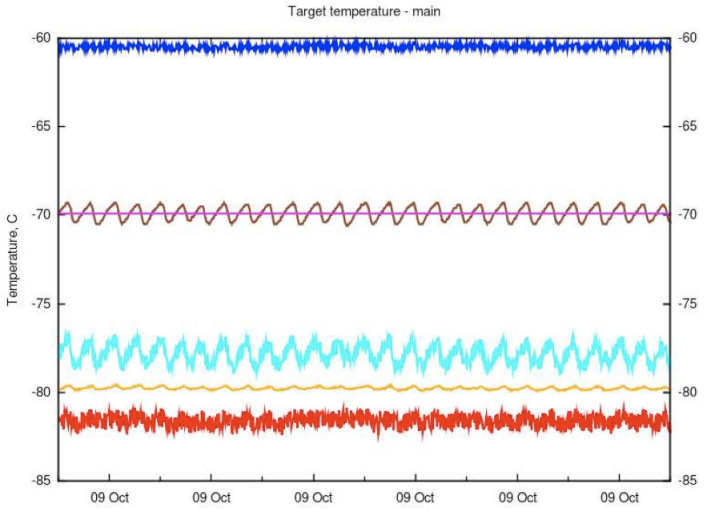

Figure 4.13: A 12 hour sample of temperature readings from internal ZEPLIN-III sensors. The temperature "set-point" is shown by the pink line. The brown line overlaying this with a 30 minute oscillation period shows the temperature of the left braid which is connected to the cooling flange below the target.

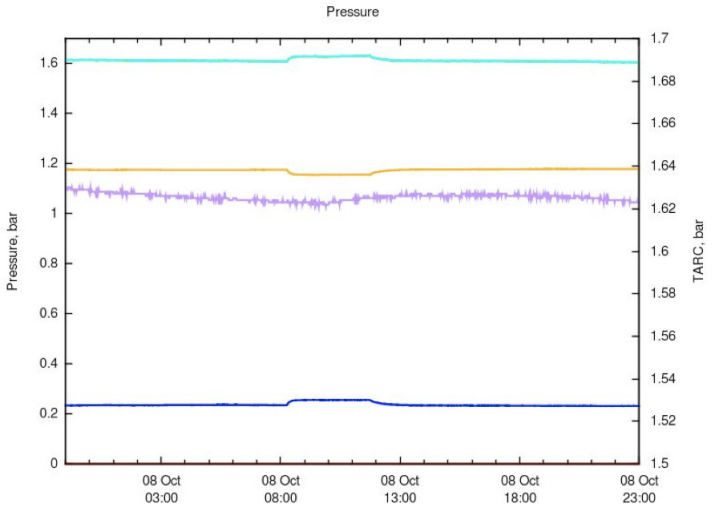

Figure 4.14: A 12 hour sample of data from ZEPLIN-III internal pressure monitors. The pressure within the target is shown by the blue line. In this example a slight deviation in pressure can be seen shortly after 6 a.m. which is in response to a change in ambient temperature (the orange line) caused by unrelated mining operations. The purple line shows the corrected pressure (TARC) and remains stable to within 0.01 bar.

about 17 μs the lower limit on the level of purity required is parts per billion (ppb). As this is beyond commercially available xenon a purification system is required. A schematic of the ZEPLIN-III gas system is shown in Figure 4.15 and a photograph showing the gas system in situ is shown in Figure 4.16. 40 kg of xenon is stored in two stainless-steel bottles, B1 and B2, fitted with ultra-high vacuum (UHV) valves and regulators. The bottles are housed in stainless-steel jackets which may be filled with LN_2 to allow cryogenic pumping. The gas delivery lines are fitted with 0.5 μm particle filters and are of an all-metal construction to allow baking. This prevents contamination of the xenon as it is transferred through the gas system. Two SAES getters are connected to the main body (or "hedgehog") to allow purification of the xenon when transferring from a bottle to the target via getter G1, or in bottle-to-bottle transfers via getter G2. Xenon may be routed to an electron lifetime monitor (ELM) for purity measurements. A hot getter is also attached for further purification. The system is pumped by both an oil-free scroll pump and a turbo-molecular pump. The gas system can achieve a base vacuum of $\sim 10^{-8}$ mbar, limited by H_2 outgassing from metal pipes. Low pressure gas may be fed through the mass spectrometer for residual gas analysis (RGA). This was also used for helium leak testing.

The gas handling system has several built in safety features. Both the target and the hedgehog are connected to a large safety reservoir (the emergency dump, 1500 l capacity) via burst discs. These burst discs are a passive system to prevent xenon leaking to the atmosphere in the event of a catastrophic coolant failure. A motorised valve (V14) connects the target to the dump in parallel to the burst disc BD1. This valve may allow the slow release of pressure from the target for a less rapid coolant failure which would prevent damage to delicate detector components which may result from the rapid pressure change in the case of a burst disc rupture.

4.4.3 Data Acquisition

The data acquisition system is also described elsewhere [262, 156]. The average signal gain during the second science run was approximately 2×10^6. The signal from each of the 31 PMTs is split into two, one is read directly and the other is first amplified by a factor of 10 by Phillips Scientific 770 amplifiers. These are

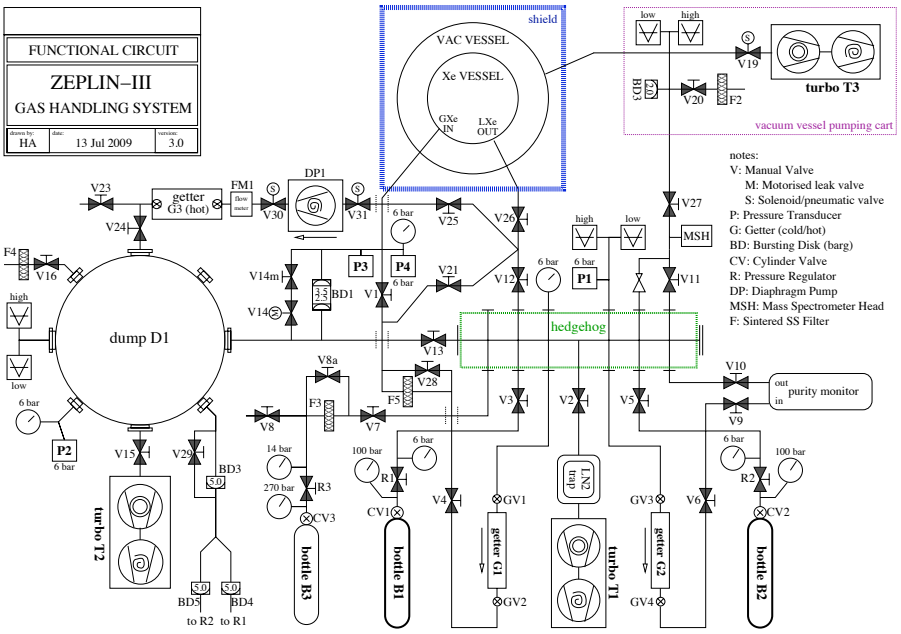

Figure 4.15: A schematic diagram of the ZEPLIN-III gas handling system. The purity monitor refers to the ELM which was attached to the system to measure the purity of the xenon [128].

called the low sensitivity (LS) and high sensitivity (HS) channels, respectively. The noise levels during the second science run were 70 μV_{rms} to 0.1 mV_{rms} and 0.2 mV_{rms} to 1 mV_{rms} for the LS and HS, respectively. All 62 individual channels, along with a summed channel from both LS and HS, are digitised by an 8-bit ACQIRIS ADCs at a rate of 500 MHz. Figure 4.17 shows the channels recorded in an example event from science run data. The PMTs used common electrodes and so the large gain variance between the PMTs used for the second science run (a factor of approximately 100) was corrected using individual Phillips Scientific 804 attenuators attached to the PMT signal cables. The trigger initiates the recording of a 36μs waveform in all channels, $\pm$18μs around the trigger point. This timing window was chosen to give a reasonable margin beyond the maximum expected fiducial drift time of 15μs and is symmetrical about the trigger point, since its possible for either the S1 or S2 to trigger the system. Where the S1 signal is below the threshold the S2 signal, being larger, may trigger the system. This ensures sensitivity to low energy events whilst reducing the number of spurious triggers as a higher threshold may be set.

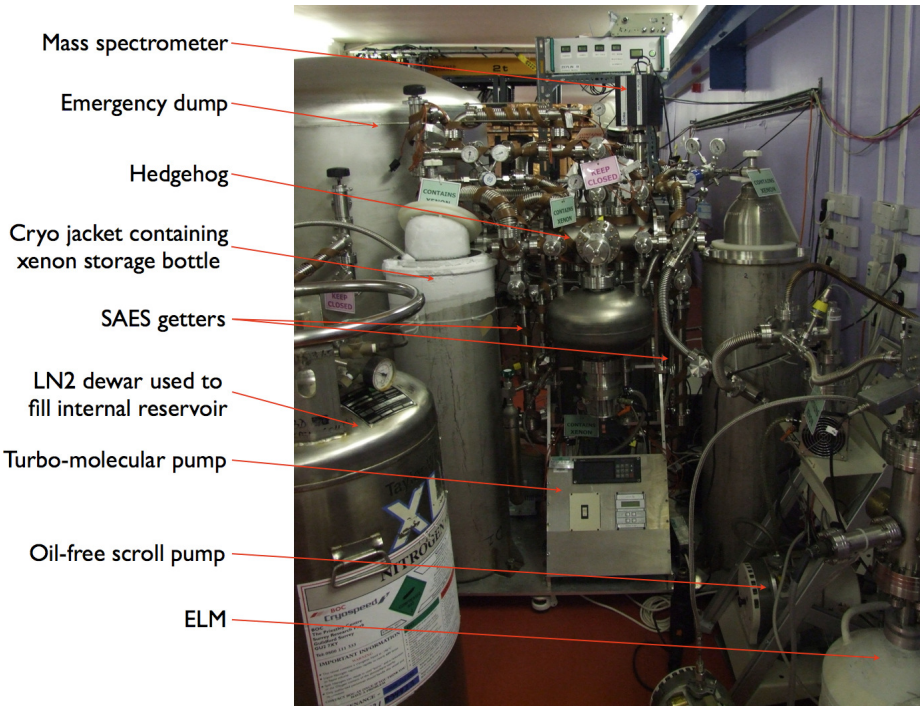

Figure 4.16: A photograph of the ZEPLIN-III gas handling system annotated with some of the key features.

The ZEPLIN-III trigger schematic is shown in Figure 4.18. This is generated by feeding the high sensitivity sum channel through a summing amplifier before integration (500 ns) and differentiation (500 ns) by a timing filer amplifier (Canberra 2111) giving a shaped sum pulse. The shaped sum pulse is then fed to a fast discriminator. The threshold of this discriminator was set to -80 mV. This threshold allows the system to trigger at a sustainable rate in terms of data rate and volume, whilst also allowing very small signals to be recorded. These extremely small signals are triggered by the secondary S2 signal and -80 mV is equivalent to ~ 11 ionisation electrons (~ 0.2 keV$_{ee}$ for nuclear recoils). An inhibit signal ensures that the system cannot trigger until all the crates containing the digitisers are ready for the next event. Additionally a gate was used to generate an inhibit of 1 ms to ensure a minimum time between events so that the PMTs have adequate time to recover after each event in order to minimise the number of spurious signals contaminating the data. Figure 4.19 shows an example of waveforms at each stage of the trigger generation.

When the system is triggered the digitised output is read in by the ZEPLIN-III DAq computer using custom linux based software. With 2 ns sampling this means that 1.8×10^4 bins have to be recorded in each 36μs timeline giving a raw data file size of ~ 1 MB per event. The DAq computer is a Viglen LX260 server with 2 CPUs and 6 hot-swap drive bays supporting Ultra320 SCSI (10,000 rpm) drives giving a maximum data writing rate of 60 MB/s. The connection to ACQIRIS is 80 MB/s but, due to the writing speed, this rate would be unsustainable for prolonged periods. In practice it was found that the maximum sustainable rate was ~ 50 Hz.

After compression, the data are written to 100 GB LTO1 data tapes. Two identical copies are made, one is retained at the Palmer lab and one is sent to RAL where it is uploaded to a central server. The data is then reduced using a custom software package called `ze3ra`, discussed in more detail in Section 8.4.1.1. Multiple instances of the program performed the reductions in parallel on an Apple XGRID system with 28 processors, giving a combined processing power of 72 GHz.

4.4.4 Other Systems

The ZEPLIN-III detector has several other smaller ancillary systems. The source delivery system was fully automated and calibration sources could be inserted above the target volume remotely. An optical fibre leads from the target to an optical connection at the base of the instrument. This was connected to an LED and used to test the response of the PMTs, as discussed in Section 8.2.5. A purity monitor is attached to the gas handling system, this apparatus measures the lifetime of electrons drifting in the xenon. The ELM is housed inside a dewar for cooling using LN_2.

4.5 FSR

The first science run of the ZEPLIN-III detector lasted for 83 days between the 27^{th} of February 2008 and the 20^{th} of May 2008 [254]. A total of 847 kg·days of raw data were gathered, which was compressed to 15.5 TB. During the first science run the detector used passive shielding only, an array of 31 ETL D730/9829Q PMTs [260] and a drift field of 3.9 kV cm^{-1} in the liquid phase and 7.8 kV cm^{-1} in the gas phase. The data were re-analysed using up to date $\mathcal{L}_{\mathbf{eff}}$ results and achieved a discrimination power between electron and nuclear recoils of 7800 : 1. A 90% C.L. result for the WIMP-nucleon cross-section of 8.8×10^{-8} pb for a 56 GeV/c^2 WIMP mass was obtained [26]. The details of the first science run analysis are given in Table 8.1. These results were also combined with the second science run data to give a total result for the ZEPLIN-III project, as outlined in Section 8.4.2.1.

Following the FSR data acquisition was halted for upgrades to the instrument. These upgrades included the addition of the veto, replacing the PMTs with custom made low background PMTs as outlined in this Chapter and Chapter 5.

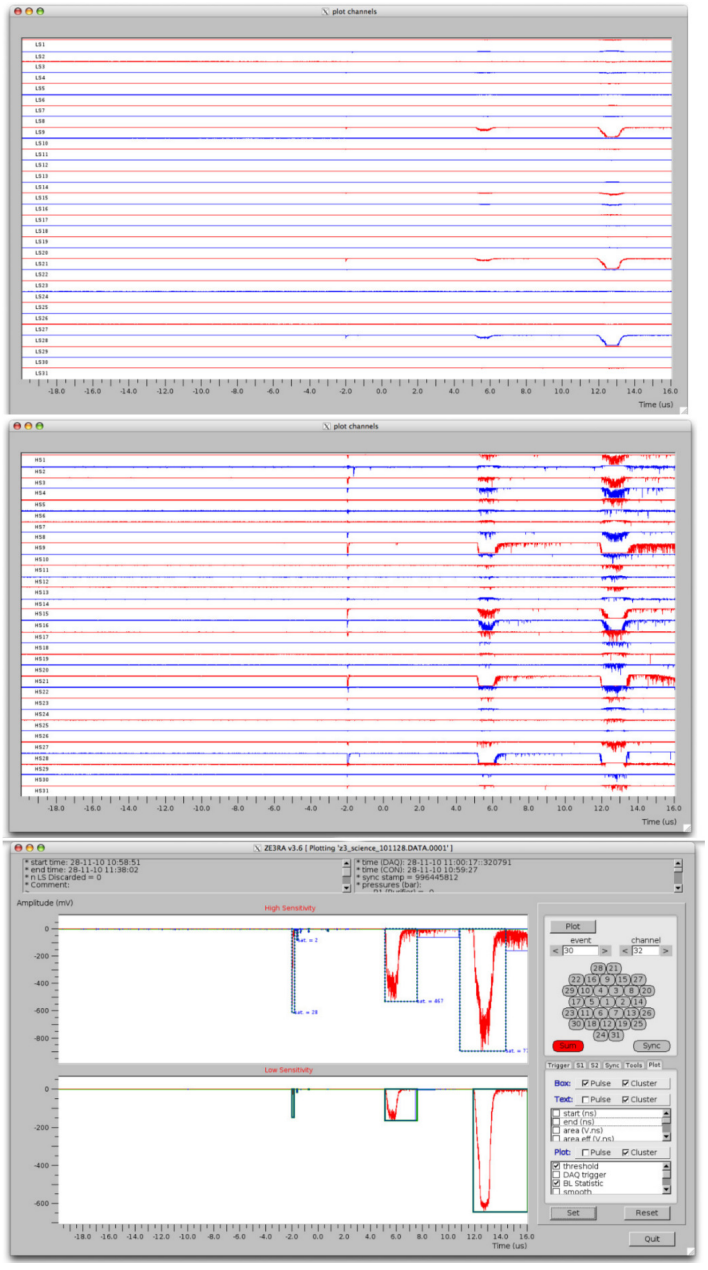

Figure 4.17: An example event recorded by the ZEPLIN-III daq and displayed by ZE3RA (see 8.4.1.1). The upper left image shows the 31 low sensitivity channels, the upper right image shows the 31 high sensitivity channels and the middle bottom image shows the summed waveforms for high sensitivity (upper window) and low sensitivity (lower window).

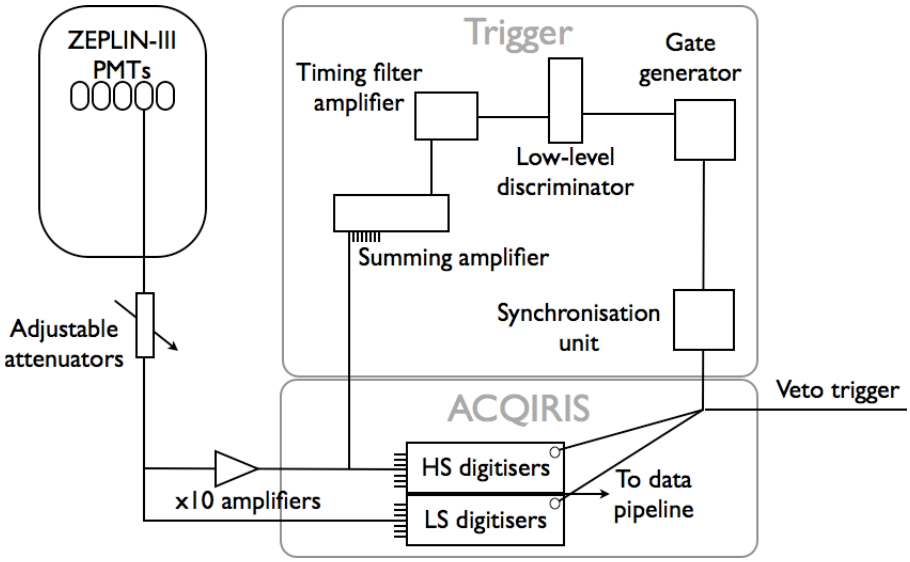

Figure 4.18: A schematic of the ZEPLI-III SSR trigger setup.

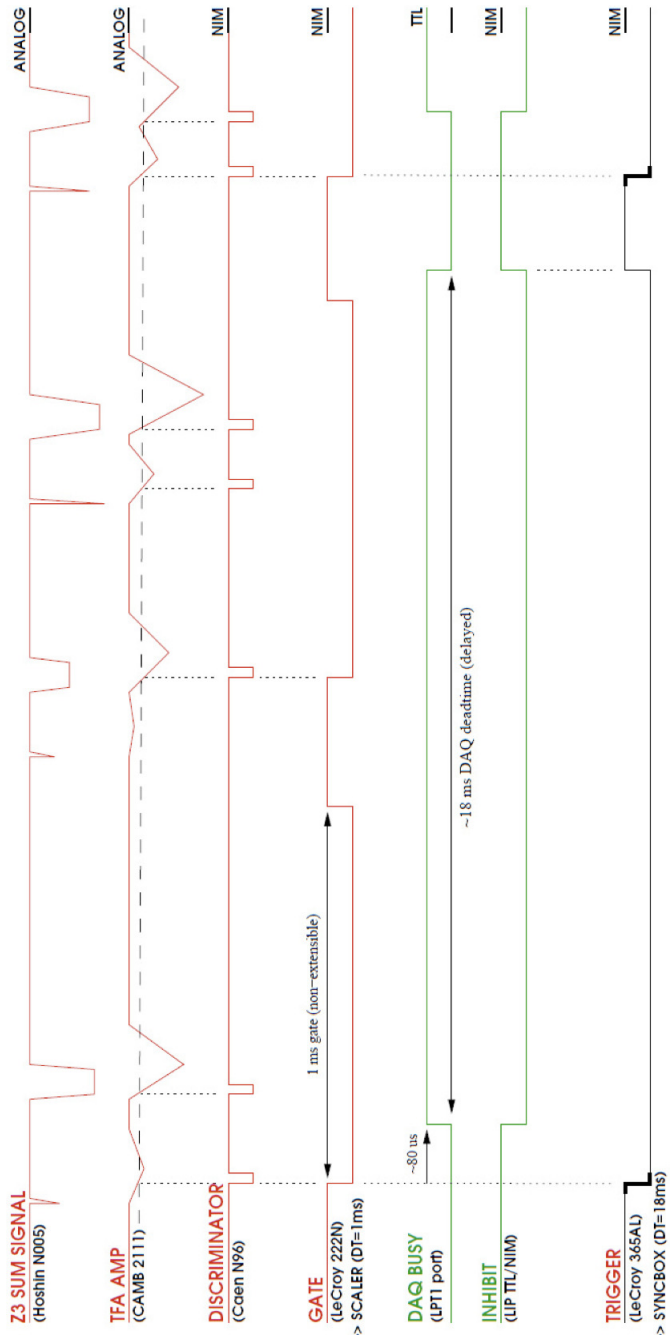

Figure 4.19: An example of the trigger generation for the ZEPLIN-III second science run. The upper waveform shows an example of the ZEPLIN-III high sensitivity sum channel generated by summing the 31 PMT signals after amplification by a factor of 10. The small thin initial pulses are the S1 signals from scintillation and the wider pulse (and also saturated in these examples) following these are the S2 signals from electroluminescence. Both triggers in this example are generated by the S1. The second signal which does not trigger due to the Daq inhibit signal would have generated a trigger from the S2 (note this is not to scale and does not represent a typical DAq busy time but is just for illustrative purposes) [128].

Chapter 5

Veto Detector Commissioning

5.1 ZEPLIN-III Veto Detector

5.1.1 Introduction

A major part of the ZEPLIN-III upgrade for its second science run was the addition of the veto detector (hereafter refereed to as the veto). This instrument was designed, constructed and commissioned by the University of Edinburgh, with help from ITEP Moscow. As such I was heavily involved in most aspects of this instrument, taking the leading role in many of them. For completeness, this chapter includes some work vital to the commissioning of this instrument in which fellow Ph.D. students working on the ZEPLIN-III project were either involved or took a lead role.

The work I was most heavily involved with includes veto assembly and testing work. I put all the modules together and I completed several test assemblies of the complete veto system, in addition to the final assembly before the science run. I also designed and machined the additional neutron shielding which surrounded the gadolinium loaded polypropylene shielding. I also completed the energy calibration of the veto, although the mote carlo simulation used for comparison was completed by a colleague. I investigated the downsampling and triggering options and then aided colleagues from ITEP in setting up the veto trigger. I wrote half of the automated veto daily checks and I was responsible for the veto data. I wrote the `raVen` software package, used to reduce the veto data, and

I also wrote most of the additional analysis codes which were used to interpret the veto data. For the quenching factor measurements of the plastic scintillator, discussed in Section 5.2.6, I obtained the data along with Lea Reichhart, and I developed the analysis technique which allowed the energy scale to be set.

This instrument had several strict requirements to meet; it was required to be a low cost device, it had to have high sensitivity to the background experienced by the ZEPLIN-III detector and it had to introduce only minimal additional background. Achieving these three aims would allow the veto to increase the significance of any WIMP signal detected, increase the ability of the experiment to reject unwanted background events and also act as a diagnostic tool whilst not compromising the excellent sensitivity already achieved, by introducing additional sources of internal background. Two vital uses of the veto as a diagnostic tool were (*i*) to characterise the ZEPLIN-III background without compromising the WIMP search results, by using a sample of vetoed events and (*ii*) to sample events with rare topologies and allow the analysis software to be trained using science run background data to avoid spurious signals from contaminating the WIMP search data. This chapter describes the design, construction and operation of the veto and its ancillary systems. The results obtained by the veto are presented in Chapter 6.

5.1.2 ZEPLIN-III Veto Detector Design

The veto is of a modular design with 52 sections of polystyrene based UPS-923A plastic, weighing a total of 1057 kg. These sections of plastic were doped with benzene based scintillator (p-terphenyal 2%, POPOP 0.02%) by Amcrys-H, Kharkov, Ukraine [38]. The veto modules each consist of one section of plastic scintillator, one PMT, one base containing the voltage divider circuit and pre-amp and the scintillator wrapping used to ensure light tightness. The properties of this material are summarised in Table 5.1. The 15 cm thick scintillator modules are mounted adjacent to 15 cm thick passive shielding, consisting of gadolinium loaded polypropylene $(C_3H_6)_n$, to form a barrel plus roof shape which covers over 3π sr with a total thickness of 30 cm. The gap in the veto corresponds to the floor shielding as the veto does not extend beneath the detector. This thickness of hydrocarbon reduces the external neutron flux into the target volume by a factor

of 10^5 [327]. Figure 5.1 shows CAD drawings of the veto. To increase the light collection efficiency, each veto module was wrapped along its length with three layers of 76 μm thick PTFE sheeting. Tests showed that this doubled the light collection efficiency [71]. A PMT (type ETEL 9302KB) was optically coupled to the far end of each scintillator module using BC-630 silicone-based optical couplant from Saint Gobain Crystals Ltd. This design kept the veto PMTs as far from the ZEPLIN-III target as possible to minimise the introduction of additional background radiation.

The main source of PMT activity is the glass required for the photocathode. The veto contains 52 PMTs. The veto roof contains 20 PMTs and the barrel contains 32 PMTs, the barrel section PMTs are housed near the base of the detector, as far as possible from the target volume. The PMT glass contains trace contamination of uranium, thorium and potassium. Measurements of the contamination in the veto PMTs were taken using a high purity germanium (HPG) crystal and the results are presented elsewhere [327]. A light-tight PVC tube was placed over each PMT and chemically bonded to the scintillator using UV activated glue. A sheet of aluminised Mylar foil was placed at the opposite end to the PMT in each module to further increase the light collection. The entire assembly was then wrapped in a black opaque PVC sheet to provide light tightness. A fibre optic cable was then inserted into the base of each module to allow for calibration. Figures 5.2 shows an unwrapped scintillator module and a fully assembled module mounted on a section of gadolinium loaded polypropylene.

The passive neutron shielding was loaded with gadolinium (in the form of 10 μm Gd_2O_3 powder) to enhance its ability to detect neutrons. A total weight of 756 kg of polypropylene was required to create the passive component of the barrel plus roof shape around the ZEPLIN-III detector. The detector and veto stand on a base of 30 cm of polypropylene to give full 4π sr neutron shielding, as in the first science run. Polypropylene has a high hydrogen content which will thermalise neutrons. The thermal neutrons may be captured by hydrogen to form deuterium releasing a 2.2 MeV γ-ray. It is much more likely however that the thermal neutrons will be captured by the gadolinium which has the highest neutron capture cross-section of any naturally occurring material, at $49,000$ barns

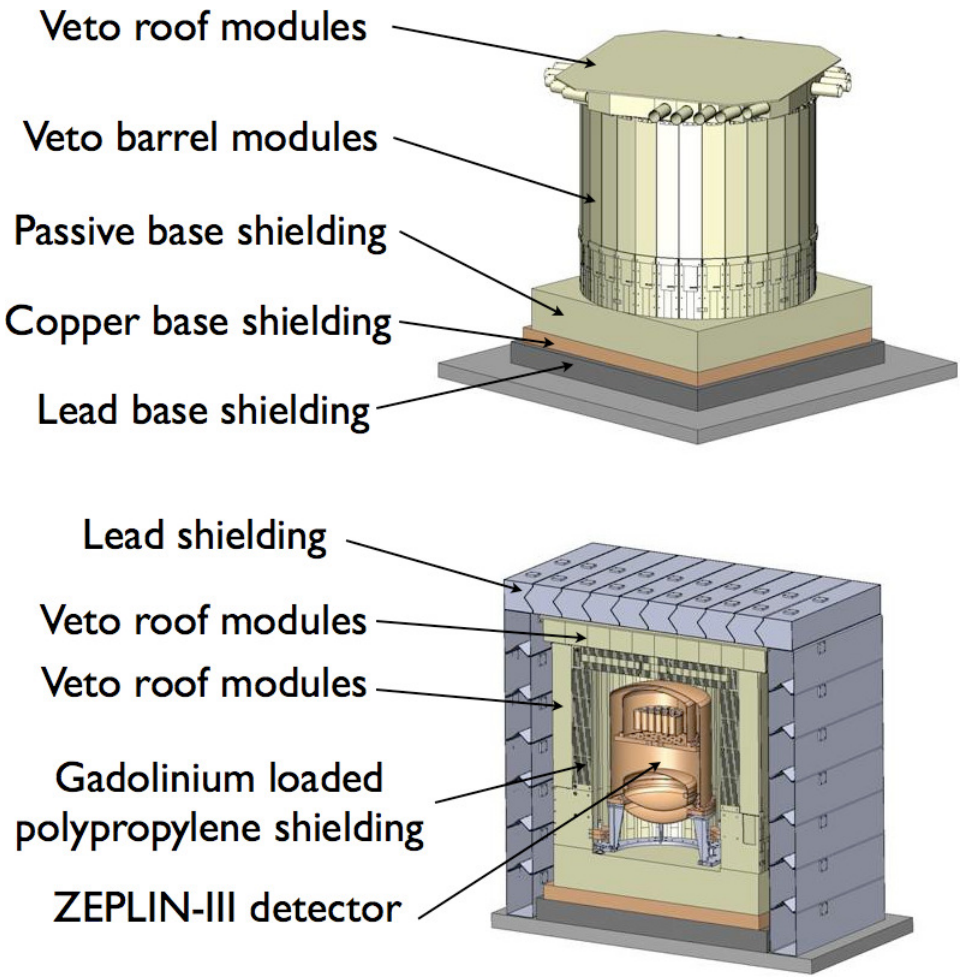

Figure 5.1: CAD drawings of the ZEPLIN-III veto. The left image shows the barrel plus roof design of the 52 active modules and the right image shows a cut away of the completely assembled system. From center moving outwards this comprises of the ZEPLIN-III detector, the passive Gd-loaded neutron shield, the veto modules and finally the lead shielding. The passive Gd-loaded shielding can be distinguished by the dark lines running thorough these sections. These lines show the slots into which the Gd was loaded. Adapted from [128].

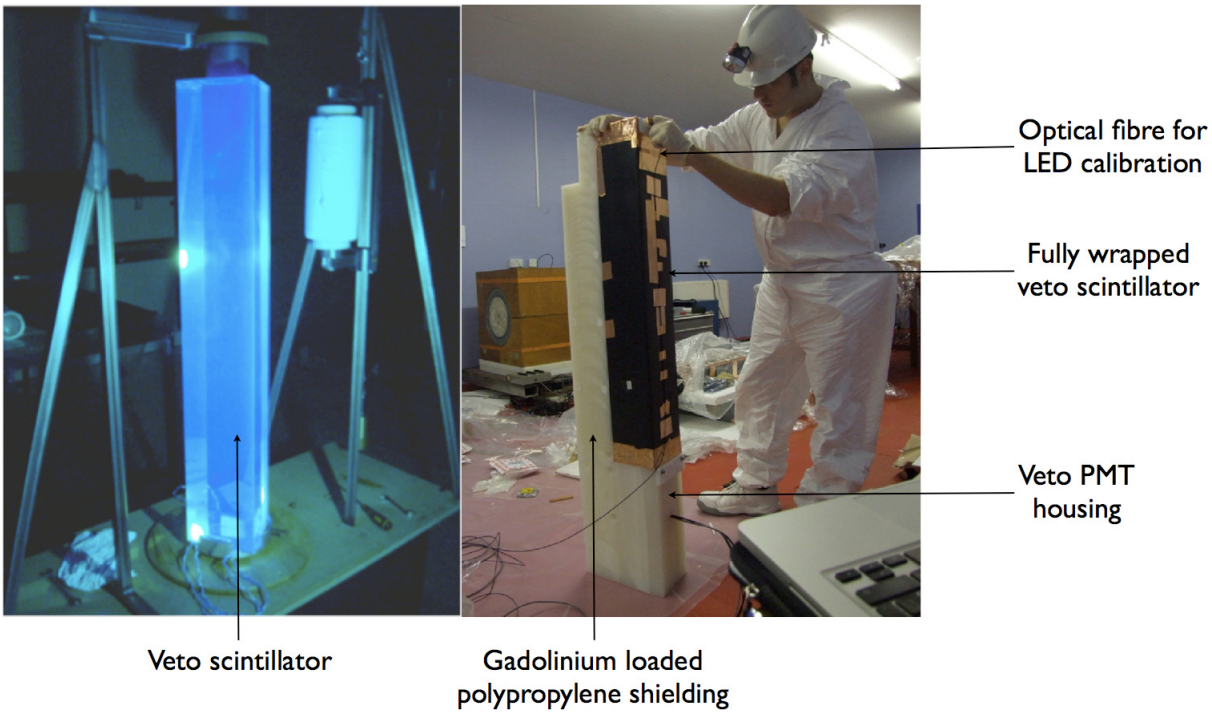

Figure 5.2: Photographs of a veto module. The left image shows a piece of scintillator prior to wrapping. The right image shows a fully constructed veto module as described in Section 5.1.2. Note that the active and passive shielding were offset by 2 cm to ensure no line-of-sight gaps could allow background neutrons into the fiducial volume.

Table 5.1: Properties of the plastic UPS-923A scintillator as stated by the manufacturer [38]. The light output is given compared to anthracene which produces an average of 20 photons per keV, giving an expected value of $\sim$ 12 photons per keV for the veto modules. The light output and bulk attenuation length were remeasured for each module, as described in Section 5.1.4.

property	value
Density	1.06 g cm^{-3}
Refractive index	1.52
Light output	60% anthrance
Emission peak	425 nm
Rise time	0.9 ns
Decay time	3.3 ns
Bulk attenuation length	50-300 cm

(4.9×10^{-20} cm^{-2}). This high cross section is predominantly due to the 15.7% abundance of the isotope ^{157}Gd in natural gadolinium. This isotope has a neutron capture cross-section of 242,000 barns. Neutron capture by ^{157}Gd is accompanied by the emission of between three and four γ-rays with energy totalling 7.94 MeV. Figure 5.3 shows the γ-ray spectrum emitted by the ^{157}Gd(n,γ)^{158}Gd reaction along with the neutron capture cross section as a function of neutron energy [323]. The required gadolinium loading fraction was calculated using Monte Carlo simulations which are described extensively in [71]. Loading the polypropylene with gadolinium showed a remarkable increase in the maximum neutron tagging efficiency of the veto, from $\sim$ 55% with no gadolinium to $\sim$ 81% for 0.5% loading by weight. This level of gadolinium loading also improved the mean neutron capture time by a factor of 10 [71] enabling a shorter veto recording time to be used and a lower chance of a non-neutron event being vetoed due to an accidental coincidence. These simulations also investigated methods of gadolinium loading. The simulations indicated that 2 mm wide, 10 mm pitch slits in the polypropylene filled with gadolinium oxide (Gd_2O_3) gave a high efficiency with minimal difficulty regarding construction. The slits were filled with Rutherford Type 71 epoxy containing the gadolinium oxide power by the RAL workshop. This epoxy was found to keep the gadolinium oxide uniform in suspension during the period of time taken to dry, ensuring uniform performance across the veto. Figure 5.4 shows the expected performance of the veto as a function of the gadolinium loading fraction. Figures 5.5 and 6.17 show results from calibration data confirming a

gadolinium concentration of $0.42 \pm 0.03\%$ (w/w). This concentration is at the centre of the plateau region from $0.3 - 0.5\%$, where the neutron tagging efficiency varies by less than 1% [27].

Polypropylene, consisting of only the light elements carbon and hydrogen, is an inherently radio-pure material. This is another advantage to its use as neutron shielding. Loading a polypropylene shield with a significant quantity of a rare earth, such as gadolinium, could pose a potential threat of neutron emission by (α, n) reactions. The isotope ^{152}Gd is present at a concentration of 0.2% in natural gadolinium. This isotope decays by α-particle emission, thus a possibility is that the α-particle released may interact with a loosely bound neutron leading to neutron emission. The SOURCES-4A code was used to calculate the expected neutron emission spectrum from gadolinium in the second science run veto [327]. The contribution was found to be negligible when compared to the integrated rate from uranium and thorium contamination of the polypropylene shielding itself, at 1.2×10^{-10} n s^{-1} cm^{-3}. This represents no threat to the instruments dark matter sensitivity. The veto PMTs are model 9302KB from Electron Tube Enterprises Ltd. (ETEL). These consist of a 78 mm diameter window with a blue-green sensitive bialkali (K-Cs-Sb) photocathode and nine dynode stages giving a gain of up to 0.7×10^6. The anode sensitivity is given as 50 (200) A/lm at nominal (peak) operating voltage. These PMTs have a spectral range covering 285-630 nm with a response that peaks at $\sim$ 30% quantum efficiency between 350 and 400 nm. The envelopes are manufactured from low background glass, with the contamination levels quoted as 30 ppb U, 30 ppb Th and 60 ppm K. This was confirmed experimentally as outlined in [327]. The dynode pins were plugged into low background B14A bases fitted with voltage divider networks also supplied by ETEL (type ETL C647BFN2-01). The contamination level of the base and components was confirmed to be consistent with (or lower than) the manufacturers stated values of 13 ppb U, 19 ppb Th and 21 ppm K. All the power supply and signal cables required for the veto detector were manufactured to order with minimal radiological content. All components were radio-assayed and the number of neutrons emitted from the veto expected to scatter only once in the ZEPLIN-III target is 0.3 events per year in anti-coincidence with the veto. The veto is also expected to contribute less than 1000 electron recoils per year

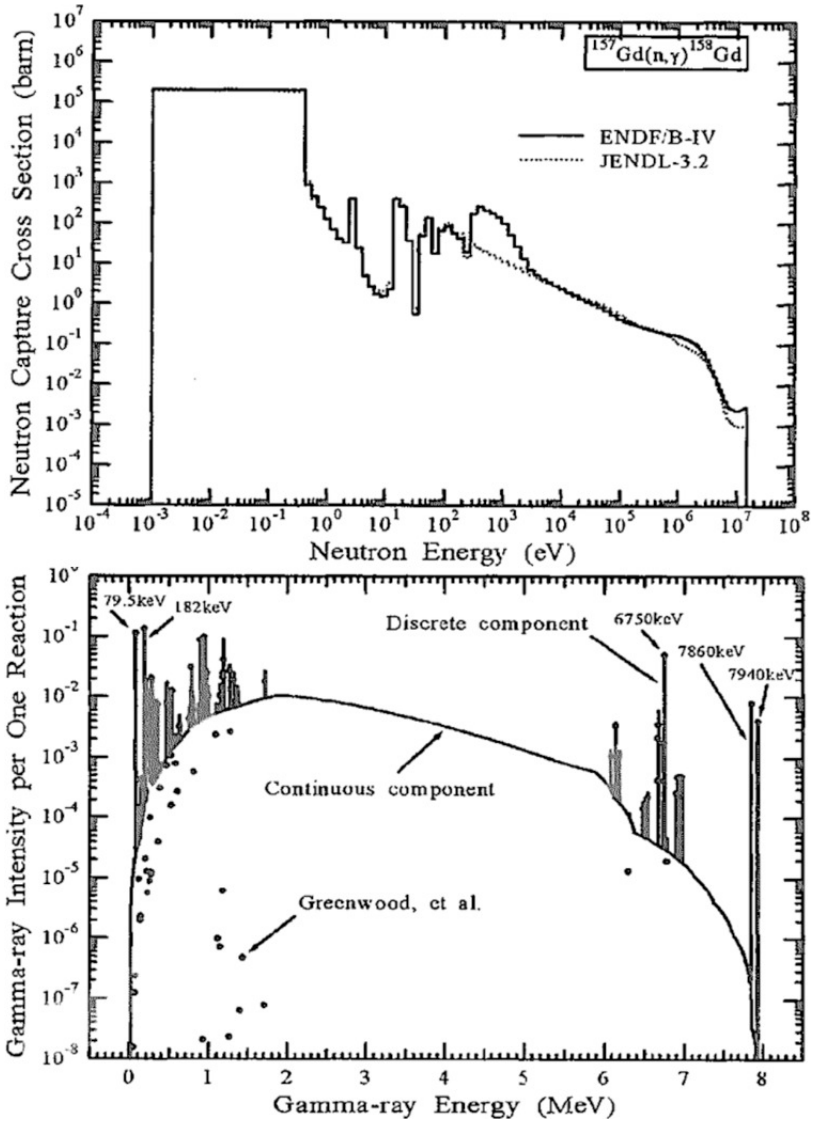

Figure 5.3: The neutron capture cross section of ^{157}Gd as a function of neutron energy (upper image) and the γ-ray energy spectrum from the ^{157}Gd(n,γ)^{158}Gd reaction (lower image) [323].

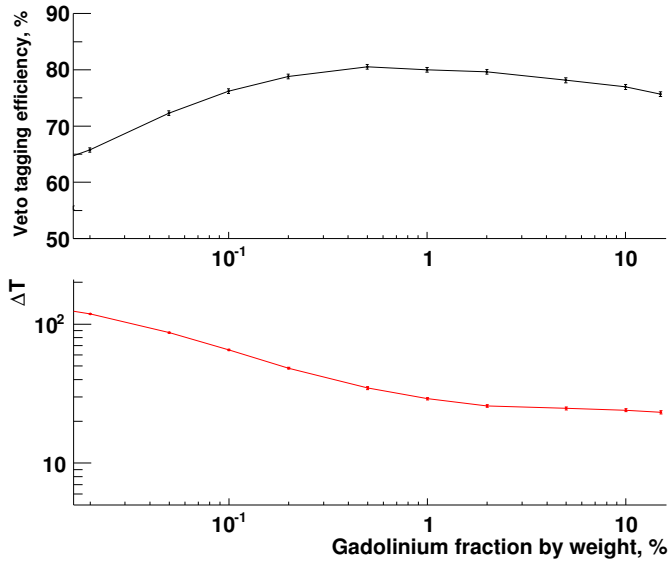

Figure 5.4: Monte Carlo simulation results of neutron detection for various gadolinium concentrations. The upper image shows the veto neutron tagging efficiency and the lower image shows the time delay (μs) between a nuclear recoil in ZEPLIN-III and neutron capture by the veto which is subsequently detected by observation of the γ-rays emitted [27].

between 2 and 16 keV$_{ee}$ [27].

Figure 5.6 shows the veto at various stages of construction between May and June 2010.

5.1.3 Data Acquisition

The veto PMTs operate with a negative bias supplied by a LeCroy 1440 HV high voltage system. This contains four LeCroy 1443NF boards which supply around -1 kV to each PMT, with the exact voltage supplied to each PMT adjusted to equalise the response of each veto module. Since the PMTs have an output impedance of 1 MΩ, preamplifiers were attached to the output to reduce the impedance to 50 Ω, in addition to providing an additional gain of 10. These preamplifiers were designed and manufactured at the University of Edinburgh by the electronics workshop [362]. The circuit design for the preamplifier plus voltage divider network is shown in Figure 5.7. The preamplifiers were tooled onto surface

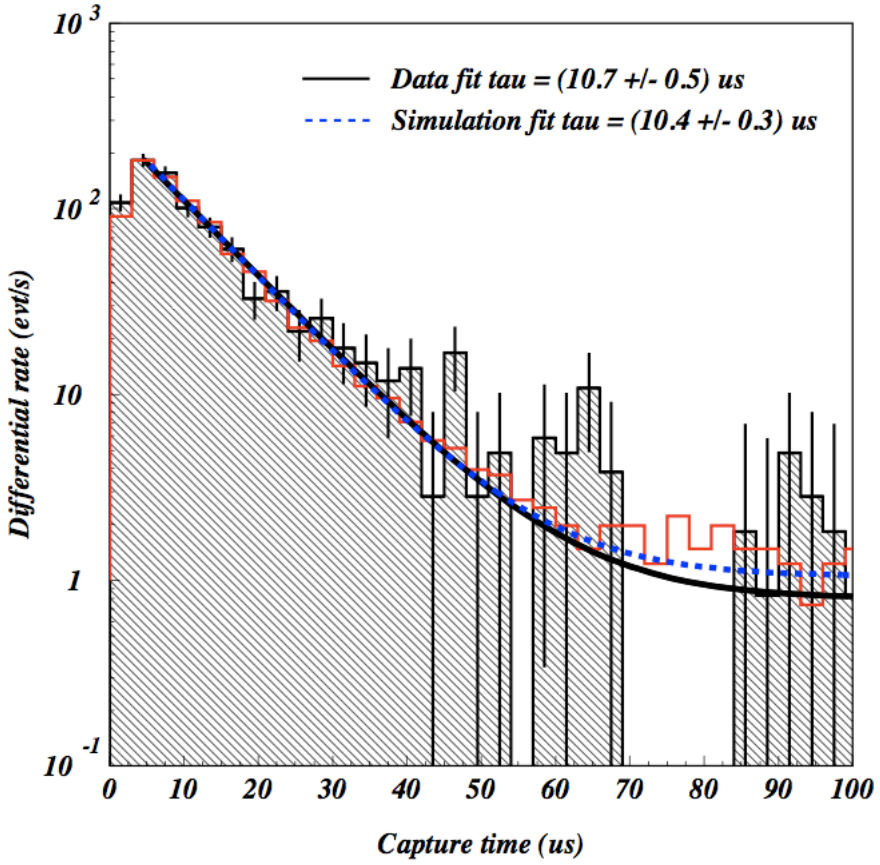

Figure 5.5: The time distribution of energy deposits in the veto relative to the primary signal in the ZEPLIN-III detector for events from the nuclear recoil band. Taken from neutron calibration data (filled black histogram) and Monte Carlo simulation (open red histogram). The elapsed time between the two signals during which the neutron is thermalised and then captured is dependent on the gadolinium loading fraction. The overall trend line (solid) is a fit to the calibration data with a characteristic decay time on 10.7 ± 0.5 μs which is in agreement with the simulated decay time (dotted blue line) showing a decay time of 10.4 ± 0.3 μs for 0.42% (w/w) gadolinium concentration [191].

Figure 5.6: Various stages of the construction of the ZEPLIN-IIII veto detector, arranged anti-clockwise in chronological order. The upper left images shows the partially completed barrel section around the ZEPLIN-III detector. The middle left image shows the ZEPLIN-III detector inside the completed barrel section including the copper source holder over the top of the target. The central pipe was used for daily energy calibration and the thicker off-center tube was used for nuclear and electron recoil band calibrations. The bottom left image shows the gadolinium loaded roof section being inserted onto the completed inner 15 cm of gadolinium loaded neutron shielding. The bottom right image shows the barrel section veto scintillator modules fully assembled and the partial assembly of the roof modules. The top right image shows the full assembled veto prior to the addition of the final outer layers of shielding (an additional 5-9 cm of polypropylene and 20 cm of lead).

mount printed circuit boards made from light-weight low-background single-sided resin bonded paper to ensure minimal additional background was introduced. The 50 Ω output signal is then fed to seven CAEN V1724 flash analogue to digital converter (FADCs) modules housed in a VME8011 crate, shown in Figure 5.8. This crate uses a CAEN V2718 PCI bridge which transfers data via an optical link to a dedicated DAq computer. The FADCs have a 14-bit resolution covering a range of 2.25 V, slightly below the PMT saturation voltage determined to be ∼2.5 V. The bandwidth is 40 MHz with a maximum sampling rate of 100 MB/s simultaneously on each channel and internal buffering to ensure zero dead time performance. Custom run-control software was designed to allow direct or remote control of the veto DAq.

Different trigger modes are permitted to be used simultaneously to record events. Each event contains timelines for the 52 veto modules as well as additional data and timelines described later in this section. The trigger options allowed by the DAq hardware are:

- **Slave mode:** In this mode the DAq records an event when a signal is received from an external source. The main purpose of this detector is to veto ZEPLIN-III events and slave mode, where the external signal is generated by ZEPLIN-III, was the main mode of operation of the veto during the second science run.

- **Master mode:** In this mode the veto is able to trigger itself. The output signals may be fed back into the trigger and a hardware threshold set. If the threshold is surpassed by a module then a trigger is generated and an event is recorded. This method was used to observe background radiation and for calibration.

- **Majority mode:** This is an extension of the master mode. Each module is capable of individually exceeding the threshold required to generate a trigger. If the threshold is surpassed then a NIM pulse is generated. If other veto modules surpass the signal threshold at the same time then multiple NIM pulses may be generated simultaneously. A further threshold can be set for the number of simultaneous NIM pulses required to trigger the recording of the event. This method was used to record background radiation. It

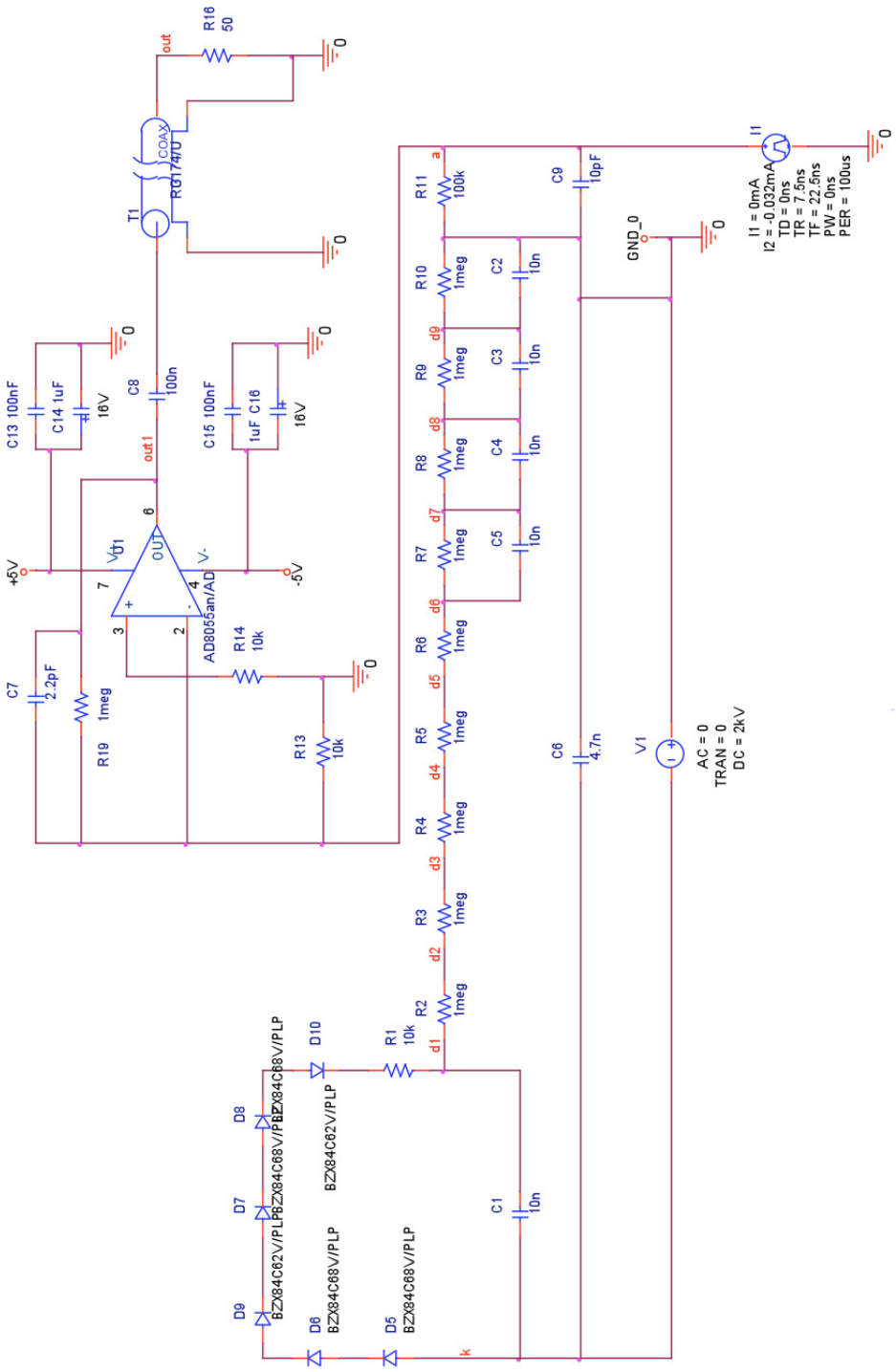

Figure 5.7: A circuit diagram for the veto PMT electronics. The bottom part of the image is the voltage divider network and the top part of the image is the preamplifier circuit. The signal cable "out" in the top right is fed to the FADC [362].

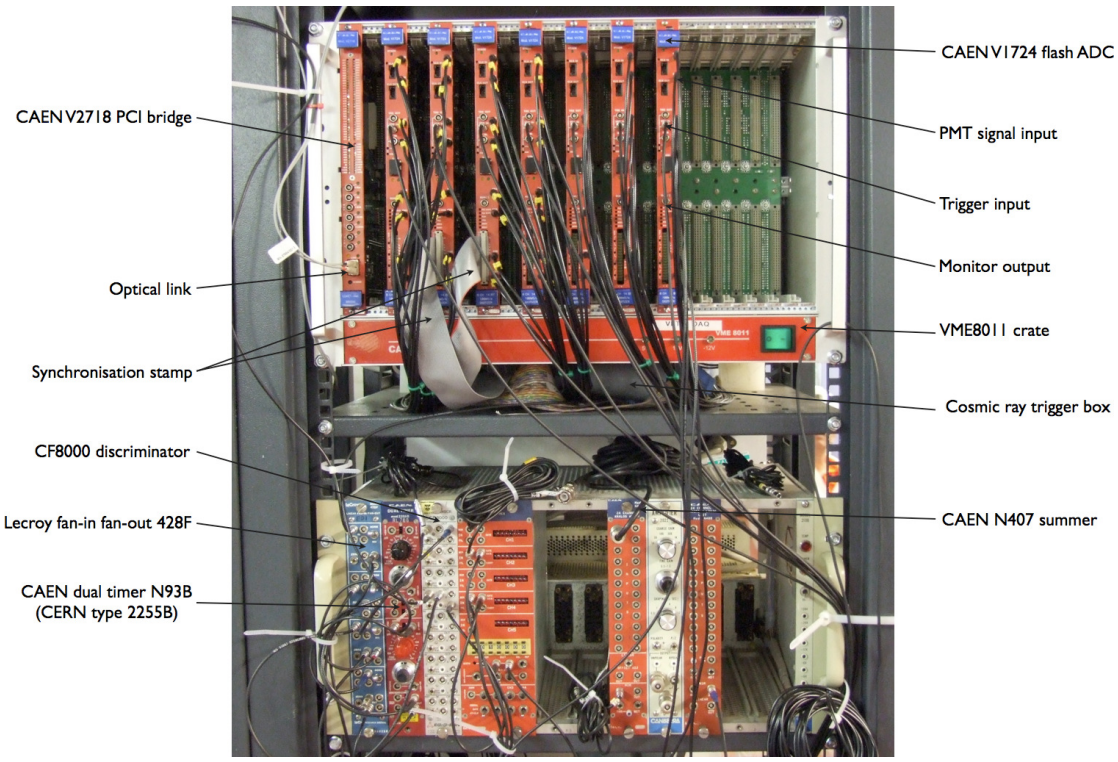

Figure 5.8: An annotated photo of the veto DAQ layout. A schematic and description of the trigger is given in Figure 5.9. This is only representative as the synchronisation unit is not shown here.

was also used for calibration with a much lower energy threshold than is possible using master mode. This was achieved using a trigger requirement of a multiplicity of two NIM pulses in coincidence with the second signal supplied by a pulser calibrated to mimic a NIM pulse. The pulser provided the maximum possible rate and ensured that a low threshold for generating a NIM pulse in the veto module would not overload the DAq by triggering at too high a rate.

- **"fancy signal" mode:** The so called "fancy signal" provides a method of recording events in delayed coincidence with ZEPLIN-III with only minimal data storage requirements (in addition to the prompt recording). The ZEPLIN-III trigger supplied to the veto is set to the equivalent of n NIM pulses in coincidence, where n is the number required to exceed the triggering threshold. This trigger also generates the fancy signal which is a long duration pulse set to the equivalent of $n-1$ NIM pulses in coincidence. The duration of this signal may be adjusted depending on the maximum time expected for the delayed signals. For the duration of this fancy signal a single veto module would be able to trigger the recording of an event by supplying the additional NIM pulse required to exceed the trigger threshold. This trigger mode allows short timelines, $\mathcal{O}$(pulse duration), to be recorded only when necessary, avoiding the recording of empty timelines.

- **Cosmic ray mode:** The output signal from each roof module was split and a copy sent to a custom made trigger unit know as the cosmic ray trigger. Due to the high rock overburden, incoming cosmic ray muons travel at angles very close to the vertical, and hence incoming muons are predominantly seen at least in the roof. The cosmic ray trigger sums and shapes the signals from roof modules with a 2 μs time constant. A high threshold can then be set on this signal to trigger recording if enough energy is deposited in the roof modules. This could be triggered by a muon passing through the roof and leaving very large energy deposits in one or more roof modules, or by a particle shower created by a cosmic ray giving smaller deposits in many modules.

The different triggers are fed into a custom made synchronisation unit. There they are summed and a copy of the trigger is sent to each FADC board. This

synchronisation unit also contains a 32 bit binary counter clocked at 1 MHz from which was derived a time stamp used for event synchronisation. This signal was fed to both the ZEPLIN-III DAq and veto DAq when ZEPLIN-III initiates the trigger. This allows off-line synchronisation of the events. For the second science run two trigger set ups were used. The slave mode trigger and cosmic ray trigger were used throughout the second science run. For the first 39 days the veto also recorded data using a multiplicity trigger. This was set to a minimum of three modules in coincidence recording an average of 10 photoelectrons each. This multiplicity and threshold were chosen to keep the event rate from self triggering at ~ 2 Hz which ensures the veto will not exceed its maximum memory usage of $\sim 20\%$ of the ZEPLIN-III data. A higher multiplicity with a lower threshold was selected over alternate combinations providing a ~ 2 Hz trigger rate as external neutrons are more likely to produce energy deposits in multiple modules, as shown in Figure 6.13. This self trigger setup provides the most efficient utilisation of the rudimentary event discrimination provided by a modular veto loaded with gadolinium. A schematic of the veto trigger is shown in Figure 5.9.

The veto DAq is capable of recording one sample every 10 ns from all channels simultaneously. The sampling rate may be adjusted to prevent excessive memory usage, this is referred to as the downsampling rate. A sampling rate of 10 MHz (a downsampling of 10) was selected for the science run as this was found to be adequate to detect all veto pulses without a substantial loss of resolution. This downsampling rate provided a significant reduction in memory usage, allowing the veto to achieve its target memory-usage rate. Figure 5.10 shows the same single photoelectron pulse at three different downsampling rates. Due to the shaping amplifier time constant of 2 μs, this pulse was detected at all the downsampling rates considered. The drop in resolution given by the reduced sampling rate is shown in Figure 5.11.

A typical timeline with a pulse is shown in Figure 5.12. The veto timelines record from 20 μs prior to the trigger until 300 μs after the trigger. This time window was chosen to cover the maximum prompt and delayed regions of ZEPLIN-III events. The -20 μs end of the window was chosen to cover events where a secondary signal from a deep event in ZEPLIN-III triggers the system and

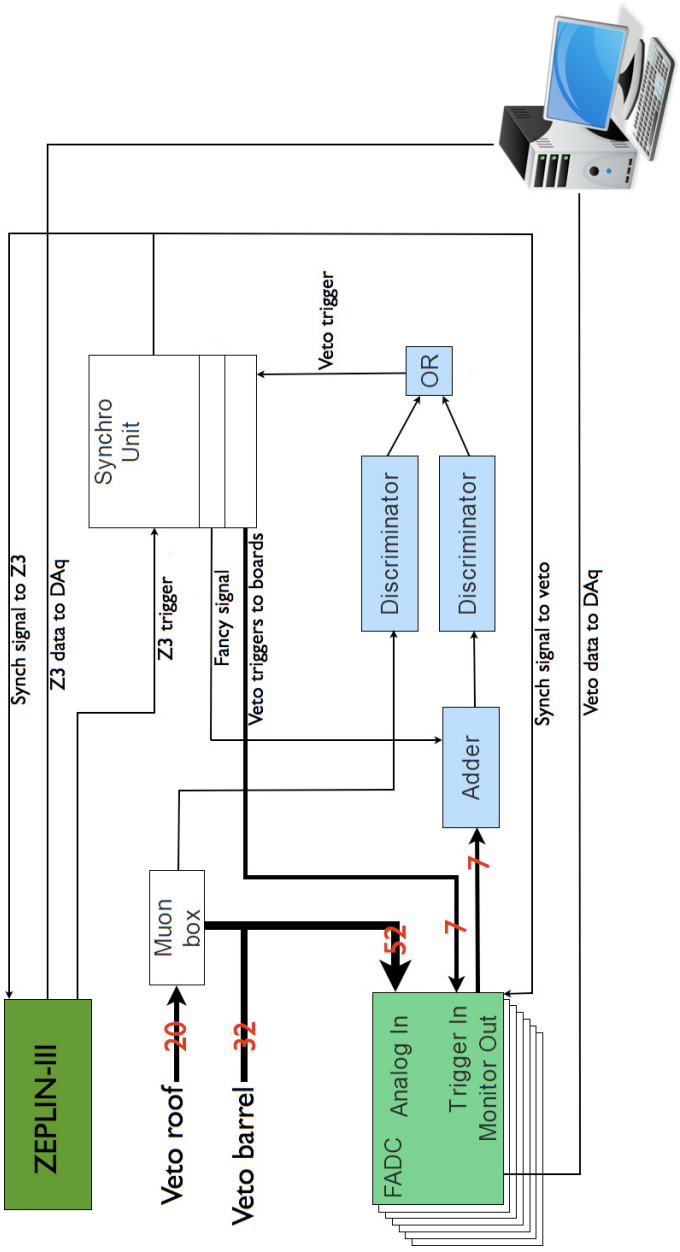

Figure 5.9: The layout of the veto trigger system. The monitor output from each board is fed to a LeCroy fan-in fan-out (adder, model 428F). There, the signals are inverted and used to assemble the majority logic. The fancy signal from the syncro unit is also sent to the LeCroy fan-in fan-out for inversion. The fully assembled majority trigger is then fed to the discriminator (ORTEC model CF 8000) which produces the veto trigger; the threshold is set on this unit. The output signal from the cosmic ray trigger unit is also fed to the discriminator where a high threshold is set. The outputs are sent to the synchronisation unit. This unit provides the overall trigger which records an event and a copy of this trigger is fed to each of the seven FADC boards. A synchronisation signal is also fed into the veto (boards 2 and 3) to provide a unique stamp linking each ZEPLIN-III event to each veto event. The multiplicity of each link, if greater than 1, is written on each in red. Information about the links is written beneath.

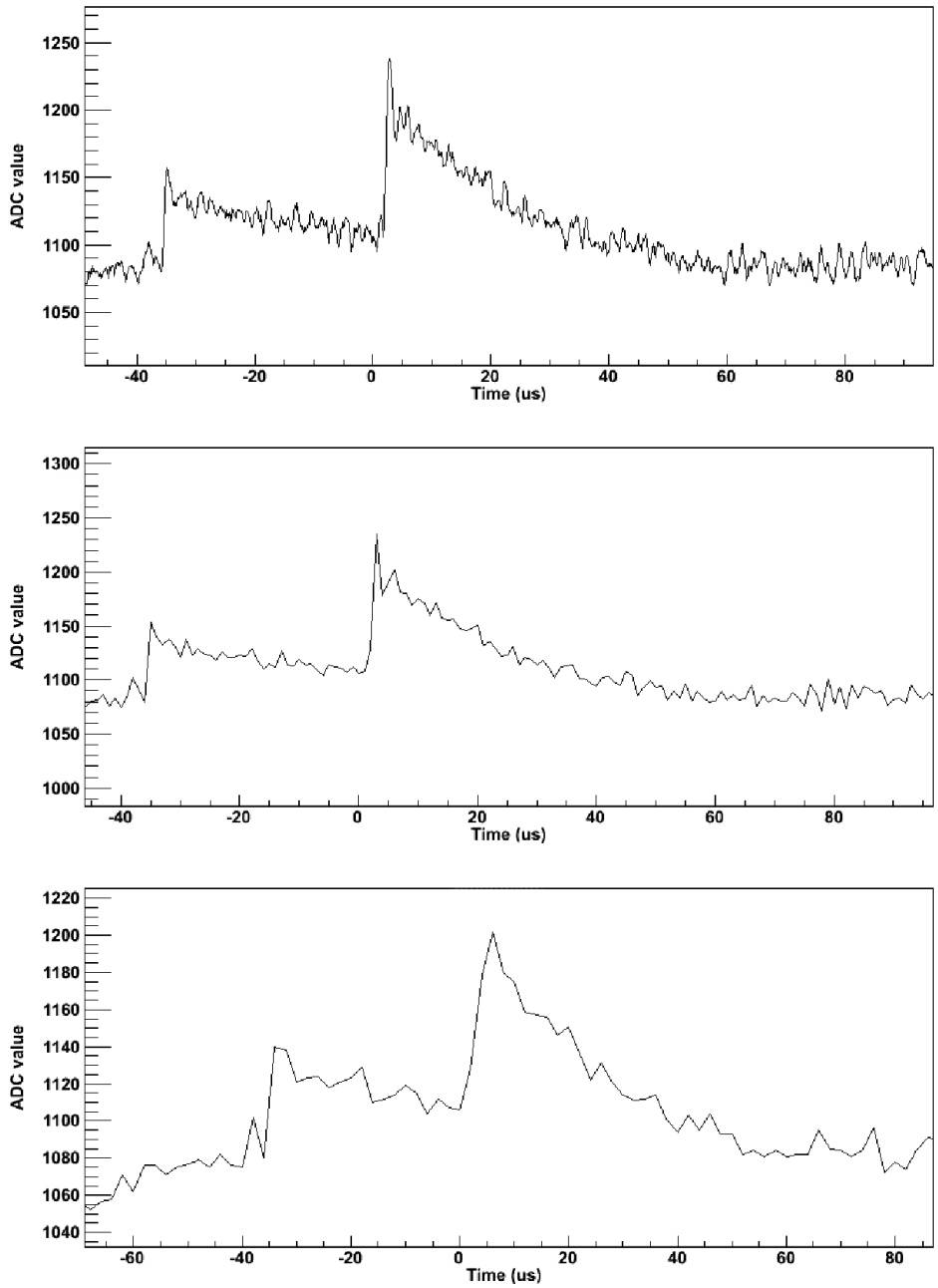

Figure 5.10: This figure shows the smallest single photoelectron pulse above noise from a calibration run taken with no downsampling. This is the first pulse at -35 μs, the second pulse beginning at 0 μs is also a singe photoelectron pulse. The same pulse shown at the three different downsampling levels considered. The top image shows the pulse with samples taken 10 ns apart (no downsampling). The middle image shows the same pulse where only 1 in 10 samples is plotted simulating a downsampling of 10. The bottom image shows a simulated downsampling of 20.

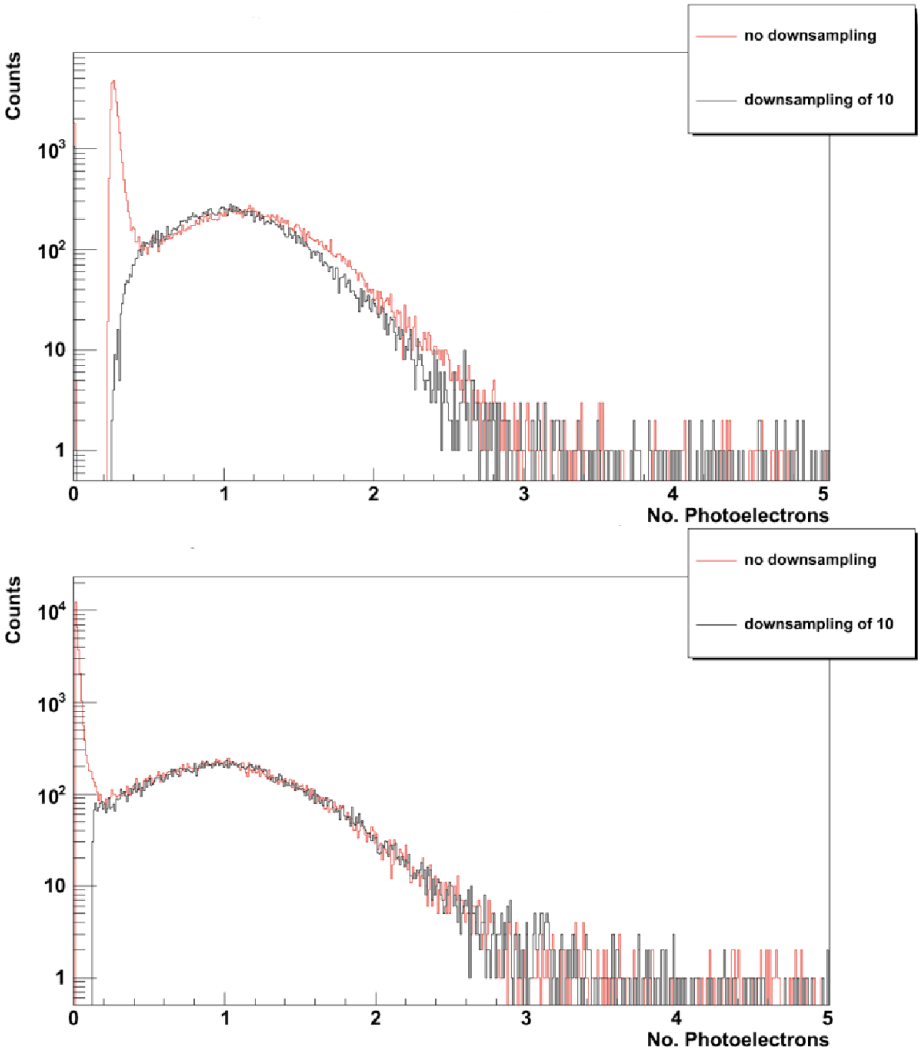

Figure 5.11: The pulse height and area spectra of single photoelectrons with no downsampling and with the science run downsampling of 10. Although the peak shifts slightly for the height spectrum due to the sharpness of the initial voltage spike (shown clearly in the example pulse in Figure 5.12), the area spectrum is very similar due to the 2 μs time constant of the shaping amplifier.

the prompt position is several microseconds before the trigger. The +300 μs part of the window following the trigger covers the delayed region for a significant time period to ensure the maximum possible chance of recording any delayed events corresponding to the original ZEPLIN-III event. The signal shown in Figure 5.12 is an example of a pulse in prompt coincidence with an energy deposit in ZEPLIN-III. The veto also records four extra timelines in addition to the 52 veto modules. Three of these record copies of triggers, shown in Figures 5.13, 5.14 and 5.15, and one records a shaped copy of the ZEPIN-III sum channel, shown in Figure 5.16. This figure shows the benefit of recording the waveform from the dark matter detector in the veto DAq. As a longer timeline is recorded signals are seen in ZEPLIN–III that would otherwise be missed. The shaped ZEPLIN-III sum channel is recorded as an extra diagnostic tool, although the veto has a lower range and sample rate it is still able to record ZEPLIN-III pulses due to the time constant of the shaping. This allows the recording of delayed events in ZEPLIN-III that would otherwise be missed.

The custom veto DAq software was designed to output ROOT [104] NTuples. The reduced data is also stored using this format. Each raw file contains an average of 5126 events and uses just over 1 GB of memory. A typical science run day contains 8 files.

5.1.4 Calibration

All the individual components of the veto detector were thoroughly tested and categorised, as outlined in this section. Components were matched to give a high degree of uniformity of performance across the detector. Following construction, the veto detector was calibrated using radioactive sources and any variations in performance between the modules were corrected, as far as possible, by adjusting the voltage supplied to each PMT.

The gain response of each PMT was assessed using the dark current. The PMT was placed in a light-tight environment and a range of voltages supplied. The output was connected to an ORTEC Multi-Channel Analyser (MCA) and Maestro software was used to produce a spectrum. In this environment the dark

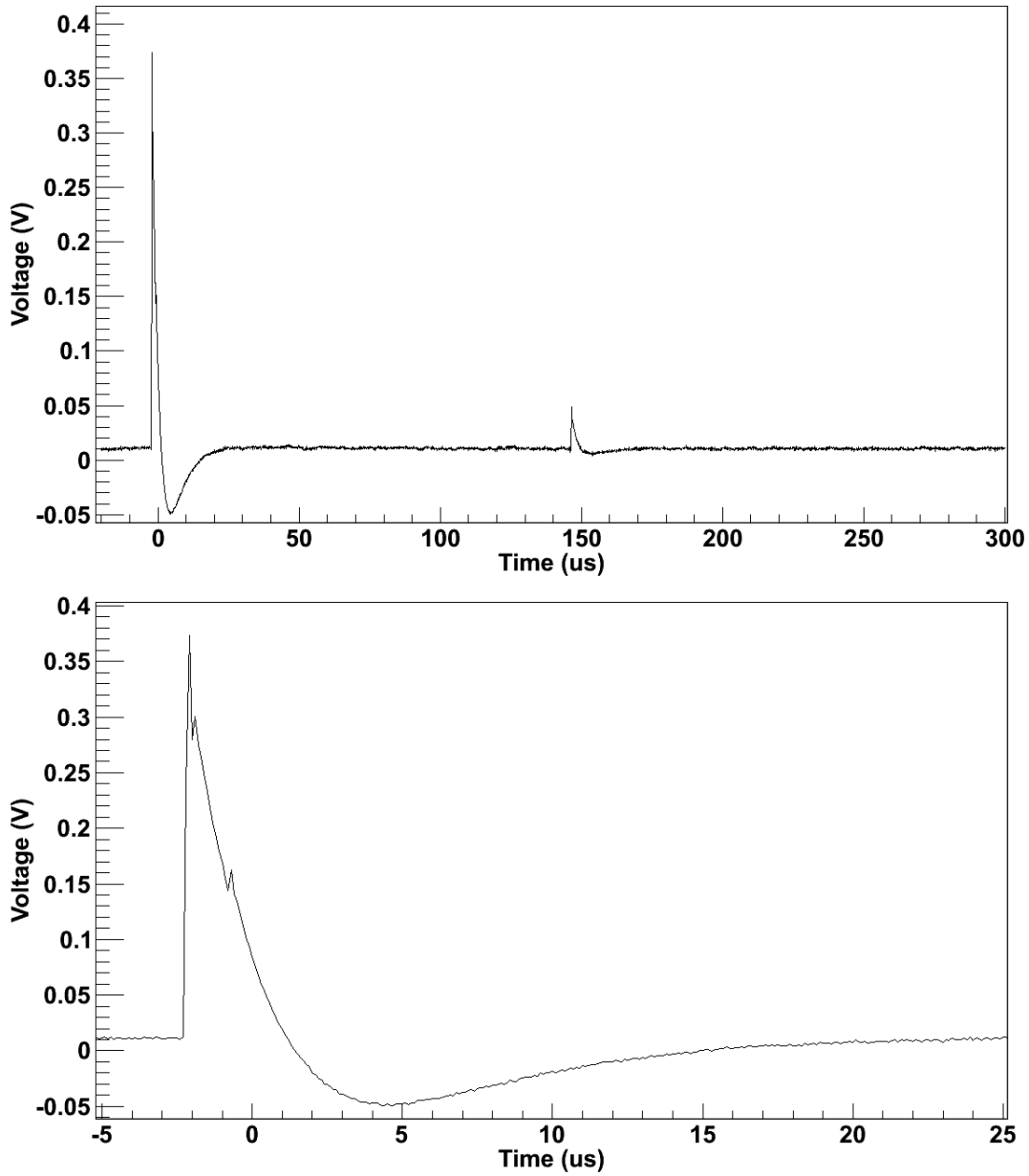

Figure 5.12: An example of an energy deposit in a veto module recorded in coincidence with ZEPLIN-III (the zero position has been slightly offset to help distinguish between trigger types). This event was in the electron recoil band and is therefore a probably a γ-ray. The size of the energy deposit is around 130 keV. The top image shows the full timeline of -20 μs to +300 μs, a single photoelectron pulse can be seen about 145 μs after the trigger. The bottom image shows a close up of the larger pulse. The features seen at -1.75 μs and -1 μs are observed for all veto signals. The height of these features is proportional to the pulse size.

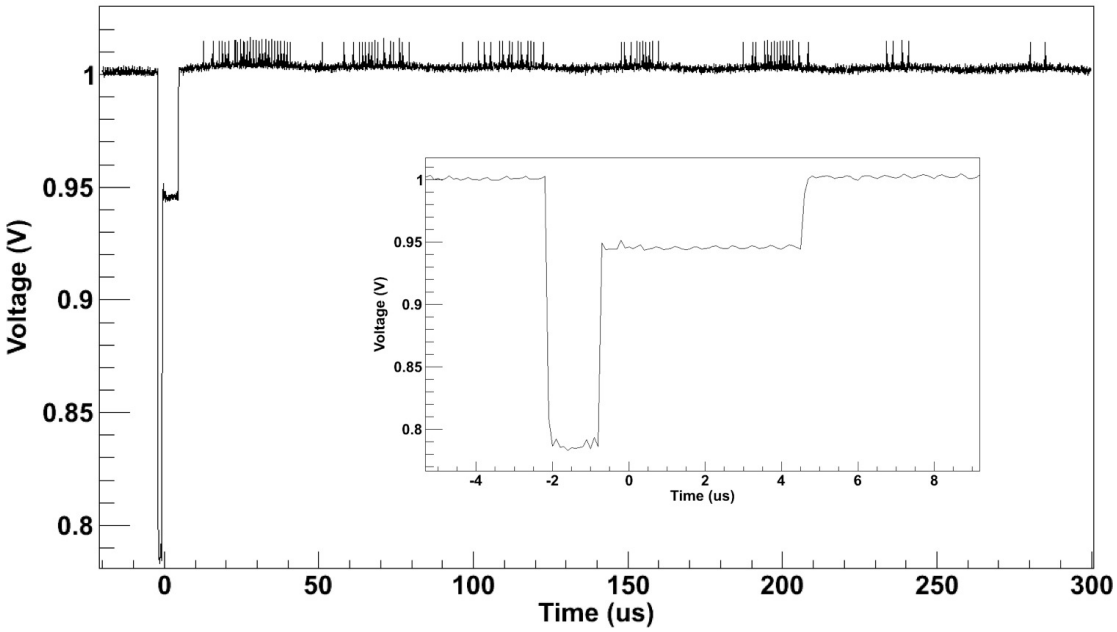

Figure 5.13: A 320 μs recording of the ZEPLIN-III trigger with a close up shown inset. The off set of $\sim$2 μs can be seen in the close up. This delay helps to distinguish between events recorded due to a trigger from the sync box and a trigger from the cosmic ray box. The ZEPLIN-III trigger is just over 0.2 V and lasts for just over a microsecond. For this event the veto DAq was configured to record a 320 μs timeline hence the "fancy signal" was not required and was set to its minimum of 0.05 V for 7 μs.

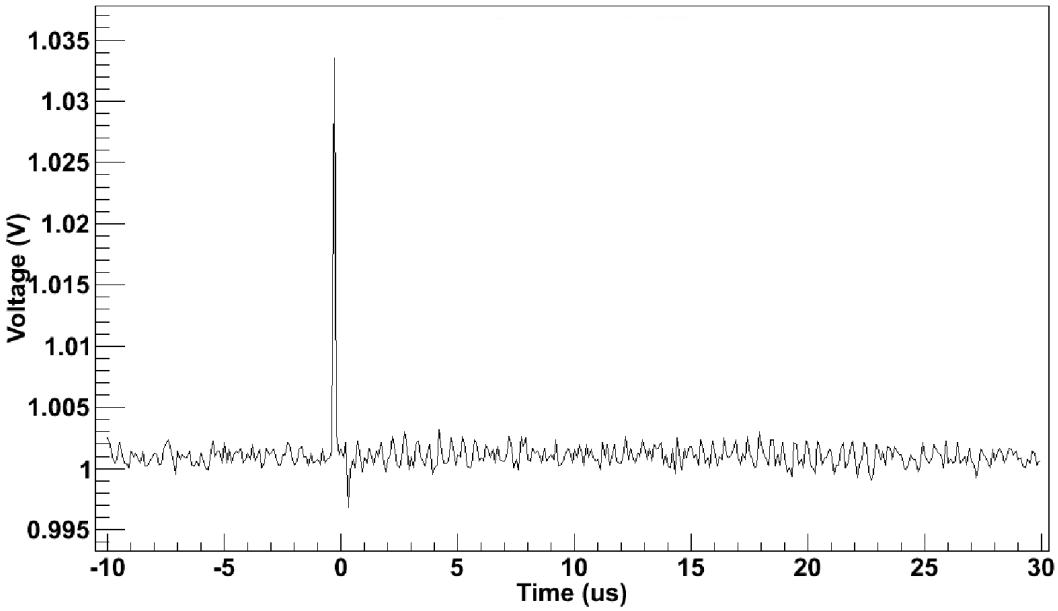

Figure 5.14: A recording of the veto LED trigger, the veto sum channel showing the LED event itself shown inset. The pulse is fed to the veto LED box, causing a flash of light to be emitted, and the veto DAq where this copy is recorded. The veto is triggered by the cosmic ray box as the light enters the roof modules. This is a typical LED calibration event where only a 40 μs timeline is recorded.

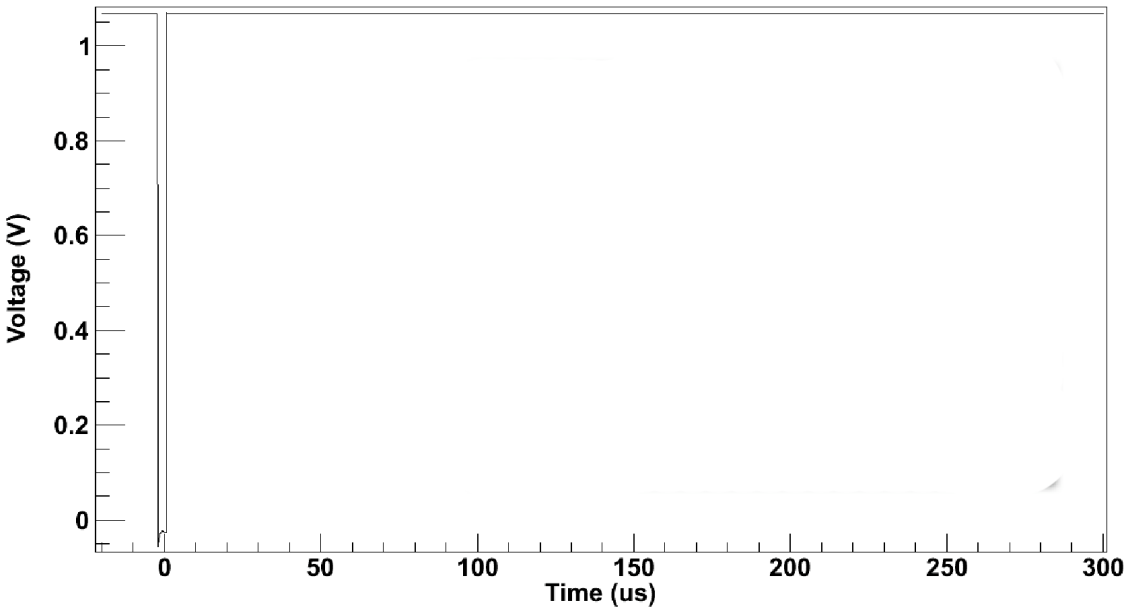

Figure 5.15: A recording of a trigger generated by the cosmic ray box , the veto sum channel showing the event is shown inset. This event also deposited energy in the ZEPLIN-III target which also generated a trigger.

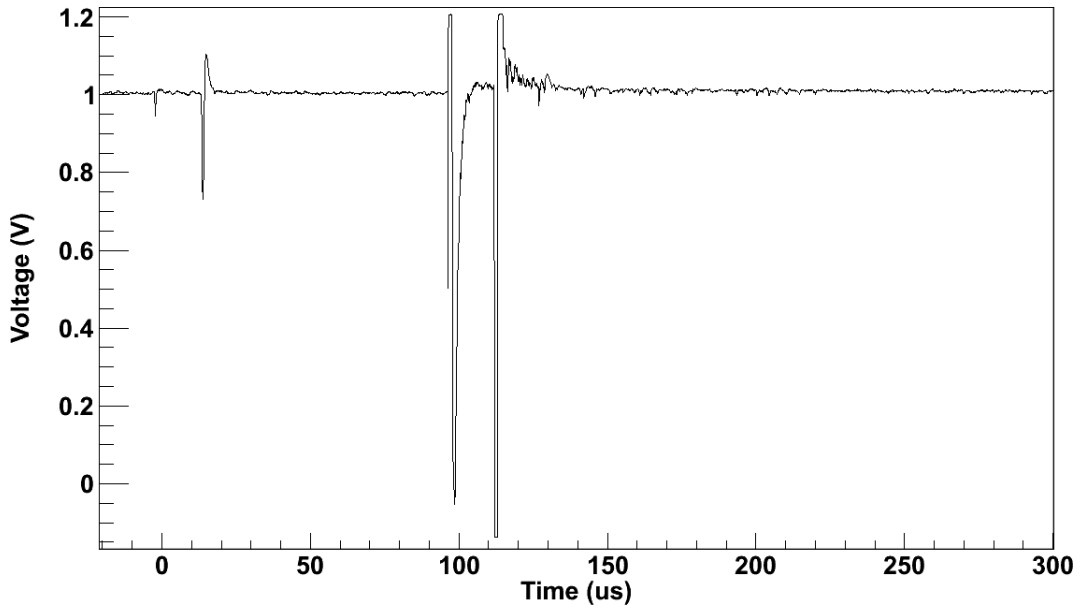

Figure 5.16: A recording of the shaped sum channel from ZEPLIN-III. This was recorded by the veto DAq. As the veto timelines extend 300 μs beyond the trigger point the second event at $\sim 100\mu$s was recorded by the veto DAq but not by the ZEPLIN-III DAq.

current is dominated by single electrons from the photocathode hitting the first dynode plate. This is equivalent to the minimum response of the PMT to a single photon. Depending on the quantum efficiency of the PMT, a certain fraction of these single photon events will produce a single photoelectron. The width of the single photoelectron peak is dominated by the intrinsic resolution of the PMT gain mechanism. An example of a single electron spectrum is shown in Figure 5.17. The gain response was found on average to be a factor of $\sim$2.5 for an additional 100 V, as is more clearly shown in Figure 5.18. This information was used to equalise the response of the PMT array so that a single photoelectron produces the same sized signal in each channel.

The quantum efficiency of the PMTs was also measured. Each PMT was placed in a dark environment (without any scintillator) and the bias was altered until the single electron peak was clearly visible. A blue LED was then introduced and provided with a small voltage such that the chances of providing more than a single photon to the photocathode at a time were minimal. The LED was driven by a pulser running at $\sim$ 100 Hz with 85 ns duration pulses. The LED voltage was

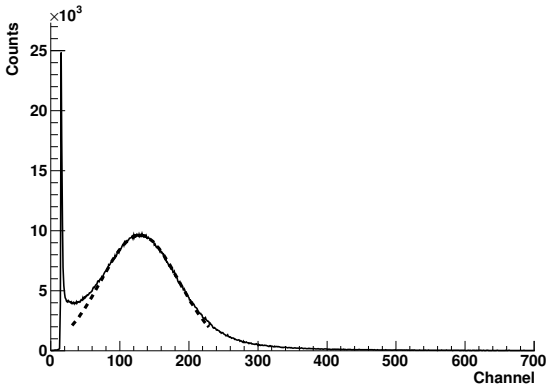

Figure 5.17: A single electron spectrum (solid line) produced by a veto PMT in a dark environment with no plastic scintillator attached. A partial Gaussian fit to the peak is shown (dashed line) [27].

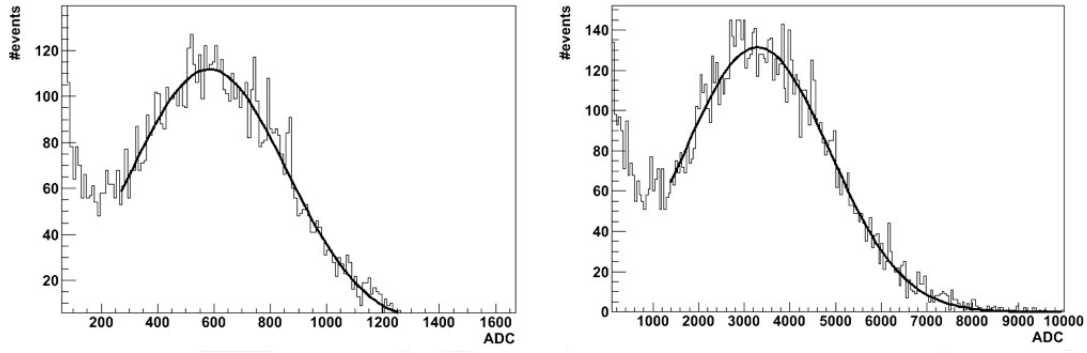

Figure 5.18: A ^{137}Cs spectrum (placed near the center of the scintillator piece) recorded at two different voltage biasses. The left image was recorded with -1 kV and the right image was recorded with -1.2 kV. A partial Gaussian fit (Thick line) is overlaid in each plot. The X-axis of this plot shows baseline corrected height in terms of ADC channel. As the full range of 2.25 V is spread over 2^{14} bits each ADC channel represents 1.37×10^{-4} V.

.

decreased until the spectrum produced peaked in the same position as the dark current single electron peak, confirming the production of single photoelectrons at the expected position. With the single photoelectron response well known for each PMT, a 100 s duration run with the LED at a higher voltage was performed. The peak position was determined in terms of number of photoelectrons using two methods. Firstly, a linear extrapolation using the known position of the single photoelectron peak, and secondly, using Poissonian statistics of photoelectron emission where the width of the peak (1 standard deviation) is given by:

$$\sigma = \frac{\mu}{\sqrt{N_{phe}}} \tag{5.1}$$

where μ is the mean of the distribution and N_{phe} is the number of photoelectrons. The integrated area of the LED peak was used to calculate the quantum efficiency by normalising to three PMTs for which the quantum efficiency was provided by ETEL on request. An example of an LED peak is shown in Figure 5.19. Figure 5.20 shows the quantum efficiency measurements for the veto PMTs. This shows that the two methods of measuring the number of photoelectrons are in agreement. The mean quantum efficiency at VUV wavelengths was measured at 27.1% assuming that all the PMT response curves are of the form stated by the manufacture.

The pieces of scintillator for each veto module were also characterised before being matched with a PMT to achieve an even response across all the veto modules. The key property required of each piece of scintillator is its attenuation length. The bulk attenuation length (BAL) was measured by the manufacturer for each batch of plastic but was only quoted with a large range, see Table 5.1 [38]. This is the length required to reduce the intensity of scintillation light to e^{-1} of the original intensity. Whilst the BAL is measured using a laser beam of appropriate wavelength, in an experimental environment this is not necessarily indicative of the true performance of the scintillator, since emitted scintillation photons encounter more than just the scintillator as they are emitted isotropically. The technical attenuation length (TAL), measured using a ^{22}Na source, is an auxiliary parameter which accounts for geometry of the scintillator, including reflection off the internal surfaces. The TAL of each scintillator piece was measured by shifting the position of the radioactive source and comparing the relative positions of the

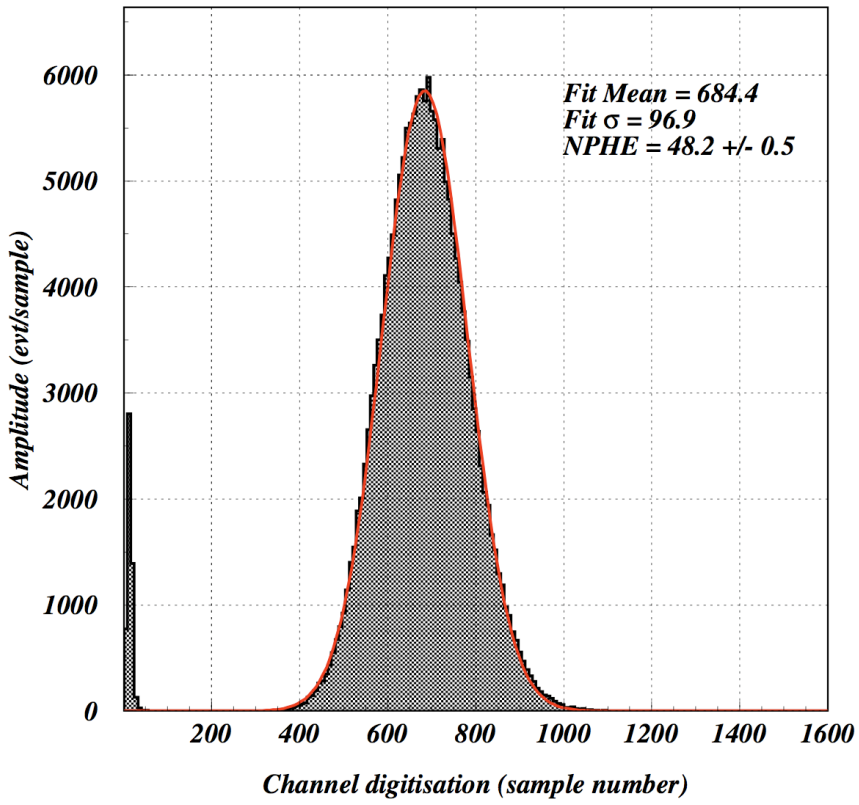

Figure 5.19: An LED spectrum used to calculate the quantum efficiency. The single photoelectron peak is at channel 14, the fit cuts off at channel 140 ensuring only the LED signal is counted.

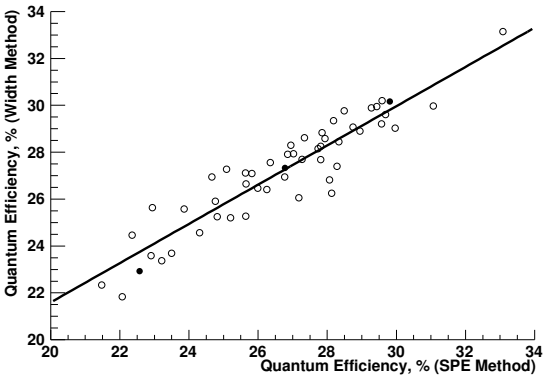

Figure 5.20: The quantum efficiency of each PMT is shown measured using two different methods. The solid circles show the three PMTs which were absolutely calibrated by the manufacture. The errors on the x-axis are 0.2% and on the y-axis are 0.5%. These calibration values are not shown on the plot which is only the response to the blue LED light [27]. The fitted line is described by $y = 0.85(5)x + 4.5(1.2)$ and has a χ^2 of 36.4.

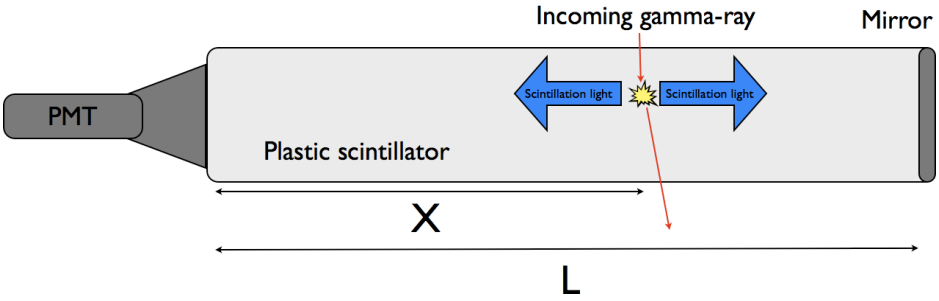

Figure 5.21: A diagram illustrating scintillation within a veto module. The incoming γ-ray interacts a distance, X, from the PMT. Light is emitted isotropically but may be approximated as light emitted towards the PMT (left) and light emitted away from the PMT (right). The light initially moving left in the diagram travels a shorter distance than light emitted to the right and so the attenuation is greater for light emitted to the right. The largest signal will be from light emitted close to the plane in this diagram. In this case light emitted to the left travels a distance X, and light emitted to the right is first reflected by the mirror before being detected and travels a distance $2L - X$. The shorter the distance the light travels within the scintillator the less attenuation occurs and the larger the signal. Thus as a radioactive source is moved along the module away from the PMT the position of the centroid of the peak shifts to lower values.

511 keV and 1274 keV γ-ray peaks. As the source is moved further from the PMT, the mean number of photoelectrons at the peak is reduced by the increased attenuation. To first order, the TAL varies as the sum of two exponentials describing the attenuation due to the distance between the source and the PMT and the distance between the source and the mirror placed at the bottom of each section. The centroid of the peak is then given by:

$$S(x) = A_1 e^{-\frac{x}{\mathrm{TAL}}} + A_2 e^{-\frac{2l-x}{\mathrm{TAL}}} \tag{5.2}$$

where x is the distance to the PMT, l is the length of the scintillator piece and $A_{1/2}$ are arbitrary scaling constants set equal for this analysis, see Figure 5.21. This function was applied to data from each scintillator piece to calculate its TAL [71]. Figure 5.22 shows the TAL for each scintillator piece plotted again the BAL results from Monte Carlo simulation. As the BAL quoted by the manufacturer had large range of possible values the measured TAL was used as an input parameter of the simulations to calculate the exact BAL for each scintillator piece.

After categorising all the components of the veto, the scintillator pieces and PMTs were matched to give a uniform performance. Following assembly of the

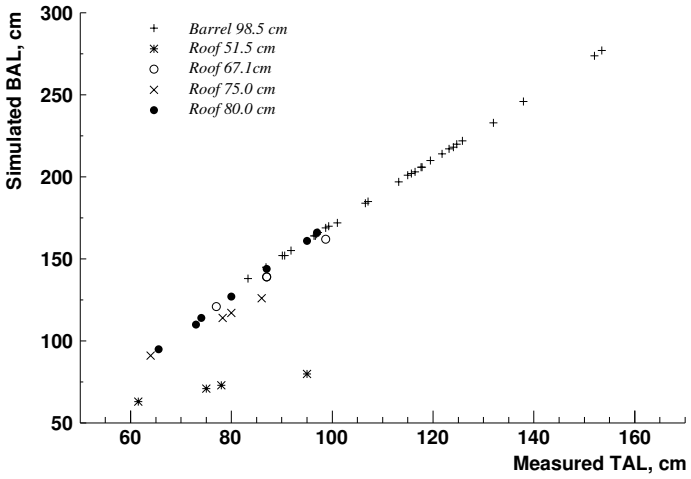

Figure 5.22: The measured technical attenuation length (TAL) and simulated bulk attenuation length (BAL) for each piece of plastic scintillator. As the TAL accounts for the geometry of the scintillator a linear relationship between the TAL and the BAL for each different set of shapes is observed [27]. This is the reason for several straight line trends appearing on this plot, notably the four smallest roof sections (51.5 cm) denoted by the star symbols.

veto, as described in Section 5.1.2, the energy scale was set. The voltages supplied to the PMTs were set to equalise the response and provide the best achievable range compatible with the main aim of the instrument as a dark matter veto. This required the single photoelectron signal to be clearly visible above the noise, providing the potential for maximum vetoing capability. As a secondary consideration, a lower voltage increases the sensitivity range of the veto (i.e. the maximum energy before saturation) and thus improves its diagnostic capabilities as less of the background is truncated by saturation.

The signals from the PMTs, after the pre-amplification, are fed into the veto data acquisition system. The full range of the veto DAq is 2.25 V. The baseline was offset to allow for any voltage drift and to record the undershoots which follow pulses as the baseline recovery is related to the signal size. The average baseline is at 0.138 V (1008 ADC channels) giving a range of 2.112 V for pulses (15376 ADC channels). Simulated calibration with a ^{137}Cs source shows a peak at 32 photoelectrons corresponding to the 661.7 keV γ-ray emitted following β decay to the $\frac{11}{2}^-$ state of ^{137}Ba. Linear extrapolation of the single photoelectron signal in ^{137}Cs spectra acquired using the veto agree with the simulations, as

shown in Figure 5.23. This provides an energy calibration for the veto, where a single photoelectron requires an energy deposit of ∼20 keV. This indicates a range of 72 photoelectrons, or ∼1.44 MeV in the veto. However this is specific to the position of the calibration source, as the source is moved closer to the PMT the number of photoelectrons detected increases leading to a decrease in energy range. The absolute decrease is proportional to the TAL and the range set for the science run was 65 photoelectrons to ensure good sensitivity to small energy deposits anywhere in the veto modules.

Given the full DAq range of 2.25 V spread over 14 bits and the sampling rate of 10 MHz, conversion factors for the pulse area and height can be calculated. The conversion factor for height is 1.37×10^{-4} V per ADC channel. As the mean single photoelectron signal is 230 ADC channels this is 3.14×10^{-2} V per photoelectron. The area of pulses at the SSR sampling rate of 10 MHz is in ADC samples × 100 ns. So the conversion factor between area as seen by the DAq and V•ns is 1.37×10^{-6}. Only the pulse height is given in terms of SPEs here since this is the parameter that was used for the SSR data. Calibration runs showed this to be adequate, see Figure 5.11, and there were initial concerns about the pulse area. Although these concerns were proven not to affect the area calculated, the pulse height was used throughout the SSR for consistency.

The single photoelectron signal was measured daily by an automatic script, discussed further in Section 5.1.5. The script examines small pulses away from the ZEPLIN-III coincident portion of the timeline. Single photoelectron calibration from science run data ensures the exact same operating conditions and produces a daily average, rather than calibration from a dedicated run which provides only a snapshot in time of the single photoelectron signal size. A separate single photoelectron calibration run would also risk the possibility of interfering effects from the new operating conditions, such as a higher rate for example, altering the signal size with respect to the science data. The single photoelectron search provides a daily energy scale calibration for each veto module. The average single photoelectron size was found to vary little over the second science run, as shown by Figure 5.24. The data show an initial increase of the single photoelectron signal size of $\sim 0.92\%$ per month for the first 6 months. After this the signal

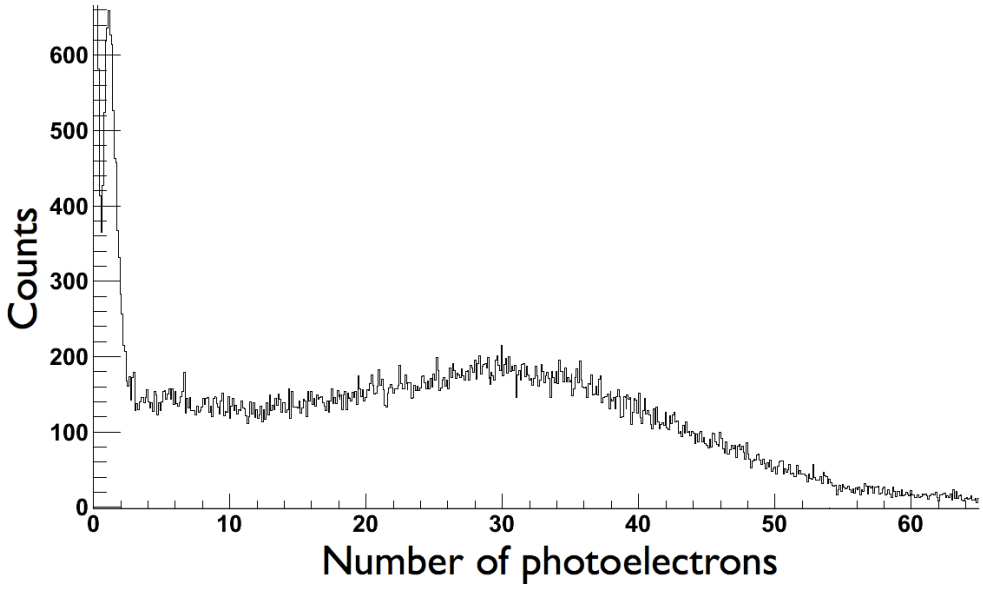

Figure 5.23: A ^{137}Cs spectrum taken using a veto module. The single photoelectron threshold is clearly visible at 1 phe, just before the noise, and the peak at 32 photoelectrons corresponds to the 661.7 keV γ-ray.

size stabilised (the average change over the remainder of the science run was a decrease of $\sim 0.27\%$ per month). Although this effect is small; it demonstrates the need for regular energy calibration during a science run of this length.

The response of the light transmission through the scintillator was also regularly checked via a calibration using blue light from an LED, discussed further in Section 5.1.5. The LED is mounted in an acrylic light guide from which 52 fibre optic cables emerge. These cables are secured into recesses in the plastic scintillator modules at the far end from the PMT. A pulse from the LED generates an average of 48 photoelectrons in each module and a partial Gaussian fit to the LED peak is used to monitor any change in the TAL of the scintillator which could effect the energy scale of the veto modules. Figure 5.25 shows the performance of the modules over the second science run. An LED calibration was selected over calibration using a radioactive source to achieve the maximum possible live time for the WIMP search data. The 122 keV γ-rays emitted during the daily ^{57}Co energy calibration did not give a large enough signal for calibration of the veto and Calibration of the veto modules using a dedicated run was not practical as it would inhibit the ZEPLIN-III WIMP search.

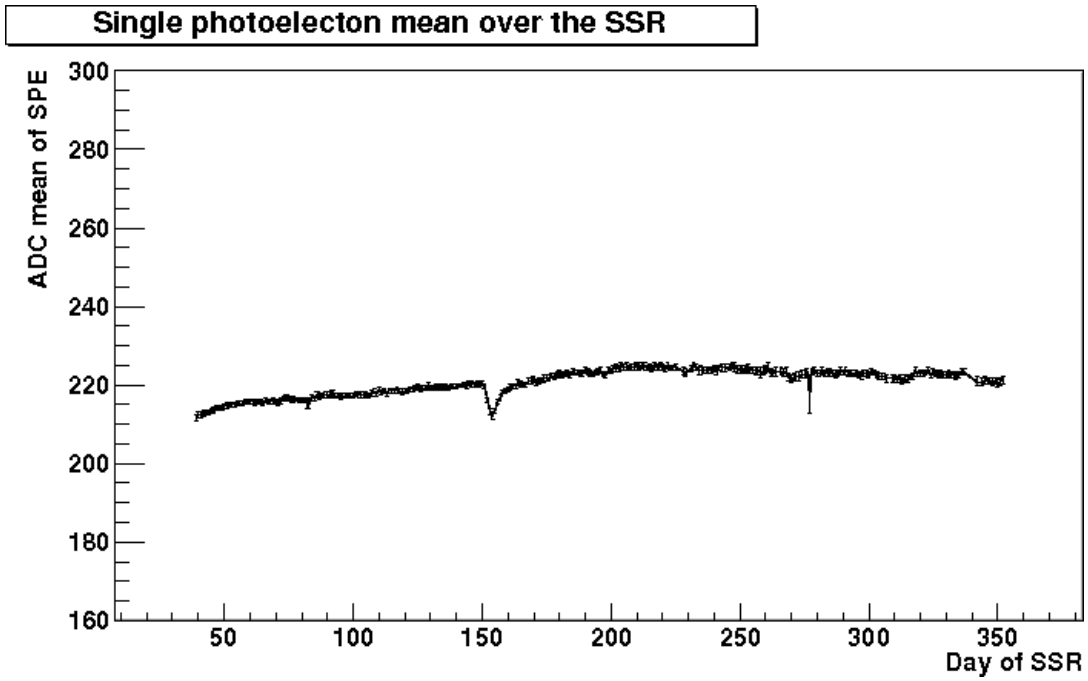

Figure 5.24: The evolution of the mean of the single photoelectron peak in the veto modules over the second science run. The dip in early January (day 155) corresponds to a failure in the laboratories air conditioning system causing a rise in the ambient temperature.

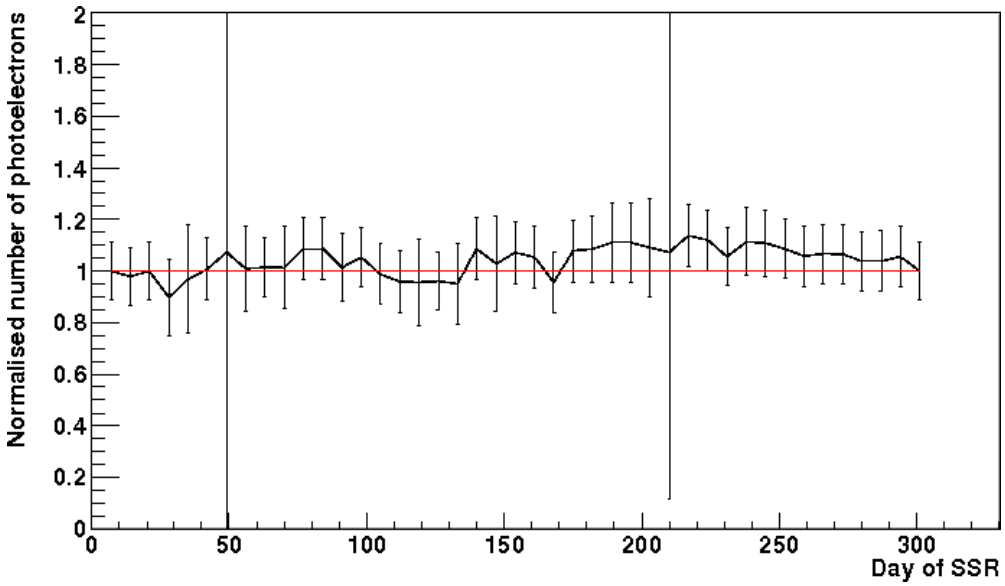

Figure 5.25: The evolution of the number of photoelectrons from LED exposures averaged over all veto modules over the full period of the second science run. The results are normalised to the first measurement. This plot shows some variation of the signal size, however, as all modules show the same trend it is unlikely that this is due to a change in the TAL. A significant change in TAL would also be seen as a change in the tagging efficiency as the threshold would be shifted. As such a slight change in TAL may be spotted by looking at both this plot and the tagging efficiency daily plot as this plot on its own could only show a significant change. The variation observed here is most likely due to the instability of the pulser used to drive the LED. The error bars on this plot are derived from an automatic fit which occasionally applied the fit too close to the noise producing excessively large errors. These plots were produced to alert the operator to changes in performance as the occur.

5.1.5 Operations

During the second science run the operation of the veto went through three distinct phases. For the initial 39 days the veto was set to trigger primarily in slave mode, with ZEPLIN-III providing the trigger, but also set to trigger by the cosmic ray box and allowed to self trigger following signals in three or more modules simultaneously. For this phase of the science run the veto was controlled in situ by a member of the ZEPLIN-III collaboration. On the 2nd of August 2010 the self triggering capability was removed to reduce memory usage and simplify analysis of vetoed ZEPLIN-III events. This reduced the number of files produced in a day from ~ 36 to ~ 8. The third stage of veto operation was

the move to automation. On the 14th of August 2010 operators spent only one or two days underground with the detector and operated the detector remotely for the remaining five or six days of each ZEPLIN-III one week shift. This section describes some of the weekly tasks required to monitor and operate the ZEPLIN-III veto.

On a daily basis the veto data were reduced by the `raVen` software discussed in Section 5.2. This was performed by the DAq computer during the one hour daily break in the science run for cryogenic refilling and energy calibration. During this period the raw datafiles were copied onto 100 GB LTO1 data tapes. The raw and reduced datafiles were processed by shell scripts to asses the performance of the veto on a daily basis. Figures 5.26, 5.27 and 5.28 show examples of the plots generated automatically each day. Once a week two, operators were required to go underground to perform weekly tasks that could not be fully automated. The veto required a weekly LED run to be performed. The LED was driven by a pulser at approximately 30 Hz for 300 s. An automatic script analysed the reduced data files and used the results to generate a plot of the historical performance of each module over time. Figure 5.26 shows an example of a partial Gaussian fit to an LED peak and Figure 5.25 shows the variation of the peak position over the second science run for a typical veto module.

The data were used to produce trend plots of the performance over time. These plots were used as a daily/weekly reference to ensure consistent performance and ensure any potential problems could be quickly investigated and resolved. Figure 5.29 shows the historic plots which were automatically reproduced each time a new daily data point was added. An example of a problem found immediately using these plots is illustrated in Figure 5.30. The synchronisation signal developed a flaw during the second month of the science run. The issue was resolved swiftly by altering the trigger setup and recording an extra data channel. The self triggering ability of the veto was removed. This ensured that the off-line synchronisation would be simplified as the number of events was greatly reduced. This also lowered the memory usage to a more manageable level. The connection to the laboratory bottlenecks between the surface building at Boulby Mine and Rutherford Appleton Laboratory as the

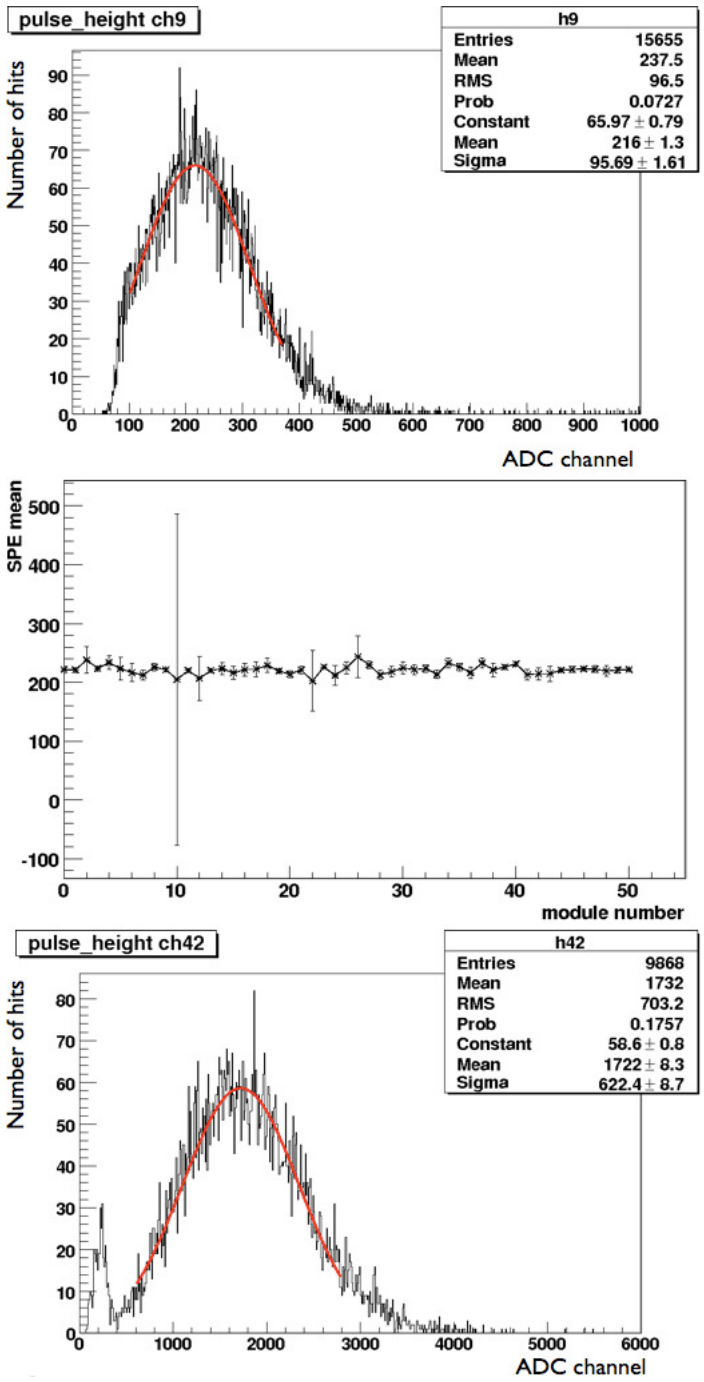

Figure 5.26: Automatically generated performance plots. The top left image shows a partial Gaussian fit to the SPE peak in module 9. ADC channel 230 corresponds to 0.0316 V. The top right image shows the results from partial Gaussian fits to the SPE signal in all modules over a one day period. The bottom image shows a partial Gaussian fit to the LED peak for module 42. The LED calibration was performed once a week to monitor any change in attenuation length of the scintillator. These plots were generated by an automated script and serve as a guide to any potential changes in the performance of the veto detector.

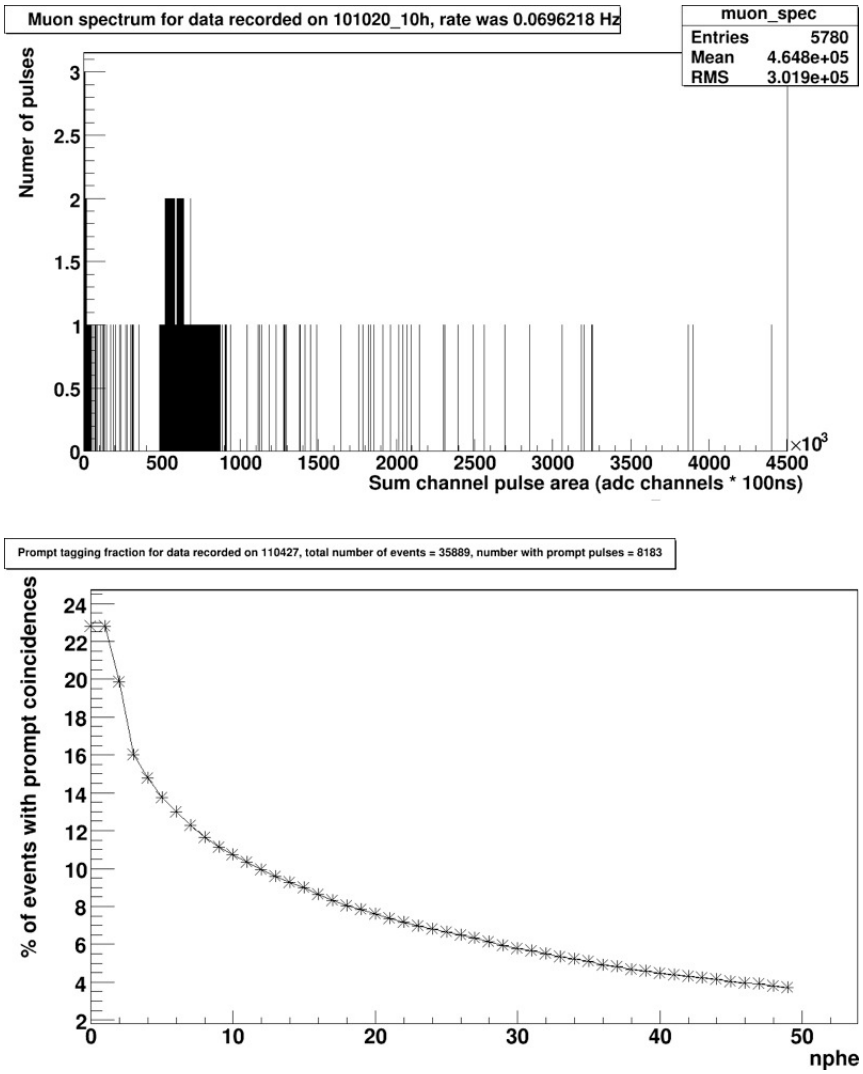

Figure 5.27: Automatically generated performance plots. The lower image shows the fraction of events with a veto signal in coincidence with the trigger position as a function of the energy deposited. This is only a rough indication of the prompt event tagging efficiency due to effects such as triggering from β radiation or the electroluminescence signal, which typically does not have a coincident event in the veto at the trigger point. The top image shows a spectrum of the pulse area in the veto sum channel for events triggered by the cosmic ray box. The events in this channel give the total energy deposited across the veto. As many of the modules are saturated by the large energy deposits which cause the cosmic ray box to trigger, the spectrum is distorted. The most important parameter calculated by the daily muon script is the trigger rate which is included in the graph title. As most of the events recorded by the cosmic ray trigger are large γ-rays, which leave energy deposits saturating several roof modules simultaneously, this value monitors part of the background spectrum experienced by the ZEPLIN-III detector as well as the muon flux. These plots were generated by an automated script and serve as a guide to any potential changes in the performance of the veto detector.

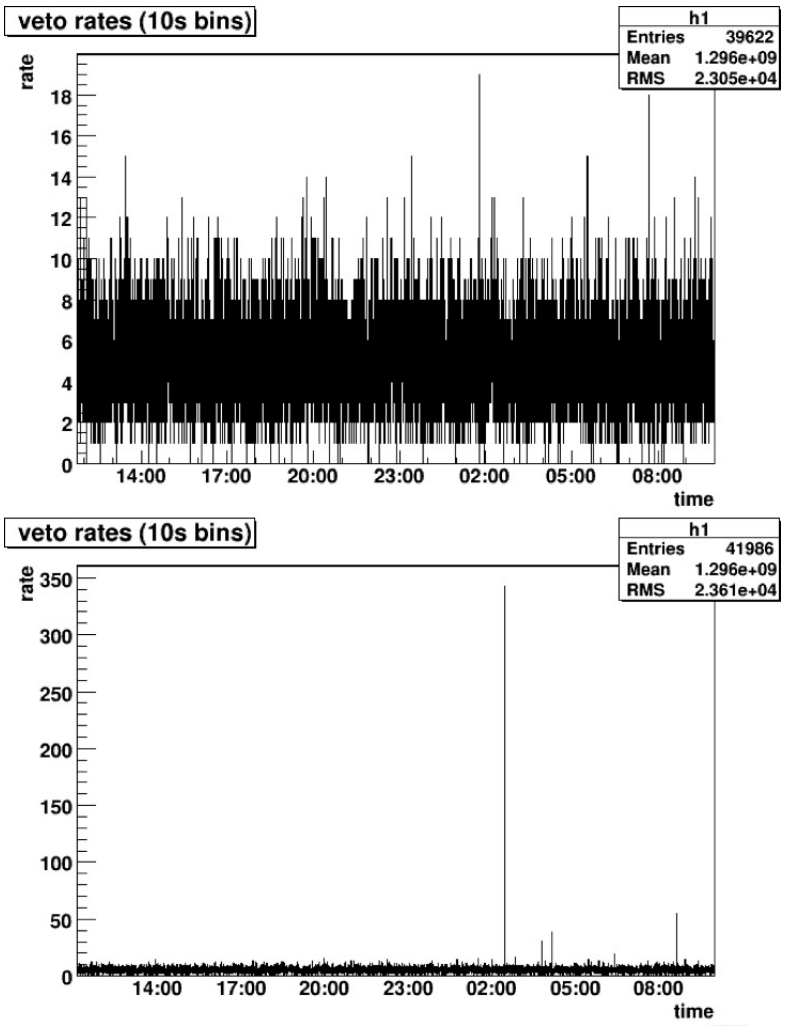

Figure 5.28: Automatically generated performance plots. These images show the trigger rate (in Hz) over a one day period. Each point is averaged over a 10 second period, this shows that the average trigger rate is ∼0.5 Hz, as expected. The lower image shows a rate spike, of unknown origin, at around 3 a.m., these were occasionally seen through the science run and some particularly bad periods were excluded from the WIMP search data set using the information from the daily plots. These plots were generated by an automated script and serve as a guide to any potential changes in the performance of the veto detector.

connection is only 0.25 Mbps so the reduction from $\sim$ 36 files per day to $\sim$ 8 meant that transfer of data was feasible with the available connection if required. An extra timeline was also recorded in a spare DAq channel. This channel recorded a copy of the ZEPLIN-III trigger as an extra aid to data synchronisation. The performance of the synchronisation is discussed in Chapter 6.

5.1.6 ZEPLIN–III Neutron Shield

It is vital to shield dark matter detectors from any potential sources of neutrons. Single scatter neutrons, although rare, may mimic a dark matter signal and compromise the sensitivity of an instrument. Figures 7.1 and 7.2 show the neutron scattering cross-section in xenon. Given that the mean free path may be calculated using the cross section these plots show that the mean free path for thermal neutrons is $\mathcal{O}$(10 cm). The mean free path of thermal neutrons in the shielding is 0.14 cm [281]. The ZEPLIN–III main neutron shield consists of 30 cm thick plastic with a high hydrogen content. Hydrogen is a good kinematic match to neutrons and will quickly thermalise any incident neutrons which may then be captured by either a hydrogen atom or the implanted gadolinium. The outer 15 cm consists of plastic scintillator to act as a veto for the main instrument, as discussed throughout this chapter. The inclusion of this veto at low cost required a modular design. The barrel consists of 32 trapezoid shaped sections of scintillator which are mounted on 32 sections of gadolinium loaded polypropylene. The modular design of the veto had several benefits in terms of rudimentary positional information, a multiplicity trigger capability and containment of any interference to individual modules. This modular design also required strict tolerances to prevent any air gaps between the sections which could lead to line of sight neutrons from the external environment reaching the target volume and contaminating the WIMP search data.

An additional 8 cm of shielding was produced by cannibalising the first science run shield. This bespoke shield was designed as a topless box to rest on stands inserted around the detector plinth. It was designed to be flush against the inner wall of lead shielding. Additionally a layer of extra shielding to cover the top of the detector was inserted above the polypropylene roof shield. Retrospective "dog-

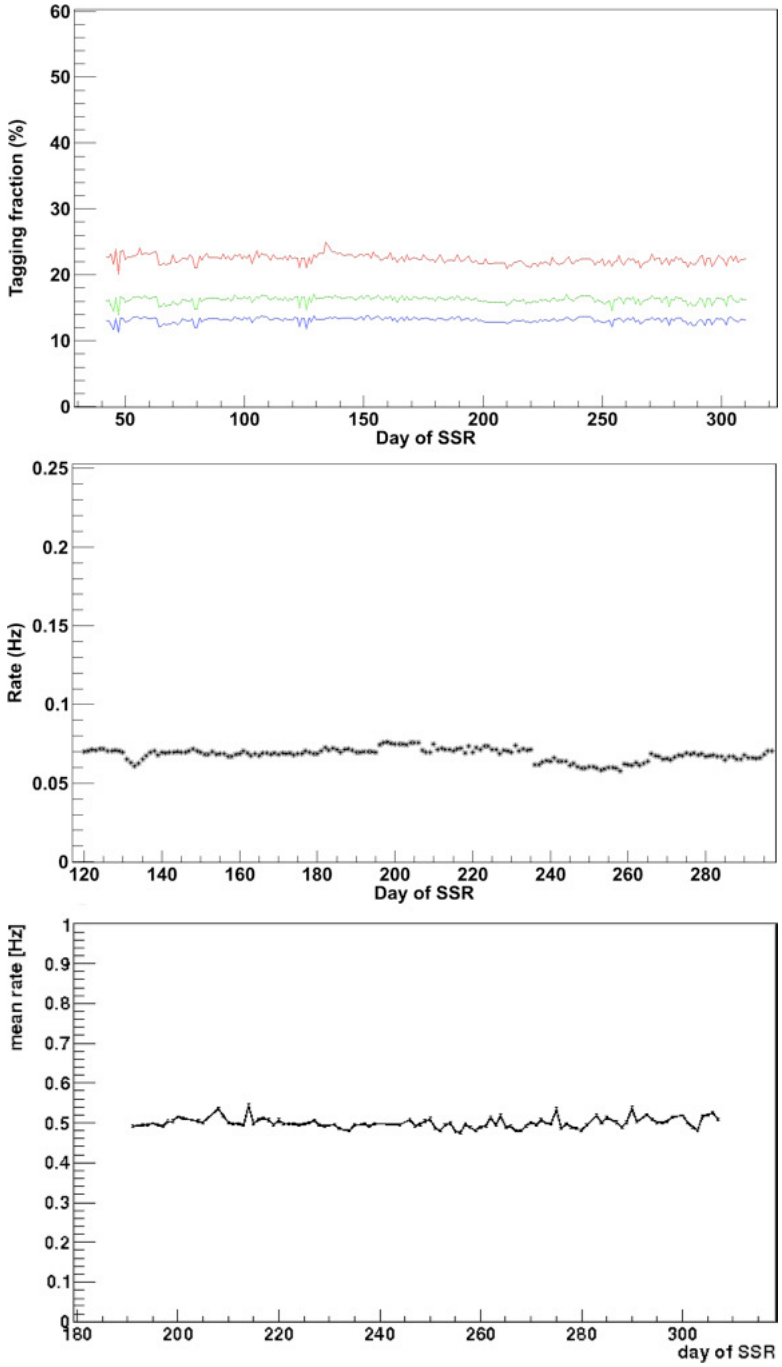

Figure 5.29: Plots of the daily mean values of the veto performance over the second science run. The top image shows the evolution of the tagging fraction (all events at trigger position (red), >3 photoelectrons at trigger position (green) and >6 photoelectrons at trigger position (blue)). This image only includes datapoints from days where the instrument operated in its main triggering mode as the datapoints are generated automatically and may be skewed by changes in trigger mode. The bottom left image shows the daily rate of cosmic ray triggers over a period of the second science run. The bottom right image shows the mean trigger rate over a period of the second science run. As the datapoints are calculated by an automatic script this plot excludes days where the results have been skewed by changes in operation.

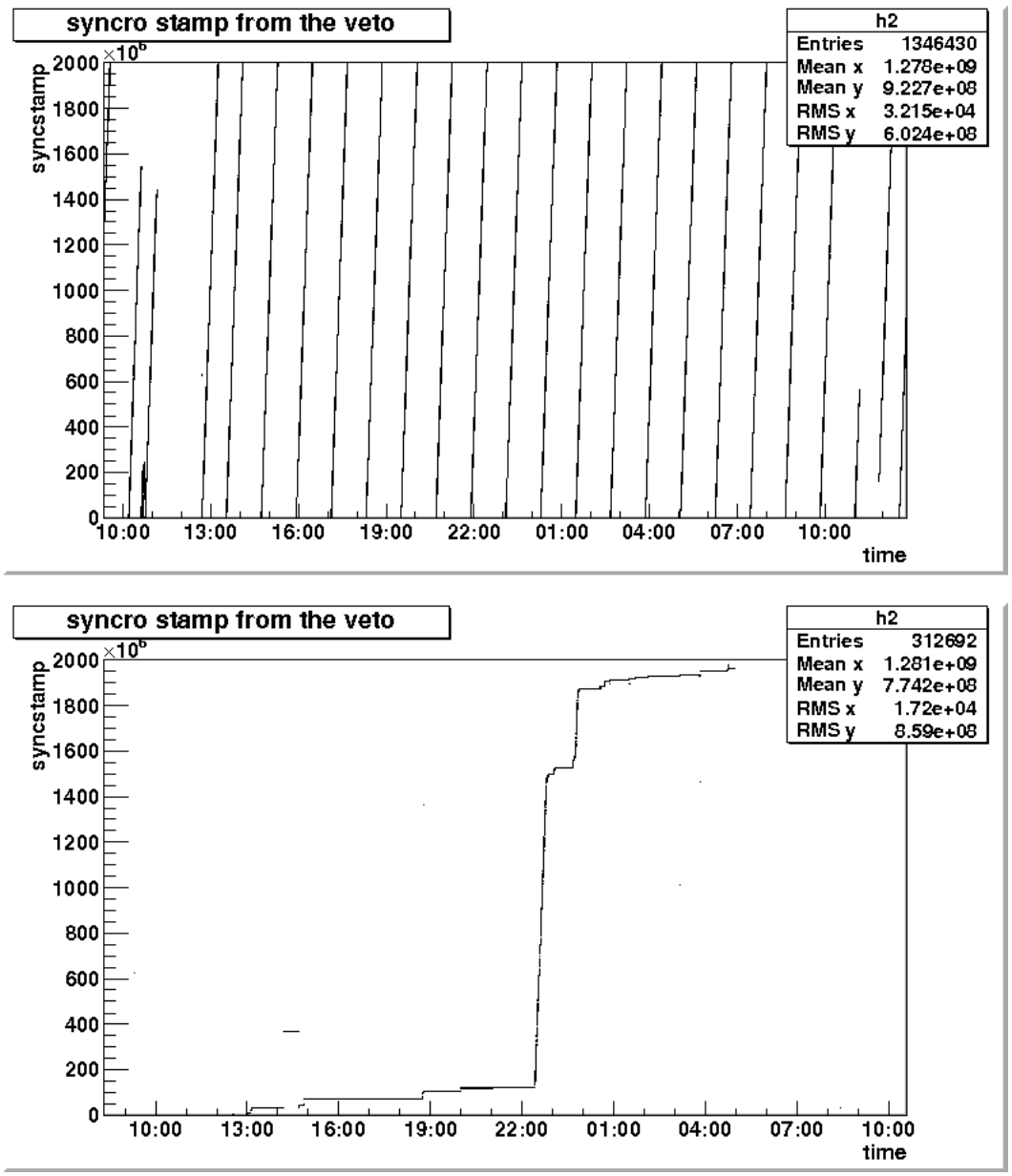

Figure 5.30: These images show the value of the synchronisation signal output by the trigger box and recorded with each event. The left image shows the synchronisation stamp performing properly. It increases over time until it reaches a maximum value then resets and begins again. The small gaps seen at 11 a.m. correspond to the daily break in the science run for cryogenic refilling and energy calibration. The plot on the right shows the same signal after several of the bits stopped functioning correctly. The synchronisation signal could not be used to match the ZEPLIN-III and veto events following this change, however this was spotted immediately in the daily performance plots and the synchronisation issue was quickly resolved with minimal impact to the science run data.

legging" (where the direct line of sight is blocked half way through by shifting part of the shielding around) was applied to the barrel sections by cutting a small recess in the side of each PMT cup hole of the passive gadolinium loaded shield sections and shifting each veto module around by 2 cm with respect to the passive shielding sections.

5.2 raVen

5.2.1 Introduction

The Reduction and Analysis of VEto sigNals (`raVen`) software package is responsible for reduction and analysis of the veto data. I designed and implemented `raVen` using a similar style to the ZEPLIN–III package ZE3RA [286] for consistency. The software package also includes a user friendly event viewer designed to mimic the geometry of the instrument. The requirements set by the needs of the experiment are a package to accurately separate small signals from the noise, allowing the maximum possible vetoing capability. It was required to reduce large quantities of data quickly, and to output the parameters to data files using an appropriate format for the subsequent data analysis. The `raVen` software is implemented in C++ using class-oriented architecture which mimics the function stages of the instrument (pulse class, module class, event class etc.). The design allows additional tools to be added easily and configuration files to be developed to target specific analyses.

The `raVen` architecture is illustrated schematically in Figure 5.31. The classes include:

- **veto:** This class manages individual events. It is structured to match the veto detector layout as each instance contains 52 instances of **veto_slab**. It also holds the additional timelines from the ZEPLIN–III trigger, the ZEPLIN–III shaped sum, the LED trigger and the cosmic ray trigger as well as the veto sum channel which is created by `raVen` by summing the timelines together during processing.
- **veto_run:** This class inherits from **veto** and manages the reduction

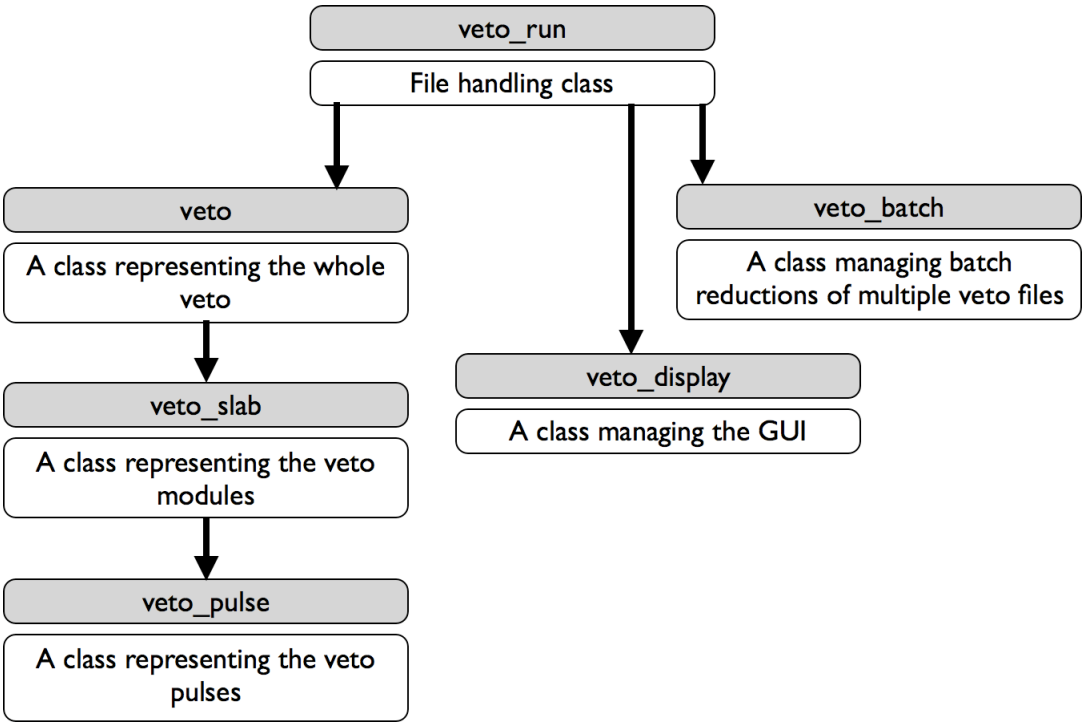

Figure 5.31: A schematic representation of the raVen software architecture. The arrows point in the direction of inheritance, each box is a class in the software.

templates and settings. This class also opens and closes raw veto DAq files and reduced data files.

- **veto_display:** This class inherits from **veto_run**. It layers the graphical user interface (GUI) with the classes managing analysis. This class may create configuration templates.

- **veto_batch:** This class inherits from **veto_run**. It controls large reductions including multiple files, allowing the reduced data to be output to either a single file or one file for each input file.

- **veto_slab:** This class stores and manages data from each DAq channel. This class contains a dynamic array of **veto_pulse** instances.

- **veto_pulse:** This class holds all the information related to each pulse detected on the veto timeline. The parameters are set according to the reduction template selected.

The following sections contain an overview of the most relevant algorithms implemented in `raVen` and a review of its performance for the various tasks required for the second science run.

5.2.2 Pulse Finding Algorithms

Prior to searching the timeline for pulses the baseline must be parameterised. Although the intended offset is recorded by the DAq and read in by `raVen`, the baseline position was also calculated using the waveforms containing the PMT signals. Two different methods were used to calculate the baseline position. The first takes the average over the whole timeline after excluding regions which contain signals. This is achieved by calculating the average voltage along the timeline and its root mean square (RMS) and then excluding regions of the timeline which fall outside a threshold set in terms of the RMS. The initial calculation of the mean position and its RMS is performed as `raVen` reads in each timeline. As the majority of the timeline is free from signals this usually gives an accurate position for the baseline, however large pulses may skew the position slightly. This would lead to small errors in the pulse parameters, and so areas of the timeline which include pulses exceeding a threshold set in terms of the RMS are excluded from the next calculation. This was initially set to repeat until the RMS reached a selected value, however in practice it was found that three iterations was sufficient even with noisy timelines. The second method of baseline calculation involved monitoring the RMS as the waveform was read in by `raVen` and halting baseline calculations once the RMS begins to increase, indicating the presence of a signal. As the baseline recovery following a signal takes several microsecond this method assumes that there were no large pulses prior to the start of the recorded timeline. As such this method was complemented by calculations of the baseline for each individual pulse, working backwards along the horizontal portion of the timeline prior to each pulse.

To suppress high frequency noise, the data was boxcar averaged over m bins. An example of the filter is shown in Figure 5.32.

Once the regions of the timelines containing pulses have been identified the

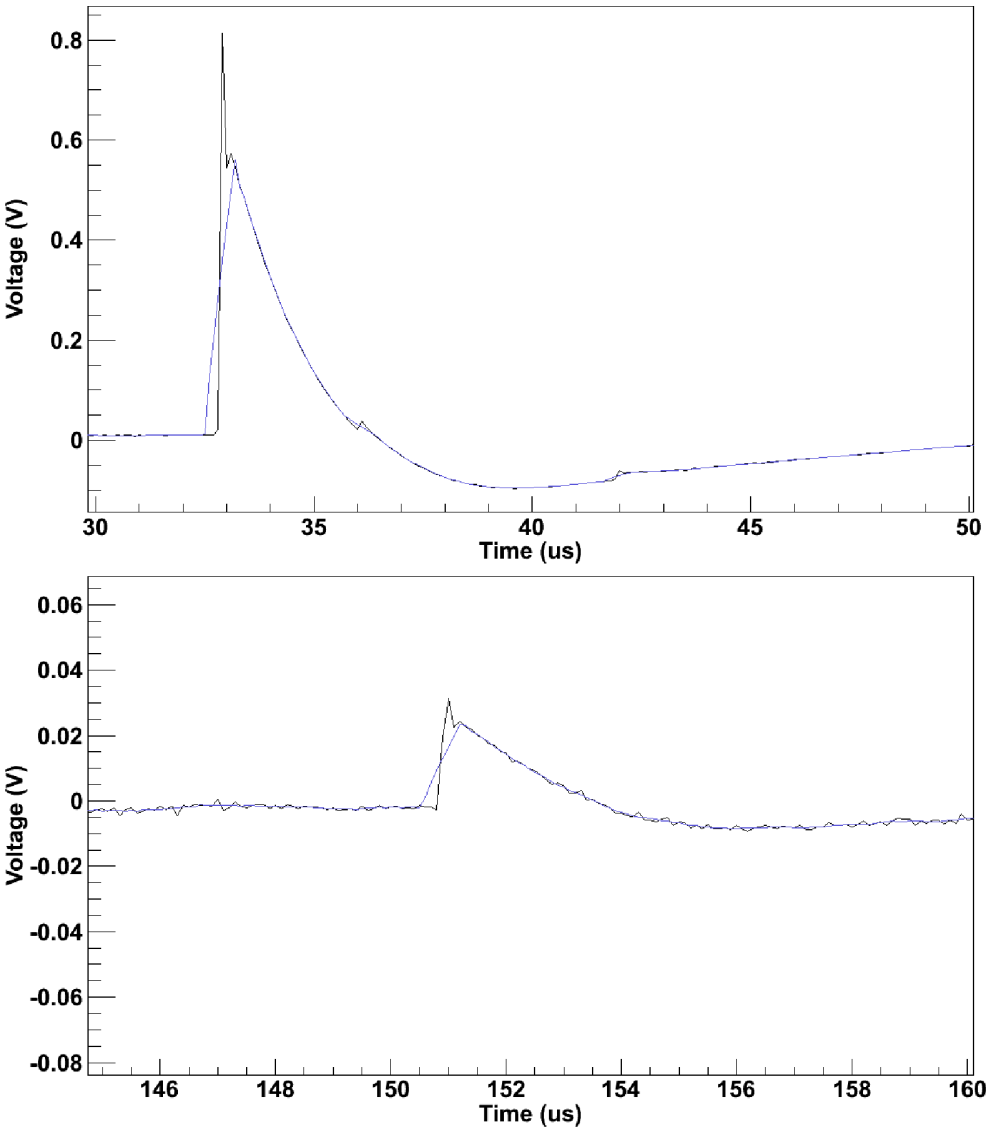

Figure 5.32: Examples of signals in the filtered buffer of raVen (blue) overlain with the original unfiltered buffer (black). The top image shows a typical signal and the bottom image shows a single photoelectron. In both cases the filter width is 0.3 μs.

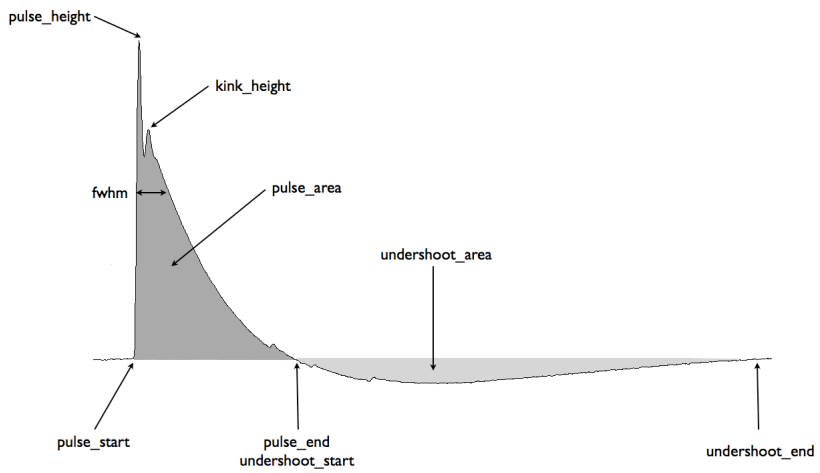

Figure 5.33: A typical veto pulse annotated with some of the parameters calculated by raVen.

parameters of each pulse are calculated. A pulse is identified as a region of timeline with n consecutive samples above a threshold. Once the existence of a pulse has been established and a pulse object created the threshold is disregarded and the parameters of the pulse are calculated with respect to the baseline. An example of a pulse found by `raVen` is shown with some of the main parameterised indicated in Figure 5.33. The beginning of each pulse is estimated by searching backwards from the peak of the pulse for a change in gradient and extrapolating. The end position is found by assuming a flat baseline and a check is performed to confirm this. The pulse area is given by the sum of all baseline subtracted heights between the begging and end of the pulse. Once each channel has been analysed individually a search is performed for coincident pulses. Once all timelines have been scanned the pulses are cross referenced for coincident energy deposits.

The voltages supplied to the PMTs were high enough to ensure single photoelectrons produced a pulse significantly above the noise level in each channel and the threshold was adjusted so that all genuine signals were detected. The ability of `raVen` to pick out small signals above the noise is demonstrated graphically in Figure 5.34. This also shows a comparison with an alternate method. The alternate method shown uses an MCA and Maestro pulse-finding software and was found to be consistent with the spectra obtained using the `raVen` software. The MCA is a peak finding ADC which uses a simple threshold to measure pulse height. The acquired spectrum was analysed using the second

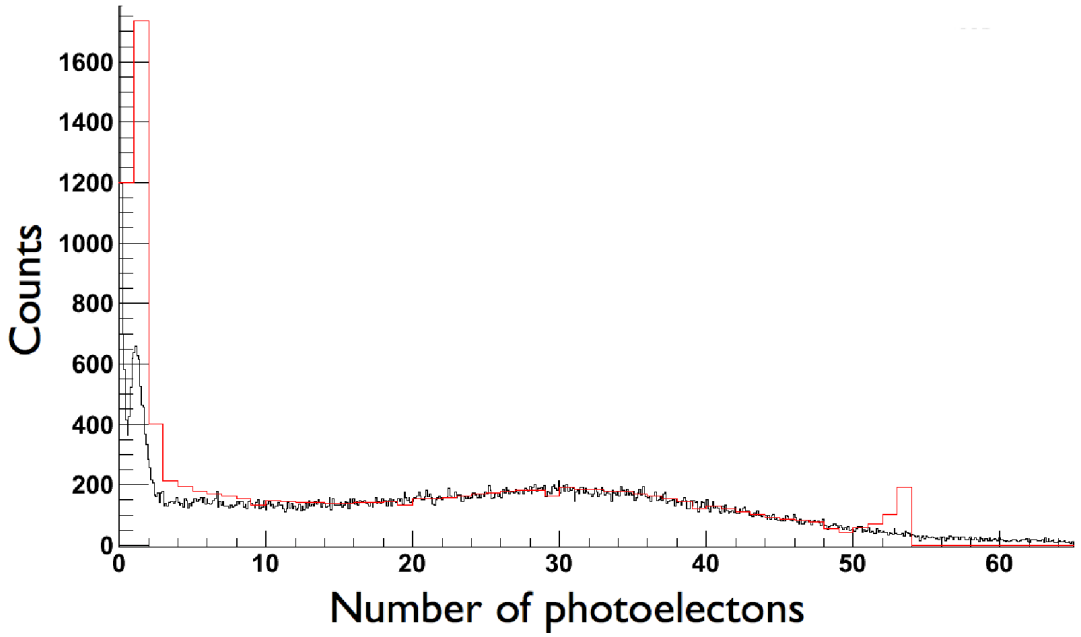

Figure 5.34: As a sanity check a comparison of ^{137}Cs calibration spectra acquired using a veto module attached to two different DAqs was obtained. The two methods of acquisition are a MCA with Maestro software (red) and the veto CAEN DAq analysed by raVen software. The two methods were found to be consistent. The single photoelectron peak is clearly visible above the noise when analysed by raVen, however the MCA has not separate these small pulses from the noise as effectively.

science run configuration file which uses an iterative method to cut out signals and find the baseline and a filterless scan of the buffer with a low threshold to find pulses. The figure shows some noise below the single photoelectron peak. The noise pickup is mostly from small fluctuations in the baseline following large energy deposits.

5.2.3 Output

The `raVen` software reads in ROOT files described in 5.1.3. These files are chained together for each run. The raw data is processed using the second science run configuration file and output as a ROOT file. The output files are typically 14 MB in size. The output file contains 4 branches:

- **run_info:** This branch contains information about the run read in directly from the raw DAq file. It also stores the settings used to parameters the pulses.

- **run_channel:** This branch contains information about each individual channel during the run.
- **events:** This branch contains information about each event. This branch also holds arrays of up to 10 pulses for each of the additional timelines. The trigger analysis is as in ZE3RA as this information is used for syncing.
- **batch_pulses:** This branch contains the pulses from the 52 veto modules.

5.2.4 User interface

Figure 5.35 shows a veto event represented in `raVen`. The `raVen` graphical user interface (GUI) incorporates all the analysis framework and allows the user to view the timelines and the analysed parameters. The interface is coded using the cross-platform GUI toolkit FLTK (Fast Light ToolKit). As well as viewing events, this GUI allows for editing of the configuration file and initiating reductions. The detector schematic in the bottom right corner of the GUI consists of a series of buttons which display different timelines. The buttons change colour, following analysis, according to the nature of the information within the timeline. This alerts the user to timelines containing important information. The "view all" button creates a pop up window showing the timelines from all modules overlaid as shown in Figure 5.36.

5.2.5 Pulse Reconstruction

As the characteristic shape of veto pulses is well known for each DAq channel, it was possible to reconstruct saturated events beyond the maximum range of the DAq which is limited to 14 bits. The most effective reconstruction is given by the relation between pulse area and width and it was possible to reconstruct saturated pulses up to the point at which the PMTs saturate. The average PMT saturation point was 2.52 V. A reconstruction algorithm in `raVen` is used to predict the height and area of saturated pulses up to this point. The range of the DAq was extended by an additional 13% using this method.

5.2.6 Performance

The `raVen` software package was designed with careful attention to speed. Much of the data was reduced using a Mac mini with a batch of 4 days of science run data taking an average of 6 hours to reduce. The veto also has a dedicated data reduction machine. A typical batch of four days worth of science run data takes ∼8 hours to reduce on this machine. The `raVen` software package also detects and avoids file corruption. The most common form of corruption is data loss due to DAq overload. To avoid this the expected file configuration, read from the DAq, is compared to the actual configuration in each file. No second science run candidate events were lost to corruption.

The ability of `raVen` to discriminate between small energy deposits and noise was used to measure the quenching factor of the plastic scintillator used in the veto modules [309]. Spectra were acquired by the veto DAq using both an Am-Be and ^{252}Cf source. A high threshold was set for triggering the DAq and the spectra contained the 2.2 MeV γ-ray peak from neutron capture onto hydrogen. This was used to set the energy scale and then the off trigger section of the timeline was searched for small energy deposits from nuclear recoils in the plastic scintillator. By matching the acquired spectra to simulations using the 2.2 MeV γ-ray peak a difference in the slope of the spectrum was observed at low energy due to nuclear quenching. This difference was also observed using MCA and maestro software but data reduced by `raVen` allowed an energy dependent quenching factor to be calculated as shown in Figures 5.37 and 5.38. I took a lead role in performing this experiment and I developed the technique which allowed the simultaneous recording of low energy neutron data and energy calibration, however the lead role in data analysis was taken by Lea Reichhart who was also the lead author of [309].

5.2.7 Conclusion

I was heavily involved in the commissioning of the ZEPLIN–III veto detector. Due to my involvement in so many aspects of the veto I was regarded by the collaboration as a key member required to be present for the assembly of the detector. After helping with the construction of the veto I developed

the calibration methods to parameterise the veto, wrote the reduction software and much of the analysis code used for the veto data. An additional analysis, measurements of the energy dependent quenching factor of the plastic scintillator, was made possible by the ability of the software I wrote to detect and accurately parameterise very small energy deposits. I took a lead role in setting up the experiment, acquiring the data and developing the analysis technique used.

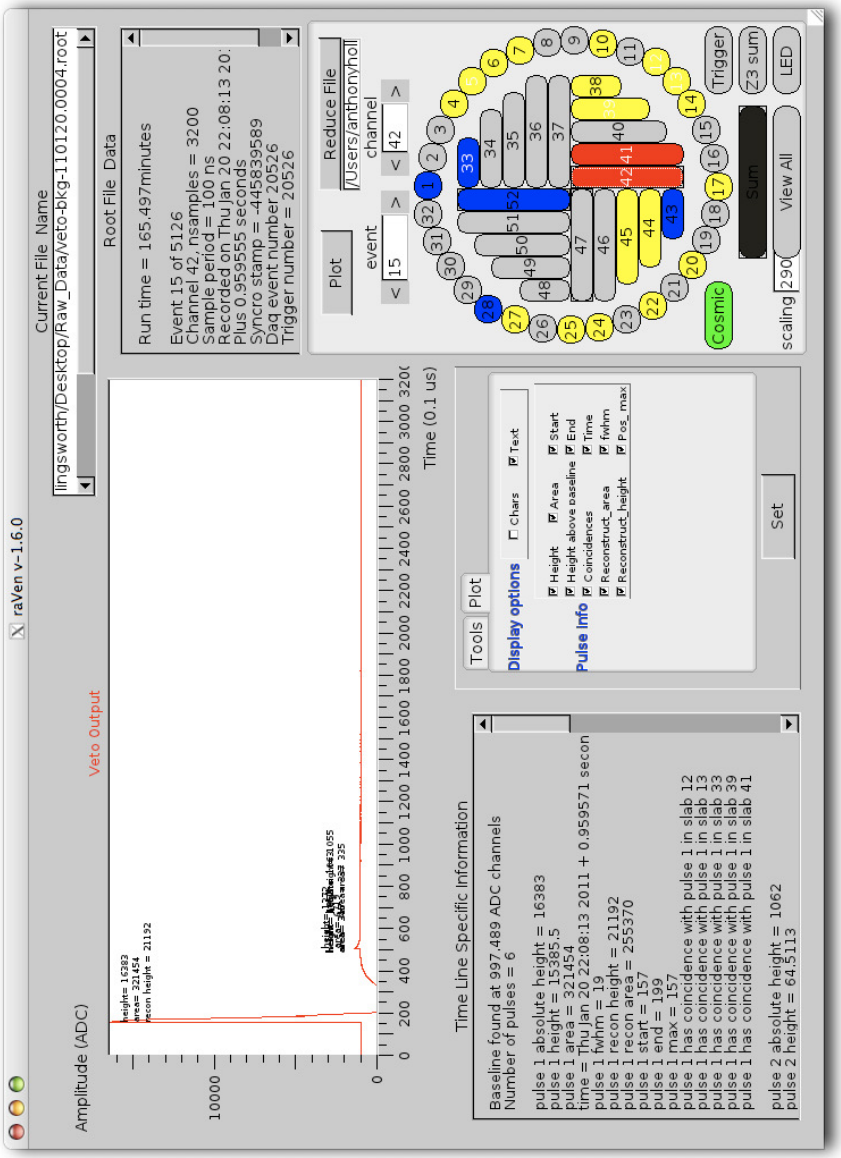

Figure 5.35: This image shows a typical event recorded following a trigger from the cosmic ray box. The lower left text box shows information about the pulses found on this channel. This information includes a list of the pulses in other channels detected in prompt coincidence with this pulse. The buttons in the lower right hand box have changed colour to indicate the presence of noteworthy features on the timeline. The schematic display of buttons shows that this event was triggered by the cosmic ray box (the "Cosmic" button is green) but was not seen by ZEPLIN–III (the "Trigger" button and "Z3 sum" are not green). Some of the module buttons are red indicating very saturated pulses are present, some are blue indicating large pulses and most are yellow indicating the presence of smaller pulses. The labels on some of the module buttons have changed from black to white which indicates the presence of pulses in coincidence. The "Sum" button is dark indicating lots of energy was deposited in the veto during this event as the shade is determined by the total area of all pulses in this event. The "view all" button displays amplitude vs. time for all 52 PMTs in the veto, see Figure 5.36.

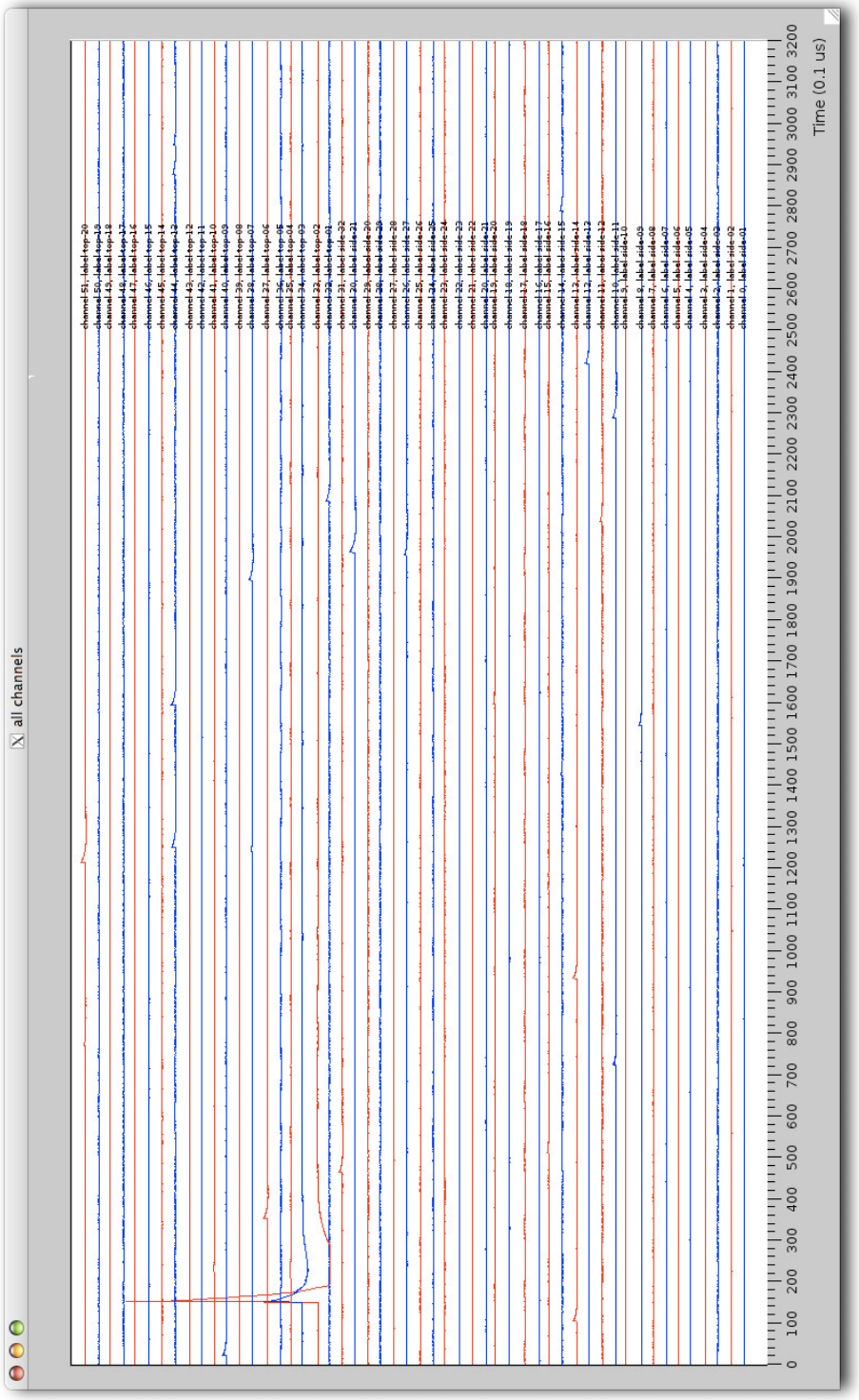

Figure 5.36: A typical output from the "Display All" button. The timelines from all 52 modules are shown simultaneously. This event shows two coincident energy deposits in adjacent modules at the prompt region of the timeline (in coincidence with the trigger). No delayed events above single photoelectron level are seen.

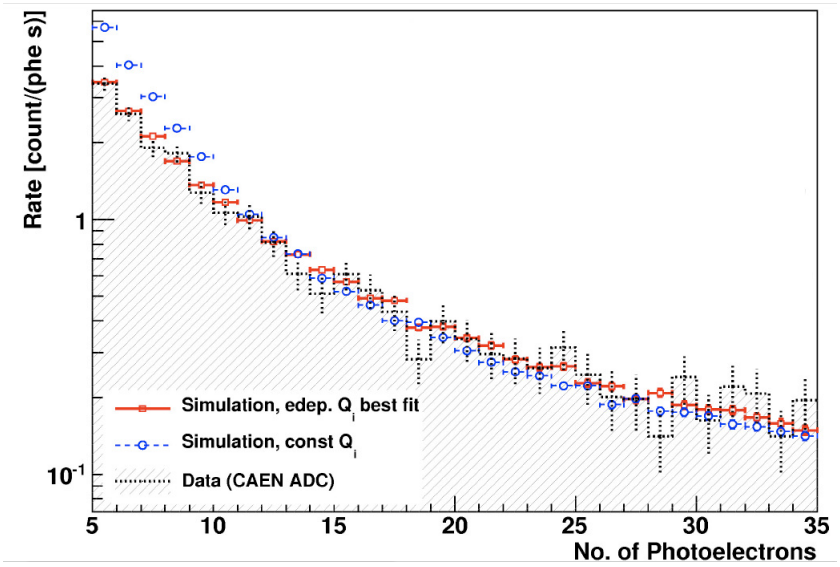

Figure 5.37: Simulations of energy deposits in a veto module from an Am-Be source. This simulations used an energy dependent nuclear quenching factor, $Q_i(E)$. The best fit using χ^2 minimisation is shown by the red histogram and the best fit using a constant quenching factor is shown by the blue histogram [309].

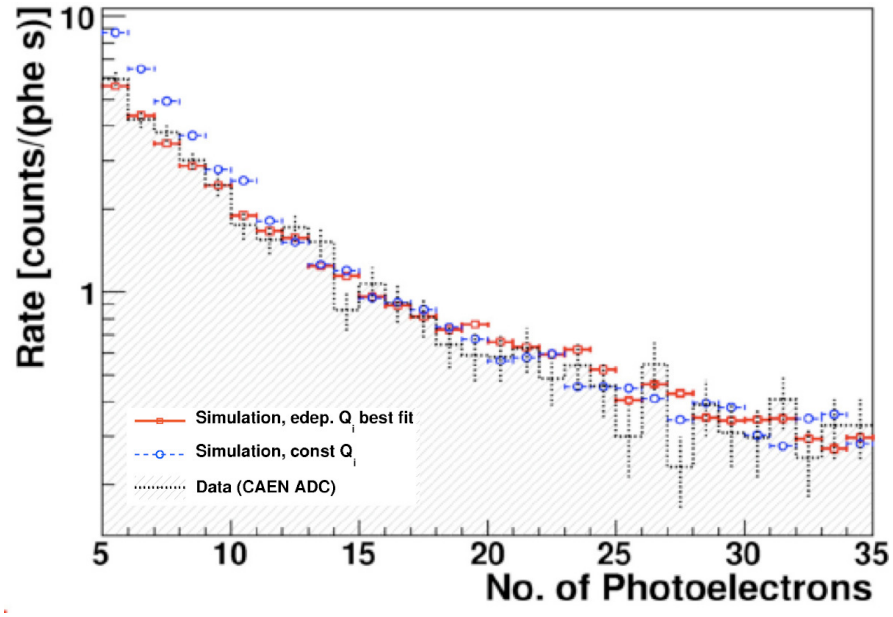

Figure 5.38: Simulations of energy deposits in a veto module from a ^{252}Cf source. This simulation used an energy dependent nuclear quenching factor, $Q_i(E)$. The best fit using χ^2 minimisation is shown by the red histogram and the best fit using a constant quenching factor is shown by the blue histogram [309].

Chapter 6

Veto Detector Performance

6.1 Introduction

The primary function of this detector is to veto ZEPLIN-III background events. To achieve this requires firstly that each ZEPLIN-III event be correctly linked with the corresponding veto event, and secondly that any delays between the trigger time and energy deposits be carefully measured. The ZEPLIN–III veto detector operated in conjunction with ZEPLIN–III for the duration of the second science run lasting from the 24^{th} of June 2010 to the 7^{th} of May 2011. This chapter details the results from the veto over the second science run.

6.2 Event Synchronisation

A method of matching each ZEPLIN–III event with the corresponding veto event is required. Initially the synchronisation used a 32 bit digital stamp generated by a custom built synchronisation unit. Additional synchronisation methods were employed for redundancy. These additional methods comprised of daily synchronisation of the DAq clocks to the same time server and identical parameterisation of the ZEPLIN–III shaped sum channel which are recorded by both DAqs. As the event rate is $\sim$ 0.5 Hz, the most effective method of synchronisation (after matching the synchronisation stamp) is the event time distribution as the clocks of the two DAq computers agree to within 4 ms when synchronised to the time server. If an event remains unsynchronised after examining the synchronisation stamp the next step is to examine the time

distribution with respect to surrounding events and the absolute time. The final attempt at synchronisation, if these methods all fail, is provided by the parameterisation of the shaped sum channel. An example of the same shaped sum channel waveform recorded by each DAq is shown in Figure 6.1. Despite the difference in sampling rate (500 MHz for ZEPLIN–III and 10 MHz for the veto) the pulse parameters match to a high enough degree of accuracy to allow events to be synchronised using this method. It should be noted that as the veto maintained a 100% live time with respect to ZEPLIN–III [191] each ZEPLIN–III event does have a corresponding veto event.

The DAq clocks are both subject to $\mathcal{O}$(ms) drifting with respect to each other over the 24 hour period between re-synching. Figure 6.2 shows the time difference between the time stamps from the two DAqs over several days of the second science run. An analysis program called '`Vesync`' was created to synchronise the events off-line. This software is discussed extensively in [327]. This program synchronised 96% of the second science run "golden" events, shown graphically in Figure 6.3, to give a total of 97% synchronisation when additional synchronised events are taken into account. The selection requirements for the golden events are described in Section 8.4.1.1. The 3% of unsynchronised events remain in the golden data. No events were synchronised incorrectly. Although the waveforms from both DAqs were examined for some of the unsynchronised events, none lay in regions of particular interest (such as at low energies or in the region below the electron recoil band).

6.3 Event Tagging

The most important aspect of the veto is its ability to provide extra information about ZEPLIN–III events. Highly penetrating radiation such as γ-rays and neutrons may be observed by both instruments. The types of ZEPLIN–III events also observed by the veto fall into two categories; events in prompt coincidence with a ZEPLIN–III event and events with a delayed energy deposit in the veto. Hereafter these are referred to as prompt tags and delayed tags respectively. The delayed tags include intermediate steps such as the thermalisation of a neutron or

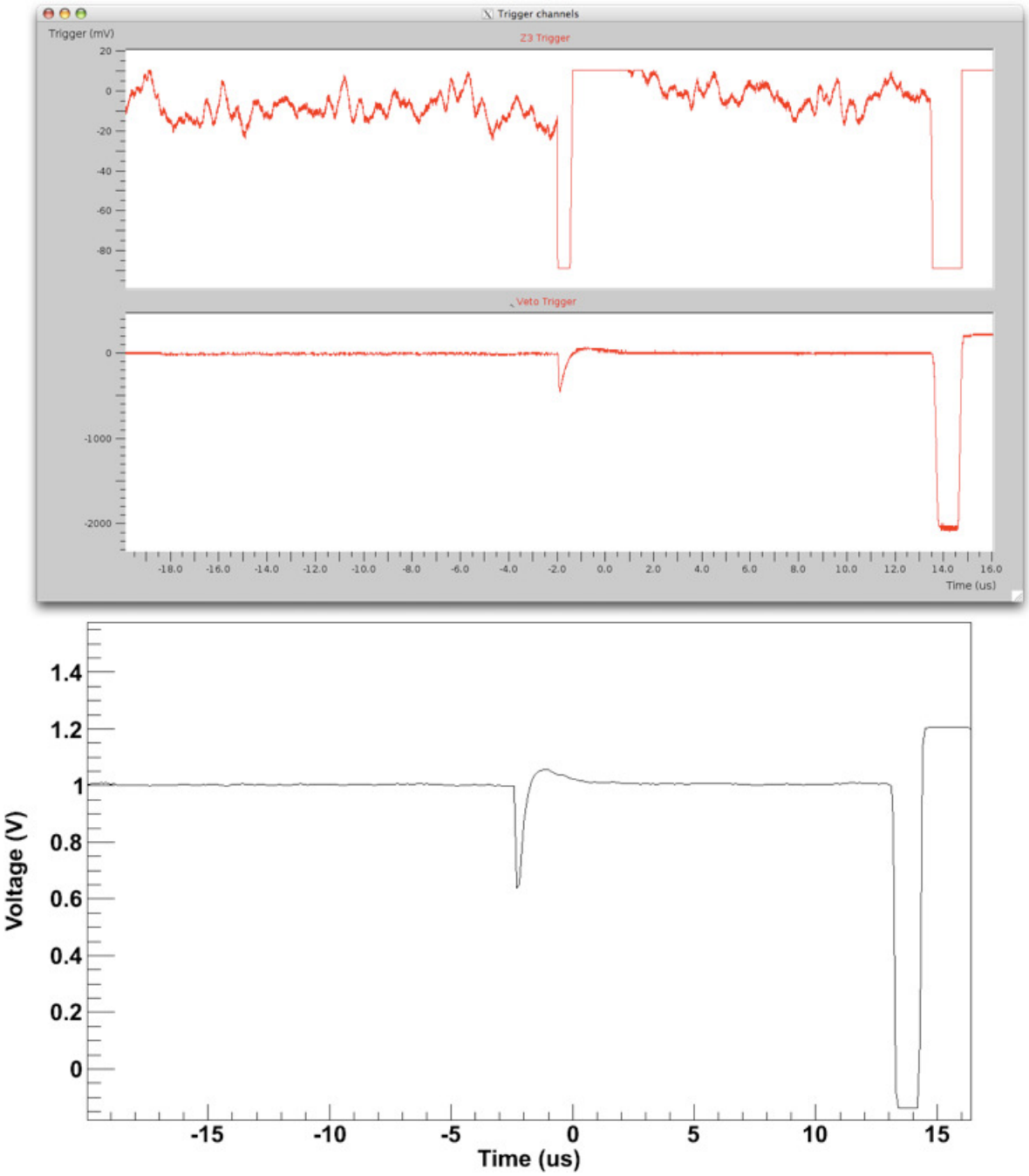

Figure 6.1: Waveforms showing the shaped sum channel of ZEPLIN–III. The top image shows the high sensitivity (upper panel, "Z3 Trigger") and low sensitivity (lower panel, "veto Trigger") channels. The lower image shows the same waveform recorded by the veto DAq. Despite the 50 times higher sampling rate of the ZEPLIN–III DAq this image shows the pulses recorded are very similar. This is due to the long time constant of the pulse shaping with respect to the sampling rate of either DAq.

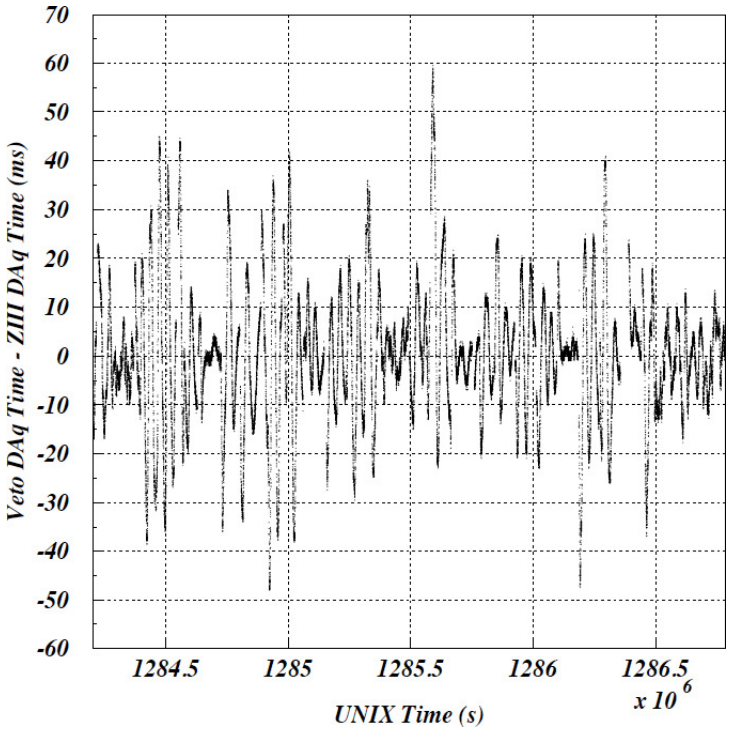

Figure 6.2: The absolute time difference between the two DAq clocks over a period of second science run days between the 12$^{\text{th}}$ of September 2010 and the 10$^{\text{th}}$ of October 2010. The synchronisation of events by time was achieved by aligning the event distribution in time in each data stream and the absolute time was used as a guide. Each X-axis division represents 5×10^5 seconds.

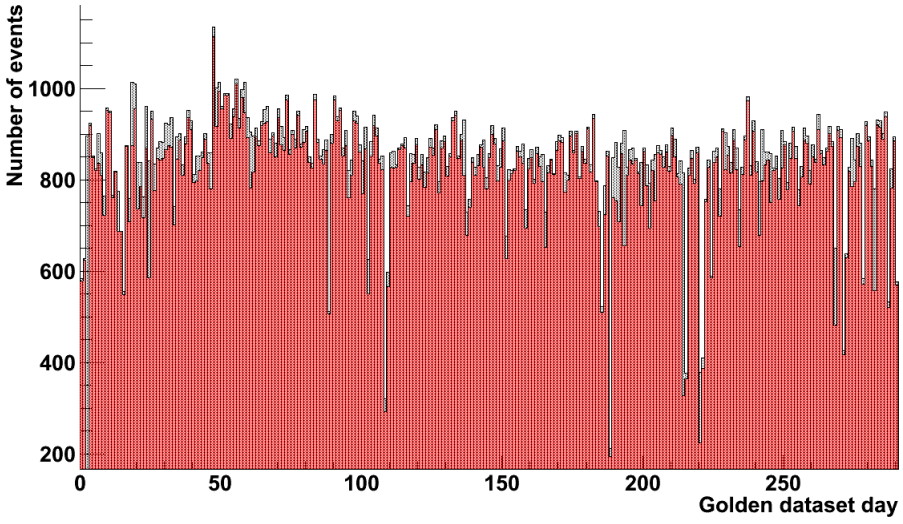

Figure 6.3: The automatic synchronisation of the two data streams for the second science run golden data set. The black histogram shows the number of golden events on each day and the red histogram shows how many of those were automatically synchronised by '`Vesync`.'

the decay time of an excited state. Prompt tags generally have no intermediate stage and the time between the signals observed in the two detectors is small due to the high velocity of the radiation. The maximum delay for a prompt tag of relativistic radiation due to distance is ∼4 ns. This is too short to be resolved considering the sampling rate of either DAq. In practice a short "prompt window" was adopted as the alignment of the prompt position between the two data streams was found to vary slightly due to the resolution of the veto DAq. The conditions for the two veto tags applied in the SSR are given below:

- **SSR prompt tag:** This uses a threshold of 2 photoelectrons across the whole veto within ±0.2 μs of the trigger point.
- **SSR delayed tag:** This uses a threshold of 10 photoelectrons across the whole veto from 0.2 μs to 70 μs from the trigger point. The minimum number of modules with coincident energy deposits was 1, as with the prompt tagging.

Figure 6.4 illustrates the veto tagging. Figure 6.5 shows the fraction of prompt events as a function of the maximum delay allowed. This shows the appropriate prompt window is ±0.2 μs about the trigger point [191]. The rate of prompt signals to background events is shown in Figure 6.6, the rate of background signals gives the accidental tagging fraction. The accidental tagging fraction is an estimate of the background that falls within the tagging window. Since there is a rate of background events it is inevitable that some of these will fall into a tagging window causing a ZEPLIN–III event to be associated with an unrelated veto event. To compensate for this the average rate of background events is measured and compared to the total rate of tagging to calculate the expected accidental tagging fraction. Figure 6.7 shows the accidental tagging fraction as a function of the threshold calculated using the measured background event rate shown in Figure 6.8. To minimise the accidental tagging fraction whilst maintaining a high tagging efficiency for prompt events a 2 photoelectron threshold was chosen. The direct measurement shown in Figures 6.5 and 6.6 both agree with the prediction, show in Figure 6.7, of a ∼0.4% accidental tagging fraction with this threshold and prompt window. The exact measurements given by the data used in Figure 6.6 show an accidental tagging fraction of $(0.43 \pm 0.01)\%$ [191].

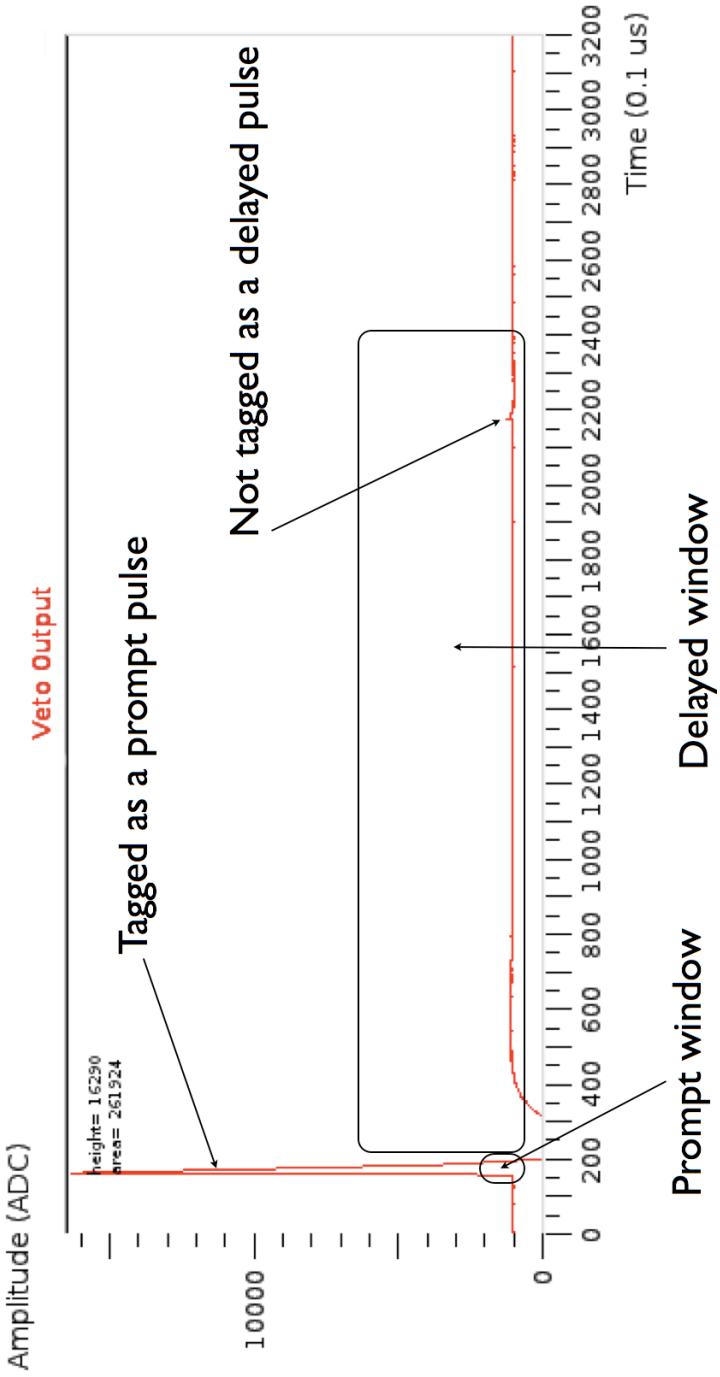

Figure 6.4: This uses an example of an event in a veto module to illustrate the veto tagging. The example timeline is shown with boxes showing the tagging regions. The prompt window shown is ± 4 μs and the threshold above the baseline is 5 photoelectrons, as such the pulse shown would be tagged as being in prompt coincidence. The larger box shows the delayed tagging window. This example extends for 220 μs following the prompt window. To reduce the chances of accidental tagging due to the larger extent of the window the delayed threshold is typically larger than the prompt window, as such the small delayed event indicated would not generate a delayed tag. The example shown here is set at 25 photoelectrons. The thresholds here are not those used in the SSR but are larger for clarity.

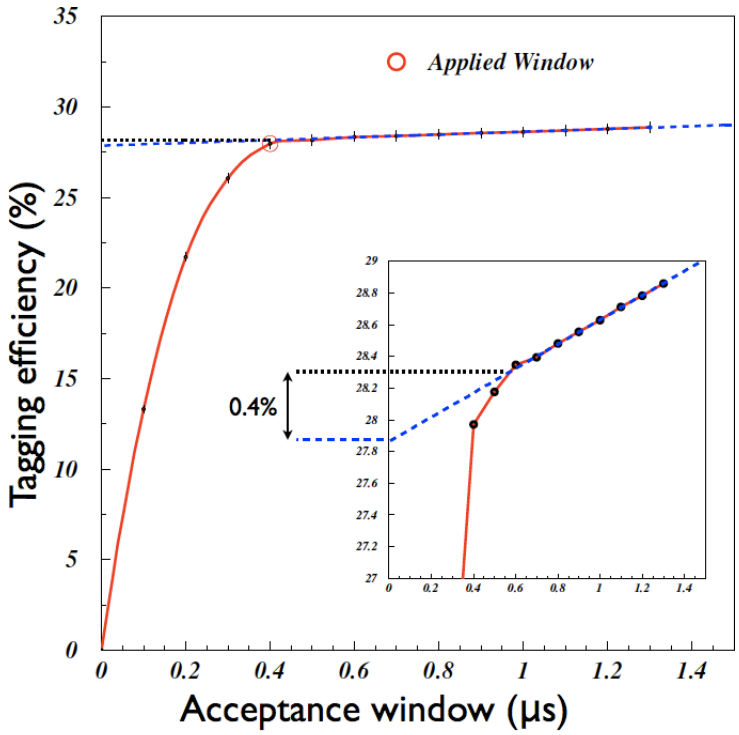

Figure 6.5: The prompt tagging efficiency of the veto as a function of the size of the prompt window for a 2 photoelectron threshold measured from second science run data. The inset image shows a close up of the turnover point where the acceptance window has accepted all prompt tags and increasing the window further only increases the tagging slightly by allowing more accidental tags. Extrapolating back from the increase in tagging due to accidental coincidences gives a measurement of the accidental tagging fraction [191].

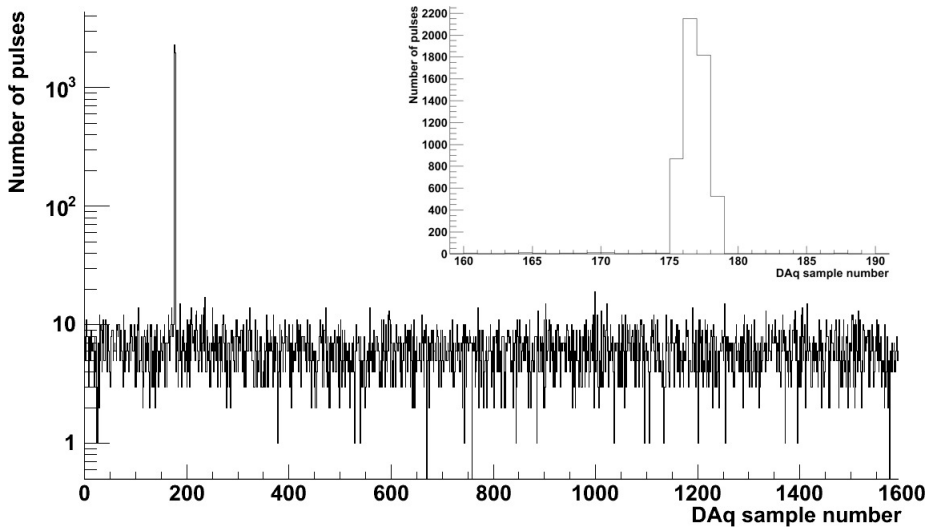

Figure 6.6: The start position of pulses of 2 or more photoelectrons seen in the whole veto when triggered by ZEPLIN–III. This is measured from test data 3 days prior to the commencement of the second science run. A close up of the prompt position is shown inset. The difference between the number of signals in prompt coincidence and the number of background events (i.e. not in channels 176-179) gives the accidental tagging fraction. This is 0.4% for this data.

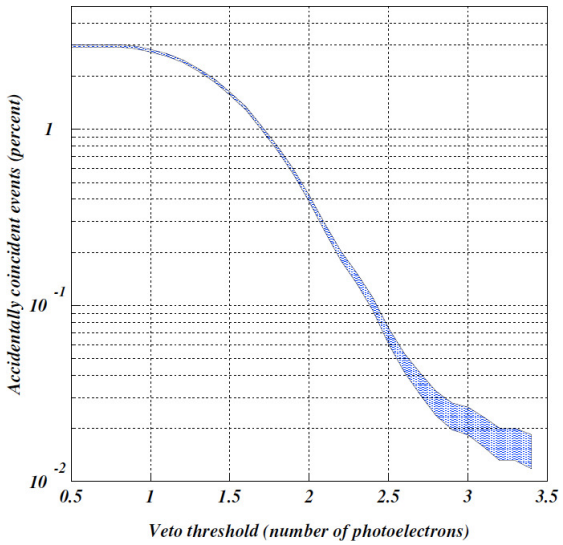

Figure 6.7: The accidental tagging fraction in the veto as a function of threshold for a 0.4 μs prompt window. This is calculated using the background rate shown in Figure 6.8 by $f_a = 1 - \exp^{-r \times w_p}$ where f_a is the accidental tagging fraction, r is the background rate and w_p is the size of the prompt window. The width of the band represents 1σ error bars [191].

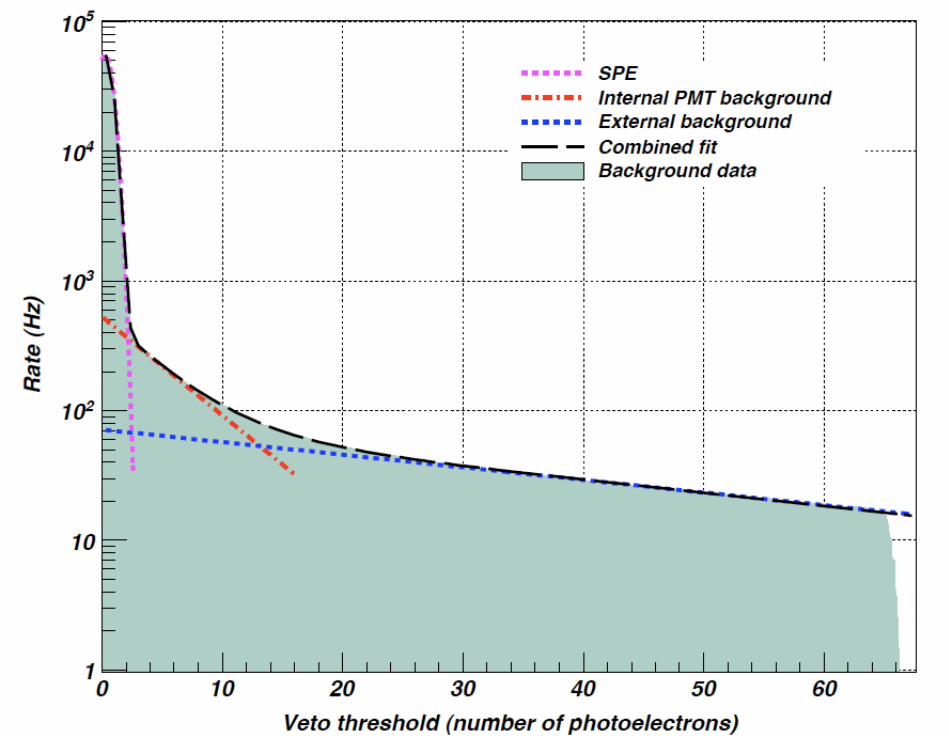

Figure 6.8: The background rate measured across the full veto array. The 3 main components which combine to produce the observed rate are illustrated. At low threshold the rate is dominated by single photoelectrons (SPE). At intermediate threshold the rate is dominated by the internal background generated by the PMT such as β emission from ^{40}K in the glass. Above ~20 photoelectrons the external background begins to dominate the rate [191].

6.3.1 Prompt Tagging

The prompt tags in the science run data are expected to be generated almost exclusively by γ-rays. This is the only type of radiation expected to be present in the science run data which is penetrative enough to leave a signal in both detectors. Other types of event could trigger ZEPLIN–III then emit a prompt γ-ray which is subsequently detected by the veto, such as (β, γ) from the decay of ^{214}Pb, but these type of events are relatively rare. The main purpose of the prompt tag is to veto an event as a potential WIMP candidate and so the origin of any vetoed event is irrelevant to the primary purpose of the instrument. Figure 6.9 shows the prompt tagging efficiency of the veto measured from the second science run data. The data selected are golden events which deposit less than 100 keV$_{ee}$ in the ZEPLIN–III target. To qualify as a prompt tag the signal in the veto must fall within the ± 0.2 μs prompt window around the primary scintillation signal observed by ZEPLIN–III and include at least 2 photoelectrons distributed across the veto. The prompt tagging efficiency of the veto is $(28.1 \pm 0.2)\%$. This measured value is in excellent agreement with Monte Carlo simulations presented in [27]. The simulated result suggests a tagging of $(27.0 \pm 0.6)\%$ which increases to $(27.4 \pm 0.6)\%$ when the accidental coincidence fraction is accounted for [191].

The prompt tagging was also explored as a function of the energy deposit in the ZEPLIN–III target. Figure 6.10 shows the differential rate of background events observed by ZEPLIN–III between 0 and 200 keV$_{ee}$. The prompt tagging fraction remains constant as a function of ZEPIN-III energy in the region of interest. In addition to providing background rejection the γ-ray tagging ability of the veto provides an unbiased sample of background events for detector characterisation in a blind analysis. It also provides an independent estimate of the γ-ray background in the xenon target which is especially important at low energies due to the finite discrimination power of the detector. Any discrepancy between the predicted and observed γ-ray background, or any significant excursions from the mean rate as a function of energy, could indicate that electron recoil backgrounds have a significant β contribution. Figure 6.11 shows the veto energy spectrum of the prompt tags (i.e energy deposited in the veto). As expected, this spectrum is featureless with a similar form to the background event rate observed in the veto.

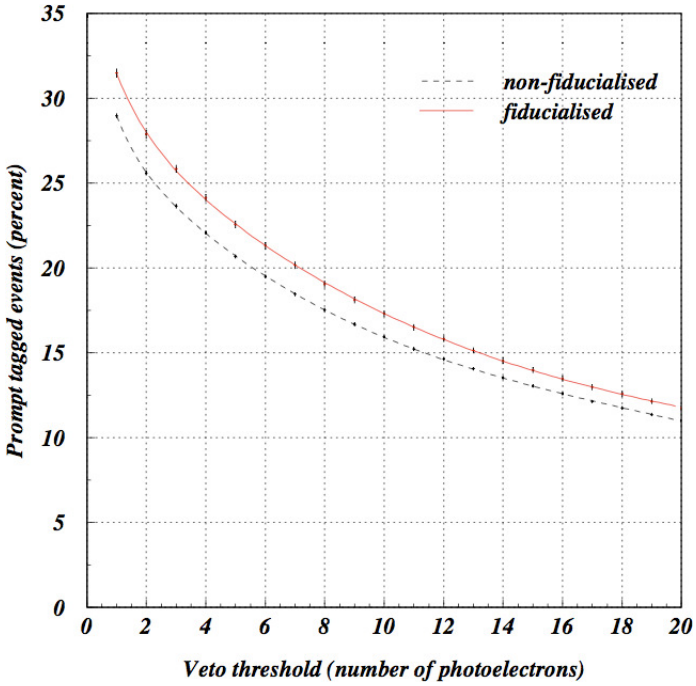

Figure 6.9: The prompt tagging efficiency of the veto as a function of threshold for ZEPLIN–III events depositing less than 100 keV$_{ee}$ in the target. This was measured from the second science run data and uses a 0.4 μs window and a 2 photoelectron threshold (distributed across the whole veto). The black curve shows the results from the golden events and the red curve shows the results following a fiducial cut ($z = 28.4$ mm, $r = 140$ mm) of the golden events [191].

6.3.2 Delayed Tagging

The most important aspect of the veto is its ability to tag neutron events. The veto provides ZEPLIN–III with the ability to discriminate between nuclear recoils due to WIMP interactions and nuclear recoils due to single scatter neutron interactions. These events would otherwise be indistinguishable and as such represent a serious threat to the detectors WIMP sensitivity. This discrimination power was measured using neutron calibration data. This measurement was performed during the nuclear recoil band calibration using an AmBe source described in Section 8.2.2. The fraction of neutron events, observed in the fiducial volume of ZEPLIN–III, which deposit energy in the veto gives the tagging efficiency. The results from Monte Carlo simulations which were used to predict the neutron tagging efficiency are shown in Figure 6.12 [27]. These simulations do not take into account background events which may lead to accidental coincidences and represent the limit of the detector's neutron vetoing efficiency.

To achieve the best tagging-efficiency to accidental-tagging ratio, several factors must be considered. As neutron capture is most likely to be on one of the gadolinium isotopes, the number of coincident energy deposits in different modules provides some discrimination power. Figure 6.13 shows the multiplicity dependence of the prompt and delayed event tagging. This figure shows that the number of modules with coincident deposits in other modules has a strong dependence on the event type. As neutron capture may lead to the emission of several γ-rays it is much more likely that several modules will observe a ZEPLIN–III neutron event in coincidence.

A significantly larger acceptance window must be used for the delayed event tagging, as demonstrated by the neutron capture time distribution shown in Figure 5.5. As such, the background rate above the chosen threshold, shown in Figure 6.8, must be taken into account when considering an appropriate window size to avoid significant accidental coincidences. A 70 μs acceptance window for delayed tagging was selected for the second science run. The window follows

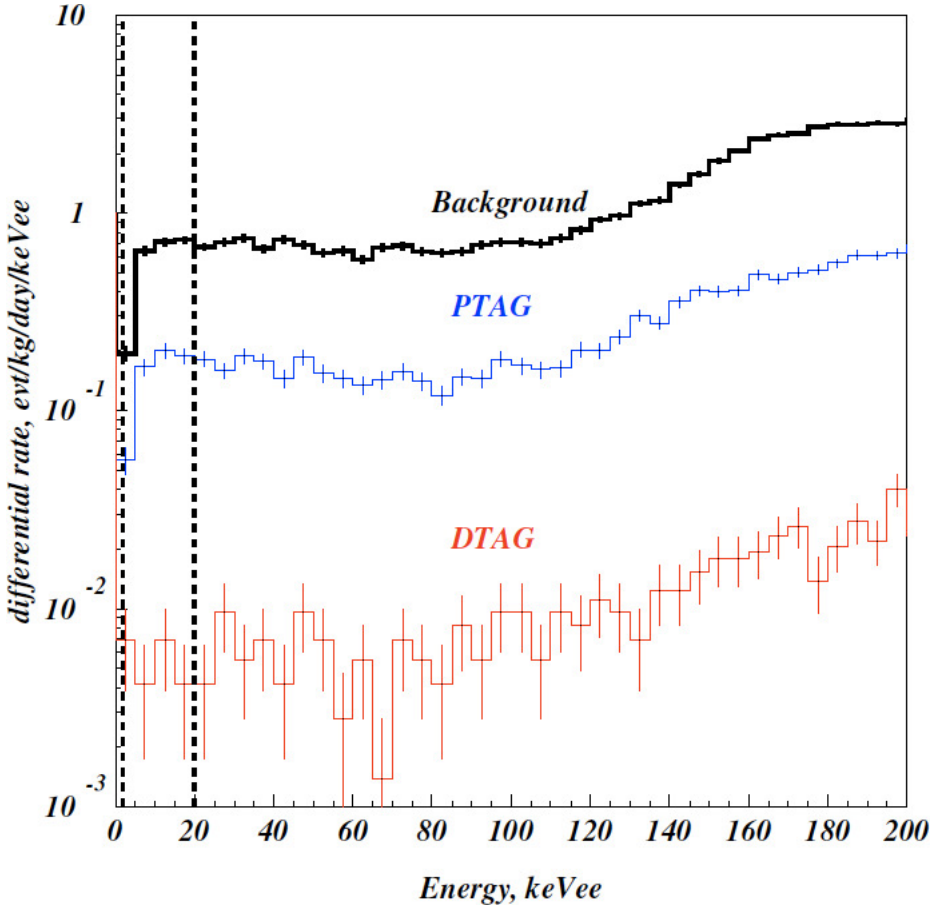

Figure 6.10: The differential background rate (black line) as a function of energy deposited in the ZEPLIN–III target. Also shown are the differential rate of prompt tags (blue line) and the differential rate of delayed tags (red line). Both of these tagging rates remain a constant fraction of the background as a function of energy in the region of interest. The delayed tagging rate is consistent with accidentally coincident delayed tags due to the unrelated background seen by the veto detector. The vertical line represents the approximate upper boundary of the WIMP acceptance region [191].

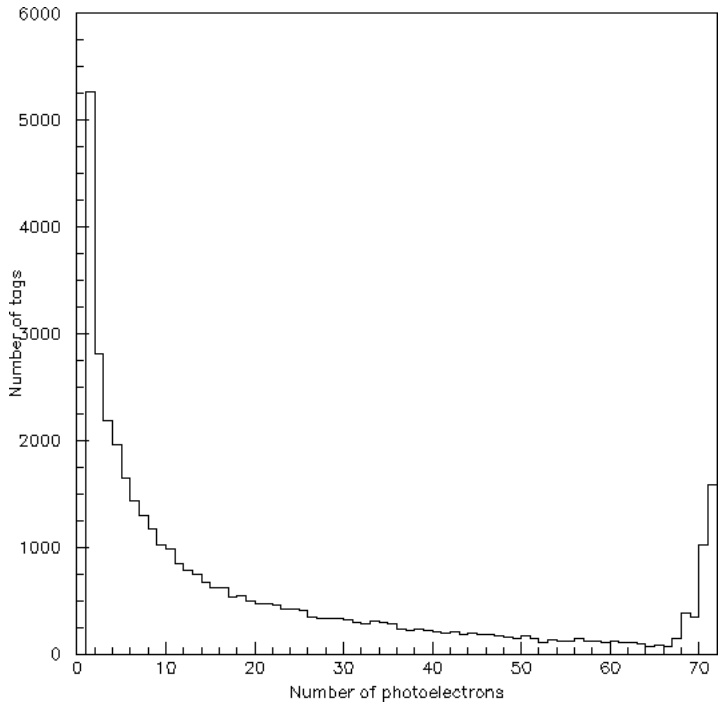

Figure 6.11: The spectrum of prompt tagged energy deposits in the veto. This spectrum shows no unexpected features, the increase beyond 65 photoelectrons is due to saturated events which would extend beyond the range of the veto DAq.

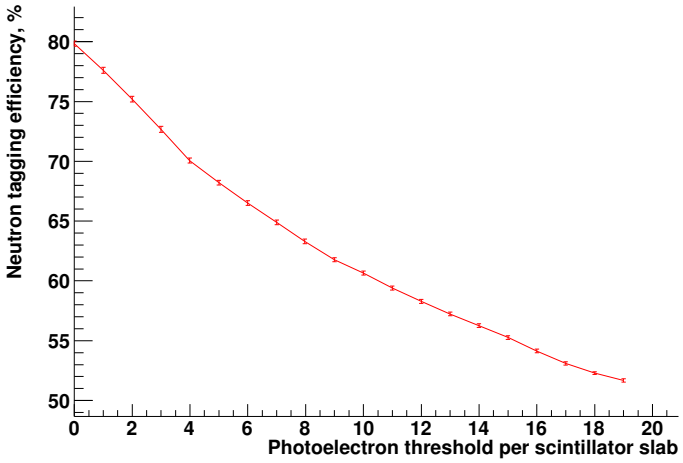

Figure 6.12: Results Monte Carlo simulations of single scatter neutron events in the ZEPLIN–III fiducial volume as a function of energy deposited in the veto [27].

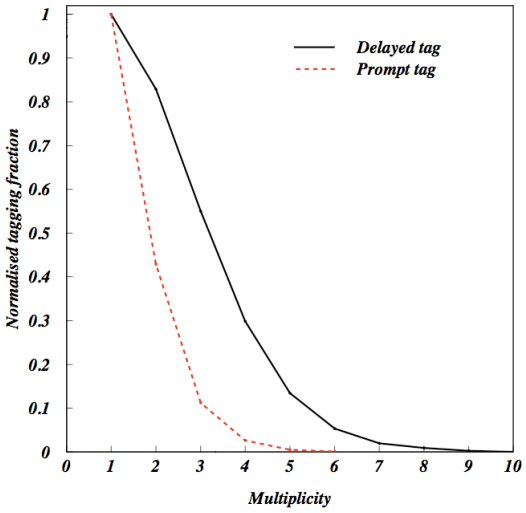

Figure 6.13: A comparison of the tagging fractions of prompt and delayed events as a function of the number of veto modules observing the event (the multiplicity). These were measured from background (with a 2 photoelectron threshold) and neutron calibration data (with a 9 photoelectron threshold) respectively. Neutron capture on gadolinium may release multiple γ-rays which can be detected in several different veto modules. This provides a rudimentary form of discrimination between event types [191].

immediately after the prompt tagging window, and so the neutron tagging is actually a combination of a 0.4 μs prompt tagging window plus a 69.6 μs delayed tagging window. As neutrons have a lifetime of 10.7 μs within the veto, this window accepts 99.86% of single scatter neutrons from the fiducial volume of ZEPLIN–III [191]. Note that although the window accepts this high fraction other efficiencies must be accounted for to calculate the total number observed by the veto.

The veto neutron tagging efficiency, measured during neutron calibration, is shown as a function of the energy deposited in the veto in Figure 6.14. Only single scatter neutrons within $\pm 2\sigma$ of the mean of the nuclear recoil band in the energy range 2 to 20 keV$_{ee}$ were selected. The selected neutrons are shown in Figure 6.15. The multiplicity dependence of the neutron tagging is shown for two different energy thresholds in Figure 6.16. The neutron tagging efficiency has a stronger dependence on energy threshold than on multiplicity threshold, hence a lower multiplicity threshold with a higher energy threshold combine to provide an overall higher neutron tagging efficiency. The main benefit of using a

multiplicity threshold is the reduction in the accidental coincidence rate as a ± 0.2 μs coincidence window is used to relate coincident pulses. This is confirmed by Figure 6.13, which shows a weaker dependence on multiplicity for γ-ray events. A 10 photoelectron threshold across the veto with no minimum multiplicity requirement was selected for the second science run. This gives a total neutron tagging efficiency of $(60.5 \pm 0.5)\%$ with less than a 1% accidental delayed tagging rate [191]. The accidental tagging of prompt pulses and delayed pulses are so similar due to the varying affects of window size and threshold, as the threshold is low for prompt pulses the rate per sample is high, but the number of samples included in the window is low. Similarly for the delayed events the threshold is much higher so the rate per sample is very low, however many more samples are included. The total tagging efficiency comprises of $(58.8 \pm 0.5)\%$ measured by delayed tagging during neutron calibration plus an additional $(1.7 \pm 0.1)\%$ from an extrapolation into the prompt window by considering the characteristic neutron capture time. A direct measurement of the neutron tagging in the prompt window was not feasible using an AmBe calibration source as high energy γ-rays emitted in coincidence with the emitted neutron in the Be(α,n) reaction may be detected in the prompt window. The simulated result shown in Figure 6.17 predicts a total neutron tagging efficiency of $(60.7 \pm 0.1)\%$ which is in excellent agreement with this measurement. The losses are accounted for by the veto coverage (3π) and the veto γ-ray detection efficiency.

After event synchronisation the science run data are assessed for veto coincidences. As the background data is dominated by γ-ray events, the prompt tagging is assessed first. This reduces the population to which the delayed tag is then applied by the prompt tagging fraction. The delayed tagging is then assessed. As no population of delayed events is expected in the background data the delayed tagging criteria (threshold size, module multiplicity and acceptance window) were selected to give a total accidental vetoing rate below 1%.

The accidental tagging of prompt events is 0.43% and the accidental tagging of delayed events for the selected criteria is 0.83%, although this is reduced by the tagging of prompt events by 28%. Summing these 2 contributions gives the accidental tagging for the second science run background events as $\sim$0.98%.

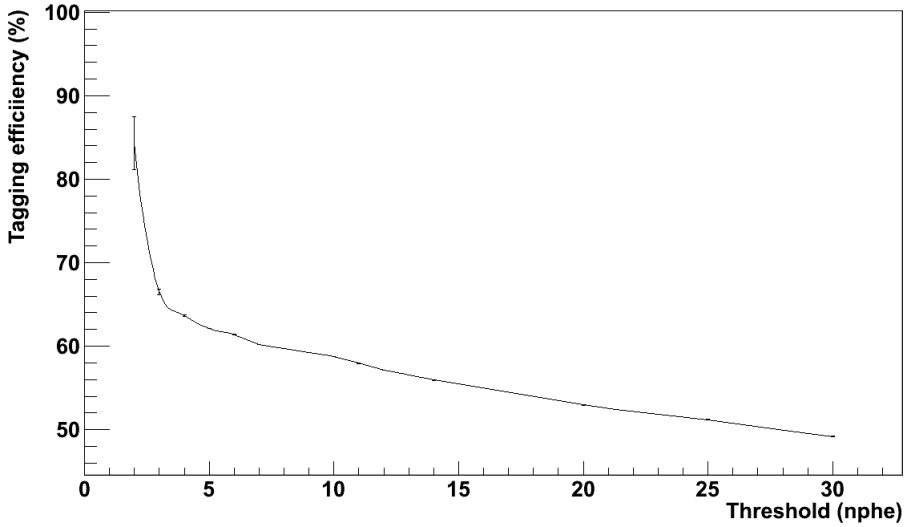

Figure 6.14: The neutron tagging efficiency of the veto as a function of energy deposited in the veto. Measured using single scatter neutrons within $\pm 2\sigma$ of the nuclear recoil band mean between 2 and 20 keV_{ee} as shown in Figure 6.15. The sharp turn up at lower thresholds is in line with expectations of accidental tagging due to the increased in event rate.

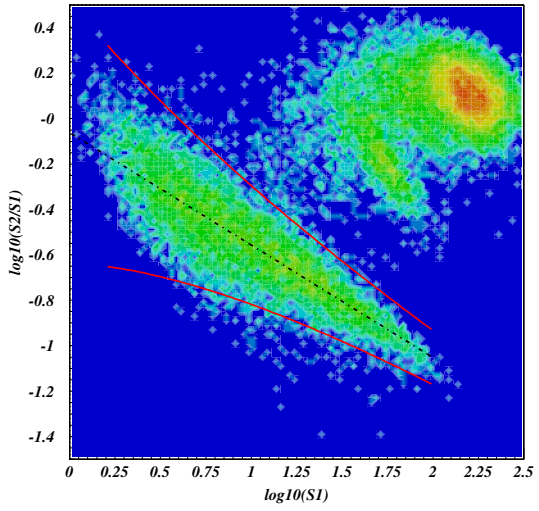

Figure 6.15: A density plot of events from a nuclear recoil band calibration with an AmBe source. The mean of the nuclear recoil band is indicated by the dashed line and the $\pm 2\sigma$ error limits are indicated with red lines. Single scatter events from the fiducial volume within these limits are selected for analysis of the response of the veto to neutrons. These are the neutrons selected for the analysis presented in [191].

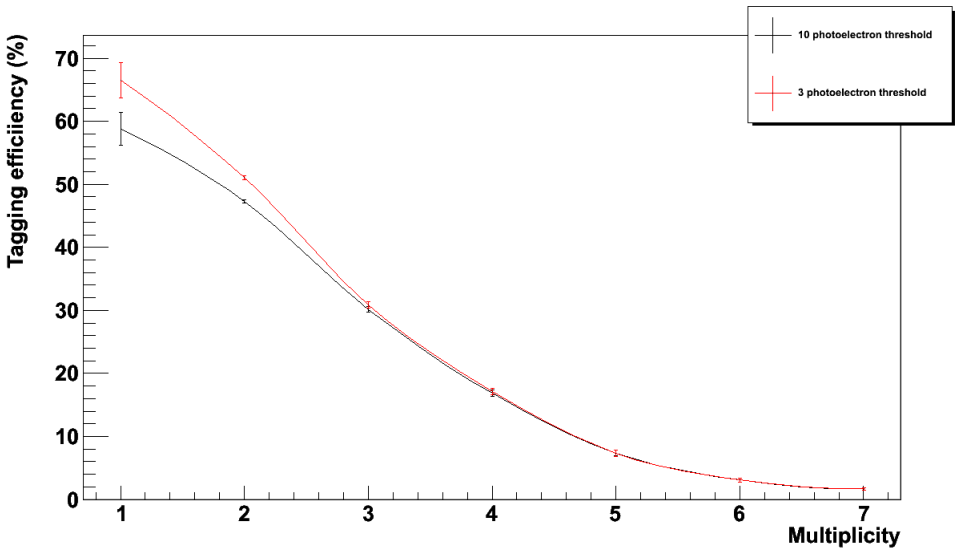

Figure 6.16: The neutron tagging efficiency of the veto as a function of multiplicity for two different energy thresholds. This shows that an energy threshold is more effective than a multiplicity threshold, for example a requirement of a minimum multiplicity of 2 modules with a 3 photoelectron threshold gives a lower tagging efficiency than a 10 photoelectron threshold with a minimum multiplicity on 1 module.

The accidental tagging rate for WIMPs, which would not interact with both detectors, is given by the sum of the 2 accidental tagging rates without any reduction in the delayed tagging exposure. With the thresholds and windows selected for the second science run data the accidental WIMP vetoing is $\sim$1.3% [191]. The differential rate of these events is shown in Figure 6.10. This confirms the expected accidental delayed tagging rate for background events assuming that no significant delayed event population is present in the data.

As previous mentioned, the neutron tagging capability of the veto is due to its sensitivity to γ-rays emitted following neutron capture. As such no significant dependence on the neutron energy is expected to be observed in the tagging efficiency at the low energies of interest to WIMP searches. An energy dependence may be manifest at very high energies due to the decrease in the thermalisation and capture rate of these neutrons, see Figure 5.3. Figure 6.17 shows the veto neutron tagging efficiency as a function of the energy deposited by the neutron. Figure 6.16 shows that an energy dependent threshold is more effective than a multiplicity threshold for vetoing neutron events from the fiducial volume of

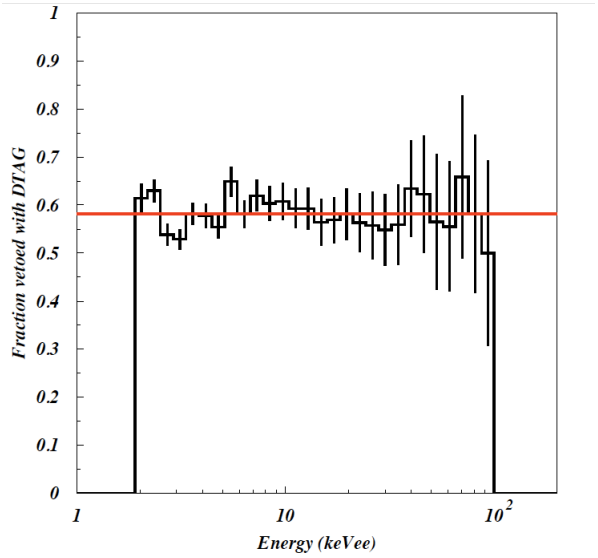

Figure 6.17: The neutron tagging efficiency of the veto as a function of the energy deposited in the ZEPLIN–III fiducial volume by the neutron. The efficiency remains constant as a function of energy as the neutrons are detected via the emission of γ-ray/s emitted after neutron capture following thermalisation [191].

ZEPLIN–III. This justifies the minimum multiplicity requirement of only a single module.

6.4 Diagnostics Using the Veto Data

The veto provides an invaluable diagnostic tool for analysis of the second science run data. ZEPLIN–III events with a veto event in prompt coincidence could be analysed during the science run without compromising the blind WIMP analysis to be conducted at the conclusion of data taking. This provided over a quarter of the background data for analysis. Previously a blind analysis was conducted by selecting 10% of the science data [254]. This method not only reduced the exposure but also risked prejudicing the WIMP search. This method using vetoed data only reduces the WIMP exposure by the accidental coincidence rate for prompt tags, which is very low. The data was used to characterise the background experienced by the instrument and check for any unusual event topologies which may compromise the WIMP sensitivity. The analysis software could also be trained using real background data without compromising the WIMP sensitivity.

One example of where this was useful is a population of background events interacting at the very top of the liquid xenon. For this type of event the S1 signal overlaps with the S2 signal and may be inseparable, an example is shown in Figure 6.18. Most of these events are rejected due to the lack of an S1 signal but some are accidentally associated with an unrelated pulse prior to the event. The veto detected large energy deposits in coincidence with the start of the S2 signal for $\sim \frac{1}{3}$ of these events. With a significant proportion of this population to analyse the analysis software could be trained to recognise these signals and cut them from the WIMP search data set. The veto is also able to detect 28% of multiple scintillation single ionisation (MSSI) events. These events are particularly dangerous and are discussed further in Section 8.4.1.2.

6.4.1 Position Dependence

The tagging efficiency of the science run background may be calculated as a function of position. Due to the geometry of the veto (*i.e.* $< 4\pi$ st coverage), the tagging efficiency will not be uniform for events across the ZEPLIN–III fiducial volume. Also events closer to the edge of the xenon have a longer average path length through the barrel sections of the veto and are therefore more likely to be observed. Cylindrical co-ordinates are appropriate to describe the ZEPLIN–III fiducial volume and the position dependence of the tagging efficiency is shown as a function of the depth co-ordinate and of the radial co-ordinate in Figure 6.19. This plot divides the fiducial volume up into slices and shows the tagging efficiency averaged across each slice. As may be expected from considering the geometry of the instrument, the strongest dependence is due to the drift time where the tagging efficiency decreases with increasing depth. There is also a slight dependence on the radial position of the initial energy deposit with the highest tagging efficiency coming from the outer part of the target. As the veto only covers $\sim 3\pi$, and the least amount of intervening material between the two sensitive volumes is found near the center of the veto roof, an increase in depth also gives an increase in the mean solid angle which is not covered by the veto and similarly with decreasing radius. Due to this gap in the veto, if the veto is considered as two detectors, the barrel modules should be sensitive to the position of the event whereas the roof modules should be less sensitive as the solid angle

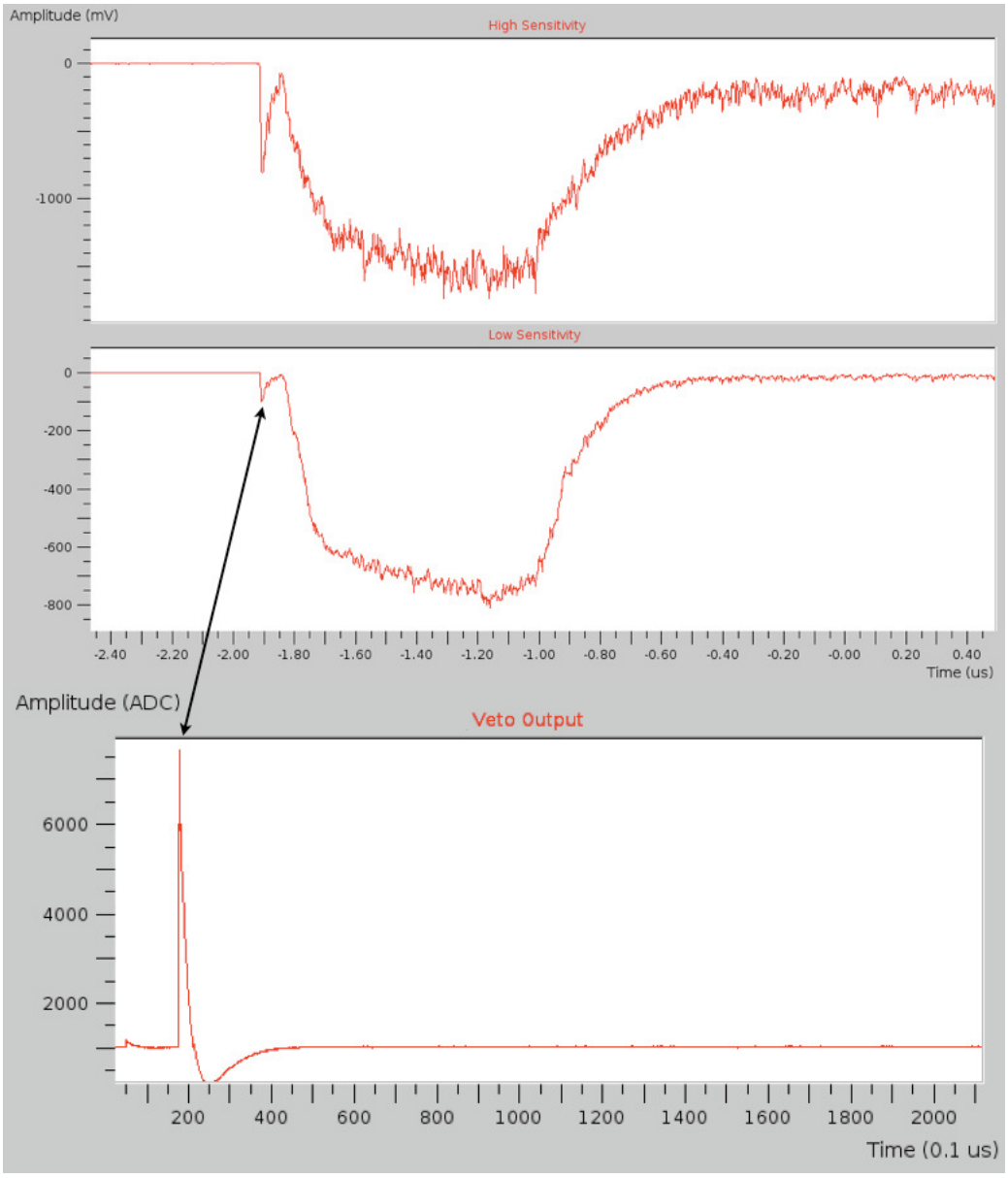

Figure 6.18: An example of an event interacting at the surface of the liquid xenon seen in ZEPLIN–III (top image). The S1 signal is buried within the S2 signal however this event was also detected by the veto (bottom image). The arrow shows the alignment of the timelines. The smaller S1 event is lined up in time with the large veto signal.

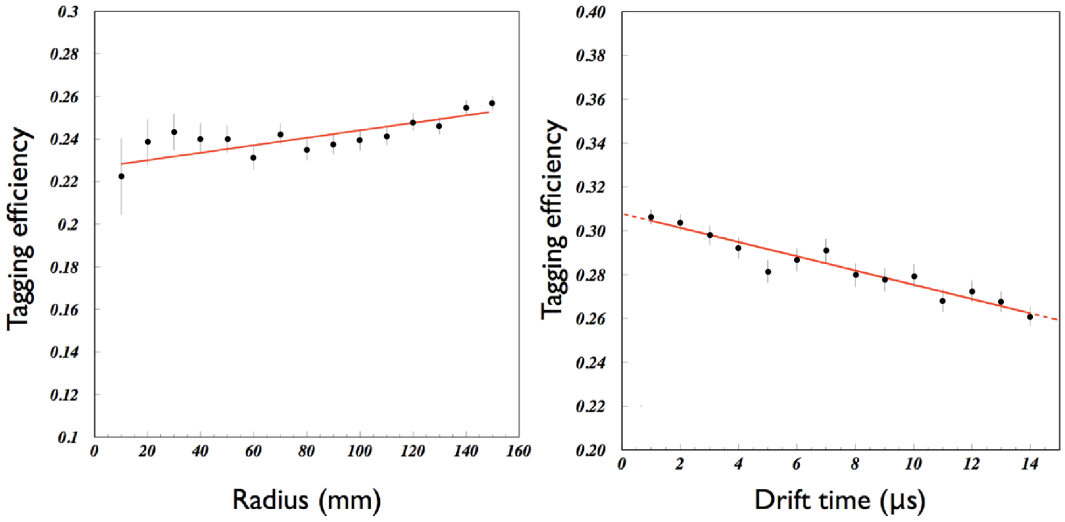

Figure 6.19: The positional dependence of the background event tagging for the whole veto. The left image shows the efficiency as a function of radius for the full height of the fiducial volume and the right image shows the efficiency as a function of depth for the full fiducial radius. The fiducial volume is divided up into slices and the average tagging efficiency for each slice is shown.

changes little with radius (averaged over 2π) and very little with depth.

To confirm this, the depth and radial dependencies may also be split into the component from the barrel and the component from the roof. The depth dependence is shown separately for the roof modules and barrel modules in Figure 6.20. This indicates that the depth dependence of the background tagging efficiency is dominated by the barrel sections. Figure 6.21 shows a similar result for the radial dependence of the background tagging efficiency.

6.5 Muon Events

The ZEPLIN–III veto data was searched for muon events. Utilising the cosmic ray trigger feature a total of 1.2×10^6 candidate events were selected for further analysis. An example of a muon event is shown in Figures 6.22 and 6.23. A spectrum of the total (sum channel) area of the veto pulse, shown in Figure 6.24, shows 2 populations of events. The absence of lower energy events is due to the hardware threshold set on the cosmic ray trigger box. Due to saturation effects

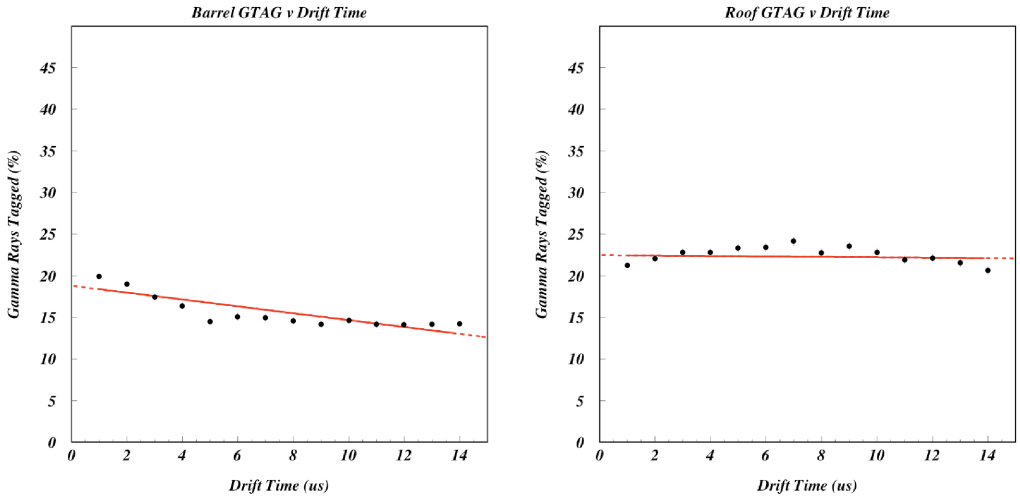

Figure 6.20: The tagging efficiency of the veto as a function of depth (drift time in the fiducial volume of ZEPLIN–III). The left image shows the tagging efficiency of the barrel modules and the right image shows the tagging efficiency of the roof modules. As expected the change in the solid angle of area with no sensitive detector effects the barrel modules more than the roof modules.

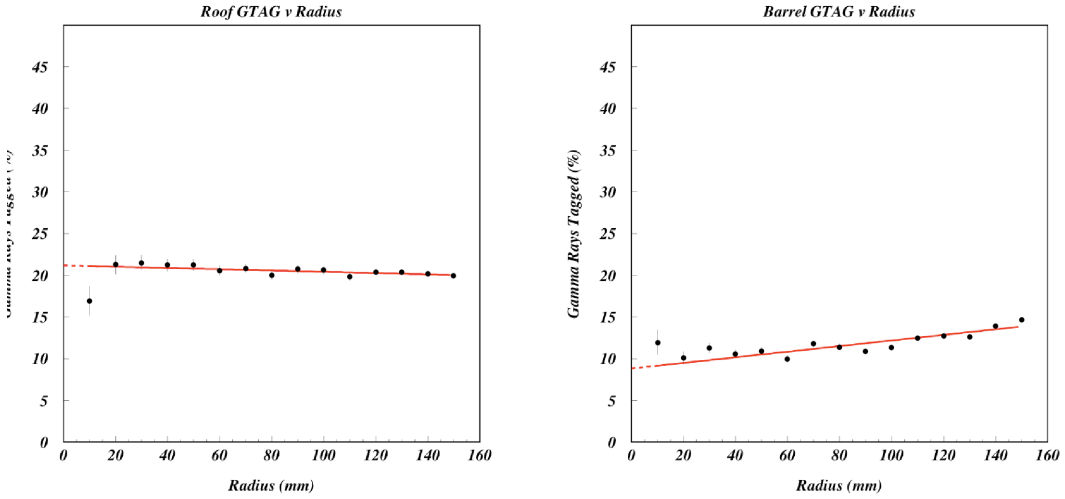

Figure 6.21: The tagging efficiency of the veto as a function of radius from the center of the fiducial volume of ZEPLIN–III. The left image shows the tagging efficiency of the barrel modules and the right image shows the tagging efficiency of the roof modules. As expected the change in the solid angle of area with no sensitive detector effects the barrel modules more than the roof modules.

the energy resolution of the veto falls with increasing energy deposited. At higher energies the area of the sum channel pulse is strongly dependent on the number of modules that are hit by the muon and its particle shower as each module hit it typically saturated. Figure 6.25 shows the area as a function of the number of saturated modules. In addition to genuine muon events the cosmic ray box may also be triggered by high energy γ-rays. These background events typically deposit energy in two of the roof modules and, despite saturating both modules, produce a much smaller sum channel signal than muon events. A threshold was applied to the size of the sum channel signal to separate the two populations of events. Figure 6.24 shows a break in the spectrum at $\sim 1.2 \times 10^6$ ADC channels $\times$100 ns (corresponding to 1.65 V ns). There are 8271 events above this threshold. Accounting for the live time and the area of the roof this corresponds to 18.8 ± 0.2 muons day^{-1} m^{-2} above this threshold.

Pervious measurements of the muon rate in this laboratory have been made using ZEPLIN-I [314] and ZEPLIN-II [52]. The muon rates were measured as $(4.09 \pm 0.15) \times 10^{-8}$ cm^{-2} s^{-1} and $(3.79 \pm 0.04(\text{stat}) \pm 0.11(\text{syst})) \times 10^{-8}$ cm^{-2} s^{-1}, respectively. The measurement in this analysis corresponds to $(2.18 \pm 0.02) \times 10^{-8}$ muons cm^{-2} s^{-1}. However, this measurement uses a threshold which excludes lower energy events. Simulations of the muon spectrum suggest that the spectrum is approximately flat at lower energies. Figure 6.26 shows a simulated neutron spectrum from Reference [261]. If, for example, a flat spectrum is assumed form the muon event threshold then an additional $\sim$ 6000 events would be added to the total number of events. This would increase the rate to 3.76×10^{-8} muons cm^{-2} s^{-1}.

The variation of the muon flux was also investigated. Figure 6.27 shows the monthly average rate of muon triggers for events over several different thresholds. No significant variation in the muon rate was detected.

Many of the muon events are followed by delayed events. Figure 6.28 shows the proportion of events with large delayed events in the veto. The delay between the muon and the first large event is shown in Figure 6.29. This plot shows the number of events falls off exponentially with time following the muon. This

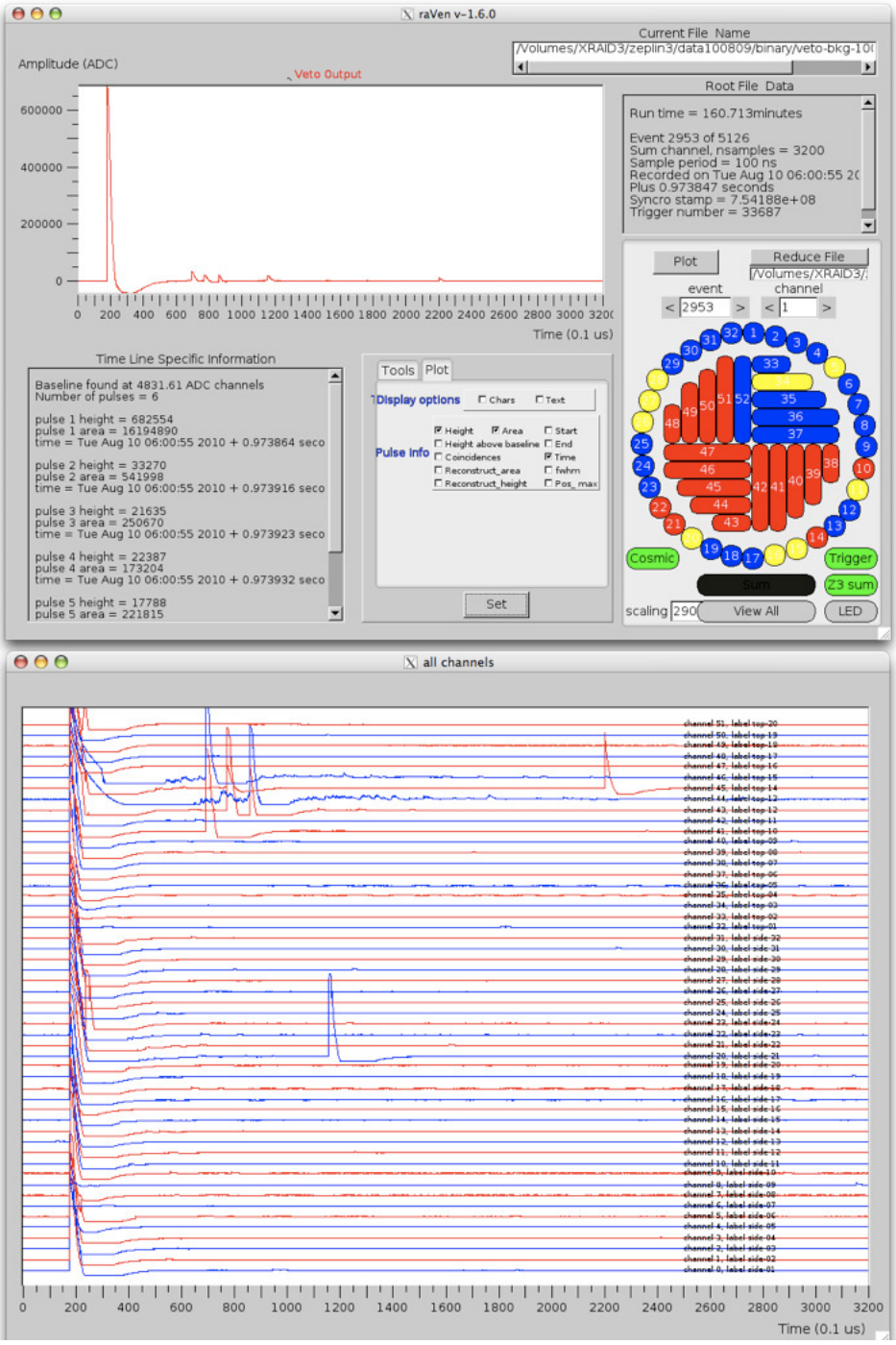

Figure 6.22: An example of a muon event recorded by the veto. This event also triggered ZEPLIN-III. The top image shows the veto sum channel. The lower image shows the time lines from all of the 52 veto modules. The muon has saturated each module at the trigger point and several delayed events can also be seen later in the timelines. Some of the delayed events are coincident in several modules. Figure 6.23 shows some timelines for individual channels for this event.

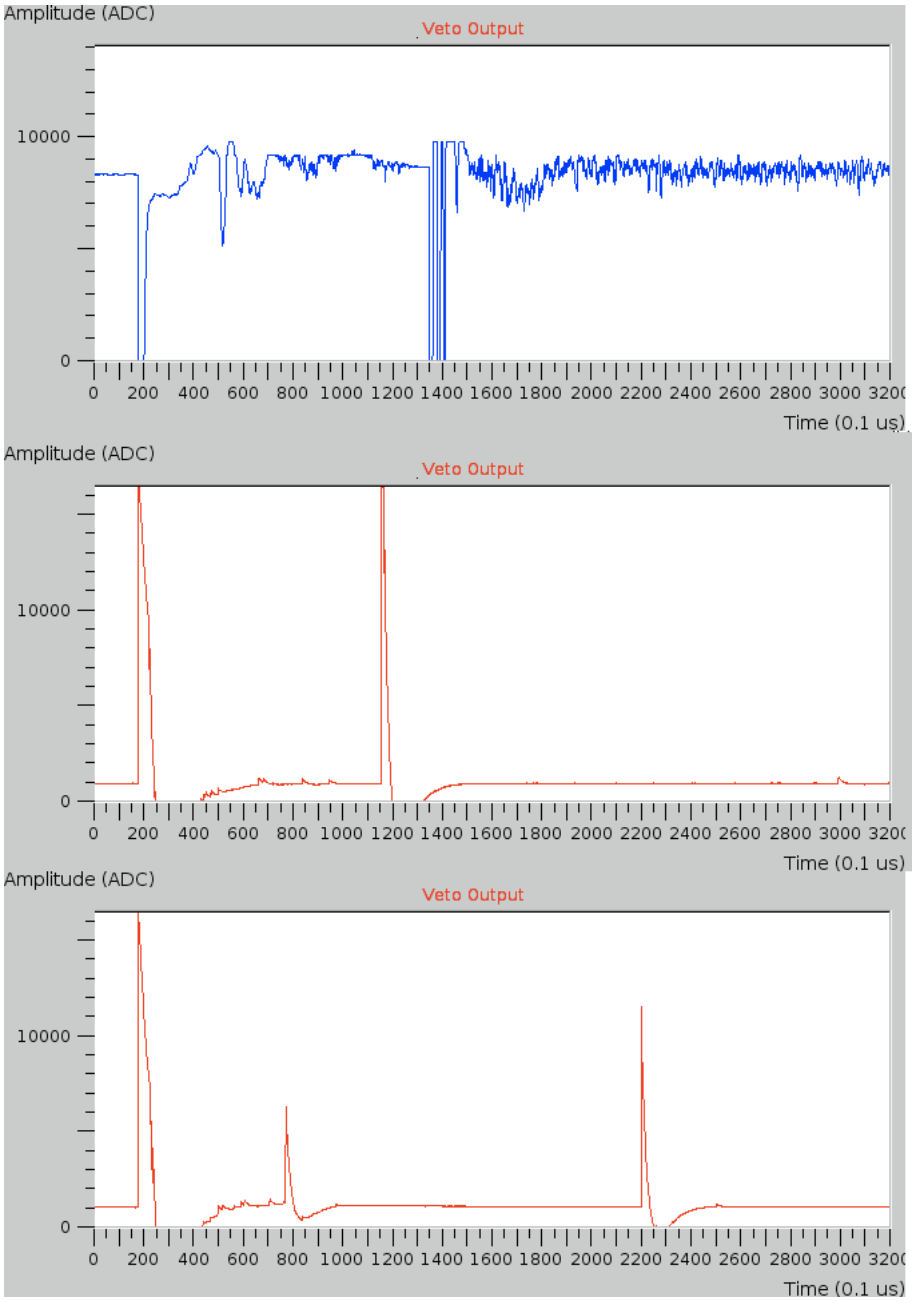

Figure 6.23: An example of a muon event recorded by the veto. The upper image shows the ZEPLIN–III shaped sum channel recorded for 320 μs by the veto DAq. The S2 signal from a delayed event in ZEPLIN-III can be seen at sample 1300. The central image shows the timeline recorded by module 21, a delayed event can be seen approximately 100 μs after the muon. The lower image shows the timeline recorded by module 46, again delayed events can be seen.

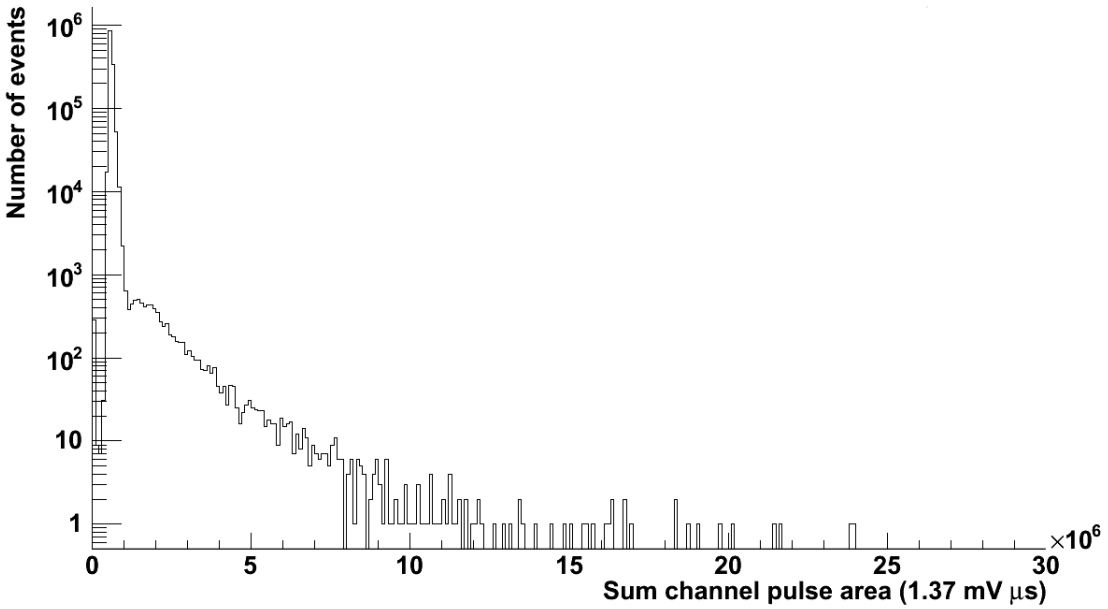

Figure 6.24: The sum channel pulse area spectrum of events triggering the veto cosmic ray box.

could be caused by activation of a relatively long lived isotope or the time taken to thermalise and capture muon induced neutrons. The rate of muon induced neutrons has been measured using ZEPLIN–II [52].

The results presented here show the ability of plastic scintillator to measure the muon flux. Due to its primary use as a veto the system was optimised for low energy events and therefore energy resolution was limited for high energy events. In a dedicated search energy resolution could be recovered somewhat by adjusting the PMT voltages. Due to the modular nature of the veto and the presence of the gadolinium loaded polypropylene this instrument could be used to study the muon induced neutron rate in lead. The expected accidental coincidence rate of large prompt energy deposits in multiple modules is low enough to ensure a reasonable discrimination factor between neutrons and γ-rays.

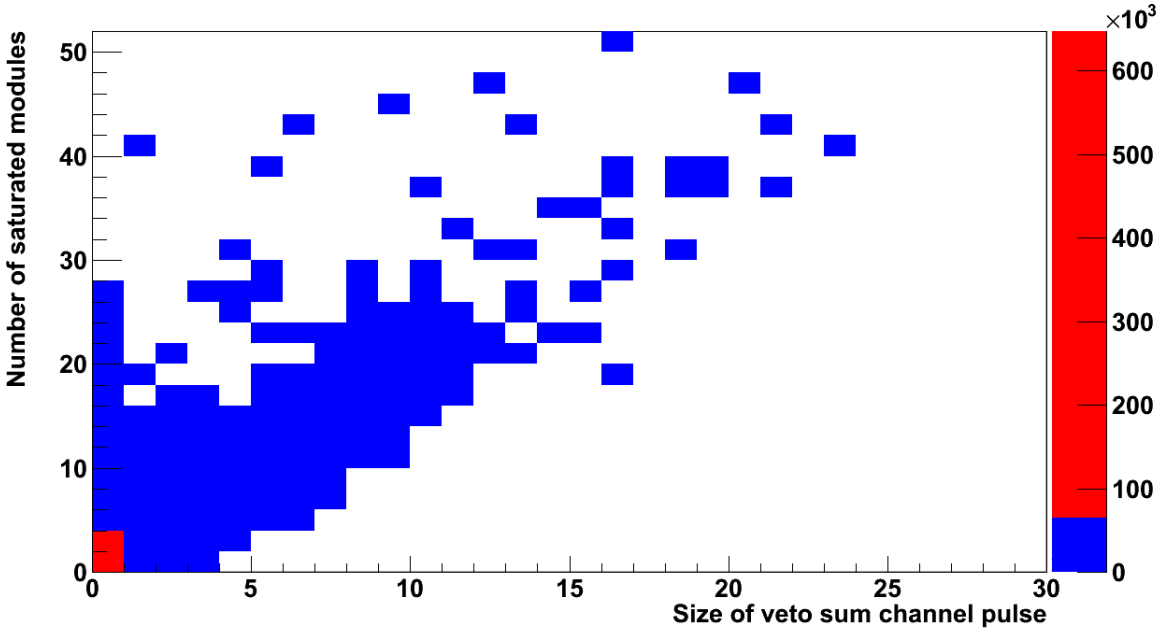

Figure 6.25: A density plot showing the area of the veto sum channel pulse against the number of saturated modules. The majority of events are γ-rays which trigger the cosmic ray box by saturating two roof modules in coincidence. At higher energies the energy resolution is limited by the maximum rage of the veto DAq since the muon and its associated particle shower usually saturate each module hit. The colours represent density, the red shows that the majority of events saturate few modules and have relatively small sum channel pulses. The red events are probably γ-rays.

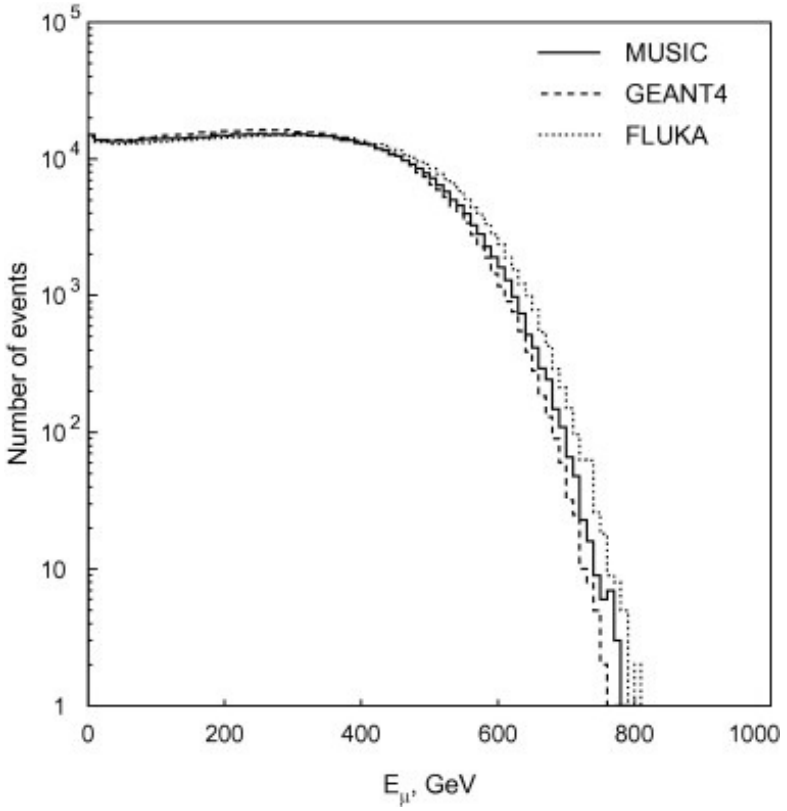

Figure 6.26: The spectrum of 2 TeV muons after crossing 3 km w.e. of standard rock (Z=11, A=22, ρ=2.65 g/cm^3) simulated using three different software packages [261]. References to the codes listed inset are; [44], [16] and [74, 176], from top to bottom.

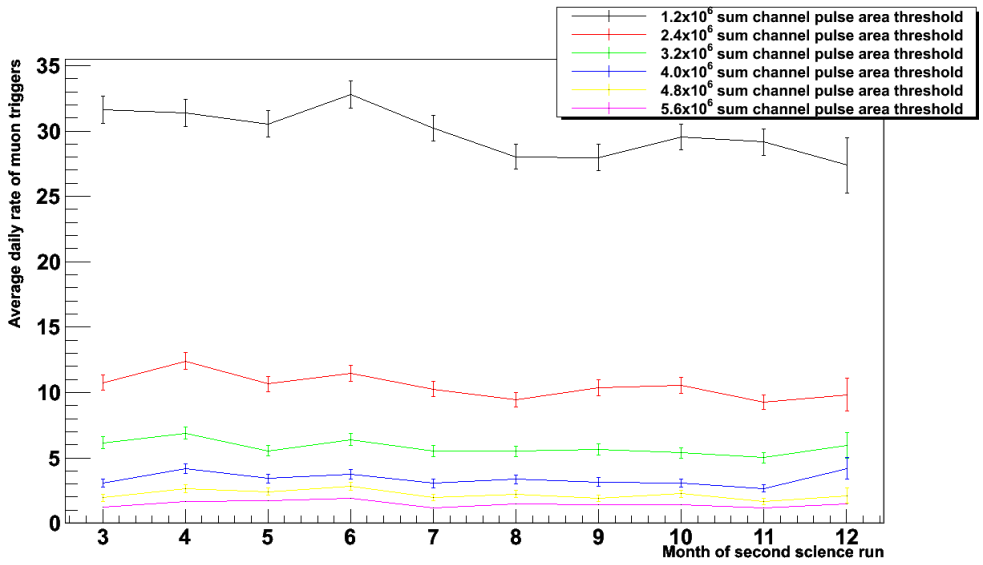

Figure 6.27: The average monthly rate of cosmic ray box triggers shown for several different sum channel pulse thresholds. The threshold unit is ADC channels · 0.1 μs, which is 0.137 V · ns.

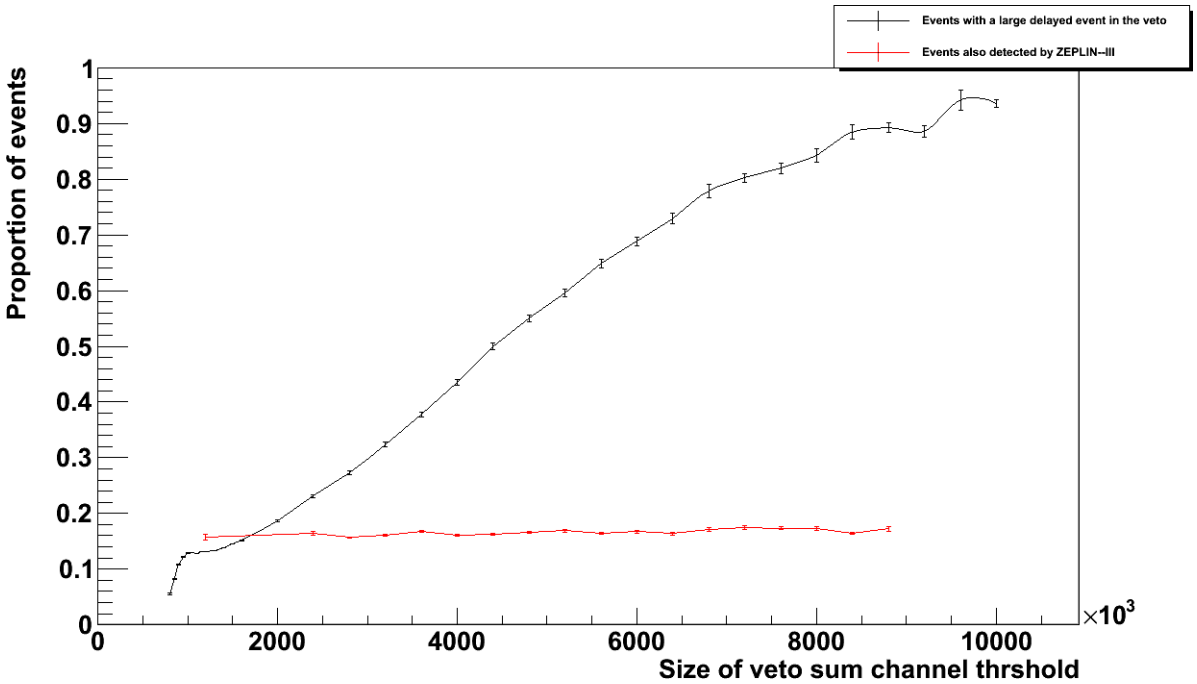

Figure 6.28: The proportion of events with a large (>20 photoelectrons) delayed event in the veto (black). A distinct change in gradient can be seen at the threshold. This plot also shows the proportion of these events also seen by ZEPLIN–III (red). This shows that the threshold for selecting muon events is effective (demonstrated by the change in gradient), and that the number of events also observed by ZEPLIN–III is not energy dependent.

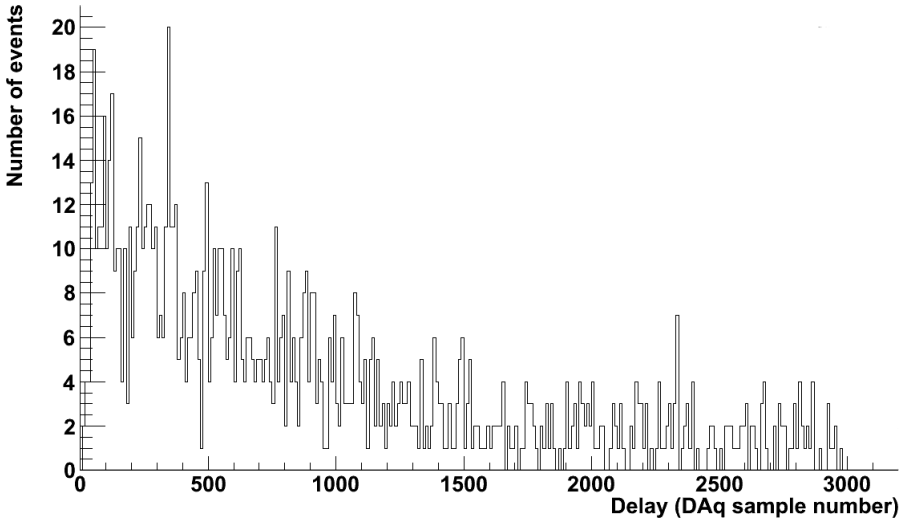

Figure 6.29: The delay between the muon event and the first delayed event in the veto above 20 photoelectrons.

6.6 Exotic Dark Matter Detection

6.6.1 Introduction

Whilst most direct dark matter searches focus on elastic scattering off nuclei, it may also be possible for dark matter to scatter inelastically. Inelastic scattering may leave the dark matter particle in an excited state. If the dark matter has a magnetic dipole moment, it is possible that particles in an excited state may decay to the ground state via emission of a photon. This exotic for of dark matter was first postulated in [116]. The magnetic dipole interaction could arise from either conventional magnetism or a hypothetical dark force. This form of dark matter could explain the DAMA signal which has not been observed by other experiments. This experiment has observed an annual modulation signal, with the expected phase for WIMP-nucleon interactions, for over a decade [82]. The lack of conformation by other experiments suggests that this signal is not due to conventional spin-independent elastic scattering of WIMPs off atomic nuclei, however, dark matter interpretations of the modulation signal are still possible. The DAMA experiment uses an iodine target. The relatively large dipole moment of iodine, combined with its high mass, make it much more sensitive to interactions with a magnetic dipole than target materials such as germanium, due to its enhanced dipole-dipole scattering. Figure 6.30 shows the

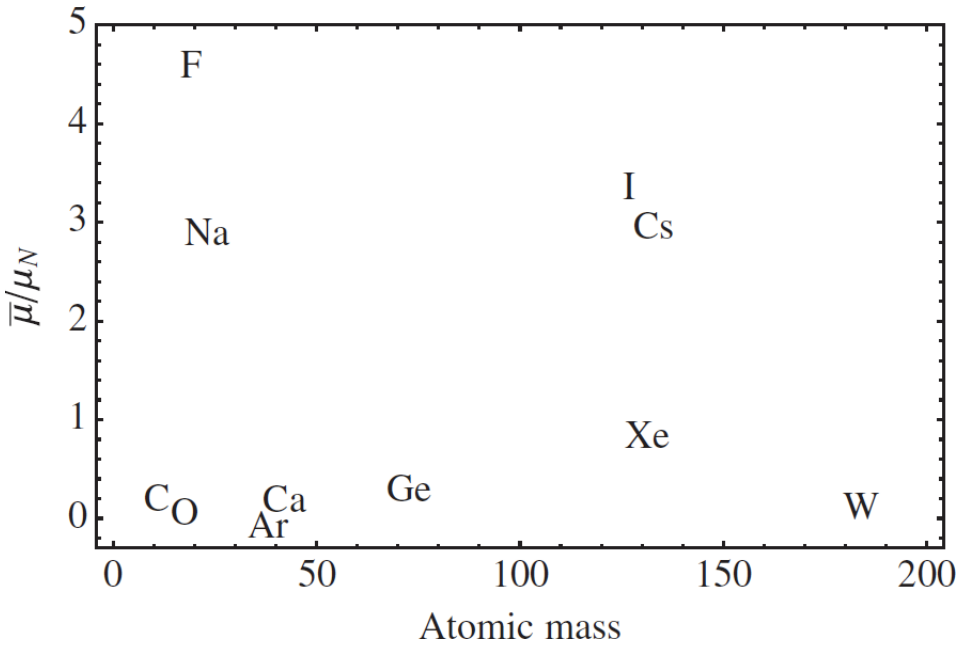

Figure 6.30: The weighted-atomic mass and weighted-magnetic dipole moment of several common target materials. C, O and Ar have been shifted slightly so as not to overlay each other [116].

weighted magnetic dipole moment:

$$\bar{\mu} = \left(\sum_{\text{isotope}} f_i \mu_i^2 \frac{S_i + 1}{S_i} \right)^{\frac{1}{2}} \tag{6.1}$$

as a function of weighted-atomic mass for several common targets. In Equation 6.1 f_i is the elemental abundance, μ_i is the nuclear magnetic moment and S_i is the spin of each isotope i. Figure 6.30 indicates that xenon has a reasonable sensitivity to dipole interactions, although this is subdominant to the velocity-suppressed interaction with the charge of the nucleus.

This section describes a search of the SSR data for this form of dark matter. The method used involves searching the veto data for the delayed photons following ZEPLIN–III events occurring near the mean of the neutron recoil band. If a large enough signal were present, then this would be seen as an excess of events at short time intervals overlaid on top of a flat background due to accidental coincidences. There are possible interfering effects which must be taken into

account, such as signals from neutron events or possible signals from ^{85}Kr decays.

6.6.2 Particle properties

Strict limits have been placed on the potential coupling of dark matter particles with the electromagnetic field [332]. These models assume that the dark matter particle is a Dirac fermion, as single-photon couplings through electron dipoles do not exist for Majorana fermions [247]. If however the dark matter does consist of Majorana fermions, then an off-diagonal coupling to the electromagnetic field may be natural [382, 153]. The ground state of this particle constitutes the dark matter, and transitions to excited states could be mediated by a dipole interaction [116]. The scattering rate, as a function of recoil energy E_R, of interest to direct dark matter searches is given by:

$$\frac{d\sigma}{dE_R} = \frac{d\sigma_{DD}}{dE_R} + \frac{d\sigma_{DZ}}{dE_R} \tag{6.2}$$

where σ_{DD} is the dipole interaction cross-section and σ_{DZ} is the velocity-suppressed interaction cross-section with the charge of the nucleus. These vary as $\propto \mu^2$ and $\propto Z^2 v^2$, respectively, and are given in full in Reference [116].

Figure 6.31 shows an example of the scattering rate of magnetic inelastic WIMPs off xenon from Reference [257]. In this example, the mass splitting between the states is 123 keV. The lifetime of the excited state may be calculated by:

$$\tau = \frac{\pi}{\mu_\chi^2 \delta^3} \tag{6.3}$$

where $\delta = m_{\chi^\star} - m_\chi$ is the mass splitting of the excited state and μ_χ is the dipole moment of the WIMP. In this example, with a mass splitting of $\delta = 123$ keV, if the dipole moment is $6.2 \times 10^{-3} \mu_N$ then $\tau = 1.2$ μs. Considering the sampling rate of the veto DAq (0.1 μs) a decay curve with this lifetime could be resolved. Furthermore, given the expected velocity of a WIMP, the average length travelled during this lifetime for a standard halo model WIMP is ~ 35 cm and so the excited WIMP is expected to decay in the region of the detector. Thus events matching this hypothesis can be searched for, and a sensitivity to

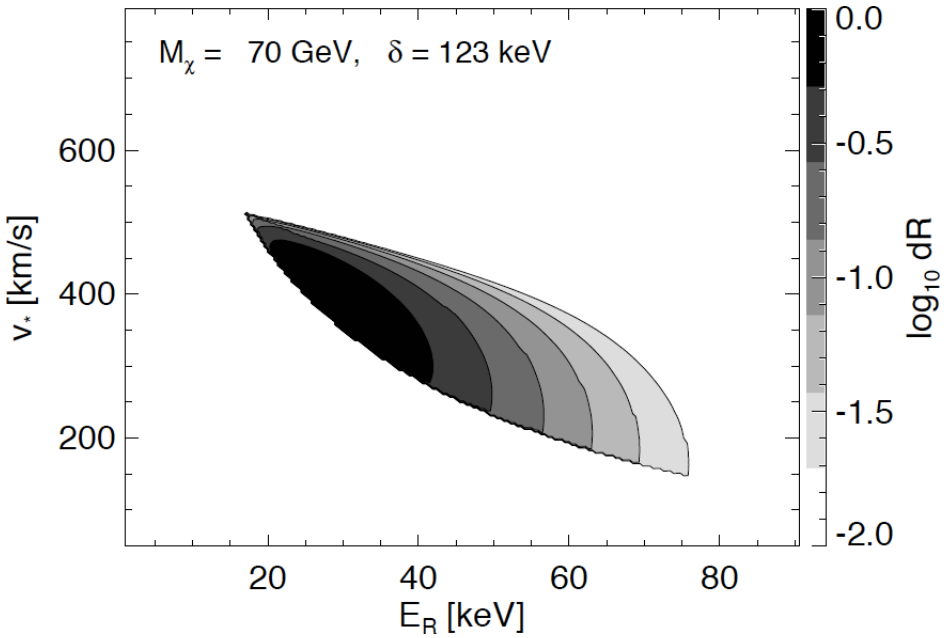

Figure 6.31: The differential scattering rate (counts per day per kg) for a 70 GeV/c^2 magnetic inelasticity WIMP scattering off xenon using an approximation for the form factor. Obtained from Reference [257].

the model calculated.

6.6.3 ZEPLIN–III Efficiency

The efficiencies of the ZEPLIN–III and veto detectors for detecting this form of dark matter are required to set limits on the interaction cross-section. To calculate the veto efficiency for detecting the delayed de-excitation γ-ray I used Monte Carlo simulations. A different simulation was required for each different particle. Firstly a simulation was used to calculate the expected recoil spectrum of WIMPs, given the standard WIMP spectrum expected at Earth over the period of the SSR as an input. As the nuclear magnetic dipole form factor required for an accurate analysis is not well known, an approximation was used. The initial program was supplied by Dr. Alex Murphy and was modified for each particle simulated. To calculate the efficiency of the veto to the decay radiation, given a magnetic inelastic WIMP interaction within the fiducial volume, I created and added custom particles to Geant4 [16] with the appropriate properties and decay

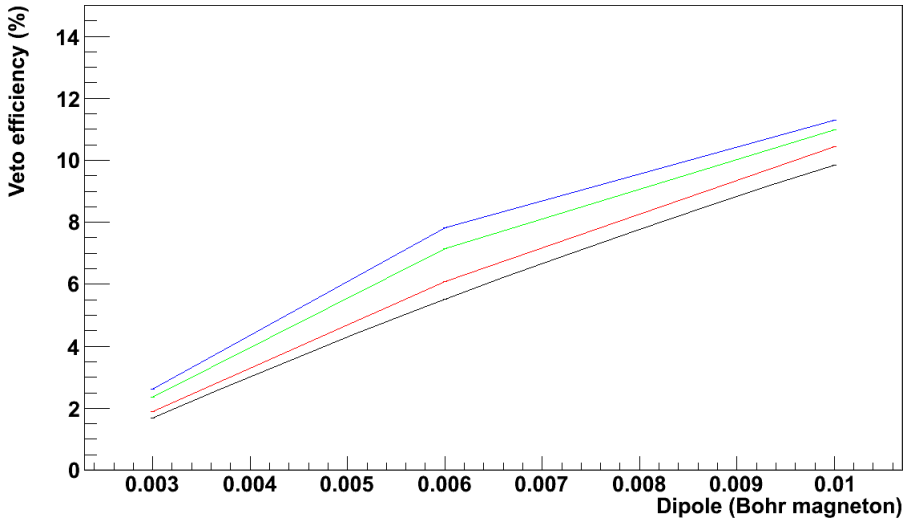

Figure 6.32: The efficiency of detection of the de-excitation γ-ray by the veto shown as a function of the dipole magnitude. The plot shows results for several different recoil spectra. The black line uses a WIMP recoil spectrum which peaks at 10 keV, the red peaks at 16 keV, the green peaks at 30 keV and the blue peaks at 50 keV. In all cases the splitting of the mass states was 80 keV.

tables. The calculated recoil spectrum was used as the input for simulations using accurate detector geometry down to the component level. The efficiency depends on the energy of the γ-ray emitted, the recoil velocity of the excited WIMP and the magnitude of the magnetic dipole. To investigate the effect of the approximation of the recoil velocity on the veto efficiency, several simulations were produced which covered some of the parameter space.

It was determined that the recoil velocity spectrum shape influences the veto efficiency to a lesser extent than other considerations. Figure 6.32 shows plots for several different recoil spectra and dipole magnitudes. Simulations covering 4 different recoil spectra, 3 different magnetic dipole moment magnitudes and 7 different mass splittings, ranging from 80 keV to 140 keV, were performed. Typically the peak efficiency is $\mathcal{O}(10\%)$, which suggests that the instrument is reasonably sensitive to magnetic inelastic dark matter via detection of the de-excitation γ-rays.

6.6.4 Results and Summary

The simulations indicate the veto has a reasonable efficiency for detection of the de-excitation γ-ray emitted by excited magnetic inelastic WIMPs scattering in the ZEPLIN–III fiducial volume. If the nuclear magnetic dipole form factor was accurately measured, then the ZEPLIN–III SSR data could be used to set limits on the interaction cross-section. A search of the SSR data for delayed veto hits was performed for ZEPLIN–III events near the nuclear recoil band. No excess of events was seen at short delay times.

There are 2 expected backgrounds which must be considered for this search. The ^{85}Kr background is negligible, considering the measurement presented in Section 7.2.2.4 and the discrimination power of ZEPLIN–III. The background from neutrons is also expected to be negligible, given the use of radiopure materials and shielding. Also, as the γ-rays emitted by neutron capture have much higher energies than the mass splittings considered, then in principle a population of neutrons could be separated from a population of delayed events caused by de-excitation of magnetic inelastic dark matter. For a large enough population, the time scale of the delayed events may also be used to discriminate against neutrons.

There are two different techniques which may be used to reveal a population of magnetic inelastic WIMPs in the data. As the parameter space is large, the time scale for decay of the excited magnetic inelastic WIMP is broad. If a population of these events were present in the data then they could be revealed by measuring the distribution of the time delays between the ZEPLIN–III nuclear recoils and the energy deposits in the veto. An exponential decay curve could be overlaid onto the flat background of accidental coincidences, to reveal the number of events present and the lifetime of the excited state. Alternately, as the number of expected accidental coincidence can be measured, the number of delayed events occurring within a given time window may be compared to the background expectation to obtain a limit on the number of signal events. This latter, more simple technique, can also be used to produce limits on the number of events in the absence of a clear signal.

The results of simulations for magnetic inelastic WIMP masses of 50, 70, 100 and 140 GeV/c^2 are shown in Tables A.3, A.4, A.5 and A.6, respectively. These tables show the results of analyses to determine the limits on the number of signal events. Although the events at short delay times are in line with background, both methods were attempted as an exercise. A maximum likelihood fit to the decay curve gave poor results, as expected, as the data do not show a curve. The ROOT class TRolke [135] was used to obtain limits by counting the total number of events present and comparing to the expected background. This method assumes a Gaussian error in the uncertainty of the background estimate and in the uncertainty in the efficiency. This class uses the Profile Likelihood Ratio method [26, 315, 92], as outlined in Section 8.4.2. Results from Profile Likelihood Ratio fits to all the different types of magnetic inelastic WIMPs considered are shown in Tables A.3, A.4, A.5 and A.6. The number of events typically produced by the fit was $\sim$0, however the error was relatively large.

The veto efficiency has some dependence on the form factor, as this effects the form of magnetic inelastic WIMP recoil spectrum. Given accurate calculations of the interaction rate and the veto efficiency it would be possible to set limits on the interaction cross-section using the information provided by the fit to the decay curve. However, the limits on the number of events provided by the maximum likelihood fits to the decay curve are usually larger than the number of events near the nuclear recoil band detected by ZEPLIN–III. The results obtained using this method on the ZEPLIN–III SSR data are thus unsuitable to be used to calculate a limit on the magnetic inelastic WIMP-nucleon interaction cross-section, as each result would need to be capped at the number of ZEPLIN–III events detected, which is known to be dominated by background.

For this analysis the events in the WIMP search box, outlined in Chapter 8, were used. Although the events observed here are in line with background expectations, the veto timelines were searched for delayed energy deposits. As the veto background event rate increases with decreasing threshold, there is a greater chance of accidental coincidences occurring for lower thresholds. As the detection efficiency for the delayed de-excitation γ-ray also increases with decreasing threshold there will be some peak threshold which maximises the

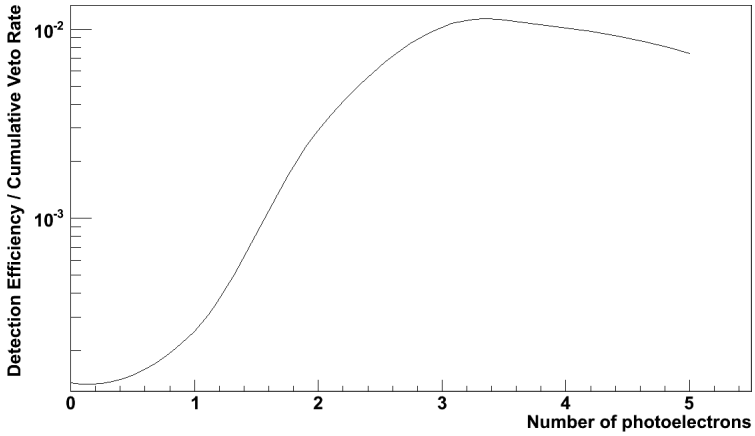

Figure 6.33: An example of the peak detection efficiency of the delayed de-excitation γ-ray magnetic inelastic dark matter. This plot shows that there is an optimum detection efficiency, using a threshold of 3 photoelectrons, due to the pay off between the decreasing efficiency as a function of number of photoelectrons and decreasing chance of an accidental coincidence as a function of number of photoelectrons. Ideally, with no background to give accidental coincidences, the minimum observable energy would be used as this gives the highest efficiency, however due to the significantly higher background rate at 1 and 2 photoelectrons, the optimum detection efficiency is achieved using a minimum threshold of 3 photoelectrons.

chances of detecting a real event while minimising the chance of an accidental coincidence. Figure 6.33 shows a typical efficiency ratio curve. This shows the peak sensitivity occurs using a threshold of 3 photoelectrons.

These results would be more appropriate to use for obtaining a limit on the magnetic inelastic WIMP-nucleon cross-section, as few events are observed near the nuclear recoil band so the signal detection efficiency must be maximised. As an example, a 70 GeV/c^2 magnetic inelastic WIMP with a mass splitting of 120 keV and a dipole moment of 6.0×10^{-3} $\mu_{\rm N}$ has a lifetime of 1.1 μs. The peak detection efficiency occurs using a threshold of 3 photoelectrons. At this threshold the veto will detect the delayed de-excitation γ-ray 5.82(2)% of the time. Given the lifetime of the excited state, a window of 5.08 μs would accept 99% of the decays back to the ground state. The background expectation from accidental coincidences within this window is 1.54×10^{-3} delayed energy deposits in the veto per ZEPLIN–III event. The lower limit on the number of signal events is 0 and the upper limit is 34.4, at 90% C.L.. The upper limit is higher than the number of ZEPLIN–III events considered for this analysis due to the efficiency for detection by the veto. For this example, as only an indication of potential

sensitivity is sought, the upper limit is capped at the number of ZEPLIN–III events observed after accounting for the efficiency loss due to event cuts. The efficiency loss for ZEPLIN–III events failing the event cuts due to detection of the delayed de-excitation γ-ray within the fiducial volume of ZEPLIN–III is 4.44(2)%. This result was used to estimate the limits which may be set on the magnetic inelastic WIMP-nucleon cross-section. Using the limit on the number of possible signal events, capped at the efficiency corrected number of events observed, and scaling the interaction rate used to calculate the SSR result (outlined in Chapter 8) to the rate presented in [257], the limit on the interaction cross-section is estimated to be $\mathcal{O}(1 \times 10^{-7}) \times \eta_{\text{ff}}(E))$ pb, where $\eta_{\text{ff}}(E)$ is the scaling due to the currently unknown nuclear dipole form factor.

In conclusion, a search of the ZEPLIN–III data was performed to determine if any magnetic inelastic WIMP events were detected. No signal was observed but the technique could be used for other detectors. A large population of these events, depending on the particle properties, would show as an excess of delayed veto coincidences due to the $\mathcal{O}(10\%)$ detection efficiency of the delayed de-excitation γ-ray. If a large population were observed, a fit to the time delay distribution could be used to constrain the properties of the particle. As no clear signal is observed, the veto timelines for the 8 events in the WIMP search region were analysed in order to estimate the order of magnitude of the limit on the magnetic inelastic WIMP-nucleon interaction cross-section which could be set using the SSR data. If the most cautious result were considered, where the upper limit on the number of signal events is 8.4 (to account for the inefficiency of events failing cuts due to the delayed de-excitation γ-ray interacting in the fiducial volume of ZEPLIN–III), then limits $\mathcal{O}(1 \times 10^{-7} \times \eta_{\text{ff}}(E))$ pb may be achievable.

Chapter 7

ZEPLIN–III Radioactive Contaminations

7.1 Introduction

Searching for a dark matter signal requires very low levels of background radiation as the event rate is expected to be relatively low. Although every effort is made to reduce background radiation, by the use of shielding and the careful selection of all materials used in construction, background radiation is still generated internally by the small amounts of contaminants present in the detector components. One of the most dangerous internal backgrounds is that generated by contaminants present in the target volume itself. The self shielding properties of xenon, which help make it so attractive for dark matter searches, also means that any background generated from xenon contamination is more likely to interact within the fiducial volume. The self shielding properties of xenon are due to its high density. Although liquid xenon is transparent at optical wavelengths, it has a very low penetration depth for higher energy photons (see Figure 7.4). Xenon also has a large neutron cross section at 2.96 barns for coherent scattering and 23.9(1.2) barns for absorption [328]. Figures 7.1 and 7.2 shows the total neutron cross section of natural xenon as a function of neutron energy.

The levels of any contaminant may be measured by searching the data for specific signals unique to each contaminant. Once the levels of contaminations are known, their threat to the dark matter sensitivity of the instrument can be

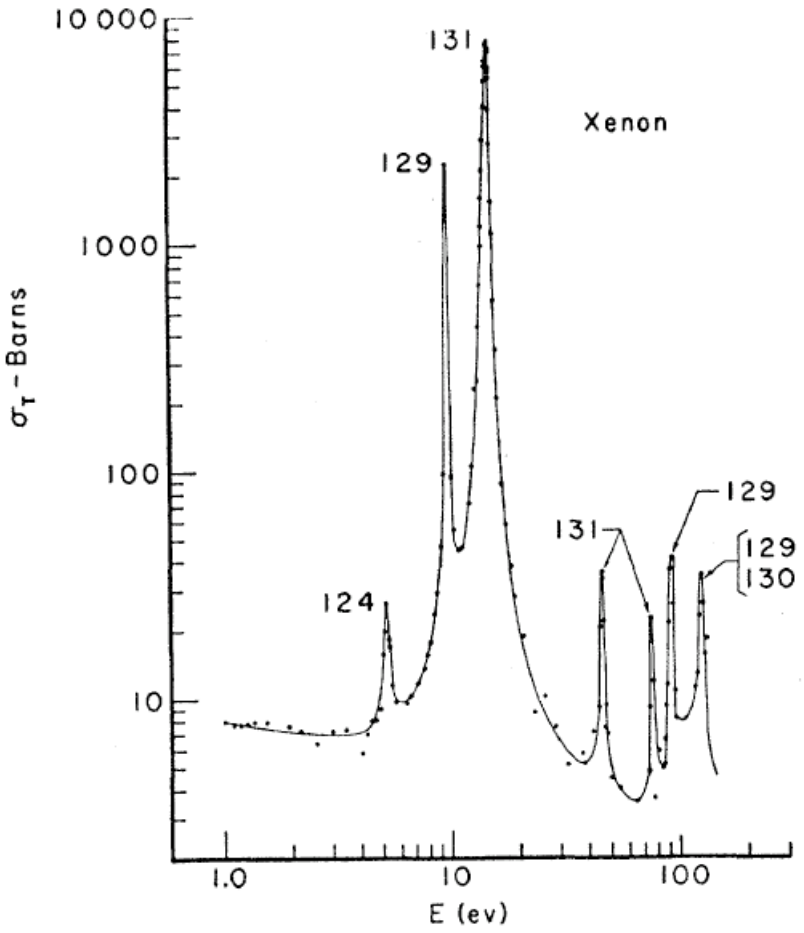

Figure 7.1: The total neutron scattering cross-section of natural xenon as a function of neutron energy. Resonance peaks due to different xenon isotopes have been marked [268]. Higher energy neutrons are shown in Figure 7.2.

assessed. A useful unit used to characterise the radioactivity due to contaminants is the differential rate unit (DRU). This is the number of events expected per kilogram per day at a certain energy, events kg^{-1} $\mathrm{day}^{-1}\mathrm{keV}^{-1}$. The canonical value to allow comparison between different instruments searching for dark matter is 10 keV_{ee}, for example by averaging the events per kg per day between 5 and 15 keV_{ee}.

This chapter details measurements of some of the radioactive contaminants present in the ZEPLIN–III instrument. These measurements were made using science run data. As a good understanding of the background is vital for a rare

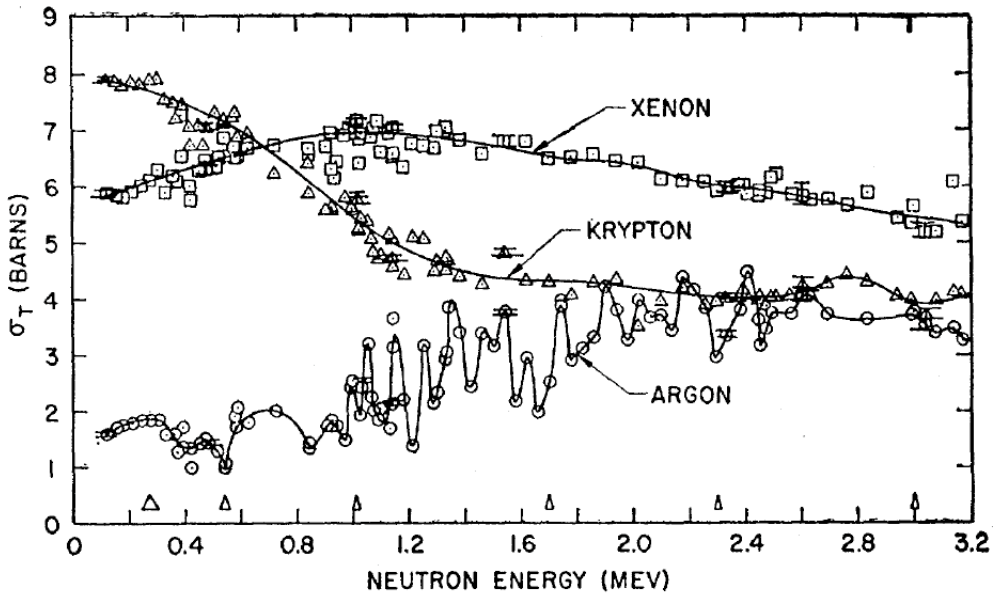

Figure 7.2: The total neutron scattering cross-section of natural xenon as a function of neutron energy for energies up to 3.2 MeV. This plot shows the results for high energy neutrons, also shown are the cross-sections for krypton and argon [378].

event search in-situ measurements are ideal as they can provide measurements which coincide with the rare event search and can monitor any changes. These types of measurements will be required for the next generation of detectors which will have considerably larger volumes than ZEPLIN–III. This chapter also illustrates the additional benefits provided by the addition of the veto.

7.2 ^{85}Kr Contamination of Xenon

7.2.1 Introduction

Krypton is an almost unavoidable contaminant of xenon. Since both are inert elements, even commercially available "krypton-free" xenon still contains ppb level contamination. Due to the presence of the isotope ^{85}Kr, this contaminant has long been recognised as a potential threat to dark matter searches using a xenon target. ^{85}Kr is a β^- emitter ($t_{\frac{1}{2}} = 10.76$ years, $\beta_{max} = 687$ keV) and thus may generate low energy electron recoils within the target volume. Depending on the discrimination power of the instrument, these low energy recoils may leak

into the nuclear recoil band and compromise the sensitivity of the instrument.

Minimising the ^{85}Kr contamination of ZEPLIN–III was achieved by using xenon of an underground origin supplied in the late 1970s. ^{85}Kr is present in the atmosphere mainly due to nuclear fuel reprocessing and nuclear weapons testing. The ^{85}Kr/Ke ratio was as low as 3×10^{-18} in the early 1950's but the present day ratio is $\sim 1 \times 10^{-11}$ [134]. Considering the source and age of the ZEPLIN–III xenon, the ratio of ^{85}Kr/Kr would be relatively low. In 1997, the activity of a test sample of the ZEPLIN–III xenon was used to measure the ^{85}Kr/Kr ratio where the krypton content was measured using residual gas analysis (RGA). The appropriately age-corrected ^{85}Kr/Kr ratio for the ZEPLIN–III xenon is 1.43×10^{-12} ppb [226, 51]. The xenon was then further purified by cryogenic distillation to achieve a Kr/Xe ratio conservatively estimated at <50 ppb (w/w). This corresponds to <0.2 DRU at 10 keV$_{ee}$ in the xenon target from ^{85}Kr contamination [51].

7.2.2 Methods

In its SSR configuration the ZEPLIN–III instrument can be used in two different ways to measure the ^{85}Kr contamination. A minor branch of ^{85}Kr decay is to an excited state of ^{85}Rb (Figure 7.3). The lifetime of this excited state is sufficiently long that the decay curve could be resolved by both the ZEPLIN–III DAq and the veto DAq. In this mode, the ^{85}Rb decays from a $\frac{9}{2}^+$ excited state with a half life of 1.015 μs to a $\frac{5}{2}^-$ ground state via emission of a 514 keV γ-ray [331]. The emitted γ-ray is penetrative enough to reach the veto and ZEPLIN–III is sensitive to both β and γ-ray radiation, hence this decay is detectable using either ZEPLIN–III alone or both instruments combined.

7.2.2.1 ^{85}Kr Detection Using The Veto

^{85}Kr can be detected by a delayed coincidence between the beta emission and the γ-ray. Since the γ-ray is energetic enough to occasionally escape from the xenon target there is a chance it may be detected by the veto. A calculation using the approximate geometry of the ZEPLIN–III target suggests the number of γ-rays escaping without interaction is about $\frac{1}{3}$ of the total. The target is a cylinder, so

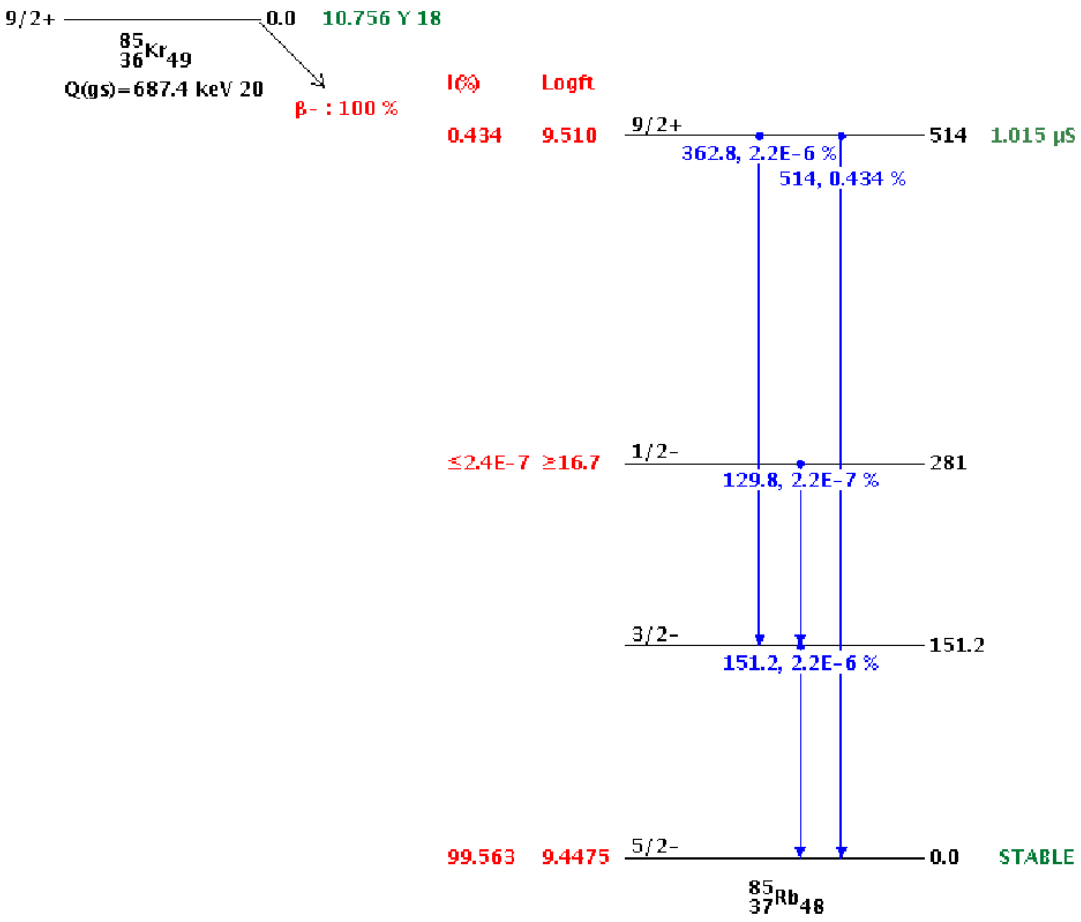

Figure 7.3: A schematic showing ^{85}Kr decay radiation. It can be seen that there are two decays possible from the $\frac{9}{2}^+$ state of ^{85}Rb. The decay to the ground state is $\sim 1.8 \times 10^6$ more intense and is thus the only one that needs to be considered for this analysis (picture obtained from the NNDC website) [331].

for isotropic emission the mean path length is determined by the column height which is ∼3.5 cm. This is approximately the interaction length for 514 keV photons (Figure 7.4). The two instruments can thus be used in conjunction to detect ^{85}Kr decays. The beta is detected with a very high efficiency by ZEPLIN–III and the γ-ray may be detected by the veto a short time later. The efficiency of detection by the veto was simulated, by the author, using a model in Geant4 with accurate geometry [50] (Figure 7.6).

The total efficiency for detection as a function of the number of photoelectrons produced in the veto is shown in Figure 7.5. The efficiency is slightly lower than one might expect from considerations of the veto performance during the SSR coupled with the loss from delayed γ-rays which interact within the xenon target. The veto detection efficiency of $\sim$ 28% would suggest an overall efficiency of $\sim$ 9%. However, it was found that the veto efficiency for tagging background radiation quoted in 6.3.1 is valid for lower energy γ-rays. Analysis of the prompt tagging efficiency of higher energy events shows a decrease with increasing energy for energies beyond those of interest for the WIMP search. Figure 7.7 shows the tagging efficiency as a function of energy.

Despite the low efficiency for detection of the γ-rays predicted by simulation this method provides a robust method of detecting ^{85}Kr events as the use of two separate detectors greatly reduces complicating effects. For example, each signal must be generated by a genuine event, whereas when only a single instrument is used secondary pulses may be generated at later times by after-effects of the original event, for example PMT afterpulsing, rather than a genuine second event. A signal from a high level of contamination should show up clearly as an excess of events at short delay times, falling off with the appropriate decay curve, superimposed onto a flat background of accidental coincidences.

7.2.2.2 ZEPLIN–III and Veto Results

Using the veto in combination with ZEPLIN–III a number of candidate events were selected. The exact number is dependant on the threshold used, for example at 6 photoelectrons there were 23793 candidate events. By plotting

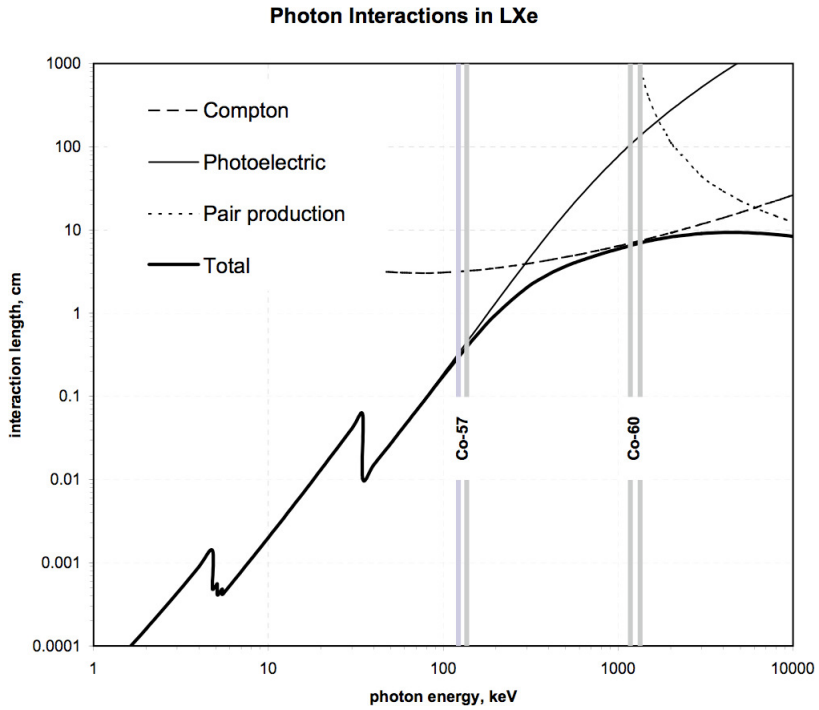

Figure 7.4: The interaction length of photons in liquid xenon as a function of energy [223].

the time distribution between the ZEPLIN–III and veto event any significant ^{85}Kr contamination would be revealed. The results show that no ^{85}Kr is detected using this method. A maximum likelihood fit of the form $y = \frac{A}{\tau}e^{\frac{-t}{\tau}} + B$ to these data was used to set a limit on the number of ^{85}Kr events during the second science run. Here B is the background level and A is the area below the exponential which gives the total number of events. The fit using a threshold of 6 photoelectrons in the veto is shown in Figure 7.8 and Figure 7.9. A value of $\frac{A}{\tau} = 0.599^{+0.730}_{-0.599}$ was obtained giving a total of $< 8.76^{+10.69}_{-8.76}$ events. The total efficiency is 0.01%, composed of the detection efficiency, the branching ratio and the triggering efficiency. The triggering efficiency was calculated by a simulation of ^{85}Kr decays showing that 99.95% of the time the β emitted by ^{85}Kr when decaying to the excited state of ^{85}Rb ($\beta_{\max} = 173.4keV$) deposits enough energy to trigger ZEPLIN–III. This was used to set a limit at 90% confidence on the contamination of the xenon of <61 ppb. A simulation of decaying ^{85}Kr nuclei in liquid xenon was used to determine the energy deposition spectrum (Figure 7.10). This was then scaled to the data to calculate the DRU. The contamination limit obtained using both the veto and ZEPLIN–III instrument is <0.3 DRU at

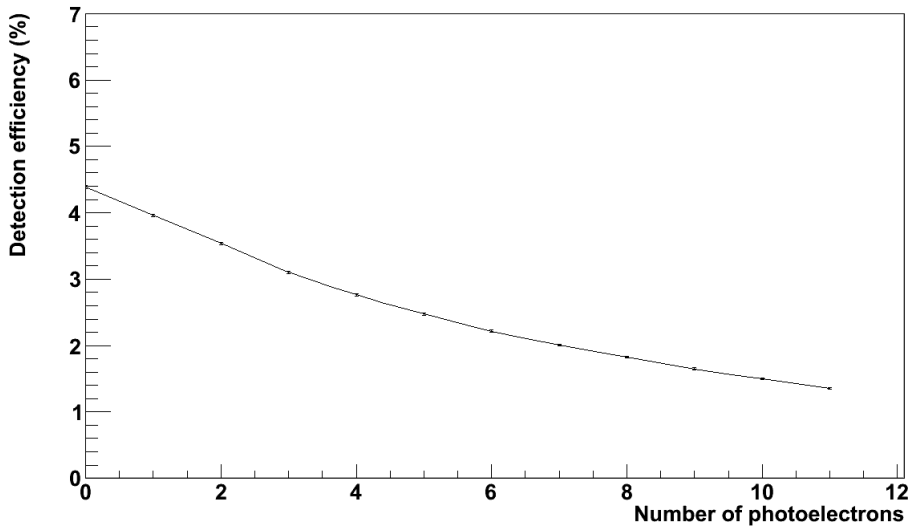

Figure 7.5:
Results from a Geant4 simulation using the veto to detect 514 keV γ-rays produced isotropically from the ZEPLIN–III fiducial volume. The number of photoelectrons was calculated assuming linearity between a single photoelectron peak and the peak observed from a 122 keV γ-ray source.

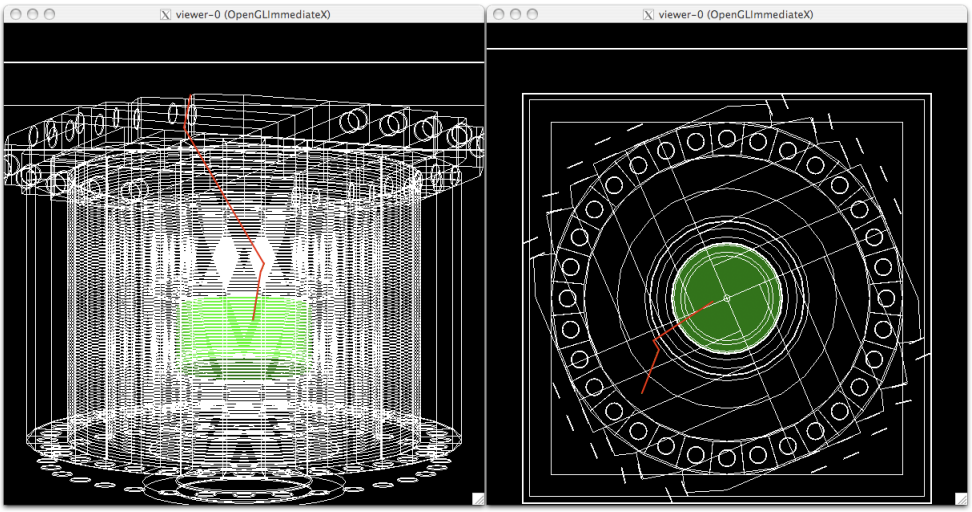

Figure 7.6: A screen grab of the Geant4 ^{85}Kr simulation showing the ZEPLIN–III instrument plus veto and shielding. The 514 keV γ-ray (red) can be seen originating from the xenon target (green) and interacting in the veto (white). The ZEPLIN–III simulation is described in [50] and the additional veto components in [71].

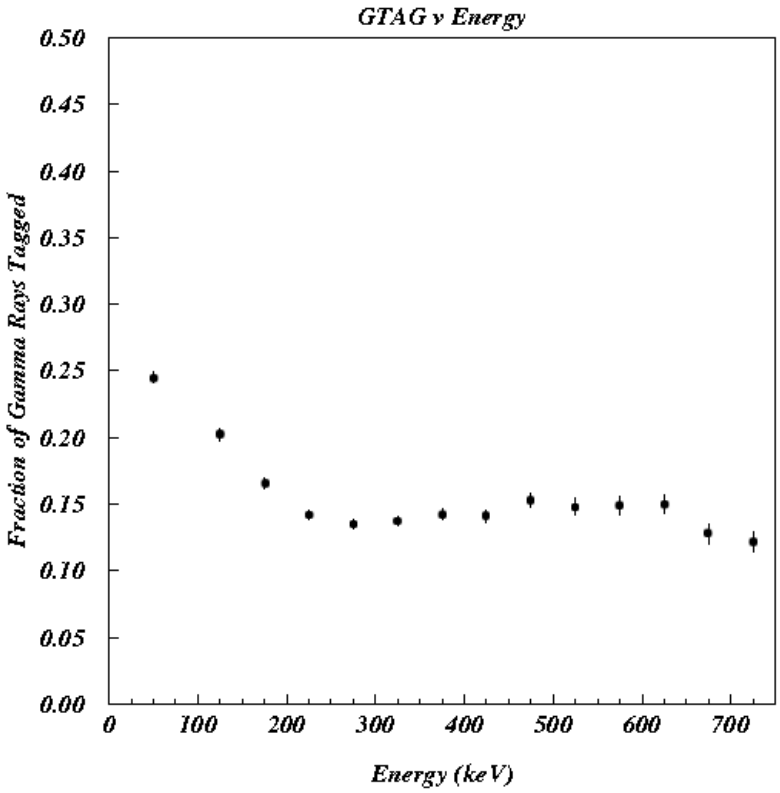

Figure 7.7: A plot of the veto tagging efficiency as a function of energy. This plot extends out to high energies where an energy dependence is observed with the tagging efficiency decreasing with increasing energy. This plot is consistent with results presented in chapter 6. The width of the first bin is the full 100 keV of the WIMP search data analysis and the same fiducial cut applied to that data also yields a prompt tag for 25% of the background events. A width of 50 keV was used for energies higher than 100 keV. This plot indicates an efficiency of ∼15% for 514 keV γ-rays and is in agreement with the prediction shown in Figure 7.5 when the fraction of events escaping the fiducial volume is taken into account.

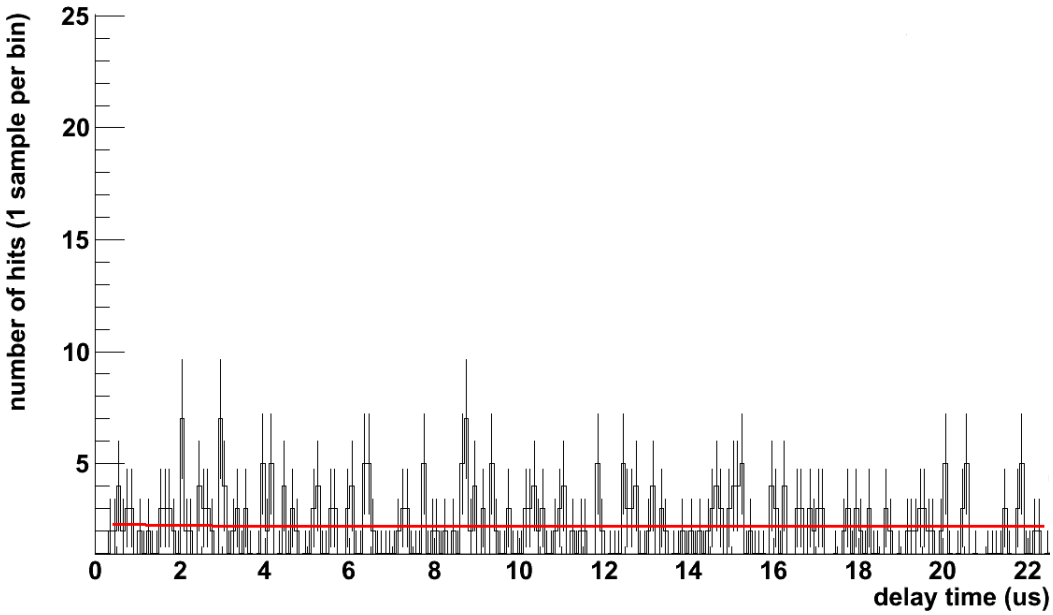

Figure 7.8: A maximum likelihood fit of $y = \frac{A}{\tau} e^{\frac{-t}{\tau}} \times B$ to the data obtained using the veto in conjunction with ZEPLIN–III to search for ^{85}Kr events.

90% confidence.

7.2.2.3 ^{85}Kr Detection Using Only ZEPLIN–III

An alternative method to detect ^{85}Kr contamination uses just the ZEPLIN–III instrument, as it has a much higher efficiency. However, since both events must be detected in the same target there are certain effects caused by the primary signal which are able to mimic or block a second signal. These must be carefully considered. Firstly, the efficiency of detecting the event must be considered. The efficiency for detecting both events within the fiducial volume is 68%. The efficiency of the β for triggering the event is 99.95% in which case there is an efficiency loss for events where the S2 signal from the γ-ray falls outside the DAq range of 1%. The S2 signal from the β may block the second S1 signal with a likelihood which decreases with depth; the average efficiency loss is 5%. Since the scintillation signals have a finite width there is an efficiency loss for events which decay too quickly to be distinguished as separate signals. The ZEPLIN–III events are recorded using a 500 MHz sampling rate and a typical scintillation

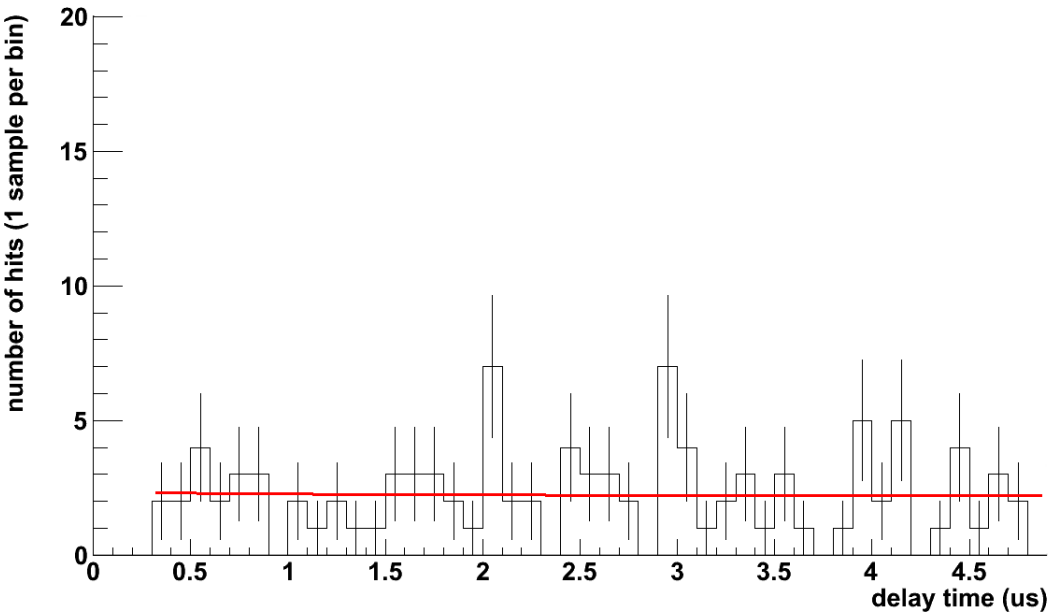

Figure 7.9: A close up of Figure 7.8, showing the first few microseconds. Although the best fit gives an exponential with a positive amplitude the error is larger than this value and may be used to set a limit.

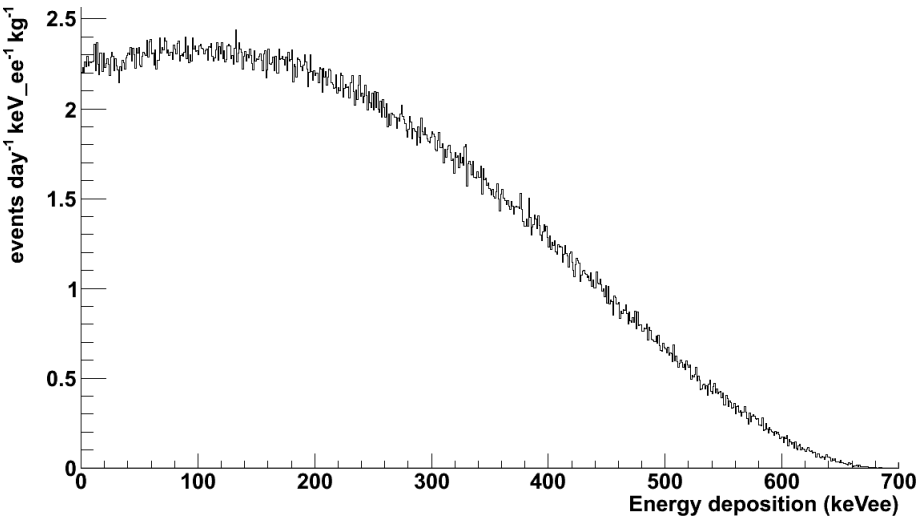

Figure 7.10: A Geant4 simulation showing the energy deposition spectrum for decaying ^{85}Kr atoms confined to the liquid xenon volume of ZEPLIN–III

pulse width for electron recoils below 174.3 keV$_{ee}$ is ∼0.1 μs. As the resolution is much higher than the typical pulse width the selection of the minimum delay was determined only by the pulse width distribution. A minimum delay between the events of 0.2 μs was used (efficiency 87%). Figure 7.11 shows the S1 pulse width distribution for the SSR golden data; this cut includes 99.7% of all S1 pulses. Secondly, and most importantly, PMT afterpulsing must be considered. The ZEPLIN–III PMT array does suffer from afterpulsing, as do all PMTs to some degree. The afterpulsing is caused by the ionisation of residual gas. Since the inside of the PMT is not a total vacuum some small amount of gas will always remain. As the electrons travel between the dynode plates they may strike the gas and ionise it. The positive ions are then attracted to the previous dynode plate. After accelerating back to the previous plate these positive ions may then knock out more electrons which will continue to cascade down the PMT leading to an afterpulse to be recorded by the DAq. These afterpulses can mimic a real signal and compromise a search for ^{85}Kr events. However, since the delayed γ-ray is considerably more energetic than the beta end point energy for the signal sought in this analysis, the condition that the second scintillation signal is larger than the first removes all the afterpulsing. A simulation was used to calculate the efficiency of this cut, giving an average efficiency of 69.6%. The results of the simulation are shown in Figure 7.12. The two features seen at the far right hand side of the γ-ray spectrum near the 514 keV total absorption peak are escape peaks. Internal conversion (IC) near the surface of the fiducial volume produces x-rays which may escape, carrying energy out of the fiducial volume (IC electrons are also produced but are much less penetrating and their contribution to the energy loss is negligible). These peaks appear at ∼30 keV$_{ee}$ and ∼34 keV$_{ee}$ before the 514 keV$_{ee}$ peak respectively. This does not affect the efficiency of the afterpulsing cut. The total efficiency for detection using these cuts is 38.1%.

7.2.2.4 ZEPLIN–III Only Results

The analysis using just the ZEPLIN–III target produced a measurement of the ^{85}Kr contamination. An example of a candidate ^{85}Kr event is shown in Figure 7.13, one of 14 such candidate events. A fit to the decay curve gives an $\frac{A}{\tau}$ value of 0.008 ± 0.002. Figure 7.14 shows a fit to the data showing a clear excess of events

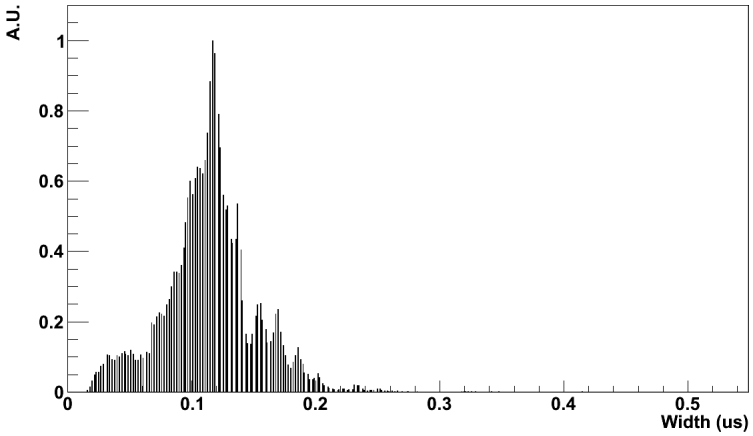

Figure 7.11: The distribution of S1 pulse widths for events below 174 keV.

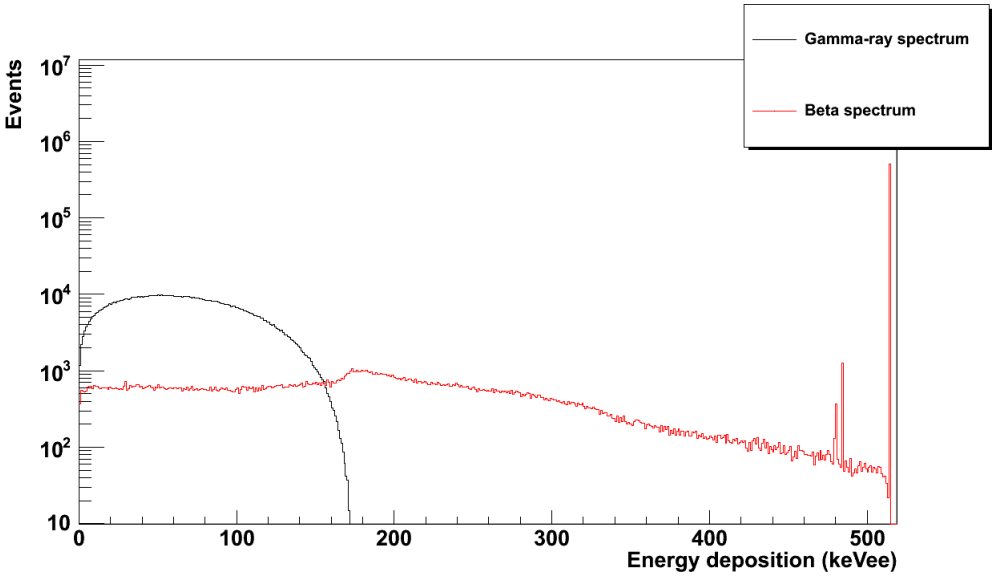

Figure 7.12: Overlaid spectra of the energy deposits in xenon from the low energy beta (black) and the delayed γ-ray (red). The efficiency penalty for requiring the γ-ray to deposit more energy than the β is 69.6%.

at shorter times consistent with the half-life of the excited state. This indicates the detection of a total of 12.1 ± 3.6 ^{85}Kr events during the SSR. This is in good agreement with simply counting the number of events in the first 5 μs (12 events with 97% efficiency timing efficiency for the delayed event). This represents a total of $(9.9 \pm 3.0) \times 10^4$ atoms of ^{85}Kr in the fiducial volume of the detector. This translates to a ^{85}Kr/Xe ratio of $(3.2 \pm 0.9) \times 10^{-21}$ which is equivalent to ~ 100 ppt krypton contamination using present-day xenon. Using a Kr/^{85}Kr ratio of 1.43×10^{-12} this gives the krypton contamination of the ZEPLIN–III xenon as 1.4 ± 0.4 ppb. The simulated ^{85}Kr spectrum was then scaled to the number of events detected to a obtain the DRU. This result represents 0.007 ± 0.002 DRU at 10 keV [51], which is insignificant. This work shows krypton contamination is not a problem for ZEPLIN–III.

7.2.3 Conclusion

The contamination result obtained using the veto in conjunction with ZEPLIN–III is enough to show that ^{85}Kr does not pose a threat to the ZEPLIN–III instrument's sensitivity to dark matter, as it has achieved a discrimination power of 1:280 between electron recoils and nuclear recoils respectively during the second science run. This limit is quite robust since the two instruments are used together and the only spurious signals are accidental coincidences which give the flat background observed in the results. Due to the higher efficiency, the result obtained using just ZEPLIN–III was much more accurate. The two results are consistent. The measurement obtained in this analysis provides a much more accurate measurement of the contamination than an RGA, which measures only the krypton contamination. This method of detection will be required in future larger dark matter detectors where the threat from ^{85}Kr is more significant and the results from an RGA, which also relies on accurate knowledge of the Kr/^{85}Kr ratio, may not be accurate enough to give a good estimate of the expected background.

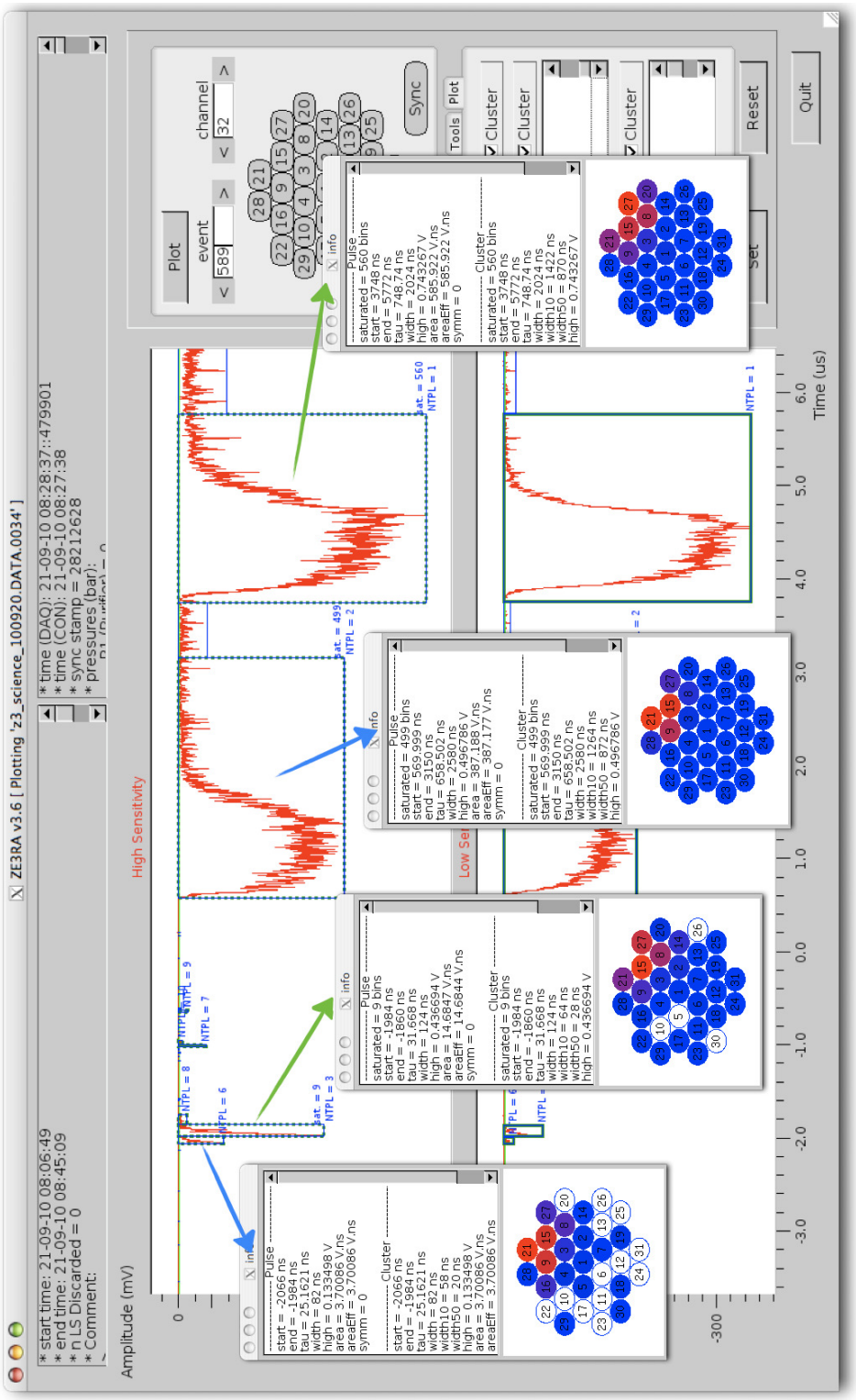

Figure 7.13: An example of a candidate ^{85}Kr event. A function was produced to calculate the X-Y position of each signal by the centroid so that the β and γ-ray signals could be distinguished in the X-Y plane, allowing for the drift time to be calculated and for fiducialisation of the primary. The PMT hit pattern can be seen with coloured arrows linking the S1 and S2 signals of the β (blue) and γ-ray (green).

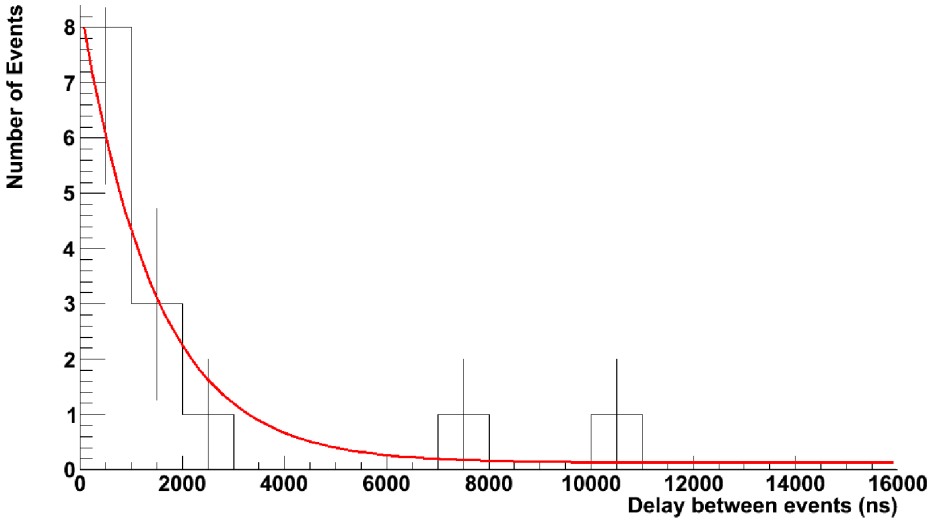

Figure 7.14: A maximum likelihood fit of $y = \frac{A}{\tau} e^{\frac{-t}{\tau}} \times B$ to the data obtained using ZEPLIN–III to search for ^{85}Kr events. This plot has been reduced to 1 μs bins to show the detection more clearly.

7.3 ^{214}Bi-^{214}Po Coincidences from ^{222}Rn Contamination

7.3.1 Introduction

Radon is a particularly problematic contaminant. It is part of both the uranium and thorium decay chains, and the longest lived isotope ^{222}Rn ($T_{\frac{1}{2}} = 3.824$ days) is part of the ^{238}U decay chain. Even if only very low levels of radon are generated internally by the instrument, its properties as a noble gas still make this a dangerous contaminant as it can decay far from its production site. Due to its chemical inertness, radon produced externally may also be able to enter the system. Emanation of radon is a potential problem for all rare event search experiments.

The ZEPLIN–III SSR configuration included the recording of the shaped sum channel by the veto DAq. Due to the relatively lower sampling rate of the veto DAq at 10 MHz the shaped sum was recorded rather than the actual sum channel. This allowed events which would otherwise be too short, such as the primary scintillation signal, to be recorded. However due to the properties of the shaping

process some of the information, such as pulse shape discrimination of the S1 signal, was lost. An example of a ZEPLIN–III event recorded by the shaped sum channel and the high sensitivity sum channel is shown in Figure 7.15. Almost all of the S2 signals can be seen in this channel, along with most of the S1 signal. Enough information is retained to allow for rudimentary analysis of the signals recorded in this channel.

7.3.2 Detection Method

Many of the isotopes in the decay chain containing radon emit α particles. These events are relatively high energy and so can easily be distinguished. A decay occurring part way through the radon decay chain (see Figure 7.16) provides the opportunity for the detection of a delayed coincidence between a β particle from ^{214}Bi and an α from ^{214}Po. Due to the short half-lives of the isotopes in this decay chain measuring any part of it may be indicative of the whole chain as secular equilibrium is quickly achieved. If the system is assumed to be closed, so that no external radon can be pumped in, then the whole chain down to ^{210}Pb would be in secular equilibrium and the radon contamination can be measured using this result. The half-life of the ^{214}Po decay is 164.3μs, which is appropriate for the veto timeline of 300 μs post trigger. Two distinct populations of events were observed in the delayed portion of the ZEPLIN–III shaped sum channel recorded by the veto DAq: events showing a high energy feature and events without one. Figure 7.17 shows the drift time of events from these two populations. The high energy events occur primarily near the cathode, and the number of lower energy events is in line with the expectations of the accidental coincidence rate and, for shorter delay times, afterpulsing.

7.3.3 Results

Events in the shaped sum channel were searched for α particles signals. It was found that α events have a very distinctive signal in the shaped sum channel, despite the high quenching factor, as the primary scintillation signal saturates the shaping amplifiers. Figure 7.18 shows an example of an alpha event seen in both ZEPLIN–III and the veto. The channels recorded through shaping amplifiers

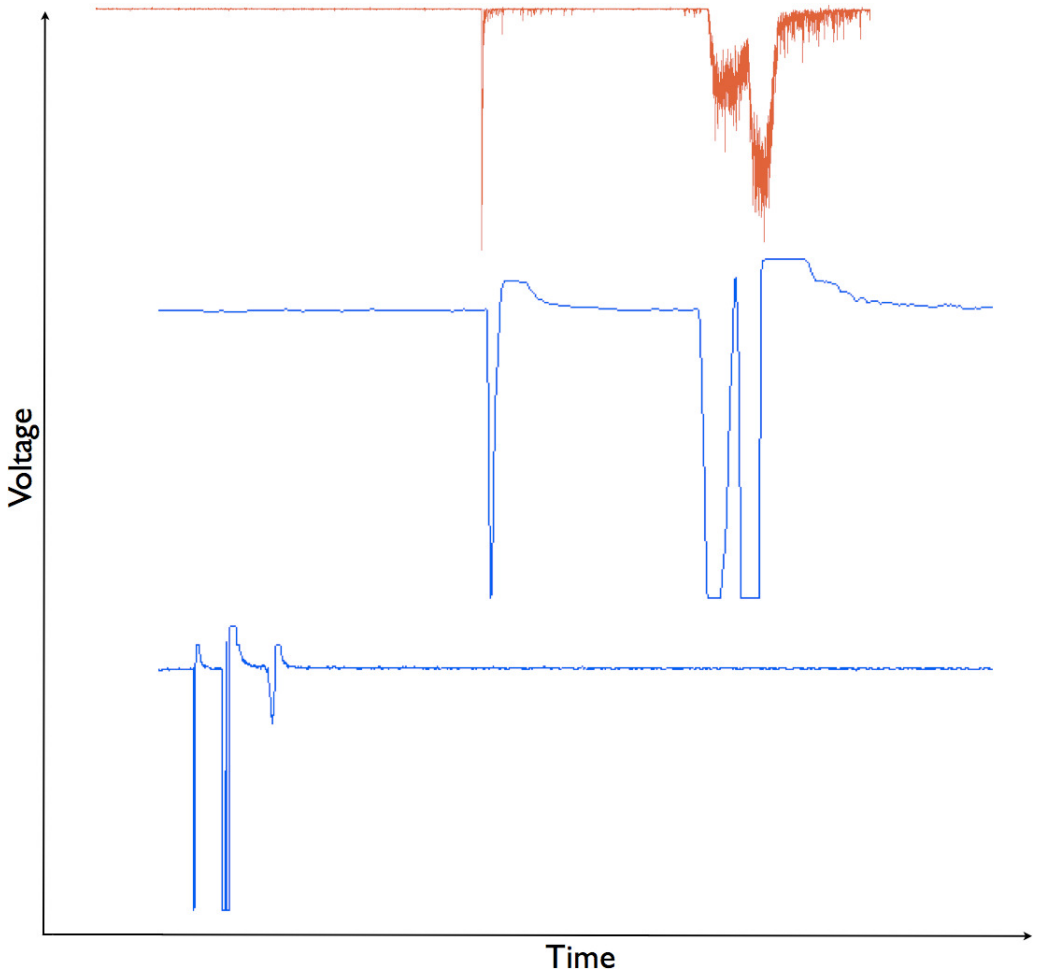

Figure 7.15: A comparison between the timelines recorded by the shaped sum channel (blue) and the high sensitivity sum channel (red) for a typical ZEPLIN–III event. The range of the shaped timeline is significantly lower at 1.8 V than the high sensitivity channel at 10 V. The top image shows the waveform recorded by the ZEPLIN–III DAq and the middle image shows the corresponding section of the veto waveform. The bottom image shows the full length of the ZEPLIN–III shaped sum timeline recorded by the veto DAq, this contains an additional 284 μs. This plot shows that the ZEPLIN–III DAq has missed a third pulse on the timeline as it does not keep sufficient data to record these delayed event. The veto DAq has recorded this event as it records a much longer timeline.

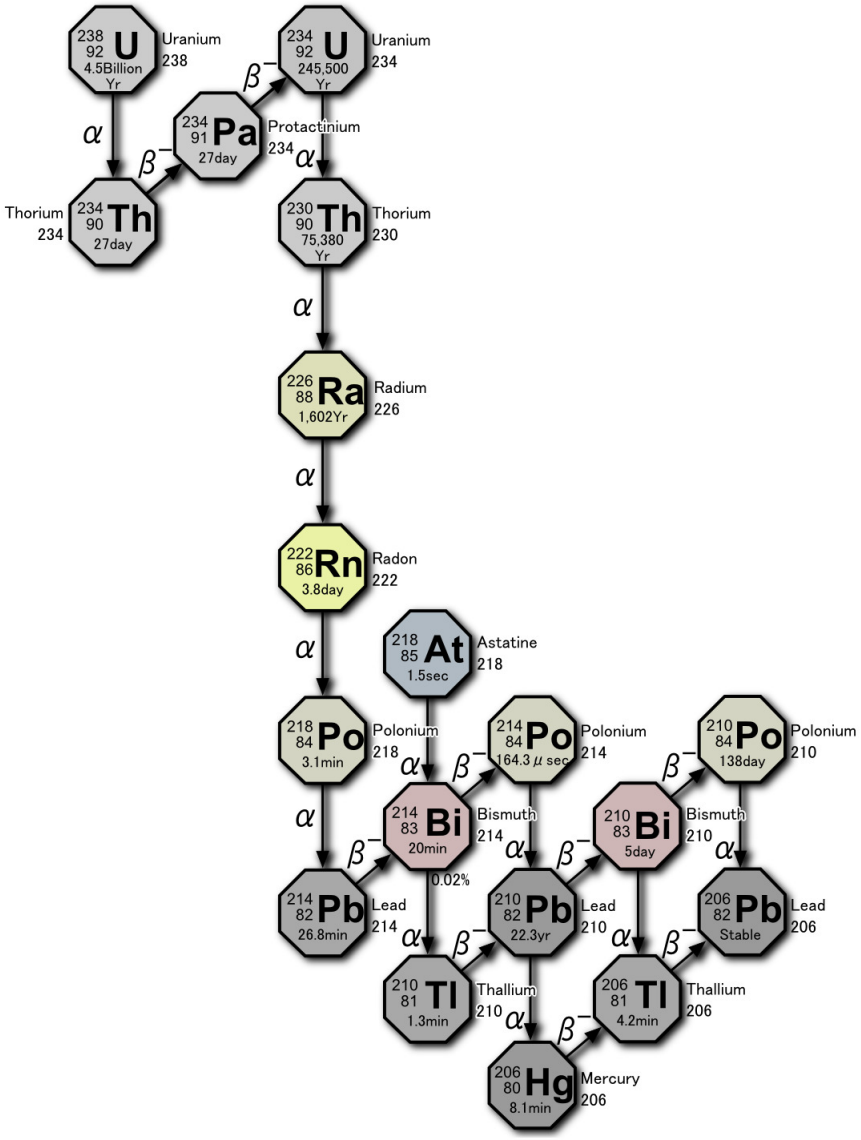

Figure 7.16: Graphical representation of the ^{238}U decay chain. Image obtained from [369].

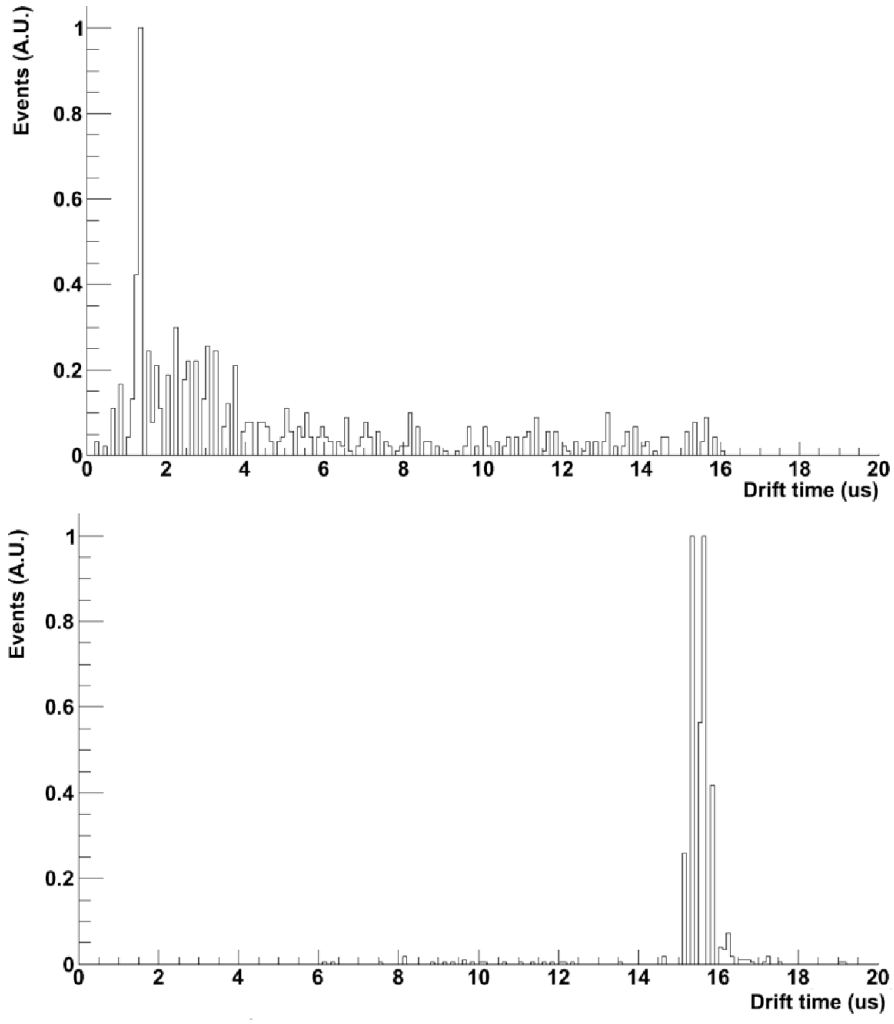

Figure 7.17: The two populations of delayed events on the ZEPLIN–III shaped sum channel recorded by the veto DAq plotted as a function of the drift time. The upper image shows the events without the high energy feature. The drift time for these events is spread over the fiducial volume, with a slight increase near the surface as would be expected from PMT afterpulsing considerations. The lower image shows events with a high energy feature. These occur almost exclusively at the cathode. This is in line with expectations of delayed ^{214}Po alpha decays as positive ions are produced earlier in the decay chain which would drift to the cathode region in the electric field.

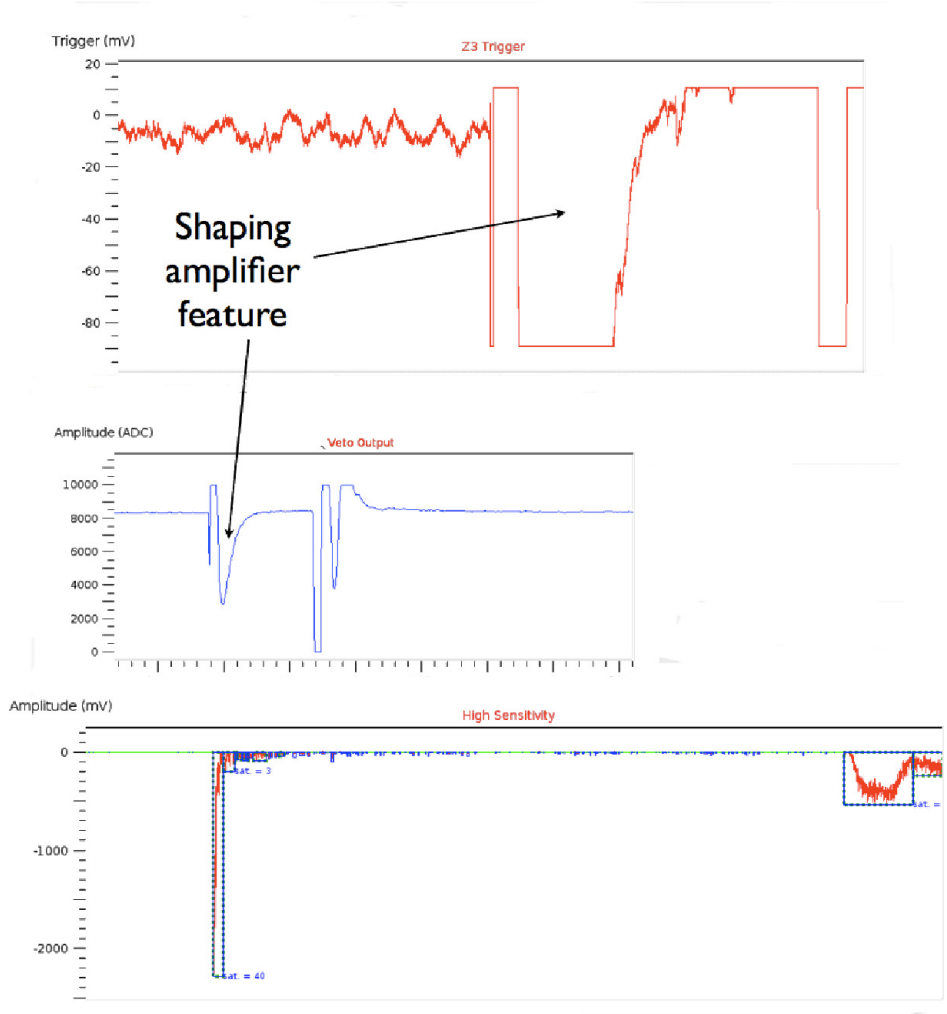

Figure 7.18: An example of an α event seen by both instruments. As these are timelines all three x-axes show time. The shaped sum channel recorded by the veto DAq is shown in the center. The upper timeline shows the shaped sum channel recorded by the ZEPLIN–III DAq. The bottom image shows the sum channel recorded by the high sensitivity channel of the ZEPLIN–III DAq. Note here that the feature marked between the S1 and S2s in both shaped timelines is not seen by the high sensitivity channel, showing that it is just a feature of the shaping amplifiers.

show the distinctive signal seen for α events. The SSR data was searched for delayed alpha events in the shaped sum channel following a ZEPLIN–III trigger. A total of 940 ± 31 candidate events were found.

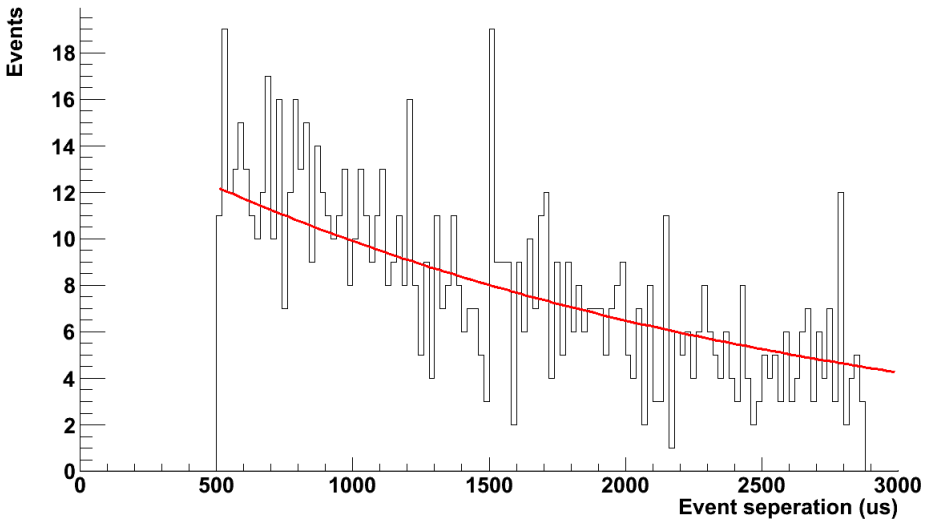

Figure 7.19: A maximum likelihood fit of the delay between the trigger event and the time of the α event. An exponential with a characteristic time matching the lifetime of ^{214}Bi fits the data very well confirming that these events are delayed α's from ^{214}Po decay.

Several selection efficiencies need to be accounted for to interpret this result. The maximum available timeline is from the trigger point to 15 μs before the end of the timeline, giving 70% efficiency. A lower bound of 50μs was selected to ensure the delayed alpha was outside the ZEPLIN–III DAq range. This allowed for analysis of the primary event using the ZEPLIN–III waveform without inference from the delayed event, for synchronised events. Although a shorter delay could be used, the additional 30 μs post trigger gives a known efficiency penalty but allows the ZEPLIN–III PMTs to fully recover after the initial energy deposit, which may be quite large. There is also an efficiency penalty due to the reverse field region. The two stages before the delayed α produce positive ions. Both ^{214}Pb^{+} and ^{214}Bi^{+} will drift to the cathode due to the strong electric field present in the target. With half lives of 28.6 minutes and 19.9 minutes respectively it would be expected that the vast majority of delayed alpha events should occur at the cathode as the ion drift time is $\mathcal{O}$(seconds).

It was observed that all delayed alphas occur in the region of the cathode, however there were some instances ($\sim 6\%$) of the primary event occurring above the cathode. Considering the half life and drift time for the positive ^{214}Pb ion these are not expected to be real bismuth-polonium coincidence events which should all occur at the cathode for a data set of this size. The number observed is in line with the expected accidental rate from large events near the cathode, discussed in Section 7.4, which produce the same high energy feature shown by α events. Figure 7.20 shows a plot of the positions of most of the ^{214}Bi β decays. Not all of the detected events could be shown since some ^{214}Bi events also emit a prompt γ-ray which does not allow for this type of analysis. The z position is given by the drift time and the x-y position was calculated by the corrected centroid of the S2 signal and then converted to polar co-ordinates to give the radial distance from the central PMT. The proportion of events falling within the fiducial volume for synchronised events with no prompt γ-ray was used to scale the total number of events.

The efficiency penalty from the reverse field region is a maximum of 50% since up to half of the recoils will be into the reverse field region above the PMT grid, where no S2 signal can be recovered. Accounting for these efficiencies gives a total of 3709 ± 121 events. A maximum likelihood fit of the form $y = \frac{A}{\tau} e^{\frac{-t}{\tau}} + B$ was applied to the data (Figure 7.19). A is the area under the exponential which gives the number of events present, B is the background level and τ is the lifetime for this decay. Analysis of prompt α events in the following section shows the expected background is very low. These α events are mostly from isotopes below ^{210}Pb in the decay chain as 97% of the delayed ^{210}Po decays lie within the 1 ms inhibit signal following the trigger. The number of events given by this fit is 3440 ± 115. This agrees well with the total number of events detected, as would be expected from the prediction of the small background for these events.

A separate analysis searching for α events in the bulk of the target, away from the cathode wire region, shows α decays occurring throughout the xenon target. These events were identified by the same feature used to select events from the veto timeline but additionally these events show up clearly on a discrimination plot, shown in Figure 7.21. The rate of these events, although relatively low, is

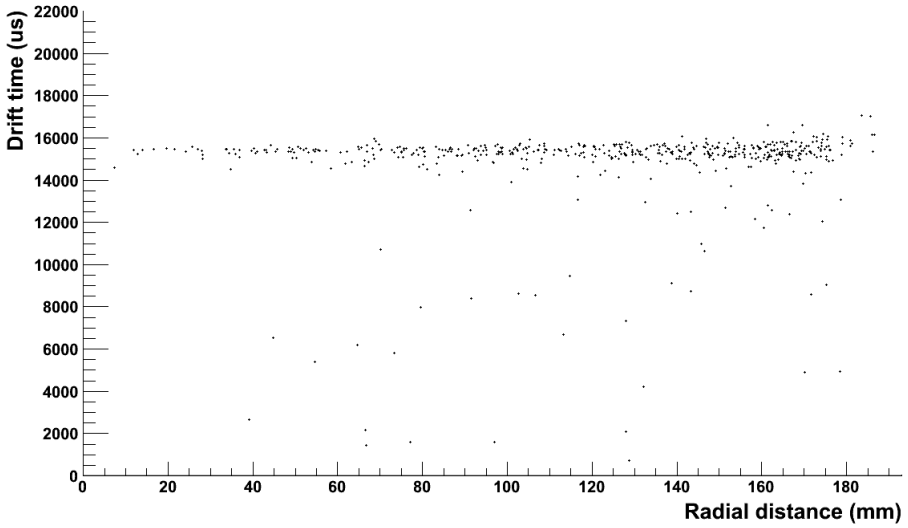

Figure 7.20: A plot of the drift time verses the corrected centroid position for candidate ^{214}Bi β decays. Note that since this is a positive ion the z position (indicated by the drift time) reflects this as most decays occur at the cathode which is located at a depth of $\sim$15.5μs.

stable over the course of the SSR, shown in Figure 7.22. Between ^{222}Rn and the positive ions which are attracted to the cathode there are two alpha decays. If some of the ^{214}Bi-^{214}Po coincidence events come from radon contaminating the xenon, rather than from contamination of the cathode grid wire, then these alpha decays within the fiducial volume are expected.

7.3.4 Conclusions

A plot of the daily rate of the ^{214}Bi–^{214}Po events from the fiducial region is shown in Figure 7.23. This shows that the rate is stable throughout the whole run. This indicates that the total rate of ^{222}Rn decays is 30.1 ± 1.0 per day. This total is from the whole of the cathode wire grid. The field near the edges is not uniform and if the cause of these events is positive ions drifting to the cathode then this total represents a volume larger than the fiducial region. To obtain a more useful result, a fiducial cut was applied to the ^{214}Bi decays recorded by the ZEPLIN–III DAq. This result was used to scale the total number of events as no radial cut can be applied to the ^{214}Po delayed α events recorded by the veto DAq. Since many

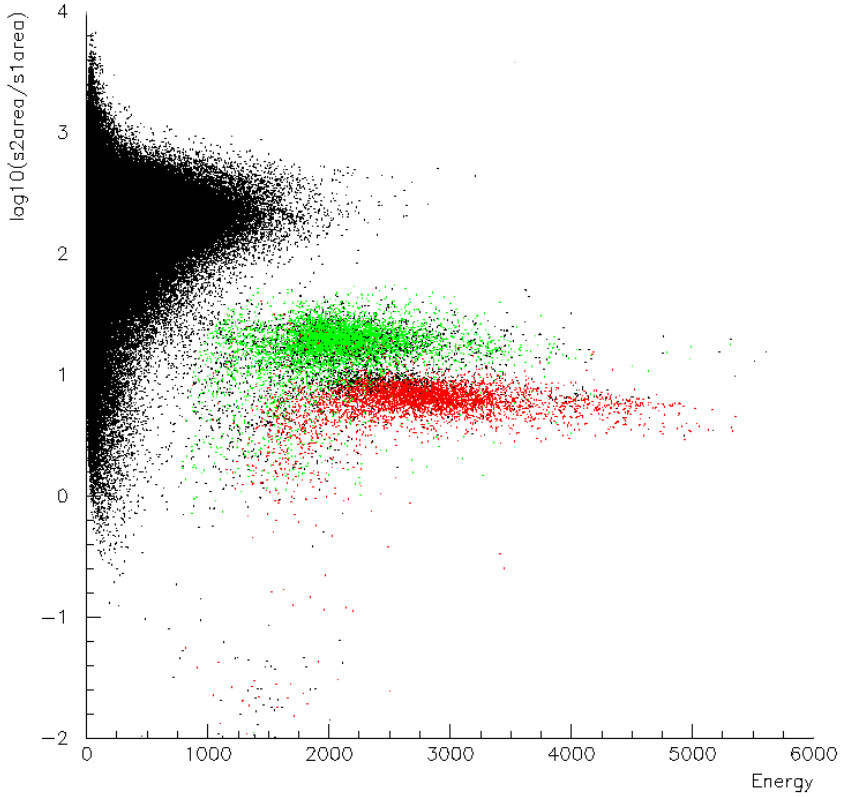

Figure 7.21: A discrimination plot of events near the cathode and high energy events from fiducial volume. The individual points are not important in this plot, which just demonstrates the separation of the different event types, which may be used to distinguish between them. Two high energy populations stand out and are shown in green (3377 ± 58 events) and red (6160 ± 78 events) showing alpha events from the region of the cathode and the fiducial volume respectively (so additional discrimination is possible using the drift time). These populations are both α events, however as the green population are emitted very close to the cathode wire they experience a different electric field from the uniform field within the fiducial volume. This causes them to be offset on the discrimination plot. The black points show other events in the cathode region. These are electron recoil events and some do extend out towards the high energy end occupied in the discrimination plot by α events. The black points are noise in this analysis.

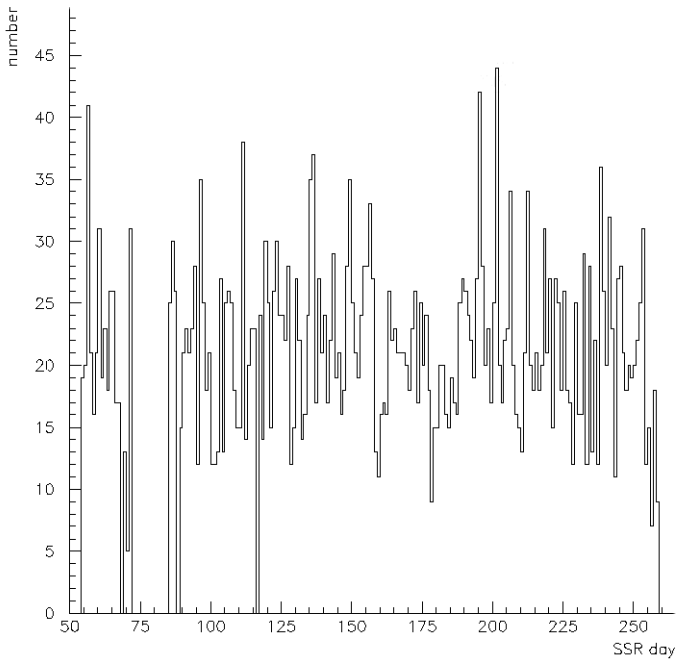

Figure 7.22: A plot of the number of α events as a function of SSR day for all days included in this data set.

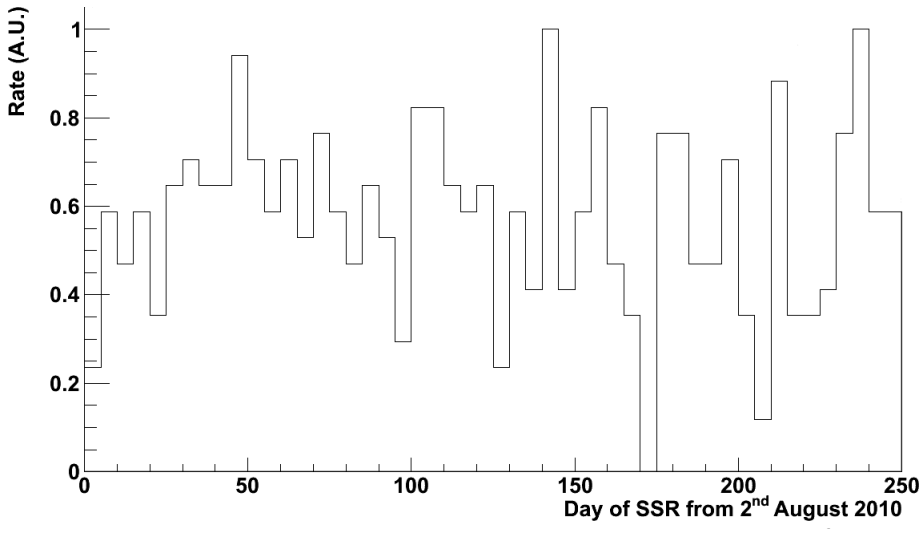

Figure 7.23: A plot of the consistency of the daily rate of ^{214}Bi decays recorded by the ZEPLIN–III DAq using 5 day bins.

of the events are accompanied by prompt γ-rays it was not possible to calculate the corrected centroid for some events. For events with a single S2 the corrected centroid and drift time were used to make a fiducial cut. Scaling the delayed α events gives a rate of 14.2 ± 0.5 per day in the SSR fiducial region. This translates to 2.0 ± 0.6 events per day per kg of xenon.

There are several possible sources for the radon. The wires of the cathode grid are contaminated with small amounts of uranium and thorium. Any contaminants at the surface of the wire could show a signal in this analysis. If this were to account for the whole signal seen in this analysis, then the steel wire would need a contamination of 3.4 ± 0.1 ppb of uranium, assuming a penetration depth of 10 μm in the wire. Although this is a plausible level for a steel wire, the presence of α events within the fiducial volume indicates that some ^{222}Rn may be mixed in with the xenon. This component of the signal could come from the inside surface of the copper vessel which houses the target, from contamination of the xenon itself, or even from radon emanating from the steel wires of the cathode. It may also be possible that radon is emanating into the system from the outside environment during the cryogenic refilling. It is not possible to determine the source from this analysis. If the worst case scenario is assumed, and the entire signal is assumed to come from uranium contamination of the xenon, then the

level of contamination would be 1.74 ± 0.06 ppt (w/w). The presence of α events in the fiducial volume suggests this worst case scenario is quite unlikely. The rate of decays per day depends on the number of isotopes in secular equilibrium. If the source of the α events is ^{222}Rn emanating into the xenon target the activity is 8.9 ± 0.2 decays per day (1.18 ± 0.02 per day per kg) as there are two α decays before decays to positive ions which drift to the cathode.

This level of contamination, whatever the source, is low enough not to represent a threat to the WIMP sensitivity of the SSR. The α decays are easily cut and β decays are typically high energy, hence the rate of low energy β decays in the fiducial volume is negligible given the discrimination power of the instrument. This is a positive result for the ZEPLIN–III instrument, and a useful proof of concept test for future experiments.

7.4 ^{210}Pb Contamination from ^{222}Rn Plateout

7.4.1 Introduction

Prior to the first science run of ZEPLIN–III, the xenon was purified using SAES PS11-MC500 getters. In addition to xenon purification, these getters are known to release 0.62 ± 0.04 atoms s^{-1} of ^{222}Rn into the system [156]. In an electric field, such as that present within the ZEPLIN–III target, positive ions produced in the decay chain of ^{222}Rn will drift to the cathode. When these positive ions, such as ^{214}Po which decays via α emission, decay close to the cathode wires the recoil may cause some of the daughter nuclei to become embedded within the wire. The decay chain has a bottle neck at ^{210}Pb ($t_{\frac{1}{2}} = 22.3$ years, $\beta_{max} = 63.5$ keV). This leads to an internal plating of ^{210}Pb on the cathode wire grid. During the SSR, which followed this internal plating by about a year, evidence of the contamination can be seen in the data. This contamination is restricted to the cathode wire grid, well away from the fiducial volume, and so does not represent a threat to the instrument sensitivity. The decays following the ^{210}Pb β^- decay are relatively rapid, hence during the SSR the isotopes between this and ^{206}Pb are in secular equilibrium. This contamination provides a constant source of ionisation at the bottom of the target during the experiment and so provides a useful tool for checking that the purity corrections applied to the science data are accurate.

The α particles emitted when ^{210}Po decays to ^{206}Pb have an energy of 5.41 MeV. The penetration is very small, about 10 μm in liquid xenon, and so, for the purposes of an independent check of the purity correction, all these events can be considered as coming from the same depth. As discussed in Section 8.2.1, the purity of the xenon effects the electron life time. This effect causes the size of the S2 signal to change depending on the depth of the interaction as some electrons will be lost as the ionisation electrons are drifted through the target. The graph shown in Figure 7.24 shows the effect of the xenon purity as a function of the drift time [220]. During the science run all the S2 signals need to be corrected for the depth they occur at, since deeper events give smaller signals due to the loss of electrons as they drift through the volume toward the gas phase. It was found in the FSR that the purity of the xenon increases over time [220]. This effect is also seen during the SSR [26] and so it would be expected that the size of S2 signals from ^{210}Po decays would increase over time. The purity correction applied to the data should compensate for this and no trend should be seen in the corrected S2 signal size.

7.4.2 Results

A search for α events at the cathode produced 6160 ± 78 candidate events. These events are shown in red on the discrimination plot in Figure 7.21. A search for events where the α recoils into the wire and the ^{206}Pb nucleus recoils into the scintillator revealed 3377 ± 58 of these events, shown on the discrimination plot in Figure 7.25. The difference in number is due several factors. The α events include a background from decays within the xenon that fall into the volume searched, subtracting the expected background leaves 5472 ± 139 α events. The ^{206}Pb nucleus is less penetrating than α particles which further decreases the relative number of events leaving the wire and interacting with the xenon. Additionally the two recoil bands overlap somewhat at low energies due to the non-uniformity of the charge extraction field around the grid wires. Hence a more strict cut was used to select events, and this may have a lower efficiency than that used to select the α recoils. The daily rates both the α and ^{210}Pb recoils remained stable over the course of the second science run, shown in figures 7.26 and 7.27. The activity

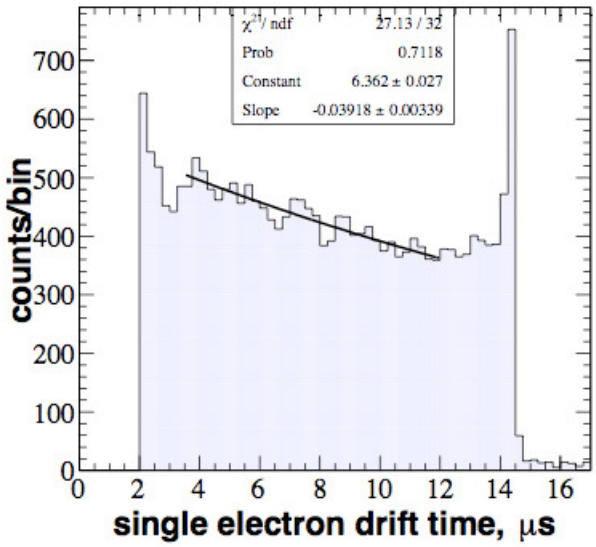

Figure 7.24: A plot showing the number of single electrons detected as a function of drift time. Due to impurities in the xenon there are less events observed with increasing depth in the fiducial region. This trend is not observed in the cathode region as there is more activity here than in the fiducial volume. The trend line may be used to calculate the electron lifetime in the xenon, the line shown gives $\tau_{e^-} = 26.4 \pm 2.0$ μs [325].

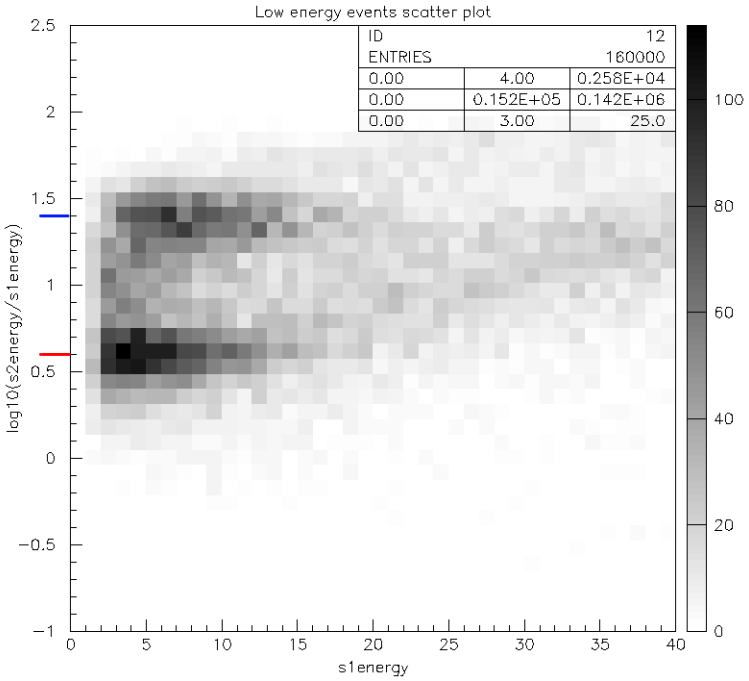

Figure 7.25: A discrimination plot of low energy events at the cathode. The nuclear and electron recoils bands are marked with red and blue respectively. The nuclear recoils are caused by recoiling ^{206}Pb nuclei. Due to nuclear quenching these events appear low energies.

averaged over the SSR is measured at 41.8 ± 0.3 events per day. As the Bateman decay equation [73] indicates, the ^{210}Pb sub chain should be in a state of transient equilibrium after ~ 2 years (the approximate period since the contamination) thus this activity level is also assumed for the isotopes ^{210}Pb and ^{210}Bi. Considering the number of ^{210}Pb atoms required to produce the rate observed along with the daily increase in the number of ^{210}Pb atoms measured from ^{214}Bi–^{214}Po coincidence events, the stable rate is consistent with expectations.

The size of the S2 signal was used to check the purity corrections were accurate. These signals provide a constant source of ionisation at the same depth throughout the SSR. The average number of electrons extracted to the gas phase is expected to increase with the increase in xenon purity measured over the course of the SSR, this effect was observed for these events. As the purity is measured each day the corrections to the ionisation signal should remove this trend for

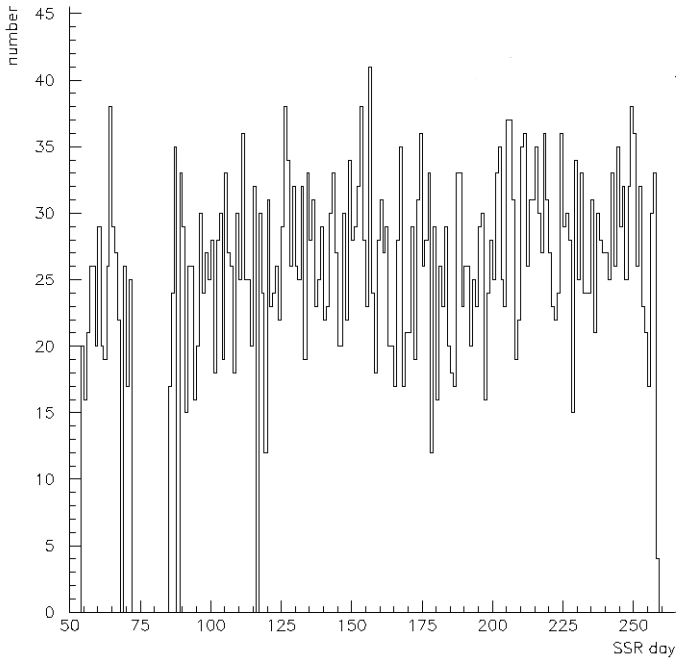

Figure 7.26: The daily rate of α events at the cathode during the SSR.

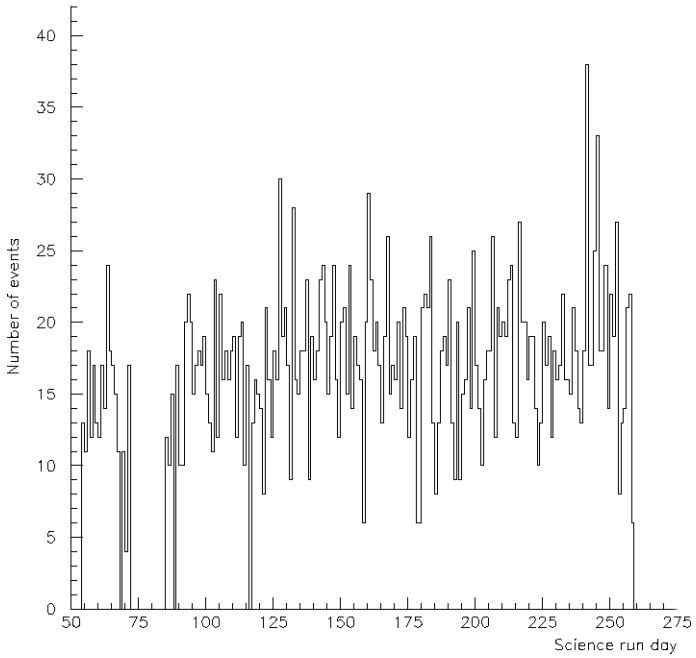

Figure 7.27: The daily rate of low energy nuclear recoils at the cathode during the SSR.

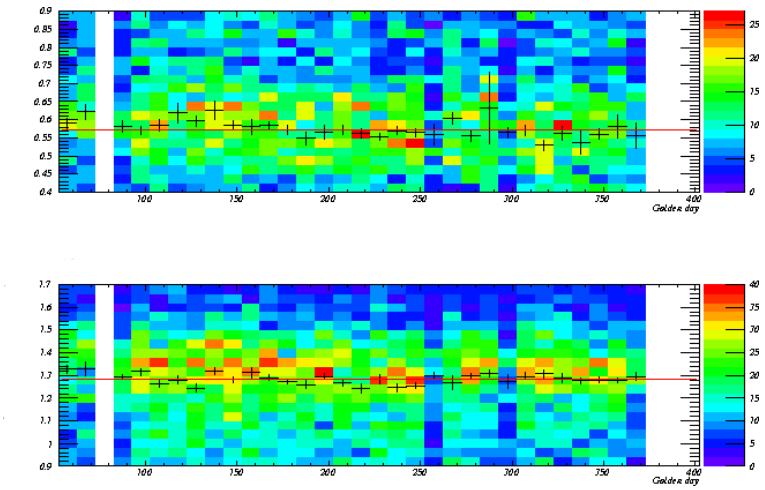

Figure 7.28: The size of the S2 signal from events at the cathode over the course of the SSR (plotted with 10 day bins). The upper image shows the size of signals from nuclear recoils and the lower image shows the size for low energy electron recoils. The mean is indicated on each plot.

these events at the cathode. Figure 7.28 shows a plot of the S2 signal size as a function of time. This shows that the purity corrections applied during the SSR are correct as the S2 size stays constant over the SSR.

7.5 Summary

Measurements of radioactive contaminants have been made using the science run data. The results show that they pose no threat to the dark matter sensitivity of the ZEPLIN–III detector. A constant source of ionisation was also found below the fiducial volume. This was useful to ensure that the corrections applied to the ionisation signal, accounting for the purity level of the xenon, were accurate throughout the science run. The techniques used here may be of use to the next generation of detectors where, due to the increased size of these targets, any contaminants present within the xenon must be measured accurately to ensure good WIMP sensitivity and a constant source of ionisation provides an additional check for ionisation energy corrections.

Chapter 8

ZEPLIN–III SSR

8.1 Introduction

The second science run of the ZEPLIN–III dark matter detector at Boulby mine acquired a raw fiducial exposure of 1343.8 kg·days during 319 days of data taking between June 2010 and May 2011, using a fiducial mass of 5.06 kg. A total of 8 events were recorded in the signal acceptance region between 7 and 29 keV_{nr}, which is compatible with background expectations. Assuming a null detection this result was used to place confidence limits on the WIMP-nucleon scattering cross section. Assuming a standard isothermal galactic halo model ($\rho_0 = 0.3$ GeV/c^2/cm^3 $v_0 = 220$ km/s, $v_{esc} = 544$ km/s and $v_E = 232$ km/s [256, 33]) the second science run data excludes a scalar cross-section above 4.2×10^{-8} pb for a WIMP mass of 51 GeV/c^2 with 90% confidence. This result was combined with the first science run data to give a limit for the ZEPLIN–III experiment of 3.5×10^{-8} pb for a 52 GeV/c^2 WIMP. The spin-dependent limit for the combined data is 7.2×10^{-3} pb for a 50 GeV/c^2 WIMP interaction with a valance neutron [26]. This chapter details the data acquisition and analysis of the second science run data used to obtain these results. Due to the nature of the ZEPLIN–III collaboration, contributions to this result were made by many members of the collaboration. I was heavily involved in the assembly of the detector, the construction and assembly of the shielding and ancillary systems, the calibration, the data acquisition and the WIMP data analysis, especially with regards to tagging events using the veto and producing background datasets. This chapter provides an overview of the ZEPLIN–III second science run which

for completeness includes work where major contributions were made by my collaborators.

8.2 Calibrations and Operations

During the second science run the ZEPLIN–III detector was operated with a 96% duty cycle. WIMP search data taking was halted for one hour each day during which the coolant was refilled and a γ-ray source was inserted above the target for energy calibration. There were also several longer breaks in WIMP search data taking, for nuclear recoil band calibration and also for electron-recoil band calibration.

8.2.1 Daily Energy Calibration

A daily calibration with ^{57}Co was used to define the S1 and S2 energy scales. The intensity of the 122 keV γ-ray used for the energy calibration is relatively high so this provides a clear peak to enable accurate fitting. This particular γ-ray has an energy that is high enough to penetrate a reasonable way into the target (mean penetration ~ 0.3 cm) whilst not being of such a high energy as to lead to significant errors when extrapolating down to the lower energies of more interest for WIMP searches. This peak is fitted daily to set the energy scale of both the S1 and S2 signals to achieve the high level of precision required for all signals recorded during the second science run. Linear interpolation between the daily measurements was used as the variance was negligible [26]. A further calibration check was also performed on the data to exploit the anti-correlation of the S1 and S2 signals, giving a more accurate estimate of the total energy deposited in the target by the interaction. Figure 8.1 shows fits to the ^{57}Co calibration data. The two left hand plots show the areas of S1 and S2 signals. The top middle plot shows the energy (in keV$_{ee}$) estimated from the S1 area. The middle bottom plot shows a parameter called E*, the anti-correlated energy. This value provides a more accurate energy estimate as lost recombination electrons that do not contribute to the S1 signal may instead contribute to the S2 signal. This is calculated by:

$$\mathrm{E}^* = (E \times \eta_{\mathrm{scintilation}}) + ((1 - \eta_{\mathrm{scintilation}}) \times (S2_{\mathrm{factor}} \times S2_{\mathrm{area}})) \qquad (8.1)$$

where $\eta_{\text{scintilation}}$ is the scintillation efficiency, E is the S1 energy, $S2_{\text{area}}$ is the area of the S2 signal and $S2_{\text{factor}} = 0.03694$ is a factor calculated using calibration data. The two plots on the right show the fits for the energy estimated by the program `mercury` which was especially designed to use likelihood estimators to reconstruct the energies and positions of the ZEPLI-III events [336]. The average energy resolution achieved using the anti-correlated energy estimate was 16.4% (FWHM)

The daily ^{57}Co data are also used to calibrate other important measurements. The purity of the xenon determines the electron lifetime. This value is the characteristic time that an electron can survive in liquid xenon. It is an important factor to measure accurately since it affects all ionisation signals as the extracted electrons are drifted through the liquid xenon by the electric field. Occasionally electrons that should contribute to the S2 signal are lost to impurities in the xenon and this effect is manifested as a decreasing S2 signal size with increasing interaction depth in the target. This effect must be accounted for and so the purity is measured every day from the ^{57}Co calibration data. The measurement is obtained by simply fitting a decay curve to a plot of the ratio of the S1 and S2 signals verses the drift time. Figure 8.2 shows a typical fit to the calibration data. Figure 8.3 shows the result from these fits for each day of the science run. It can be seen that the purity increases substantially during the second science run so long as the electric field is present. Several dips in the purity can been seen at various stages of the science run and these all correspond to shutting off of the electric field. The mean electron lifetime correction for the second science run was 37% of the S2 signal size. The electron lifetime may also be calculated by measuring the number of single electron events as a function of depth [325]. An example of this is shown in figure 7.24.

The ^{57}Co calibration data are also used to train the position reconstruction algorithms in `mercury`. A copper grid, known as the "phantom grid", was placed between the position of the ^{57}Co source (during calibration, as the source was retracted for science data taking) and the target. The thickness of the copper was selected to reduce the intensity of the 122 keV gamma-rays by half. Figure 8.4 shows the reconstructed positions of ^{57}Co events during a daily calibration.

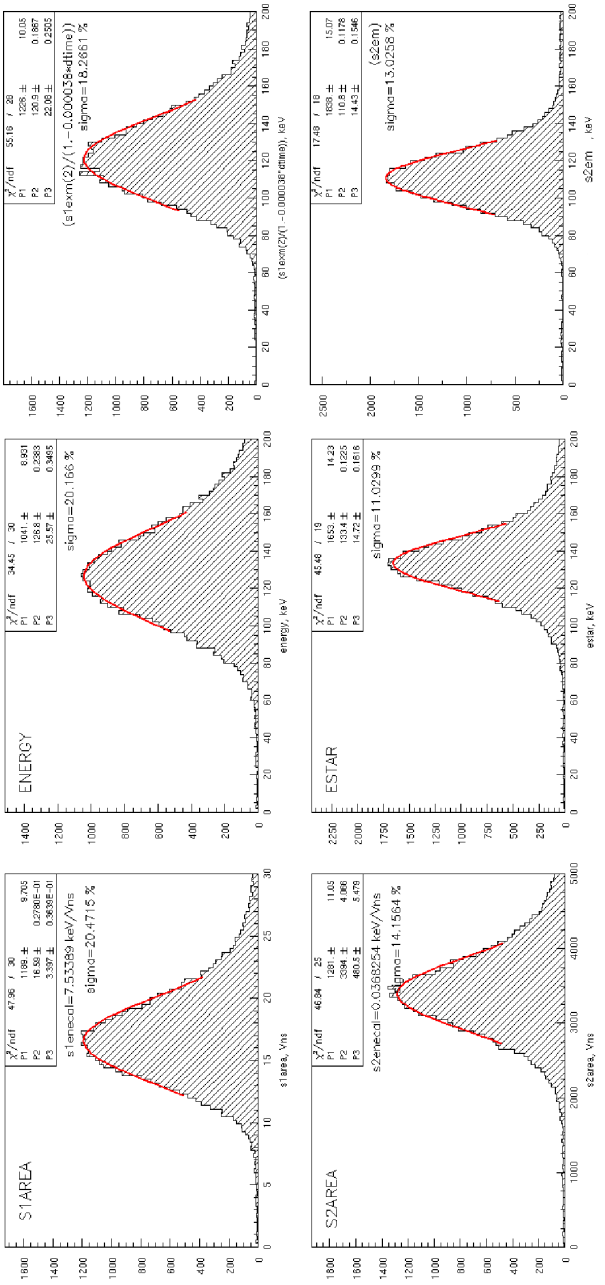

Figure 8.1: Results from ^{57}Co energy calibration. The upper left image shows the area of the S1 signal. The upper middle image shows the energy estimated from the S1 signal size, calculated by energy = S1 area $\times$7.73953. The upper right image shows the energy estimated from the S1 signal by `mercury` [336]. The lower left image shows the area of the S2 signal. The lower middle image shows the anti-correlation energy calculated as in Equation 8.1. The lower right image shows the energy estimated from the S2 signal by `mercury`.

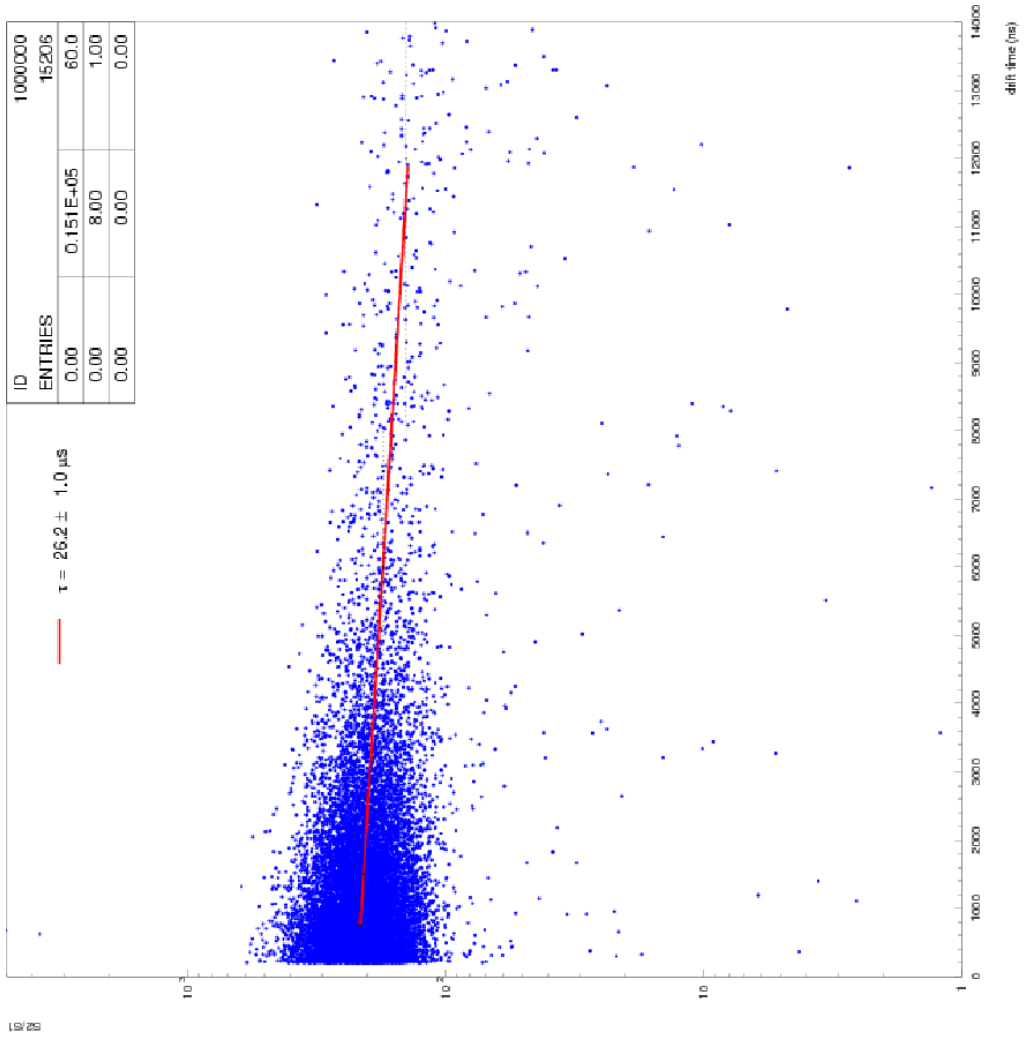

Figure 8.2: An example of a purity measurement using one days data from a ^{57}Co calibration.

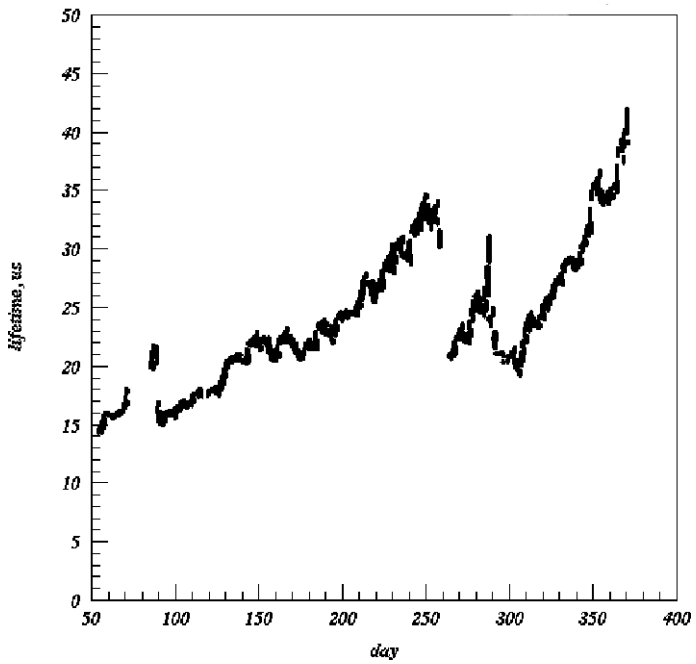

Figure 8.3: Purity measurements of the ZEPLIN–III xenon over the period of the second science run. Calculated by measuring the electron lifetime using daily ^{57}Co calibration data.

The accuracy achieved by the position reconstruction using `mercury` was 13 mm for S1 signals and 1.1 mm for S2 signals. The `mercury` program was also able to produce χ^2 maps for event checking. These maps could be used to help find multiple scatter events missed by other cuts, if multiple minima are found in the map. An example of a mercury χ^2 map is shown in figure 8.5.

8.2.2 Neutron Calibration

During the second science run there were three neutron calibrations. A total exposure of 10 hours was obtained using an Am-Be (α,n) source which emitted 1321 $\pm$ 14 neutrons per second [282]. The recoil band populated by single elastic scattering neutron events is representative of the nuclear recoil band that interacting WIMPs would populate. This band was parameterised by Gaussian fitting to the discrimination parameter (the ratio of the ionisation and scintillation energies) in 1 or 2 keV$_{ee}$ bins, an example of a fit to one energy slice is shown in figure 8.6. The mean and width of the distribution were used to define an energy dependent signal acceptance region in the energy range 2-12 keV$_{ee}$. The mean of

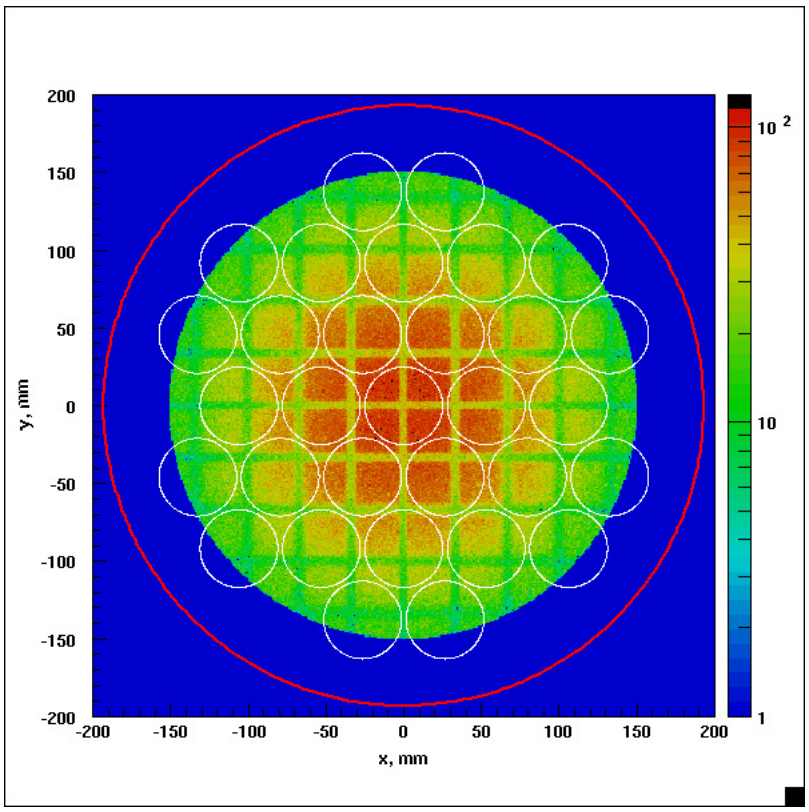

Figure 8.4: Results showing the effectiveness of the position reconstruction algorithms of `mercury` [336]. The calibration source was placed at the origin in the x-y plane and the position of the S2 signal was recorded. The colour represents event density. The phantom grid can clearly be seen with well defined edges indicating that the program has successfully reconstructed the positions of the events.

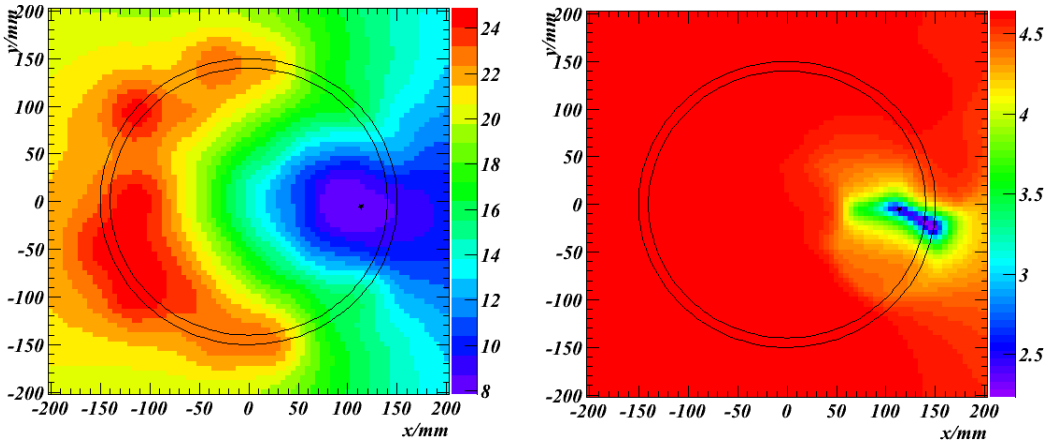

Figure 8.5: An example of a χ^2 map of an event with a relatively large uncertainty in the position. The S1 signal is shown on the left and is much less accurate due to the lower statistics. The S2 event is seen on the right. In both pictures a $\star$ is used to show the position of the minimum.

this distribution and its width for the largest of the neutron calibration runs are shown in figure 8.7. Figure 8.8 shows the resulting WIMP search box overlaid onto the Am-Be data discrimination plot. The acceptance is approximately the lower half of the low energy nuclear recoil band, from $2.3\%(\mu-2\sigma)$ to $45\%(\mu-0.126\sigma)$. This was set to maximise the sensitivity to any population of nuclear recoils and was selected by examining properties of both the nuclear recoil band and the electron recoil band. Since the background radiation experienced by ZEPLIN–III consists of electron recoils, selecting the lower half of the nuclear recoil band cuts the efficiency for nuclear recoils in the required energy range to 42.7% but reduces the electron recoil background leaking into the WIMP search region by $\sim 99.996\%$.

The relative scintillation efficiency for nuclear recoils was also measured from the Am-Be data. The light yield from scintillation differs depending on the type of interaction for the same energy deposited. Nuclear recoils give off less light than electron recoils and since the energy scale is calibrated using a γ-ray source a good measurement of the relative yields is essential. The conventional definitions of the important factors here are $\mathcal{L}_{eff}$(E) which is the scintillation yield for nuclear recoils of energy E (where E is the true energy deposited by the nuclear recoil in keV_{nr}) relative to that of electron recoils of 122 keV photoabsorption at zero

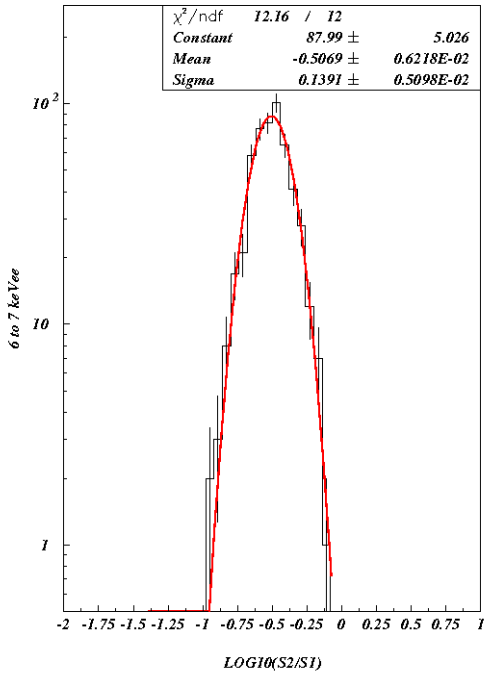

Figure 8.6: An example of a fit to a 1 keV$_{ee}$ energy slice of AmBe calibration data. The mean is used to define a point on the discrimination plot. A fit to several of these points then defines the nuclear recoil band.

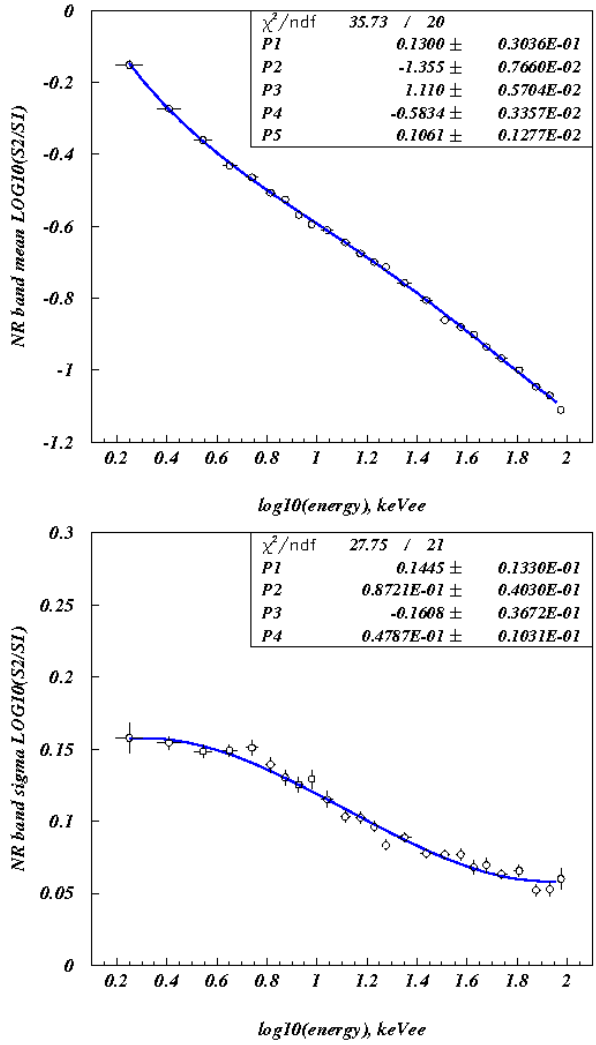

Figure 8.7: The ZEPLIN–III second science run nuclear recoil band. The top image shows the mean of the nuclear recoil band and the lower image shows the error of the mean. Both are calculate using energy slices as shown in Figure 8.6.

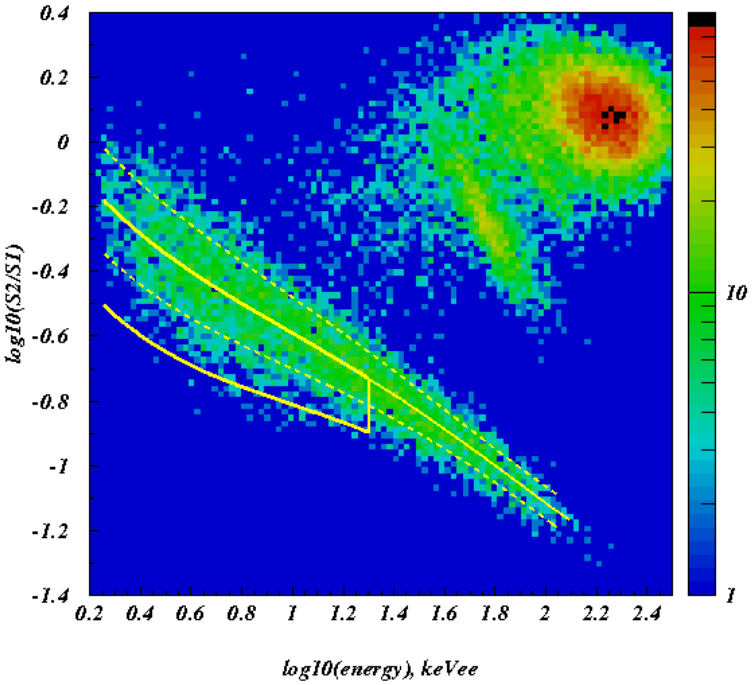

Figure 8.8: The ZEPLIN–III second science run WIMP search region (solid yellow curve) overlaid onto a discrimination plot showing neutron calibration data. Also shown is the nuclear recoil mean and its 2 σ error (dashed yellow line) [26].

electric field. $\mathcal{Q}_y$(E) is the yield of ionisation charge leaving the interaction site (in electrons per unit energy, independent of other efficiencies). The electron recoil equivalent energy, ⟨S1⟩, is calculated for nuclear recoils by:

$$\langle S1\rangle = \frac{\mathcal{S}_{nr}}{\mathcal{S}_{ee}}\mathcal{L}_{eff}(E)E \tag{8.2}$$

Where $\mathcal{S}_{nr}$ and $\mathcal{S}_{ee}$ account for the suppression of scintillation light due to charge extraction by an electric field for nuclear recoils and electron recoils respectively. These factor are both defined as unity in zero electric field. $\mathcal{Q}_y$ is defined by:

$$\mathcal{Q}_y(E) = \frac{\langle S2\rangle}{W\frac{q_0}{q(|E|)}} \tag{8.3}$$

where the relative fraction of charge collected is represented by $\frac{q_0}{q(|E|)}$ and the minimum energy required to create an electron-ion pair in liquid xenon is given by W.

The Am-Be data scintillation and ionisation spectra were compared to Geant4 simulations in order to obtain a measurement of both of these factors [220]. A χ^2 technique was used to obtain the $\mathcal{L}_{\mathbf{eff}}$ shown in figure 8.9. A similar technique was used to find $\mathcal{Q}_y$, shown as a function of energy in figure 8.10. The W-value for liquid xenon was obtained from the second science run data by rearranging equation 8.3. The W-value was found as 16.5 ± 0.8 eV.

In addition to the relative scintillation yield, the nuclear recoil acceptance must be considered to correctly interpret the sensitivity of the detector in the region of interest. Firstly, several constant factors were combined to give an energy independent efficiency of 39.8%. These include the DAQ livetime fraction of 99.2%, the quality cuts on the waveforms 98.3% (affected by the performance of the electronics in the waveform digitiser, most of the inefficiency here comes from misalignment of the high and low sensitivity channels), pulse parameter cuts were 96.9% efficient for nuclear recoils, accidental coincidences with the veto detector were measured at 0.43% and 0.83% for the thresholds used (as explained in Section 6.3) and finally the above signal acceptance calculated from the mean ratio of S2/S1 from the AmBe data. Combined these give a total efficiency of

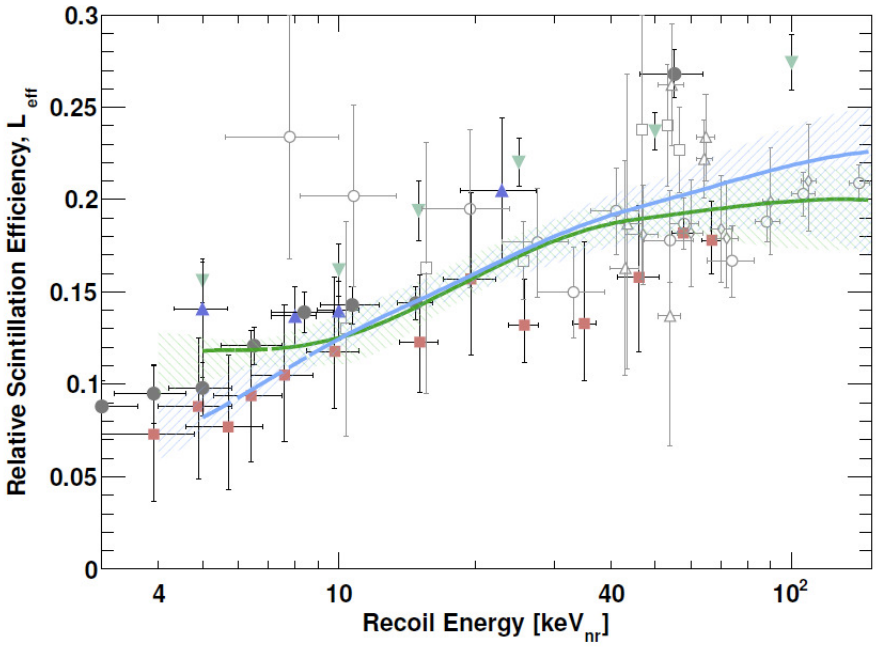

Figure 8.9: The energy-dependent relative scintillation yield for nuclear recoils ($\mathcal{L}_{\mathbf{eff}}$). The ZEPLIN–III first science run is indicated by a solid green curve with the hashed green area showing the 68% C.L. band and the ZEPLIN–III second science run result is indicated by the solid blue curve with 85% C.L. band shown by the blue hashed area [220]. Also shown are previous published measurements using mono-energetic neutron beams: (•) [302], (■) [269], (▲) [47], (○) [57], (△) [24], (▽) [119] and (◊) [48], or obtained using a Monte Carlo matching procedure similar to that used for the ZEPLIN–III results (▼) [340].

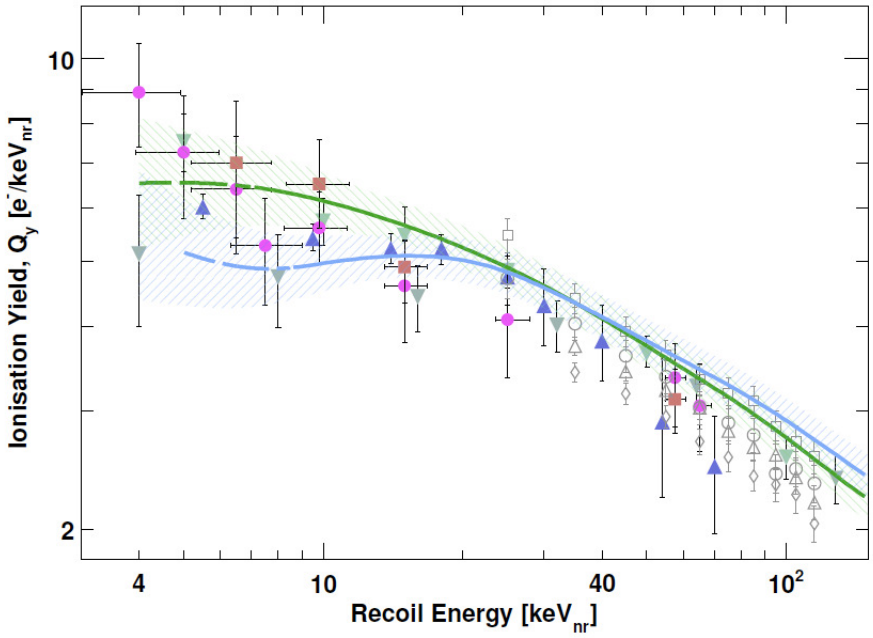

Figure 8.10: The ionisation yield, Q_y, for nuclear recoils as a function of energy. The ZEPLIN–III first science run result is shown by the solid green curve with 68% C.L. band shown by the green hashed area. The ZEPLIN–III second science run result is shown by the solid blue curve and the 68% C.L. band is shown by the blue hashed area [220]. Also shown are previous measurements at 1.0 kV cm^{-1} (•) and 4.0 kV cm^{-1} (■) from Reference [269], at 2 kV cm^{-1} (□), (△), 0.3 kV cm^{-1} (○) and 0.1 kV cm^{-1} (◊) from Reference [48] and spectra obtained using a Monte Carlo simulation matching that used by the ZEPLIN–III analysis at 0.73 kV cm^{-1} (▲) [340] and (▼) [342].

42.7% for nuclear recoils.

Three energy dependent efficiencies were also considered. The scintillation detection efficiency drops sharply at lower energies, more so than $\mathcal{L}_{\mathbf{eff}}$ alone would suggest since a 3-fold PMT coincidence is required for any signal to be considered. A curve showing the efficiencies is shown in figure 8.11. This considers the chance of detection considering the quantum efficiency of the PMT array and the number of scintillation photons generated by low energy nuclear recoils. Also shown in this figure is an energy dependent efficiency incurred from the data quality cuts (these cuts were used to further separate the electron and nuclear recoil bands in calibration data to achieve the best possible discrimination for the detector). A further energy dependent efficiency also shown relates to a timing cut on scintillation pulses to utilise the small amount of pulse shape discrimination possible with the ZEPLIN–III PMT array. This is due to the luminescence having two components, one fast ($\mathcal{O}(2)$ ns) and one slow ($\mathcal{O}(30)$ ns), see section 4.3. Hence a waveform sampling of 2 ns is adequate to utilise pulse shape discrimination since the fast component dominates for nuclear recoils.

8.2.3 Neutron Activation

Following the nuclear recoil band calibration, prior to the second science run evidence of some activation was seen in the data, as would be expected. During the calibration, isomers were created by thermal neutron capture onto ^{128}Xe and ^{130}Xe or by fast neutron inelastic scattering by ^{129}Xe or ^{131}Xe nuclei. The two isomers created are ^{129m}Xe and ^{131m}Xe which have half lives of 11.86 and 8.88 days, respectively, as shown in figure 8.12. Both these isomers de-excite via the emission of γ-rays. The excited $\frac{11}{2}^-$ state of ^{129}Xe decays to the $\frac{1}{2}^+$ ground state by the emission of two γ-rays totalling 236.2 keV (196.56 keV M4 γ-ray to the $\frac{3}{2}^+$ state followed by a 39.578 keV prompt M1+E2 γ-ray to the ground state). The excited $\frac{11}{2}^-$ state of ^{131}Xe decays to the $\frac{3}{2}^+$ ground state by the emission of a 163.9 keV M4 γ-ray.

The long lifetimes of these isomers allows them to be seen in the detector for several days following a calibration with a neutron source. Figure 8.13 shows

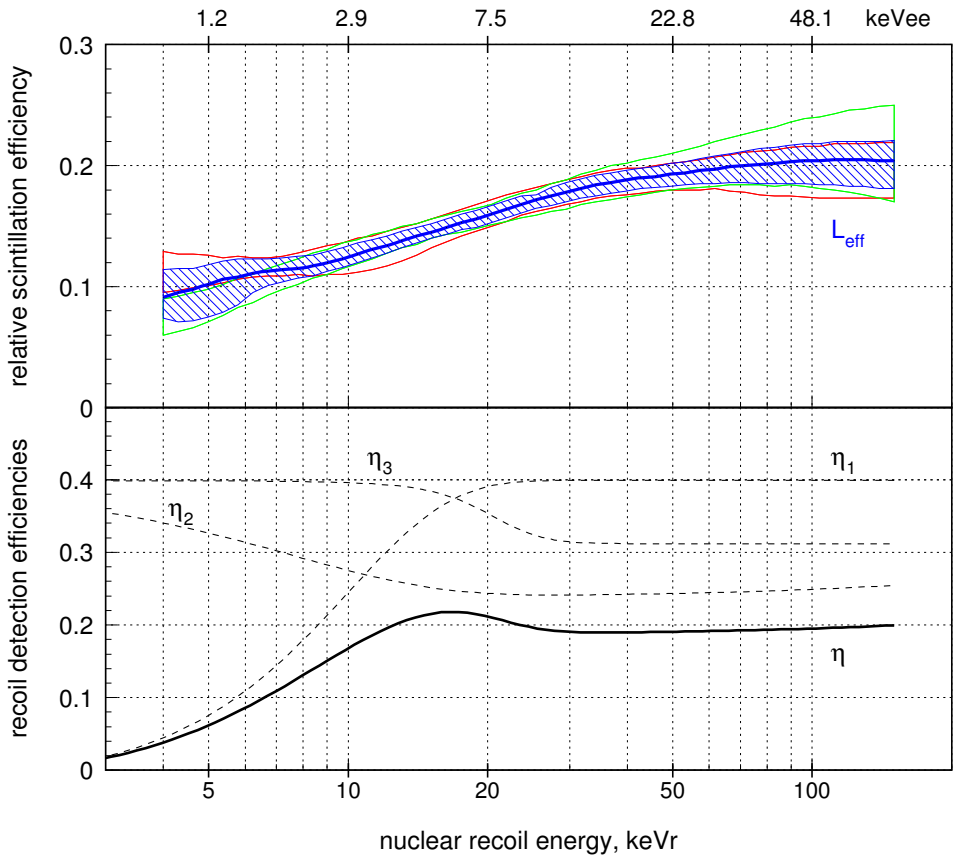

Figure 8.11: Nuclear recoil efficiencies [26]. The upper image shows the relative scintillation efficiency for nuclear recoils in liquid xenon with zero electric field; the thick blue curve (adopted for the second science run) combines the measurements and uncertainties reported in Reference [220] for the first science run data (68% C.L. band shown in red) and the second science run data (68% C.L. band shown in green). The hashed blue area shown the 68% confidence region. The lower image shows recoil detection efficiencies; η consists of a flat component ($\eta_0 = 39.8\%$) dominated by signal acceptance in S2/S1 and 3 energy-dependent factors: the S1 detection efficiency (η_1), the quality cuts (η_2) and the timing cut on S1 pulses (η_3).

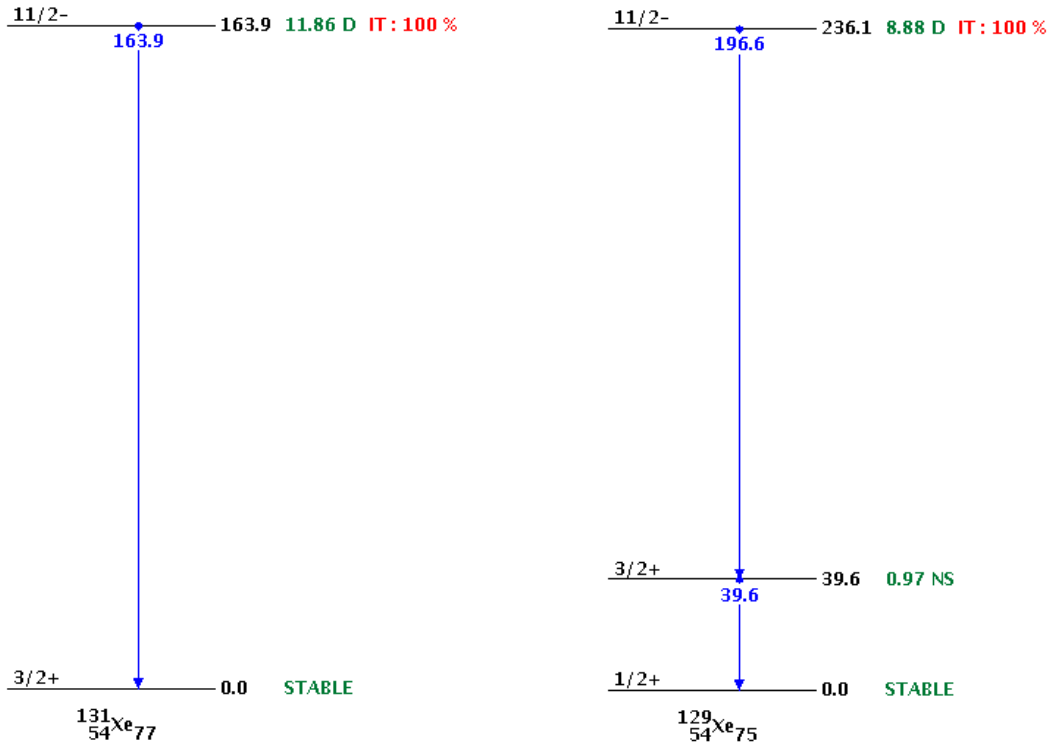

Figure 8.12: The decay modes of ^{129m}Xe [364] and ^{131m}Xe [388]

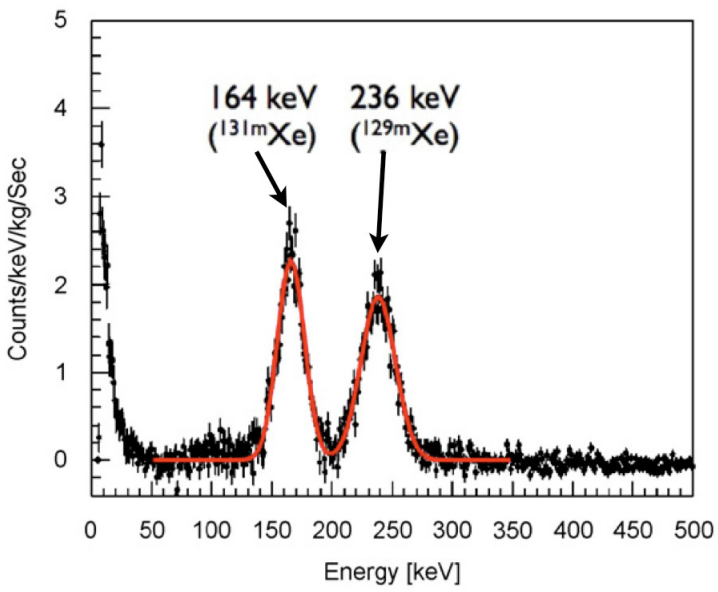

Figure 8.13: An energy spectrum seen in ZEPLIN–III following a calibration with a ^{252}Cf source. The peaks from decays of activated xenon isotopes can clearly be seen.

an energy spectrum seen in ZEPLIN–III following a five day neutron calibration before the SSR. These data are not part of the second science run. This length of exposure leads to significant activation which is shown clearly by the two peaks corresponding to the energy levels of the isomers (N.B. that since the second γ-ray produced by the decay of ^{129m}Xe is low enough in energy as to have a much higher chance of interacting than the first, and so is usually seen in coincidence with it leading to the peak at the combined energy). After neutron calibrations during the second science run these peaks can again be seen in the data, figure 8.14, but much less clearly due to the shorter exposures involved. These energy deposits are clearly very far from the region of interest for WIMP interactions and combined with the relatively short lifetime compared to the science run time-scale and the low rates observed they pose no threat to the WIMP sensitivity of the instrument.

8.2.4 Electron-recoil Band Calibration

The ZEPLIN–III electron recoil band for the second science run was calibrated using a 4.6 kBq ^{137}Cs source. The source was inserted above the target volume

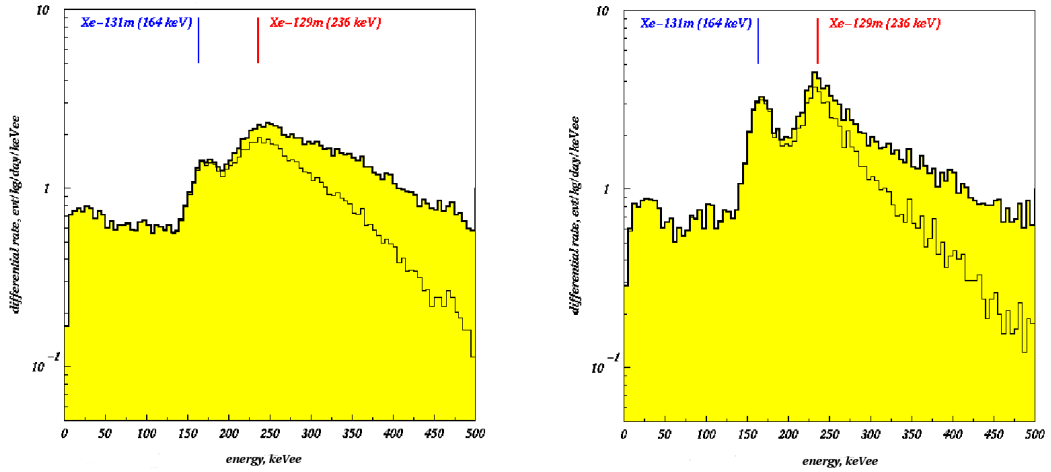

Figure 8.14: Plots showing the DRU (differential rate unit) seen in the detector before (left) and after (right) an AmBe neutron calibration.

and produced 150 counts per second in the detector. ^{137}Cs emits 661.7 keV γ-rays with 94.7% intensity [103]. These γ-rays populate the low energy region of the electron recoil band through Compton scattering, giving a reasonable calibration of the electron recoil background. The main draw back to this method is due to the difference in rate. The much higher trigger rate from the ^{137}Cs calibration leads to an increase in the resistivity of the bialkali plates in the PMTs [287] (in addition to saturation of the photocathode). This in turn leads to localised charging of the photocathode which distorts the electric fields of the input optics. This effect causes a decrease in the mean response of the PMTs proportional to the event rate, to first order [287].

The combined exposure from two ^{137}Cs calibration runs produced a similar total number of events to the science run data, the equivalent of 96% of the SSR exposure. A direct comparison of the two, shown in figure 8.15, shows a very similar number of events leaking into the WIMP search area. There were 10 ^{137}Cs events in this region for compared to 8 in the SSR. The box shown here contains an extra partition at 35% acceptance which was added before the science run data contained within was revealed. This was necessary once extrapolation of the electron recoil background produced non-zero results for events leaking

into the WIMP search box. Figure 8.16 shows the events from ^{137}Cs calibration defining the electron recoil band on a discrimination plot. This plot also shows the WIMP search box defined by neutron calibration.

A comparison of the two recoil bands gives the discrimination power of the detector. This is of vital importance for detecting rare events above the background. For the second science run the ZEPLIN–III detector achieved a discrimination power of 1 : 280 between nuclear and electron recoils, respectively. The difference between the this and the discrimination achieved during the first science run is due to the second science run PMT array. The lower discrimination power is offset by a relatively greater drop in the level of background radiation.

8.2.5 LED Calibration

A weekly calibration of the response of each PMT was carried out using an LED connected to the target via a fibre optic cable. A pulse generator was used to drive the LED and the resulting waveforms were searched for single photo-electrons (SPEs). The SPE mean area was calculated from the mean area above a certain threshold, as show for PMT 3 in figure 8.17. The mean area of the ^{57}Co peak at 122 keV was then used to calculate each PMTs response in photoelectrons per keV. For the second science run the average light yield of the chamber was calculated as 1.3 phe/keV$_{ee}$ [220].

8.2.6 Operations

During the second science run the ZEPLIN–III detector ran from the 24^{th} of June 2010 until the 7^{th} of May 2011. During this period the detector maintained an average duty cycle of 96% over 319 days of operation. The science run was halted, as planned, to allow analysis of the WIMP search data, but as the system was still stable at this point and the run could have potentially been extended. At the time of publication this was the longest continuous data taking run ever performed by a liquefied noble gas dark matter detector. Continuous monitoring and maintenance by the ZEPLIN–III collaboration was required.

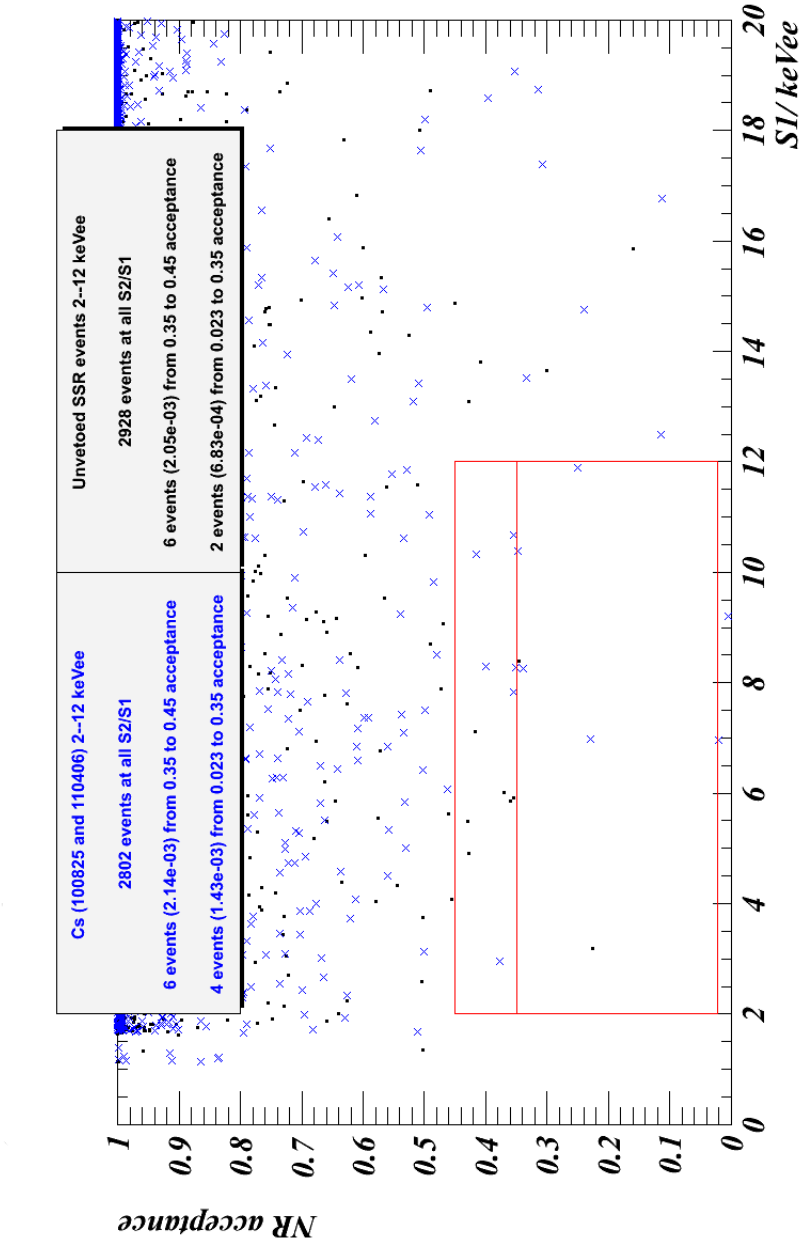

Figure 8.15: A comparison of the distribution in signal acceptance between the second science run data and the electron recoil calibration data. Recoils from WIMPs and neutrons are distributed uniformly in the y-axis. The science run data show seven (one) events in the upper (lower) region [26].

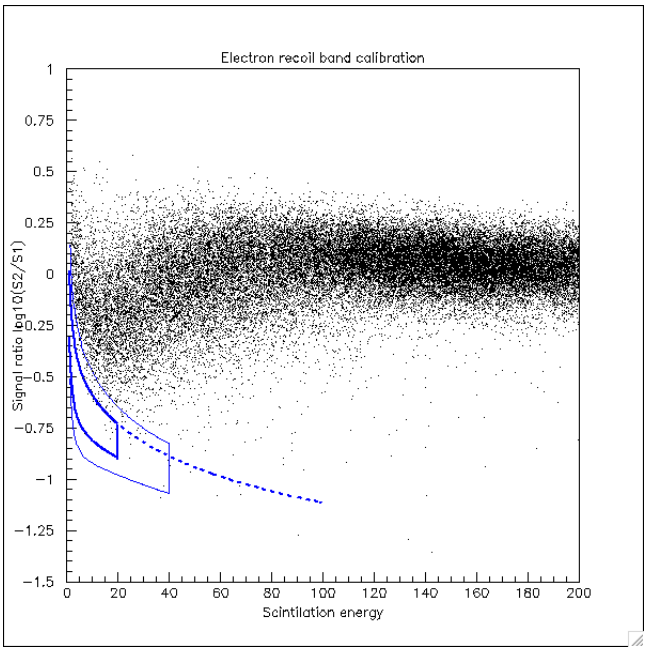

Figure 8.16: A discrimination plot showing the electron recoil band calibration data. The electron recoil band is populated using a ^{137}Cs source. The blue box shows the WIMP search box.

On a daily basis the internal liquid nitrogen vessel was refilled from a large external dewar. During this cryogenic refilling period a ^{57}Co source was inserted into place above the target using the custom built automated machinery. Once the stability of the detector was assured these daily operations were fully automated. On a weekly basis the large external dewar was refilled with liquid nitrogen. During this refill the LED calibration was performed and the detector was re-levelled to account for any geological shifts. This levelling was required to keep the gas gap uniform so that the ionisation response of the detector was constant in the x-y plane.

Significant tilting could jeopardise the science data, and slight tilting can be corrected therefore it was vital to have an accurate measurement of the detector tilt. The width of the gas gap was determined above each PMT in the detector by measuring the width of ionisation signals half way between their baseline and peak height above each PMT, since a larger gas gap produces a longer ionisation signal (i.e. a wider S2). The mean value of this parameter above each PMT can

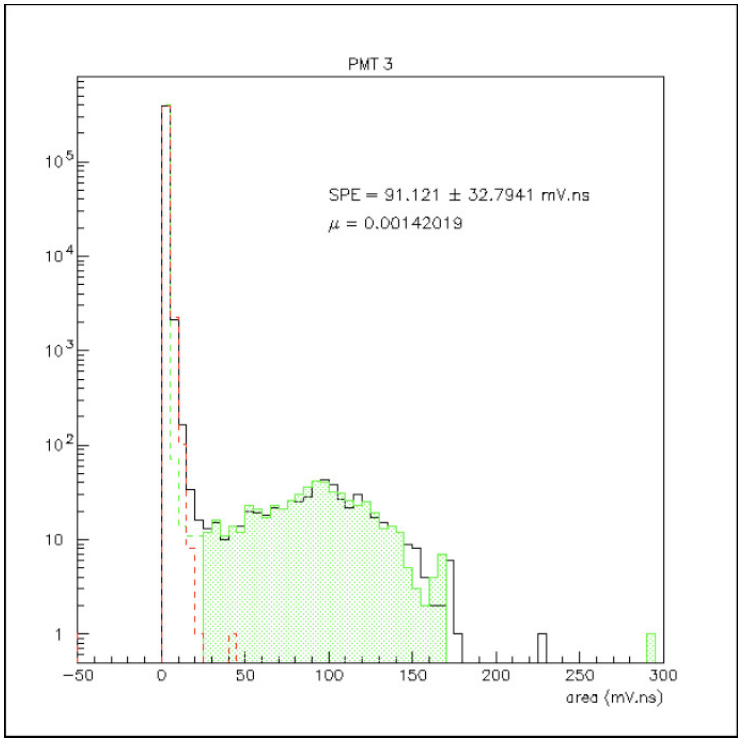

Figure 8.17: The results of an LED calibration showing a single photoelectron peak with a fit for a ZEPLIN–III second science run PMT. The area and error are marked on the plot.

be used to measure the tilt of the detector. A Gaussian distribution was fitted to the parameter to determine the tilt of the detector and the levelling screws on either side of the detector were adjusted to level the detector. A graphical representation of the tilt is shown in figure 8.18

During the second science run the xenon gas gap was maintained at approximately 3.5 mm thickness at a pressure of 1.6 bar with a 13 mbar rms variation over the whole dataset.

8.3 Signal Confirmation Using the Veto

As the vetoed events provide a sample of the background this information can be incorporated into the limits on the signal rate. Although the detector has several discrimination aids, such as the separation of the electron and nuclear recoil bands, the pulse shape and the energy deposited, the improvement given by the veto is mostly clearly demonstrated by considering a generic rare event search with a single background and no additional discrimination beyond the veto. The vetoing efficiency, η, of background events gives the relative exposure of vetoed to un-vetoed background samples: $\frac{\eta}{1-\eta}$. This allows a confidence interval to be set using the profile likelihood ratio, discussed in Section 8.4.2, as implemented in the ROOT [104] class TRolke [135]. Figure 8.19 shows how the number of un-vetoed events in the signal region effects the 3σ evidence of a signal as a function of the veto efficiency. This clearly shows the capacity of a veto to reject the background only hypothesis and increase the discovery potential of a rare event search. In the case of the ZEPLIN–III second science run, with $\eta = 0.28$, about 15 un-vetoed events along with no vetoed events would be required in the signal region to give a 3σ signal [191]. Although this plot does not account for the accidental tagging the rate of both prompt and delayed accidental tagging is low enough not to significantly effect this result.

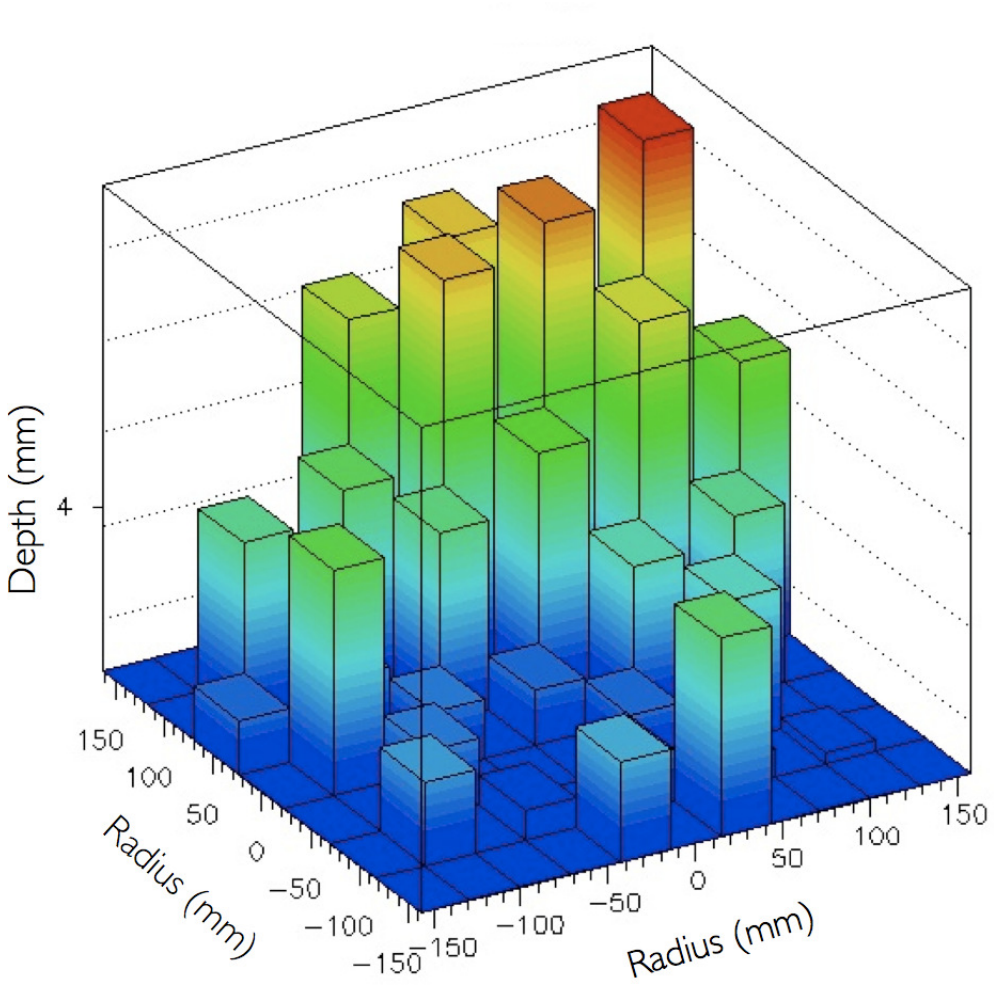

Figure 8.18: A graphical representation of the typical tilt of the ZEPLIN–III detector measured by fitting a Gaussian distribution to the width of the ionisation signal produced in the xenon gas gap above the target. The x and y axes are in mm, with the center at (0,0) and the z axis is plotted on a log scale so that the very slight tilt can be seen.

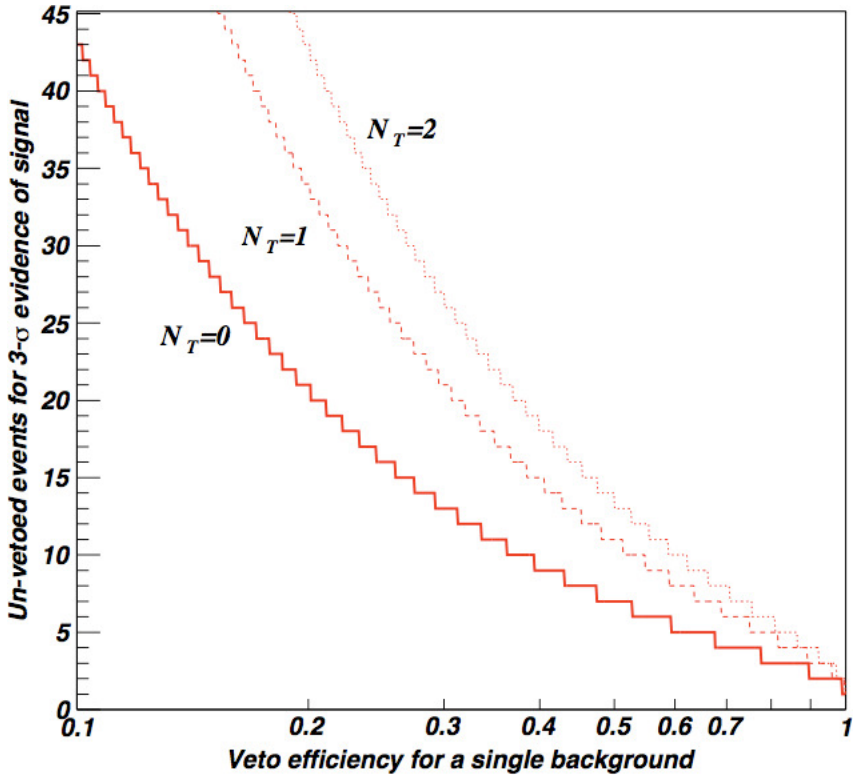

Figure 8.19: The effect of veto efficiency on discovery power for a rare event search with a single background and no additional discrimination [191]. N_T is the number of tagged events observed and the confidence intervals are calculated as in [315].

8.4 WIMP Search Data

8.4.1 Data Analysis

During the second science run the ZEPLIN–III detector collected a raw fiducial exposure of 1343.8 kg·days. Due to the presence of the veto detector, which was able to tag γ-rays with 28% efficiency, a subset of the data containing only background events was available for analysis during the second science run without compromising the blindness of the experiment.

This dataset was useful to asses the stability and effectiveness of the detector early in the science run. This subset was also useful after data taking had finished. It was used to give a representation of the γ-ray background experienced by the detector during the science run without prejudicing the WIMP result. This was more effective than using the ^{137}Cs data since that radiation is emitted from a point source whereas the true background of the experiment may come from any direction with a much broader range of possible energies, many of which may be detected by the veto.

8.4.1.1 Event Selection

The raw data were processed by a custom software package written in C++ and fluid called `ze3ra` (**ZE**PLIN **3 R**eduction & **A**nalysis) [286]. This software was carefully designed to cope with the problems associated with this type of rare event search whilst assuming minimal knowledge of the physical processes involved in order not to bias the data. Two significant challenges posed by dark matter searches are the small size of the signal expected, which must be picked out over the noise, and unusual event topologies, which may not appear in short calibration runs but are much more likely to occur in the very long science runs required to search for dark matter interactions.

Unusual event topologies require `ze3ra` to be flexible enough to cope with new types of event as they are discovered. During the second science run the veto was a useful tool to ensure unexpected events would not contaminate the WIMP search data, since any event with a prompt veto signal could be analysed as soon

as the neutron calibration was complete. The `ze3ra` package contained an event viewer which was blinded to all events near the region of interest, in addition to selection of randomly chosen events. Viewing the waveforms in this subset during data taking allowed unusual events to be accounted for before the data were searched for WIMPs. For this reason, the reduction software assumes only minimal knowledge of the physical processes involved and theses interpretations were deferred to a later analysis stage.

A section of each waveform, of up to 2μs, in the pre-trigger region was analysed to set the baseline. An F-distribution probability function was used to check the variances were statistically consistent, and portions of the timeline failing this test (i.e. including signal) were disregarded for baseline calculation [286]. This method allowed the baseline used for analysis to be flexible enough to cope with any drift introduced by the DAq and also be accurate enough as to allow `ze3ra` to accurately parameterise all genuine signals seen by the detector. The inefficiencies of signal acceptance due to the reduction software improved from $\sim 4\%$ during the first science run to $\sim 0\%$ during the second science run.

`ze3ra` uses a moving average pulse finding algorithm [286] to search the waveform for signals. A threshold of $3\times$ the RMS of the baseline was used to find genuine pulses over the noise level, and once found, the pulses were parameterised and stored as *hbook* n-tuples. The largest 10 pulses were stored in this way for the next stage of data processing, along with all the information about the configuration of the DAq (high voltage levels, event number, time etc.) and the information from the slow control system reading out all the data from the detectors other sensors (temperature, pressure etc.).

A processor called the "golden code" was then used to select good events from the data. This code read in information from detector calibrations to correct the raw pulse information for factors such and drift time and purity. Good events were defined as containing only a single S1 and a single S2, as would be expected from a WIMP event which is highly unlikely to interact more than once in the detector. The S1 and S2 are only loosely defined at this stage using the mean charge arrival time of the pulse; PMT afterpulsing can be differentiated from genuine signals

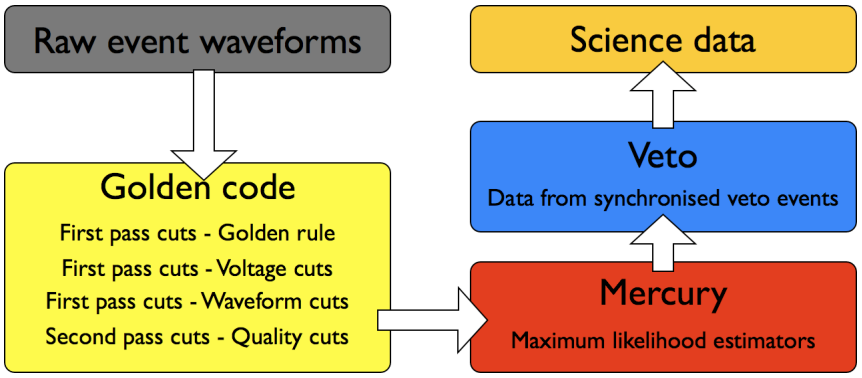

Figure 8.20: A schematic showing how the reduced data was processed to produce a WIMP search data set. Firstly the golden rule is applied. This required each event to have just one S1 signal and one S2 signal. The voltage cuts remove any data recorded during any current fluctuations and the waveform cuts remove any events with HS/LS inconsistencies, DAq mis-triggers etc. The second pass cuts refine the event selection using parameters calculated from calibrations. The program '`mercury`' then processes the remaining events and estimates the position and energy of each event. Finally the data from synchronised veto events is added to give a completed data set.

and be excused at this stage. The events are also checked for consistency between low and high sensitivity channels. Further checks on the voltage levels and on the waveform itself were used to remove any obviously spurious events at this stage. These initial checks were known as the first pass cuts.

Following this initial stage of data processing a series of more stringent cuts were applied to the event, checking the S1 and S2 signals were genuine and consistent with each other as well as further checks using parameters calculated from calibration data. All events surviving this check were then written into new "golden" n-tuples. The `mercury` code [336] was used to reconstruct the energies and positions of the signals and the veto data was then added for each synchronised event. Figure 8.20 shows a schematic of the data processing stages.

8.4.1.2 Cuts Applied to Science Run Data

Following the creation of the golden dataset a final set of cuts were applied to select the science data, to obtain a result for the experiment. As the data were blinded these cuts were created by analysis of calibration data and also the prompt veto subset of the science run data. These cuts were used to both fiducialise the detector by selecting events only from a certain volume and to

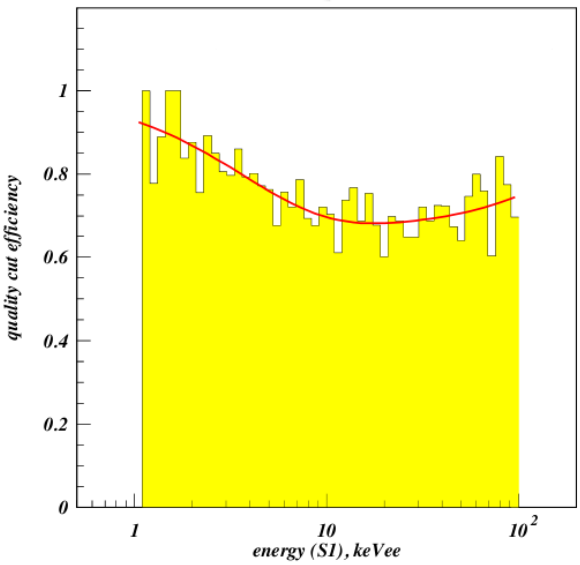

Figure 8.21: The energy dependent efficiency penalty from the second science run data quality cuts as measured by the effect on neutron calibration data.

remove outlying events by observing typical event trends. These cuts had a certain efficiency penalty which was measured by testing the cuts on nuclear recoil band calibration data, as seen in figure 8.21. Since these calibrations were performed using neutrons the efficiency losses are always conservative as WIMPs would only interact once so there are no interfering effects from multiple interactions (whilst most double scatter events are cut by requiring only a single S1 and S2 signal it is possible that some multiple scatters could survive this cut).

A particularly problematic population of events are known as MSSI (multiple scintillation single ionisation) events. These events contain scintillation light from two interactions within the target, where one vertex is within the reverse field region above the PMT array. This region is required to suppress the background events generated from radioisotopes within the PMTs and also to protect the PMT electronics from the high electric field within the target. No ionisation is extracted from interactions within this region so any multiple scatter events with a vertex in this region will have an incorrect scintillation to ionisation ratio. If the

two interactions are close in the X-Y plane then the quality cuts may not remove such an event. This could lead to additional leakage of electron recoils into the nuclear recoil band. These events could be removed by `mercury` in conjunction with data from the veto as 28% MSSI events would have a prompt tag. Following calibrations using the phantom grid (see Figure 8.4), the position reconstruction ability of `mercury` was sufficient to remove most MSSI events. The χ^2 maps of the S1 signal produced by this program should show two separated minima, or a misalignment of the S1 and S2 signal, for most of these events. Only MSSI events very close to the vertical axis could avoid being cut by `mercury` and would rely solely on the veto.

8.4.2 SSR WIMP Results

The second science run dataset contained a total of 20142 events from a 5.1 kg fiducial volume. After the final set of event quality cuts, a total of 19516 events remained for consideration. Figures 8.22 and 8.23 show the distribution of events within the target volume. The γ-rays identified by the veto are uniformly distributed; along with the energy independence discussed in section 6.3.1 this shows no significant populations of un-vetoed events. The delayed veto event tagging is also shown. The number of delayed veto events seen in the dataset is consistent with the rate expected from accidental coincidences. None of these events are seen below the median of the nuclear recoil band which confirms that there is no neutron population present in the low energy data. This achievement was vital for achieving a high sensitivity to WIMP interactions. This is consistent with expectations, the predicted rate of neutrons is 3.05 ± 0.5 events per year between 5 and 50 keV_{nr}. The portion of this expectation in the second science run effective exposure of 251 kg·days (for WIMPS of mass 50 $\mathrm{GeV/c^2}$) and within the WIMP search region is 0.06 ± 0.01 events in anti-coincidence with the veto [26]. These data allow an upper limit (90% CL) of 0.75 neutron events in the search region.

The rate of low energy electron recoils seen in the fiducial region of the science data (with no event quality cuts applied) was 0.75 ± 0.05 events per kilogram per day per keV_{ee} (or 'dru' for differential rate unit) [51]. This confirms

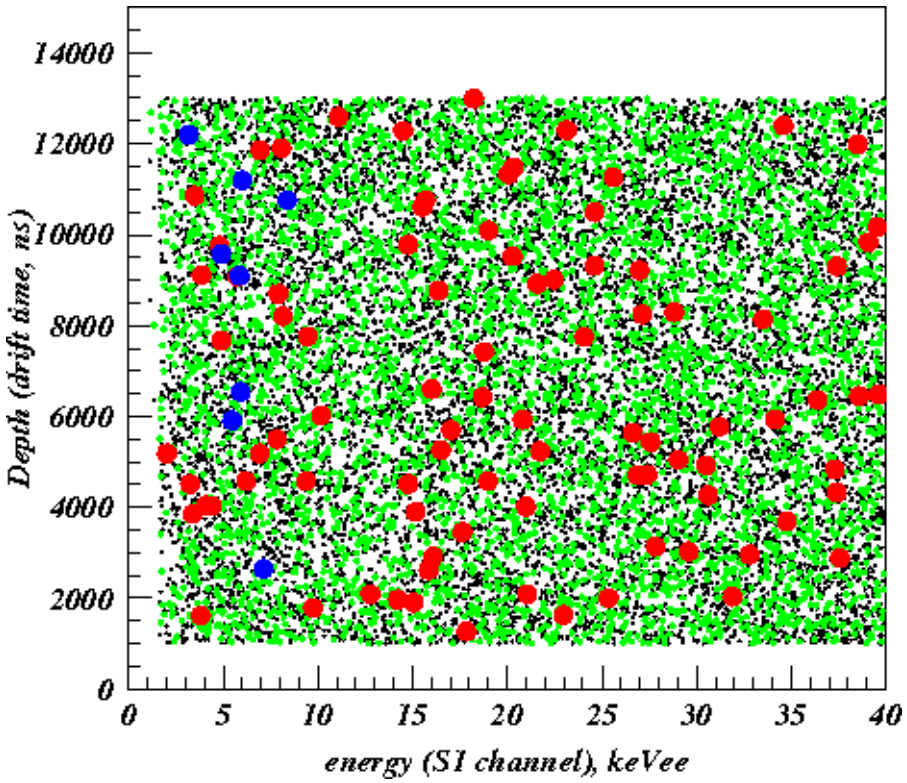

Figure 8.22: A plot showing the depth of events tagged by the veto during the SSR overlaid on-top of all the SSR events (black points). The prompt tags are shown by green dots, the delayed tags are shown by red dots and the unvetoed events within the WIMP search region are shown by blue dots.

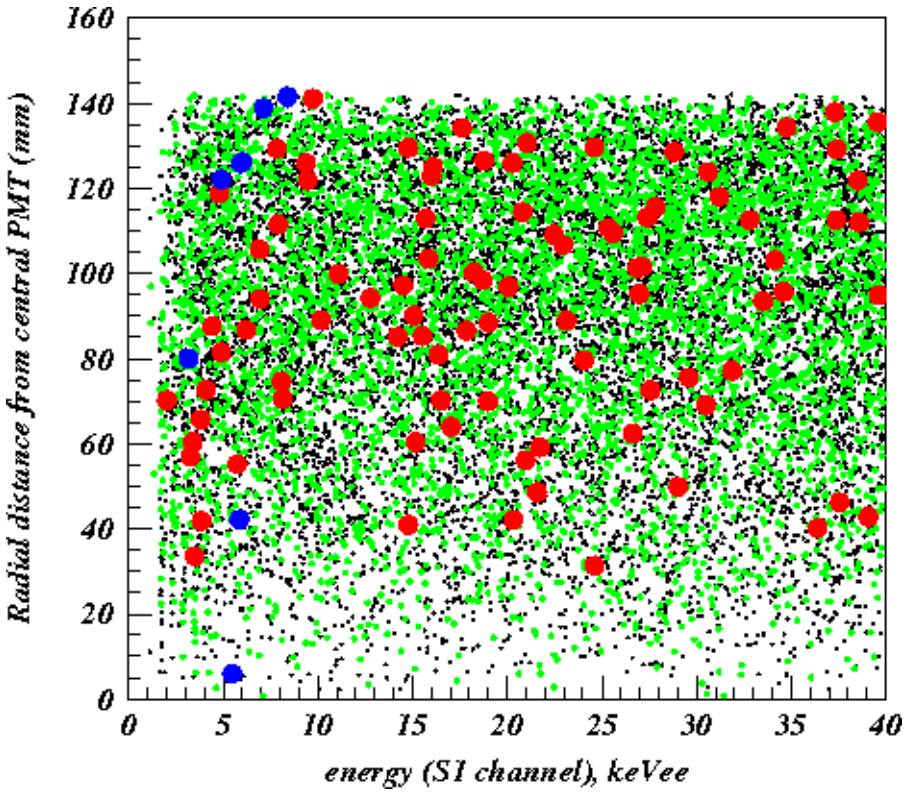

Figure 8.23: A plot showing the radial positions of events tagged by the veto during the SSR overlaid on-top of all the SSR events (black points). The prompt tags are shown by green dots, the delayed tags are shown by red dots and the unvetoed events within the WIMP search region are shown by blue dots.

a significant improvement over the first science run ($\sim$ 20 fold) due to the lower internal background generated by the new PMT array. Monte Carlo predictions accounting for a comprehensive list of background sources suggested 0.86 ± 0.05 dru [51]. The radioactivity measurements used to predict this rate were always conservative but this still shows excellent agreement, as shown by figure 8.24 where the results shown are not scaled to fit.

The data from the ZEPLIN–III second science run are shown in the form of a discrimination plot in figure 8.25. The data is also shown distributed according to WIMP acceptance in figure 8.15. The data show 8 un-vetoed events within the acceptance region. These events are distributed in acceptance as would be expected from leakage from the electron recoil band.

To obtain the WIMP result from the dataset it was first necessary to predict the leakage from the electron recoil background into the WIMP search region. Two different methods were used to estimate the number of electron recoil events. Firstly a binned skew-Gaussian of the form:

$$G(x|A, x_c, w, \alpha) = \frac{A\sqrt{2}}{w\pi} e^{-\frac{(x-x_c)^2}{2w}} \int_{-\infty}^{\alpha \frac{x-x_c}{w}} \frac{1}{\sqrt{2\pi}} e^{-\frac{t^2}{2}} dt \tag{8.4}$$

which reduces to:

$$G(x|A, x_c, w, \alpha) = \frac{1}{w\sqrt{2\pi}} e^{\frac{(x-x_c)^2}{2w}} \left[1 + \mathit{erf}\left(\frac{\alpha}{\sqrt{2}} \frac{x - x_c}{w}\right)\right] \tag{8.5}$$

was fitted to the unblinded data above the WIMP search region. Here A is the amplitude parameter which can be scaled to the number of electron recoil events at the electron recoil mean, and w is the scale parameter defining the spread of the distribution. This factor is a function of the discrimination parameter, $\log_{10}\left(\frac{S2}{S1}\right)$, and is determined by the PMT response. α is the shape of the skew-Gaussian and is also set by the detector's ability to discriminate between electron and nuclear recoils. The Gaussian error function, *erf*, is related to the Gaussian by:

$$\mathit{erf}\left(\frac{x}{\sigma\sqrt{2}}\right) = \int_{-x}^{x} G(x) dx \tag{8.6}$$

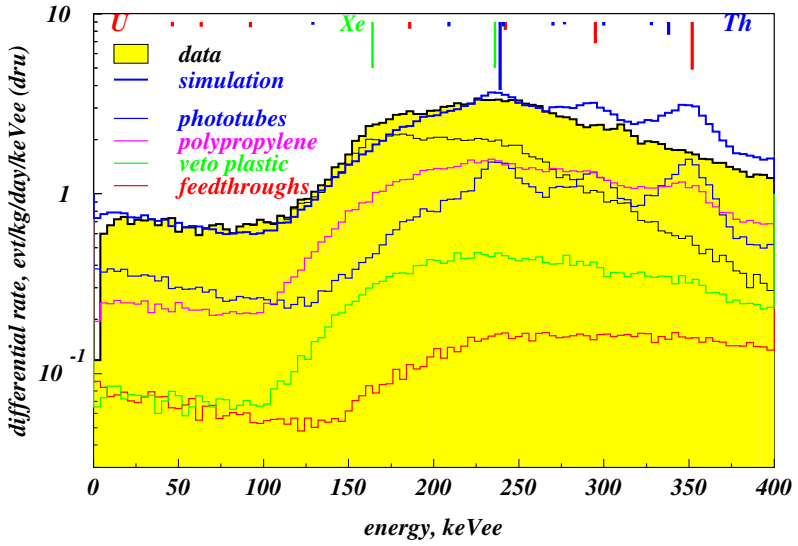

Figure 8.24: A comparison of the simulated electron recoil background in ZEPLIN–III to second science run data. U/Th and Xe activation γ-rays are indicated. Note that the dynamic range of the data is restricted by saturation effects which become significant around 150 keV$_{ee}$. The simulated results were not scaled to the data in this plot.

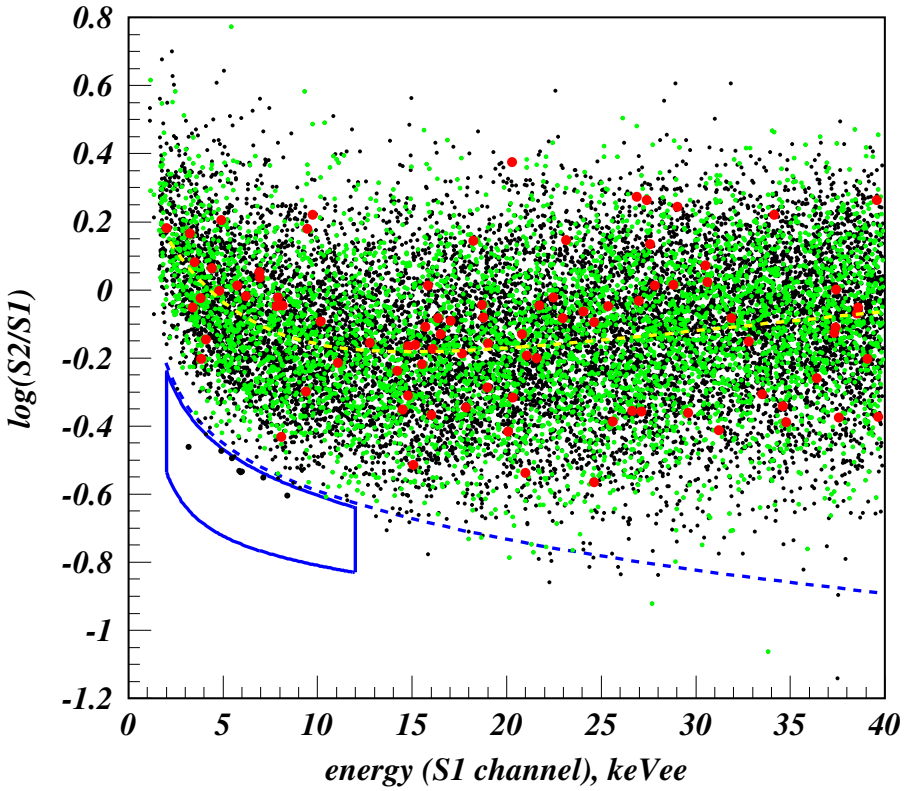

Figure 8.25: A scatter plot of the ZEPLIN–III second science run data (black points). This plot shows the discrimination between electron recoils and nuclear recoils as a function of energy. The mean of the electron recoil band is shown by the dashed yellow line and the mean of the nuclear recoil band is shown by the dashed blue line. The WIMP search region is shown by the blue box. Inside the WIMP search box 8 events can be seen located near the upper boundary closest to the electron recoil band. The green points show events with a prompt veto tag (mostly γ-rays) and the red points show events with delay veto tags (consistent with accidental coincidences) [26]. Assuming these outliers are background rather than signal these events are currently poorly understood.

The mean and standard deviation of the distribution given in equation 8.5 are given by:

$$\mu = x_c + w\delta\sqrt{\frac{2}{\pi}} \tag{8.7}$$

$$\sigma^2 = w^2\left(1 - \frac{2\delta^2}{\pi}\right) \tag{8.8}$$

The mean and variance are related to the shape of the skew by $\delta = \frac{\alpha}{\sqrt{1+\alpha^2}}$ in equations 8.8 and 8.7. Although there is as yet no good physical motivation behind this form of fit, in practice it was found that a non Gaussian tail from rare topology events combined with a Gaussian distribution of electron recoil events was best approximated by a skew-Gaussian. The number of events predicted to leak into the WIMP search box in each energy bin is given by extrapolation using the formula:

$$n_{est} = \int_{box_{lower}}^{box_{upper}} G(x|A, x_c, w, \alpha)dx \tag{8.9}$$

where $box_{upper/lower}$ are defined by the nuclear recoil band as described in section 8.2.3. A example of a skew-Guassian fit to the second science run data is shown in figure 8.26. Fitting to the science run data does leave the possibility of biasing the fits by the presence of a signal, however this method gave excellent agreement with the second method used to estimate the background in the box. This method simply involved scaling the ^{137}Cs calibration data to the exposure of the second science run. A summary of the predictions given by both methods along with the observed number of events is given in Table 8.1. This table also lists the relevant signal acceptance parameters and quotes the upper limit on the number of possible signal events that could be present along with the background events. Due to the probability of finding background events leaking into the WIMP search box this region was further partitioned in order to maximise sensitivity given by the skew-Gaussian fits. Monte Carlo sampling of the background was used to calculate optimum partition. The Feldman-Cousins (FC) method [172] gave maximum sensitivity with a partition at 24% acceptance. Table 8.1 shows good agreement between background predictions in these regions and the number of events observed once the data was unblinded.

A confidence interval for the signal expectation in the second science run was calculated with a Profile Likelihood Ratio (PLR) [26, 315, 92]. This method is

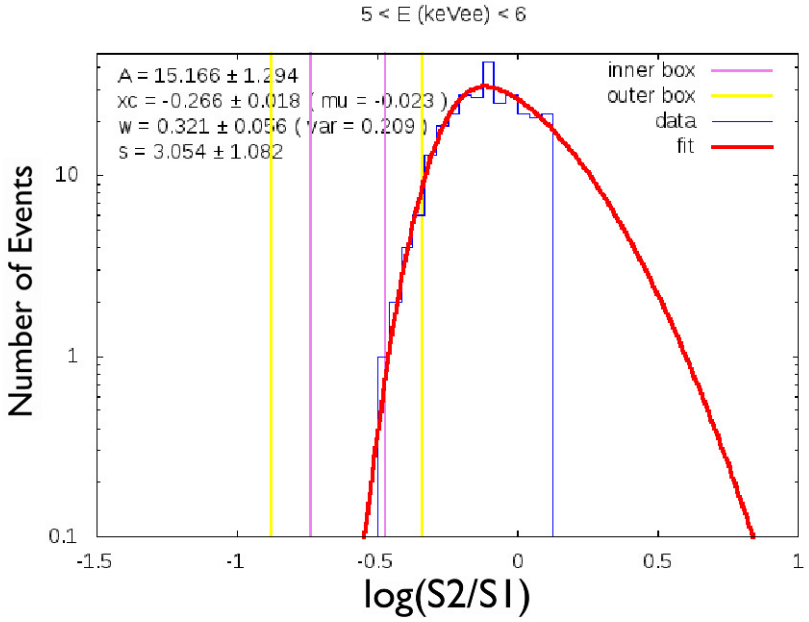

Figure 8.26: An example of a skew-Gaussian fit to the electron recoil background to predict the number of events leaking into the WIMP search box. The WIMP search box used in the second science run is shown in purple.

Table 8.1: Observations (n_{obs}), background estimations ($\mu_{b1,b2}$) and limits on the expected signal (μ_{signal}) for the first and second science run (FRS and SSR respectively). Effective exposures are presented for 50 GeV/c^2 WIMP mass along with relevant signal acceptance parameters. The electron recoil background expectations are calculated using skew-Gaussian (SG) fits to the WIMP search region in 2 keV$_{ee}$ bins and also from an equivalent exposure to a ^{137}Cs source. The 90% CL limits on the number of signal events were derived using the profile likelihood ratio method.

Run	kg·days (net)	acceptance keV$_{nr}$	acceptance fraction	n_{obs}	neutrons μ_{b1}	electrons recoils, μ_{b2} GS fit	^{137}Cs	μ_{signal}
FSR	437.0	7-35	29-35%	4	0.5±0.3	5.3±3.1	-	<4.2
	(107.3)		2-29%	1	0.7±0.3	1.5±1.7	-	
SSR	1,343.8	7-29	24-45%	7	0.03±0.005	5.5±2.2	8.3±2.9	<5.1
	(251.0)		2-24%	1	0.03±0.005	1.0±1.2	1.0±1.0	

outlined in Appendix A.18.

8.4.2.1 Excluding WIMP-nucleon Cross Section Parameter Space

The limit on the number of signal events in the data was then used to set upper limits on the scalar WIMP-nucleon elastic scattering cross-section. The cross-section limit is dependent on the astrophysical model assumed and so to compare direct detection searches a standard model is used. These calculations assume a standard galactic halo of WIMPs characterised by $\rho_0 = 0.3$ GeV/c^2/cm^2, $v_0 = 220$ km/s, $v_{escape} = 544$ km/s and $\langle v_\oplus \rangle = 232$ km/s [256]. Also using a Helm form factor [208] parameterised as in [32], given by equation 3.9.

The detector characteristics must be included in equation 3.3 to obtain the WIMP spectrum that ZEPLIN–III would expect to see. The energy resolution was first accounted for. The expectation in each energy bin was altered to account for the smearing effect caused by the finite energy resolution discussed in section 8.2.1. Also the characteristic efficiencies of the detector are folded in, these are as seen in figure 8.11. Once these effects have been considered the expected WIMP spectrum seen by ZEPLIN–III can be compared to the SSR data and used to set limits on the WIMP-nucleon interaction cross section. Figure 8.27 shows an example of the differential WIMP spectrum expected in the SSR.

The final step before comparing the expected spectrum to the data is to convert the expected recoil spectrum to the correct energy scale, using the energy dependent relative scintillation efficiency calculated in section 8.2.2. Once the data are on the correct energy scale the limit on the number of events was divided by the exposure to give the differential rate, r, of events·kg^{-1}·day^{-1}. This result was then compared to the expected WIMP spectrum to obtain a limit on the interaction cross-section.

The event rate is related to the interaction cross-section, $\sigma_{\chi-T}$, by:

$$\frac{R_0}{r} = \frac{D \cdot \sigma_{\chi-T}}{\mu^2_{\chi-T}} \tag{8.10}$$

R_0 is the integrated predicted WIMP spectrum in the WIMP search box, the

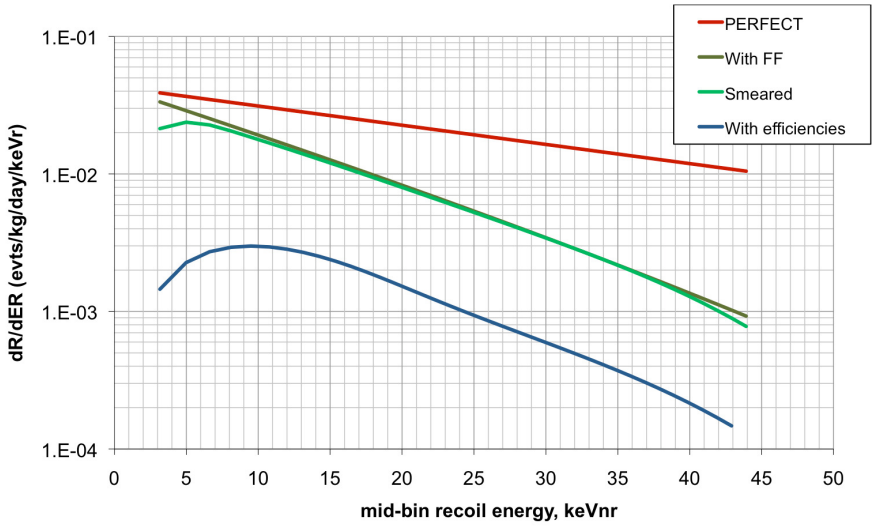

Figure 8.27: The differential spectrum expected to be observed by the ZEPLIN–III detector. The spectrum for perfect detection is shown by the red curve. The brown curve shows the effect of folding in the nuclear form factor, the green curve shows the effect after smearing is considered and the blue curve shows the effect of also folding in the detector efficiency (shown as a function of energy in Figure 8.21).

reduced mass of the colliding particles is given by $\mu_{\chi-T} = \frac{M_T \cdot M_\chi}{(M_T+M_\chi)}$ and $D = 94.3$ is a numerical factor accounting for the density of dark matter [256]. Since different targets are used for dark matter searches the convention is to report the WIMP-nucleon cross-section, $\sigma_{\chi-n}$, to give a target independent result. For the spin independent limit this is given by:

$$\sigma_{\chi-n} = \left(\frac{\mu_{A=1}}{\mu_T}\right)^2 \left(\frac{1}{A_T}\right)^2 \sigma_{\chi-T} \tag{8.11}$$

hence the limit for the experiment is calculated by:

$$\sigma_{\chi-n} = \left(\frac{\mu^2_{A=1}}{A^2 D}\right) \frac{R_0}{r} \tag{8.12}$$

solving this equation for an array of different WIMP masses leads to a WIMP-nucleon cross-section limit curve for spin independent scattering. This is calculated across the full range of theoretical WIMP masses from 10 to 1×10^5 GeV/c^2. The ZEPLIN–III second science run limit plot is shown in figure 8.28 along with the combined limit for the whole ZEPLIN–III experiment and limits

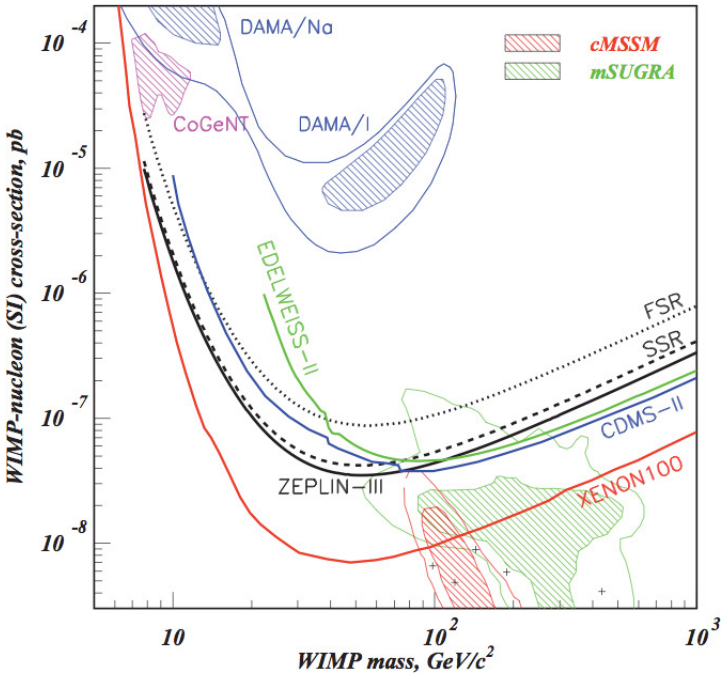

Figure 8.28: Limits at 90% confidence on the WIMP-nucleon scalar cross-section. This shows both the ZEPLIN–III limits and also the combined limit for the whole experiment [26]. Also shown are limits from XENON100 [46], CDMS-II [136] and EDELWEISS-II [55]. Blue contours are used to represent the 3σ and 5σ DAMA/LIBRA results from Ref.[326] (2008 data, no ion channelling [81]). The magenta contour is the fit to the CoGeNT data under a light WIMP hypothesis [2]. The crosses show the SUSY benchmark points from Ref [161]. Favoured regions of a Bayesian analysis in mSUGRA [371] and the likelihood analysis of LHC data within cMSSM [106] is also shown.

from some other dark matter searches. The limits shown cover a range of possible WIMP masses centred around the region of highest sensitivity. The minimum of the curve for the second science run is at 4.8×10^{-8} pb for a WIMP mass of 55 GeV/c^2. This result assumes the mean value for the relative scintillation efficiency, or $\mathcal{L}_{\mathbf{eff}}$, shown in figure 8.9. Adopting the $\mathcal{L}_{\mathbf{eff}}$ mean$+1\sigma$ would give a minimum of 4.7×10^{-8} pb for a 51 GeV/c^2 WIMP mass and 2.2×10^{-6} pb for a WIMP mass of 10 GeV/c^2. Adopting $\mathcal{L}_{\mathbf{eff}}$ mean-1σ gives minima of 5.2×10^{-8} pb for a 51 GeV/c^2 WIMP mass and 9.3×10^{-6} pb for a WIMP mass of 10 GeV/c^2. The combined (FSR+SSR) result was obtained from a four-bin PLR calculation; this shows a sensitivity reach for the ZEPLIN–III experiment of 3.9×10^{-8} pb for a WIMP mass of 52 GeV/c^2.

Spin-dependent (axial-vector) interaction cross-section limits were also calcu-

Table 8.2: Values of $\Lambda^2 J(J+1)$ for the two isotope of xenon which contribute to spin interactions.

Isotope	J	$\Lambda^2 J(J+1)$	
		single particle	odd group
^{129}Xe	1/2	0.75	0.124
^{131}Xe	3/2	0.15	0.055

lated for the ZEPLIN–III experiment. This type of interaction arises from the final term in the spin-dependent cross-section given in equation 3.14. Here the interaction cross-section is proportional to $J(J+1)$ where J is the nuclear spin. Although the spin-dependent interaction with the nucleus is still coherent in the sense that the scattering amplitudes are summed, any paired nucleons cancel out and only residual unpaired nucleons contribute to the scattering amplitude. Hence in this experiment the two neutron-odd isotopes ^{129}Xe ($J^\pi = 1/2^+$) and ^{131}Xe ($J^\pi = 3/2^+$) provide sensitivity to spin interactions. The xenon used in the ZEPLIN–III target is depleted in ^{134}Xe and ^{136}Xe and so consists of 29.5%^{129}Xe and 23.7%^{131}Xe. This composition slightly enhances its sensitivity so spin interactions compared to natural isotope levels (26.4% and 21.2% respectively). The isotope specific WIMP-proton and WIMP-neutron interaction cross-sections were calculated by:

$$\frac{\sigma_p}{\sigma_{\chi-T}} = \frac{\mu_p^2}{\mu_T^2} \frac{[\Lambda^2 J(J+1)]_p}{[\Lambda^2 J(J+1)]_T} \left(\frac{C_{\chi-p}}{C_{\chi-N}} \right)^2 \tag{8.13}$$

this equation has been normalised to the WIMP-proton cross section as denoted by the sub-script p, $C_{\chi-N}$ is the WIMP-nucleon spin factor (a linear combination of neutron or proton couplings to $\tilde{\gamma}, \tilde{H}, \tilde{B}$ and $\tilde{Z}$ as given in Ref. [256]) and values for the typical target element spin factors, $\Lambda^2 J(J+1)$, are given in Table 8.2.

The resulting WIMP-neutron spin-dependent interaction cross-section limits are shown in figure 8.29. A peak sensitivity was reached for a 50 GeV/c^2 WIMP mass at 8.0×10^{-3} pb by combining the first and second science run data.

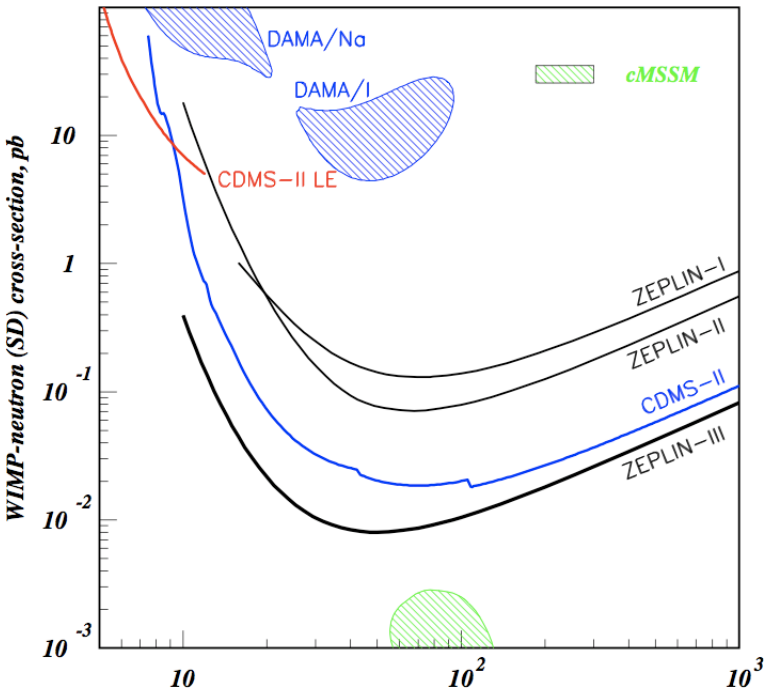

Figure 8.29: Limits on the spin-dependent WIMP-neutron cross-section from the ZEPLIN–III experiment (combined FRS and SSR) [26] assuming no proton interaction and Bonn CD nucleon-nucleon potential [368]. Also shown are the limits from previous ZEPLIN experiments [32] [34], CDMS-II data (2004-9) [136] [20] plus low-energy (LE) analysis [21]. The blue contours show the 3σ DAMA region (2008 data with no ion channelling [81]) from Ref. [326]. The green hatched area shows the 95% probability region of cMSSM neutralinos [319].

Chapter 9

Summary

A significant body of evidence now exists suggesting that almost a quarter of the energy density of the Universe is in the form of dark matter. The most favoured candidate is cold dark matter particles in the form of WIMPs. As dark matter exists within galactic halos these WIMPs are detectable via their occasional interactions with baryonic matter. One of the most promising methods of detection is via measurement of the energy deposited by nuclear recoils off xenon atoms in a two-phase time projection chamber. Using two phases allows for the measurement of energy deposited in 2 different channels, scintillation and ionisation, which allows discrimination between nuclear recoils and the dominant electron recoil background. The time projection allows accurate 3D event reconstruction which enables the self shielding properties of xenon to be exploited. During its 2 science runs the ZEPLIN–III detector has successfully demonstrated the use of a two-phase xenon time projection chamber to produce very competitive limits of WIMP-nucleon interaction cross-sections.

The detector was based at the Boulby Mine in Cleveland, UK. The 2800 m.w.e rock overburden provides a $\sim 10^6$ reduction in the muon flux. Combined with the effects of locating the laboratory within a seam of low radioactivity salt, and the use of lead and polypropylene shielding, which reduce the γ-ray and neutron flux by a factor of $\sim 10^5$, this provides an excellent low background environment in which to conduct a rare event search.

During the first science run of ZEPLIN–III the instrument acquired science

data for 83 days. The results from this exposure allowed a limit to be set on the WIMP-nucleon spin-independence cross-section of 8.8×10^{-8} pb for a 56 GeV/c^2 WIMP mass at 90% C.L.. The power of the discrimination achieved during the first science run between nuclear and electron recoils was 1:7800. This is the highest achieved by any liquid xenon dark matter detector. Following an upgrade, the second science run lasted for 305 days with an exposure of 1750 kg days (Figure 9.1). At the time of publication this was the longest run of any liquid xenon dark matter detector. Furthermore this run was halted, as planned, for analysis to produce a science run rather than due to a loss of system stability. When combined with the first science run data this allows the exclusion of a spin-dependent WIMP-nucleon cross-section above 3.5×10^{-8} pb for a 52 GeV/c^2 WIMP mass at 90% C.L., making ZEPLIN–III one of the most sensitive instruments in the world. Due to valence neutrons present in xenon the data also allow the exclusion of a spin-dependent WIMP-neutron cross-section above 7.2×10^{-3} pb for a 50 GeV/c^2 WIMP mass at 90% C.L.. This is the world's best limit.

The upgrade of the instrument before the second science run included the replacement of the PMT array with new custom made low-background PMTs. The first science run demonstrated the limitations which may be caused by dead regions within the detector. The reverse field region used to protect the PMTs and suppress unwanted background from them also allowed for the possibility of multiple scattering single ionisation events. These events contain scintillation light from interactions in both the dead region and the fiducial volume, but contain only electroluminescence from ionisation cause by the interaction within the fiducial volume. The second science run PMT array represents a 40 fold reduction in background activity which significantly reduced the chances of this type of event occurring. The upgrade also included the addition of an active veto. This detector was able to detect (28.1 ± 0.2)% of background events from the fiducial volume of ZEPLIN–III, including the multiple scintillation single ionisation events. The veto also detects (60.5 ± 0.5)% of single scattering neutrons from the fiducial volume of ZEPLIN–III. As these events represent the greatest potential threat to the WIMP sensitivity of the instrument this demonstrates the vital nature of an effective veto to a dark matter detector. An additional

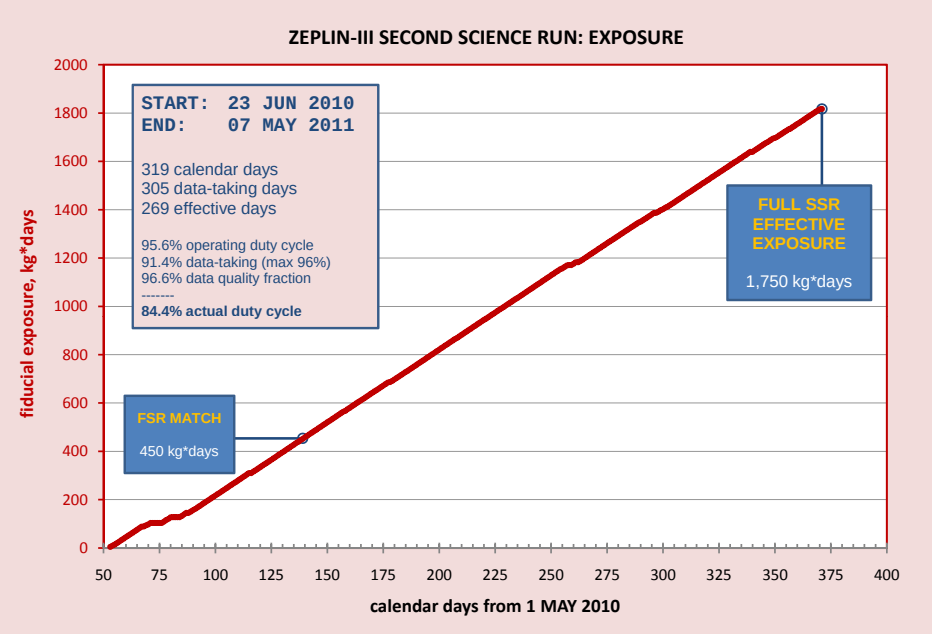

Figure 9.1: The progress of the ZEPLIN–III second science run.

benefit of including a separated veto detector was demonstrated by its use during a blind data analysis. The veto provided over a quarter of the background data for analysis during the science run without risking biasing of the WIMP results. By simply requiring a veto event be present, above some threshold, at the trigger point in an event triggered by ZEPLIN–III, it could be guaranteed that, aside from a 0.43% accidental coincidence chance, the event was not a WIMP interaction. This allowed any anomalies to be quickly detected and rectified (for example problems with the DAq or rare event topologies unaccounted for by the data analysis software).

I was involved in many aspects of this experiment and made a valuable contribution leading to the SSR result. The majority of my contribution was to the veto detector. After assembling the veto I was responsible for the data it produced. I wrote the reduction software and the analysis code and produced datasets of vetoed data that could be analysed without compromising the blindness of the WIMP analysis. I also demonstrated how the veto may be used in

conjunction with the main instrument for additional analyses, such as searching for exotic forms of dark matter and measuring radiological contamination. I also demonstrated the benefits of recording a low resolution version of the main detectors sum channel in the veto DAq, which records a much longer timeline. I made valuable contributions to the analysis of the main SSR result, setting a competitive limit on the WIMP-nucleon interaction cross-section.

Future liquid xenon dark matter detectors could benefit from the techniques used during the ZEPLIN–III experiment. The measurement of radioactive contaminants, such as ^{85}Kr, from science run data have proved much more accurate than previous techniques using, for example, RGA. Purifying the xenon using cryogenic pumping negated the possibility of introducing contaminants from the getters. The purity was maintained, and even increased, by the application of the drift field during the science run. Future detectors will require very high levels of purity, due to their increased target size. Detector stability, such as that achieved by ZEPLIN–III, will also be required for the success of these experiments. As the veto recorded a much longer timeline than ZEPLIN–III this allowed for additional analyses to be carried out, such as an accurate measurement of the radon contamination and the analysis of muon events and their after affects.

The future of liquid xenon dark matter detectors looks bright. The LUX detector, with a 350 kg target, is currently being moved underground ready to commence science operations. The XMASS experiment, with an 800 kg target, will shortly be ready to recommence science operations following an early hiccup during calibration and construction of the XENON1T detector is underway. With the recent probable discovery of the Higgs boson the phase space in which dark matter particles may exist can further be constrained. The Higgs boson is a key ingredient of the neutralino, a theoretical particle to which dark matter particle detectors are usually tuned. However, as these detectors perform rare event searches they are sensitive to many forms of dark matter particle which may arise from this discovery. As discussed in Section A.14 the announcement of the potential discovery of the Higgs boson at around 125 GeV/c^2 heavily constraints the phase space for SUSY particles. Dark matter detectors may also constrain this parameter space and if the Higgs boson is confirmed then a $\sim$ton scale

noble liquid detector could be expected to either discover mixed higgsino CDM or essentially rule out thermally-produced neutralino-only CDM in the mSUGRA model [62].

Appendix A

Appendix

A.1 The Age of the Universe

Information from the cosmic microwave background can be used to deduce the age of the Universe. The fundamental mode of vibration in the early Universe can be measured from the angular size of the strongest temperature fluctuation in the cosmic microwave background. This is measured as 0.601 ± 0.005 degrees [383]. Plasma physics tells us that the longest acoustic wave that could be supported is 143 ± 4 Mpc [383], in-fact the sound horizon at the release of the CMB can be measured as discussed in Section 2.3.3, this shows $r_s = 146.2 \pm 1.1$ Mpc [231]. Combining these two gives the longest distance through spacetime from today to the release of the cosmic microwave background as $\sim$44 billion light years, so the upper bound on the age of the Universe is $\sim$44 billion years. Other astronomical measurements, such as the expansion rate and the Universe's contents, are combined with this result to determine the exact age. The contents are significantly different today than they were at the time of last scattering, as shown in Figure A.1. Combining all this information gives an age of 13.75 ± 0.11 Gyr [231].

This age measurement relies on cosmological models. The significance of this measurement, and the parameters of the model used to produce it (including attributing a significant proportion of the Universe's energy density to dark matter), can be increased by checking if this measurement is in line with other independent measurements of the Universe's age. Historically this was often

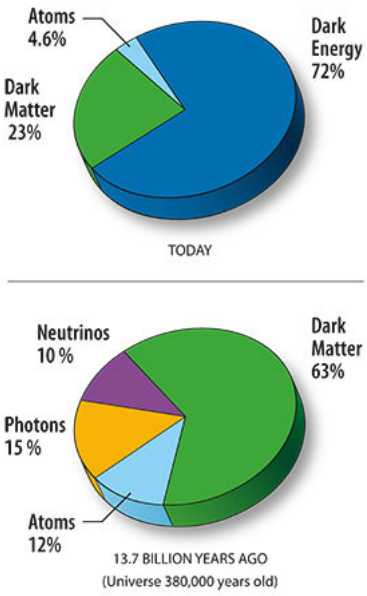

Figure A.1: The contents of the Universe now and at the epoch of the release of the cosmic microwave background. Image obtained from the WMAP website [284].

a source of controversy, with the very early scientific estimates indicating a relatively young Earth. The first successful attempts to calculate the age of the Universe began with ageing rocks here on Earth, since this would set a lower limit on the age. The oldest rocks found on Earth come from the Nuvvuagittuq greenstone belt in Northwest Canada. These rocks are estimated to be $4.28^{+0.05}_{-0.08}$ billion years (Gyr) old [290]. Older meteors have been found, the oldest of these containing specks of calcium-aluminium-rich inclusions (CAIs). These were found in carbonaceous chondrites from the meteor Efremovka which landed in Kazakhstan in 1962. These deposits are estimated to have formed 4.5647 ± 0.0006 Gyr ago [39]. These dates are consistent with the estimated age of the Sun (although much more accurate) from current knowledge of stellar evolution. With a well established lower limit on the age of the Universe (by measuring the age of the solar system) determined in laboratories on Earth we know that the Universe must of course be older than this since all elements above lithium were produced by stars. The age of the Milky Way galaxy can be estimated by measuring the relative abundance of ^{187}Re and ^{187}Os, giving an age range of 11.5 to 15.5 Gyr [94]. A better estimate of the age of the Milky Way can be determined from estimating the age of the oldest objects it contains. The oldest white dwarves

found are in the globular cluster NGC 6121, measured at 12.7 ± 0.7 Gyr [201]. It should be noted however that globular clusters are quite difficult to age with much variation within the literature. The oldest known globular clusters are the Messier clusters NGC 7078, NGC 4590 and NGC 6341. Their ages are estimated at 12.2 ± 1.8 Gyr [324]. Radioactive dating of the metal poor star CS 31082-001 via ^{238}U and ^{232}Th gives the age of this star as 14.1 ± 2.5 Gyr [380]. Observations of the accelerating expansion of the Universe can also be used to date the length of the expansion, although this relies on the cosmological model somewhat as it requires dark energy. This gives an age of 14.2 ± 1.7 Gyr [312].

The measurements used by many of these independent methods require the Universe to be older than their respective results as the rely on some amount of evolution before the phenomena occur. They are all in good agreement with the age measured by the WMAP probe using the CMB observations and a model of the Universe containing approximately 23% dark matter and 72% dark energy.

A.2 Riemann Curvature Tensor

The Ricci tensor and Ricci scalar are contractions of the general Riemann curvature tensor:

$$R^{\alpha}{}_{\mu\sigma\nu} \equiv \Gamma^{\alpha}{}_{\nu\mu,\sigma} - \Gamma^{\alpha}{}_{\sigma\mu,\nu} + \Gamma^{\alpha}{}_{\sigma\beta}\Gamma^{\beta}{}_{\mu\nu} - \Gamma^{\alpha}{}_{\nu\beta}\Gamma^{\beta}{}_{\mu\sigma} \tag{A.1}$$

where the Γ's are the Christoffel symbols describing parallel transport of vectors over curved surfaces. In general, by considering two geodesics $x^{\alpha}(\tau)$ and $x^{\alpha}(\tau) + y^{\alpha}(\tau)$ for a general τ and by considering how the small separation $y^{\alpha}(\tau)$ grows it can be shown that the covariant derivative is:

$$\frac{D^2 y^{\alpha}}{D\tau^2} = R^{\alpha}{}_{\mu\sigma\nu}\dot{x}^{\mu}\dot{x}^{\sigma}y^{\nu} \tag{A.2}$$

which establishes the connection between curvature ($R^{\alpha}{}_{\mu\sigma\nu}$) and gravity (through $\frac{D^2 y^{\alpha}}{D\tau^2}$). In flat space the Riemann tensor is zero, and initially parallel paths will always remain parallel. Non zero values represent curved space where initially parallel lines may not remain so. This curvature tensor is contracted to give the

Ricci tensor as:

$$R^{\alpha}{}_{\mu\alpha\nu} \equiv R_{\mu\nu} \tag{A.3}$$

and to give the Ricci scalar as:

$$R^{\mu}{}_{\mu} \equiv R. \tag{A.4}$$

A.3 Einstein Tensor with a Robertson-Walker Metric

Applying the Eular-Lagrange equations to the Robertson-Wlaker metric gives the Christoffel symbols for each parameter, by defining $a \equiv 1 - kr^2$ these can be written in matrix form as:

$$\Gamma_t = \begin{pmatrix} \cdot & \cdot & \cdot & \cdot \\ \cdot & \frac{\dot{R}}{R} & \cdot & \cdot \\ \cdot & \cdot & \frac{\dot{R}}{R} & \cdot \\ \cdot & \cdot & \cdot & \frac{\dot{R}}{R} \end{pmatrix} \quad \Gamma_r = \begin{pmatrix} \cdot & \frac{\dot{R}R}{a} & \cdot & \cdot \\ \frac{\dot{R}}{R} & \frac{kr}{a} & \cdot & \cdot \\ \cdot & \cdot & \frac{1}{r} & \cdot \\ \cdot & \cdot & \cdot & \frac{1}{r} \end{pmatrix}$$

$$\Gamma_\theta = \begin{pmatrix} \cdot & \cdot & \dot{R}Rr^2 & \cdot \\ \cdot & \cdot & -ar & \cdot \\ \frac{\dot{R}}{R} & \frac{1}{r} & \cdot & \cdot \\ \cdot & \cdot & \cdot & \cot\theta \end{pmatrix} \quad \Gamma_\phi = \begin{pmatrix} \cdot & \cdot & \cdot & R\dot{R}r^2\sin^2\theta \\ \cdot & \cdot & \cdot & -ar\sin^2\theta \\ \cdot & \cdot & \cdot & -\sin\theta\cos\theta \\ \frac{\dot{R}}{R} & \frac{1}{r} & \cot\theta & \cdot \end{pmatrix}$$

where zeros are represented by dots.

These can be combined using Equation A.1 to give the Riemann tensor. The (anti-)symmetry of this tensor, $R^{\alpha}{}_{\mu\sigma\nu} = -R^{\alpha}{}_{\mu\nu\sigma}$, can be used to give the Ricci tensor as:

$$R_{\mu\nu} = \begin{pmatrix} -\frac{3\ddot{R}}{R} & \cdot & \cdot & \cdot \\ \cdot & \frac{A}{a} & \cdot & \cdot \\ \cdot & \cdot & Ar^2 & \cdot \\ \cdot & \cdot & \cdot & Ar^2\sin^2\theta \end{pmatrix} \tag{A.5}$$

where $A \equiv R\ddot{R} + 2(\dot{R}^2 + k)$. The Ricci scalar is then:

$$R = -6\left(\frac{\ddot{R}}{R} + \frac{\dot{R}^2 + k}{R_2}\right) \tag{A.6}$$

then using the definition of the Einstein tensor in terms of the Ricci tensor and scalar gives:

$$G_{\mu\nu} = \begin{pmatrix} -\frac{3(\ddot{R}^2+k)}{R^2} & \cdot & \cdot & \cdot \\ \cdot & a\left(\frac{2\ddot{R}}{R} + \frac{\dot{R}^2+k}{R^2}\right) & \cdot & \cdot \\ \cdot & \cdot & a\left(\frac{2\ddot{R}}{R} + \frac{\dot{R}^2+k}{R^2}\right) & \cdot \\ \cdot & \cdot & \cdot & a\left(\frac{2\ddot{R}}{R} + \frac{\dot{R}^2+k}{R^2}\right) \end{pmatrix} \tag{A.7}$$

A.4 The Space-time Curvature

The space-time curvature can be related to the contents of the Universe by equation 2.5. The source of gravity, ρ, can be related to the potentials ($g_{\mu\nu}$) to give a tensor. From a relativistic treatment $\rho = \gamma^2\rho_0$ where ρ_0 is the density of the matter in its rest frame, one factor of γ is gained by Lorentz contraction and another factor is due to the increase in relative mass of the matter particles due to their velocity. The four vector of the matter is given by $U^\mu = \gamma(c, \vec{u})$, as transforming a second rank tensor brings in two factors of γ. The energy-momentum tensor is given by:

$$T^{\mu\nu} = \rho_0 U^\mu U^\nu \tag{A.8}$$

which is the energy-momentum tensor of dust, or a pressure-free and viscosity-free perfect fluid. Allowing for a fluid with pressure, p, this becomes:

$$T^{\mu\nu} = (\rho + p)U^\mu U^\nu - p g_{\mu\nu} \tag{A.9}$$

the pressure and density are related by :

$$p = (\kappa - 1)\rho \tag{A.10}$$

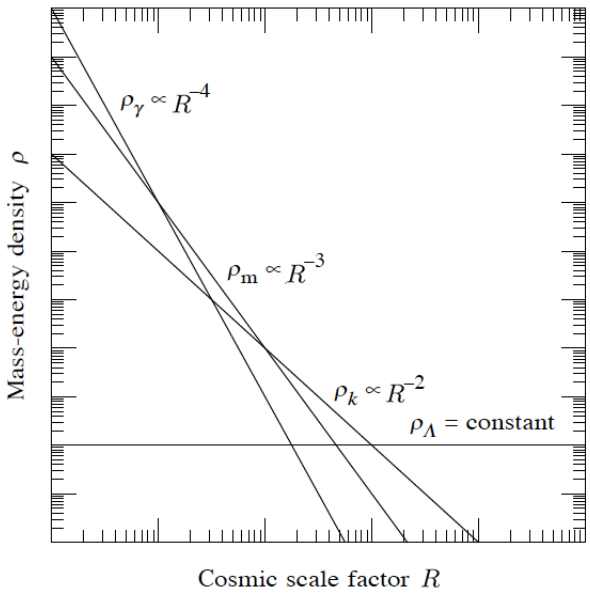

Figure A.2: The behaviour of the mass-energy density, ρ, of various species as a function of cosmic time. Image obtained from [360].

where the contents of the Universe describe its evolution by the equation of state parameter, $w = (\kappa - 1)$, which depends on how the density varies in the volume. In a radiation dominated Universe the number density scales with the volume, $n \propto R^{-3}$, multiplied by an additional factor since photons are relativistic and the energy per particle varies as $E \propto R^{-1}$, so that the density scales as $\rho_\gamma \propto R^{-4}$. The energy-momentum tensor from equation A.8 has trace $-\rho + 3p$ yet must be traceless, hence the equation of state for a radiation dominated Universe is $p_\gamma = \frac{1}{3}\rho$ and $\kappa = \frac{4}{3}$. This is a good approximation for the hot, dense, early Universe with its blackbody spectrum. In a non-interacting matter dominated Universe the density varies as $\rho_m \propto R^{-3}$ and $\kappa = 1$, there is no pressure so $p_m = 0$. A vacuum energy dominated Universe has negative pressure, $\kappa = 0$ as the vacuum density is constant giving the equation of state as $p_\Lambda = -\rho_\Lambda$. This is the likely future of the Universe since observations show the expansion is accelerating [312]. It is also believed that a similar equation of state was present during the early inflationary period discussed in Section 2.2.1. The effect of the equation of state on the evolution of the Universe is shown in Figure A.2; this also includes the curvature density which is defined in Equation A.14.

A.5 The Density Parameter

The dimensionless density parameter is defined as:

$$\Omega = \frac{\rho_T(0)}{\rho_c(0)} = \frac{8\pi G\rho_T}{3H^2} \tag{A.11}$$

such that the Friedmann equation from 2.20 becomes:

$$\frac{k}{H^2R^2} = \Omega - 1 \tag{A.12}$$

where the total density is defined as the sum of all the components of the Universe $\Omega = \Omega_\gamma + \Omega_m + \Omega_\Lambda$ and the individual components are given by:

$$\Omega_\gamma \equiv \frac{\rho_\gamma(0)}{\rho_c(0)} \ , \ \Omega_m \equiv \frac{\rho_m(0)}{\rho_c(0)} \ , \ \Omega_\Lambda \equiv \frac{\Lambda}{3H_0^2}. \tag{A.13}$$

If these components do not sum to unity then the difference gives rise to a 'curvature density' $\rho_k \equiv \frac{3k}{8\pi GR^2}$. Although this is not a form of mass-energy it is convenient to treat it as such in the Friedmann equations. The curvature density parameter is given by:

$$\Omega_k = 1 - \Omega \tag{A.14}$$

The Ω parameter then defines how the Universe evolves. There are three different scenarios, illustrated in Figure A.3. If the different components of the Universe sum to give $\Omega = 1$ then the right hand side of equation A.12 is zero, hence $k = 0$ and the Universe is flat and infinite. If the density exceeds the critical density then $k > 0$, or by normalising to R_0 then $k = 1$. In this scenario the Universe has positive curvature as described by spherical surfaces. This type of Universe is finite and closed; the gravitation attraction of the mass of the Universe could potentially cause its eventual collapse in a 'big crunch', however this scenario is very unlikely due to the effects of Λ. The third scenario is a combination of densities which sum to less than the critical density so $\Omega < 1$. In this scenario $k < 0$ (or $k = -1$ by normalising to $R(t)$) and the Universe has negative curvature, as described by saddle shaped surfaces. This type of Universe is open and infinite.

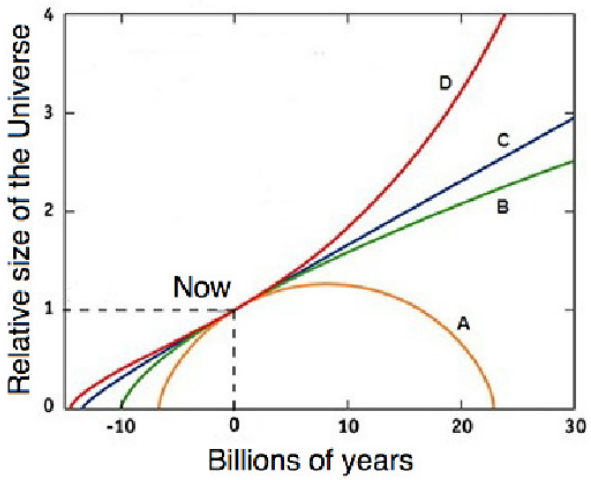

Figure A.3: The expansion of the Universe described by $R(t)$ for four different scenarios. If $k = 1$ space-time has positive curvature and the Universe is closed and will eventually collapse in on itself due to the gravitational attraction of the matter contained within it, curve A. If $k = 0$ the Universe is at critical density, space-time is flat with no curvature and the Universe will expand forever at an increasingly slower rate. Curves B and C show this where B shows a flat critical Universe that will eventually stop expanding and C shows a coasting Universe which is flat but expands forever. If $k = -1$ then space-time has negative curvature (as described by a hyperbolic surface or saddle), in this case the rate of expansion will increase at an exponential rate shown by curve D. Image adapted from [284].

By rearranging equation A.12 for k and substituting this equation back into the solution to the field equation, 2.17, and using the definition of red shift $z + 1 = \frac{R_0}{R(t)}$, the expansion rate of the Universe can be defined in terms of observables, in this case the redshift z, as:

$$\tilde{H}(z) = \left[\Omega_\gamma(1+z)^4 + \Omega_m(1+z)^3 + \Omega_\Lambda + \Omega_k(1+z)^2\right]^{\frac{1}{2}}. \tag{A.15}$$

This is known as the Friedmann-Lemaitre equation (for a review see [227]). The first term shows that radiation acts to increase the expansion rate with increasing z, hence reducing the expansion rate over time. The second term shows matter has a similar effect although with a less strong dependence on z. The third term accounting of dark energy has no dependence on z and remains constant over time. This indicates that a vacuum energy $\Lambda > 0$ would eventually come to dominate the Universe as the matter and radiation components diminish with increasing volume. The last term acts to decrease the expansion rate of an over-critical Universe ($\Omega > 1$) with positive curvature, but would act to increase the expansion rate of an under-critical Universe ($\Omega < 1$) with negative curvature.

In the limit $t \to \infty$ all terms except the dark energy term tend to zero such that:

$$\left(\frac{H_\infty}{H_0}\right)^2 = \Omega_\Lambda \tag{A.16}$$

where H_∞ is the value of H at $t = \infty$. By the definition given in equation A.13 this means:

$$\Lambda = 3H_\infty^2 \tag{A.17}$$

and if initially $\Lambda > 0$ then at late times $\Omega_\Lambda \to 1$.

The time-scale of the evolution can be calculated by integrating $\frac{H(t)}{H_0} = \sqrt{\frac{\rho_c(t)}{\rho_c(t_0)}}$ with respect to cosmic time (via the time dependent cosmological expansion scale factor):

$$t = \int \frac{dR}{RH} \tag{A.18}$$

writing H in terms of the densities of the components of the Universe, $H_0(\Omega_\gamma R^{-4} +$

Table A.1: How the Universe scales with cosmic time depending on the nature of the dominant species.

Dominant species		R$\propto$
Radiation	Ω_γ	$t^{\frac{1}{2}}$
Matter	Ω_m	$t^{\frac{2}{3}}$
Curvature	Ω_k	t
Vacuum	Ω_Λ	e^{Ht}

$\Omega_m R^{-3} + \Omega_k R^{-2} + \Omega_\Lambda$), gives an expression for the time-scale:

$$t = \frac{1}{H_0} \int \frac{dR}{R\sqrt{\Omega_\gamma R^{-4} + \Omega_m R^{-3} + \Omega_k R^{-2} + \Omega_\Lambda}} \tag{A.19}$$

if a single species dominates the Universe then this equation can be integrated to give the scale-factor time-scale, as shown in Table A.1.

A.6 Inflation

Inflation is described by a transitory scalar-field represented by Λ in Equations 2.17 and 2.18, acting as negative-pressure on space-time. This scalar-field drives the rapid expansion as it relaxes to the vacuum, eventually falling to $\Lambda \rightarrow 0$ where normal expansion once again resumes. The mechanism for the inflation is currently not understood, but one possible explanation is symmetry breaking at the GUT unification point, as discussed in Section 2.4, at $\sim 10^{-36}$ seconds. The energy released here may have caused an over-pressure that was applied directly to space-time itself [28]. The dynamics of the inflation may be described using the Klein-Gordon equation:

$$\frac{\ddot{\phi}}{c^2} - \left(\nabla^2 - \frac{m^2 c^2}{\hbar^2} \right) \phi = 0 \tag{A.20}$$

where ϕ represents the scalar-field (or 'inflaton'). If an initial domain is considered where the field is uniform then the subsequent dynamics of $\phi(t)$ are synchronised throughout the observable Universe (i.e. the inflated patch). Adding in a 'Hubble drag' friction term, $3H\dot{\phi}$, which opposes clumping allows this to be written in the

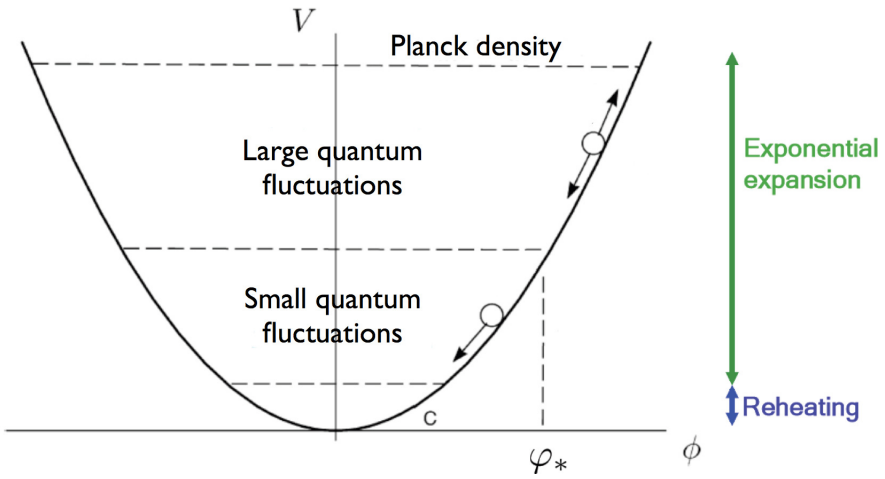

Figure A.4: An illustration representing the slow roll regime. $\phi^\star$ represents the crossover between quantum and classical fluctuations in the scalar-field where $\phi > \phi^\star$ when $\delta\phi_{quantum} > \delta\phi_{classical}$. Image adapted from [258].

form of a harmonic oscillator in a potential $V(\phi)$:

$$\ddot{\phi} + 3H\dot{\phi} = -\frac{d}{d\phi}V(\phi) \tag{A.21}$$

where $V(\phi) = \frac{\phi^2 m^2 c^4}{2\hbar^2}$. The energy is conserved between pure potential at the top and kinetic energy (which is thought to cause the re-heating) at the bottom, as illustrated in Figure A.4. The ability of the scalar-field oscillations to have a state of pure potential is what allows inflation to take place. When the energy is all potential, $\dot{\phi}^2 \ll V(\phi)$, this is like a time varying vacuum energy with $E = V(\phi)$. This limit is called the "slow-roll" regime because the scalar-field moves down the potential slowly relative to the expansion rate and the energy remains almost constant.

A scalar-field synchronised as mentioned above so that $\phi = \phi(t)$ has an energy-momentum tensor:

$$T_{\alpha\beta} = \partial_\alpha\phi\partial_\beta\phi - \frac{1}{2}g_{\alpha\beta}g^{\mu\nu}\partial_\mu\phi\partial_\nu\phi - g_{\alpha\beta}V(\phi) \tag{A.22}$$

which reduces to:

$$T_{00} = \frac{1}{2}\dot{\phi}^2 + V(\phi) \ , \ T_{ij} = \left(\frac{1}{2}\dot{\phi}^2 - V(\phi)\right) g_{ij} \tag{A.23}$$

hence the pressure and density are given by:

$$\rho(t) = \frac{1}{2}\dot{\phi}^2 + V(\phi) \ , \ p(t) = \frac{1}{2}\dot{\phi}^2 - V(\phi) \tag{A.24}$$

which leads to a time-dependent equation of state parameter:

$$w(t) = \frac{p(t)}{\rho(t)} = \frac{\frac{1}{2}\dot{\phi}^2 - V(\phi)}{\frac{1}{2}\dot{\phi}^2 + V(\phi)} \tag{A.25}$$

where w is related to equation A.10 simply by $w = \kappa - 1$. During slow roll this mimics the cosmological constant, $w = -1$, and the pressure of the scalar-field is $-V(\phi)$. In this model the Universe begins in a potential dominated state until the onset of inflation. This was a period of super-cooled expansion with a temperature drop from $\sim 10^{27}$ K to $\sim 10^{22}$ K [192]. This low temperature was maintained during the inflationary period until the potential energy of the scalar-field decayed into particles, a process known as reheating. Although weakly interacting, the field does couple to other particles, and its oscillations can generate other particles - thus transforming the scalar-field energy into the energy of the radiation dominated Universe which followed the inflationary period.

A.7 Eras of the Universe

During the radiation dominated era of the Universe the importance of gravity was greatly diminished. The dynamics of the Universe were relativistic and baryonic matter could not begin to clump together when dominated by radiation. The dark matter though was unaffected by radiation and began to fall towards over-densities. This phase of the Universe persisted until the matter density, ρ_m, became larger that the radiation density, ρ_γ. The cross over point where the Universe became matter dominated can be found using $(1 + z) = \frac{\rho_0^m}{\rho_0^\gamma} = \frac{\Omega_m h^2}{\Omega_\gamma h^2}$. Using a simple calculation from the temperature of the CMB for the radiation density, $\rho_\gamma = 4\sigma T^4 c^{-3}$, and the matter density from the ΛCDM model gives a

redshift for this change in global equation of state as $(1 + z_{eq}) = 40208\Omega_m h^2$. However the neutrinos are relativistic and should be counted with the radiation, as their density scales the same (rather than scaling like matter), despite having some mass. At the later stages of the big bang only light particles (γ,ν,e) survive in equilibrium, as the temperature drops below $T \sim 10^{9.7}$ K, the electron pair threshold, the electrons and positrons annihilate. The annihilations could in principle yield equal numbers of pairs of photons and neutrinos, however, since weak reactions freeze out earlier at $T \sim 10^{10}$ K the number of photons is enhanced relative to the number of neutrinos. Entropy is conserved in this process so the relative abundances can be calculated by:

$$s(\gamma, e^+, e^-) = s(1 + 2 \times \frac{7}{8})s(\gamma) = \frac{11}{4}s(\gamma) \tag{A.26}$$

where the degeneracy $g = 2$, for polarisation and spin, gives the factor of two and the factor of $\frac{7}{8}$ comes from the different equilibrium occupancy numbers for bosons ($\propto 1$) and fermions ($\propto \frac{3}{4}$). Since entropy $\propto T^3$ the temperature of the radiation field is a factor of $\left(\frac{11}{4}\right)^{\frac{1}{3}}$ higher than the background neutrinos hence this implies a current neutrino background with a temperature of:

$$T_\nu = \left(\frac{4}{11}\right)^{\frac{1}{3}} T_\gamma = 1.95 \text{ K}. \tag{A.27}$$

Adding this to the density for relativistic species gives an extra factor of:

$$\frac{\rho_\nu}{\rho_\gamma} = 3 \times \frac{7}{8}\left(\frac{T_\nu}{T_\gamma}\right)^4 = \frac{21}{8}\left(\frac{4}{11}\right)^{\frac{4}{3}} \approx 0.68 \tag{A.28}$$

where the factor of three represents three neutrino species. The redshift of radiation-matter equality is divided by 1.68 and so occurs much later at $(1+z_{eq}) = 23933\Omega_m h^2 \approx 3200$ [231].

This era was followed by a period of matter domination. During the radiation dominated era of the Universe, the radiation density produced almost all of the gravitational force. During this era fluctuations in the dark matter density can only grow if the dark matter and radiation fall into over-densities together. This does not occur for small perturbations as the photons move out of the potential

well at the speed of light. These small fluctuations therefore do not grow until the Universe becomes matter dominated. Growth in a radiation dominated Universe only occurs for the large perturbations where there has not been sufficient time for the matter and radiation to separate. The length-scale that separates the two regimes will be the horizon distance. Once the Universe becomes matter dominated there should be a characteristic break in the fluctuation spectrum around the comoving horizon length at this time. This is known as the Mészáros effect [277] measuring the comoving horizon size at z_{eq} it is possible to determine $\Omega_m h^2$.The current era of the Universe, domination by vacuum energy, began after the matter dominated era, when the Universe was about five billion years old.

A.8 Nucleosynthesis and Freezeout

The number density of particles per mode is given by:

$$n(\vec{p})d^3p = f\frac{d^3p}{h^3} \tag{A.29}$$

where the equilibrium occupancy number for a state of given energy ϵ is given by:

$$\langle f\rangle = \frac{1}{e^{\frac{\epsilon(p)-\mu}{kT}} \pm 1} \tag{A.30}$$

where the $+1$ is for Fermions, the -1 is for Bosons and μ is the chemical potential. The distribution of momenta depends on the energy per particle, $\epsilon^2 = m^2c^4 + p^2c^2$. The total number density is calculated by integrating over energy:

$$n = g\int n(\vec{p})d^3p = \frac{4\pi g}{c^3h^3}\int \frac{\sqrt{\epsilon^2 - m^2c^4}}{e^{\frac{\epsilon-\mu}{kT}} \pm 1} \tag{A.31}$$

In the relativistic limit where $kT \gg mc^2$ the masses of the particles are insignificant and they behave like radiation, if the chemical potential is also negligible ($\mu \ll m$, non-degenerate) then:

$$n = \frac{g\delta\zeta(3)}{\pi^2}\left(\frac{kT}{\hbar c}\right)^3 \tag{A.32}$$

where δ is $\frac{3}{4}$ for Fermions, 1 for Bosons and $\zeta(3) \simeq 1.202$ is the Riemann zeta function. The energy density can be found using a similar calculation to the number density:

$$\epsilon = g \int \epsilon(p) n(\vec{p}) d^3p. \tag{A.33}$$

In the relativistic limit this gives:

$$\epsilon = g\delta \frac{\pi^2 (kT)^4}{30(\hbar c)^3} \tag{A.34}$$

where δ is $\frac{7}{8}$ for Fermions and 1 for Bosons. The pressure can be calculated as $p = \frac{\epsilon}{3}$ and the ratio of the energy density to number density gives the average energy per particle:

$$\langle E \rangle = \frac{\epsilon}{n} \simeq \begin{cases} 3.15kT & \text{Fermions} \\ 2.70kT & \text{Bosons} \end{cases} \tag{A.35}$$

At earlier times the temperature was higher by the redshift factor, $T = (1+z)T_0$. For any particle of mass m there is a redshift such that the $kT \gg mc^2$ limit is satisfied and the particles behave like radiation; therefore the number density of particles behaving as radiation increases with red shift. As the Universe expands and cools the number density changes so that in the non-relativistic limit the ± 1 in the occupancy number may be neglected and bosons and fermions behave the same with:

$$n = g \left(\frac{mkT}{2\pi\hbar^2} \right)^{\frac{3}{2}} e^{-\frac{(mc^2 - \mu)}{kT}}. \tag{A.36}$$

This shows that at the threshold value of $kT \sim mc^2$ a background of particle antiparticle pairs will be produced. As the temperature falls below the threshold annihilations take over and the number density decays exponentially. A notable problem with this is that it also suggests the Universe should be barren of all matter (and anti-matter) due to symmetric annihilations. This clearly did not occur in the observable Universe. Since the pressure in the ultra-relativistic limit is $p = \frac{\epsilon}{3}$ so that the entropy scales as $\propto T^3$ and the number density here scales as $\propto T^3$, this shows that the entropy just counts the number of particles. The entropy per baryon may be calculated from the ratio of the number density of photons in the Universe to the number density of baryons. The blackbody number

density of photons at a frequency ν is given by the Planck function:

$$n(\nu)d\nu = \frac{8\pi}{c^3}\frac{\nu^2 d\nu}{e^{\frac{h\nu}{kT}} - 1}. \tag{A.37}$$

Integrating gives the total number density in a proper volume as:

$$n_\gamma = \left(\frac{kT}{hc}\right)^3 16\pi\zeta(3) \simeq 413 \text{ cm}^3 \tag{A.38}$$

which is the density of CMB photons at $T_0 = 2.7$ K. Using the WMAP measurement of $\Omega_b h^2 \simeq 0.023$ and the average mass of a proton and neutron the number density of baryons is:

$$n_b = \Omega_b h^2 / m_b \simeq 2.6 \times 10^{-7} \text{ cm}^{-3} \tag{A.39}$$

therefore there are

$$\eta \equiv \frac{n_b}{n_\gamma} \sim 10^{-9} \tag{A.40}$$

baryons per photon, which has been approximately constant since the big bang. This ratio justifies the adiabatic assumption since most of the entropy is in the photons. In the relativistic limit this would have been ∼unity so the fractional violation of the matter anti-matter symmetry should be at about the 10^{-9} level. At around 10^{13} K, the Universe had a thermal background of protons and antiprotons, this ratio suggests there was about one extra proton per 10^9 antiprotons once the temperature dropped below the threshold and annihilations took over. In order for the Universe to develop asymmetry, as observed, the Sakharov conditions must be met by some interaction [322]. These conditions assume the Universe began in a symmetric initial state. The mechanism by which the observed asymmetry was produced is currently not known. Possible solutions to this include the difference in the oscillations of neutrinos and antineutrinos [370]. The Long Baseline Neutrino Experiment (LBNE) proposed at Fermi lab is one of the experiments which will investigate this possibility. Another possibility is strong CP violation, discussed in Section 2.4.

A.9 Big Bang Nucleosynthesis

Following baryogenesis, when stable protons and neutrons were formed, nuclear reactions assembled progressively heavier nuclei until the temperature became too low a few minutes after the big bang. After the initial thermal background of protons and neutrons (at $\sim 10^{13}$ K) the neutrons and protons were then kept in thermal equilibrium via weak interactions with the electron-positron and neutrino backgrounds:

$$p + e^- \leftrightarrow n + \nu_e$$
$$n + e^+ \leftrightarrow p + \bar{\nu}_e$$

and the relative number densities of neutrons and protons varied according to a Boltzmann factor based on their mass difference:

$$\frac{n_n}{n_p} = e^{-\frac{\Delta mc^2}{kT}}. \tag{A.41}$$

This neutron-proton ratio undergoes freeze-out at some characteristic value. Since most helium is ^{4}He, the helium fraction, by mass, which is observed to be 0.249(9) [289], can be used to determine the freeze-out ratio of $\frac{n_n}{n_p} \simeq \frac{1}{7}$. The weak reaction rates are known so this ratio can also be calculated by considering the reaction time-scale for a proton in a thermal background of electrons or a neutron in a thermal background of neutrinos (the rates are the same as this occurs above the e^+e^- threshold). When this time-scale equals the local Hubble time the proton-neutron ratio is frozen out, which happens at:

$$T(\text{neutron freeze-out}) \simeq 10^{10.14} \text{ K} \tag{A.42}$$

so by equation A.41 this gives:

$$\frac{n_n}{n_p} \simeq 0.34. \tag{A.43}$$

This is clearly higher than the observed helium fraction indicates. This is due to the close proximity of the electron-positron freeze-out and also due to neutron decay. Free neutrons decay spontaneously into protons with a lifetime of 881.5 ± 1.5 seconds [283]. Neutrons can be "locked up" in deuterium once

conditions become favourable. The binding energy of a deuteron is 2.22 MeV, so high energy photons from the tail of the black body spectrum destroy most Deuterium shortly after it forms until the thermal energy drops below $\sim$ 0.1 MeV. This deuterium bottleneck held back the formation of heavier nuclei as is required as an intermediate step. Due to the higher binding energy per nucleon of ^{4}He (7 MeV, as opposed to 1.1 MeV for Deuterium) its formation is favoured thermodynamically and eventually almost all of the neutrons end up in ^{4}He. Observations of deuterium in quasar absorption systems gives the ratio of deuterium to protons as $\frac{D}{H} = 2.82(21) \times 10^{-5}$ [299].

The main nuclear reactions during big bang nucleosynthesis are given below:

$$
\begin{aligned}
& n \rightarrow p + e^- + \bar{\nu}_e && p + n \rightarrow D + \gamma \\
& D + p \rightarrow {}^3He + \gamma && D + D \rightarrow {}^3He + n \\
& D + D \rightarrow T + p && T + D \rightarrow {}^4He + n \\
& T + {}^4He \rightarrow {}^7Li + \gamma && {}^3He + n \rightarrow T + p \\
& {}^3He + D \rightarrow {}^4He + p && {}^3He + {}^4He \rightarrow {}^7Be + \gamma \\
& {}^7Li + p \rightarrow {}^4He + {}^4He && {}^7Be + n \rightarrow {}^7Li + p
\end{aligned}
$$

Due to the low density ($\propto$ air) at this stage only two-body reactions are significant. Elements past lithium and beryllium were not formed as there are no stable isotopes with five or eight nucleons. The nucleosynthesis period ended too quickly for this gap to be overcome. Figure A.5 illustrates the isotope ratios during the big bang nucleosynthesis process.

A.10 Dark Matter in Clusters

The virial velocities method assumes that the cluster is spherically symmetric and its components are in a relaxed equilibrium state. The galaxies then act similarly to a fluid in hydrostatic equilibrium where orbits in random directions play the role of pressure so that $p = \rho\sigma_v^2$ where σ_v is the rms dispersion of velocities. For

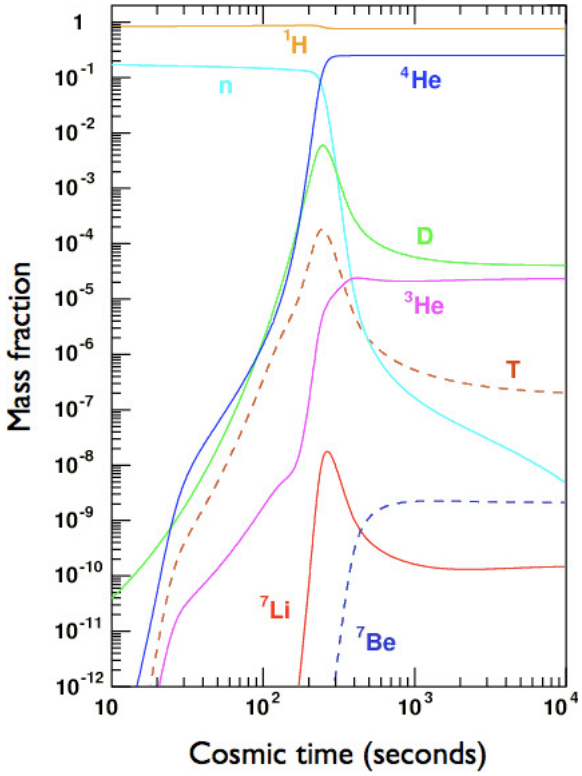

Figure A.5: The mass fraction of light elements against cosmic time shows the evolution of the light elements during big bang nucleosynthesis [127].

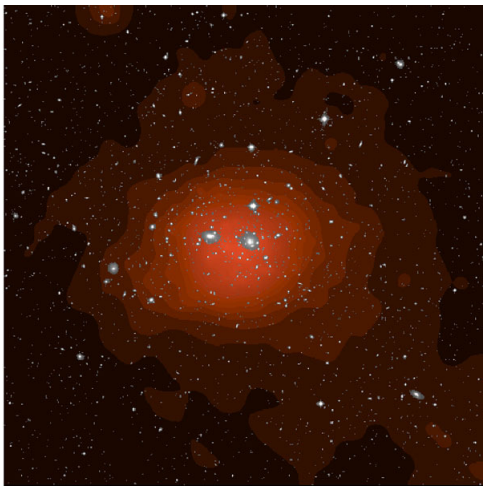

Figure A.6: An X-ray image of the Coma cluster obtained by the ROSAT all sky survey (red) [146], overlaid with an optical image from the Palomar Sky Survey [137].

equilibrium this means:

$$-\frac{\partial\Phi}{\partial r} = -\frac{GM(<r)}{r^2} = \frac{1}{\rho_g}\frac{\partial}{\partial r}\rho_g\sigma_v^2 \tag{A.44}$$

where Φ is the gravitational potential and ρ_g is the mass density. Hence the mass can be found by deprojecting the galaxy surface brightness, yielding a value of M up to an unknown factor, which predicts the shape of $\sigma_v^2(r)$ if it is assumed that light traces mass. Scaling to the velocity dispersion gives an estimate of the mass-to-light ratio from which an estimate of the total mass can be made. More accurate measurements have since been made of the Coma cluster giving a mass of $1.88^{+0.65}_{-0.56} \times 10^{15} h^{-1} M_\odot$, whereas the combined mass of the galaxies (optical) and gas (X-ray) account for only $\sim 1.66 \times 10^{14} M_\odot$ [250], which still implies a significant dark matter component. Figure A.6 shows an optical and X-ray map of the Coma cluster.

This modern result relies on measurements of X-rays emitted by gas in the cluster to both estimate the total mass and to calculate the mass of the major baryonic component, as most of the mass is in the form of X-ray emitting gas rather than stars. This gas is known as the intracluster medium and mostly consists of ionised hydrogen and helium that has been superheated to millions of degrees as it responds to the large potential of the cluster. This gas has extremely

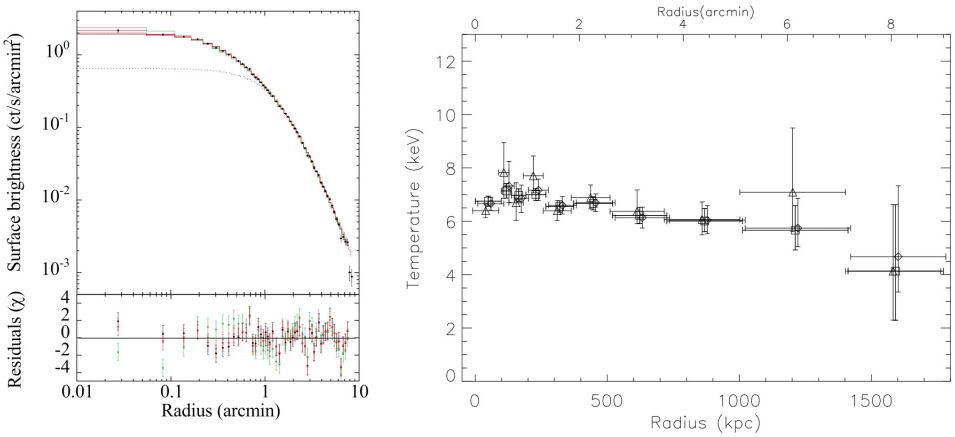

Figure A.7: Measurements taken using the XMM-Newton instrument by [304].
Left image: The surface brightness profile of the galaxy cluster Abell 1413 in the energy range $0.3 - 1.4$ keV. The black, red and green lines show fits using different models, as outlined in [304].
Right image: The temperature profile of the intracluster medium of Abel 1413. Squares show the projected temperature profile, diamonds show the data after correction for the point spread function (PSF) and the deprojected profile is shown with triangles.

low density (with mean free path typically ∼light year) but occasionally a hydrogen nucleus encounters a free electron and emits Bremsstrahlung radiation. Assuming that the gas is in hydrostatic equilibrium, the radial mass distribution can be deduced in terms of the radial temperature and density gradients:

$$\frac{GM(<r)}{r} = -\frac{kT(r)}{\mu m_p}\left(\frac{d\ln T}{d\ln r} + \frac{d\ln \rho_{gas}}{d\ln r}\right) \tag{A.45}$$

where the chemical potential μ depends on the metallicity of the gas. The X-ray emissivity is proportional to the density squared (ion density × electron density) so the total X-ray luminosity scales as $L \propto \rho_{gas}(0) r_c^3$ where r_c is the 'core radius' of the X-ray emitting region. The temperature of the gas can be determined by X-ray spectroscopy and the spectral form depends only on the temperature and the chemical composition of the gas. Figure A.7 shows measurements taken using the XMM-Newton telescope [304]. These data were used to calculate the total mass and the fraction which is x-ray emitting gas, as shown in Figure A.8.

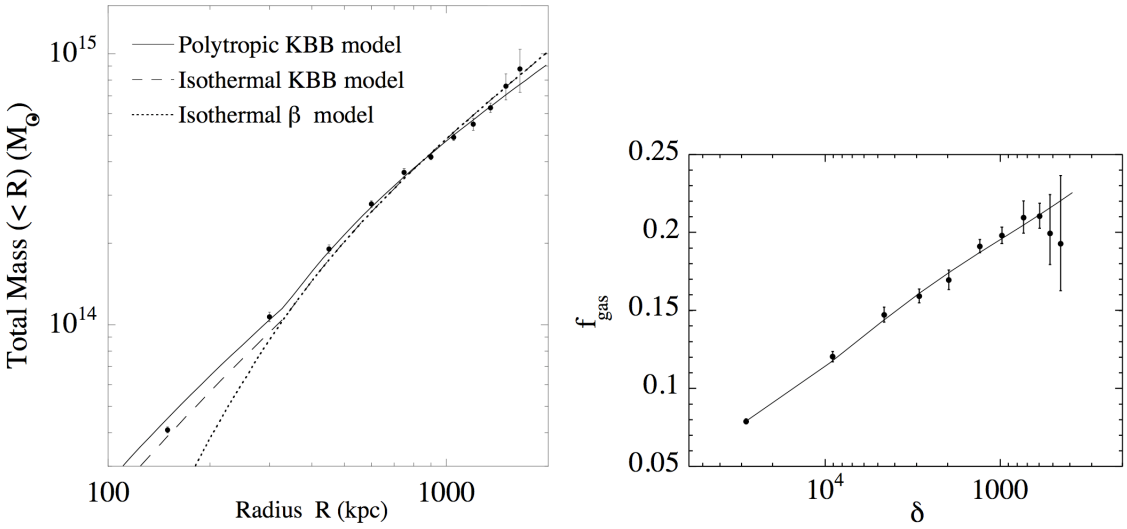

Figure A.8: Mass estimates for the components of the galaxy cluster Abel 1413, using data from [304].
Left image: The mass profile derived from the data used to plot Figure A.7. Three fits using models outlined in [304] are shown on the plot.
Right image: The gas mass fraction as a function of overdensity, δ, Obtained using Monte-Carlo simulations, the best fit is obtained from the MQGSL model as outlined in [304]. Although dominant over the stars mass, the gas only makes up a small proportion of the mass of the cluster.

A.11 The Sunyaev-Zeldovich Effect

Another method of detecting the presence of hot intracluster gas is by measuring its effect on the background radiation field [356]. Free electrons in the intracluster medium will have a temperature $T \sim \frac{GMm}{2kR}$, and therefore interactions with the CMB will typically be at low energy as this distribution peaks in the microwave region. The scattering optical depth for low energy interactions is given by:

$$\tau_e \approx n_e \sigma_T R_{eff} \sim 10^{-2} \tag{A.46}$$

where σ_T is the Thomson scattering cross section. The CMB photons inverse-Compton scatter off the electrons, and since the electrons have much higher energy than the photons, up-scattering is more likely and the CMB spectrum hardens slightly, as illustrated in Figure A.9. The mean shift in frequency is given by:

$$\frac{\Delta\nu}{\nu} \approx \frac{kT}{m_e c^2} \sim 10^{-2}. \tag{A.47}$$

This effect can be divided into three parts; the thermal effect due to the high temperature of the electrons, the kinematic effect due to the bulk motion of the gas, and polarisation effects. These measurements are an extremely useful cosmological tool as they are redshift independent. They are also complementary to X-ray emission measurements as Equation A.46 shows that they are proportional to density, n_e, whereas X-ray measurements are proportional to the density squared.

Measurements of this effect agree well with X-ray observations [248], as is shown in Figure A.10, indicating a significant dark matter component of the Universe. This effect also allows the detection of clusters that would otherwise not be visible to us [349].

A.12 The Cosmic Microwave Background

Although the temperature profile of the CMB is close to uniform there are small fluctuations which provide measurements of cosmological parameters. The temperature map must first be corrected for lower order anisotropies. The main correction is the dipole anisotropy, 3.355 ± 0.008 mK, which is thought to be due

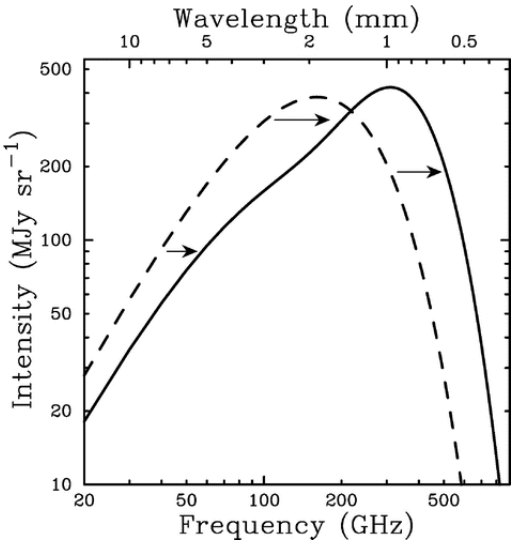

Figure A.9: An illustration of the Sunyaev-Zeldovich effect, the CMB spectrum shifts up to slightly higher energy after passing through an intracluster medium [307].

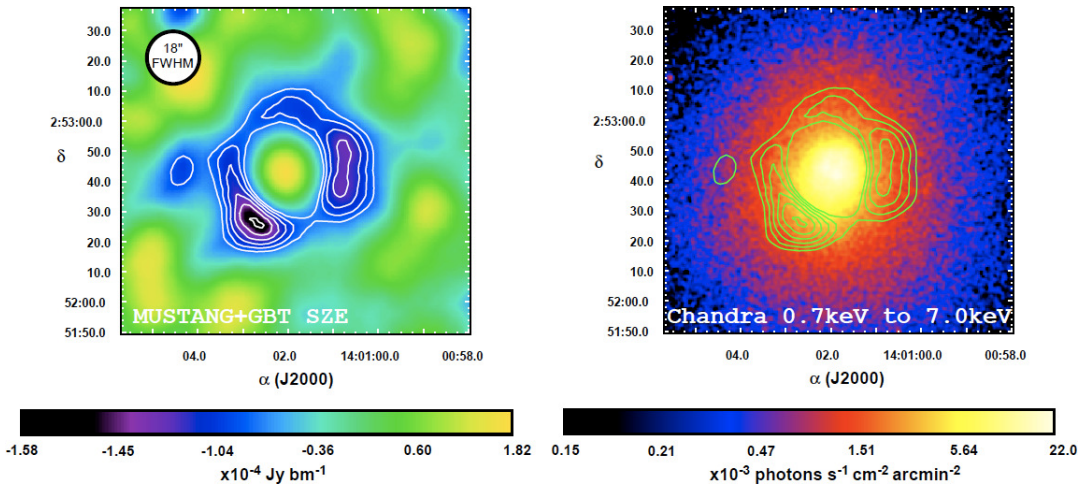

Figure A.10: A comparison of results from MUSTANG and CHANDRA [248]:
Left image: MUSTANG SZE [130] image of Abell 1835 smoothed to 18" resolution. Contours begin at 2.5σ and are in units of 0.5σ.
Right image: CHANDRA [129] image of Abel 1835 from $0.7 - 7.0$ keV smoothed with a 1.5" Gaussian. Contours begin at 2.5σ and are in units of 0.5σ.

to the Earth's relative motion to the CMB as it falls towards an over-density (in the direction of the Virgo cluster). Although we cannot distinguish between an intrinsic dipole and one due to our relative motion, the quadrupole term is only ∼1% of the dipole field, which suggests the dipole is purely due to the Earth's relative motion and agrees with the cosmological principle. The Earth's relative motion through the Universe has been measured as $v_{\oplus} = 369.0 \pm 0.9$ $\mathrm{km\,s^{-1}}$ towards $(l, b) = (263.99 \pm 0.14°, 48.26 \pm 0.03°)$ [211]. There are also secondary anisotropies generated by scattering along the line of sight. Although at the release of the CMB most of the baryons were neutral, once stars began to form, ultra-violet radiation was released which re-ionised the neutral hydrogen. Although the expansion diluted the ultra-violet radiation sufficiently for it not to affect the CMB significantly, most of the baryons remain in an ionised state. During the period after the first stars began to shine, up until the Universe expanded enough to dilute the scattering plasma, between 150 million and a billion years after the big bang, the CMB photons scattered off free electrons. The effect of this has been observed and the most recent WMAP study gives the re-ionisation optical depth as 0.088 ± 0.015 at a redshift of 10.5 ± 1.2 [231].

The CMB data must also be corrected for other low modes and Galactic emissions before the most interesting primary anisotropies can be measured. Galactic emission is minimised using Internal Linear Combination (ILC) of WMAP data from independent frequency bands [79]. The quadrupole ($l = 2$) and octupole ($l = 3$) anisotropies are compensated for, as shown in Figure A.11. There have been suggestions of anomalies in low multipoles [230, 318] such as a lower than expected quadrupole amplitude and an anomalous alignment of the quadrupole and octupole modes. However analysis of the full seven year data set shows a good fit to the ΛCDM model [79]. The results show the quadrupole amplitude is within 95% of the expected value, see Figure A.12, and although the alignment does appear to be significant there is no model providing a compelling retrodiction. Indeed, with a data set as rich as the CMB there are bound to be several occurrences with low intrinsic probabilities: for example, the discovery of Stephen Hawking's initials in the correct order, matching font size and style [79]. A calculation would show the chances of this occurrence are vanishingly small; however it does not indicate non-standard cosmology.

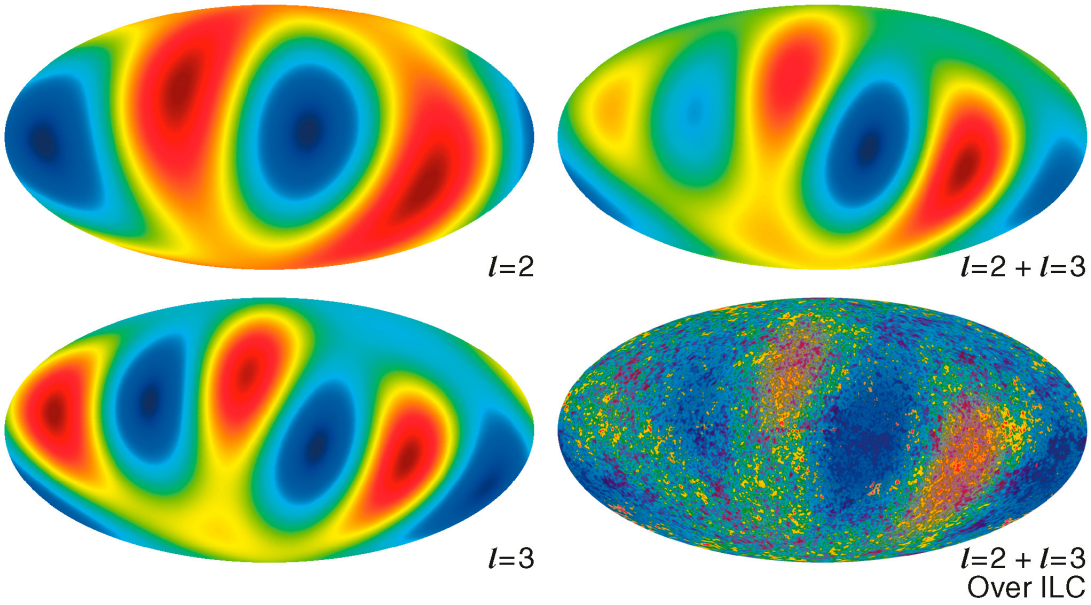

Figure A.11: The quadrupole ($l = 2$) and octopole ($l = 3$) WMAP maps are shown, along with both combined and overlaid with the ILC map. The high degree of quadrupole-octopole alignment results from statistical distribution of anisotropy power across the whole sky and single-void models are ruled out, the alignment behaves as may be expected from chance random anisotropy amplitudes and phases [79].

The primary anisotropies created by effects at or before the photon decoupling were caused by three mechanisms:

- **Gravitational perturbations (Sachs-Wolfe effect).** Photons from high-density regions at photon decoupling must climb out of the gravitational potential causing a redshift, this produces fluctuations of:

$$\frac{\Delta T}{T} = \frac{\Phi}{3c^2} \tag{A.48}$$

  where Φ is the gravitational potential [321].

- **Adiabatic oscillations.** Density perturbations on all scales are thought to have been produced from quantum fluctuations that were magnified by inflation. An over-density will begin to gravitationally collapse once it enters its own particle horizon, at which time every point within is in causal contact. Adiabatic oscillations occur when baryons fall towards a

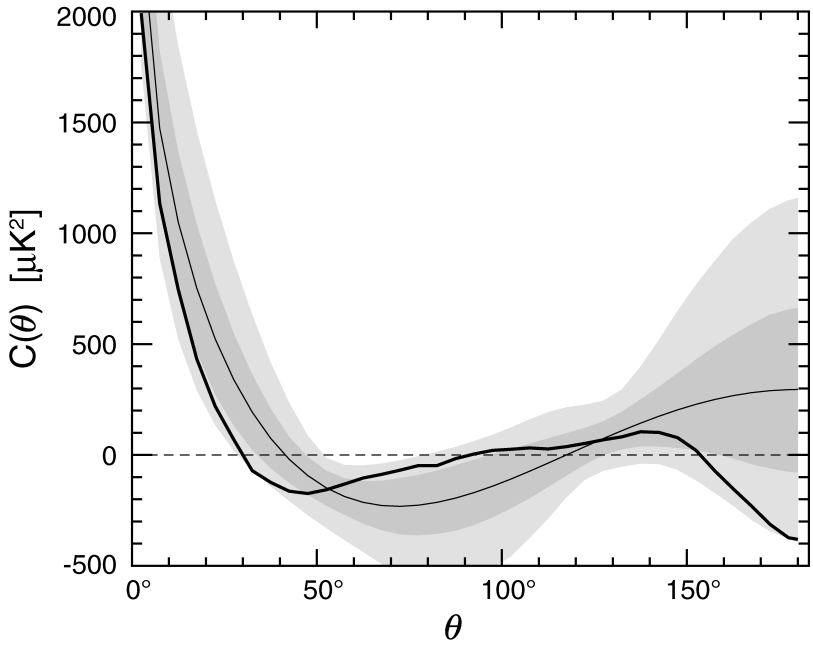

Figure A.12: The angular correlation function of the full-sky WMAP ILC map is shown by a heavy black curve. The thin black curve shows the best-fit ΛCDM model along with associated 68% and 95% confidence ranges. This shows no strong evidence of a lack of large-scale power [79].

dark matter potential well. The radiation is also compressed due to its coupling to the baryons. Once the density perturbation collapses to it Jeans length, the radiation pressure builds up enough to push the baryons back out of the over-density. This effect repeats and leads to fluctuations in the CMB temperature power spectrum known as baryonic acoustic oscillations (BAO). The anisotropies introduced are:

$$\frac{\Delta T}{T} = \frac{4\partial\rho_b}{3\rho_b}. \tag{A.49}$$

The other fundamental type of density perturbation is isocurvature. Here the sum of the fractional over-densities is zero, so if one component gains energy in some region of space then another component loses it (so for example an energy gain in baryons and photons as they fell into an over-density would lead to an energy loss in neutrinos). This is opposed to the adiabatic type discussed above where all components fluctuate in the same way. Inflation predicts adiabatic perturbations, with a series of peaks whose angular scales have a $1 : 2 : 3...$ ratio, rather than isocurvature perturbations, with peaks in a $1 : 3 : 5...$ ratio [222]. Measurements of the CMB show only adiabatic density perturbations providing further support for inflation theory.

- **Diffusion damping (Silk damping).** There is a net flux of photons out of overdense regions. As the photons have non-zero mean free path, due to scattering by the plasma, the radiation random-walks out of overdense regions convecting the plasma with it. This smoothes out the smaller scale temperature variations. This dampens fluctuations in the temperature as:

$$\frac{\Delta T}{T}(l) \propto \exp^{-0.5l^2\theta_H^2}, \tag{A.50}$$

where θ_H is the angular size of the horizon at recombination. There is also collisionless damping caused by the dilution due to expansion. This increases the optical depth during the period of decoupling, which lasted for 115 ± 5 thousand years [347] as discussed in Section 2.2.

The angular dependence of the fluctuations are related to the properties of the Universe and so measuring them can be used to constrain parameters of a model.

Equations A.48 and A.49 show that gravity dominates on larger angular scales and adiabatic perturbations dominate smaller scales so there is a critical wavenumber where these two effects are equal, $k_c^2 \sim \frac{G\rho}{c^2}$. The age of the Universe at any stage is $t \sim (G\rho)^{-\frac{1}{2}}$ so the critical wavenumber is:

$$k_c \sim \frac{1}{ct} \tag{A.51}$$

so photon decoupling perturbations with wavelengths above the horizon scale generate temperature fluctuations primarily via gravitational redshift. On shorter scales than this adiabatic perturbations dominate. The distance-redshift relation in a matter dominated Universe is given by:

$$R_0 dr = \frac{cdz}{H_0(1+z)\sqrt{1+z\Omega_m}} \tag{A.52}$$

and so the comoving horizon size is then given by:

$$D_H(z) \equiv R_0 \int_z^\infty dr = \frac{2c}{Ho}\left[(1+z)\Omega_m\right]^{-\frac{1}{2}}. \tag{A.53}$$

Then at the time of photon decoupling this gives $D_{dc} \simeq 181\Omega_m^{-\frac{1}{2}}h^{-1}$. The critical angle on the sky now can be calculated using the current horizon size by

$$\theta = \frac{D_{dc}}{D_H} \tag{A.54}$$

for $\Omega_m + \Omega_\Lambda = 1$ then $D_H \simeq \frac{2c}{\Omega_m^{0.4}H_0}$. So measurements of the CMB should show a change over from scale-invariant Sachs-Wolfe fluctuations to adiabatic perturbations at a critical angle of $\theta = 1.8\Omega_m^{\frac{1}{2}\circ}$ for a matter dominated Universe or $\theta = 1.8\Omega_m^{\frac{5}{4}\circ} \sim 1^\circ$ for the $\Omega_m + \Omega_\Lambda = 1$ case.

The temperature field can be decomposed into spherical harmonics. These modes have angular wavenumber l and the temperature deviation is given by $\Delta T(\theta\phi) = \sum_{l=0}^{\infty}\sum_{m=-l}^{l} a_{ml}Y_{ml}(\theta\phi)$. Figure A.13 shows the CMB power spectrum. The amplitude of the temperature variations can be predicted empirically. Massive clusters with velocity dispersions of order 1000 kms^{-1} can give an indication of the depth of potential wells since $v^2 \sim \frac{GM}{r}$ so $\frac{\Phi}{c^2} \sim \frac{v^2}{c^2}$ indicating a well depth of $\sim 10^{-5}$.

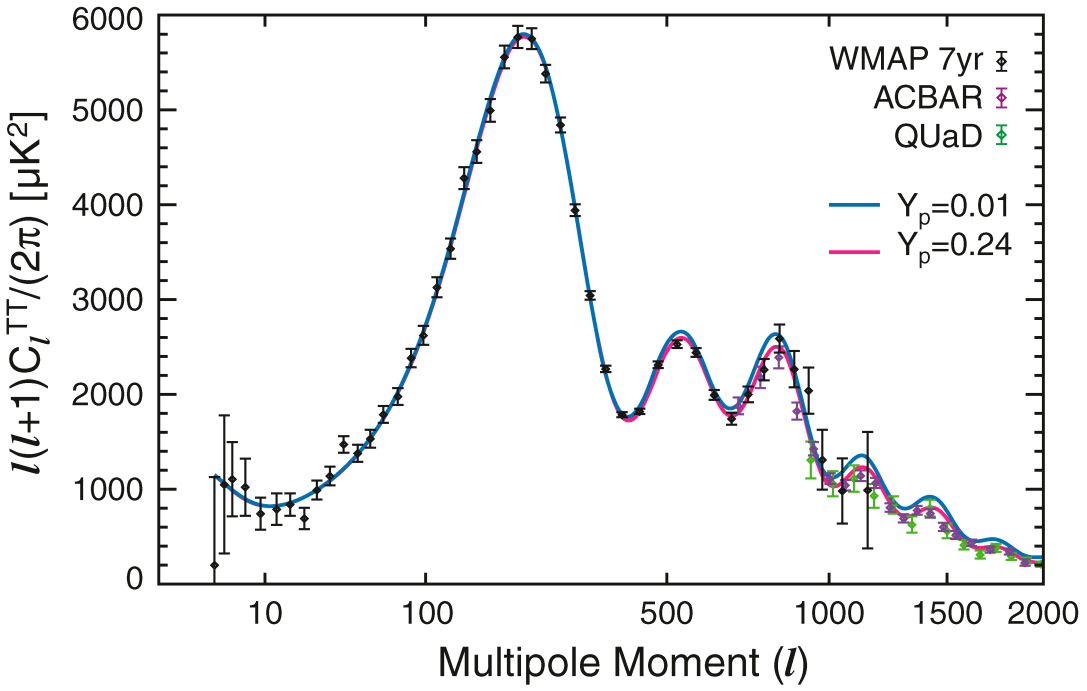

Figure A.13: The CMB angular power spectrum plotted against wavenumber l in radians^{-1}, the power spectrum estimator $C_l = \sum_{m=-1}^{l} \frac{|a_{ml}|^2}{2l+1}$. The blue and pink curves show ΛCMB fits with parameters $(\Omega_b h^2, \Omega_m h^2, \Omega_\Lambda, \tau, n_s, \Delta_R^2, A_{SZ}) = (0.0227, 0.1107, 0.086, 0.969, 2.38 \times 10^{-9}, 0.52)$, see Table 2.1 for details. A_{SZ} results from the SPT collaboration [265]. High-l data has been added from the Arcminute Cosmology Bolometer Array Receiver (ACBAR) [308] and the QUaD (QUEST [Q and U Extragalactic Sub-mm Telescope] at DASI [Degree Angular Scale Interferometer]) [102] experiments. The two curves shown differ in primordial helium abundance. This shows the He fraction can be measured from the power spectrum alone by measuring the Silk dampening [245].

The cosmological parameters are derived from the WMAP data using a multi parameter maximum-likelihood fit [231], however some approximate relations exist between cosmological parameters and the visible parameters of the best ft curve. The first peak in the power spectrum corresponds to a wave that only had time to fully compress once before decoupling. Since it is observed through a lens, due to the curvature of space-time, this peak can be analysed to constrain the total density of the Universe, Ω. Higher order peaks yield information about weakly interacting matter. Odd numbered peaks in the spectrum are seen where the baryons were maximally compressed at decoupling and even peaks correspond to regions where the baryons have maximally rebounded due to photon pressure.

For a high baryon-to-photon ratio the compression is enhanced whereas rarefied regions are retarded so the ratio of the first two peaks can be used to measure the baryon density. The magnitude of higher peaks depends on the density relativistic species. Following maximum compression the relativistic species would redshift with the expansion of the Universe as the density perturbation rebounded. In the CMB the temperature perturbation would be enhanced as the gravitational potential decays due to the falling density. The gravitational potential of non-relativistic matter does not redshift away and so temperature fluctuations would be smaller for this material. The density of non-relativistic matter can be measured by the relative strength of higher order peaks and is found to be significantly higher than the baryon density. Table 2.1 lists some of the WMAP results and a ΛCDM fit to the power spectrum using these results is shown in Figure A.13. As expected, the dampening causes an exponential decay at larger l.

A.13 Beyond the Standard Model of Particle Physics

The standard model of particle physics is known to be incomplete and Equation 2.31 requires new physics (Λ). Several experimental results show that an extension is needed, most notably the existence of matter (it being dominant over anti-matter). Furthermore, the standard model does not include gravity, though this is not surprising as gravity cannot be written as a renormalisable quantum field theory. Also, graviton emission is highly suppressed due to its low relative strength (for example the branching ratio of kaon decay to a pion and graviton scales as $(M_K/M_{planck})^2 \sim 10^{-38}$). Further evidence of physics beyond the standard model comes from observations of neutrino oscillations. This implies that, unlike the standard models prediction of massless neutrinos, the neutrinos do have a mass and that the different families have different masses. This mass is unlikely to be due to a simple linear (Yukawa) coupling to the Higgs field as with the other known particles and may include a "Majorana" mass allowing neutrinos to be their own antiparticles. There is no *a priori* reason that neutrino mass would not only be the Dirac mass, but this would require seemingly unnatural fine tuning. A neutrino with both Dirac and Majorana mass can lead to a much

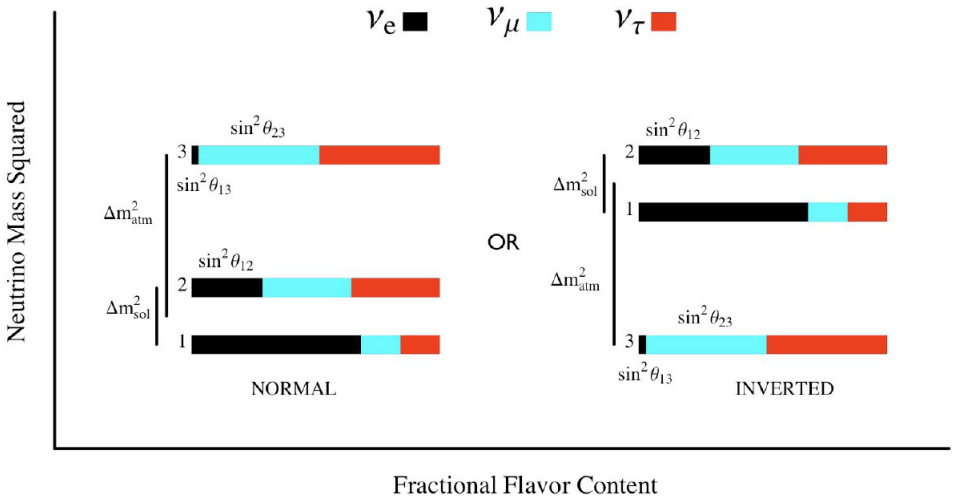

Figure A.14: A graphical representation of the leptonic mixing matrix. The left image shows a normal quark-like spectrum and the right image shown an inverted spectrum as expected if the neutrinos are Majorana particles. The masses are currently unknown and the value on the y-axis shows the mass difference. Image obtained form [59].

more natural explanation of the observed mass for the left-handed neutrinos via the See-Saw mechanism [279]. The neutrinos of definite mass, $\nu_{1,2,3}$, are coherent quantum mechanical super-positions of the three flavours, electron, muon and tau as shown in Figure A.14.

Two of the standard model forces, the electromagnetic and weak force, are seen to unify into the electroweak force at high energy (the elecroweak scale). It is expected that at very high energies all forces unify into a single force. Before this complete unification, it is also expected that the SM forces (i.e. the electroweak and strong forces) will unify. This is known as Grand Unification Theory (GUT), however the fits miss by $\sim 12\sigma$ unless complex symmetry breaking patterns are considered [255], shown in Figure 2.29.

Baryon number is violated by any GUT [189], leading to nucleon decay. With a GUT coupling and scale (α_{GUT}, M_{GUT}) the lifetime of a proton, which is the limiting factor for GUT theories, is calculable since $\tau_p \propto \frac{M^4_{GUT}}{\alpha^2_{GUT} m^5_p}$. Results from Super-Kamiokande indicate, for several decay channels, that $\tau_p > \mathcal{O}(10^{33})$ years [288]. The SM also has a gauge hierarchy problem where a natural explanation is sought for the different strengths of the gravitational and weak forces, as the weak

force is 10^{32} times stronger than the gravitational force. Although this is not a physical problem, it is in conflict with the expectation that the renormalisation parameters are closely related to the fundamental parameters. The Higgs-boson mass must be less than a TeV [387], yet the scalar mass communicates quantum-mechanically with scales up to the GUT scale, 10^{16} GeV, where fine tuning would seem to be required for stability, and eventually even to the Plank scale, 10^{19} GeV, where gravitational interactions become comparable in magnitude to the gauge interactions. All particles get radiative corrections to their mass. While Fermion masses increase only logarithmically as $\delta m_f \propto m_f \ln \frac{\Lambda^2}{m_f^2}$, the scalar masses increase quadratically with energy giving corrections at 1-loop $\propto \Lambda^2$, as seen in Equation 2.31. A larger mismatch is observed when considering the cosmological constant given the strength of the gravitational constant. The gravitational result for vacuum energy density gives $\Lambda_{vacuum} = \left(\frac{8\pi G}{c^4}\right) \rho_\Lambda \approx 10^{-47}$ GeV^4 [363] which is ∼55 orders of magnitude below the result obtained from the Higgs field density $\rho_H \equiv \frac{M_H^2 v^2}{8}$ where $v \sim 246$ GeV is the scale of elecroweak symmetry breaking, for $M_H \geq 114$ GeV the density is $\rho_H \geq 10^8$ GeV^4.

Charge Parity (CP) violation has been observed in the weak force [120] and CP is also expected be violated by the strong force providing a possible explanation for the observed matter anti-matter asymmetry in the Universe. CP-symmetry states that the laws of physics are identical for a particle and its antiparticle (*i.e.*, if the particle's charge is reversed) and independent of parity (*i.e.*, if spatial dimensions are reversed). As previously mentioned, the violation of this symmetry is the most obvious evidence of physics beyond the SM as clearly matter is dominant over anti-matter in the Universe, and the mechanism provided by the current SM is too small to account for the imbalance. If there were no violation of CP in the strong sector this should allow an electric dipole moment in neutrons of order $10^{-18} e{\cdot}$cm. No dipole has yet been observed and current upper limits on the neutron dipole set it below $2.9 \times 10^{-26} e{\cdot}$cm [65]. This is a subset of CPT (Charge conjugate Parity and Time) symmetry, although conservation of time, or CPT, is still an open question [195].

A.14 SUSY models

The Minimal Supersymmetric Standard Model (MSSM) is a SUSY extension to the SM which introduces the least number of new particles. Listed in Table A.2 are the SM particles and their MSSM superpartners. The Higgs sector in this theory consists of two doublet fields, $H_{u,d}$, which result in five physical Higgs bosons after electroweak symmetry breaking. This form of SUSY introduces "soft symmetry breaking" as the minimal way of breaking SUSY symmetry. This adds over 120 free parameters to the model [151] but this number may be reduced by making assumptions about relative masses giving a constrained Minimal Supersymmetric Standard Model (cMSSM) [236]. The minimal SUper GRAvity model (mSUGRA) [113] assumes that SUSY-breaking occurs in a hidden sector which communicates with the visible sector via gravity. This model may be reduced to five parameters which are the coefficient of the universal mass term for scalars, m_0, and for gauginos, $m_{\frac{1}{2}}$, the coefficient of the trilinear soft breaking coupling, A_0, the sign of the Higgs mass term sgn(μ) and the ratio between the vacuum expectation values of the Higgs bosons, $\tan\beta = \frac{v_2}{v_1}$, which characterises the relative fraction that the two Higgs doublets contribute to the electroweak symmetry breaking $v = \sqrt{v_1^2 + v_2^2} \approx 246$ GeV. Searches for SUSY at the ATLAS and CMS experiments have constrained the parameter space for these models [1, 239]. Including direct dark matter detection constraints also allows some branches of cMSSM, such as the focus point region (FP) [175] to be ruled out completely [83].

Recent results from the LHC [1, 239] also indicate the possibility of a Higgs mass of $\sim$ 125 GeV (2.5σ significance if the excess signal in $\gamma\gamma$, $ZZ^\star \rightarrow 4l$ and $WW^\star \rightarrow 2l$ is a sign of the Higgs). More recently CERN press releases, currently unpublished [365, 366], have announced the discovery of a new "Higgs like" particle. The ATLAS preliminary results show a particle with a mass of $\sim$126.5 GeV. Combining the 2011 with the two channels with the highest energy resolution, $\gamma\gamma$ and ZZ*, give a significance of 5σ shown in Figure A.15. The CMS preliminary results indicate a particle with a mass of 125.3$\pm$0.6 GeV with 5σ significance in the $\gamma\gamma$ channel, shown in Figure A.16. The two other channels which are equally sensitive in this mass range, WW* and ZZ*, currently show excesses in a similar mass region at 3.2σ and 1.5σ significance levels, respectively.

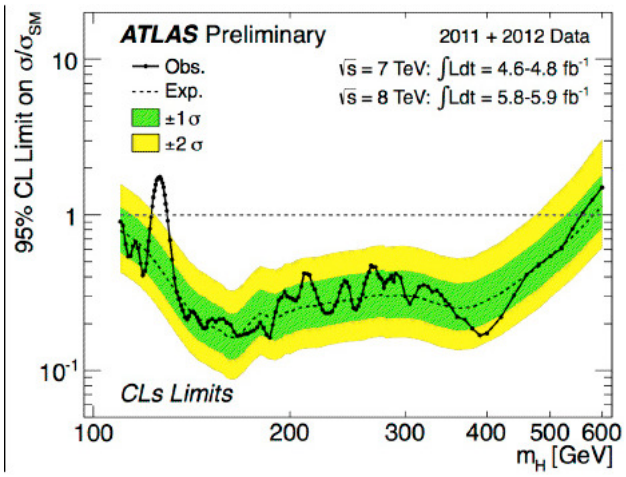

Figure A.15: Experimental limits from ATLAS on Standard Model Higgs production in the mass range 110-600 Gev/c^2. The solid curve reflects experimental limits for the production of a Higgs of each possible mass values. The dashed curve shows the expected limit in the absence of the Higgs boson, based on simulations. The green (yellow) band shows the 95% (68%) confidence level region. The region for which the solid curve dips below the horizontal dashed line at a value of 1 $\left(\frac{\sigma}{\sigma_{\mathrm{SM}}}\right)$ is excluded with 95% C.L.. Image obtained from [365].

This value would place strict constraints on SUSY theories, pushing allowed cMSSM particle masses to higher values and reducing the favoured values of both spin-independent and spin-dependent neutralino-proton cross-sections [353]. Although this is still within the expected range of MSSM [61]. Figure A.17 shows the constraints placed on $\tan\beta$ and Figure A.18 shows the restrictions placed on the supersymmetric top squark (stop) mass requiring large values of A_0 and significant stop mixing, $X_t \equiv A_t - \mu \cot\beta$ [53, 150]. Super gravity theories are less constrained by the implied large A_0 as this is a largely independent parameter [61]. The non-observation of squarks and gluinos in the current LHC data sample may be seen as a hint of an alternative theory to the SUSY flavour and CP problems. Decoupling the first and second generation squark and slepton masses, known as effective SUSY (ESUSY), would allow sub-TeV third generation squarks but with multi-TeV first and second generation squarks [171]. Such split spectrum SUSY models satisfy naturalness considerations as third generation particles have much more mild CP constraints [186].

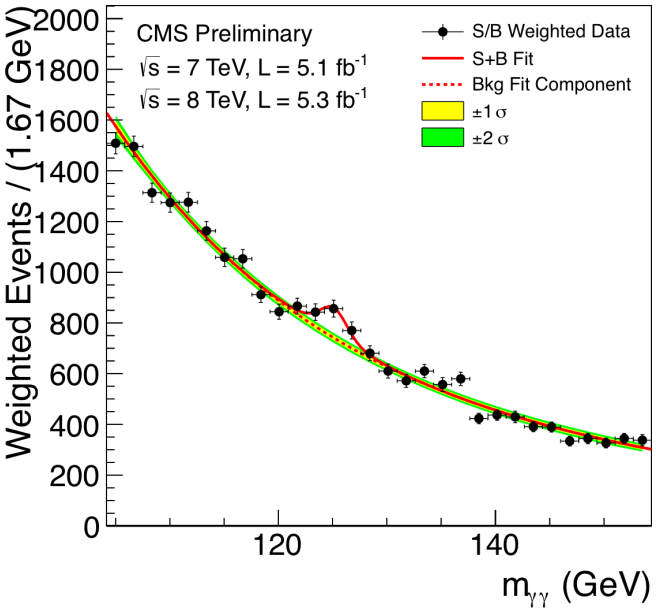

Figure A.16: Di-photon ($\gamma\gamma$) invarient mass distribution for the CMS data of 2011 and 2012 (black points). This shows Higgs decay to photons via a virtual top loop. The data are weighted by the signal to background ratio for each sub-category of events. The solid red line shows the fit result for signal plus background; the dashed red line shows only the background and the yellow (green) band shows the 95% (68%) confidence region. Image obtained from [366]

Table A.2: The MSSM particles and their superpartners [190].

MSSM chiral content

Names		Spin 0	Spin $\frac{1}{2}$	$SU(3)_C$, $SU(2)_L$, $U(1)_Y$
squarks, quarks	Q	$(\tilde{u}_L \tilde{d}_L)$	$(u_L d_L)$	$(3,2,\frac{1}{6})$
(3 families)	$\bar{u}$	$\tilde{u}_R^\star$	$u_R^\dagger$	$(\bar{3},1,-\frac{2}{3})$
	$\bar{d}$	$(\tilde{d}_R^\star)$	$(d_R^\dagger)$	$(\bar{3},1,\frac{1}{3})$
sleptons, leptons	L	$(\tilde{\nu}\tilde{e}_L)$	(νe_L)	$(1,2,-\frac{1}{3})$
(3 families)	$\bar{e}$	$\tilde{e}_R^\star$	$e_R^\dagger$	$(1,1,1)$
Higgsinos, Higgs	H_u	$(\tilde{H}_u^+ \tilde{H}_u^0)$	$(H_u^+ H_u^0)$	$(1,2,\frac{1}{2})$
	H_d	$(\tilde{H}_d^0 \tilde{H}_d^-)$	$(H_d^0 H_d^-)$	$(1,2,-\frac{1}{2})$

MSSM gauge content

Names		Spin $\frac{1}{2}$	Spin 1	$SU(3)_C$, $SU(2)_L$, $U(1)_Y$
gluino, gluon		$\tilde{g}$	g	(8,1,0)
wino, W bosons		$\tilde{W}^\pm \tilde{W}^0$	$W^\pm W^0$	(1,3,0)
bino, B boson		$\tilde{B}^0$	B^0	(1,1,0)

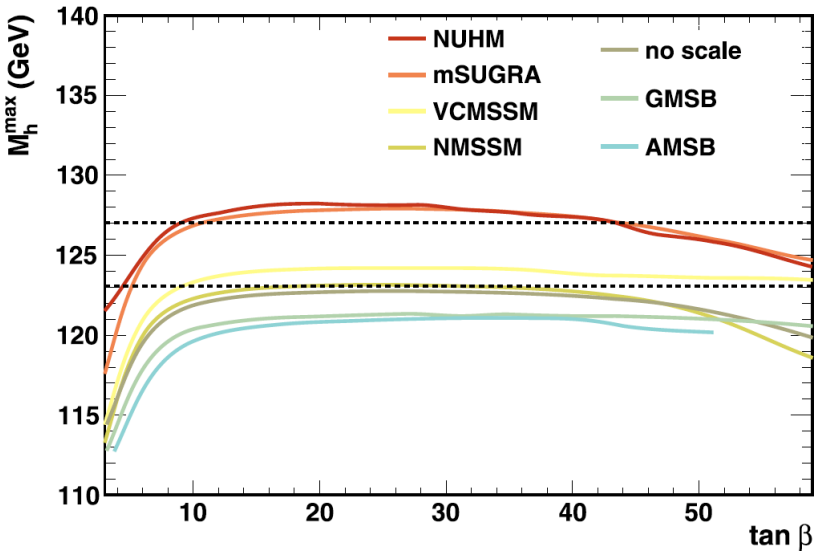

Figure A.17: Results from a full scan of the Gauge Mediated SUSY Breaking (GMSB), Anomaly Mediated SUSY Breaking (AMSB) and mSUGRA scenarios using the *Softsusy* and *Suspect* programmes in light of the recent results from the LHC indicating a possible Higgs mass of ~ 125 GeV. The maximal value of the Higgs mass defined as the value for which 99% of the scan points have a smaller mass, shown as a function of $\tan\beta$ for the various constrained MSSM models [53].

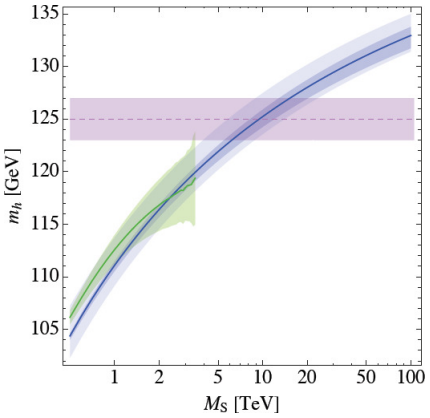

Figure A.18: The Higgs mass (m_h) as a function of supersymmetric top squark mass (M_S) with no mixing ($X_t = 0$). The green band is the output of FeynHiggs along with its uncertainty which becomes too large to consider beyond 3 TeV. The blue line represents 1-loop renormalisation group evolution in the SM matched to MSSM at M_S. The blue bands give the errors from the varying top mass between 172 and 174 GeV (darker band) and the renormalisation scale between $\frac{M_t}{2}$ and $2M_t$ (lighter band) [150].

A.15 SUSY Neutralinos

The SUSY neutralino may be expressed as:

$$\tilde{\chi}_i^0 = f_{i1}\tilde{W}_3 + f_{i2}\tilde{B}^0 + f_{i3}\tilde{H}_1^0 + f_{i4}\tilde{H}_2^0 \tag{A.55}$$

where $i = 1 - 4$ and f_{ij} encompasses the parameters $m_{\frac{1}{2}}$, μ and $\tan\beta$. The masses of the four neutralino mass eigenstates are (M_1, M_2, μ, μ) and although the neutralino may be a mix, there are three limiting cases. For the pure Bino case, $M_1 \ll M_2, \mu \rightarrow \tilde{\chi}_1^0 \approx b^0$, the relic density tends to be too large as annihilation channels suffer from suppression factors, unless the sfermions are light. For the pure Wino case $M_2 \ll M_1, \mu \rightarrow \tilde{\chi}_1^0 \approx w^0$. Again the annihilation channels to fermions and Higgs suffer from suppression however the annihilation channel to $W^{\pm}$ is unsuppressed and the Wino relic density would be too small. For the pure Higgsino case $\mu \ll M_1, M_2 \rightarrow \tilde{\chi}_1^0 \approx \frac{h_u^0 + h_d^0}{\sqrt{2}}$. In this case the annihilation channels to $W^{\pm}$ and Z^0 are unsuppressed and allow rapid annihilation leaving a very small relic density.

For the partially mixed cases there are three possibilities. A mixed Wino-Higgsion LSP where $M_2 \sim \mu \ll M_1$ still produces a negligible relic density [274]. The mixed Bino-Higgsino LSP with $M_1 \sim \mu \ll M_2$ would allow for an acceptable relic density however the parameter space has been highly constrained by LHC and direct detection results [83]. For the mixed Bino-Wino case where $M_1 \sim M_2 \ll \mu$ the relic density may also be acceptable. This model is compatible with rSUGRA, an extension to mSUGRA adding one extra parameter $r = \frac{M_1}{M_2}$ accounting for nonuniversiality of gaugino mass [89]. These cases show the more extreme limits where the lightest neutralino may be composed primarily of a single particle, or be Higgsino-like or gaugeino-like but in general the mixing is not heavily restricted to some components being more dominant, although the parameter space becomes quite large outside these considerations.

Limits have been placed on the lightest neutralino mass. An upper limit of 500 GeV c^{-2} has been set by WMAP measurements of Ω_m [164] and a lower limit of 47 Gev c^{-2} (52 GeV c^{-2}) for high (low) $\tan\beta$, shown in Figure A.19 [187]. These lower limits apply to the coupling to W and Z bosons and lighter neutralino

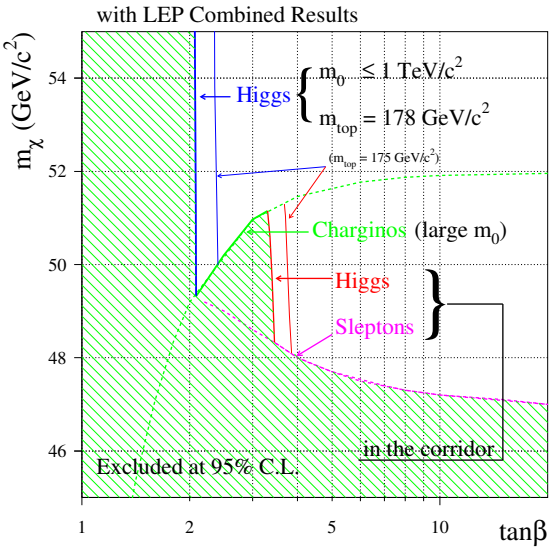

Figure A.19: 95% C.L. lower limits of the neutralino mass obtained using methods outlined in [68], valid for $m_0 < 1$ TeV and $m_{top} = 178$ GeV although $m_{top} = 175$ GeV is also shown for comparison. Image from [187].

masses are still possible in some scenarios, for example photon coupling. For non-universal gaugeino masses the lower limit is set by observations of supernovae at $m_\chi \geq 0.2$ GeV [152].

A.16 Alternate Dark Matter Theories to SUSY

A.16.1 Axions

Axions represent a possible solution to naturalness problems in QCD. The parameter Θ introduced in Section 2.4.2 has two contributions, one from the quark mass matrix and the other from instanton tunnelling. That these two components should sum to zero by chance seems unlikely and so a mechanism beyond the standard model is sought to force the parameter to zero. A proposed mechanism is the global spontaneous breaking of axial $U(1)$ symmetry, resulting in a massless Nambu-Goldstone (NG) boson associated with the new $U(1)_{PQ}$ field [296]. The presence of a small explicit symmetry breaking allows the boson (now

a pseudo-NG boson known as an axion) to acquire a non-pertubative mass:

$$m_A^2 \propto \frac{m_\star |\langle \bar{q}q \rangle|}{f_A^2} \tag{A.56}$$

where $m_\star = (m_u^{-1} + m_d^{-1})^{-1}$ is the combination of quark masses, $\langle \bar{q}q \rangle$ is the quark condensate and f_A is the axion coupling scale. This particle plays the role of Θ and allows the CP violating parameter to naturally relax to 0, restoring CP symmetry. The resulting axion is similar to the neutral pion, gaining mass when chiral symmetry is broken. The two may therefore be related by $m_A f_A \approx m_\pi f_\pi$; with $m_\pi = 135$ MeV and $f_\pi \approx 92$ MeV the axion mass is given by:

$$m_A = \frac{z^{\frac{1}{2}}}{1+z} \frac{f_\pi m_\pi}{f_A} = \frac{0.60 \text{ meV}}{\frac{f_A}{10^{10} \text{ GeV}}} \tag{A.57}$$

where $z = \frac{m_{up}}{m_{down}} = 0.56$, although it may lie in the range $0.35 \leq z \leq 0.60$ [40]. As standard axions, with $f_A \sim v_{weak}$, have been excluded [72, 70] the focus is now on axions with $f_A \gg v_{weak}$ where there are two leading classes of models. The Kim, Shifman, Vainshtein and Zakharov (KSVZ) model introduces a scalar field, σ, with $f_A = \langle \sigma \rangle \gg v_{weak}$ and a super-heavy quark with $m_q \sim f_A$ as the only fields carrying PQ charge [330]. The Dine, Fischler, Srednicki and Zhitnisky (DFSZ) model adds a scalar field ϕ which carries PQ charge, so that at least two Higgs doublets and ordinary quarks and leptons carry PQ charge, and $f_A = \langle \phi \rangle \gg v_{weak}$ [145].

Axions would be most easily detectable by the two photon interaction $A \rightarrow \gamma\gamma$. This allows search techniques for low-mass axions involving strong magnetic fields or observations of stellar cooling as axions transport energy out of hot astrophysical plasmas, as discussed in Section 3.2.8. The cooling effect of axions implies $f_A \geq 10^{10}$ GeV from red giants [142] and $f_A \geq 2 \times 10^{11}$ GeV from supernovae [163]. Considerations of the critical energy density limits $f_A \leq 10^{12}$ GeV [6] and the axion mass is constrained by the decay time given the age of the Universe so that $m_A \leq 20$ meV. This leaves only a narrow window in which axions may exist as a viable dark matter candidate. In the early Universe axions would have been produced by quark and gluon interactions [273]. Following colour confinement the dominant thermalisation process is then $\pi + \pi \leftrightarrow \pi + A$ [376].

Thermal production of axions leaves a hot relic, however the thermal production is negligible and the relative lack of interaction with the other constituents allows a cold axion relic as the dominant production method is non-thermal [377, 316]. The resulting axion population would be a relic whose mass density may be given by:

$$\Omega_A h^2 \approx 0.7 \left(\frac{f_A}{10^{12}\ \text{GeV}} \right)^{\frac{7}{6}} \left(\frac{\Theta_i}{\pi} \right)^2 \tag{A.58}$$

where Θ_i is the initial "misalignment angle" relative to the CP-conserving value [333].

In some theories, the axions may make up only part of the dark matter. These theories include axinos as the LSP [9] and the possibility of a mixed dark matter relic consisting of neutralinos and axions [63, 64]. A mixed neutralino-axion model may account for the low thermal neutralino abundance expected from wino-like and Higgsino-like neutralinos as decays from axinos boost the density.

A.16.2 Neutrinos

The number of neutrino species has been constrained by data from particle accelerators. The ratio of widths of the Z decay to invisible channels and leptonic channels is $\frac{\Gamma_{inv}}{\Gamma_{ll}} = 5.961 \pm 0.023$ and the ratio to neutrinos and charged leptons is $\frac{\Gamma_{\nu\nu}}{\Gamma_{ll}} = 1.991 \pm 0.001$ [5]. The ratio of these two gives the number of neutrino species (with masses $< \frac{M_Z}{2}$) as:

$$N_\nu = 2.994 \pm 0.011 \tag{A.59}$$

This result indicates that there are only three fermion families in nature. The number of neutrinos is also constrained by cosmological observations. This latter result seems to also allow for a fourth neutrino type. However, a fourth generation of particles seems unlikely as accelerator results have ruled out weakly interacting neutrinos with less than ~ 45 GeV [143] and no sign of a fourth generation has been observed [40]. As the weak force would only effect these particle generations this indicates that any additional neutrino families would be sterile.

Experimental results have shown that detected and produced neutrinos are predominantly left-handed whereas antineutrinos are right handed [283] as predicted by the SM. However observations of neutrino oscillations indicate they have non-zero mass, and since helically is relativistically invariant, it is possible that left and right-handed neutrinos and antineutrinos exist as separate particles. If the neutrino is a Majorana particle then, by the See-Saw mechanism, its right-handed partner is a weak isosinglet and does not couple directly to fermions or bosons. The masses of the left and right handed neutrinos are inversely related, so as the left-handed neutrinos are all relatively light, $m_{tot} = \sum_{\nu} m_{\nu} \leq 28$ eV [357], the right-handed partners must be extremely heavy. The sterile neutrinos may decay into a lighter neutrino and a photon [294]. This photon could be detectable over the background as line emission at a particular wavelength. Notably recent result from the Chandra X-ray telescope have detected an excess in the Willam 1 feint dwarf galaxy at 68% C.L., which would correspond to a sterile neutrino mass of 5.0 ± 0.2 keV [263]. Results from the Liquid Scintillator Neutrino Detector (LSND) using antineutrinos [147], suggested there may be a fourth neutrino. Follow up experiments with the Mini Booster Neutrino Experiment (MiniBooNE) using neutrinos did not indicate a fourth (sterile) neutrino, however when antineutrinos were used a scenario of three active plus one sterile, (3+1), neutrinos was a good fit to the data [237]. More recent results from the Main Injector Neutrino Oscillation Search (MINOS) experiment found no evidence of a fourth neutrino, severely constraining the parameter space for sterile neutrinos [14].

A.16.3 Kaluza Klein Dark Matter

Extra spatial dimensions have been proposed as a route to unify the fundamental forces of nature. The framework used to describe extra spatial dimensions was originally developed by Kaluza and Klein [233, 243]. The initial attempts to describe extra spatial dimensions were unsuccessful but the formalisation developed by Kaluza and Klein is still used and the theories are collectively known as "Kaluza-Klein" theories. Many of these theories provide a candidate for dark matter in the form of the Lightest Kaluza-Klein Particle (LKP). The simplest model contains one extra dimension so that for a five-dimensional (the

extra dimension is indicated by the superscript ^{5}) space-time the metric is:

$$ds^2 = -dt^2 + dx^2 + (dx^5)^2 \tag{A.60}$$

where x^5 is a coordinate on a circle with radius R. A massless scalar field, ϕ in five-dimensional space-time would satisfy the five-dimensional Klein-Gordon equation:

$$\Box\phi(x^\mu, x^5) = g^{\beta\nu}\partial_\beta\partial_\nu\phi(x^\mu, x^5) = 0 \tag{A.61}$$

where $\Box$ is the four-dimensional d'Alembertian operator. Here x^5 is periodic with period $2\pi R$. Using the Fourier expansion of $\phi = \sum_n \phi_n(x^{/mu})e^{\frac{inx^5}{R}}$ equation A.61 gives an infinite number of decoupled equations for ϕ, one for each mode:

$$(\Box - m_n^2)\phi_n = 0 \tag{A.62}$$

where the mass term arises from the x^5-derivative. From a four-dimensional point of view, a massless scalar field in five-dimensional space-time gives a massless scalar field and an infinite number of massive fields. The masses of these Klauza-Klein modes are inversely related to the size of the topology of the extra spatial dimension:

$$m_n \sim \frac{n}{R}. \tag{A.63}$$

This is characteristic of the massive fields that may arise from dimensional reduction from some higher dimensional space.

A.16.4 Baryonic Dark Matter

A certain fraction of the total baryonic matter in the Universe is expected to be very difficult to detect. These objects, known as Massive Astrophysical Compact Halo Objects (MACHOs), contribute to the dark matter content to some extent. Microlensing searches for MACHOs by the Expérience pour la Recherche d'Objets Sombres (EROS-2) survey show at 95% confidence that they make up less than 8% of the Milky Way halo [367]. This result indicates that baryons do not make a significant contribution to the dark matter content of the Universe.

A.16.5 Modified Gravity

The observations of galaxy rotation curves deviating from Newtonian expectations also lead to theories of modified gravity as an alternative to dark matter. The original MOdified Newtonian Dynamics (MOND) theory [278] was an *ad hoc* method to match the observed rotation curves by altering the strength of gravity depending on the scale. This theory does not fare well on larger scales though and has considerable difficulty explaining phenomena such as low surface brightness galaxies and observations of colliding clusters such as the bullet cluster. More sophisticated theories have been developed using a general relativistic approach, such as Tensor-Vector-Scalar gravity (TeVeS) [76]. While the standard gravitational theory describes a single rank-2 tensor field there is, no *a priori* reason why there should only be a single field. There may be additional tensor, vector or scalar fields but the coupling must be weak, or otherwise suppressed, on scales where the current theory of gravity has been well tested. Although it is possible to construct theories which explain the observed dynamics quite well, the Hubble constant would be ~ 5 times lower with no cold dark matter [124]. To explain the observed value of the Hubble constant within TeVeS some form of dark matter is needed: aside from particle candidates previously mentioned the scalar field itself provides a possible candidate [334]. This must be balanced with the correct diameter distance to the last scattering surface which leads to strict constraints on form of the additional fields [177].

Another class of modified gravity theories are collectively known as as $f(R)$ gravity, a review of these theories is given in [343]. The R here is the Ricci scalar, see Equation 2.4. These theories generalise the Lagrangian of the GR action, S (known as the Einstein-Hilbert action), which yields the field equations. The action is then:

$$S = \frac{1}{2k} \int d^4x \sqrt{g} f(R) \tag{A.64}$$

where $f(R)$ has replaced the standard general relativity R in this equation, $k = 8\pi G$ and $c = \hbar = 1$. In addition to the possibility of providing an an explanation for the dark sectors of the Universe, as outlined in [169], f(R) gravity may offer a route to quantum gravity [351, 373].

There are 3 main classes of $f(R)$ gravity, these are:

- **Metric formalisation:** This is the simplest modification to the action [109, 111].
- **Palatini formalisation:** Here the metric, g, and the connection, Γ, are treated as independent variables and the action is varied with respect to both [105]. This means that particle trajectories are governed by Γ and the chronology of the Universe is governed by g.
- **Metric-affine gravity:** This is similar to the Palatini formalisation, however the metric and connection are no longer treated as entirely independent [344, 345]. As the matter action depends on the connection, a quantity called the hypermomentum [206] is defined to represent the variation of the action with respect to the connection.

A review of the successes of $f(R)$ gravity, as well as the challenges it still faces is given in [343]. There are several more modified gravity theories such as Dvali-Gabadadze-Porrati (DGP) gravity [155], brane world gravity [266] and the Einstein-Aether theory [228].

A.17 Results of a Search of the SSR Data for Magnetic Inelastic Dark Matter

The following tables show the results of a search for the de-exitation γ-ray interacting in the veto, following the scattering of exotic dark matter into an excited state in the ZEPLIN–III target. Tables A.3, A.4, A.5 and A.6 show the results are for magnetic inelastic WIMP masses of 50, 70, 100 and 140 GeV/c^2 respectively. The two search methods used are fitting a decay curve to the time delay between the ZEPLIN–III and veto events and simply counting the number of observed background events and comparing this to the expectation, as outlined in Section 6.6.4.

Table A.3: Results from simulations of 50 GeV/c^2 magnetic inelastic WIMPs. Given that a scattering occurred in the ZEPLIN–III fiducial volume, the veto efficiency for detecting the delayed de-excitation γ-ray is given (for an energy deposit of over 20 keV in the veto). The 90% C.L. limit on the number of events is shown, calculated by fitting an exponential decay onto a flat background. The number of events is entirely dominated by the error on the area below the exponential. Values with † are for a fit to the whole SSR data set rather than just events near the nuclear recoil band. These fits occasionally produced better results due to the much higher statistics producing a better estimate for the background level. The last columns show the 90% C.L. limits from a Profile Likelihood Ratio (PLR) calculation applied to the events in the WIMP search box. Here 0 delayed events were observed in the veto. The expectation for accidental coincidences was calculated for a delayed coincidence window scaled to accept 99% of decays from the excited state. These two values, along with the efficiency for detection calculated by Monte Carlo simulation, were used as the input for the TRolke method "`SetGaussBkgGaussEff`" to produce the limits shown.

Mass	Dipole	Lifetime	Veto peak	Maximum	PLR 90% C.L. limits	
splitting (keV)	(μ_χ/μ_N)	(μs)	efficiency (%)	likelihood fit	Lower	Upper
80	3×10^{-3}	17.2	1.16	$1.67 \times 10^{4\dagger}$	0	397.4
80	6×10^{-3}	4.30	3.78	$4.29 \times 10^{3\dagger}$	0	129.2
80	1×10^{-2}	1.55	6.72	3.16×10^{4}	0	74.9
90	3×10^{-3}	12.1	1.62	$6.33 \times 10^{3\dagger}$	0	319.4
90	6×10^{-3}	3.00	5.12	$3.67 \times 10^{4\dagger}$	0	106.0
90	1×10^{-2}	1.09	8.28	1.53×10^{3}	0	67.1
100	3×10^{-3}	8.80	2.07	$7.90 \times 10^{3\dagger}$	0	238.6
100	6×10^{-3}	2.20	6.27	$3.82 \times 10^{3\dagger}$	0	81.1
100	1×10^{-2}	0.79	9.53	5.74×10^{2}	0	54.5
110	3×10^{-3}	6.60	2.65	5.93×10^{3}	0	165.9
110	6×10^{-3}	1.65	7.67	3.05×10^{3}	0	59.3
110	1×10^{-2}	0.60	10.47	3.47×10^{2}	0	44.2
120	3×10^{-3}	5.10	2.32	$6.79 \times 10^{3\dagger}$	0	170.9
120	6×10^{-3}	1.40	6.71	2.73×10^{3}	0	60.9
120	1×10^{-2}	0.51	11.1	2.56×10^{7}	0	37.3

Table A.4: As Table A.3 but from simulations of 70 GeV/c^2 magnetic inelastic WIMPs.

Mass splitting (keV)	Dipole (μ_χ/μ_N)	Lifetime (μs)	Veto peak efficiency (%)	Maximum likelihood fit	PLR 90% C.L. limits Lower	Upper
80	3×10^{-3}	17.2	1.29	$1.49 \times 10^{4\dagger}$	0	358.6
80	6×10^{-3}	4.30	4.17	$3.89 \times 10^{3\dagger}$	0	118.7
80	1×10^{-2}	1.55	7.14	2.98×10^{3}	0	70.6
90	3×10^{-3}	12.1	1.98	$5.18 \times 10^{3\dagger}$	0	263.6
90	6×10^{-3}	3.00	5.97	$3.14 \times 10^{3\dagger}$	0	91.0
90	1×10^{-2}	1.09	8.69	1.46×10^{3}	0	64.5
100	3×10^{-3}	8.80	2.66	$6.13 \times 10^{3\dagger}$	0	185.5
100	6×10^{-3}	2.20	7.42	$3.22 \times 10^{3\dagger}$	0	68.7
100	1×10^{-2}	0.79	9.45	5.79×10^{2}	0	55.3
110	3×10^{-3}	6.60	3.39	$4.64 \times 10^{3\dagger}$	0	131.8
110	6×10^{-3}	1.65	8.83	2.65×10^{3}	0	51.8
110	1×10^{-2}	0.60	9.94	3.66×10^{2}	0	47.4
120	3×10^{-3}	5.10	4.07	$3.87 \times 10^{3\dagger}$	0	98.1
120	6×10^{-3}	1.40	9.68	1.89×10^{3}	0	42.3
120	1×10^{-2}	0.51	10.37	2.74×10^{2}	0	40.9
130	3×10^{-3}	4.00	5.06	$3.26 \times 10^{3\dagger}$	0	73.1
130	6×10^{-3}	1.10	11.00	1.17×10^{3}	0	34.4
130	1×10^{-2}	0.40	10.01	1.38×10^{2}	0	39.1
140	3×10^{-3}	3.20	5.63	$3.21 \times 10^{4\dagger}$	0	61.6
140	6×10^{-3}	0.83	11.97	6.65×10^{2}	0	29.6
140	1×10^{-2}	0.32	10.12	9.77×10^{1}	0	36.5

Table A.5: As Table A.3 but from simulations of 100 GeV/c^2 magnetic inelastic WIMPs.

Mass	Dipole	Lifetime	Veto peak	Maximum	PLR 90% C.L. limits	
splitting (keV)	(μ_χ/μ_N)	(μs)	efficiency (%)	likelihood fit	Lower	Upper
80	3×10^{-3}	17.2	1.61	$1.20 \times 10^{4\dagger}$	0	289.0
80	6×10^{-3}	4.30	4.87	$3.33 \times 10^{3\dagger}$	0	100.6
80	1×10^{-2}	1.55	7.52	2.83×10^{3}	0	67.4
90	3×10^{-3}	12.1	2.32	$4.43 \times 10^{3\dagger}$	0	225.0
90	6×10^{-3}	3.00	6.67	$2.81 \times 10^{3\dagger}$	0	81.5
90	1×10^{-2}	1.09	8.75	1.45×10^{3}	0	63.7
100	3×10^{-3}	8.80	3.15	$5.19 \times 10^{3\dagger}$	0	157.7
100	6×10^{-3}	2.20	8.3	$2.88 \times 10^{3\dagger}$	0	62.2
100	1×10^{-2}	0.79	9.08	6.03×10^{2}	0	57.7
110	3×10^{-3}	6.60	4.04	$3.88 \times 10^{3\dagger}$	0	110.2
110	6×10^{-3}	1.65	9.65	2.42×10^{3}	0	47.2
110	1×10^{-2}	0.60	8.97	4.05×10^{2}	0	52.6
120	3×10^{-3}	5.10	5.07	$3.11 \times 10^{3\dagger}$	0	79.3
120	6×10^{-3}	1.40	10.6	1.73×10^{3}	0	39.2
120	1×10^{-2}	0.51	8.94	3.17×10^{2}	0	47.9
130	3×10^{-3}	4.00	6.3	$2.62 \times 10^{3\dagger}$	0	58.7
130	6×10^{-3}	1.10	11.77	1.09×10^{3}	0	32.2
130	1×10^{-2}	0.40	7.99	1.73×10^{2}	0	49.8
140	3×10^{-3}	3.20	7.38	$2.46 \times 10^{3\dagger}$	0	46.9
140	6×10^{-3}	0.83	12.53	6.35×10^{2}	0	28.4
140	1×10^{-2}	0.32	7.23	1.37×10^{2}	0	52.3

Table A.6: As Table A.3 but from simulations of 140 GeV/c^2 magnetic inelastic WIMPs.

Mass	Dipole	Lifetime	Veto peak	Maximum	PLR 90% C.L. limits	
splitting (keV)	(μ_χ/μ_N)	(μs)	efficiency (%)	likelihood fit	Lower	Upper
80	3×10^{-3}	17.2	1.79	$1.08 \times 10^{4\dagger}$	0	256.3
80	6×10^{-3}	4.30	5.35	$3.03 \times 10^{3\dagger}$	0	92.5
80	1×10^{-2}	1.55	7.71	2.76×10^{3}	0	66.1
90	3×10^{-3}	12.1	2.63	$3.91 \times 10^{3\dagger}$	0	197.5
90	6×10^{-3}	3.00	7.18	$2.61 \times 10^{3\dagger}$	0	75.6
90	1×10^{-2}	1.09	8.51	1.48×10^{3}	0	65.9
100	3×10^{-3}	8.80	3.59	$4.54 \times 10^{3\dagger}$	0	137.0
100	6×10^{-3}	2.20	8.78	$2.73 \times 10^{3\dagger}$	0	58.4
100	1×10^{-2}	0.79	8.58	6.38×10^{2}	0	61.4
110	3×10^{-3}	6.60	4.58	$3.43 \times 10^{3\dagger}$	0	96.7
110	6×10^{-3}	1.65	10.15	2.30×10^{3}	0	45.1
110	1×10^{-2}	0.60	8.09	4.49×10^{2}	0	58.5
120	3×10^{-3}	5.10	5.74	$2.74 \times 10^{3\dagger}$	0	70.4
120	6×10^{-3}	1.40	11.05	1.66×10^{3}	0	37.6
120	1×10^{-2}	0.51	7.86	3.61×10^{2}	0	55.0
130	3×10^{-3}	4.00	7.11	$2.32 \times 10^{3\dagger}$	0	52.0
130	6×10^{-3}	1.10	11.86	1.09×10^{3}	0	32.1
130	1×10^{-2}	0.40	6.69	2.06×10^{2}	0	60.6
140	3×10^{-3}	3.20	8.37	$2.16 \times 10^{3\dagger}$	0	41.7
140	6×10^{-3}	0.83	12.34	6.45×10^{2}	0	29.1
140	1×10^{-2}	0.32	5.74	1.72×10^{2}	0	67.5

A.18 Profile Likelihood Ratio Method

A confidence interval for the signal expectation in the second science run was calculated with a Profile Likelihood Ratio (PLR) [26, 315, 92]. This method can be adapted to treat problems with nuisance parameters which are not known exactly, in this case the leakage of the electron recoil background events into the WIMP search area and to a much lesser extent the neutron background. The full likelihood function is given by:

$$L(\pi, \theta|X) = \prod_{i=1}^{n} f(X_i|\pi, \theta) \tag{A.65}$$

where $f(z|\pi, \theta)$ is the probability density function for parameters of interest $\pi = (\pi_1, ..., \pi_k)$, with nuisance parameters $\theta = (\theta_1, ..., \theta_l)$ given the independent observables $\mathbf{X} = (X_1, ..., X_n)$. To cope with the uncertainty in the nuisance parameters they can be factored out. When constructing confidence intervals this may be accomplished by finding a hypothesis test and then inverting that test. For example a hypothesis test $H_0 : \pi = \pi_\mathbf{0}$ and its inverse $H_a : \pi \neq \pi_\mathbf{0}$ give a likelihood test statistic of:

$$\lambda(\pi_\mathbf{0}|X) = \frac{sup\{L(\pi_\mathbf{0}, \theta|X); \theta\}}{sup\{L(\pi, \theta|X); \pi, \theta\}} \tag{A.66}$$

where λ is just a function of π_0 given the data and is not dependent on the nuisance parameters θ. In the context of the electron recoil background as a nuisance parameter λ is the profile likelihood. The nuisance parameter μ_{b2} (see Table 8.1) included estimators from the Poisson distributed ^{137}Cs calibration and also SG predictions treated as a Gaussian truncated at 0. The distribution of the function $-2\log\lambda$ converges to a χ^2 random variable with k degrees of freedom [112]. To get the required confidence interval, $100(1-\alpha)\%$, the true value of the parameter of interest would be covered $100(1-\alpha)\%$ of the time after many repetitions of the experiment. Monte-Carlo sampling over a grid of (π, θ) values was used to obtain the distribution of the profile likelihood ratio. From this the appropriate double sided limit is found by moving out from the minimum (the maximum likelihood estimator) to find the points where the function increases by the α percentile of the distribution.

For the case of a dark matter search with an unknown potential signal s and background b we have the data $X = (N, M)$ where N and M have Poisson distributions with mean $b + s$ and τb respectively, where τ is the probability that a background event falls into the background region (the electron recoil band) divided by the probability that it falls into the signal region (the nuclear recoil band). Here $N = B + S$ where B and S are independent Poisson random variables with mean b and s respectively. b and s are unknown but τ is assumed to be known. The from of the function f used to calculate the likelihood function in equation A.65 is then given by:

$$f(n, m|b, s) = \frac{(s+b)^n}{n!} \exp^{-(s+b)} \cdot \frac{(\tau b)^m}{m!} \exp^{-\tau b} \tag{A.67}$$

using the estimated background from the SG fits and also the estimate from the ^{137}Cs calibration as the nuisance parameters μ_{b2} and the result for the limit of neutron events as the other nuisance parameter μ_{b1} a double-sided 90% CL interval for the signal from the second science run was $0-5.1$ events [26]. Two-bin FC calculations were also made, as in the FSR [254]. The background predictions were capped at the observed levels when the estimated number was higher than that seen, so that the results were not unreasonable due to downward fluctuations of background. This result yielded a maximum of 4.8 signal events at 90% CL, in good agreement with the PLR calculations.

Appendix B

Glossary

- **ADC :**Analogue to digital converter.
- **BAL :** Bulk attenuation length.
- **BAO :** Baryonic acoustic oscillations.
- **CAI :** Calcium-aluminium-rich inclusions, sometimes found in meteors.
- **CCD :** Charge coupled device.
- **CERN :** The Organisation europeenne pour la recherche nucleaire, situated in Geneva. This lab currently houses the large hadron collider (LHC).
- **CDM :** Cold dark matter. These relic dark matter particles have non-relativistic velocities.
- **CMB :** The cosmic microwave background. The photon relic from the big bang.
- **cMSSM :** Constrained minimal supersymmetric standard model. The minimal supersymmetric extension to the standard model.
- **CPT :** Charge conjugate, parity and time. Symmetries of particles which are usually conserved. A subset (CP) has occasionally been observed to be violated.
- **CPU :** Central processing unit.
- **DAq :** Data acquisition. This usually refers to the data acquisition system.

- **DRU :** Differential rate unit (events kg^{-1} day^{-1} keV^{-1}).
- **DTAG :** An energy deposit in the veto which is delayed with respect to a ZEPLIN–III event.
- **ELM :** The electron lifetime monitor.
- **FADC :** Flash analog-to-digital converter.
- **FC :** Feldman Cousins analysis.
- **FLRW :** The Friedmann-Lemaitre-Robertson-Walker solutions to Einstein's field equations.
- **FSR :** The first science run of the ZEPLIN–III instrument.
- **FWHM :** The full width of a pulse at half of its maximum height.
- **golden event :** A golden event is defined as having only a single S1 signal and a single S2 signal.
- **GUI :** Graphical user interface.
- **GUT :** Grand unification theory. The convergence of standard model forces at high energy.
- **Gyr :** A period of 1 billion years.
- **HPG :** High-purity germanium.
- **HS :** High-sensitivity output signal.
- **IC :** Internal conversion.
- **ΛCDM :** The currently favoured cosmological model where the vast majority of the energy density of the Universe is split between cold dark matter (CDM) and dark energy (Λ).
- **LED :** Light emitting diode.
- $\mathcal{L}_{eff}$: The relative scintillation yield between electron and nuclear recoils.

- **LET :** Linear energy transfer. The energy transferred to a material as an ionizing particle travels through it.
- LKP : The lightest Kaluza-Klein particle.
- **LN_2**Liquid nitrogen.
- **LS :** Low-sensitivity output signal.
- **LSP :** The lightest supersymmetric particle.
- **LXe :** Liquid xenon.
- **MACHO :** Massive compact halo object.
- **MCA :** Multi-channel analyser.
- **MEt :** Missing transverse energy. A signature of the creation of dark matter particles.
- **MOND :** Modified Newtonian dynamics. A theory of modified gravity.
- **MSSI :** Multiple scintillation single ionisation events.
- **mSUGRA :** The minimal super gravity model, combining supersymmetry and general relativity.
- **NIM :** Nuclear instrumentation module. These have standardised mechanical and electrical specifications.
- **PLR :** Prole likelihood ratio.
- **PMT :** Photomultiplier tube.
- **PTAG :** An energy deposit in the veto which is in prompt coincidence with a ZEPLIN–III event.
- **QCD :** Quantum chromodynamics. The theory of the strong nuclear force using colour charge.
- **RAM :** Random-access memory.
- **raVen :** The reduction and analysis of veto signals software package.

- **RGA :** Residual gas analysis.
- **RMS :** Root mean square.
- **S1 :** The primary scintillation signal.
- **S2 :** The secondary signal. This is generated by electroluminescence in the gas phase and provides a measurement of the ionisation.
- **SG :** Skew-Gaussian.
- **SM :** The standard model of particle physics.
- **SN1a :** A type 1a supernova, resulting from the explosion of a white dwarf star.
- **SPE :** Single photoelectron.
- **SSR :** The second science run of the ZEPLIN–III instrument.
- **SUSY :** Supersymmetry, an theoretical extension to the standard model of particle physics.
- **TAL :** Technical attenuation length.
- **TeVeS :** Tensor-vector-scalar theory. A theory of modified gravity.
- **TPC :** Time projection chamber.
- **UHV :** Ultra-high vacuum.
- **VUV :** Vacuum ultra-violet photons ranging from 150 to 200 nm.
- **WIMP :** Weakly interacting massive particle.
- **ZE3RA :** The ZEPLIN–III reduction and analysis package.
- **ZEPLIN :** ZonEd Proportional scintillation in LIquid Noble gases.
- $\oplus$ **:**The symbol for Earth.
- $\odot$ **:**The symbol for Sol.

Bibliography

[1] G. Aad and the ATLAS collaboration. Combined search for the standard model higgs boson using up to 4.9 fb1 of pp collision data at with the atlas detector at the lhc. *Physics Letters B*, 0, 2012.

[2] C. E. Aalseth, P. S. Barbeau, and et. al. Results from a search for light-mass dark matter with a *p*-type point contact germanium detector. *Phys. Rev. Lett.*, 106:131301, Mar 2011.

[3] C. E. Aalseth, P. S. Barbeau, and et. al. Search for an annual modulation in a *p*-type point contact germanium dark matter detector. *Phys. Rev. Lett.*, 107:141301, Sep 2011.

[4] C. E. Aalseth et al. Results from a Search for Light-Mass Dark Matter with a P-type Point Contact Germanium Detector. *Phys. Rev. Lett.*, 106:131301, 2011.

[5] D. Abbaneo and et. al. Cern lep report. The LEP collaborations technical report No. CERN-EP/99-15 (unpublished), 1999.

[6] L.F. Abbott and P. Sikivie. A cosmological bound on the invisible axion. *Physics Letters B*, 120(1-3):133 – 136, 1983.

[7] K. Abe, J. Hosaka, and et. al. Distillation of liquid xenon to remove krypton. *Astroparticle Physics*, 31(4):290 – 296, 2009.

[8] K Abe and the XMASS Collaboration. The xmass experiment. *Journal of Physics: Conference Series*, 120(4):042022, 2008.

[9] Nobutaka Abe, Takeo Moroi, and Masahiro Yamaguchi. Anomaly-mediated supersymmetry breaking with axion. *Journal of High Energy Physics*, 2002(01):010, 2002.

[10] A. Abramowski, F. Acero, and H.E.S.S. Collaboration. Search for dark matter annihilation signals from the fornax galaxy cluster with h.e.s.s. *The Astrophysical Journal*, 750(2):123, 2012.

[11] A. Abramowski, F. Acero, and et. al. Search for a dark matter annihilation signal from the galactic center halo with h.e.s.s. *Phys. Rev. Lett.*, 106:161301, Apr 2011.

[12] P. Abreu and et al. Publisher's note: Search for ultrahigh energy neutrinos in highly inclined events at the pierre auger observatory [phys. rev. d 84, 122005 (2011)]. *Phys. Rev. D*, 85:029902, Jan 2012.

[13] N. Ackerman, B. Aharmim, and et. al. Observation of two-neutrino double-beta decay in ^{136}xe with the exo-200 detector. *Phys. Rev. Lett.*, 107:212501, Nov 2011.

[14] P. Adamson, C. Andreopoulos, and et. al. Search for sterile neutrino mixing in the minos long-baseline experiment. *Phys. Rev. D*, 81:052004, Mar 2010.

[15] M. Ageron, J.A. Aguilar, and et. al. Antares: The first undersea neutrino telescope. *Nuclear Instruments and Methods in Physics Research Section A: Accelerators, Spectrometers, Detectors and Associated Equipment*, 656(1):11 – 38, 2011.

[16] S. Agostinelli, J. Allison, K. Amako, and et. al. Geant4, a simulation toolkit. *Nuclear Instruments and Methods in Physics Research Section A: Accelerators, Spectrometers, Detectors and Associated Equipment*, 506(3):250 – 303, 2003.

[17] B. Aharmim, S. N. Ahmed, and et. al. Measurement of the cosmic ray and neutrino-induced muon flux at the sudbury neutrino observatory. *Phys. Rev. D*, 80:012001, Jul 2009.

[18] S. Ahlen, J.B.R. Battat, and et. al. First dark matter search results from a surface run of the 10-l dmtpc directional dark matter detector. *Physics Letters B*, 695(14):124 – 129, 2011.

[19] Z. Ahmed, D. S. Akerib, and et. al. Search for axions with the cdms experiment. *Phys. Rev. Lett.*, 103:141802, Oct 2009.

[20] Z. Ahmed, D. S. Akerib, and et. al. Search for weakly interacting massive particles with the first five-tower data from the cryogenic dark matter search at the soudan underground laboratory. *Phys. Rev. Lett.*, 102:011301, Jan 2009.

[21] Z. Ahmed, D. S. Akerib, and et. al. Results from a low-energy analysis of the cdms ii germanium data. *Phys. Rev. Lett.*, 106:131302, Mar 2011.

[22] Z. Ahmed and et. al. Search for annual modulation in low-energy cdms-ii data. *ArXiv*, 2012. arXiv:1203.1309v1.

[23] D.S. Akerib, X. Bai, and et. al. Data acquisition and readout system for the lux dark matter experiment. *Nuclear Instruments and Methods in Physics Research Section A: Accelerators, Spectrometers, Detectors and Associated Equipment*, 668(0):1 – 8, 2012.

[24] D Akimov, A Bewick, D Davidge, J Dawson, A.S Howard, I Ivaniouchenkov, W.G Jones, J Joshi, V.A Kudryavtsev, T.B Lawson, V Lebedenko, M.J Lehner, P.K Lightfoot, I Liubarsky, R L?scher, J.E McMillan, C.D Peak, J.J Quenby, N.J.C Spooner, T.J Sumner, D.R Tovey, and C.K Ward. Measurements of scintillation efficiency and pulse shape for low energy recoils in liquid xenon. *Physics Letters B*, 524(3-4):245 – 251, 2002.

[25] D.Yu. Akimov, G.J. Alner, H.M. Araùjo, A. Bewick, C. Bungau, A.A. Burenkov, M.J. Carson, H. Chagani, V. Chepel, D. Cline, D. Davidge, E. Daw,

J. Dawson, T. Durkin, B. Edwards, T. Gamble, C. Chag, R.J. Hollingworth, A.S. Howard, W.G. Jones, M. Joshi, K. Mavrokoridis, E. Korolkova, A. Kovalenko, V.A. Kudryavtsev, I.S. Kuznetsov, T. Lawson, V.N. Lebedenko, J.D. Lewin, P. Lightfoot, A. Lindote, I. Liubarsky, M.I. Lopes, R. L?scher, J.E. McMillan, P. Majewski, B. Morgan, D. Muna, A.S. Murphy, F. Neves, G.G. Nicklin, S.M. Paling, D. Muna, J. Pinto da Cunha, S.J.S. Plank, R. Preece, J.J. Quenby, M. Robinson, C. Silva, V.N. Solovov, N.J.T. Smith, P.F. Smith, N.J.C. Spooner, V. Stekhanov, T.J. Sumner, C. Thorne, D.R. Tovey, E. Tziaferi, R.J. Walker, H. Wang, J. White, and F. Wolfs. The zeplin-iii dark matter detector: Instrument design, manufacture and commissioning. *Astroparticle Physics*, 27(1):46 – 60, 2007.

[26] D.Yu. Akimov, H.M. Araùjo, E.J. Barnes, V.A. Belov, A. Bewick, A.A. Burenkov, V. Chepel, A. Currie, L. DeViveiros, B. Edwards, C. Ghag, A. Hollingsworth, M. Horn, W.G. Jones, G.E. Kalmus, A.S. Kobyakin, A.G. Kovalenko, V.N. Lebedenko, A. Lindote, M.I. Lopes, R. L?scher, P. Majewski, A.St.J. Murphy, F. Neves, S.M. Paling, J. Pinto da Cunha, R. Preece, J.J. Quenby, L. Reichhart, P.R. Scovell, C. Silva, V.N. Solovov, N.J.T. Smith, V.N. Stekhanov, T.J. Sumner, C. Thorne, and R.J. Walker. Wimp-nucleon cross-section results from the second science run of zeplin-iii. *Physics Letters B*, 709(1-2):14 – 20, 2012.

[27] D.Yu. Akimov, H.M. Araùjo, E.J. Barnes, V.A. Belov, A.A. Burenkov, V. Chepel, A. Currie, B. Edwards, V. Francis, C. Ghag, A. Hollingsworth, M. Horn, G.E. Kalmus, A.S. Kobyakin, A.G. Kovalenko, V.N. Lebedenko, A. Lindote, M.I. Lopes, R. L?scher, K. Lyons, P. Majewski, A.St.J. Murphy, F. Neves, S.M. Paling, J. Pinto da Cunha, R. Preece, J.J. Quenby, L. Reichhart, P.R. Scovell, V.N. Solovov, N.J.T. Smith, P.F. Smith, V.N. Stekhanov, T.J. Sumner, R. Taylor, C. Thorne, and R.J. Walker. The zeplin-iii anti-coincidence veto detector. *Astroparticle Physics*, 34(3):151 – 163, 2010.

[28] Andreas Albrecht and Paul J. Steinhardt. Cosmology for grand unified theories with radiatively induced symmetry breaking. *Phys. Rev. Lett.*, 48:1220–1223, Apr 1982.

[29] J. Alcaraz, D. Alvisi, and et. al. Search for antihelium in cosmic rays. *Physics Letters B*, 461(4):387 – 396, 1999.

[30] J. Aleksić, E.A. Alvarez, and et. al. Searches for dark matter annihilation signatures in the segue 1 satellite galaxy with the magic-i telescope. *Journal of Cosmology and Astroparticle Physics*, 2011(06):035, 2011.

[31] S. Allen. Chandra website. http://chandra.harvard.edu/, 2008.

[32] G.J. Alner, H. Araujo, G.J. Arnison, J.C. Barton, A. Bewick, C. Bungau, B. Camanzi, M.J. Carson, D. Davidge, J.V.Dawson, G.J. Davies, J.C. Davies, T. Durkin, T. Gamble, S.P. Hart, R.J. Hollingworth, G.J. Homer, A.S. Howard, I. Ivaniouchenkov, W.G. Jones, M.K. Joshi, V.A. Kudryavtsev, T.B. Lawson, V. Lebedenko, J.D. Lewin, P.K. Lightfoot, I. Liubarsky, M.J. Lehner, R. L?scher,

J.E. McMillan, B. Morgan, A. Nicholls, G. Nicklin, S.M. Paling, R.M. Preece, J.W. Roberts, M. Robinson, J.J. Quenby, N.J.T. Smith, P.F. Smith, N.J.C. Spooner, T.J. Sumner, and D.R. Tovey. First limits on nuclear recoil events from the zeplin i galactic dark matter detector. *Astroparticle Physics*, 23(5):444 – 462, 2005.

[33] G.J. Alner, H.M. Araùjo, A. Bewick, C. Bungau, B. Camanzi, M.J. Carson, R.J. Cashmore, H. Chagani, V. Chepel, D. Cline, D. Davidge, J.C. Davies, E. Daw, J. Dawson, T. Durkin, B. Edwards, T. Gamble, J. Gao, C. Ghag, A.S. Howard, W.G. Jones, M. Joshi, E.V. Korolkova, V.A. Kudryavtsev, T. Lawson, V.N. Lebedenko, J.D. Lewin, P. Lightfoot, A. Lindote, I. Liubarsky, M.I. Lopes, R. L?scher, P. Majewski, K. Mavrokoridis, J.E. McMillan, B. Morgan, D. Muna, A.St.J. Murphy, F. Neves, G.G. Nicklin, W. Ooi, S.M. Paling, J. Pinto da Cunha, S.J.S. Plank, R.M. Preece, J.J. Quenby, M. Robinson, G. Salinas, F. Sergiampietri, C. Silva, V.N. Solovov, N.J.T. Smith, P.F. Smith, N.J.C. Spooner, T.J. Sumner, C. Thorne, D.R. Tovey, E. Tziaferi, R.J. Walker, H. Wang, J.T. White, and F.L.H. Wolfs. First limits on wimp nuclear recoil signals in zeplin-ii: A two-phase xenon detector for dark matter detection. *Astroparticle Physics*, 28(3):287 – 302, 2007.

[34] G.J. Alner, H.M. Araùo, A. Bewick, C. Bungau, B. Camanzi, M.J. Carson, R.J. Cashmore, H. Chagani, V. Chepel, D. Cline, D. Davidge, J.C. Davies, E. Daw, J. Dawson, T. Durkin, B. Edwards, T. Gamble, J. Gao, C. Ghag, A.S. Howard, W.G. Jones, M. Joshi, E.V. Korolkova, V.A. Kudryavtsev, T. Lawson, V.N. Lebedenko, J.D. Lewin, P. Lightfoot, A. Lindote, I. Liubarsky, M.I. Lopes, R. L?scher, P. Majewski, K. Mavrokoridis, J.E. McMillan, B. Morgan, D. Muna, A.St.J. Murphy, F. Neves, G.G. Nicklin, W. Ooi, S.M. Paling, J. Pinto da Cunha, S.J.S. Plank, R.M. Preece, J.J. Quenby, M. Robinson, G. Salinas, F. Sergiampietri, C. Silva, V.N. Solovov, N.J.T. Smith, P.F. Smith, N.J.C. Spooner, T.J. Sumner, C. Thorne, D.R. Tovey, E. Tziaferi, R.J. Walker, H. Wang, J. White, and F.L.H. Wolfs. Limits on spin-dependent wimp-nucleon cross-sections from the first zeplin-ii data. *Physics Letters B*, 653(2-4):161 – 166, 2007.

[35] R. A. Alpher, H. Bethe, and G. Gamow. The origin of chemical elements. *Phys. Rev.*, 73:803–804, Apr 1948.

[36] A. Alton and E. Zetterlund. Direct detection of dark matter with the DarkSide experiment. In *APS Prairie Section Meeting Abstracts*, page C1008, November 2011.

[37] Ambrosioetal. and MACRO collaboration. Final results of magnetic monopole searches with the macro experiment. *The European Physical Journal C - Particles and Fields*, 25:511–522, 2002.

[38] Amcrys-H. http://www.amcrys-h.com. 60, Lenin Ave., Kahrkov, 310001, Ukraine, 1998.

[39] Yuri Amelin, Alexander N. Krot, and et. al. Lead isotopic ages of chondrules and calcium-aluminum-rich inclusions. *Science*, 297(5587):1678–1683, 2002.

[40] C. Amsler, M. Doser, and et. al.r. Review of particle physics. *Physics Letters B*, 667(1-5):1 – 6, 2008.

[41] V. Chepel anf H. Araùjo. Liquid noble gas detectors for low energy particle physics. *ArXiv*, 2012. submitted to JINST.

[42] J. Angle, E. Aprile, and et. al. First results from the xenon10 dark matter experiment at the gran sasso national laboratory. *Phys. Rev. Lett.*, 100:021303, Jan 2008.

[43] G. Angloher, M. Bauer, and et. al. Results from 730 kg?days of the cresst-ii dark matter search. *The European Physical Journal C - Particles and Fields*, 72:1–22, 2012. 10.1140/epjc/s10052-012-1971-8.

[44] P. Antonioli, C. Ghetti, E.V. Korolkova, V.A. Kudryavtsev, and G. Sartorelli. A three-dimensional code for muon propagation through the rock: Music. *Astroparticle Physics*, 7(4):357 – 368, 1997.

[45] E. Aprile, M. Alfonsi, K. Arisaka, and et. al. Dark matter results from 225 live days of xenon100 data. *ArXiv*, 2012. arXiv:1207.5988v1.

[46] E. Aprile, K. Arisaka, and et. al. Dark matter results from 100 live days of xenon100 data. *Phys. Rev. Lett.*, 107:131302, Sep 2011.

[47] E. Aprile, L. Baudis, and et. al. New measurement of the relative scintillation efficiency of xenon nuclear recoils below 10 kev. *Phys. Rev. C*, 79:045807, Apr 2009.

[48] E. Aprile, C. E. Dahl, and et. al. Simultaneous measurement of ionization and scintillation from nuclear recoils in liquid xenon for a dark matter experiment. *Phys. Rev. Lett.*, 97:081302, Aug 2006.

[49] E. Aprile and T. Doke. Liquid xenon detectors for particle physics and astrophysics. *Rev. Mod. Phys.*, 82:2053–2097, Jul 2010.

[50] H.M. Araùjo, D.Yu. Akimov, G.J. Alner, A. Bewick, C. Bungau, B. Camanzi, M.J. Carson, V. Chepel, H. Chagani, D. Davidge, J.C. Davies, E. Daw, J. Dawson, T. Durkin, B. Edwards, T. Gamble, C. Ghag, R. Hollingworth, A.S. Howard, W.G. Jones, M. Joshi, J. Kirkpatrick, A. Kovalenko, V.A. Kudryavtsev, V.N. Lebedenko, T. Lawson, J.D. Lewin, P. Lightfoot, A. Lindote, I. Liubarsky, M.I. Lopes, R. Lscher, P. Majewski, K. Mavrokoridis, J. McMillan, B. Morgan, D. Muna, A.S. Murphy, F. Neves, G. Nicklin, S. Paling, J. Pinto da Cunha, S. Plank, R. Preece, J.J. Quenby, M. Robinson, C. Silva, V.N. Solovov, N.J.T. Smith, P.F. Smith, N.J.C. Spooner, V. Stekhanov, T.J. Sumner, D.R. Tovey, C. Thorne, E. Tziaferi, and R.J. Walker. The zeplin-iii dark matter detector: Performance study using an end-to-end simulation tool. *Astroparticle Physics*, 26(2):140 – 153, 2006.

[51] H.M. Araùjo, D.Yu. Akimov, E.J. Barnes, V.A. Belov, A. Bewick, A.A. Burenkov, V. Chepel, A. Currie, L. DeViveiros, B. Edwards, C. Ghag, A. Hollingsworth, M. Horn, G.E. Kalmus, A.S. Kobyakin, A.G. Kovalenko, V.N. Lebedenko, A. Lindote, M.I. Lopes, R. L?scher, P. Majewski, A. St. J. Murphy, F. Neves, S.M. Paling, J. Pinto da Cunha, R. Preece, J.J. Quenby, L. Reichhart, P.R. Scovell, C. Silva, V.N. Solovov, N.J.T. Smith, P.F. Smith, V.N. Stekhanov, T.J. Sumner, C. Thorne, and R.J. Walker. Radioactivity backgrounds in zeplin-iii. *Astroparticle Physics*, 35(8):495 – 502, 2012.

[52] H.M. Araùjo, J. Blockley, C. Bungau, M.J. Carson, H. Chagani, E. Daw, B. Edwards, C. Ghag, E.V. Korolkova, V.A. Kudryavtsev, P.K. Lightfoot, A. Lindote, I. Liubarsky, R. L?scher, P. Majewski, K. Mavrokoridis, J.E. McMillan, A.St.J. Murphy, S.M. Paling, J. Pinto da Cunha, R.M. Preece, M. Robinson, N.J.T. Smith, P.F. Smith, N.J.C. Spooner, T.J. Sumner, R.J. Walker, H. Wang, and J. White. Measurements of neutrons produced by high-energy muons at the boulby underground laboratory. *Astroparticle Physics*, 29(6):471 – 481, 2008.

[53] A. Arbey, M. Battaglia, A. Djouadi, F. Mahmoudi, and J. Quevillon. Implications of a 125 gev higgs for supersymmetric models. *Physics Letters B*, 708(1-2):162–169, 2012.

[54] S. Archambault, F. Aubin, and et. al. Dark matter spin-dependent limits for wimp interactions on 19f by picasso. *Physics Letters B*, 682(2):185 – 192, 2009.

[55] E. Armengaud, C. Augier, and et. al. Final results of the edelweiss-ii wimp search using a 4-kg array of cryogenic germanium detectors with interleaved electrodes. *Physics Letters B*, 702(5):329 – 335, 2011.

[56] E. Armengaud and et. al. A search for low-mass wimps with edelweiss-ii heat-and-ionization detectors. *ArXiv*, 2012. arXiv:1207.1815v1.

[57] F Arneodo, B Baiboussinov, and et. al. Scintillation efficiency of nuclear recoil in liquid xenon. *Nuclear Instruments and Methods in Physics Research Section A: Accelerators, Spectrometers, Detectors and Associated Equipment*, 449(12):147 – 157, 2000.

[58] S. J. Asztalos, R. F. Bradley, and et. al. Improved rf cavity search for halo axions. *Phys. Rev. D*, 69:011101, Jan 2004.

[59] S Parke B. Kayser. The neutrinos. *Fermilab notes*, 2009.

[60] David J. Bacon and Bjrn Malte Schfer. Twist and turn: weak lensing image distortions to second order. *Monthly Notices of the Royal Astronomical Society*, 396(4):2167–2175, 2009.

[61] H. Baer, V. Barger, and A. Mustafayev. Implications of a 125 gev higgs scalar for lhc susy and neutralino dark matter searches. *ArXiv*, 2011. arXiv:1112.3017v2, Report number: UMN-TH-3024/11; FTPI-MINN-11/32.

[62] H. Baer, V. Barger, and A. Mustafayev. Neutralino dark matter in msugra/cmssm with a 125 gev light higgs scalar. *ArXiv*, 2012. arXiv:1202.4038v1.

[63] H. Baer, A. Lessa, S. Rajagopalan, and W. Sreethawong. Mixed axion/neutralino cold dark matter in supersymmetric models. *ArXiv*, 2011. arXiv:1103.5413v1.

[64] Howard Baer, Andre Lessa, and Warintorn Sreethawong. Coupled boltzmann calculation of mixed axion/neutralino cold dark matter production in the early universe. *Journal of Cosmology and Astroparticle Physics*, 2012(01):036, 2012.

[65] C. A. Baker, D. D. Doyle, and et. al. Improved experimental limit on the electric dipole moment of the neutron. *Phys. Rev. Lett.*, 97:131801, Sep 2006.

[66] S. N. Balashov and et. al. https://www.neutronedm.org/. arXiv:0709.2428v1, 2007.

[67] E. A. Baltz, B. Berenji, and et. al. Pre-launch estimates for GLAST sensitivity to dark matter annihilation signals. *jcap*, 7:13, jul 2008.

[68] R. Barate, I. De Bonis, and et. al. Search for supersymmetric particles in e+e collisions at s up to 202 gev and mass limit for the lightest neutralino. *Physics Letters B*, 499(12):67 – 84, 2001.

[69] P S Barbeau, J I Collar, and O Tench. Large-mass ultralow noise germanium detectors: performance and applications in neutrino and astroparticle physics. *Journal of Cosmology and Astroparticle Physics*, 2007(09):009, 2007.

[70] William A. Bardeen, R.D. Peccei, and T. Yanagida. Constraints on variant axion models. *Nuclear Physics B*, 279(3-4):401 – 428, 1987.

[71] E. J. Barnes. *A veto for the ZEPLIN-III dark matter detector*. PhD thesis, The University of Edinbugh School of Physics and Astronomy, 2010.

[72] Augusto Barroso and Nimai C. Mukhopadhyay. Axions: To be or not to be? *Physics Letters B*, 106(1-2):91 – 94, 1981.

[73] H. Bateman. Solution of a system of differential equations occurring in the theory of radio-active transformations. *Proc. Cambridge Phil. Soc.*, 15, 1910.

[74] G. Battistoni, S. Muraro, P.R. Sala, and et. al. The fluka code: Description and benchmarking. *AIP Conference Proceeding*, 896, 2007.

[75] V. Bednyakov and H. Klapdor-Kleingrothaus. Direct search for dark matterstriking the balanceand the future. *Physics of Particles and Nuclei*, 40:583–611, 2009. 10.1134/S1063779609050013.

[76] Jacob D. Bekenstein. Relativistic gravitation theory for the modified newtonian dynamics paradigm. *Phys. Rev. D*, 70:083509, Oct 2004.

[77] Bell. http://www.bell-labs.com/org/physicalsciences/pro jects/darkmatter/. Bell Labs.

[78] P. Benetti, R. Acciarri, and et. al. First results from a dark matter search with liquid argon at 87 k in the gran sasso underground laboratory. *Astroparticle Physics*, 28(6):495 – 507, 2008.

[79] C. L. Bennett, R. S. Hill, and et. al. Seven-year wilkinson microwave anisotropy probe (wmap) observations: Are there cosmic microwave background anomalies? *The Astrophysical Journal Supplement Series*, 192(2):17, 2011.

[80] Berkeley. http://cedar.berkeley.edu/plotter. Berkeley dark matter detector limit plotter.

[81] R. Bernabei, P. Belli, and et. al. First results from dama/libra and the combined results withdama/nai. *The European Physical Journal C - Particles and Fields*, 56:333–355, 2008. 10.1140/epjc/s10052-008-0662-y.

[82] R. Bernabei, P. Belli, and et. al. New results from dama/libra. *The European Physical Journal C - Particles and Fields*, 67:39–49, 2010.

[83] Gianfranco Bertone, David G. Cerdeo, and et. al. Global fits of the cmssm including the first lhc and xenon100 data. *Journal of Cosmology and Astroparticle Physics*, 2012(01):015, 2012.

[84] Gianfranco Bertone, Dan Hooper, and Joseph Silk. Particle dark matter: evidence, candidates and constraints. *Physics Reports*, 405(5-6):279 – 390, 2005.

[85] Fedor Bezrukov, Felix Kahlhoefer, and Manfred Lindner. Interplay between scintillation and ionization in liquid xenon dark matter searches. *Astroparticle Physics*, 35(3):119 – 127, 2011.

[86] S. Biagi. http://consult.cern.ch/writeup/magboltz/, 1995. Magboltz - transport of electrons in gas mixtures.

[87] C. Moni Bidin, G. Carraro, R. A. Mendez, and R. Smith. No evidence of dark matter in the solar neighbourhood. *ArXiv*, 2012. arXiv:1204.3919v1.

[88] J Billard, F Mayet, C Grignon, and D Santos. Directional detection of dark matter with mimac: Wimp identification and track reconstruction. *Journal of Physics: Conference Series*, 309(1):012015, 2011.

[89] A. Birkedal-Hansen. rsugra: Putting nonuniversal gaugino masses on the (w)map. *ArXiv*, 2003. arXiv:hep-ph/0306144v1.

[90] Abhijit Biswas and Krishnan Mani. Relativistic perihelion precession of orbits of venus and the earth. *Central European Journal of Physics*, 6:754–758, 2008. 10.2478/s11534-008-0081-6.

[91] Michael R. Blanton, David W. Hogg, and et. al. The galaxy luminosity function and luminosity density at redshift z = 0.1. *The Astrophysical Journal*, 592(2):819, 2003.

[92] Michael Woodroofe Bodhisattava Sen, Matthew Walker. On the unified method with nuisanc parameters. *Statistical Sinica*, 19:301 – 314, 2009.

[93] W J Bolte, J I Collar, and et. al. A bubble chamber for dark matter detection (the coupp project status). *Journal of Physics: Conference Series*, 39(1):126, 2006.

[94] F. Bosch, T. Faestermann, and et. al. Observation of bound-state beta minus decay of fully ionized 187-re: 187-re 187-os cosmochronometry. *Phys. Rev. Lett.*, 77:5190–5193, Dec 1996.

[95] Mark Boulay, Bei Cai, and the Deap/Clean Collaboration. Dark matter search at snolab with deap-1 and deap/clean-3600. *Journal of Physics: Conference Series*, 136(4):042081, 2008.

[96] J. Bovy and S. Tremaine. On the local dark matter density. *ArXiv*, 2012. arXiv:1205.4033v2.

[97] M. Boylan-Kolchin, V. Springel, and et. al. Resolving cosmic structure formation with the Millennium-II Simulation. *Monthly Notices of the Royal Astronomical Society*, 398:1150–1164, September 2009.

[98] Marusa Bradac, Tim Schrabback, and et. al. Dark matter and baryons in the x-ray luminous merging galaxy cluster rx j1347.51145. *The Astrophysical Journal*, 681(1):187, 2008.

[99] Torsten Bringmann, Michele Doro, and Mattia Fornasa. Dark matter signals from draco and willman 1: prospects for magic ii and cta. *Journal of Cosmology and Astroparticle Physics*, 2009(01):016, 2009.

[100] P.L. Brink, B. Cabrera, and et. al. First test runs of a dark-matter detector with interleaved ionization electrodes and phonon sensors for surface-event rejection. *Nuclear Instruments and Methods in Physics Research Section A: Accelerators, Spectrometers, Detectors and Associated Equipment*, 559(2):414 – 416, 2006.

[101] Andrew Brown, Sam Henry, Hans Kraus, and Christopher McCabe. Extending the cresst-ii commissioning run limits to lower masses. *Phys. Rev. D*, 85:021301, Jan 2012.

[102] M. L. Brown, P. Ade, and The QUaD collaboration. Improved measurements of the temperature and polarization of the cosmic microwave background from quad. *The Astrophysical Journal*, 705(1):978, 2009.

[103] E. Browne and J. K. Tuli. Nuclear data sheets 108, 2173. National Nuclear Data Center, Brookhaven National Laboratory, 2007.

[104] Rene Brun and Fons Rademakers. Root - an object oriented data analysis framework. *Nuclear Instruments and Methods in Physics Research Section A: Accelerators, Spectrometers, Detectors and Associated Equipment*, 389(1-2):81 – 86, 1997.

[105] H. A. Buchdahl. Non-linear lagrangians and cosmological theory. *Monthly Notices of the Royal Astronomical Society*, 150:1, 1970.

[106] O. Buchmueller, R. Cavanaugh, and et. al. Implications of initial lhc searches for supersymmetry. *The European Physical Journal C - Particles and Fields*, 71:1–13, 2011. 10.1140/epjc/s10052-011-1634-1.

[107] O. Buchmueller, R. Cavanaugh, and et. al. Supersymmetry and dark matter in light of lhc 2010 and xenon100 data. *The European Physical Journal C - Particles and Fields*, 71(8):1–22, 2011-08-01.

[108] S Burgos, E Daw, and et. al. Low energy electron and nuclear recoil thresholds in the drift-ii negative ion tpc for dark matter searches. *Journal of Instrumentation*, 4(04):P04014, 2009.

[109] S. Capozziello, S. Carloni, and A. Troisi. Quintessence without scalar fields. *Recent Res. Dev. Astron. Astrophys*, 1, 2003.

[110] S. Caron, J. Laamanen, I. Niessen, and A. Str"ubig. Higgs and non-universal gaugino masses: no susy signal expected yet? *ArXiv*, 2012. arXiv:1202.5288v2.

[111] Sean M. Carroll, Vikram Duvvuri, Mark Trodden, and Michael S. Turner. Is cosmic speed-up due to new gravitational physics? *Phys. Rev. D*, 70:043528, Aug 2004.

[112] George Casella and Roger L. Berger. *Statistical Inference*. Duxbury Press, 2 edition, June 2001.

[113] A. H. Chamseddine, R. Arnowitt, and Pran Nath. Locally supersymmetric grand unification. *Phys. Rev. Lett.*, 49:970–974, Oct 1982.

[114] J. Chang. An excess of cosmic ray electrons at energies of 300-800 gev. *Nature*, 456:362 – 365, 2008.

[115] Spencer Chang, Jia Liu, and et. al. Cogent interpretations. *Journal of Cosmology and Astroparticle Physics*, 2010(08):018, 2010.

[116] Spencer Chang, Neal Weiner, and Itay Yavin. Magnetic inelastic dark matter. *Phys. Rev. D*, 82:125011, Dec 2010.

[117] D. M. Chen. Flux-limited strong gravitational lensing and dark energy. *A&A*, 418(2):387–392, 2004.

[118] V. Chepel, M.I. Lopes, and V. Solovov. Primary scintillation yield and ratio in liquid xenon. *Radiation Physics and Chemistry*, 74(3-4):160 – 167, 2005.

[119] V. Chepel, V. Solovov, F. Neves, A. Pereira, P.J. Mendes, C.P. Silva, A. Lindote, J. Pinto da Cunha, M.I. Lopes, and S. Kossionides. Scintillation efficiency of liquid xenon for nuclear recoils with the energy down to 5.0 kev. *Astroparticle Physics*, 26(1):58 – 63, 2006.

[120] J. H. Christenson, J. W. Cronin, V. L. Fitch, and R. Turlay. Evidence for the 2π decay of the k_2^0 meson. *Phys. Rev. Lett.*, 13:138–140, Jul 1964.

[121] CLASH. *http://archive.stsci.edu/prepds/clash/.* CLASH website.

[122] K. Clausen and C. Winkler. "integral" - a challenging scientific mission. *ESA Bulletin*, 79:6 – 3, 1994.

[123] G. M. Clemence. The relativity effect in planetary motions. *Rev. Mod. Phys.*, 19:361–364, Oct 1947.

[124] Timothy Clifton, Pedro G. Ferreira, Antonio Padilla, and Constantinos Skordis. Modified gravity and cosmology. *Physics Reports*, 513(13):1 – 189, 2012.

[125] D. Clowe. Chandra website. http://chandra.harvard.edu/, 2006.

[126] Douglas Clowe, Marusa Bradac, and et. al. A direct empirical proof of the existence of dark matter. *The Astrophysical Journal Letters*, 648(2):L109, 2006.

[127] Alain Coc, Stphane Goriely, Yi Xu, Matthias Saimpert, and Elisabeth Vangioni. Standard big bang nucleosynthesis up to cno with an improved extended nuclear network. *The Astrophysical Journal*, 744(2):158, 2012.

[128] The ZEPLIN-III collaboration. *http://www.hep.ph.ic.ac.uk/ZEPLIN-III-Project/.* ZEPLIN–III website.

[129] The CHANDRA collaboration website. *http://nssdc.gsfc.nasa.gov/nmc/spacecraftdisplay.do?id=040b. CHANDRA website, 2013.*

[130] The MUSTANG collaboration website. http://www.gb.nrao.edu/mustang/. MUSTANG website, 2013.

[131] J. I. Collar. A comparison between the low-energy spectra from cogent and cdms. ArXiv*, 2011. arXiv:1103.3481v1.*

[132] J. I. Collar. A realistic assessment of the sensitivity of xenon10 and xenon100 to light-mass wimps. ArXiv*, 2011. arXiv:1106.0653v3.*

[133] Matthew Colless, Gavin Dalton, and the 2dFGRS team. The 2df galaxy redshift survey: spectra and redshifts. Monthly Notices of the Royal Astronomical Society*, 328(4):1039–1063, 2001.*

[134] P. Collon, T. Antaya, and et. al. Measurement of 81kr in the atmosphere. Nuclear Instruments and Methods in Physics Research Section B: Beam Interactions with Materials and Atoms*, 123(1-4):122 – 127, 1997.*

[135] J. Conrad. Cern, root. ROOT class, 2004.

[136] J. Cooley and The CDMS-II Collaboration. Dark matter search results from the cdms ii experiment. Science*, 2010.*

[137] Cornell. Cornell university dept. of astronomy. Palomar observatory.

[138] *N. Coron et al. 2010 update on the ROSEBUD project.* PoS, *IDM2010:054, 2011.*

[139] *Richard H Cyburt, Brian D Fields, and Keith A Olive. An update on the big bang nucleosynthesis prediction for 7 li: the problem worsens.* Journal of Cosmology and Astroparticle Physics, *2008(11):012, 2008.*

[140] *G. Czapek, A. Federspiel, and et. al. Branching ratio for the rare pion decay into positron and neutrino.* Phys. Rev. Lett., *70:17–20, Jan 1993.*

[141] *F. De Lorenzi, O. Gerhard, and et. al. Dearth of dark matter or massive dark halo? mass-shape-anisotropy degeneracies revealed by nmagic dynamical models of the elliptical galaxy ngc 3379.* Monthly Notices of the Royal Astronomical Society, *395(1):76–96, 2009.*

[142] *David S. P. Dearborn, David N. Schramm, and Gary Steigman. Astrophysical constraints on the couplings of axions, majorons, and familons.* Phys. Rev. Lett., *56:26–29, Jan 1986.*

[143] *D. DeCamp, B. Deschizeaux, and et. al. Determination of the number of light neutrino species.* Physics Letters B, *231(4):519 – 529, 1989.*

[144] *J. P. Dietrich, N. Werner, and D. Clowe et. al. A filament of dark matter between two clusters of galaxies.* Nature, *487, 2012.*

[145] *Michael Dine, Willy Fischler, and Mark Srednicki. A simple solution to the strong cp problem with a harmless axion.* Physics Letters B, *104(3):199 – 202, 1981.*

[146] *DLR. http://www.dlr.de/dlr/en/desktopdefault.aspx/tabid-10424. ROSAT website.*

[147] *Scott Dodelson, Alessandro Melchiorri, and Anze Slosar. Is cosmology compatible with sterile neutrinos?* Phys. Rev. Lett., *97:041301, Jul 2006.*

[148] *T. Doke, A. Hitachi, and et. al. Estimation of fano factors in liquid argon, krypton, xenon and xenon-doped liquid argon.* Nuclear Instruments and Methods, *134:353–357, apr 1976.*

[149] *Tadayoshi Doke and Kimiaki Masuda. Present status of liquid rare gas scintillation detectors and their new application to gamma-ray calorimeters.* Nuclear Instruments and Methods in Physics Research Section A: Accelerators, Spectrometers, Detectors and Associated Equipment, *420(1-2):62 – 80, 1999.*

[150] *P. Draper, P. Meade, M. Reece, and D. Shih. Implications of a 125 gev higgs for the mssm and low-scale susy breaking.* ArXiv, *2011. arXiv:1112.3068v1.*

[151] *H. Dreiner. Hide and seek with supersymmetry.* ArXiv:hep-ph, *1999. arXiv:hep-ph/9902347v1.*

[152] *H. K. Dreiner, C. Hanhart, and et. al. Supernovas and light neutralinos: Sn 1987a bounds on supersymmetry reexamined.* Phys. Rev. D, *68:055004, Sep 2003.*

[153] *Herbi K. Dreiner, Howard E. Haber, and Stephen P. Martin. Two-component spinor techniques and feynman rules for quantum field theory and supersymmetry.* Physics Reports, *494(12):1 – 196, 2010.*

[154] *Gintaras Dūda, Ann Kemper, and Paolo Gondolo. Model-independent form factors for spin-independent neutralinonucleon scattering from elastic electron scattering data.* Journal of Cosmology and Astroparticle Physics, *2007(04):012, 2007.*

[155] *Gia Dvali, Gregory Gabadadze, and Massimo Porrati. 4d gravity on a brane in 5d minkowski space.* Physics Letters B, *485(1-3):208 – 214, 2000.*

[156] *B. N. V. Edwards.* The ZEPLIN Dark Matter Search: Two Phase Xenon as a WIMP Target. *PhD thesis, Department of Physics, Imperial College London, 2009.*

[157] *Klaus Ehret, Maik Frede, and et. al. New alps results on hidden-sector lightweights.* Physics Letters B, *689(45):149 – 155, 2010.*

[158] *A. Einstein. Die feldgleichungen der gravitation.* Königlich Preußische Akademie der Wissenschaften, *6:233–243, 1915.*

[159] *A. Einstein. Die grundlage der allgemeinen relativittstheorie.* Annalen der Physik, *354(7):769–822, 1916.*

[160] *Daniel J. Eisenstein, Idit Zehavi, and et. al. Detection of the baryon acoustic peak in the large-scale correlation function of sdss luminous red galaxies.* The Astrophysical Journal, *633(2):560, 2005.*

[161] *J. Ellis, J.L. Feng, and et. al. Prospects for detecting supersymmetric dark matter at post-lep benchmark points.* The European Physical Journal C - Particles and Fields, *24:311–322, 2002. 10.1007/s100520200897.*

[162] *John Ellis, S. Kelley, and D.V. Nanopoulos. Probing the desert using gauge coupling unification.* Physics Letters B, *260(12):131 – 137, 1991.*

[163] *John Ellis and K.A. Olive. Constraints on light particles from supernova sn 1987a.* Physics Letters B, *193(4):525 – 530, 1987.*

[164] *John Ellis, Keith A. Olive, Yudi Santoso, and Vassilis C. Spanos. Supersymmetric dark matter in light of wmap.* Physics Letters B, *565(0):176 – 182, 2003.*

[165] *J. Engel. Nuclear form factors for the scattering of weakly interacting massive particles.* Physics Letters B, *264(1-2):114 – 119, 1991.*

[166] *J. Engel, S. Pittel, and P. Vogel. Nuclear physics of dark matter detection.* Int. J. Mod. Phys. E, *1, 1992.*

[167] D. Fabricant and P. Gorenstein. Further evidence for m87's massive, dark halo. ApJ, 267:535–546, April 1983.

[168] Daniele S. M. Fantin, Anne M. Green, and Michael R. Merrifield. Ultrafine dark matter structure in the solar neighbourhood. Monthly Notices of the Royal Astronomical Society, 418(4):2648–2655, 2011.

[169] V. Faraoni and T. P. Sotiriou. f(r) gravity: successes and challenges. In XVIII Congresso SIGRAV proceedings, 2008.

[170] M. Feast and P. Whitelock. Galactic kinematics of cepheids from hipparcos proper motions. mnras, 291:683, nov 1997.

[171] Daniel Feldman, Gordon Kane, Eric Kuflik, and Ran Lu. A new (string motivated) approach to the little hierarchy problem. Physics Letters B, 704(12):56 – 61, 2011.

[172] Gary J. Feldman and Robert D. Cousins. Unified approach to the classical statistical analysis of small signals. Phys. Rev. D, 57:3873–3889, Apr 1998.

[173] M. Felizardo, T. Morlat, and et. al. First results of the phase ii simple dark matter search. Phys. Rev. Lett., 105:211301, Nov 2010.

[174] Jonathan L. Feng, Jason Kumar, Danny Marfatia, and David Sanford. Isospin-violating dark matter. Physics Letters B, 703(2):124 – 127, 2011.

[175] Jonathan L. Feng, Konstantin T. Matchev, and Takeo Moroi. Focus points and naturalness in supersymmetry. Phys. Rev. D, 61:075005, Mar 2000.

[176] A. Ferrari, P.R. Sala, A. Fasso, and J. Ranft. Fluka: a multi-particle transport code. CERN-2005-10, 2005.

[177] P. G. Ferreira, C. Skordis, and C. Zunckel. Dark matter, modified gravity, and the mass of the neutrino. Phys. Rev. D, 78:044043, Aug 2008.

[178] Brian D. Fields. The primordial lithium problem. Annual Review of Nuclear and Particle Science, 61(1):47–68, 2011.

[179] D. J. Fixsen. The temperature of the cosmic microwave background. The Astrophysical Journal, 707(2):916, 2009.

[180] A. Fontana, L. Pozzetti, and et. al. The k20 survey. A&A, 424(1):23–42, 2004.

[181] W. Forman, C. Jones, and W. Tucker. Hot coronae around early-type galaxies. apj, 293:102–119, jun 1985.

[182] Patrick J. Fox, Joachim Kopp, Mariangela Lisanti, and Neal Weiner. A cogent modulation analysis. Phys. Rev. D, 85:036008, Feb 2012.

[183] Mads T. Frandsen, Ulrich Haisch, and et. al. Loop-induced dark matter direct detection signals from gamma-ray lines. ArXiv, 2012. arXiv:1207.3971v1.

[184] *Mads T. Frandsen, Felix Kahlhoefer, and et. al. On the dama and cogent modulations.* Phys. Rev. D*, 84:041301, Aug 2011.*

[185] *A. Fruchter. Strong lensing by abel 2218. Image obtained by NASA using the Hubble space telescope, 2010.*

[186] *F. Gabbiani, E. Gabrielli, A. Masiero, and L. Silvestrini. A complete analysis of fcnc and cp constraints in general susy extensions of the standard model.* Nuclear Physics B*, 477(2):321 – 352, 1996.*

[187] *G. Ganis. Lepsusywg note 04-07.1. http://lepsusy.web.cern.ch/lepsusy, 2004.*

[188] *Raphal Gavazzi, Tommaso Treu, and et. al. The sloan lens acs survey. iv. the mass density profile of early-type galaxies out to 100 effective radii.* The Astrophysical Journal*, 667(1):176, 2007.*

[189] *M. Gell-Mann and et. al.* Supergravity: proceedings of the Supergravity Workshop at Stony Brook, 27-29 September 1979*. North-Holland Pub. Co., p. 315, 1979. P. van Nieuwenhuizen and D. Z. Freedman.*

[190] *C. Ghag.* Simulation, Calibration & Exploitation of the DRIFT-II Directional Dark Matter Detector*. PhD thesis, The University of Edinburgh, School of Physics and Astronomy, 2006.*

[191] *C. Ghag, D.Yu. Akimov, H.M. Araùjo, E.J. Barnes, V.A. Belov, A.A. Burenkov, V. Chepel, A. Currie, L. DeViveiros, B. Edwards, V. Francis, A. Hollingsworth, M. Horn, G.E. Kalmus, A.S. Kobyakin, A.G. Kovalenko, V.N. Lebedenko, A. Lindote, M.I. Lopes, R. L?scher, K. Lyons, P. Majewski, A.St J. Murphy, F. Neves, S.M. Paling, J. Pinto da Cunha, R. Preece, J.J. Quenby, L. Reichhart, P.R. Scovell, C. Silva, V.N. Solovov, N.J.T. Smith, P.F. Smith, V.N. Stekhanov, T.J. Sumner, C. Thorne, and R.J. Walker. Performance of the veto detector incorporated into the zeplin-iii experiment.* Astroparticle Physics*, 35(2):76 – 86, 2011.*

[192] *G. W. Gibbons, S. W. Hawking, and S. T. C. Siklos.* The Very Early Universe: Proceedings Of The Nuffield Workshop, Cambridge 21 June To 9 July, 1982*. Cambridge University Press, 1985. ISBN-10: 0521316774.*

[193] *G. Gilmore, D. Zucker, and et. al. What Is a Galaxy? How Cold Is Cold Dark Matter? Recent Progress in Near Field Cosmology. In* Panoramic Views of Galaxy Formation and Evolution*, volume 399 of* Astronomical Society of the Pacific Conference Series*, page 453, oct 2008.*

[194] *Mark W. Goodman and Edward Witten. Detectability of certain dark-matter candidates.* Phys. Rev. D*, 31:3059–3063, Jun 1985.*

[195] *O. W. Greenberg. CPT Violation Implies Violation of Lorentz Invariance.* Physical Review Letters*, 89(23):231602, November 2002.*

[196] *E. M. Gushchin, A. A. Kruqlov, and et. al. Electron emission from condensed noble gases.* JEPT*, 1979. Russian original in ZhETF, vol. 76, no. 5, p. 1685.*

[197] *Alan H. Guth. Inflationary universe: A possible solution to the horizon and flatness problems.* Phys. Rev. D*, 23:347–356, Jan 1981.*

[198] *Jacek Guzik and Uroš Seljak. Virial masses of galactic haloes from galaxygalaxy lensing: theoretical modelling and application to sloan digital sky survey data.* Monthly Notices of the Royal Astronomical Society*, 335(2):311–324, 2002.*

[199] *C. Hagmann and H. Murayama amd et. al. http://pdg.web.cern.ch/pdg/2011/reviews/rpp2011-rev-axions.pdf. CERN particle data group website, 2012.*

[200] *C. Hagmann, P. Sikivie, N. S. Sullivan, and D. B. Tanner. Results from a search for cosmic axions.* Phys. Rev. D*, 42:1297–1300, Aug 1990.*

[201] *Brad M. S. Hansen, James Brewer, and et. al. The white dwarf cooling sequence of the globular cluster messier 4.* The Astrophysical Journal Letters*, 574(2):L155, 2002.*

[202] *M. Haraǹczyk, C. Amsler, and et. al. The ardm experiment.* Acta Phys. Polon. B*, 41:1441–1446, 2010.*

[203] *Fiona Harrison, Finn Christensen, and et. al. Development of the heft and nustar focusing telescopes.* Experimental Astronomy*, 20:131–137, 2005. 10.1007/s10686-006-9072-z.*

[204] *A. Hashizume. Nuclear data sheets 112, 1647. National Nuclear Data Center, Brookhaven National Laboratory, 2011.*

[205] *A. Heavens. General relativity course notes, 2008. The University of Edinburgh.*

[206] *FriedrichW. Hehl and G.David Kerlick. Metric-affine variational principles in general relativity. i. riemannian space-time.* General Relativity and Gravitation*, 9:691–710, 1978.*

[207] *A. Heister and ALEPH Collaboration. Search for stable hadronizing squarks and gluinos in e+e- collisions up to sqrts=209 gev.* The European Physical Journal C - Particles and Fields*, 31:327–342, 2003. 10.1140/epjc/s2003-01376-0.*

[208] *Richard H. Helm. Inelastic and elastic scattering of 187-mev electrons from selected even-even nuclei.* Phys. Rev.*, 104:1466–1475, Dec 1956.*

[209] *P.W. Higgs. Broken symmetries, massless particles and gauge fields.* Physics Letters*, 12(2):132 – 133, 1964.*

[210] *H. Hildebrandt, T. Erben, and et. al. Cfhtlens: Improving the quality of photometric redshifts with precision photometry.* submitted to MNRAS*, 2011.*

[211] G. Hinshaw, J. L. Weiland, and et. al. *Five-year wilkinson microwave anisotropy probe observations: Data processing, sky maps, and basic results.* The Astrophysical Journal Supplement Series, *180(2):225, 2009.*

[212] A. Hitachi. *Properties of liquid xenon scintillation for dark matter searches.* Astroparticle Physics, *24(3):247 – 256, 2005.*

[213] A. Hitachi, T. Doke, and A. Mozumder. *Luminescence quenching in liquid argon under charged-particle impact: Relative scintillation yield at different linear energy transfers.* Phys. Rev. B, *46:11463–11470, Nov 1992.*

[214] Akira Hitachi, Tan Takahashi, Nobutaka Funayama, Kimiaki Masuda, Jun Kikuchi, and Tadayoshi Doke. *Effect of ionization density on the time dependence of luminescence from liquid argon and xenon.* Phys. Rev. B, *27:5279–5285, May 1983.*

[215] Henk Hoekstra, H. K. C. Yee, and Michael D. Gladders. *Properties of galaxy dark matter halos from weak lensing.* The Astrophysical Journal, *606(1):67, 2004.*

[216] W. Hofmann, M. Martnez, and et. al. *Design concepts for the cherenkov telescope array cta: an advanced facility for ground-based high-energy gamma-ray astronomy.* Experimental Astronomy, *32:193–316, 2011. 10.1007/s10686-011-9247-0.*

[217] G.'t Hooft. *Magnetic monopoles in unified gauge theories.* Nuclear Physics B, *79(2):276 – 284, 1974.*

[218] Dan Hooper and Edward A. Baltz. *Strategies for Determining the Nature of Dark Matter.* ANNUAL REVIEW OF NUCLEAR AND PARTICLE SCIENCE, *58:293–314, 2008.*

[219] Dan Hooper and Chris Kelso. *Implications of cogent's new results for dark matter.* Phys. Rev. D, *84:083001, Oct 2011.*

[220] M. Horn, V.A. Belov, D.Yu. Akimov, H.M. Araùjo, E.J. Barnes, A.A. Burenkov, V. Chepel, A. Currie, B. Edwards, C. Ghag, A. Hollingsworth, G.E. Kalmus, A.S. Kobyakin, A.G. Kovalenko, V.N. Lebedenko, A. Lindote, M.I. Lopes, R. L?scher, P. Majewski, A.StJ. Murphy, F. Neves, S.M. Paling, J. Pinto da Cunha, R. Preece, J.J. Quenby, L. Reichhart, P.R. Scovell, C. Silva, V.N. Solovov, N.J.T. Smith, P.F. Smith, V.N. Stekhanov, T.J. Sumner, C. Thorne, L. de Viveiros, and R.J. Walker. *Nuclear recoil scintillation and ionisation yields in liquid xenon from zeplin-iii data.* Physics Letters B, *705(5):471 – 476, 2011.*

[221] J. Hoskins, J. Hwang, and et. al. *Search for nonvirialized axionic dark matter.* Phys. Rev. D, *84:121302, Dec 2011.*

[222] Wayne Hu and Martin White. *Acoustic signatures in the cosmic microwave background.* The Astrophysical Journal, *471(1):30, 1996.*

[223] *J.H. Hubbell. Photon mass attenuation and energy-absorption coefficients.* The International Journal of Applied Radiation and Isotopes, *33(11):1269 – 1290, 1982. Graph obtained from the NIST XCOM database.*

[224] *E. Hubble. A Relation between Distance and Radial Velocity among Extra-Galactic Nebulae.* Proceedings of the National Academy of Science, *15:168–173, March 1929.*

[225] *Francesco Iachello, Lawrence M Krauss, and Giuseppe Maino. Spin-dependent scattering of weakly interacting massive particles in heavy nuclei.* Physics Letters B, *254(1-2):220 – 224, 1991.*

[226] *et al. J. Gavrilyuk. Proc. first int. workshop on nonaccelerator new physics (nanp 97). In* Physics of Atomic Nuclei, *1997.*

[227] *P. S. Wesson J. M. Overduin.* Dark Sky, Dark Matter. *Taylor & Francis, 2002.*

[228] *Ted Jacobson and David Mattingly. Gravity with a dynamical preferred frame.* Phys. Rev. D, *64:024028, Jun 2001.*

[229] *A. Jaffe. Cosmology lecture notes. Imperial college, 2012.*

[230] *T. R. Jaffe, A. J. Banday, and et. al. Evidence of vorticity and shear at large angular scales in the wmap data: A violation of cosmological isotropy?* The Astrophysical Journal Letters, *629(1):L1, 2005.*

[231] *N. Jarosik, C. L. Bennett, and et. al. Seven-year wilkinson microwave anisotropy probe (wmap) observations: Sky maps, systematic errors, and basic results.* The Astrophysical Journal Supplement Series, *192(2):14, 2011.*

[232] *Gerard Jungman, Marc Kamionkowski, and Kim Griest. Supersymmetric dark matter.* Physics Reports, *267(56):195 – 373, 1996.*

[233] *T. Kaluza. Zum unitatsproblem in der physik.* Sitzungsber. Preuss Akad. Wiss. Berlin. (Math. Phys.), *1921.*

[234] *M. Kamionkowski. Possible relics from new physics in the early universe: Inflation, the cosmic microwave background, and particle dark matter.* arXiv:astro-ph/9809214v1, *1998.*

[235] *Marc Kamionkowski, Lawrence M. Krauss, and M. Ted Ressell. Implications of recent nucleon spin structure measurements for neutralino dark matter detection.* ArXiv, *1994.*

[236] *G. L. Kane, Chris Kolda, Leszek Roszkowski, and James D. Wells. Study of constrained minimal supersymmetry.* Phys. Rev. D, *49:6173–6210, Jun 1994.*

[237] *G. Karagiorgi, Z. Djurcic, and et. al. Viability of* $\delta m^2 \sim 1$ ev^2 *sterile neutrino mixing models in light of miniboone electron neutrino and antineutrino data from the booster and numi beamlines.* Phys. Rev. D, *80:073001, Oct 2009.*

[238] *Lilian Kaufmann and Andr Rubbia. The ardm project: a dark matter direct detection experiment based on liquid argon.* Journal of Physics: Conference Series, *60(1):264, 2007.*

[239] *V. Khachatryan and et. al. Search for supersymmetry in pp collisions at 7 tev in events with jets and missing transverse energy.* Physics Letters B, *698(3):196 – 218, 2011.*

[240] *S K Kim, H J Kim, and Y D Kim. Scintillator-based detectors for dark matter searches i.* New Journal of Physics, *12(7):075003, 2010.*

[241] *S K Kim and the KIMS Collaboration. New results from the kims experiment.* Journal of Physics: Conference Series, *120(4):042021, 2008.*

[242] *H.V. Klapdor-Kleingrothaus, L. Baudis, and et. al. Genius-tf: a test facility for the genius project.* Nuclear Instruments and Methods in Physics Research Section A: Accelerators, Spectrometers, Detectors and Associated Equipment, *481(13):149 – 159, 2002.*

[243] *Oskar Klein. Quantentheorie und fnfdimensionale relativittstheorie.* Zeitschrift fr Physik A Hadrons and Nuclei, *37:895–906, 1926.*

[244] *M. Kleinheinrich, P. Schneider, and et. al. Weak lensing measurements of dark matter halos of galaxies from combo-17.* ArXiv Astrophysics e-prints, *dec 2004.*

[245] *E. Komatsu, K. M. Smith, and et. al. Seven-year wilkinson microwave anisotropy probe (wmap) observations: Cosmological interpretation.* The Astrophysical Journal Supplement Series, *192(2):18, 2011.*

[246] *L. V. E. Koopmans and T. Treu. The structure and dynamics of luminous and dark matter in the early-type lens galaxy of 0047-281 at z = 0.485.* apj, *583:606–615, feb 2003.*

[247] *Joachim Kopp, Thomas Schwetz, and Jure Zupan. Global interpretation of direct dark matter searches after cdms-ii results.* Journal of Cosmology and Astroparticle Physics, *2010(02):014, 2010.*

[248] *P. M. Korngut, S. R. Dicker, and et. al. Mustang high angular resolution sunyaev-zel'dovich effect imaging of substructure in four galaxy clusters.* apj, *734:10, June 2011.*

[249] *H. Kraus, M. Bauer, and et. al. Eureca the european future of dark matter searches with cryogenic detectors.* Nuclear Physics B - Proceedings Supplements, *173(0):168 – 171, 2007. Proceedings of the 7th UCLA Symposium on Sources and Detection of Dark Matter and Dark Energy in the Universe.*

[250] *Jeffrey M. Kubo, Albert Stebbins, and et. al. The mass of the coma cluster from weak lensing in the sloan digital sky survey.* The Astrophysical Journal, *671(2):1466, 2007.*

[251] S Kubota, M Hishida, and J Raun. *Evidence for a triplet state of the self-trapped exciton states in liquid argon, krypton and xenon.* Journal of Physics C: Solid State Physics, *11(12):2645, 1978.*

[252] Tomislav Kundic, Edwin L. Turner, and et. al. *A robust determination of the time delay in 0957+561a, b and a measurement of the global value of hubble's constant.* The Astrophysical Journal, *482(1):75, 1997.*

[253] A. Leauthaud, J. Tinker, and et. al. *New constraints on the evolution of the stellar-to-dark matter connection: A combined analysis of galaxy-galaxy lensing, clustering, and stellar mass functions from z = 0.2 to z =1.* Apj, *744:159, 2012.*

[254] V. N. Lebedenko, H. M. Araújo, E. J. Barnes, A. Bewick, R. Cashmore, V. Chepel, A. Currie, D. Davidge, J. Dawson, T. Durkin, B. Edwards, C. Ghag, M. Horn, A. S. Howard, A. J. Hughes, W. G. Jones, M. Joshi, G. E. Kalmus, A. G. Kovalenko, A. Lindote, I. Liubarsky, M. I. Lopes, R. Lüscher, P. Majewski, A. St. J. Murphy, F. Neves, J. Pinto da Cunha, R. Preece, J. J. Quenby, P. R. Scovell, C. Silva, V. N. Solovov, N. J. T. Smith, P. F. Smith, V. N. Stekhanov, T. J. Sumner, C. Thorne, and R. J. Walker. *Results from the first science run of the zeplin-iii dark matter search experiment.* Phys. Rev. D, *80:052010, Sep 2009.*

[255] Dae-Gyu Lee, R. N. Mohapatra, and et. al. *Predictions for the proton lifetime in minimal nonsupersymmetric so(10) models: An update.* Phys. Rev. D, *51:229–235, Jan 1995.*

[256] J.D. Lewin and P.F. Smith. *Review of mathematics, numerical factors, and corrections for dark matter experiments based on elastic nuclear recoil.* Astroparticle Physics, *6(1):87 – 112, 1996.*

[257] Tongyan Lin and Douglas P. Finkbeiner. *Magnetic inelastic dark matter: Directional signals without a directional detector.* Phys. Rev. D, *83:083510, Apr 2011.*

[258] Andrei Linde. *Inflationary cosmology. In Martin Lemoine, Jerome Martin, and Patrick Peter, editors,* Inflationary Cosmology, *volume 738 of* Lecture Notes in Physics, *pages 1–54. Springer Berlin / Heidelberg, 2007.*

[259] J. Lindhard, V. Nielsen, M. Sharff, and P. V. Thomsen. *Integral equations governing radiation effects.* Mat. Fys. Medd. Dan. Vid. Selsk., *33, 1963.*

[260] A. Lindote, H.M. Araùjo, J. Pinto da Cunha, D.Yu. Akimov, V. Chepel, D. Davidge, J.V. Dawson, M. Joshi, V.N. Lebedenko, I. Liubarsky, M.I. Lopes, F. Neves, J.J. Quenby, C. Silva, V. Solovov, T.J. Sumner, C. Thorne, and R.J. Walker. *Preliminary results on position reconstruction for zeplin iii.* Nuclear Instruments and Methods in Physics Research Section A: Accelerators, Spectrometers, Detectors and Associated Equipment, *573(1-2):200 – 203, 2007.*

[261] *A. Lindote, H.M. Araùo, V.A. Kudryavtsev, and M. Robinson. Simulation of neutrons produced by high-energy muons underground.* Astroparticle Physics, *31(5):366 – 375, 2009.*

[262] *A. M. F. Lindote.* Dark matter searches using the ZEPLIN detectors. *PhD thesis, Universidade de Coimbra, 2008.*

[263] *Michael Loewenstein and Alexander Kusenko. Dark matter search using chandra observations of willman 1 and a spectral feature consistent with a decay line of a 5 kev sterile neutrino.* The Astrophysical Journal, *714(1):652, 2010.*

[264] *M. Longair.* QJRAS, *34:157, 1993.*

[265] *M. Lueker, C. L. Reichardt, and et. al. Measurements of secondary cosmic microwave background anisotropies with the south pole telescope.* The Astrophysical Journal, *719(2):1045, 2010.*

[266] *Roy Maartens. Brane-world gravity.* Living Reviews in Relativity, *7(7), 2004.*

[267] *Rachel Mandelbaum, Uroš Seljak, and et. al. Galaxy halo masses and satellite fractions from galaxygalaxy lensing in the sloan digital sky survey: stellar mass, luminosity, morphology and environment dependencies.* Monthly Notices of the Royal Astronomical Society, *368(2):715–731, 2006.*

[268] *D. P. Mann, W. W. Watson, and et. al. Total neutron cross section of xenon and krypton.* Phys. Rev., *116:1516–1520, Dec 1959.*

[269] *A. Manzur, A. Curioni, and et. al. Scintillation efficiency and ionization yield of liquid xenon for monoenergetic nuclear recoils down to 4 kev.* Phys. Rev. C, *81:025808, Feb 2010.*

[270] *R. Massey. Cosmos. 3D dark matter map using COSMOS survey data, 2007.*

[271] *R. Massey, J. Rhodes, and et. al. COSMOS: Three-dimensional Weak Lensing and the Growth of Structure.* Apjs, *172:239–253, sep 2007.*

[272] *Richard Massey, Thomas Kitching, and Johan Richard. The dark matter of gravitational lensing.* Reports on Progress in Physics, *73(8):086901, 2010.*

[273] *Eduard Massó, Francesc Rota, and Gabriel Zsembinszki. Axion thermalization in the early universe.* Phys. Rev. D, *66:023004, Jul 2002.*

[274] *K. Matchev. Lecture notes on susy and cosmology. SLAC, Stanford, 2004.*

[275] *D N McKinsey, D Akerib, and et. al. The lux dark matter search.* Journal of Physics: Conference Series, *203(1):012026, 2010.*

[276] *A. McWilliam and M. Rauch.* Origin and Evolution of the Elements, *volume 4. Cambridge University Press, 2010. http://arxiv.org/abs/astro-ph/0310557.*

[277] *P. Mészáros. The behaviour of point masses in an expanding cosmological substratum.* aap, *37:225–228, December 1974.*

[278] *M. Milgrom. A modification of the newtonian dynamics as a possible alternative to the hidden mass hypothesis.* The Astrophysical Journal*, 270:365–370, jul 1983.*

[279] *Peter Minkowski. mu to e gamma at a rate of one out of 109 muon decays?* Physics Letters B*, 67(4):421 – 428, 1977.*

[280] *Kentaro Miuchi, Hironobu Nishimura, and et. al. First underground results with newage-0.3a direction-sensitive dark matter detector.* Physics Letters B*, 686(1):11 – 17, 2010.*

[281] *A. Munter. www.ncnr.nist.gov/resources/sldcalc.html. NIST resources website, 2012.*

[282] *Tech. Rep. N887. Cern technical report. National Physics Laboratory (UK), 2009.*

[283] *K Nakamura and Particle Data Group. Review of particle physics.* Journal of Physics G: Nuclear and Particle Physics*, 37(7A):075021, 2010.*

[284] *NASA. Wmap website. http://map.gsfc.nasa.gov/.*

[285] *Aravind Natarajan, Christopher Savage, and Katherine Freese. Probing dark matter streams with cogent.* Phys. Rev. D*, 84:103005, Nov 2011.*

[286] *F Neves, D Yu Akimov, H M Araùjo, E J Barnes, V A Belov, A A Burenkov, V Chepel, A Currie, L DeViveiros, B Edwards, C Ghag, A Hollingsworth, M Horn, G E Kalmus, A S Kobyakin, A G Kovalenko, V N Lebedenko, A Lindote, M I Lopes, R L?scher, P Majewski, A StJ Murphy, S M Paling, J Pinto da Cunha, R Preece, J J Quenby, L Reichhart, S Rodrigues, P R Scovell, C Silva, V N Solovov, N J T Smith, P F Smith, V N Stekhanov, T J Sumner, C Thorne, and R J Walker. Ze3ra: the zeplin-iii reduction and analysis package.* Journal of Instrumentation*, 6(11):P11004, 2011.*

[287] *F. Neves, V. Chepel, D.Yu. Akimov, H.M. Arajo, E.J. Barnes, V.A. Belov, A.A. Burenkov, A. Currie, B. Edwards, C. Ghag, M. Horn, A.J. Hughes, G.E. Kalmus, A.S. Kobyakin, A.G. Kovalenko, V.N. Lebedenko, A. Lindote, M.I. Lopes, R. L?scher, K. Lyons, P. Majewski, A.St.J. Murphy, J. Pinto da Cunha, R. Preece, J.J. Quenby, P.R. Scovell, C. Silva, V.N. Solovov, N.J.T. Smith, P.F. Smith, V.N. Stekhanov, T.J. Sumner, C. Thorne, and R.J. Walker. Calibration of photomultiplier arrays.* Astroparticle Physics*, 33(1):13 – 18, 2010.*

[288] *H. Nishino, S. Clark, and et. al. Search for proton decay via* $p \to e^+\pi^0$ *and* $p \to \mu^+\pi^0$ *in a large water cherenkov detector.* Phys. Rev. Lett.*, 102:141801, Apr 2009.*

[289] *Keith A. Olive and Evan D. Skillman. A realistic determination of the error on the primordial helium abundance: Steps toward nonparametric nebular helium abundances.* The Astrophysical Journal*, 617(1):29, 2004.*

[290] *Jonathan O'Neil, Richard W. Carlson, and et. al. Neodymium-142 evidence for hadean mafic crust.* Science, *321(5897):1828–1831, 2008.*

[291] *L. Onsager. Initial recombination of ions.* Phys. Rev., *54:554–557, Oct 1938.*

[292] *E. O'Sullivan and T. J. Ponman. The isolated elliptical ngc 4555 observed with chandra.* Monthly Notices of the Royal Astronomical Society, *354(3):935–944, 2004.*

[293] *P. Schneider and X. Er. Weak lensing goes bananas: what flexion really measures.* A&A, *485(2):363–376, 2008.*

[294] *Palash B. Pal and Lincoln Wolfenstein. Radiative decays of massive neutrinos.* Phys. Rev. D, *25:766–773, Feb 1982.*

[295] *J. A. Peacock.* Cosmological Physics. *Cambridge University Press, 2003.*

[296] *R. D. Peccei and Helen R. Quinn. Constraints imposed by cp conservation in the presence of pseudoparticles.* Phys. Rev. D, *16:1791–1797, Sep 1977.*

[297] *A. A. Penzias and R. W. Wilson. A measurement of excess antenna temperature at 4080 mc/s.* apj, *142:419–421, July 1965.*

[298] *D. H. Perkins.* Particle Astrophysics. *Oxford University Press, 2009.*

[299] *Max Pettini, Berkeley J. Zych, and et. al. Deuterium abundance in the most metal-poor damped lyman alpha system: converging on b,0h2.* Monthly Notices of the Royal Astronomical Society, *391(4):1499–1510, 2008.*

[300] *P. Picozza, R. Sparvoli, and the "PAMELA collaboration". Understanding cosmic rays and searching for exotic sources with pamela.* Astrophysics and Space Sciences Transactions, *7(2):85–91, 2011.*

[301] *Lidia Pieri, Julien Lavalle, Gianfranco Bertone, and Enzo Branchini. Implications of high-resolution simulations on indirect dark matter searches.* Phys. Rev. D, *83:023518, Jan 2011.*

[302] *G. Plante, E. Aprile, and et. al. New measurement of the scintillation efficiency of low-energy nuclear recoils in liquid xenon.* Phys. Rev. C, *84:045805, Oct 2011.*

[303] *M. Postman. Cluster lensing and supernova survey with hubble (clash): An overview.* arXiv:1106.3328v2 [astro-ph.CO], *2011.*

[304] *G. W. Pratt and M. Arnaud. The mass profile of a1413 observed with xmm-newton: Implications for the m-t relation.* A&A, *394(2):375–393, 2002.*

[305] *C. Quigg. arxiv:hep-ph/0404228v1. ArXiv, 2004.*

[306] *Katherine Rawlinsfor, A. Achterberg, and et. al. Icecube: A multipurpose neutrino telescope.* Journal of the Physical Society of Japan, *77SB(Supplement B):71–75, 2008.*

[307] *E. D. Reese. Measuring the hubble constant with the sunyaev-zel'dovich effect.* ArXiv:0306073, *2003.*

[308] *C. L. Reichardt, P. A. R. Ade, and et. al. High-resolution cmb power spectrum from the complete acbar data set.* The Astrophysical Journal, *694(2):1200, 2009.*

[309] *L. Reichhart, D.Yu. Akimov, H. M. Araújo, E. J. Barnes, V. A. Belov, A. A. Burenkov, V. Chepel, A. Currie, L. DeViveiros, B. Edwards, V. Francis, C. Ghag, A. Hollingsworth, M. Horn, G. E. Kalmus, A. S. Kobyakin, A. G. Kovalenko, V. N. Lebedenko, A. Lindote, M. I. Lopes, R. Lüscher, P. Majewski, A.St J. Murphy, F. Neves, S. M. Paling, J. Pinto da Cunha, R. Preece, J. J. Quenby, P. R. Scovell, C. Silva, V. N. Solovov, N. J. T. Smith, P. F. Smith, V. N. Stekhanov, T. J. Sumner, C. Thorne, and R. J. Walker. Quenching factor for low-energy nuclear recoils in a plastic scintillator.* Phys. Rev. C, *85:065801, Jun 2012.*

[310] *B. Reindl, G. A. Tammann, A. Sandage, and A. Saha. Reddening, absorption, and decline rate corrections for a complete sample of type ia supernovae leading to a fully corrected hubble diagram to $v < 30{,}000$ km s1.* The Astrophysical Journal, *624(2):532, 2005.*

[311] *R. Reyes, R. Mandelbaum, U. Seljak, and et. al. Confirmation of general relativity on large scales from weak lensing and galaxy velocities.* Nature, *464, 2010.*

[312] *Adam G. Riess, Alexei V. Filippenko, and et. al. Observational evidence from supernovae for an accelerating universe and a cosmological constant.* The Astronomical Journal, *116(3):1009, 1998.*

[313] *Adam G. Riess, Lucas Macri, and et. al. A 3% solution: Determination of the hubble constant with the hubble space telescope and wide field camera 3.* The Astrophysical Journal, *730(2):119, 2011.*

[314] *M Robinson, V.A Kudryavtsev, and et. al. Measurements of muon flux at 1070 m vertical depth in the boulby underground laboratory.* Nuclear Instruments and Methods in Physics Research Section A: Accelerators, Spectrometers, Detectors and Associated Equipment, *511(3):347 – 353, 2003.*

[315] *Wolfgang A. Rolke, Angel M. L?pez, and Jan Conrad. Limits and confidence intervals in the presence of nuisance parameters.* Nuclear Instruments and Methods in Physics Research Section A: Accelerators, Spectrometers, Detectors and Associated Equipment, *551(2-3):493 – 503, 2005.*

[316] *Leslie J Rosenberg and Karl A. van Bibber. Searches for invisible axions.* Physics Reports, *325(1):1 – 39, 2000.*

[317] *Nicholas P. Ross, Adam D. Myers, and et. al. The sdss-iii baryon oscillation spectroscopic survey: Quasar target selection for data release nine.* The Astrophysical Journal Supplement Series, *199(1):3, 2012.*

[318] G. Rossmanith, C. Rth, and et. al. *Non-gaussian signatures in the five-year wmap data as identified with isotropic scaling indices.* Monthly Notices of the Royal Astronomical Society, *399(4):1921–1933, 2009.*

[319] Leszek Roszkowski, Roberto Ruiz de Austri, and Roberto Trotta. *Implications for the constrained mssm from a new prediction for b ? s ?* Journal of High Energy Physics, *2007(07):075, 2007.*

[320] V. C. Rubin, W. K. J. Ford, and N. Thonnard. *Rotational properties of 21 sc galaxies with a large range of luminosities and radii, from ngc 4605 r = 4kpc to ugc 2885 r = 122 kpc.* apj, *238:471–487, jun 1980.*

[321] R. K. Sachs and A. M. Wolfe. *Perturbations of a cosmological model and angular variations of the microwave background.* Apj, *147:73, jan 1967.*

[322] Andrei D Sakharov. *Violation of cp in variance, c asymmetry, and baryon asymmetry of the universe.* Soviet Physics Uspekhi, *34(5):392, 1991.*

[323] Y. Sakurai and T. Kobayashi. *Experimental verification of the nuclear data of gadolinium for neutron capture therapy.* Nuclear Science and Technology, *2:1294–1297, 2002.*

[324] M. Salaris, S. Degl'Innocenti, and A. Weiss. *The age of the oldest globular clusters.* The Astrophysical Journal, *479(2):665, 1997.*

[325] E. Santos, B. Edwards, V. Chepel, H. Araùjo, D. Akimov, E. Barnes, V. Belov, A. Burenkov, A. Currie, L. DeViveiros, C. Ghag, A. Hollingsworth, M. Horn, G. Kalmus, A. Kobyakin, A. Kovalenko, V. Lebedenko, A. Lindote, M. Lopes, R. Lscher, P. Majewski, A. St J. Murphy, F. Neves, S. Paling, J. Pinto da Cunha, R. Preece, J. Quenby, L. Reichhart, P. Scovell, C. Silva, V. Solovov, N. Smith, P. Smith, V. Stekhanov, T. Sumner, C. Thorne, and R. Walker. *Single electron emission in two-phase xenon with application to the detection of coherent neutrino-nucleus scattering.* Journal of High Energy Physics, *2011:1–20, 2011. 10.1007/JHEP12(2011)115.*

[326] C. Savage, K. Freese, and et. al. *Compatibility of dama/libra dark matter detection with other searches in light of new galactic rotation velocity measurements.* Journal of Cosmology and Astroparticle Physics, *2009(09):036, 2009.*

[327] P. Scovell. Results from the ZEPLIN-III Dark Matter Search Experiment. *PhD thesis, The University of Edinbugh School of Physics and Astronomy, 2011.*

[328] V. F. Sears. *Neutron scattering lengths and cross-sections.* Neutron News, *3(3), 1992.*

[329] F. Shankar, A. Lapi, and et. al. *New relationships between galaxy properties and host halo mass, and the role of feedbacks in galaxy formation.* The Astrophysical Journal, *643(1):14, 2006.*

[330] *M.A. Shifman, A.I. Vainshtein, and V.I. Zakharov. Can confinement ensure natural cp invariance of strong interactions?* Nuclear Physics B*, 166(3):493 – 506, 1980.*

[331] *H. Sievers. Nuclear data sheets 62, 271. National Nuclear Data Center, Brookhaven National Laboratory, 1991.*

[332] *Kris Sigurdson, Michael Doran, Andriy Kurylov, Robert R. Caldwell, and Marc Kamionkowski. Dark-matter electric and magnetic dipole moments.* Phys. Rev. D*, 70:083501, Oct 2004.*

[333] *Pierre Sikivie. Axion cosmology. In Markus Kuster, Georg Raffelt, and Berta Beltrn, editors,* Axions*, volume 741 of* Lecture Notes in Physics*, pages 19–50. Springer Berlin / Heidelberg, 2008.*

[334] *C. Skordis, D. F. Mota, P. G. Ferreira, and C. Bœhm. Large scale structure in bekenstein's theory of relativistic modified newtonian dynamics.* Phys. Rev. Lett.*, 96:011301, Jan 2006.*

[335] *Y. Sofue, Y. Tutui, and et. al. Central rotation curves of spiral galaxies.* The Astrophysical Journal*, 523(1):136, 1999.*

[336] *V.N. Solovov, V.A. Belov, D.Y. Akimov, H.M. Araùjo, E.J. Barnes, A.A. Burenkov, V. Chepel, A. Currie, L. DeViveiros, B. Edwards, C. Ghag, A. Hollingsworth, M. Horn, G.E. Kalmus, A.S. Kobyakin, A.G. Kovalenko, V.N. Lebedenko, A. Lindote, M.I. Lopes, R. Luscher, P. Majewski, A.S.J. Murphy, F. Neves, S.M. Paling, J. Pinto da Cunha, R. Preece, J.J. Quenby, L. Reichhart, P.R. Scovell, C. Silva, N.J.T. Smith, P.F. Smith, V.N. Stekhanov, T.J. Sumner, C. Thorne, and R.J. Walker. Position reconstruction in a dual phase xenon scintillation detector. In* Nuclear Science Symposium and Medical Imaging Conference (NSS/MIC), 2011 IEEE*, pages 1226 –1233, oct. 2011.*

[337] *V.N Solovov, V Chepel, and et. al. Measurement of the refractive index and attenuation length of liquid xenon for its scintillation light.* Nuclear Instruments and Methods in Physics Research Section A: Accelerators, Spectrometers, Detectors and Associated Equipment*, 516(2-3):462 – 474, 2004.*

[338] *Yong-Seon Song, Gong-Bo Zhao, and et.al. Complementarity of weak lensing and peculiar velocity measurements in testing general relativity.* Current*, 1:8, 2010.*

[339] *P. Sorensen.* A Position Sensitive Liquid Xenon Time-Projection Chamber for Direct Detection of Dark Matter*. PhD thesis, Brown University Astrophysics group, 2008.*

[340] *P. Sorensen, A. Manzur, and et. al. The scintillation and ionization yield of liquid xenon for nuclear recoils.* Nuclear Instruments and Methods in Physics Research Section A: Accelerators, Spectrometers, Detectors and Associated Equipment*, 601(3):339 – 346, 2009.*

[341] *Peter Sorensen and Carl Eric Dahl. Nuclear recoil energy scale in liquid xenon with application to the direct detection of dark matter.* Phys. Rev. D*, 83:063501, Mar 2011.*

[342] *P. Sorenson, E. Aprile, J. Angle, and et. al. Lowering the low-energy threshold of xenon detectors. In* Proceedings of Science, PoS(IDM2010)017*, 2010. arXiv:1011.6439.*

[343] *Thomas P. Sotiriou and Valerio Faraoni. $f(r)$ theories of gravity.* Rev. Mod. Phys.*, 82:451–497, Mar 2010.*

[344] *Thomas P Sotiriou and Stefano Liberati. The metric-affine formalism of f (r) gravity.* Journal of Physics: Conference Series*, 68(1):012022, 2007.*

[345] *Thomas P. Sotiriou and Stefano Liberati. Metric-affine f(r) theories of gravity.* Annals of Physics*, 322(4):935 – 966, 2007.*

[346] *D. N. Spergel, R. Bean, and et. al. Three-year wilkinson microwave anisotropy probe (wmap) observations: Implications for cosmology.* The Astrophysical Journal Supplement Series*, 170(2):377, 2007.*

[347] *D. N. Spergel, L. Verde, and et. al. First-year wilkinson microwave anisotropy probe (wmap) observations: Determination of cosmological parameters.* The Astrophysical Journal Supplement Series*, 148(1):175, 2003.*

[348] *Volker et. al. Springel. Simulating the joint evolution of quasars, galaxies and their large-scale distribution.* Nature*, 435:629–636, 2005.*

[349] *Z. Staniszewski, P. A. R. Ade, and et. al. Galaxy clusters discovered with a sunyaev-zel'dovich effect survey.* The Astrophysical Journal*, 701(1):32, 2009.*

[350] *M. Steinmetz and J. F. Navarro. The hierarchical origin of galaxy morphologies.* New Astronomy*, 7(4):155 – 160, 2002.*

[351] *K. S. Stelle. Renormalization of higher-derivative quantum gravity.* Phys. Rev. D*, 16:953–969, Aug 1977.*

[352] *L. Stodolsky and et. al. The cresst ii dark matter search.* ArXiv*, 2012. arXiv:1203.6835v1.*

[353] *C. Strege, G. Bertone, and et. al. Updated global fits of the cmssm including the latest lhc susy and higgs searches and xenon100 data.* Journal of Cosmology and Astroparticle Physics*, 2012(03):030, 2012.*

[354] *N. Strobel. Astronomy notes. Astronomy notes website: http://www.astronomynotes.com, 2010.*

[355] *T.J. Sumner. The zeplin iii dark matter project.* New Astronomy Reviews*, 49(2-6):277 – 281, 2005.*

[356] *R. A. Sunyaev and Y. B. Zeldovich. Small-scale fluctuations of relic radiation.* apss*, 7:3–19, April 1970.*

[357] *A. S. Szalay and G Marx. Neutrino rest mass from cosmology.* Astro-particle Physics*, 49:437–441, June 1976.*

[358] *T. Takahashi, S. Konno, and et. al. Average energy expended per ion pair in liquid xenon.* Phys. Rev. A*, 12:1771–1775, Nov 1975.*

[359] *J. Tauber. Plank results papers. http://www.sciops.esa.int/index.php, 2011.*

[360] *A. Taylor. Cosmology course notes, 2008. The University of Edinburgh.*

[361] *James E. Taylor, Richard J. Massey, and et. al. Measuring the geometry of the universe from weak gravitational lensing behind galaxy groups in the hst cosmos survey.* The Astrophysical Journal*, 749(2):127, 2012.*

[362] *R. Taylor and D. Munro.* Veto PMT base schematics*. The University of Edinburgh electronics workshop, 2008.*

[363] *Max Tegmark, Michael A. Strauss, and et. al. Cosmological parameters from sdss and wmap.* Phys. Rev. D*, 69:103501, May 2004.*

[364] *Y. Tendow. Nuclear data sheets 77, 631. National Nuclear Data Center, Brookhaven National Laboratory, 1996.*

[365] *the ATLAS collaboration. Observation of an excess of events in the search for the standard model higgs boson with the atlas detector at the lhc. ATLAS Note: ATLAS-CONF-2012-093, 2012.*

[366] *the CMS Experiment. Observation of a new particle with a mass of 125 gev. http://cms.web.cern.ch/news/observation-new-particle-mass-125-gev, 2012.*

[367] *P. Tisserand, L. Le Guillou, and The EROS-2 collaboration. Limits on the macho content of the galactic halo from the eros-2 survey of the magellanic clouds.* A&A*, 469(2):387–404, 2007.*

[368] *P. Toivanen, M. Kortelainen, and et. al. Dark-matter detection by elastic and inelastic lsp scattering on 129xe and 131xe.* Physics Letters B*, 666(1):1 – 4, 2008.*

[369] *Tosaka. http://en.wikipedia.org/wiki/uranium_series. wikipedia, 2008.*

[370] *Mark Trodden. Electroweak baryogenesis.* Rev. Mod. Phys.*, 71:1463–1500, Oct 1999.*

[371] *Roberto Trotta, Farhan Feroz, and et. al. The impact of priors and observables on parameter inferences in the constrained mssm.* Journal of High Energy Physics*, 2008(12):024, 2008.*

[372] *M.S. Turner. The case for lambdacdm.* ArXiv Astrophysics e-prints*, 1997.*

[373] *Ryoyu Utiyama and Bryce S. DeWitt. Renormalization of a classical gravitational field interacting with quantized matter fields.* Journal of Mathematical Physics, *3(4):608–618, 1962.*

[374] *A. Vale and J. P. Ostriker. Linking halo mass to galaxy luminosity.* Monthly Notices of the Royal Astronomical Society, *353(1):189–200, 2004.*

[375] *F. Della Valle, G. Di Domenico, and et. al. Towards a direct measurement of vacuum magnetic birefringence: Pvlas achievements.* Optics Communications, *283(21):4194 – 4198, 2010.*

[376] *K. Van Bibber, N. R. Dagdeviren, and et. al. Proposed experiment to produce and detect light pseudoscalars.* Phys. Rev. Lett., *59:759–762, Aug 1987.*

[377] *K. van Bibber and L. J. Rosenberg. Ultrasensitive searches for the axion.* Physics Today, *2006.*

[378] *F. J. Vaughn, W. L. Imhof, R. G. Johnson, and M. Walt. Total neutron cross sections of helium, neon, argon, krypton, and xenon.* Phys. Rev., *118:683–686, May 1960.*

[379] *M. Wagner, T. Pitchard, and E. Shaghoulian. Berkley lensing group. Smoot lensing subgroup, Berkeley Lab, 2007.*

[380] *Shinya Wanajo, Naoki Itoh, and et. al. The r-process in the neutrino winds of core-collapse supernovae and u-th cosmochronology.* The Astrophysical Journal, *577(2):853, 2002.*

[381] *Anne-Marie Weijmans, Davor Krajnovic, and et. al. The shape of the dark matter halo in the early-type galaxy ngc 2974.* Monthly Notices of the Royal Astronomical Society, *383(4):1343–1358, 2008.*

[382] *Neal Weiner and Itay Yavin. How Dark Are Majorana WIMPs? Signals from MiDM and Rayleigh Dark Matter. 2012.*

[383] *D. A Weintraub.* How old is the Universe. *Princeton university press, 2010.*

[384] *C. Weniger. A tentative gamma-ray line from dark matter annihilation at the fermi large area telescope.* ArXiv, *2012. arXiv:1204.2797v1.*

[385] *B. C. Whitmore, D. B. McElroy, and F Schweizer. The shape of the dark halo in polar-ring galaxies.* apj, *314:439–456, March 1987.*

[386] *M. Wood, G. Blaylock, and et. al. A search for dark matter annihilation with the whipple 10 m telescope.* The Astrophysical Journal, *678(2):594, 2008.*

[387] *W-M Yao and et.al. Review of particle physics.* Journal of Physics G: Nuclear and Particle Physics, *33(1):1, 2006.*

[388] *A. Rodinov YU. Khazov, I. Mitropolsky. Nuclear data sheets 107, 2715. National Nuclear Data Center, Brookhaven National Laboratory, 2006.*

[389] J. A. Tyson et. al. Z. Lvezic. Lsst: from science drivers to reference design and anticipated data products. arXiv:0805.2366v2 [astro-ph]*, 2011.*

[390] F. Zwicky. Die rotverschiebung von extragalaktischen nebeln. Helvetica Physica Acta*, 6:110–127, 1933.*

[391] F. Zwicky. Nebulae as gravitational lenses. Phys. Rev.*, 51:290–290, Feb 1937.*

Publications

WIMP-nucleon cross-section results from the second science run of ZEPLIN-III.
Published in Physics Letters B in 2012, volume 709, number 1-2, pages 14 to 20.

Radioactivity backgrounds in ZEPLIN-III.
Published in Astroparticle Physics in 2012, volume 35, number 8, pages 495 to 502.

Quenching factor for low-energy nuclear recoils in a plastic scintillator.
Published in Phys. Rev. C in 2012, issue 6, article 065801.

Performance data from the ZEPLIN-III second science run.
Published in the Journal of Instrumentation in 2012, volume 7, number 3, article C03044.

Nuclear recoil scintillation and ionisation yields in liquid xenon from ZEPLIN-III data.
Published in Physics Letters B in 2011, volume 705, number 5, pages 471 to 476.

Performance of the veto detector incorporated into the ZEPLIN-III experiment.
Published in Astroparticle Physics in 2011, volume 35, number 2, pages 76 to 86.

Single electron emission in two-phase xenon with application to the detection of coherent neutrino-nucleus scattering.
Published in the Journal of High Energy Physics in 2011, issue 12, pages 1 to 20.

Position reconstruction in a dual phase xenon scintillation detector.

Published in the Nuclear Science Symposium and Medical Imaging Conference proceedings in 2011, pages 1226 to 1233.

ZE3RA: the ZEPLIN-III Reduction and Analysis package.
Published in the Journal of Instrumentation in 2011, volume 6, number 11, article P11004.

Limits on inelastic dark matter from ZEPLIN-III.
Published in Physics Letters B in 2010, volume 692, number 3, pages 180 to 183.

The ZEPLIN-III anti-coincidence veto detector.
Published in Astroparticle Physics in 2010, volume 34, number 3, pages 151 to 163.